

# Electromagnetic Scattering and Filtering in Random Media for Image Sensing

Yasumitsu Miyazaki

Department of Media Informatics, Aichi University of Technology  
50-2 Manori, Nishihasama-cho, Gamagori 443-0047, Japan

**Abstract**— In special session in memory of Prof. J. A. Kong at PIERS 2008, Cambridge, studies on electromagnetic guided waves in irregular waveguides, and scattered field in random media for microwave and millimeter wave technologies and optical technologies are discussed. Further, recent X-rays problems in random biological media are shown. Wave filtering for signal and image processing are also discussed.

## 1. INTRODUCTION

Prof. J. A. Kong investigated electromagnetic characteristics in complex anisotropic and moving media, since 1967. And later, electromagnetic scattering by periodic structures and in random surfaces and media for remote sensing technologies were investigated. After 2000, he studies on electromagnetic wave properties of artificial meta materials and application to antenna problems [1–3].

In 1964, I presented mode conversions and reflections in irregular millimeter waveguides such as tilted and bent waveguides using conformal mapping method with integral equations [4]. Using asymptotic methods, mode conversions and reflections in millimeter waveguide junction between conical and circular waveguides were discussed in 1968. After 1965, I studied guided and scattered waves of optical waveguides with inhomogeneous and random refractive index distributions and random boundary surfaces, and further, investigated asymptotic fields in beam waveguides [5–7]. Mode filtering characteristics in millimeter waveguides and optical waveguides were studied for signal processing of high bit transmissions. Integrated optics with anisotropic crystals for optical modulators and isolators were also discussed using hybrid vector field equations. Optical wave coupling and mode conversions in acousto-optic waveguides with periodic structures induced by surface acoustic waves were also studied [8–10]. Optical scattering of laser beams in random media were shown [12]. Beam scatterings and reflections on curved complex dielectric surfaces were studied by spectral functions. This method could be applied to space-time response analysis of electromagnetic beams for remote sensing. Numerical calculation of sub-surface radar pulses in random media was studied by FDTD techniques. Analysis of electromagnetic wave scattering characteristics for satellite microwave remote sensing was also shown by FDTD method. These FDTD methods for scattering analysis of sensing could be applied to time response of automobile radar for auto cruising, and measurement analysis of water film sensor using microwaves [13].

For high bit-rate wireless communications and wireless LAN, FDTD method was used to analyze radio propagation in big urban areas with combinations of streets and buildings, and also, in indoor areas with several rooms through open doors [14]. Recently, for optimum design of RFID for school children securities, FDTD methods could be applied to study on radio propagation around schools. Also, for WiMAX wireless communications, FDTD methods are applied to analysis of propagation and scattering characteristics of microwaves over forests and through rain falls.

For X-ray fibers and devices, electromagnetic theoretical analysis is shown for propagation, focusing and attenuation characteristics in X-ray waveguides with bent and tapered parts [7]. X-ray scattering in bio-medical media with nano-meter structures of atoms are studied by statistical theory of electromagnetic waves, and also numerical methods of FDTD techniques, using correlation functions of random indexes [15]. Spatial filtering characteristics of waveguide-type grids are discussed for scattered field filtering to obtain precise image diagnosis. These theoretical and numerical methods are also applied to cases of optical and acoustical CT techniques for medical diagnosis [16].

## 2. ELECTROMAGNETIC WAVES IN PERTURBED DIELECTRIC WAVEGUIDES

This section considers the electromagnetic field in the irregular dielectric waveguide perturbed from the normal straight waveguide. The waveguide with the refractive index  $\varepsilon_1 = \varepsilon_1^{(1)} + \varepsilon_1^{(2)}$  which is

surrounded by the dielectric material of constant  $\varepsilon_2 = \varepsilon_2^{(1)} + \varepsilon_2^{(2)}$  is bent in  $(X, Y, Z)$  space and its cross section may be nonuniform. The conformal transformation given by the metrical relation  $ds^2 = dX^2 + dY^2 + dZ^2 = h_x^2 dx^2 + h_y^2 dy^2 + h_z^2 dz^2$ , where  $h_x = h_1(x, y)h_2(x, z)$ ,  $h_y = h_1(x, y)h_3(y, z)$ ,  $h_z = h_2(x, z)h_3(y, z)$ ,  $\left|\frac{d\dot{z}}{d\dot{z}}\right| = h_2$  etc., (for example, in case of bend on the  $XZ$  plane whose radius is  $R$ ,  $X + jZ = R(1 + x/R)^{j\frac{z}{R}}$ ,  $h_x = h_y = 1$ ,  $h_z = 1 + x/R$ ) maps the deformed waveguide into the straight waveguide. The wave equation and the boundary condition in  $(X, Y, Z)$  space are transformed into following equation in  $(x, y, z)$  space, representing in a form of the functional analysis as follows, using wave operators  $L_\varepsilon$  and  $L_F$ ,

$$LE = J + L_\varepsilon E + L_F E \tag{1}$$

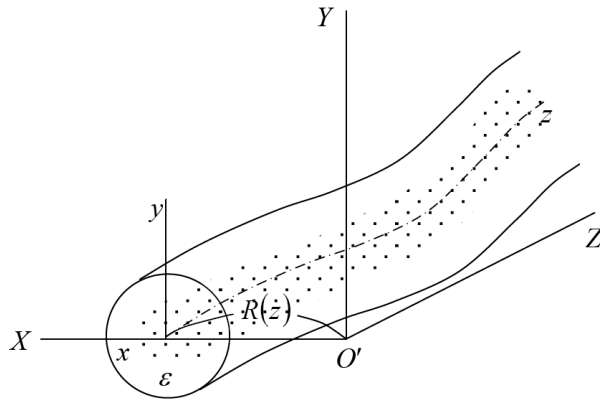


Figure 1: Randomly inhomogeneous waveguide with irregular bend.

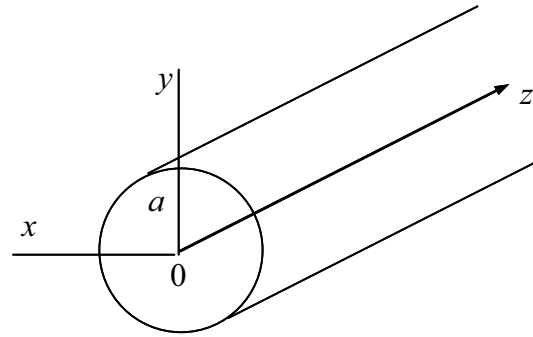


Figure 2: Curved waveguide in a new coordinate system.

For random refractive index  $\varepsilon^{(2)}(\mathbf{r})$ , correlation functions are assumed to be

$$\langle \varepsilon^{(2)}(\mathbf{r})\varepsilon^{(2)}(\mathbf{r}') \rangle = \varepsilon'^2 \langle \varepsilon^{(2)}(x, y)\varepsilon^{(2)}(x', y') \rangle \langle \varepsilon^{(2)}(z)\varepsilon^{(2)}(z') \rangle \tag{2}$$

For axial randomness of the refractive index and random bent, correlation functions are

$$\langle \varepsilon^{(2)}(\mathbf{r})\varepsilon^{(2)}(\mathbf{r}') \rangle = \langle \delta\varepsilon_z \rangle e^{-\frac{|z-z'|}{\gamma z r}} \cos \frac{|z-z'|}{\gamma z i}$$

For dominant  $(0, 0)$  mode incident case, intensities  $\langle J \rangle$  is given as, at the output, when intensities of  $(m, n)$  modes are  $\langle J_{mn} \rangle$ , using mode conversion coefficients

$$\langle J \rangle = \langle J_{00} \rangle + \sum_{m, n \neq 0} \langle J_{mn} \rangle \tag{3}$$

where,  $\langle J_{00} \rangle = 1 - \sum_{m, n \neq 0} \langle J_{mn} \rangle = 1 - \sum_{m, n \neq 0} [F_{mn}^{(t)} \cdot S_z F_{mn}^{(z)} + S_R F_{mn}^{(R)} \delta_{m1} \delta_{n0}]$ .

When a gradient fibre with the parabolic index profile has lossy inhomogeneous cladding with  $\varepsilon_1 = \varepsilon'(1 - (\ell_t r)^2 + D_{IV}(\ell_t r)^4 + D_{VI}(\ell_t r)^6)$  where  $D_{IV, VI} = D_{IV, VI}^{(r)} - jD_{IV, VI}^{(i)}$  are complex coefficients, propagation constants  $\beta_{mnx, y}$  and attenuation constants  $-\text{Im}\beta_{mnx, y} = \alpha_{mnx, y}$  of the  $(m, n)$  mode are obtained as follows, for the linear polarization in the  $x$  and  $y$  directions.

$$\beta_{mnx, y} = \beta_1 \left\{ 1 - (2n + 2m + 2) \frac{\ell_t}{\beta_1} - \frac{\ell_t^2}{\beta_1^2} - \frac{\ell_t^3 (1 - 2D_{IV}^{(r)})}{\beta_1^3} \left[ 3 \binom{m}{n} + \binom{n}{m} + 2 \right] + \frac{D_{IV}^{(r)} \ell_t^2}{4 \beta_1^2} A_{mn} + \frac{D_{VI}^{(r)}}{8 \beta_1^3} \ell_t^3 B_{mn} \right\}^{1/2} \tag{4}$$

and

$$\alpha_{mnx,y} = \frac{D_{IV}^{(i)}}{2} \left\{ \frac{\ell_t^2}{\beta_1} \frac{A_{mn}}{4} + \frac{\ell_t^3}{\beta_1^2} \left[ 3 \binom{m}{n} + \binom{n}{m} + 2 \right] \right\} + \frac{D_{VI}^{(i)}}{16\beta_1^2} \ell_t^3 B_{mn} \quad (5)$$

Some numerical examples are shown in Fig. 3 for the mode filtering properties of lossy inhomogeneous claddings. When the maximum mode number of guided modes in the gradient fibre of  $\epsilon_1(\mathbf{r}) = \epsilon' [1 - (\ell_t r)^2]$ ,  $r \leq a$ ,  $\epsilon_2 = \epsilon' [1 - (\ell_t a)^2]$ ,  $r \geq a$  is approximately  $(M, N)$ ,  $M+N+1 \cong \beta_1 \ell_t a^2 / 2$ , the scattering loss due to mode conversion for the dominant mode excitation at the input and output pulses are shown in Fig. 4, for several filtering parameters  $D_{VI}^{(i)}$  of lossy inhomogeneous claddings.

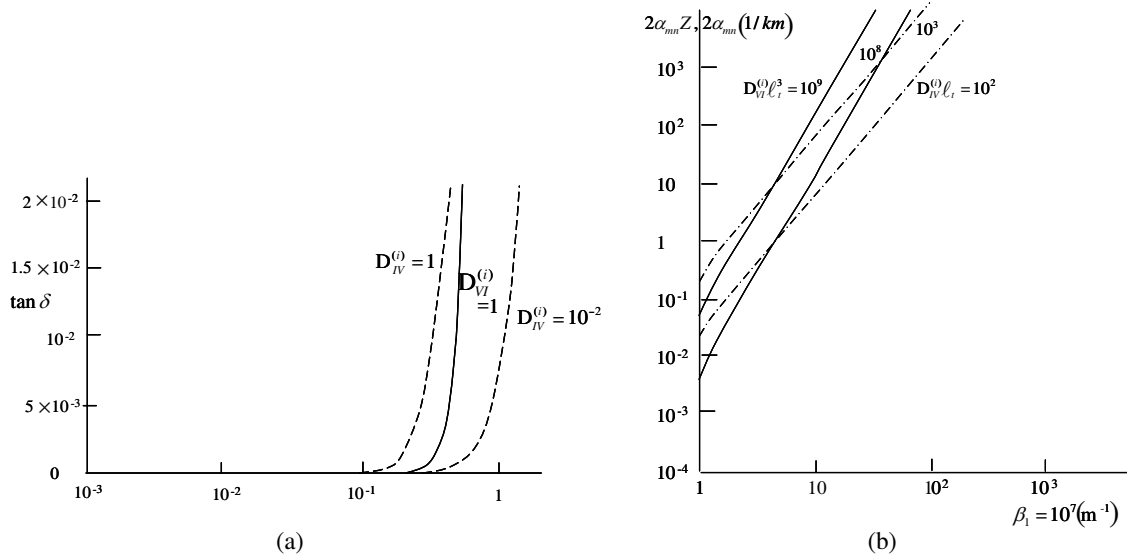


Figure 3: (a)  $\tan \delta$  distribution in graded-index fibre with lossy inhomogeneous cladding. (b) Attenuation constant  $2\alpha_{mn}$  of guided  $(m, n)$  mode,  $\beta_1 = 10^7 \text{ (m}^{-1}\text{)}$ .

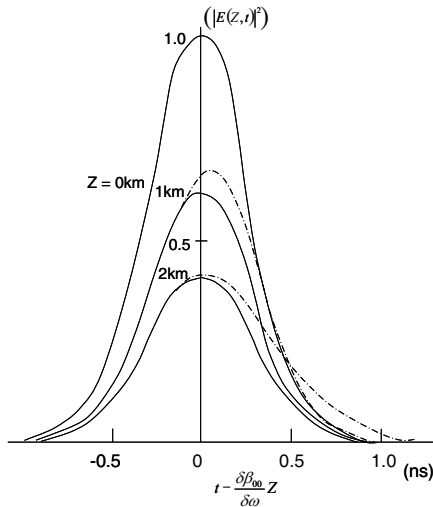


Figure 4: Pulse broadening of output pulse in the case of  $\gamma_z = 10 \mu\text{m}$ ,  $\gamma_t = 0.1 \mu\text{m}$ ,  $\beta_1 = 10^7 \text{ (m}^{-1}\text{)}$ ,  $\ell_t = \sqrt{10} \times 10^3 \text{ (m}^{-1}\text{)}$ ,  $\langle \delta^{(2)} \epsilon \rangle = (2 \times \sqrt{10}) \times 10^{-9}$ ,  $a = 50 \mu\text{m}$ ,  $M + N = 50$ ,  $T = 1.0 \text{ ns}$ . solid line  $D_{VI}^{(i)} = \sqrt{10} \times 10^{-2}$ , dashed line  $D_{VI}^{(i)} = \sqrt{10} \times 10^{-4}$ .

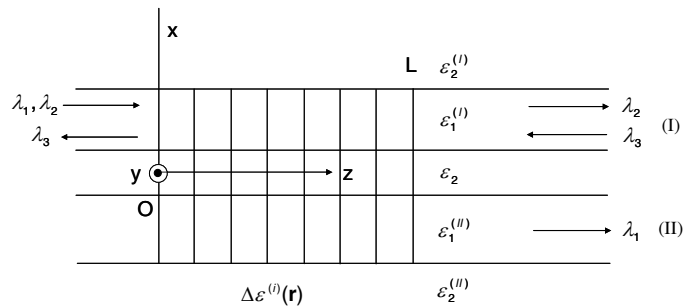


Figure 5: Coupled waveguides controlled by SAW.

### 3. SWITCH AND FILTERING OF GUIDED MODES BY SAW

When permittivity variations of waveguides are assumed to be  $\Delta\varepsilon^{(i)}(\mathbf{r})$  for waveguide (I) and (II), electromagnetic fields  $\hat{\mathbf{E}}(\mathbf{r}, \omega)$  are given

$$\nabla \times \nabla \times \hat{\mathbf{E}}(\mathbf{r}, \omega) - \mu\varepsilon_j^{(i)} \omega^2 \hat{\mathbf{E}}(\mathbf{r}, \omega) = -\omega^2 \mu \Delta\varepsilon^{(i)}(\mathbf{r}) \hat{\mathbf{E}}(\mathbf{r}, \omega) \quad (6)$$

SAW propagating in the middle layer of coupled waveguides induces variations of permittivity

$$\Delta\varepsilon^{(i)} = \sum_a u_a(\mathbf{r}_t) e^{-j\beta_a z} \quad (7)$$

Guided waves are given as

$$\hat{\mathbf{E}}_i(\mathbf{r}_t, \omega) = \sum_a a_{\alpha_i}(z) \phi_{\alpha_i}(\mathbf{r}, \omega) e^{-j\beta_{\alpha_i} z} \quad (8)$$

Using coupling coefficient  $c$ , mode amplitude  $b_j$  of wavelength  $\lambda_j$  in waveguide I, II is given

$$|b_j| = \frac{|c|^2}{|c|^2 + |\Delta\beta|^2} \sin^2 \left( \sqrt{|c|^2 + |\Delta\beta|^2} z \right) \quad (9)$$

where,  $\Delta\beta = \beta_{\alpha} \pm |\Delta\beta'|$ ,  $\Delta\beta' = |\beta_i - \beta_j|$ . Fig. 6 shows optical filtering switch by SAW for coupled waveguides.

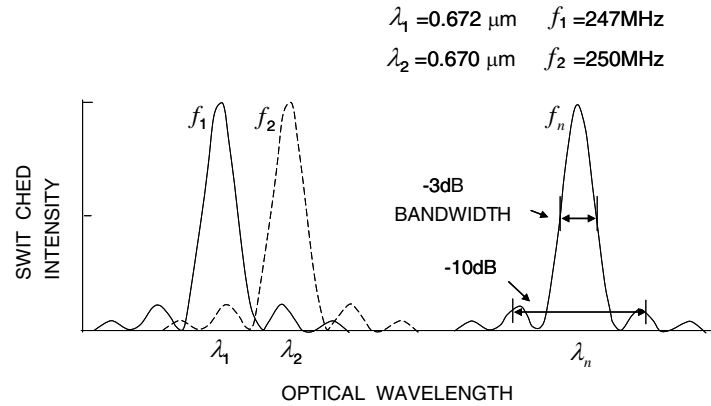


Figure 6: Optical filtering by SAW.

### 4. OPTICAL SCATTERING WAVES IN RANDOM MEDIA

Optical transmitted and scattered waves through random media are studied by statistical theory in two dimensional case. Optical waves are incident on random media (I) ( $0 \leq z \leq \ell$ ) from left side in Fig. 7. Incident optical wave has  $y$ -direction linearly polarization  $\mathbf{E} = \phi(x, z)\mathbf{i}_y$ . Dielectric constants of random media (I) are  $\varepsilon_t = \varepsilon + \varepsilon\Delta\eta(\mathbf{r}_t)$  where  $\Delta\eta$  is random function and  $\varepsilon = \varepsilon' - j\varepsilon''$ . The electric field satisfies

$$\nabla_{xy}^2 E(\mathbf{r}_t) + k^2 E(\mathbf{r}_t) = -\omega^2 \varepsilon \Delta\eta E(\mathbf{r}_t) \quad (10)$$

where  $k^2 = \omega^2 \varepsilon \mu = (k_r - jk_i)^2$ .

Incident Gaussian beam is

$$\mathbf{E}_{inc}(\mathbf{r}_t) = \mathbf{i}_y \frac{A}{\sqrt{1 - j\zeta}} e^{-jk(z+z_0)} e^{-\frac{x^2}{x_0^2(1-j\zeta)}} \quad (11)$$

where beam parameters are  $\zeta = \frac{2(z+z_0)}{kx_0^2}$ , beam waist is  $z = -z_0$  and beam spot size is  $x_0$ .

We assume that the statistical average  $\langle \Delta\eta \rangle$  of fluctuations in the sample is equal to zero and the correlation function is defined by

$$\langle \Delta\eta(\mathbf{r}'_t) \Delta\eta(\mathbf{r}''_t) \rangle = B_\eta(\mathbf{r}'_t - \mathbf{r}''_t) \quad (12)$$

The correlation function is assumed to be  $B_\eta(\rho_t) = \overline{\Delta\eta^2} e^{-\rho^2/\rho_0^2}$  with  $\rho_t = \mathbf{r}'_t - \mathbf{r}''_t$ , where variances of fluctuations are  $\Delta\eta^2$  and correlation lengths of fluctuations are  $\rho_0$ .

When  $\rho_0 < x_0$ , length of random media  $z_\ell$  for coordinate  $(r, \theta)$ , we have scattering intensity as shown in Eq. (13) and Fig. 8.

$$\langle \mathbf{I}_s \rangle = \mathbf{i}_r \frac{k}{\omega\mu} \frac{\sqrt{2\pi}}{16} \overline{\Delta\eta^2} A^2 k^3 x_0 \rho_0^2 \frac{1}{|\mathbf{r}|} e^{-k^2 \rho_0^2 \sin^2 \frac{\theta}{2}} e^{-2k_i(z_\ell + z_0)} z_\ell \quad (13)$$

3-dimensional scattering is shown similarly, as in Fig. 11 for incident Gaussian beam with beam waist  $z = -z_0$ , beam spot size  $r_0$ , and polarization of  $\tau$  direction,

$$\langle \mathbf{I}_s \rangle = \mathbf{i}_R \frac{k^4 \pi^{1/2}}{32} I_0 \sum_i r_{0z}^2 \rho_{0i}^3 \overline{\Delta\eta_i^2} \sin^2(\mathbf{i}_R, \tau) \frac{\ell}{R^2} \cdot e^{-k^2 \rho_{0i}^2 \sin^2 \frac{\theta}{2}} \quad (14)$$

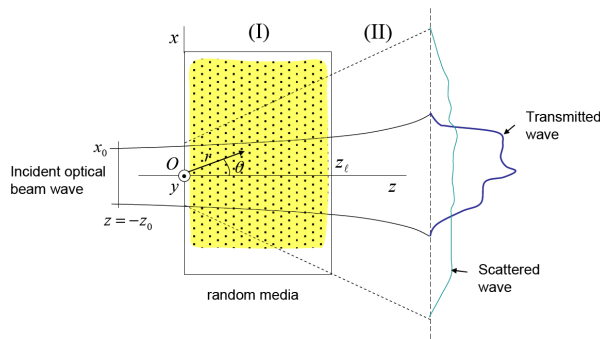


Figure 7: Transmitted and scattered waves of optical beam waves in random media.

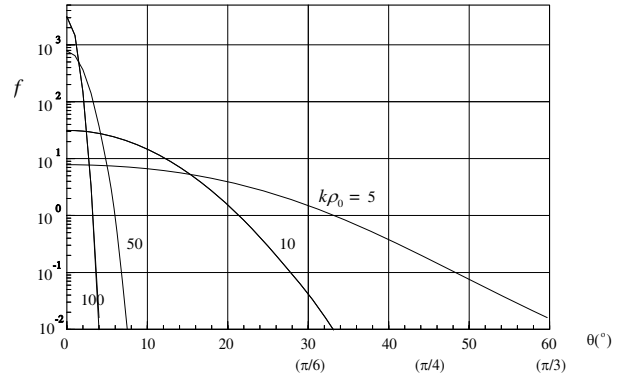


Figure 8: Angular distribution of scattering intensity.  $\frac{|\mathbf{I}_s|}{|\mathbf{I}_0|} = \overline{\Delta\eta^2}(kx_0) \left( \frac{z_\ell}{|\mathbf{r}|} \right) f$ ,  $f = \frac{\sqrt{2\pi}}{8} (k\rho_0)^2 e^{-(k\rho_0)^2 \sin^2 \frac{\theta}{2}}$ .

## 5. SPACE-TIME PULSE RESPONSE OF ELECTROMAGNETIC BACKSCATTERING FOR SENSING

Electromagnetic pulses of beam waves are radiated from antenna at height  $z = -z_0$  and transverse position  $x = -x_0$ , and are incident at the surface with incident angle  $\theta_0$ , as shown in Fig. 9. The incident wave is TE wave with  $y$ -polarization of the electric field, and two dimensional model is used. We define here that the region of incident wave is region I, the scattering object is region II' and ground region is region II.

The incident beam pulse is

$$\mathbf{E}^{(i)}(\mathbf{r}, t) = \frac{1}{2\pi} \int_{-\infty}^{\infty} \hat{V}(\omega) \hat{\mathbf{E}}^{(i)}(\mathbf{r}, \omega) e^{i\omega t} d\omega \quad (15)$$

where, the temporal function is,  $V(t) = e^{-(2t/T)^2} e^{j\omega_0 t}$  and spectral function is,  $\hat{V}(\omega) = \frac{\sqrt{\pi}T}{2} e^{-[(\omega - \omega_0)T/4]^2}$ .

Boundary  $z = f(x)$  separates the region I and region II. Scattering object II' may be a rectangular target of height  $h$  and width  $2W$ .

Electromagnetic fields  $\mathbf{E}^{(1)}$  and  $\mathbf{E}^{(2)}$  in the region I and II are represented, using coordinates  $x_n = x_i, x_r, x_t$ .

$$\hat{\mathbf{E}}_n(\mathbf{r}_n, \omega) = \int_{-\infty}^{\infty} \tilde{\mathbf{E}}_n(\beta_{tn}) e^{-j\beta_{tn}x_n - j\sqrt{k_n^2 - \beta_{tn}^2}z} d\beta_{tn} \quad (16)$$

In Eq. (16), wave numbers  $k_n$  are  $k_i = k_r = k_1 = \omega \sqrt{\varepsilon_1^* \mu_1}$  and  $k_t = k_2 = \omega \sqrt{\varepsilon_2^* \mu_2}$ ,  $\varepsilon_i^* = \varepsilon_i - j\sigma/\omega$  when region II' is included in region II. And also  $\beta_{tn}$  are  $\beta_{ti}$ ,  $\beta_{tr}$  and  $\beta_{tt}$ . If  $\beta_{tn}$  are small, and we can use approximation of  $\sqrt{k_n^2 - \beta_{tn}^2} \cong k_{tn} - \frac{1}{2} \frac{\beta_{tn}^2}{k_n} - \frac{1}{8} \frac{\beta_{tn}^4}{k_n^3}$ ,  $\tilde{\mathbf{E}}_n(\beta_{tn})$  can be expanded as series of

Hermite Gaussian functions as

$$\tilde{\mathbf{E}}_n(\beta_{tn})e^{-j\beta_{tn}x_n} = \sum_{m=0}^{\infty} a_{mn}f_m(\beta_{tn}x_n)\tau_n \quad (17)$$

where

$$f_m(\beta_{tn}x_n) = \frac{1}{(2^m m! \sqrt{\pi})^{1/2}} e^{-\frac{x_n'^2}{2}} H_m(x_n'), \quad x_n' = \beta_{tn}x_n.$$

From the boundary condition of field continuity on the boundary of the earth  $z = f(x)$ , spectral function of reflected waves  $E_r(\beta_t)$  can be given by spectral function  $B_r(\beta_t)$  as

$$B_r(\beta_t) = \int_{-\infty}^{\infty} e^{\mp j\sqrt{k_1^2 - \beta_t^2}f(x)} e^{-j\beta_t x} \varphi^{(0)}(x) dx \quad (18)$$

From Eq. (18), we obtain asymptotically scattered field of backward direction. The radar impulse responses are derived in the results as dynamic responses due to targets on the earth, namely spatial and temporal responses of backward scattering and bi-directional scattering. For TM incident beam waves, the similar discussions are obtained.

Electromagnetic backscattering characteristics of car body imaging using scanning millimeter wave radars can be analyzed by this spectral function method with synthetic aperture techniques, as Fig. 10.

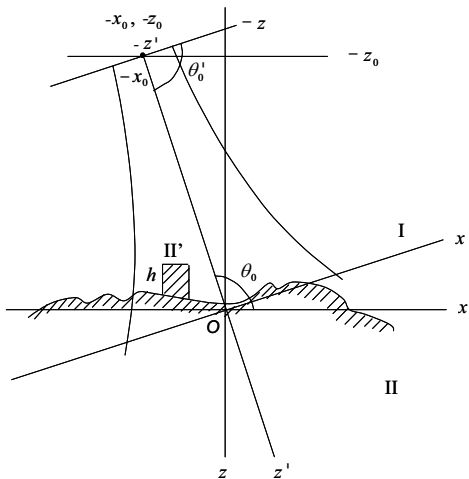


Figure 9: Electromagnetic pulses of beam waves and antenna.

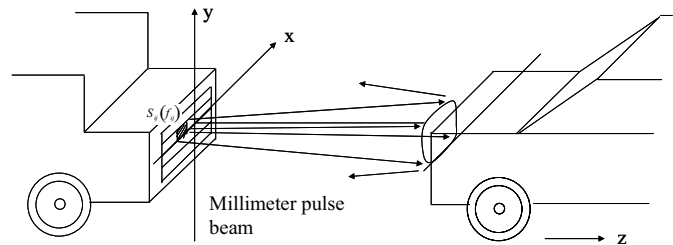


Figure 10: Scanning millimeter wave radar.

## 6. SPATIAL FILTERING OF OPTICAL SCATTERED WAVES IN RANDOM BIO-MEDICAL MEDIA

Medical image diagnosis using optical waves of lasers is very important technical tools for physiological examination of human body interior structures. Image responses of optical transmitted projection include, with optical absorption characteristics, optical scattering characteristics, that disturb transmission properties through biological structures depending on optical absorption effects due to biological characteristics consisting of atomic and molecular structure. Technical methods of spatial filtering for optical scattering superposed on attenuated transmission waves improve image diagnosis as shown in Fig. 11. Spatial filtering of grid structure yield exact image optical projection excluding scattering effects through physiological media. Spatial filtering characteristics for off-axial scattering optical waves are given by mode propagation properties with large attenuation for higher order modes in inhomogeneous waveguide-type grids.

Scattered fields of incident optical beams in bio-medical media (I) are given by Eqs. (13) and (14). Waveguide type grid of region (II) filters scattered fields in bio-medical media of region (I), and output fields of grid yield image fields of region (III) as shown in Fig. 11.

If we describe filtering characteristics using spatial frequencies  $k_x = \sqrt{k^2 - k_z^2}$ , in these three regions, for  $t = \text{I, II, III}$ , Fourier components are

$$E^{(t)}(k_x) = \int_{-\infty}^{\infty} E^{(t)}(x) e^{+jk_x x} dx \quad (19)$$

Filtering characteristics of lossy waveguide grids  $\hat{F}(k_x^{(II)})$  are defined as

$$\hat{E}^{(I)}(k_x^{(I)}) \hat{F}(k_x^{(II)}) = \hat{E}^{(III)}(k_x^{(III)}) \quad (20)$$

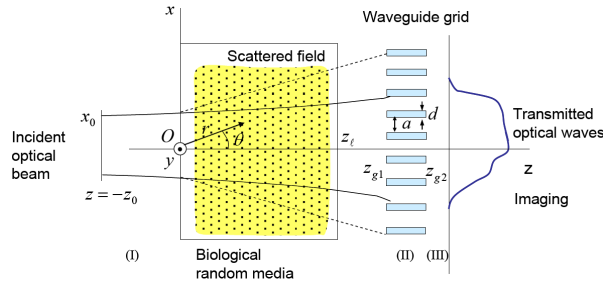


Figure 11: Optical scattering and optical grid.

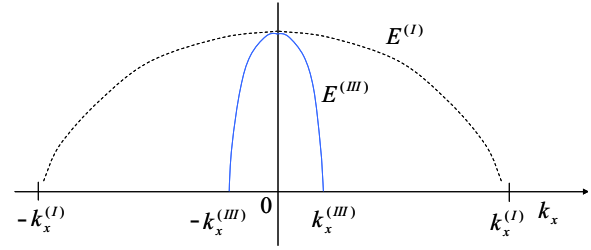


Figure 12: Spatial frequency and filtering characteristics.

Spatial frequency  $k_x^{(II)}$  of lossy waveguide grid filter is proportional to mode number  $m$ . Fig. 12 shows filtering characteristics for spatial frequencies  $k_x$ . Grid arrays shown in Fig. 13 consisting of inhomogeneous waveguides with lossy clads as given in Eqs. (4) and (5) shows excellent spatial filters for optical CT imaging.

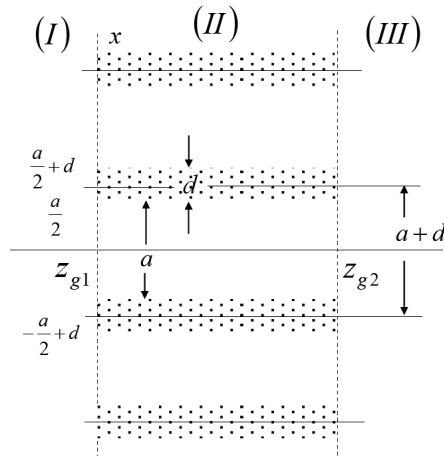


Figure 13: Waveguide type grid structure for scattering filtering.

Lossy waveguides with absorption clad layers have large propagation losses for higher modes and may have filtering characteristics of incident waves of large incident angles. When scattered waves with scattered angles  $\theta$  are incident to lossy waveguide (II) at the input  $z = z_{g1}$  from region (I), fields in the waveguide region (II) can be expressed as, for one grid section,

$$E_y^{(II)}(x, z) = \sum_m a_m \Psi_m(x) e^{-j\beta_m(z-z_{g1})}, \quad a_m = \int_{-\frac{a+d}{2}}^{\frac{a+d}{2}} E_{scatt}(x, z_{g1}) \Psi_m^*(x) dx \quad (21)$$

where  $\Phi_m(x, z) = \Psi_m(x) e^{-j\beta_m z}$ ,  $\int_{-\frac{a+d}{2}}^{\frac{a+d}{2}} \Psi_m(x) \Psi_n^*(x) dx = \delta_{mn}$ ,  $\beta_m = \beta_m^{(r)} - j\beta_m^{(i)}$ . Mode coefficients  $a_m$  show filtering characteristics. At the output of waveguide grids,  $z = z_{g2}$ , only lower modes propagate through lossy waveguides that couple with incident fields of small scattering angles and

Table 1: Optical parameters of random media and lossy waveguide grids.

Parameters	Values
$f$ : Frequency of incident wave	300 THz
$\lambda_0$ : Wavelength of incident wave	1 $\mu\text{m}$ ( $c/f$ )
$\ell_y$ : Length of an analysis space ( $y$ )	150 $\mu\text{m}$ ( $150\lambda_0$ )
$\ell_z$ : Length of an analysis space ( $z$ )	100 $\mu\text{m}$ ( $100\lambda_0$ )
$y_0$ : Center point of incident beam	75 $\mu\text{m}$ ( $\ell_y/2 = 75\lambda_0$ )
$r_0$ : Beam spot at $z = z_0$	15 $\mu\text{m}$ ( $r_0/\lambda_0 = 15$ )
$\Delta s$ : Length of a cell	0.05 $\mu\text{m}$ ( $\Delta s/\lambda_0 = 1/20$ )
$\Delta t$ : Time increment	$1.15 \times 10^{-16}$ s
$N$ : A number of polymers	2300
$a$ : Length of a side of polymers	0.5 $\sim$ 1.0 $\mu\text{m}$ ( $a/\lambda_0 = 0.5 \sim 1.0$ )
$n^*$ : Refractive index of polymers	1.4 - $j$ 0.001
$n_g^*$ : Refractive index of waveguide walls	2.0 - $j$ 0.5
$d$ : Width of waveguide walls	1 $\mu\text{m}$ ( $d/\lambda_0 = 1$ )
$D$ : Distance of waveguide walls	5 $\mu\text{m}$ ( $D/\lambda_0 = 5$ )
$\ell_g$ : Length of waveguide walls	20 $\mu\text{m}$ ( $\ell_g/\lambda_0 = 20$ )

higher modes that couple with high angle scattered fields can not pass through the waveguides. Filtered fields in the region (III) are derived by, using Green's function, for one grid section,

$$E_{fil}^{(III)}(x, z) = \int_{-\frac{a+d}{2}}^{\frac{a+d}{2}} \left\{ -G \frac{\partial E_y^{(II)}}{\partial z} + E_y^{(II)} \frac{\partial G}{\partial z} \right\} dx$$

$$= \left( -\frac{j}{4} \right) \sum_m (jk + j\beta_m) \sqrt{\frac{2}{\pi k z'}} e^{-jkz' + j\frac{\pi}{4}} a_m e^{-j\beta_m z'} \int_{-\frac{a+d}{2}}^{\frac{a+d}{2}} e^{-j\frac{k}{2z}(x-x')^2} \Psi_m(x') dx' \quad (22)$$

where  $z' = z - z_{g2}$  and  $a_m$  for large  $m$  is very small. When  $x_0$  is larger than core width, coupling coefficients  $a_m$  are given by, using  $C_2 = e^{-jk_s z'_0} e^{-j\beta_m z_{g1}}$ ,  $\beta' = k_s \sin \theta$

$$a_m = \int_{-\infty}^{\infty} E_{scatt}(x, z_{g1}) \Phi_m(x, z) dx = b_m C_2 \int_{-\infty}^{\infty} e^{-jk_s z'} \Psi_m(x) dx,$$

$$a_{2m'} = \sqrt{2\pi} (-1)^{m'} e^{-\frac{1}{2} \left( \frac{\beta'}{a_x} \right)^2} \frac{1}{a_x} H_{2m'} \left( \frac{\beta'}{a_x} \right), \quad a_{2m'+1} = -j\sqrt{2\pi} (-1)^{m'} e^{-\frac{1}{2} \left( \frac{\beta'}{a_x} \right)^2} \frac{1}{a_x} H_{2m'+1} \left( \frac{\beta'}{a_x} \right) \quad (23)$$

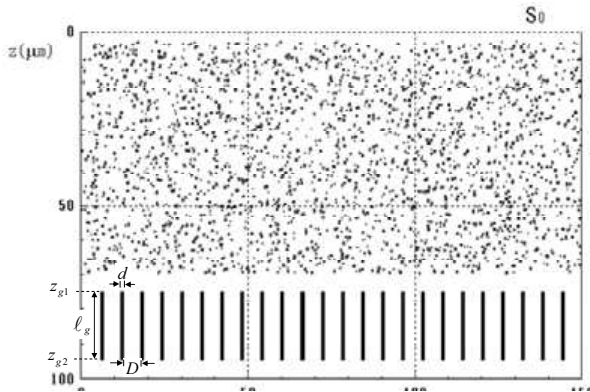
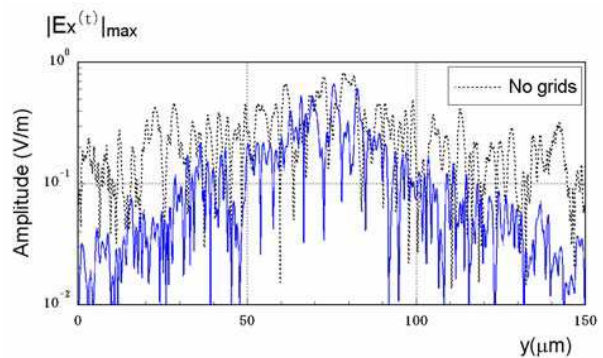


Figure 14: Random bio-medical media and lossy waveguide grids for scattering.

Figure 15: Electric field amplitude of transmitted optical waves  $\max |E_x^{(t)}|$  at  $z = \ell_z = 100 \mu\text{m}$ .

Coupling coefficients  $a_m$  show small mode coupling for large scattered angles and for large incident angle  $\theta$ , corresponding higher modes with large attenuation constants are coupled and filtered.

Computer simulation of optical scattering in random bio-medical media consisting of polymer particles with complex refractive indexes are studied by FDTD methods as Fig. 14.

Filtering characteristics of scattered fields by lossy waveguide grids are shown by FDTD method in case of  $x$ -polarization in Fig. 15 for imaging processing of medical diagnosis. Filtering characteristics of scattered fields by lossy waveguide grids for image processing are shown also in X-ray and ultrasonic medical diagnoses.

## 7. CONCLUSIONS

Mode conversions concerned with Scattered fields in perturbed dielectric waveguides with irregular bent and random dielectric constants in case of microwaves, optical waves and also X-ray, nanometer electromagnetic waves are studied. Switch and filtering characteristics of optical waves in integrated acousto-optic devices consisting of parallel coupled waveguide are discussed for multi-wavelengths transmission systems of WDM technology. Periodical waveguide structures for mode couplings are induced by SAW. Statistical properties of scattering fields in random media for Gaussian beams are shown by using correlation functions for two and three dimensional spaces. Back scattering characteristics by random surfaces are discussed by spectral function methods and applied to car body imaging for auto cruising of ITS by scanning millimeter wave radars.

Medical diagnosis with spatial filtering of scattered fields by lossy waveguide grids are shown for precise image processing of biological organizations in random biological media.

## REFERENCES

1. Kong, J. A. and D. K. Cheng, "On guided waves in moving anisotropic media," *IEEE Trans. Microwave Theory and Techniques*, Vol. 16, 99–103, 1968.
2. Kong, J. A., *Electromagnetic Wave Theory*, Wiley-Interscience, New York, 1990.
3. Tsang, L., J. A. Kong, and R. T. Shin, *Theory of Microwave Remote Sensing*, Wiley-Interscience, New York, 1985.
4. Udagawa, K. and Y. Miyazaki, "Deflection and mode conversion in tilted millimeter circular waveguides — A study by conformal mapping technique," *Jour. of IEC*, Vol. 48, 1186–1195, Japan.
5. Miyazaki, Y., "Propagation properties of optical signal waves in perturbed dielectric waveguide by conformal mapping technique," *Topical Meeting on Integrated Optics*, MA6-1, Las Vegas, USA, 1972.
6. Miyazaki, Y., "Partially coherent optical waves in random gradient fibers," *Optical and Quantum Electronics*, Vol. 9, 153–165, 1977.
7. Miyazaki, Y., "Beam propagation and radiation fields in a uniformly curved X ray dielectric gradient waveguides," *Trans. IEE of Japan*, Vol. 120-C, No. 1, 68–73, 2000.
8. Kondo, T., Y. Miyazaki, and Y. Akao, "Optical tunable switched directional couplers consisting of two thin-film waveguides using surface acoustic waves," *Jpn. Jour. Appl. Phys.*, Vol. 17, 1231–1243, 1978.
9. Goto, N. and Y. Miyazaki, "Integrated optical multi-/demulti-plexer using acoustooptic effect for multiwavelength optical communications," *IEEE J. on Sel. Areas in Comm.*, Vol. 8, 1160–1168, 1990.
10. Miyazaki, Y., "Nonlinear interaction of optical modes with multi-electromagnetic waves in optical functional devices," *Trans. IEE Japan*, Vol. 118-C, 99–104, 1998.
11. Miyazaki, Y., "Light scattering of laser beams by random micro-inhomogeneities in glasses and polymers," *Jpn. Jour. Appl. Phys.*, Vol. 13, 1238–1248, 1974.
12. Miyazaki, Y., "Spectral expansion method of beam guiding and scattering at arbitrary dielectric boundary interfaces," *Electromagnetic Waves and Electronic Systems*, Vol. 7, 13–21, 2002.
13. Takahashi, K. and Y. Miyazaki, "Scattering analysis of millimeter wave radar for collision avoidance using FDTD method," *Trans. IEE Japan*, Vol. 120-C, 111–116, 2000.
14. Rodriguez, G., Y. Miyazaki, and N. Goto, "Matrix-based FDTD parallel algorithm for big areas and its applications to high-speed wireless communications," *IEEE Trans. Antennas and Propagation*, Vol. 54, 785–796, 2006.
15. Miyazaki, Y. and K. Takahashi, "Computer simulation of X-ray scattering characteristics for medical image diagnosis," *Trans. IEE Japan*, Vol. 126-C, 1431–1440, 2006.
16. Miyazaki, Y., "Spatial filtering of optical scattered waves in Bio-medical media by inhomogeneous waveguide grids for optical CT," *Proc. APMC*, 527–530, TH-A-D, Bangkok, 2007.

# Parallel Transmission: A Comprehensive RF Safety Concept

I. Graesslin

Philips Research Europe, Hamburg, Germany

**Abstract**— RF safety is an important aspect for MRI systems. However, patient safety in parallel RF transmission systems is more complex due to the extra degree of freedom in the RF pulse design, as existing SAR limits may be violated in case of a system failure or miscalibration.

This abstract describes a comprehensive safety concept for such a system. Part of the concept is the verification of the SAR limits *before* the scan in combination with RF waveform monitoring *during* the scan to ensure patient safety for RF parallel transmit systems.

## 1. INTRODUCTION

RF safety is a prerequisite for in vivo parallel transmission [1, 2] MRI experiments. This abstract describes a comprehensive safety concept for parallel transmission MRI systems. Part of the concept is the verification of the SAR limits [3, 4] prior to the scan in combination with RF waveform monitoring during the scan. The scan is terminated, as soon as an unsafe condition is detected.

## 2. METHODS

The safety concept consists of the following two parts:

SAR calculation prior to the scan: For the SAR limit verification before a scan, the electric fields  $E$  were pre-calculated using finite-difference time-domain simulations (“XFDTD,” Remcom Inc., USA) with 5 mm spatial grid resolution and perfectly matched layer boundaries (16 layers). As an example, an ideally decoupled 3T multi-channel body coil (MBC) [5] was used, which was loaded with bio-mesh models, including the “Visible Human Male” [6]. The pre-calculated  $E$ -fields of the individual coil elements were averaged according to [7] and stored in a database. This pre-calculated information is used for the pre-scan calculation of the SAR, which is obtained by a superposition of the weighted  $E$ -fields with the RF pulses.

Waveform monitoring during the scan: To ensure patient safety during scanning, existing solutions such as the monitoring of the RF with a power-monitoring unit (PMU) are not sufficient. The reason is that only the maximum peak and average power can be monitored, so that neither, potential phase deviations at the transmit coil elements nor other potential channel failures, are detected. In addition, in parallel transmission experiments at higher field strengths, the local SAR and not the global SAR, which is PMU controlled, is the limiting factor for the allowed maximum duty cycle. The ratio between local and global SAR is not constant and may vary significantly based on the coil/patient interaction as well as the form of the parallel RF transmission pulses [8–10].

To ensure patient safety, an individual pick-up coil (PUC) monitoring (see Fig. 1) is used. The PUCs were placed near each coil element of the MBC, which was integrated into a Philips 3T Achieva system (Philips Healthcare, The Netherlands) equipped with eight transmit channels [11]. Each PUC was connected to a dedicated monitoring input. Thus, the current of each coil element of the MBC can be monitored and subsequently compared with the demand RF waveform. To compensate for RF coil coupling, active decoupling is used [12]. The RF pulses are pre-compensated, which is equivalent to a virtual decoupling of the MBC elements. This compensation is necessary to match the RF simulation model to the real coil configuration, so that the SAR calculations are correct for the simulated ideally decoupled MBC. Furthermore, it is advantageous to keep the safety margin small for the RF demand monitoring. The selection of the safety margin is important for the correct functioning of the monitoring system. For the margin definition, amplitude as well as phase changes were investigated for different volunteers including their positions in the coil as well as their motion (e.g., breathing). For the demonstration of a hazardous situation, a tuned single channel receive coil ( $\phi = 10$  cm) was placed inside the MR scanner, and the influence on RF amplitude and phase was investigated.

## 3. RESULTS AND DISCUSSION

The SAR can be calculated for (accelerated) multi-transmit RF pulses, and its conformity with existing SAR limits [3, 4] can be verified before the scan. From the database, a bio-mesh model

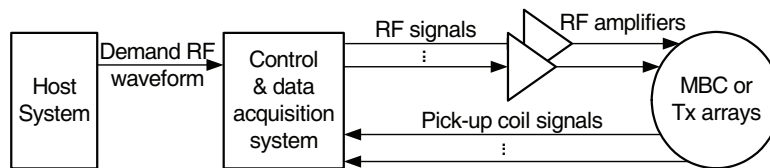


Figure 1: To ensure patient safety, one PUC per coil element is integrated into the MBC. Each pick-up coil is connected to a dedicated monitoring input of the control & data acquisition system. The current, which is induced by the transmit pulse in each of the RF transmit coil elements, can be monitored and compared with the demand RF waveform.

is selected that optimally matches the actual patient shape. Two examples for a possible safety margin violation are shown in Fig. 2. After one second of scanning, a surface coil was forced to remain in its tuned state during transmission, causing a decrease of the transmit amplitude of 55% in combination with a transmit phase deviation of  $10^\circ$  (Fig. 2(a)).

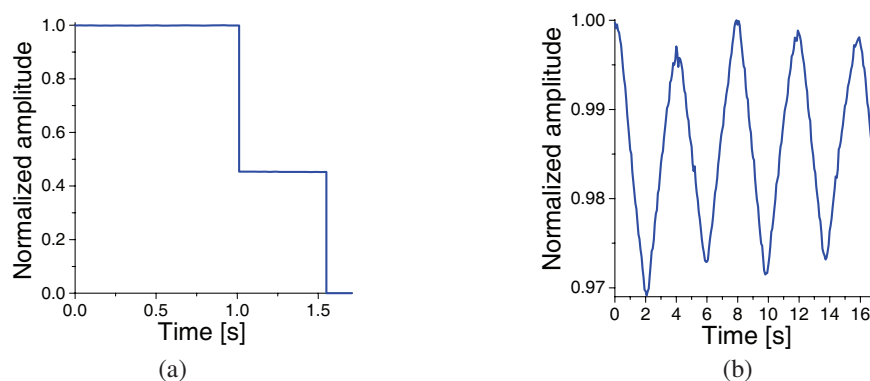


Figure 2: The deviation from RF demand is induced by (a) a resonant object in the MR scanner, which leads to a scan termination and (b) respiration.

The reason for the amplitude decrease is the detuning of the RF transmit coils, which results in an unpredictable behavior in terms of SAR. The malfunctioning of the receive coil is detected in real-time and leads to a scan termination within a few hundred milliseconds. In Fig. 2(b)), a respiration induced amplitude change in the order of 3% can be observed, which, however, should not lead to a scan termination. The calculated SAR deviation was investigated for four subjects and led to a negligible increase of smaller than 0.01% for the breathing situation and less than 3% for the worst case breath-hold situation (with respect to SAR). As a side remark, the influence of the respiration on the PUC signal might be utilized in the framework of motion compensation [13].

#### 4. CONCLUSIONS

Patient safety in parallel RF transmission systems is more complex due to the extra degree of freedom in the RF pulse design, as existing SAR limits may be violated in case of system failure or miscalibration. Furthermore, many variables may affect the SAR as e.g., the dielectric heterogeneity of human tissue as well as its loading of the coil.

A SAR determination before the scan in combination with RF waveform monitoring during the scan can ensure patient safety for RF parallel transmit systems.

#### ACKNOWLEDGMENT

The author would like to thank D. Glaesel, S. Biederer, F. Schweser, P. Vernickel, P. Börnert, and U. Katscher (Philips Research Europe, Hamburg, Germany) as well as H. Dingemans, G. Mens, and P. Harvey (Philips Healthcare, Best, The Netherlands).

#### REFERENCES

1. Katscher, U., P. Börnert, C. Leussler, and J. van den Brink, "Transmit SENSE," *Magn. Reson. Med.*, Vol. 49, No. 1, 144–150, 2003.
2. Zhu, Y., "Parallel excitation with an array of transmit coils," *Magn. Reson. Med.*, Vol. 51, 775–784, 2004.

3. IEC 60601-2-33, “Medical electrical equipment and particular requirements for the safety of magnetic resonance equipments for medical diagnosis and §51 protection against hazardous output,” *Internat. Electrotech. Commis.*, 2002.
4. FDA, “Criteria for significant risk investigations of magnetic resonance diagnostic devices,” 2003.
5. Vernickel, P., P. Röschmann, C. Findekle, K. M. Luedeke, C. Leussler, J. Overweg, U. Katscher, I. Graesslin, and K. Schuenemann, “Eight-channel transmit/receive body MRI coil at 3T,” *Magn. Reson. Med.*, Vol. 58, No. 2, 381–389, 2007.
6. National Library of Medicine, “Visible human male,” <http://www.nlm.nih.gov>, 1996.
7. IEEE Std C95.3-2002, “IEEE recommended practice for measurements and computations of radio frequency electromagnetic fields with respect to human exposure to such fields, 100 kHz–300 GHz,” *Inst. of Electrical and Electronics Eng.*, 2002.
8. Wang, Z., J. C. Lin, W. Mao, W. Liu, M. B. Smith, and C. M. Collins, “SAR and temperature: Simulations and comparison to regulatory limits for MRI,” *Journ. of Magn. Reson. Imag.*, Vol. 26, 437–441, 2007.
9. Collins, C. M., Z. Wang, and M. B. Smith, “A conservative method for ensuring safety within transmit arrays,” *Proc. Intl. Soc. Mag. Reson. Med.*, 1092, Berlin, Germany, May 2007.
10. Graesslin, I., K. Falaggis, S. Biederer, D. Glaesel, P. Vernickel, P. Röschmann, C. Leussler, A. Thran, Z. Zhai, M. Morich, and U. Katscher, “SAR simulations and experiments for parallel transmission,” *Proc. Intl. Soc. Mag. Reson. Med.*, 1090, Berlin, Germany, May 2007.
11. Graesslin, I., P. Vernickel., J. Schmidt, C. Findekle, P. Röschmann, C. Leussler, P. Haaker, K. Laudan, K. M. Luedeke, J. Scholz, S. Buller, J. Keupp, P. Börnert, H. Dingemans, G. Mens, G. Vissers, K. Blom, N. Swennen, J. van der Heijden, L. Mollevanger, P. Harvey, and U. Katscher, “Whole body 3T MRI system with eight parallel RF transmission channels,” *Proc. Intl. Soc. Mag. Reson. Med.*, 129, Toronto, USA, May 2006.
12. Vernickel, P., C. Findekle, J. Eichmann, and I. Graesslin, “Active digital decoupling for multi-channel transmit MRI Systems,” *Proc. Intl. Soc. Mag. Reson. Med.*, 170, Berlin, Germany, May 2007.
13. Graesslin, I., D. Glaesel, P. Börnert, H. Dingemans, G. Mens, and P. Harvey, “An alternative concept of selfnavigation for patient respiration monitoring,” *Proc. Intl. Soc. Mag. Reson. Med.*, 867, Berlin, Germany, May 2007.

# Basic and Tailored RF Shimming in a Multi-transmit Whole Body MR System

U. Katscher

Philips Research Europe, Hamburg, Germany

**Abstract**— Wave propagation effects diminish the quality of MR images at main fields of 3T or above. Parallel RF transmission has the potential of compensating for these effects through RF shimming. RF shimming can be performed in two different ways. The basic way of RF shimming is to adjust the global amplitude and phase of the currents in each transmit element, aiming at a constant  $B_1$  in the region of interest. For 3D volume imaging, 3D RF shimming is facilitated using multiple frequencies for the different transmit elements. On the other hand, “tailored” RF shimming can be performed via multi-dimensional RF pulses designed to achieve a spatially constant excitation pattern. Using an MR system equipped with parallel RF channels, these multi-dimensional RF pulses can be accelerated via Transmit SENSE.

The potential of both, basic and tailored RF shimming, can be enhanced significantly, if only a constant  $B_1$  amplitude is demanded, and an arbitrary spatial distribution of the resulting  $B_1$  phase is allowed. This is the case, if only magnitude images are of interest. However, this approach introduces a non-linear problem, requiring corresponding numerical techniques.

Optimal results for basic RF shimming are obtained with transmit arrays owning preferably homogeneous sensitivity distributions of the individual elements. On the other hand, for tailored shimming, the transmit elements require orthogonal sensitivity distributions, which are easier to achieve with inhomogeneous sensitivity distributions. Thus, the transmit coil array cannot be optimized for both, basic and tailored RF shimming simultaneously, and a suitable compromise has to be found.

This study compares the different RF shimming approaches using a whole-body, 8-channel Tx/Rx system at 3T. It shows, that basic RF shimming is able to remove  $B_1$  inhomogeneities to a high degree, both in phantoms and in vivo. Tailored RF shimming is able to achieve even higher levels of  $B_1$  homogeneity, which, however, might not be necessary for the majority of clinical applications.

## 1. INTRODUCTION

Wave propagation effects diminish the quality of MR images at main fields of 3T or above. Parallel RF transmission has the potential of compensating for these effects through RF shimming. RF shimming can be performed in two different ways. The basic way of RF shimming is to adjust the global amplitude and phase of the currents in each transmit element, aiming for a constant  $B_1$  amplitude in the region of interest [1, 2]. For 3D volume imaging, 3D RF shimming is facilitated using multiple frequencies for the different transmit elements [3]. On the other hand, “tailored” RF shimming can be performed via multi-dimensional RF pulses [4], accelerated via parallel transmission [5, 6], designed to achieve a spatially constant excitation pattern [7–9]. This study compares the different RF shimming approaches using a whole-body, 8-channel Tx/Rx system at 3T [10, 11].

## 2. THEORY

The central equation for both, the basic and tailored RF shimming, is given by

$$\sum_{n=1}^N T_n(\mathbf{x})P_n(\mathbf{x}) = C(\mathbf{x}). \quad (1)$$

This equation states, that the superposition of the transmit sensitivity profiles  $T_n(\mathbf{x})$  of the  $N$  transmit coils, weighted with  $P_n(\mathbf{x})$ , yields the desired constant  $B_1$  distribution  $C(\mathbf{x}) = const.$  For the basic RF shimming,  $P_n(\mathbf{x})$  are constant, leading to a global (complex) scaling of the different sensitivity profiles  $T_n(\mathbf{x})$ . For 3D volume imaging, 3D RF shimming might be performed via a technique called “Multi-Frequency Excitation” (“MULTIFEX”, [3]). Here, the elements of a transmit array are driven with different frequencies to excite different slabs in the excitation volume via the underlying gradient. Amplitudes and phases can be optimized for each slab individually to achieve

maximum  $B_1$  homogeneity. For the tailored RF shimming,  $P_n(\mathbf{x})$  of Eq. (1) define spatial excitation patterns of the individual transmit elements, which can be converted to (multi-dimensional) RF pulses [4]. The simultaneous use of multiple transmit elements allows the shortening of the different pulses [5, 6]. By discretizing Eq. (1) on a spatial grid, it can be solved via linear algebra for both basic and tailored RF shimming.

In the majority of applications, only a constant amplitude  $|C|$  is required, and an arbitrary spatial phase distribution  $\varphi(\mathbf{x})$  is acceptable  $C(\mathbf{x}) = \text{const} \exp(i\varphi(\mathbf{x}))$ . This is the case, if only magnitude images are of interest. The resulting degree of freedom enhances the power of (basic and tailored) RF shimming considerably, however, Eq. (1) is no longer linear and corresponding non-linear inversion techniques are required.

Optimal results for basic RF shimming are obtained with transmit arrays showing preferably homogeneous sensitivity distributions of the individual elements. On the other hand, for tailored shimming, the transmit elements require orthogonal sensitivity distributions, which are easier to achieve with inhomogeneous sensitivity distributions. Thus, the transmit coil array cannot be optimized for both, basic and tailored RF shimming simultaneously, and a suitable compromise has to be found.

### 3. METHODS

Experiments has been performed using a 3T MR system (Philips Achieva, Philips Medical System, The Netherlands) equipped with an 8-element Tx/Rx body coil and corresponding parallel RF channels [10, 11]. Since it is expected that basic RF shimming will be the preferred way of shimming, the transmit elements were designed to be slightly more suitable for basic than for tailored RF shimming. However, the differences are small, and might be outperformed by other system parameters.

The transmit sensitivities have been determined via “Actual Flip angle Imaging” [12]. Basic and tailored RF shimming has been performed as described in the previous section.

For the phantom experiments, a water bottle with a diameter of 20 cm has been used. Images without and with basic RF shimming have been acquired using a FFE sequence with  $TR = 8.0$  ms,  $TE = 2.6$  ms, a spatial resolution of  $1.5 \times 1.5 \times 10$  mm<sup>3</sup>, and a flip angle of  $\alpha = 15^\circ$ . Tailored RF shimming has been performed with a reduction factor of  $R = 2$  via a spiral  $k$ -space trajectory with 8 revolutions for a field of excitation of  $32^2$  pixels. For the acquisition, a 3D-FFE sequence was used with  $TR = 40.0$  ms,  $TE = 1.4$  ms, and a spatial resolution of  $9 \times 9 \times 10$  mm<sup>3</sup>.

Furthermore, basic RF shimming has been applied in vivo for mammography. For these experiments, a FFE sequence was chosen with  $TR = 4.14$  ms,  $TE = 2.0$  ms, a spatial resolution of  $1.5 \times 1.5 \times 10$  mm<sup>3</sup>, and a flip angle of  $\alpha = 15^\circ$ . Written consent was obtained from all participants of this study.

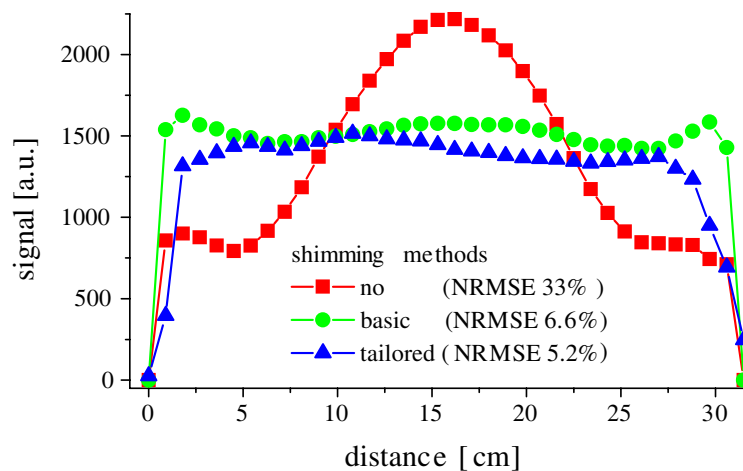


Figure 1: Experimental phantom results. Without shimming, the normalized root-mean square error (NRMSE) is 33% (red line/symbols). The NRMSE reduces to 6.6% for basic (green line/symbols) and 5.2% for tailored shimming (blue line/symbols).

#### 4. RESULTS/DISCUSSION

Experimental phantom results are shown in Fig. 1. Without shimming, the normalized root-mean square error (NRMSE) is 33%. The NRMSE reduces to 6.6% for basic and 5.2% for tailored shimming. Thus, both RF shimming approaches show a high potential to homogenise the overall  $B_1$  transmit field. However, at least for this scenario, the potential of tailored RF shimming seems to be only slightly higher than the potential of basic RF shimming. For Fig. 1, no phase demand was given for basic RF shimming. The solution of the resulting non-linear optimization problem took roughly 35 s on a standard PC. The RF pulses for tailored RF shimming were calculated using a spatially constant phase demand. The solution of the resulting matrix/vector equation took roughly 10 s on a standard PC.

The high potential of basic RF shimming is also found in the framework of the mammography study (Fig. 2). Within the breasts, an NRMSE of 37.4% is found without RF shimming. With basic RF shimming, an NRMSE inside the breasts of 18.7% is found. Thus, using basic RF shimming reduced the left-right signal imbalance of the image significantly.



Figure 2: RF shimming for mammography. Left: without RF shimming (NRMSE inside breast = 37.4%). Right: using basic RF shimming (NRMSE inside breasts = 18.7%). The left-right signal imbalance is reduced significantly. It is expected that the small residual inhomogeneities, particularly on the right portion of the torso, will disappear using tailored RF shimming.

#### 5. CONCLUSIONS

Basic RF shimming is able to remove  $B_1$  inhomogeneities to a high degree, both in phantoms in vivo. Tailored RF shimming is able to achieve even higher levels of  $B_1$  homogeneity, which, however, might not be necessary for the majority of clinical applications.

#### ACKNOWLEDGMENT

The author would like to thank Ingmar Graesslin, Peter Vernickel, Kay Nehrke, and Peter Börnert for their support.

#### REFERENCES

1. Hoult, D. I. and D. Phil, "Sensitivity and power deposition in a high-field imaging experiment," *J Magn. Reson. Imaging*, Vol. 12, No. 1, 46–67, 2000.
2. Ibrahim, T. S., R. Lee, B. A. Baertlein, A. Kangarlu, and P. L. Robitaille, "Application of finite difference time domain method for the design of birdcage RF head coils using multi-port excitations," *J Magn. Reson. Imaging*, Vol. 18, No. 6, 733–742, 2000.
3. Katscher, U., H. Eggers, I. Graesslin, G. Mens, and P. Börnert, "3D RF shimming using multi-frequency excitation," *16 Proceedings of International Society of Magnetic Resonance in Medicine*, 1263, Toronto, Canada, May 2008.
4. Pauly, J., D. Nishimura, and A. Macovski, "A  $k$ -space analysis of small-tip-angle excitation," *J Magn. Reson.*, Vol. 81, 43–56, 1989.
5. Katscher, U., P. Börnert, C. Leussler, and J. van den Brink, "Transmit sense," *Magn. Reson. Med.*, Vol. 49, No. 1, 144–150, 2003.
6. Zhu, Y., "Parallel excitation with an array of transmit coils," *Magn. Reson. Med.*, Vol. 51, No. 4, 775–784, 2004.
7. Saekho, S., F. E. Boada, D. C. Noll, and V. A. Stenger, "Small tip angle three-dimensional tailored radiofrequency slab-select pulse for reduced  $B_1$  inhomogeneity at 3T," *Magn. Reson. Med.*, Vol. 53, No. 2, 479–484, 2005.

8. Ullmann, P., S. Junge, M. Wick, F. Seifert, W. Ruhm, and J. Hennig, “Experimental analysis of parallel excitation using dedicated coil setups and simultaneous RF transmission on multiple channels,” *Magn. Reson. Med.*, Vol. 54, No. 4, 994–1001, 2005.
9. Setsompop, K., L. L. Wald, V. Alagappan, B. Gagoski, F. Hebrank, U. Fontius, F. Schmitt, and E. Adalsteinsson, “Parallel RF transmission with eight channels at 3 tesla,” *Magn. Reson. Med.*, Vol. 56, No. 5, 1163–1171, 2006.
10. Graesslin, I., P. Vernickel, J. Schmidt, C. Findekle, P. Röschmann, C. Leussler, P. Haaker, H. Laudan, K. M. Luedeke, J. Scholz, S. Buller, J. Keupp, P. Börnert, H. Dingemans, G. Mens, G. Vissers, K. Blom, N. Swennen, L. Mollevanger, P. Harvey, and U. Katscher, “Whole body 3T MRI system with eight parallel RF transmission channels,” *14 Proceedings of International Society of Magnetic Resonance in Medicine*, 129, Seattle, USA, May 2006.
11. Vernickel, P., P. Roschmann, C. Findekle, K. M. Luedeke, C. Leussler, J. Overweg, U. Katscher, I. Graesslin, and K. Schuenemann, “Eight-channel transmit/receive body MRI coil at 3T,” *Magn. Reson. Med.*, Vol. 58, No. 2, 381–389, 2007.
12. Yarnykh, V. L., “Actual flip-angle imaging in the pulsed steady state: A method for rapid three-dimensional mapping of the transmitted radiofrequency field,” *Magn. Reson. Med.*, Vol. 57, No. 1, 192–200, 2007.

## SAR in Parallel Transmission

I. Graesslin<sup>1</sup>, D. Glaesel<sup>1</sup>, S. Biederer<sup>2</sup>, F. Schweser<sup>1</sup>  
 P. Vernickel<sup>1</sup>, P. Börnert<sup>1</sup>, B. Annighoefer<sup>1</sup>, H. Stahl<sup>1</sup>  
 H. Dingemans<sup>3</sup>, G. Mens<sup>3</sup>, P. Harvey<sup>3</sup>, and U. Katscher<sup>1</sup>

<sup>1</sup>Philips Research Europe, Hamburg, Germany

<sup>2</sup>Institute of Medical Engineering, University of Lübeck, Lübeck, Germany

<sup>3</sup>Philips Healthcare, Best, The Netherlands

**Abstract**— Parallel transmission bears the potential of compensating B1 field inhomogeneities induced by wave propagation effects in (ultra) high field whole body MR imaging. However, with increasing field strength, the RF power deposition and the associated local specific absorption rate (SAR) represent an important attention point with respect to patient safety.

This paper presents simulations of a 3T whole body eight-channel transmit/receive body coil loaded with a human bio-mesh model. Phantom SAR simulations were carried out and validated by temperature measurements. A good correlation between SAR simulations and measured temperature was obtained, so that the FDTD method can be considered to be a valuable tool in determining (local) SAR for patient safety in multi-channel transmission MRI systems.

### 1. INTRODUCTION

With increasing field strength, the RF power deposition and the associated local specific absorption rate (SAR) are becoming more important with respect to patient safety. SAR represents the limiting factor for the allowed RF duty cycle of an MR scan. This paper presents simulations using a whole body human bio-mesh model and a cuboid phantom for an eight-channel transmit/receive body coil [1] operating at 128 MHz. Furthermore, the SAR simulations of the cuboid phantom were validated by temperature measurements for the assessment of safety and coil performance.

### 2. METHODS

SAR for parallel transmission is assessed by simulating a 3T multi-channel body coil (MBC) with eight ideally decoupled transversal electro magnetic transmit elements using the finite-difference time-domain method (“XFDTD”, Remcom, Inc., USA). The coil sensitivities were calculated on a 5 mm grid using perfectly matched layer boundaries (16 layers) and the bio-mesh model of the “Visible Human Male” [2] as an example (see Fig. 1). The SAR was obtained from the superposition of the spatially averaged [3] pre-calculated fields  $E$  of the individual coil elements and weighted with the RF pulses.

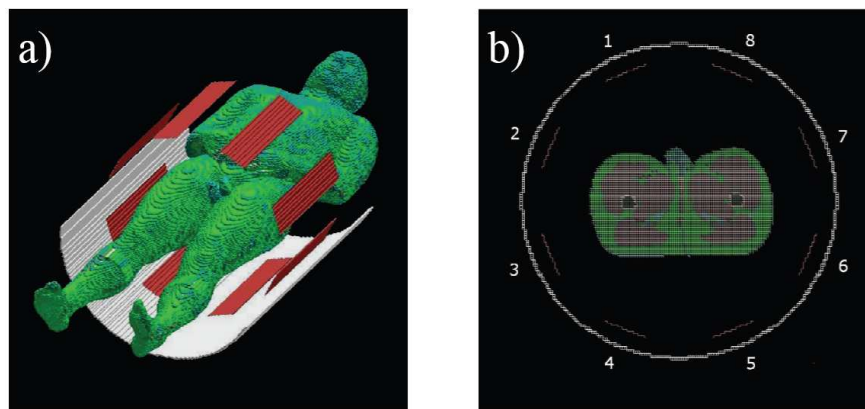


Figure 1: An eight-channel multi-channel body coil loaded with the NLM “Visible Human” [2] bio-mesh (a) and a transversal slice (b).

The 2D spatially selective RF excitation pulses were calculated iteratively in the spatial domain using a conjugate-gradient method [4] as well as directly using a SAR optimized RF pulse design method according to Ref. [5–7]. Furthermore, the VERSE approach [8] was adopted for parallel

transmission [9, 10]. Target excitation pattern used were, for instance, a segmented region of the kidneys (Fig. 2, top row) and a segmented region of the liver (Fig. 2, bottom row). Other patterns, such as a disc (Fig. 2(d)), have been employed as well, all using spiral k-space trajectories with a numerical field-of-excitations between  $32 \times 32$  and  $64 \times 64$  pixels. Reduction factors  $R$  of up to eight were used for the calculated (accelerated) Transmit SENSE RF pulses [7].

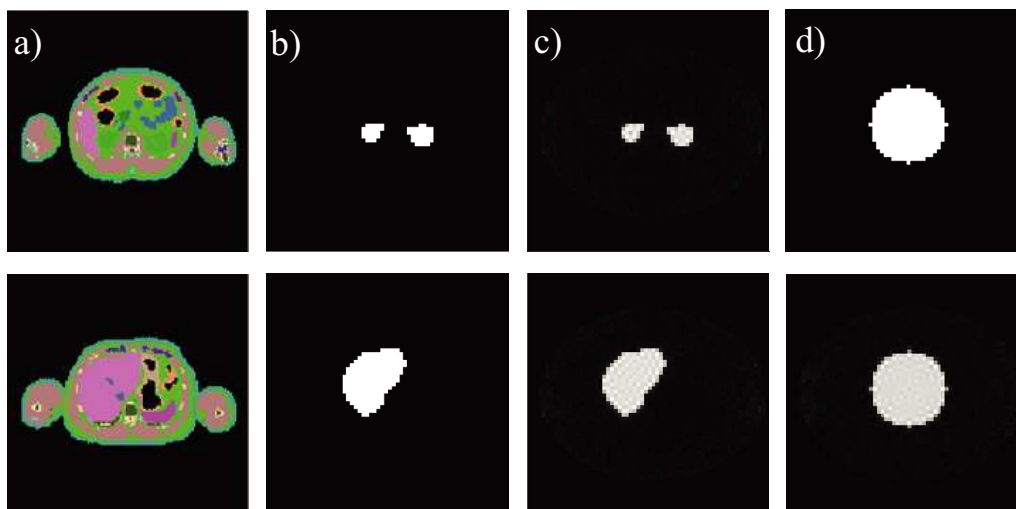


Figure 2: Selected transversal slices of the bio-mesh with color-coded material properties. (a) Target- (b) and calculated excitation pattern (Bloch-simulation) (c) of the kidneys (top) and liver (bottom). (d) Disc target- (top) and calculated (bottom) excitation pattern.

The experiments were carried out on an integrated 3T MRI prototype system [11], based on a 3T Achieva system (Philips Healthcare, The Netherlands), which is equipped with an eight-channel body coil. For the SAR verification experiments [12], the coil was loaded with a homogeneous cuboid phantom ( $h = 10$  cm,  $w = 20$  cm,  $l = 30$  cm), which was filled with a lipid-doped  $H_2O$ -NaCl-TX150 (Oil Center Research, USA) solution ( $\sigma = 0.5$  S/m,  $\epsilon_r = 78$ ). The heating experiments were carried out using two of the eight transmit coil elements of the body coil and a phase deviation of  $0^\circ$  and  $180^\circ$  between the elements. The temperature was measured using a 4-channel fiber optic probe (Luxtron790, Santa Clara, CA) and an IR-camera (Vario-THERM, JENOPTIC, Jena, Germany).

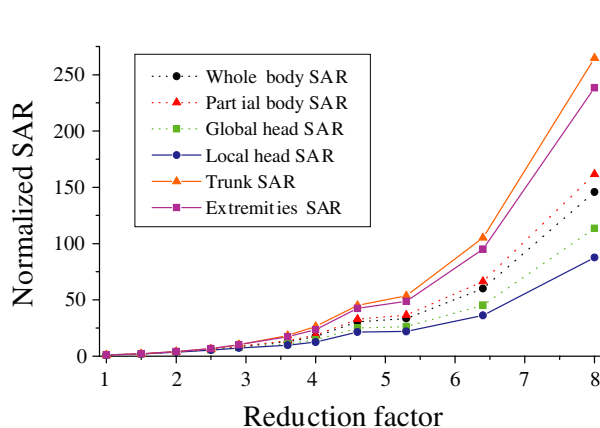


Figure 3: Normalized SAR for the local excitation pattern of the kidneys.

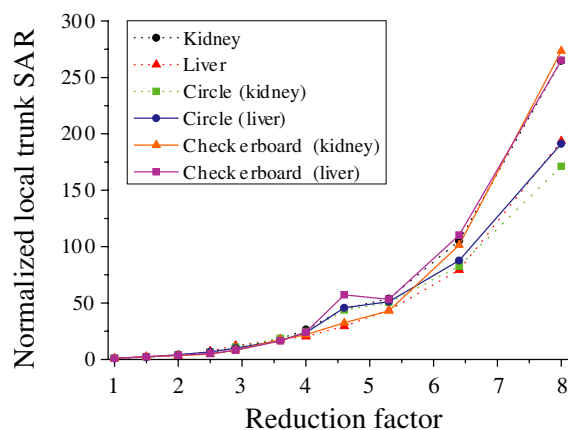


Figure 4: Normalized local trunk SAR for several different excitation patterns.

### 3. RESULTS AND DISCUSSION

In Fig. 3, the global and local SAR is shown for the local excitation pattern of the kidneys using the iterative spatial domain approach. The SAR increases about with the square of the reduction factor,

for lower  $R$  up to six. For higher  $R$ , an even higher increase is observed. With increasing  $R$ , the spacing between the spiral revolutions in k-space increases. Its relation with the desired excitation pattern seems to have a significant impact on the pulse energy and SAR. In Fig. 4, the normalized local trunk SAR is shown for different excitation patterns. For the different local excitation patterns investigated, a rather small variability can be observed for smaller  $R$ , which becomes larger with increasing  $R$ . Thus, the SAR depends on the excitation patterns as well as the reduction factors for whole body Transmit SENSE applications. Moreover, it strongly depends on additional boundary conditions, e.g., the selected k-space trajectory [8], the regularization parameter, and the coil geometry [13]. Fig. 5 shows the results of SAR simulations for global whole body and local torso SAR for the local excitation patterns of the kidneys for a reduction factor  $R$  of up to 8. For all cases, the SAR optimized algorithm outperforms the algorithm without SAR optimization. However, the improvement becomes smaller with increasing  $R$ , as the degrees of freedom decrease that can be deployed for SAR reduction. For a reduction factor equal to the number of coils ( $R = 8$ ) both algorithms yield the same SAR because the solution is unique.

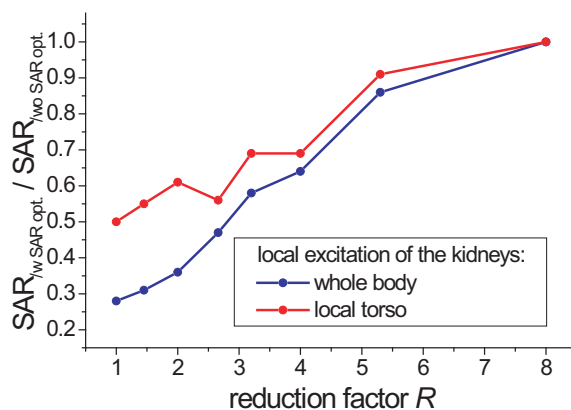


Figure 5: SAR ratio of the two different algorithms (conjugate-gradient method vs. SAR optimized) for local excitation of the kidneys for global whole body and local torso SAR.

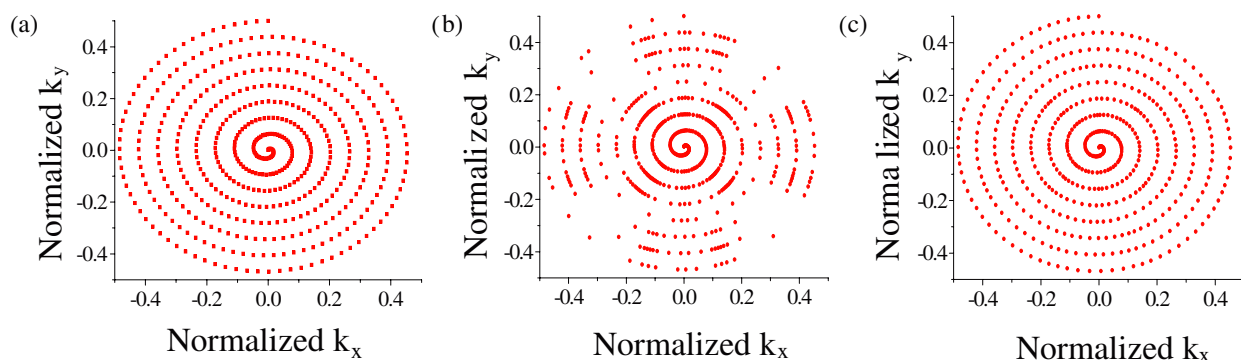


Figure 6: Comparison of (a) the standard trajectory for a 2D spatially selective RF pulse for  $R = 2$ , (b) The corresponding k-space filtered and VERSE adapted trajectory, and (c) the VERSE trajectory with limited gradient and slew rate.

An alternative SAR reduction technique, such as VERSE, represents a method to reduce the SAR for Transmit SENSE pulses by adaptation of the k-space trajectory. In turn, the peak RF amplitudes can be reduced leading to a lower pulse power as well as SAR. The VERSE trajectory is determined before the calculation of the RF pulse to stabilize Transmit SENSE calculation due to the very high amplitude and phase variations of consecutive RF samples. Fig. 6(a) shows the initial trajectory of a 2D spatially selective RF pulse, Fig. 6(b) shows the trajectory, which is optimized via k-space filtering and VERSE, and Fig. 6(c) shows a gradient amplitude  $G$  and slew rate  $S$  limited trajectory ( $G_{\max} = 40$  mT/m,  $S_{\max} = 140$  mT/m/s).

Figure 7 shows the RF amplitudes for a selected RF channel corresponding to the three k-space trajectories (Figs. 7(a)–(c)). For an unlimited slew rate, compared to a slew rate reserve of 25%

with a reduction factor of  $R = 2$ , the peak suppression is reduced from a factor of 11.8 to a factor of 4.2. For this example, the pulse power was reduced by a factor of 1.49, the global SAR by 1.51, and the local SAR by 1.59.

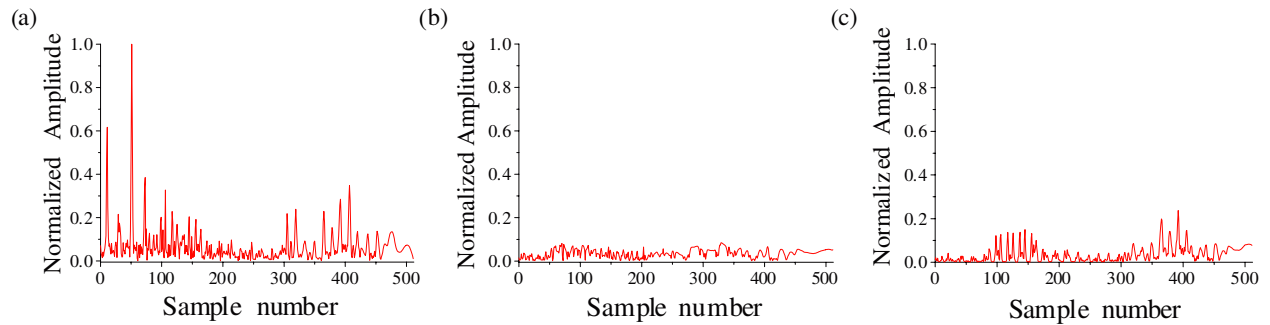


Figure 7: Comparison of the RF amplitude for a 2D spatially selective RF pulse for  $R = 2$ . (a) The ideal trajectory, (b) The corresponding k-space filtered and VERSE adapted trajectory, and (c) VERSE trajectory with limited gradient amplitude and slew rate.

The  $B_{1+}$  distribution can be measured in MRI systems via  $B_1$ -mapping [14]. However, the electric field distribution is unknown and cannot easily be obtained. In a homogeneous cuboid phantom experiment, the temperature distribution, which corresponds to the electric field distribution, was obtained via FDTD simulation for the given phantom. A high correlation between the spatial distribution of simulated SAR and the temperature measurements was obtained (see Fig. 8).

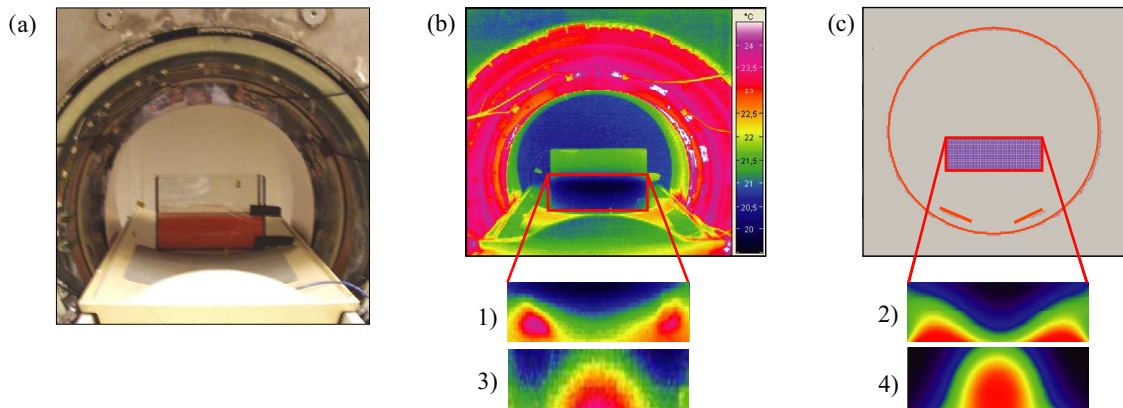


Figure 8: Experimental phantom setup located in the MBC of the MRI system. (a) Photo of the setup, (b) Thermal image and (c) simulation. Spatial SAR distribution simulation 2) & 4) and measured temperature 1) & 3) after heating the phantom with constant amplitudes and  $0^\circ$  phase difference (1 & 2) and  $180^\circ$  phase difference (3 & 4).

#### 4. CONCLUSIONS

SAR strongly depends on the excitation pattern and reduction factor used in whole body Transmit SENSE applications. Furthermore, it strongly depends on additional boundary conditions, e.g., the selected k-space trajectory [8], the regularization parameters, and the coil geometry [13]. SAR reduction techniques, as, e.g., VERSE [9,10] or SAR optimized RF pulse design [5–7], are an interesting possibility in reducing the RF pulse power and in turn the SAR for parallel transmission.

A good correlation between the experimental RF induced temperature changes and SAR simulations was obtained, confirming that the FDTD method can be considered as a valuable tool in determining (local) SAR for patient safety in multi-channel transmission MRI systems.

#### ACKNOWLEDGMENT

The authors would like to thank Z. Zhai and M. Morich, Philips Healthcare, Cleveland, USA, C. Collins, The Penn State College of Medicine, Hershey, USA, and C. vd. Berg and B. vd. Bergen, University Medical Center Utrecht, The Netherlands, for discussions and support.

## REFERENCES

1. Vernickel, P., P. Röschmann, C. Findeklee, K. M. Luedeke, C. Leussler, J. Overweg, U. Katscher, I. Graesslin, and K. Schuenemann, "Eight-channel transmit/receive body MRI coil at 3 T," *Magn. Reson. Med.*, Vol. 58, No. 2, 381–389, 2007.
2. National Library of Medicine, "Visible human male," <http://www.nlm.nih.gov>, 1996.
3. IEEE Std C95.3-2002, "IEEE recommended practice for measurements and computations of radio frequency electromagnetic fields with respect to human exposure to such fields, 100 KHz–300 GHz," *Inst. of Electrical and Electronics Eng.*, 2002.
4. Graesslin, I., U. Katscher, F. Schweser, M. Niemann, and P. Börnert, "Iterative solution of transmit SENSE using a conjugate gradient method," *Proc. Intl. Soc. Mag. Reson. Med.*, 2470, Toronto, USA, May 2006.
5. Grissom, W. A., C.-Y. Yip, Z. Zhang, V. Stenger, J. A. Fessler, and D. C. Noll, "A spatial domain method for the design of RF pulses in multi-coil parallel excitation," *Proc. Intl. Soc. Mag. Reson. Med.*, 3015, Toronto, USA, May 2006.
6. Zhu, Y., "RF power deposition and "g-factor" in parallel transmit," *Proc. Intl. Soc. Mag. Reson. Med.*, 599, Toronto, USA, May 2006.
7. Katscher, U., P. Börnert, C. Leussler, and J. S. van den Brink, "Transmit SENSE," *Magn. Reson. Med.*, Vol. 49, No. 1, 144–150, 2003.
8. Conolly, S., D. G. Nishimura, A. Macovski, and G. Glover, "Variable-rate selective excitation," *J. Magn. Reson.*, Vol. 78, 440–458, 1988.
9. Graesslin, I., S. Biederer, F. Schweser, K.-H. Zimmermann, U. Katscher, and P. Börnert, "SAR reduction for parallel transmission using VERSE and k-space filtering," *Proc. Intl. Soc. Mag. Reson. Med.*, 674, Berlin, Germany, May 2007.
10. Wu, X., C. Akgun, J. T. Vaughan, K. Ugurbil, and P.-F. van de Moortele, "SAR reduction in transmit SENSE using adapted excitation k-space trajectories," *Proc. Intl. Soc. Mag. Reson. Med.*, 673, Berlin, Germany, May 2007.
11. Graesslin, I., P. Vernickel, J. Schmidt, C. Findeklee, P. Röschmann, C. Leussler, P. Haaker, K. Laudan, K. M. Luedeke, J. Scholz, S. Buller, J. Keupp, P. Börnert, H. Dingemans, G. Mens, G. Vissers, K. Blom, N. Swennen, J. van der Heijden, L. Mollevanger, P. Harvey, and U. Katscher, "Whole body 3 T MRI system with eight parallel RF transmission channels," *Proc. Intl. Soc. Mag. Reson. Med.*, 129, Toronto, USA, May 2006.
12. Graesslin, I., K. Falaggis, S. Biederer, D. Glaesel, P. Vernickel, P. Röschmann, C. Leussler, A. Thran, Z. Zhai, M. Morich, and U. Katscher, "SAR simulations and experiments for parallel transmission," *Proc. Intl. Soc. Mag. Reson. Med.*, 1090, Berlin, Germany, May 2007.
13. Katscher, U., J. Röhrs, and P. Börnert, "Basic considerations on the impact of the coil array on the performance of transmit SENSE," *MAGMA*, Vol. 18, No. 2, 81–88, 2005.
14. Yarnykh, V. L., "Actual flip-angle imaging in the pulsed steady state: A method for rapid three-dimensional mapping of the transmitted radiofrequency field," *Magn. Reson. Med.*, Vol. 57, No. 1, 192–200, 2006.

# Hypercapnia-induced Changes in Loss Tangent at Microwave Frequencies

G. Jerome Beers<sup>1,2,3</sup>, Y. Iris Chen<sup>1,2</sup>, Kenneth K. Kwong<sup>1,2</sup>  
Giorgio Bonmassar<sup>1,2</sup>, Leonardo Angelone<sup>1,2,4</sup>, and Jerome L. Ackerman<sup>1,2</sup>

<sup>1</sup>Athinoula A. Martinos Center for Biomedical Imaging, USA

<sup>2</sup>Department of Radiology, Massachusetts General Hospital, USA

<sup>3</sup>Department of Radiology, Brigham and Women's Hospital, USA

<sup>4</sup>Department of Biomedical Engineering, Tufts University, USA

## 1. INTRODUCTION

Prior authors have used *in situ* probes to demonstrate changes in permittivity-related parameters at microwave frequencies associated with changes in blood flow, ischemia, and death [1–4]. We have previously described changes in reflection coefficient from 100 to 3000 MHz associated with cerebral blood flow (via hypercapnia) and death (via administration of KCl) in a pilot study in which a coaxial probe was directly applied to exposed rat skulls [5]. In order to express the prior data more in terms of the inherent electrical properties of tissue, we now present change in loss tangent ( $\tan \delta$ ) as a response to onset and cessation of hypercapnia.

## 2. TECHNIQUE

A probe, modified from semirigid coaxial cable was fashioned to be applied to exposed calvarium of rats. The outer conductor terminated as a ground-plate. The inner conductor protruded  $\sim 0.6$  mm beyond it. Both were gold-plated.

Following general anesthesia with  $\sim 1\%$  halothane or isoflurane (in 1 : 1  $O_2$  :  $N_2O$ ) ventilation and local analgesia, intravenous and intra-arterial femoral catheters were placed, and the calvarium of adult male Sprague-Dawley rats, was exposed. A small hole was drilled to or just through the inner table of the calvarium overlying the parietal cortex. The probe was connected to a HP/Agilent 4191A vector network analyzer, and  $S_{11}$  1-port calibration was performed. The probe was then immobilized with the inner conductor fitting into the drilled hole and the ground-plate (outer conductor) firmly applied to the outer table of the calvarium. During the experiment the rat was in a stereotactic frame, the contact site was kept wet with saline, and a heat bath applied to maintain body temperature. There were 15 total hypercapnic episodes (1–3 per rat, lasting 1.98 to 4.85 minutes) during which 33%  $CO_2$  was administered. Arterial  $pCO_2$  was measured before, during, and after each hypercapnic episode: mean ( $\pm$  SD)  $pCO_2 = 133.8$  ( $\pm 23.2$ ) during hypercapnia; 48.5 ( $\pm 7.9$ ) baseline. Euthanasia was with overdose with intravenous KCl injection during anesthesia.

The complex reflection coefficient at 51 frequencies from 100 to 3000 MHz was measured continuously every  $\sim 2.4$  sec from soon after application of the probe until after death. Later,  $\tan \delta$  was calculated for each of 7 selected frequencies (100, 506, 1028, 1492, 2014, 2420, and 3000 MHz). In a number of cases the baseline drifted considerably before, after, and presumably during hypercapnia. Therefore baseline drift correction was performed using linear regression of a baseline defined as consisting of 4 minutes' data up until hypercapnia and 1 minute's data beginning 1 minute after its cessation. The baseline-corrected values ( $=$  " $\tan \delta_{\text{corrected}}$ ") were used for further data analysis. The time course of  $\tan \delta_{\text{corrected}}(t)$  was normalized to the value at the start of hypercapnia ( $t = 0$ ) (i.e.,  $(|\tan \delta_{\text{corrected}}(t) - \tan \delta_{\text{corrected}}(0)|) / \tan \delta_{\text{corrected}}(0)$ ). Effect of hypercapnia was calculated by comparing the time course of the final  $\tan \delta$  values during hypercapnia and baseline periods using student t-test (two-tailed with equal-variance).

## 3. RESULTS

A nearly immediate effect of hypercapnia (both its onset and its cessation) on calculated  $\tan \delta$  was often readily apparent. An example in which there was no appreciable baseline drift is given in Figure 1.

However, averaging baseline-corrected values and comparing them to baseline or  $t = 0$  values was often helpful. For example, a clear-cut effect was frequently not obvious at 3000 MHz, which

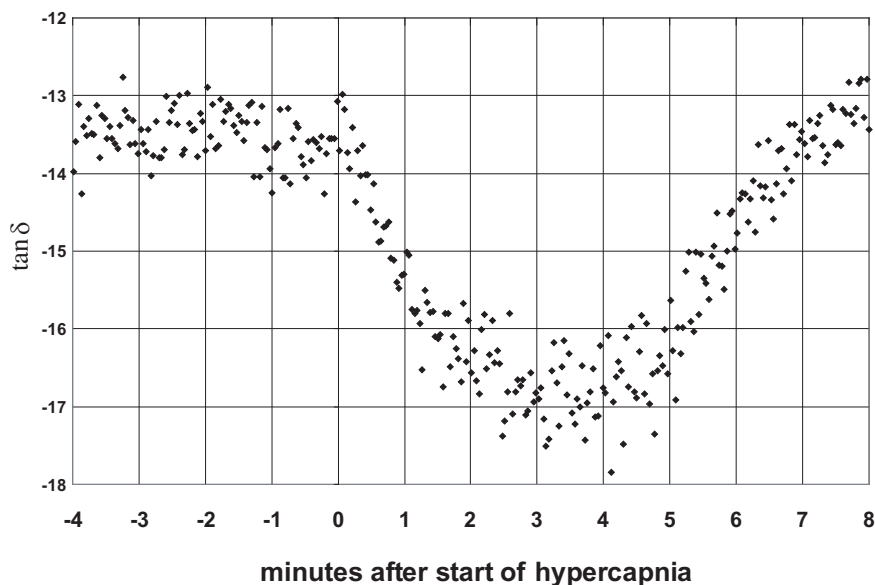


Figure 1: Uncorrected  $\tan \delta$  vs. time — hypercapnic lasts 4.35 minutes (a single hypercapnic episode, 506 MHz)

typically yielded some of the noisiest data. Yet Figure 2, which shows the results of a 31-point moving average of pooled data from all 15 hypercapnic events at 3000 MHz, clearly demonstrates an effect. (At other frequencies the appearance of averaged pooled data was similar, or more pronounced.)

Statistical analysis for the effect of hypercapnia was done by comparing the normalized  $\tan \delta_{corrected}(t)$  during the first  $\sim 1.98$  minutes of hypercapnia to  $\sim 1.98$  minutes of baseline values immediately preceding hypercapnia. Of the 105 cases analyzed (7 frequencies  $\times$  15 episodes), 78% of the cases showed increased  $\tan \delta$  (baseline corrected and normalized) in response to hypercapnia, and 65% of the cases reached a statistically significance ( $p < 0.05$ ). Of these statistically significant

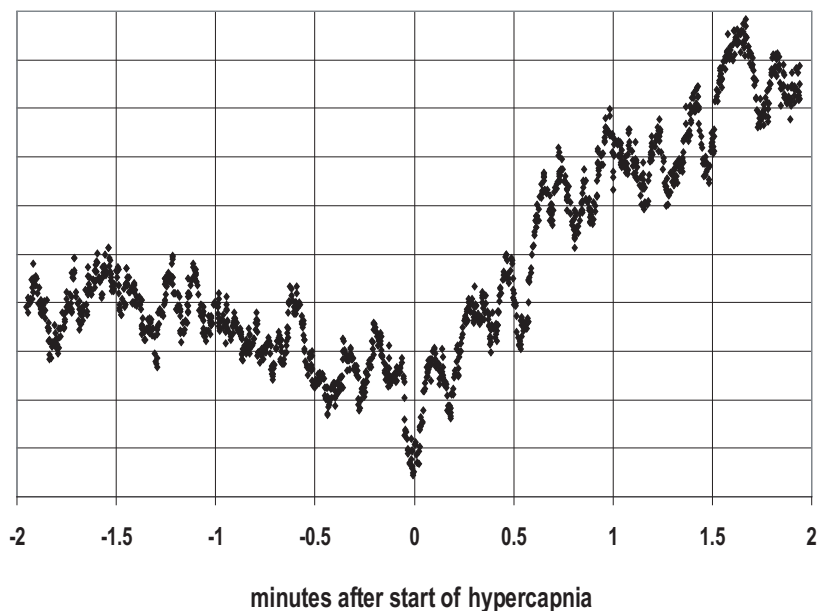


Figure 2: 31-point moving average of pooled baseline-corrected data from all 15 episodes at 3000 MHz. Unprocessed data from this frequency from a single hypercapnic episode often did not show unambiguous effects.

$$y\text{-axis: } (|\tan \delta_{corrected}(t) - \tan \delta_{corrected}(0)|) / \tan \delta_{corrected}(0)$$

cases, the increased  $\tan \delta$  values were maintained 90% of the time during hypercapnia. Statistical analysis has not been performed on effects of cessation of hypercapnia, but prompt changes in measured  $\tan \delta$  were repeatedly seen to occur soon after hypercapnia stopped (as in Figure 1).

#### 4. DISCUSSION

A change in measured  $\tan \delta$  occurred almost immediately when hypercapnia was started, and again soon after it was stopped. Depending on the particular frequency studied, and on the hypercapnic event, the change varied from being obvious (such as in Figure 1) to being but more commonly the former. Frequently, however, the response to hypercapnia was unambiguous even without data processing, particularly after the group analysis. Statistical analysis confirmed the change to hypercapnia from baseline status in the majority of cases. The cause or causes of variability of results is unknown. Noise may be one explanation. Especially the small minority of cases in which there was a significant difference between  $|\tan \delta_c - \tan \delta_c(t = 0)|$  values from before onset of hypercapnia and those after, employment of linear baseline correction in the face of nonlinear baseline drift might have played a role. Also, the baseline physiologic status presumably varied from rat to rat, and perhaps within a single experiment if physiology changed by anesthesia, or with accumulated stress from repetition of hypercapnia. Limitations of this pilot study include that we do not know the sampled volume, and its tissue composition. Thus we do not know whether or to what extent the results reflect changes in brain, or merely dilatation of meningeal vessels, or perhaps changes in sampled cerebrospinal fluid volume caused by expansion/contraction of brain. We have focussed on changes in measured  $\tan \delta$  values rather than in their accuracy. We have not yet calculated relative permittivity and conductivity to determine how they might change with hypercapnia. Nevertheless the results confirm that the technique can be used to monitor physiological changes with rather high temporal resolution. Also, these results, like those obtained at the time of death [3], suggest that physiological changes in permittivity may affect RF/MW SAR, though it is unclear that such changes would be meaningful physiologically. Finally, these results, like others, hold open the eventual possibility of permittivity-based physiologic imaging [4].

#### REFERENCES

1. Burdette, E. C., P. G. Friederich, R. L. Seaman, and L. E. Larsen, "In situ permittivity of canine brain: regional variations and postmortem changes," *IEEE Trans. Microwave Theory Tech.*, Vol. 34, No. 1, 38–49, 1986.
2. Burdette, E. C., F. L. Cain, and J. Seals, "In-situ tissue permittivity at microwave frequencies: perspective, techniques, results," *Medical Applications of Microwave Imaging*, L. E. Larsen, J. H. Jacobi, eds. IEEE Press, 18–40, 1986.
3. Schmid, G., G. Neubauer, U. M. Illievich, and F. Alesch, "Dielectric properties of porcine brain tissue in the transition from life to death at frequencies from 800 to 1900 MHz," *Bioelectromagnetics*, Vol. 24, No. 6, 413–22, 2003.
4. Semenov, S. Y., R. H. Svenson, V. G. Posukh, A. G. Nazarov, Y. E. Sizov, A. E. Bulyshev, A. E. Souvorov, W. Chen, J. Kasell, and G. P. Tatsis, "Dielectrical spectroscopy of canine myocardium during acute ischemia and hypoxia at frequency spectrum from 100 kHz to 6 GHz," *IEEE Trans Med Imaging*, Vol. 21, No. 6, 703–7, Jun. 2002.
5. Beers, G. J., Y. I. Chen, K. K. Kwong, G. Bonmassar, and J. L. Ackerman, "Monitoring intracranial hypercapnea-provoked changes in the rat with permittivity-based measurements (0.1 GHz to 3.0 GHz): A pilot study (abstr)," 35, *BioEM*, 2005.

# Self-organized Propagation of Spatiotemporal Dissipative Solitons in Saturating Nonlinear Media

V. Skarka<sup>1</sup> and N. B. Aleksić<sup>2</sup>

<sup>1</sup>Laboratoire POMA, UMR 6136 CNRS, Université d'Angers  
2, Boulevard Lavoisier, Angers 49045, Cedex 1, France

<sup>2</sup>Institute of Physics, Pregrevica 118, Belgrade 11000, Serbia

**Abstract**— Light bullets as localized self-organized spatiotemporal dissipative structures are studied from the point of view of propagation and stability. Experimental conditions involve consideration of asymmetric inputs. Squeezed input optical pulse evolves toward stable dissipative light bullet, whenever its dissipative parameters belong to the established domain of stability. Such a domain of attraction is found following an extension of our analytical stability criterion confirmed by numerical simulations. Stable and robust dissipative light bullets are generated during a self-organizing propagation due to the cross compensation of various linear and nonlinear effects.

Ultra-short optical pulses have a variety of applications in modern physics and technology. Among them are: optical communication systems, solid-state spectroscopy, ultra-cold atom studies, optical memory devices, quantum computers and various security devices. It is desirable that pulses are not only extremely short in length but also have high power. Developing powerful ultra-short pulse generating devices is crucial for all these applications. High-power ultra-short pulses generated in optics using laser systems are self-shaped in saturating nonlinear media due to the compensation of diffraction and dispersion by nonlinearity and essentially are solitons [1]. Optical solitons may soon become the principal carrier in telecommunication in all-optical transmission lines because they propagate long distances without changing shape [2]. Spatiotemporal solitons are good candidates in all-optical signal processing since they are self-guided in bulk media carrying big power for a small dissipated energy [3]. Stable operation of laser systems, closely related to the issue of dissipative soliton stability, is crucial for practical purposes [4]. Dynamics of dissipative solitons can be described by the complex cubic-quintic Ginzburg-Landau equation (CQGLE) which is nonintegrable and can be solved only numerically [5]. However, an analytical approach, even though approximate, is needed in order to guide simulations and to avoid tedious numerical computations necessary to determine the stability domain point by point [6, 7]. In a recent publication [8] we used the variational method extended to dissipative systems, to establish this stability domain of parameters for spherically symmetric input pulses with radius  $r = \sqrt{x^2 + y^2 + t^2}$  imposing a constraint to independent transverse space ( $x$  and  $y$ ) and time ( $t$ ) variables. In order to meet experimental conditions [9], for instance, a pulse have to be squeezed in order to be injected in optical guide, we study in the present work the generation of dissipative solitons from inputs with no spherical symmetry. Therefore, (3 + 1)-dimensional complex cubic-quintic Ginzburg-Landau equations for the normalized field envelope  $E$ , describes separately diffractions following  $x$  and  $y$  coordinates and anomalous group velocity dispersion in time  $t$  without such a constraint.

$$i \frac{\partial E}{\partial z} - i\delta E + (1 - i\beta) \left( \frac{\partial^2 E}{\partial x^2} + \frac{\partial^2 E}{\partial y^2} + \frac{\partial^2 E}{\partial t^2} \right) + (1 - i\varepsilon)|E|^2 E + (\nu - i\mu)|E|^4 E = 0. \quad (1)$$

In order to prevent the wave collapse the saturating nonlinearity is required [6, 7]. As a consequence, cubic and quintic nonlinearity have to have opposite signs, i.e., parameter  $\nu$  is negative. The stability of the pulse background involves the linear loss, thus the parameter  $\delta$  must be negative [8]. Parameters  $\varepsilon$  and  $\mu$  are associated respectively with cubic gain and quintic loss terms. The parabolic gain ( $\beta > 0$ ) is taken also with respect to each transverse coordinate separately. The prerequisite for generation of a completely confined spatiotemporal structure, the dissipative light bullet, is a simultaneous balance of diffraction and dispersion with self-focusing and gain with loss.

In order to generalize variational approach to asymmetric conditions, we construct for Eq. (1) the total Lagrangian  $\mathbb{L} = \mathbb{L}_c + \mathbb{L}_Q$  that contains a conservative part

$$\mathbb{L}_c = \frac{i}{2} \left( E \frac{\partial E^*}{\partial z} - E^* \frac{\partial E}{\partial z} \right) + |\partial E / \partial x|^2 + |\partial E / \partial y|^2 + |\partial E / \partial t|^2 - \frac{|E|^4}{2} - \frac{\nu |E|^6}{3}, \quad (2)$$

and a dissipative part

$$\mathbb{L}_Q = i\delta |E|^2 + i\frac{\varepsilon|E|^4}{2} + i\frac{\mu|E|^6}{3} - i\beta \left( |\partial E/\partial x|^2 + |\partial E/\partial y|^2 + |\partial E/\partial t|^2 \right). \quad (3)$$

The independent treatment of all three transverse coordinates involves an asymmetric trial function

$$E = A \exp \left[ i \left( Cx^2 + Gy^2 + St^2 + \Psi \right) - \frac{x^2}{2X^2} - \frac{y^2}{2Y^2} - \frac{t^2}{2T^2} \right] \quad (4)$$

as functional of amplitude  $A$ , temporal ( $T$ ) and spatial ( $X$  and  $Y$ ) pulse widths, anisotropic wave front curvatures  $C$  and  $G$ , chirp  $S$ , and phase  $\Psi$ . Each of these functions of the independent variable  $z$  is optimized giving one of eight Euler-Lagrange equations. Within variational approximation, to the partial differential CQGLE corresponds a set of eight coupled first order differential equations (FODE) resulting from the variations in unequal widths.

$$\frac{dX}{dz} = 4CX - \frac{\varepsilon A^2}{R^2 B^2} X - \frac{\mu A^4}{R^2 B^4} X + \frac{\beta}{X} - 4\beta X^3 C^2 = \mathbb{X}, \quad (5)$$

$$\frac{dY}{dz} = 4CY - \frac{\varepsilon A^2}{R^2 B^2} Y - \frac{\mu A^4}{R^2 B^4} Y + \frac{\beta}{Y} - 4\beta Y^3 G^2 = \mathbb{Y}, \quad (6)$$

and

$$\frac{dT}{dz} = 4CT - \frac{\varepsilon A^2}{R^2 B^2} T - \frac{\mu A^4}{R^2 B^4} T + \frac{\beta}{T} - 4\beta T^3 S^2 = \mathbb{T}, \quad (7)$$

asymmetric wave front curvatures

$$\frac{dC}{dz} = -4C^2 + \frac{1}{X^4} - \frac{1}{R^2 B^2} \frac{A^2}{X^2} - \frac{\nu}{R^2 B^4} \frac{A^4}{X^2} - 4\frac{\beta}{X^2} C = \mathbb{C}, \quad (8)$$

$$\frac{dG}{dz} = -4G^2 + \frac{1}{Y^4} - \frac{1}{R^2 B^2} \frac{A^2}{Y^2} - \frac{\nu}{R^2 B^4} \frac{A^4}{Y^2} - 4\frac{\beta}{Y^2} G = \mathbb{G}, \quad (9)$$

and

$$\frac{dS}{dz} = -4S^2 + \frac{1}{T^4} - \frac{1}{R^2 B^2} \frac{A^2}{T^2} - \frac{\nu}{R^2 B^4} \frac{A^4}{T^2} - 4\frac{\beta}{T^2} S = \mathbb{S}, \quad (10)$$

amplitude

$$\frac{dA}{dz} = A \left( \delta + \frac{7\varepsilon}{2R^2 B^2} A^2 + \frac{3\mu}{R^2 B^4} A^4 - \frac{\beta}{X^2} - \frac{\beta}{Y^2} - \frac{\beta}{T^2} - 2C - 2G - 2S \right) = \mathbb{A}, \quad (11)$$

and phase

$$\frac{d\Psi}{dz} = -\frac{1}{X^2} - \frac{1}{Y^2} - \frac{1}{T^2} + \frac{7}{2R^2 B^2} A^2 + \nu \frac{3}{R^2 B^4} A^4 + 2\beta C + 2\beta G + 2\beta S = \mathbb{\Omega} \quad (12)$$

where  $B = 3^{5/4}/2^{7/4}$  and  $R = 8/3^{5/4}$ . For convenience reasons, all dissipative parameters, considered as small, are divided by  $\delta_o = |\delta|$ :  $\varepsilon_o = \varepsilon/\delta_o$ ,  $\mu_o = \mu/\delta_o$ , and  $\beta_o = \beta/\delta_o$ . The exact steady state solutions are obtained from Eqs. (5)–(11) for zero derivatives of amplitude, widths, and curvatures with respect to  $z$ . The only possible steady state solutions are symmetric with equal widths  $X = Y = T$  and curvatures  $C = G = S$ . In the dissipative case the power  $P = A^2XYT$  is no longer a constant [6–8]. However, in steady state the power  $P_o = (\sqrt{\pi}RB^2)^3 A_o^{-1} (A_o^2 B^2 + \nu A_o^4)^{-3/2}$ , the width  $X_o = RB^2 (A_o^2 B^2 + \nu A_o^4)^{-1/2}$ , and the propagation constant  $\Omega = 2^{-7/2} A_o^2$  depend, up to  $\theta = \max(\delta_o, |\varepsilon|, |\mu|, |\beta|)$ , only on the amplitude as in the conservative case [6, 7]. Variationally obtained family of conservative steady state solutions reduces to a fixed double solution for a given set of dissipative parameters. Indeed, the steady state amplitude has two discrete values  $A^+$  and  $A^-$ . A double solution ( $A^- > A^+$ ) exists for a cubic gain ( $\varepsilon_o > 0$ ) and a quintic loss ( $\mu_o < 0$ ) in the  $(\varepsilon_o, \mu_o)$ -domain between parabola and straight line in Fig. 1. The striking difference with conservative systems is the negative wave front curvature  $C_o = 3^{-5/2} 2^{-1} \delta_o A_o^2 [(\varepsilon_o - \beta_o) B^2 + (\mu_o - \nu \beta_o) A_o^2]$  [6–8].

In order to become a soliton a steady state solution must be stable. Our stability criterion based on the variational approach and the method of Lyapunov's exponents, has to be generalized for

non spherically symmetric conditions [8]. In steady state (*st*), right hand sides of Eqs. (5)–(11) are differentiated with respect to amplitude (e.g.,  $\mathbb{A}_A$ ), widths (e.g.,  $\mathbb{S}_Y$ ), and curvatures (e.g.,  $\mathbb{X}_C$ ) in order to construct a Jacoby matrix. The steady state solutions of seven coupled FODE are stable if and only if the real parts of solutions  $\lambda$  of equation  $(\lambda^3 + a\lambda^2 + b\lambda + c)(\lambda^2 + d\lambda + e) = 0$  are non positive [10]. That is fulfilled when the Hurwitz's conditions are satisfied. The stability criterion for steady state solutions of CQGLE is explicitly expressed up to  $\theta$  as

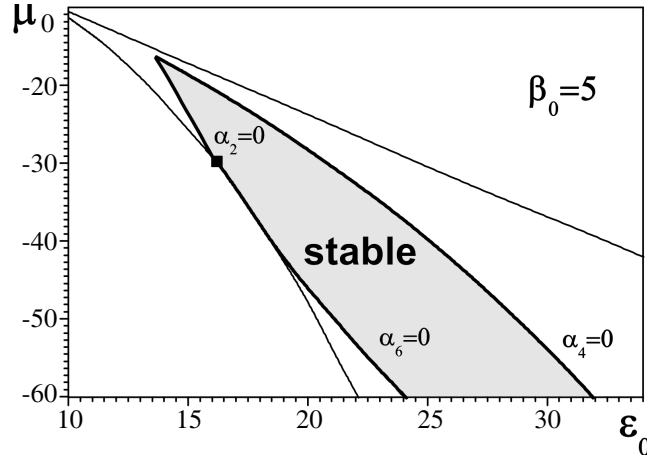


Figure 1: Stability domain of solutions.

$$b = (\mathbb{A}_A \mathbb{X}_X + \mathbb{A}_A \mathbb{C}_C + \mathbb{X}_X \mathbb{C}_C - 3\mathbb{A}_C \mathbb{C}_A - 3\mathbb{C}_C \mathbb{X}_A - 3\mathbb{X}_C \mathbb{C}_X)_{st} > 0, \quad (13)$$

$$c = (\mathbb{A}_A (\mathbb{X}_C \mathbb{C}_X - \mathbb{X}_X \mathbb{C}_C) + 3\mathbb{A}_X (\mathbb{C}_C \mathbb{X}_A - \mathbb{C}_A \mathbb{X}_C) + 3\mathbb{A}_C (\mathbb{X}_X \mathbb{C}_A - \mathbb{C}_X \mathbb{X}_A))_{st} > 0, \quad (14)$$

$$d = -(\mathbb{X}_X + \mathbb{C}_C)_{st} > 0, \quad (15)$$

$$e = (\mathbb{X}_X \mathbb{C}_C - \mathbb{X}_C \mathbb{C}_X)_{st} > 0, \quad (16)$$

and  $f = ab - c > 0$ , where  $a = -(\mathbb{A}_A + \mathbb{X}_X + \mathbb{C}_C)_{st}$ . As a consequence, in the  $(\epsilon_o, \mu_o)$ -domain

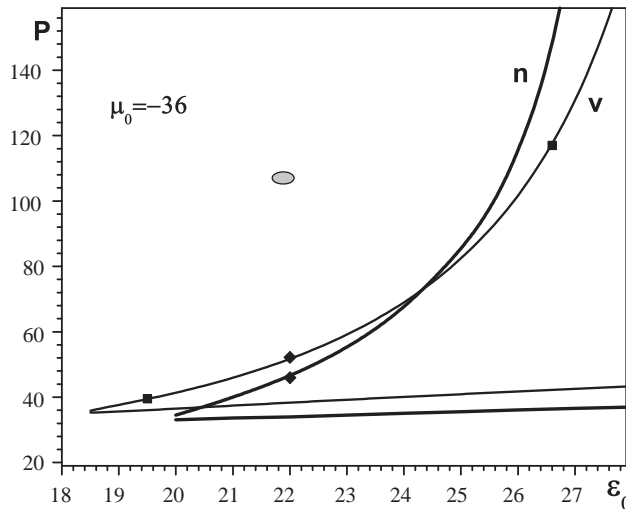


Figure 2: Upper stable and lower unstable branch of variational (*v*) and numerical (*n*) curves.

in Fig. 1 only  $A^-$  solution is stable in the shaded region between curves  $\alpha_2 = 0$ , and  $\alpha_6 = 0$  (separated by a square), as well as  $\alpha_4 = 0$  obtained from Eqs. (5)–(11) solved parametrically. Input pulse chosen in the stable domain of parameters, i.e., on the upper stable branch of the variationally obtained bifurcation curve *v* in Fig. 2, is not yet a light bullet. This curve is only a good approximation of exact bifurcation curve *n* obtained by numerical solving of Eq. (1). For illustration, let us take as an input for numerical simulations the stable solution  $A^-$  for the set of

dissipative parameters  $\delta_o = 0.01$ ,  $\varepsilon_o = 22$ ,  $\mu_o = -36$ ,  $\nu = -1$ , and  $\beta_o = 5$  labeled by a diamond on the upper branch  $v$  which is stable between squares. The triangle labeling the corresponding  $A^+$  solution is on the lower unstable branch. During the evolution the pulse will self-organize into a dissipative light bullet. Therefore, the diamond will reach the stable branch of the curve  $n$ . This exact soliton solution of CQGLE is an attractor for each of input pulses corresponding to the same set of dissipative parameters from established domain of stability. It is worthwhile to stress that even very squeezed input pulse, like the ellipsoid, far from bifurcation curves in Fig. 2, is trapped shrinking towards the stable dissipative soliton. The movie of numerical simulations demonstrates self-stabilizing dynamics of such an ellipsoidal input shown in Fig. 3. Analytically established domain of attraction (shaded in Fig. 1) is confirmed by numerical simulations of Eq. (1). Establishing of such a large domain of stability can be useful for tuning experiments.

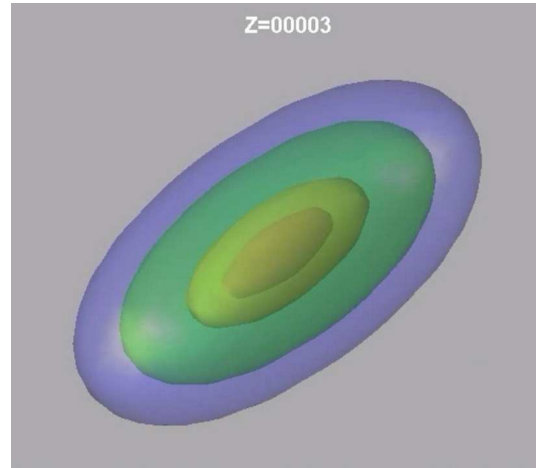


Figure 3: Numerical evolution of an asymmetric input pulse towards a stable dissipative light bullet.

Therefore, we demonstrated that light bullets are exceptionally stable and robust dissipative self-organized structures due to the cross compensation between the loss, the gain, and the excess of the saturating nonlinearity that is a consequence of negative curvature. Consequently, light bullets appear to be the best candidate for carrying the information that has to be treated in all-optical logic circuits. In order to guide light by light saturating nonlinear materials are needed. Following our recent measurements of organic materials, polydiacetylene *para*-toluene sulfonate (PTS) exhibits large cubic — quintic saturating nonlinearity. As a consequence, either imbedded in porous silicon nanocomposites [11] or as bulk, PTS may be promising for elaboration of reconfigurable guides. Light bullets during their propagation modify nonlinear properties of the sample, inducing a guideable network. Modification of bullets timing and paths reconfigures the guide altering its geometry in real time.

The atmosphere exhibits saturating nonlinearity too. A laser pulse having above critical power is self-focused due to focusing Kerr nonlinearity of the air. Therefore, the intensity of the field is increasing and the plasma is generated due to multiphoton (or tunneling) ionization of neutral molecules. The plasma acts as a defocusing medium suppressing field blow up. A balance between the nonlinear focusing and plasma defocusing results in self-guiding solitons. In contrast to the non-singular beams, the dynamics of beams with nonzero topological charge is more robust leading to vortex solitons. A laser beam with phase singularity, i.e., with vortex structure contributes in general, if not to suppress the breakup of ring into modulation instability induced filaments, at least to distribute filaments symmetrically around the singularity in order to conserve the angular momentum. Hence, a vortex structure prevents chaotic filamentation so often observed in powerful laser beams without singularity. We demonstrated the possibility of filaments coalescence that seems to be related with the attraction to the equilibrium vortex soliton state [12]. These observations can be used for controlled triggering of lightning discharge, lightning protection, remote sensing, and long distance air communications. The lightning, is itself a self-organizing phenomenon based on the self-focusing without blow up, hence, it may be related to dissipative solitons.

The opportunity to treat in synergy analytically and numerically asymmetric input pulses propagation toward stable and robust dissipative light bullets, opens possibilities for diverse practical applications including experiments.

**ACKNOWLEDGMENT**

Work at the Institute of Physics is supported by the Ministry of Science of the Republic of Serbia, under the project OI 141031. This research has been in part supported by French-Serbian cooperation, CNRS/ MSCI agreement No. 20504.

**REFERENCES**

1. Kivshar, Yu. S. and B. A. Malomed, *Rev. Mod. Phys.*, Vol. 61, 763, 1989.
2. Gabitov, I. and S. K. Turitsyn, *Opt. Lett.*, Vol. 21, 327, 1996.
3. Mihalache, D., et al., *Phys. Rev. Lett.*, Vol. 97, 073904, 2006.
4. Chen, C.-J., P. K. A. Wai, and C. R. Menyuk, *Opt. Lett.*, Vol. 19, 198, 1994.
5. Akhmediev, N. N. and A. A. Ankiewicz, *Solitons, Nonlinear Pulses and Beams*, Chapman and Hall, London, 1997.
6. Skarka, V., V. I. Berezhiani, and R. Miklaszewski, *Phys. Rev. E*, Vol. 56, 1080, 1997.
7. Skarka, V., V. I. Berezhiani, and R. Miklaszewski, *Phys. Rev. E*, Vol. 59, 1270, 1999.
8. Skarka, V. and N. B. Aleksic, *Phys. Rev. Lett.*, Vol. 96, 013903, 2006.
9. Liu, X., L. J. Qian, and F. W. Wise, *Phys. Rev. Lett.*, Vol. 82, 4631, 1999.
10. Nicolis, G. and I. Prigogine, *Self-organization in Nonequilibrium Systems*, John Wiley and Sons, New York, 1977.
11. Simos, C., L. Rodriguez, V. Skarka, X. Nguyen Phu, N. Errien, G. Froyer, T. P. Nguyen, P. Le Rendu, and P. Pirastesh, *Phys. Stat. Sol. (C)*, Vol. 2, 3232, 2005.
12. Skarka, V., N. Aleksić, and V. I. Berezhiani, *Phys. Lett. A*, Vol. 319, 317, 2003.

# Light Scattering by Human Erythrocyte: Different Shape Models

Elena Eremina<sup>1</sup> and Natalia Grishina<sup>2</sup>

<sup>1</sup>University of Bremen, Badgasteiner Str. 3, Bremen 28359, Germany

<sup>2</sup>Moscow Lomonosov State University, Lenin's Hills, Moscow 119991, Russia

**Abstract**— The Discrete Sources Method is applied to model the human erythrocyte. Several shape models are investigated. The influence of the incident wavelength on the scattering characteristics is discussed.

## 1. INTRODUCTION

Light scattering by blood cells is recently of great interest both in mathematical modeling and in practical applications. In particular, studying of light scattering by erythrocytes is a suitable method for detection of some blood diseases. Between other blood cells, erythrocyte has an advantage for modeling, as it demonstrates no internal structure and can be modeled as homogeneous object with a certain refractive index. In the same time it has some features, which complicate modeling, such as relatively large size and complicated biconcave shape. To simplify erythrocyte modeling often classical shapes of oblate discs and spheroids are used to approximate a real shape.

During the last years different simulation methods have been applied to this problem: Finite Difference Time Domain (FDTD), Discrete Dipole Approximation (DDA), Multipole Multiple Technique (MMP), T-matrix and many others. Some of these methods are not applicable to the real biconcave shape of erythrocyte, others are rather time consuming, and some methods are restricted to small dimensions. Between others the Discrete Sources Method (DSM) looks very attractive, as it allows accounting for the axial symmetry of the particle and the polarization of an incident excitation, which sufficiently reduces the time of computations. Besides, the DSM allows calculation of all the incident angles and polarizations at once [1] unlike volume-based methods, such as DDA and FDTD. Additionally the DSM gives opportunity to control the accuracy of obtained results by surface residual estimation. The DSM outlines are given in the next part of the paper.

In this work the DSM is applied to investigate the influence of the incident wavelength for different shape models of erythrocyte.

## 2. METHOD OUTLINES

Consider scattering in an isotropic homogeneous medium in  $R^3$  of an electromagnetic wave by a local homogeneous penetrable obstacle  $D_i$  with a smooth boundary. Let us introduce a cylindrical coordinate system  $(z, \theta, \varphi)$  where  $z$  is the axis of symmetry of the particle and  $\theta_i$  is an incident angle with respect to  $z$ . Then the mathematical statement of the scattering problem can be formulated in the following form

$$\nabla \times \mathbf{H}_{e,i} = jk\varepsilon_{e,i}\mathbf{E}_{e,i}, \quad \nabla \times \mathbf{E}_{e,i} = -jk\mu_{e,i}\mathbf{H}_{e,i} \quad \text{in } D_{e,i}, \quad D_e := R_3/\overline{D_i}, \quad (1)$$

$$\mathbf{n}_P \times (\mathbf{E}_i(P) - \mathbf{E}_e(P)) = \mathbf{n}_P \times \mathbf{E}^0(P), \quad \mathbf{n}_P \times (\mathbf{H}_i - \mathbf{H}_0) = \mathbf{n}_P \times \mathbf{H}^0(P), \quad P \in \partial D \quad (2)$$

and Silver-Muller radiation conditions for the scattered field at infinity.

Here  $\{\mathbf{E}^0, \mathbf{H}^0\}$  is an exciting field,  $\mathbf{n}_P$  is the outward unit normal vector to  $\partial D$ , index  $e$  belongs to the external domain  $D_e$ ,  $k = \omega/c$ ,  $\varepsilon, \mu$  are permittivity and permeability,  $\text{Im}\varepsilon_e, \mu_e \leq 0$  (time dependence for the fields is chosen as  $\exp\{j\omega t\}$ ) and the particle surface is smooth enough  $\partial D \in C^{(1,\alpha)}$ . Then the above boundary-value problem is uniquely solvable.

The DSM is based on the conception of an approximate solution. The approximate solution is constructed as a finite linear combination of Discrete Sources (DS): dipoles and multipoles deposited in a supplementary domain inside the particle with certain amplitudes. Usually as such a domain the axis of symmetry of the particle is used. In case of an oblate particle like erythrocyte, disk or oblate spheroid it is not always possible to use the axis of symmetry [3]. For this purpose an analytical continuation to a complex plane is constructed. More detailed information can be found in [4]. The deposition of DS in a complex plane allows reducing calculation errors and time of computations.

In case of  $P$ -polarized plane wave the exciting field accepts the following form:

$$\begin{aligned}\mathbf{E}^0 &= (\mathbf{e}_x \cos \theta_0 + \mathbf{e}_z \sin \theta_0) \exp \{-jk_e (x \sin \theta_0 - z \cos \theta_0)\} \\ \mathbf{H}^0 &= -\mathbf{e}_y \cos \theta_0 \exp \{-jk_e (x \sin \theta_0 - z \cos \theta_0)\},\end{aligned}$$

where  $k_e = k\sqrt{\varepsilon_e \mu_e}$ .

To take into account the polarization of the external excitation we use linear combinations of electrical and magnetic multipoles. For this special vector potentials are used. For the  $P$ -polarized wave in a cylindrical coordinate system they can be represented as:

$$\begin{aligned}\mathbf{A}_{mn}^{1,e,i} &= \{Y_m^{e,i}(\eta, w_n^{e,i}) \cos(m+1)\varphi; -Y_m^{e,i}(\eta, w_n^{e,i}) \sin(m+1)\varphi; 0\}, \\ \mathbf{A}_{mn}^{2,e,i} &= \{Y_m^{e,i}(\eta, w_n^{e,i}) \sin(m+1)\varphi; Y_m^{e,i}(\eta, w_n^{e,i}) \cos(m+1)\varphi; 0\}, \\ \mathbf{A}_n^{3,e,i} &= \{0; 0; Y_0^{e,i}(\eta, w_n^{e,i})\}.\end{aligned}\quad (3)$$

Here  $Y_m^e(\eta, w_n^e) = \frac{k_e}{i} h_m^{(2)}(k_e R_{\eta w_n^e}) \left(\frac{\rho}{R_{\eta w_n^e}}\right)^m$ ,  $Y_m^i(\eta, w_n^i) = j_m(k_i R_{\eta w_n^i}) \left(\frac{\rho}{R_{\eta w_n^i}}\right)^m$ ,  $R_{\eta w_n^e}^2 = \rho^2 + (z - w_n^e)^2$ ,  $\eta = (\rho, z)$ ,  $h_m^{(2)}$  is a spherical Hankel function and  $j_m$  is a spherical Bessel function.

Hence, the approximate solution for the  $P$ -polarized wave accepts the form:

$$\begin{aligned}\begin{pmatrix} \mathbf{E}_{e,i}^N \\ \mathbf{H}_{e,i}^N \end{pmatrix} &= \sum_{m=0}^M \sum_{n=1}^{N_m^c} \left\{ p_{mn}^{e,i} \mathbf{D}_1 \mathbf{A}_{mn}^{1,e,i} + q_{mn}^{e,i} \frac{j}{\varepsilon_c} \mathbf{D}_2 \mathbf{A}_{mn}^{2,e,i} \right\} + \sum_{n=1}^{N_0^c} r_n^{e,i} \mathbf{D}_1 \mathbf{A}_n^{3,e,i}; \\ \mathbf{D}_1 &= \begin{pmatrix} \frac{j}{k\varepsilon_{e,i}\mu_{e,i}} \nabla \times \nabla \times \\ -\frac{j}{\mu_{e,i}} \nabla \times \end{pmatrix}, \quad \mathbf{D}_2 = \begin{pmatrix} \frac{1}{\varepsilon_{e,i}} \nabla \times \\ \frac{j}{k\varepsilon_{e,i}\mu_{e,i}} \nabla \times \nabla \times \end{pmatrix}.\end{aligned}\quad (4)$$

The approximation solution for the case of a  $S$ -polarized excitation is constructed in a similar way and has the form:

$$\begin{pmatrix} \mathbf{E}_{e,i}^N \\ \mathbf{H}_{e,i}^N \end{pmatrix} = \sum_{m=0}^M \sum_{n=1}^{N_m^c} \left\{ p_{mn}^{e,i} \mathbf{D}_1 \mathbf{A}_{mn}^{1,e,i} + q_{mn}^{e,i} \frac{j}{\varepsilon_c} \mathbf{D}_2 \mathbf{A}_{mn}^{2,e,i} \right\} + \sum_{n=1}^{N_0^c} r_n^{e,i} \mathbf{D}_2 \mathbf{A}_n^{3,e,i}\quad (5)$$

where the vector potentials have forms:

$$\begin{aligned}\mathbf{A}_{mn}^{1,e,i} &= \{Y_m^{e,i}(\eta, w_n^{e,i}) \sin(m+1)\varphi; Y_m^{e,i}(\eta, w_n^{e,i}) \cos(m+1)\varphi; 0\}, \\ \mathbf{A}_{mn}^{2,e,i} &= \{Y_m^{e,i}(\eta, w_n^{e,i}) \cos(m+1)\varphi; -Y_m^{e,i}(\eta, w_n^{e,i}) \sin(m+1)\varphi; 0\}, \\ \mathbf{A}_n^{3,e,i} &= \{0; 0; Y_0^{e,i}(\eta, w_n^{e,i})\}.\end{aligned}\quad (6)$$

More details can be found in [4].

The constructed approximate solutions (4), (5) satisfy Maxwell equations (1) and radiation conditions for the scattered fields at infinity. The unknown vector of amplitudes of DS

$$\mathbf{P}_m = \{p_{mn}^{e,i}, q_{mn}^{e,i}, r_n^{e,i}\}_{n=1}^{N_m^c},$$

is to be determined from the transmission conditions (2). As it was mentioned above, DS are situated in a complex plane adjoined to the symmetry axis of the particle. The approximate solutions (4) and (5) are finite linear combinations of Fourier harmonics with respect to the  $\varphi$  angle variable. Therefore, after resolving the plane wave excitation into Fourier series with respect to the  $\varphi$  angle we reduce the two-dimensional approximation problem enforced at the particle surface to a set of 1-dimensional problems at the particle generatrix. For solving these problems the General Matching-Point Technique is applied, more details can be found in [5].

The accuracy of the result is provided by stabilization of the scattering diagram and a-posteriori residual calculation.

After DS amplitudes have been determined the far-field pattern  $\mathbf{F}(\theta, \varphi)$  can be computed as:

$$\frac{\mathbf{E}(\mathbf{r})}{|\mathbf{E}^0(\mathbf{r})|} = \frac{\exp(-jk_e r)}{r} \mathbf{F}(\theta, \varphi) + o\left(\frac{1}{r}\right), \quad \text{where } r \rightarrow \infty\quad (7)$$

The components of the vector  $\mathbf{F}(\theta, \varphi)$  can be found in [2].

For experimental studies of blood cells Scanning Flow Cytometers (SCF) are used. The SCF permits measurements of the angular dependency of light scattering intensity in an angle range from 5 to 100 degrees. The design and basic principles of the SCF are described in [6]. The output signal of the SCF is proportional to the following combination of Mueller matrix elements [7]:

$$I_s(\theta) = \int_0^{2\pi} (S_{11}(\theta, \varphi) + S_{14}(\theta, \varphi)) d\varphi. \quad (8)$$

The Mueller matrix elements are connected with far-field pattern elements [8] and can be easily computed as a combination of elementary functions [2].

Another important light scattering characteristic we consider in our paper is the differential scattering cross-section (DSC), which can be calculated on the base of far-field pattern components as follows:

$$\text{DSC}^{P,S} = |F_\theta^{P,S}(\theta, \varphi)|^2 + |F_\varphi^{P,S}(\theta, \varphi)|^2. \quad (9)$$

### 3. NUMERICAL RESULTS

In papers [2,9] different shape models of erythrocyte has been investigated. In this work we concentrated on two of them: the experimental shape model suggested by Skalak, and Cassini ovals based shape. Cassini shape demonstrates relatively good fitting to experimental erythrocyte shape (Skalak) and is easy for modelling. It looks very promising as it can easily be changed by varying of just 3 parameters. Cassini shape can be a good base for development of appropriate shape model of erythrocyte under osmotic lysis, when erythrocyte changes its shape from biconcave one to nearly spherical.

Both models we use here have typical for real erythrocyte biconcave form with overall length of 6.3  $\mu\text{m}$ . The exact equation for Skalak model and parameters for Cassini model we use can be found in [9]. For modelling we took the refractive index of erythrocyte of  $n = 1.4$ . We investigate a typical case, when erythrocyte is immersed in water with refractive index of  $n = 1.33$ .

In many practical investigations of the erythrocyte the wavelength of  $\lambda = 632.8 \text{ nm}$  is used [7]. At the same time, the longer wavelength of  $\lambda = 873 \text{ nm}$  [10] can be more preferable for such investigations. Here we would like to present some exemplary numerical results. In Fig. 1 the simulation results for DCS versus scattering angle for erythrocyte under different wavelengths are presented. With increase of the wavelength the relative size of erythrocyte gets smaller and the number of distinctive maxima and minima gets less. The last fact can efficiently help in experimental data interpretation and for solving of inverse problems. In Fig. 2 numerical results for different erythrocyte shapes under  $\lambda = 873 \text{ nm}$  are presented. Results demonstrate relatively good agreement between both models in the scattering angles area of  $-180^\circ - 120^\circ$ , which is most interesting for practical investigations.

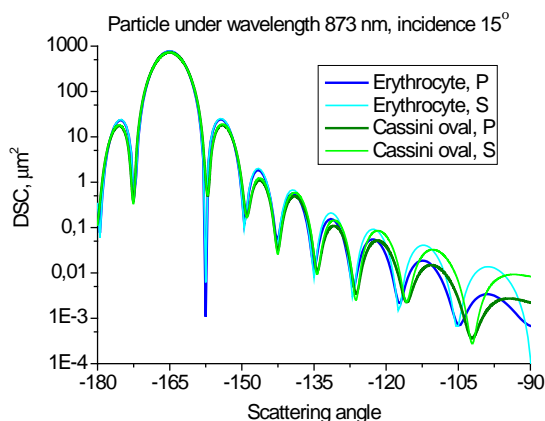


Figure 1: DSC versus scattering angle for different erythrocyte shapes for  $P$  and  $S$  polarizations,  $\lambda = 873 \text{ nm}$ .

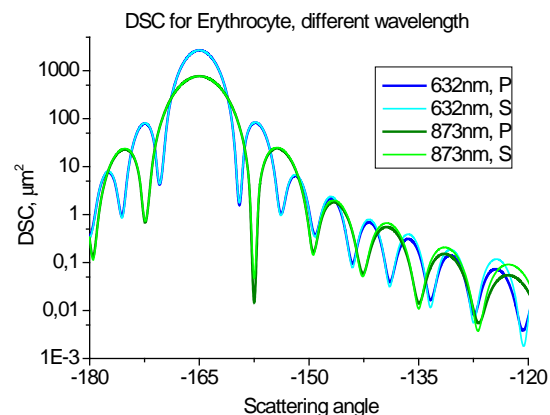


Figure 2: DSC (9) versus scattering angle for erythrocyte under different wavelengths for  $P$  and  $S$  polarizations.

More calculation results will be shown in oral presentation.

#### ACKNOWLEDGMENT

Authors would like to acknowledge financial support of this work by Deutsche Forschungsgemeinschaft (DFG) and the Russian Foundation for Basic Research (RFBR).

#### REFERENCES

1. Eremin, Y. A., “The method of discrete sources in electromagnetic scattering by axially symmetric structures,” *J. Comm. Technology and Electronics*, Vol. 45, No. 2, 269–280, 2000.
2. Eremina, E., J. Hellmers, Y. Eremin, and T. Wriedt, “Different shape models for erythrocyte: Light scattering analysis based on the discrete sources method,” *JQSRT*, Vol. 102, 3–10, 2006.
3. Doicu, A., Y. Eremin, and T. Wriedt, *Acoustic and Electromagnetic Scattering Analysis Using Discrete Sources*, Academic Press, London, 2000.
4. Eremina, E., Y. Eremin, and T. Wriedt, “Analysis of light scattering by different shape models of erythrocyte based on Discrete Sources Method,” *Opt. Comm.*, Vol. 244, 15, 2005.
5. Voevodyn, V. and A. Kuznetsov, “Matrices and calculations,” *Science*, Moscow, 1982 (in Russian).
6. Maltsev, V. P., “Scanning flow cytometry for individual particle analysis,” *Rev. Sci. Instrum.*, Vol. 71, 243, 2000.
7. Maltsev, V. P. and K. A. Semyanov, *Characterisation of Bio-Particles from Light Scattering VSP*, Utrecht, Boston, 2004.
8. Bohren, C. F. and D. R. Huffman, *Absorption and Scattering of Light by Small Particles*, Wiley, New York, 1983.
9. Wriedt, T., J. Hellmers, E. Eremina, and R. Schuh, “Light scattering by the erythrocyte: Comparison of different methods,” *JQSRT*, Vol. 100, 444, 2006.
10. Yilmaz, S., A. Kalkandelen, and N. Isayeva (Mamedova), “Comparison of the T-matrix calculations for erythrocytes with oxygenated hemoglobin and immersed in water,” *Journal of Quantitative Spectroscopy & Radiative Transfer*, Vol. 97, 20–28, 2006.

# An Efficient Space Domain Formulation of the MOM Method for Planar Circuits

Chaker Essid<sup>1</sup>, M. Bassem Ben Salah<sup>1</sup>, Faleh Yassine<sup>1</sup>  
Abdelaziz Samet<sup>1</sup>, and Ammar B. Kouki<sup>2</sup>

<sup>1</sup>URCSE, École Polytechnique de Tunisie, Tunisia

<sup>2</sup>LACIME, École de Technologie Supérieure, Montréal, Canada

**Abstract**— In this paper, we present a new technique for the evaluation of spatial-domain method of moment matrix entries, in conjunction with a DCIM two-level approximation. This technique is based on the Taylor series expansion of the complete expression of each complex image, where the integrands are expressed only by polynomial functions. The MOM matrix elements are again evaluated analytically in an efficient and a fast manner. The proposed technique has been implemented and compared with previous techniques in the analysis of microstrip structure. It has been found to yield considerable computational time savings without compromising the precision.

## 1. INTRODUCTION

The electromagnetic characterization of discontinuities in the printed circuits planar microwaves plays an important role in the design of the digital circuits at high speed and in the integrated circuits monolithic microwave (MMICs: Monolithic micro-wave Integrated Circuits). Indeed, several numerical approaches were developed to determine the characteristics of the planar structures like the Finite Element Method (FEM) [1], the Finite Difference Time Domain (FDTD) [2] and Method of Moments (MOM) in the spatial and spectral domains [3–6]. The mixed potential integral equation (MPIE) in conjunction with the spatial-domain MOM is the best suited and most robust approach for planar circuit analysis. This method is based on the closed-form expression of the Green's functions in the space domain using a finite number of discrete complex images (DCIM) that approximate it in the spectral domain and thus avoid the numerical evaluation of Sommerfeld integrals [7, 8]. Using this representation, the matrix elements that arise in the MOM formulation can be evaluated analytically as proposed in [3, 6] where the closed-form Green's functions expressions were approximated by Taylor series expansions of the exponential terms. The resulting integrals are then evaluated analytically, this gives rise to mathematical functions with singularities requiring special programming precautions [4]. In this paper, we present an efficient and fast method, which is based on a new Taylor series expansion without singularity problems, where entire integrands are expressed in terms of polynomial functions. The proposed technique can be successfully used because it is less time consuming than other techniques in the literature without compromising the precision and the improvement in the computational efficiency is demonstrated for a microstrip structure.

## 2. ANALYTICAL SPATIAL FORMULATION OF THE METHOD OF MOMENT (AS-MOM)-DCIM

In this section, the AS-MOM formulation is applied to microstrip line structure with a dielectric parameter  $\epsilon_r$  and Perfect electric conductor plane. The surface current densities on conductors are expressed as follows:

$$\vec{J}(x, y) = J_x(x, y)\vec{x} + J_y(x, y)\vec{y} \quad (1)$$

where  $J_x(x, y)$  and  $J_y(x, y)$  are decomposed in basis functions. By using the Mixed Potential Integral Equation (MPIE), we can express the tangential electric field on the plane of conductors in terms of the surface current density and Green's functions for the vector  $(G_A^{xx}, G_A^{yy})$  and the scalar  $(G_q)$  potential.

$$\begin{cases} E_x(x, y) = -j\omega\mu G_A^{xx} * J_x + \frac{1}{j\omega\epsilon} \frac{\partial}{\partial x} \left( G_q * \left( \frac{\partial J_x}{\partial x} + \frac{\partial J_y}{\partial y} \right) \right) \\ E_y(x, y) = -j\omega\mu G_A^{yy} * J_y + \frac{1}{j\omega\epsilon} \frac{\partial}{\partial y} \left( G_q * \left( \frac{\partial J_x}{\partial x} + \frac{\partial J_y}{\partial y} \right) \right) \end{cases} \quad (2)$$

$J_x(x, y)$  and  $J_y(x, y)$  in Equation (2) are substituted by their expressions given in Equation (1). The following step in MOM procedure consists in using testing functions leading to a linear system:

$$V_m = \sum_{n=0}^M Z_{mn} I_n \quad m = 1, \dots, M \quad (3)$$

where  $I(x, y)$  is the unknown coefficients.  $V = (V_1, V_2, \dots, V_M)^T$  is the excitation vector, and  $Z_{mn}$  is the impedance reaction between the  $m$ th test function  $J_{xn}$  and the  $n$ th basis function  $J_{xm}$ .

The inner products in MOM matrix are reduced to double integral over finite range by transferring the convolution over basis and testing functions. In this paper, the spatial-domain Green's functions employed in (2) are obtained in closed form using the DCIM two-level approximation described in [7] and they are given by:

$$G_A^{xx}(u, v) = \sum_{i=1}^{M1+1} a_i \frac{e^{-jk_0 r_i}}{r_i} \quad (4)$$

Using this approximation, the integrals correspond to matrix entries of method of moment can be written as the following:

$$\iint \frac{e^{-jk_0 r_i}}{r_i} u^k v^l dudv \quad \text{for } k = 0, \dots, 3, \quad l = 0, 1 \quad (5)$$

These double integrals which are expressed in (5) can be evaluated analytically, Al and Aksun have described in details the analytical evaluation of matrix elements involved in the MOM without any numerical integration, they use the fifth-order Taylor series expansion of the exponential term  $e^{-jk_0 r}$  [3] around  $r_0 = \sqrt{u_0^2 + v_0^2 - S^2}$ . Another approach is presented in [4] based on a new Taylor series expansion of the exponential term  $\frac{e^{-jk_0 r}}{r}$  for larger  $r_0$  without singularity problems and only one level approximation of DCIM is used.

Recently, a two-level approximation of DCIM has been proposed and demonstrated that this approach is very robust and it improves the computational efficiency [8]. So that it is necessary to include this approximation in the evaluation of MOM matrix entries. In this work, we apply the analytical method based on AS-MOM approach developed in [4] in conjunction with the two-level DCIM. The AS-MOM approach is based on the combination of two Taylor series expansion, the first one is for smaller  $r_0$ , we use the evaluation technique in [3] and the second is for the larger  $r_0$  a Taylor series expansion of the exponential term  $\frac{e^{-jk_0 r}}{r}$  is used, when the integrals are given by:

$$\iint u^k v^l dudv \quad \text{for } k = 0, \dots, 8 \quad \text{et } l = 0, \dots, 6 \quad (6)$$

where the term  $\frac{e^{-jk_0 r}}{r}$  is approximated as follows:

$$\frac{e^{-jkr}}{r} = \frac{e^{-jkr_0}}{r_0} \sum_{m+n \leq 5} \beta_{mn} u^m v^n \quad (7)$$

And  $\beta_{mn}$  are the Taylor series coefficients.

### 3. RESULTS AND DISCUSSION

To check the efficiency and the accuracy of our method proposed in this paper, an example is presented. This formulation is applied to a microstrip line, where the dielectric constant of the substrate  $\epsilon_r = 2.33$ ; the thickness of the substrate  $h = 0.79$  mm, the length of the microstrip line  $L = 12$  cm and the chosen frequency  $f = 1$  GHz. Figure 1 shows the magnitude of the current distribution computed using our method and the technique outline in [3]. A good agreement between the two techniques is observed. In order to improve the computational efficiency of our method, the CPU times of evaluation of matrix entries is given in Table 1. We note that our method is about four times faster than the method given in [3] and 60 times faster than numerical integration.

Table 1: CPU times in second for different methods.

Frequency (GHz)	Numerical integration	Technique [3]	AS-MOM 2
1	42	3.01	0.55
5	160	13.73	0.79
10	688	58.64	3.65

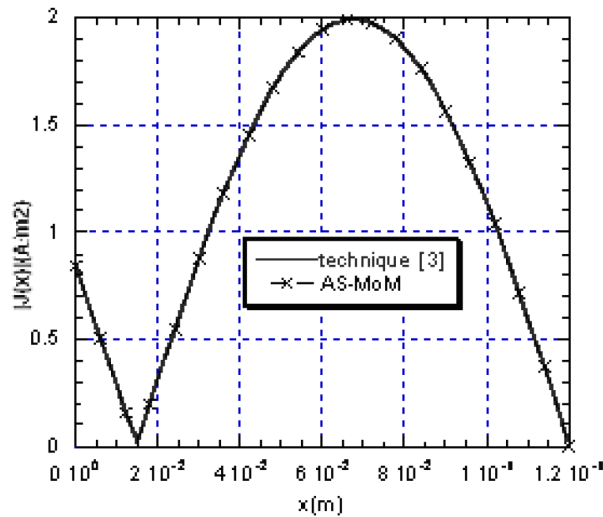


Figure 1: Current distribution on a microstrip line.

#### 4. CONCLUSION

This paper presents an efficient and a fast spatial-domain MOM formulation in conjunction with a two-level approximation of Green's functions for planar microstrip structure analysis. The results obtained from our proposed method improve the computational efficiency without compromising the precision.

#### REFERENCES

1. Ferrari, R. L. and R. L. Naidu, "Finite element modeling of high frequency electromagnetic problems with material discontinuities," *IEEE Proc.*, Vol. 137, 313–320, Nov. 1990.
2. Cherry, P. C. and M. F. Iscandar, "FDTD analysis of high frequency electronic interconnection effects," *IEEE Trans. Microwave Theory Tech.*, Vol. 43, 2445–2451, Oct. 1995.
3. Alatan, L., M. I. Aksun, K. Mahadevan, and M. Tuncay Birand, "Analytical evaluation of the MOM matrix elements," *IEEE Trans. Microwave Theory Tech.*, Vol. 44, No. 4, Apr. 1996.
4. Samet, A. and A. Bouallegue, "Fast and rigorous calculation method for MoM matrix elements in planar microstrip structures," *Electronics Letters*, Vol. 36, No. 9, Apr. 2000.
5. Ge, Y. and K. P. Esselle, "A fast method of moments based on a new closed-form Green's function for microstrip structures," *IEEE Antennas and Propagation Society International Symposium*, 2001.
6. Aksun, M. I., F. Caliskan, and L. Gurel, "An efficient method for electromagnetic characterization of 2-D geometries in stratified media," *IEEE Trans. Microwave Theory Tech.*, Vol. 50, 1264–1274, May 2002.
7. Chow, Y. L., J. J. Yang, D. G. Fang, and G. E. Howard, "A closed-form spatial Green's function for the thick microstrip substrate," *IEEE Trans. Microwave Theory Tech.*, Vol. 39, 588–592, 1991.
8. Aksun, M. I., "A robust approach for the derivation of closed-form Green's function for a general microstrip geometry," *IEEE Trans. Microwave Theory Tech.*, Vol. 44, 651–658, May 1996.

# Scattering from the Flat Strip Geometries in the Layered Medium by Using the Sinc Based Method of Moments

Fadıl Kuyucuođlu<sup>1</sup>, Taner Ođuzer<sup>2</sup>, and İbrahim Avgin<sup>1</sup>

<sup>1</sup>Electrical and Electronics Eng. Department, EGE University, Bornova, İzmır, Turkey

<sup>2</sup>Electrical and Electronics Eng. Department, Dokuz Eylöl University, Buca, İzmır, Turkey

**Abstract**— In this study, we solved the electromagnetic scattering from the strip in the layered medium. The sinc type basis functions are used with their mathematical properties and GPOF technique provides us fast computation of the Green's functions in the layered medium. Therefore we obtain an algebraic matrix equation without using integration instead we used the approximated analytical forms with a specified error criteria like the few digits accuracy in the ordinary MoM.

## 1. INTRODUCTION

One of the popular technique in the electromagnetic scattering problems is Method of the Moments in 2D or in 3D. In this method, the integral equation (IE) is formulated depending on the electromagnetic boundary conditions related with the fields. Then this IE is discretized and the Green's function in the layered medium has to be evaluated efficiently. One of the popular way of this computation of the Green's function in the layered medium is Generalized Pencil of Functions (GPOF). This provides us a fast solution of the IE solution of the MoM [1, 2]

We had already studied the free space case in [3] ad our results were compatible with the given in the previous literature [1, 2]. We also worked on the E polarization case of the strip scattering in the layered medium by using the GPOF technique [4]. The GPOF technique is used in [1] and provides one to compute the Green's function in the layered media without using the complete integrals instead we used the serial solutions with the reasonable truncation level.

In all these mentioned studies in [3] and [4] we used sinc type basis functions in MoM and Galerkin procedure is applied. The application of the sinc function provides us some advantages especially in the numerical integrating. The finite set of sinc functions are independent and orthogonal set. The feature of this set of sinc functions provides some mathematical properties. These can be stated that the convolution of the two sinc function is again a sinc function. Also the infinite integral of sinc function Hankel function is also a Hankel function at the position of the sinc.

However here we approached to the solution using the sinc based MoM in the layered medium as a Galerkin procedure and this case only  $H$ -polarization is studied. Again the GPOF technique is used here to find a closed form expression of the Green's function in the solution process.

The previous studies in [1, 2] the authors also used GPOF but in the MoM procedure they firstly obtain new function from the convolution of the sub domain functions. Then integration over this new function is required. This is the basic condition for the ordinary MoM formulation. But here we found the new sinc function as the convolution of the given two sinc as the basis and testing ones. Then the integrals of this new sinc function can be obtained analytically i.e., Hankel function with a spatial error criteria. Therefore the MoM is reduced to the IE as an algebraic matrix equation not using integration process. Also we can say that the increasing  $W$  i.e., bandwidth of the spatial domain sinc functions, reduces the relative error in the computation of the main matrix elements.

Therefore we can find fast solutions in a few digits accuracy with an available desktop computer. There are some related studies using sinc basis functions in the recent literature but they are not applied to singular problems and the computation of the main matrix elements are not specified.

The present formulation is applied to strip structures in the layered medium. Upper loaded and multi strips inside the multilayer geometries are tested. The surface current densities are obtained and compared with the previous results given in [1] and [2]. The far field scattering also is obtained and basic concepts of the physics are checked.

## 2. FORMULATION

The geometry given in Figure 1 is illuminated by a plane electromagnetic wave. In this geometry, the strip is located at different regions of the two layered media. In Figure 2(a), single strip is located in the upper layer with a height  $z = z_p = h$ . In Figure 2(b), three strips with equal widths

are located inside the slab layer with different heights. The mathematical expressions for the single strip in the layered medium can be given as

$$E_x^{inc}(x) = -j\omega\mu\vec{J}(\vec{r}) * G^A(\vec{r}) + \nabla \left[ \frac{\nabla \cdot \vec{J}(\vec{r})}{j\omega\epsilon} * G^q(\vec{r}) \right] \quad (1)$$

where the above IE given in (1) indicates the required boundary condition. After applying convolution integral and operators to the equation, integral equation takes the form.

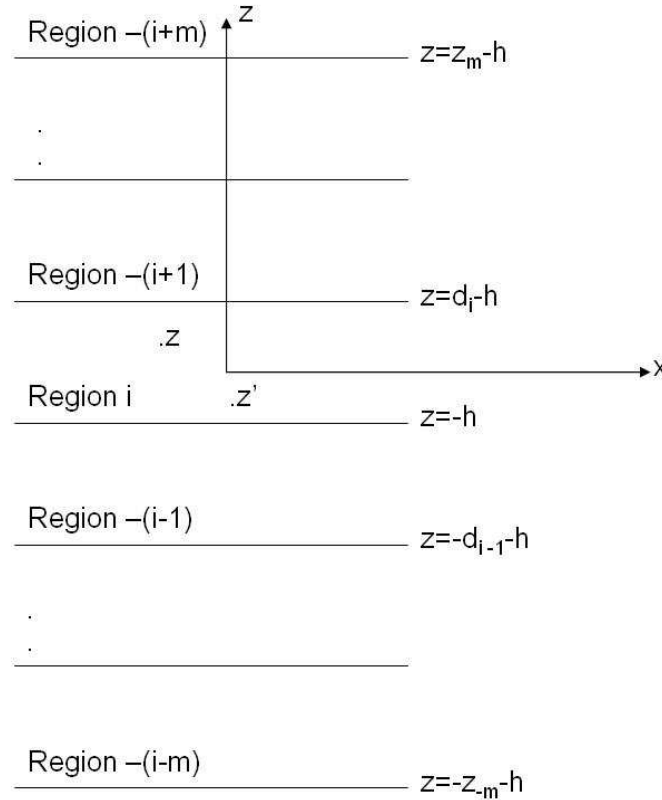


Figure 1.

$$E_x^{in}(x) = \frac{\omega\mu}{4} \int_{-w}^w J_x(x') (4j) G_{yy}^A(k_i|x-x'|) dx' - \frac{1}{4\omega\epsilon} \left( \frac{\partial J_x(x')}{\partial x'} (4j) G_q(k_i|x-x'|) \right) \Big|_{x'=-w}^{x'=w} + \frac{1}{4\omega\epsilon} \int_{-w}^w \frac{\partial^2 J_x(x')}{\partial x'^2} (4j) G_q(k_i|x-x'|) dx' \quad (2)$$

$J_x$  denotes current distribution;  $G^A$  and  $G^q$  are the Green's functions of the layered geometry. The derivatives in (2) are evaluated in the finite difference manner. Unknown current density is approximated by orthogonal sinc functions.

$$J_x(x) = \sum_{n=0}^N a_n \sin c(2Wx - n) \quad (3)$$

$W$  is the bandwidth of the function.  $N$  is number of sample points on the strip. By using current expansion of sinc functions in (2) and then applying test functions to the (2) also, IE equation takes the following matrix form.

$$t_x E_x^{in}(pt_x) = \frac{\omega\mu}{4} t_x [A_{np}] [J_x] - \frac{1}{4\omega\epsilon t_x} [A_{np}^q] [J_x] + \frac{1}{4\omega\epsilon t_x} [\gamma_{np}] [J_x] \quad (4)$$

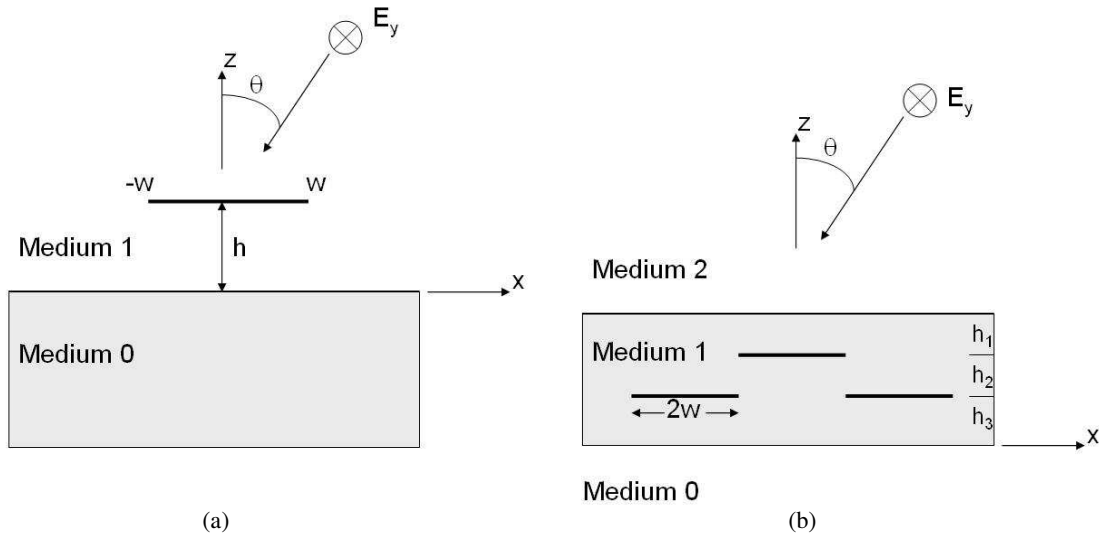


Figure 2. (a)  $2w = 2\lambda_1$  and  $h = 5\lambda_1$ ,  $\epsilon_r = 4$  and  $\theta = 0$ . (b)  $h_1 = h_2 = h_3 = 0.1\lambda_2$ ,  $2w = 0.2\lambda_2$  and  $\epsilon_r = 4$  and  $\theta = 0$ .

In this equation, A matrix can be written as follows,

$$A_{np} = \begin{cases} t_x(4j)G_{yy}^A(k_i|p-n|t_x) & p \neq n \\ \int_{-\infty}^{\infty} \sin c(2Wu - p + n)(4j)G_{yy}^A(k_i R)du & p = n \end{cases} \quad (5)$$

Also  $A^q$  matrix including  $G^q$  can be evaluated as

$$A_{np}^{(q)} = \begin{cases} t_x(4j)G_q(k_i|p-n|t_x) & p \neq n \\ \int_{-\infty}^{\infty} \sin c(2Wu - p + n)(4j)G_q(k_i R)du & p = n \end{cases} \quad (6)$$

In (4), third term can be written as the sum of matrices.

$$\gamma_{np} = \bar{F}_{np} + \bar{G}_{np} \quad (7)$$

where

$$\bar{F}_{np} = [C_p | A_{(n-1)p}^{(q)}] \quad (8)$$

$$\bar{G}_{np} = [A_{(n+1)p}^{(q)} | D_p] \quad (9)$$

Also  $C$  and  $D$  matrix coefficients are given as in (10) and (11)

$$C_p = \int_{-\infty}^{\infty} \sin c(2Wu - p)G_q(k_i |u + w|)du \quad (10)$$

$$D_p = \int_{-\infty}^{\infty} \sin c(2Wu - p)G_q(k_i |u - w|)du \quad (11)$$

### 3. NUMERICAL RESULTS

The presented formulation given above verified by using the following figures. One PC with 3 GHz Pentium processor and desktop software is used. It seen that not too large  $W$  values are required and the results are very close to the ones in the literature [1, 2]. Also at most a few minutes are enough for the computation. Figure 3 shows a that 3 strip in 3 layer geometry and it is almost same with given in [1]. Also in Figure 4(a) and (b) present the far field and surface current that the  $2\lambda$  width and  $5\lambda$  height from the layer surface and the results are given in the figure.

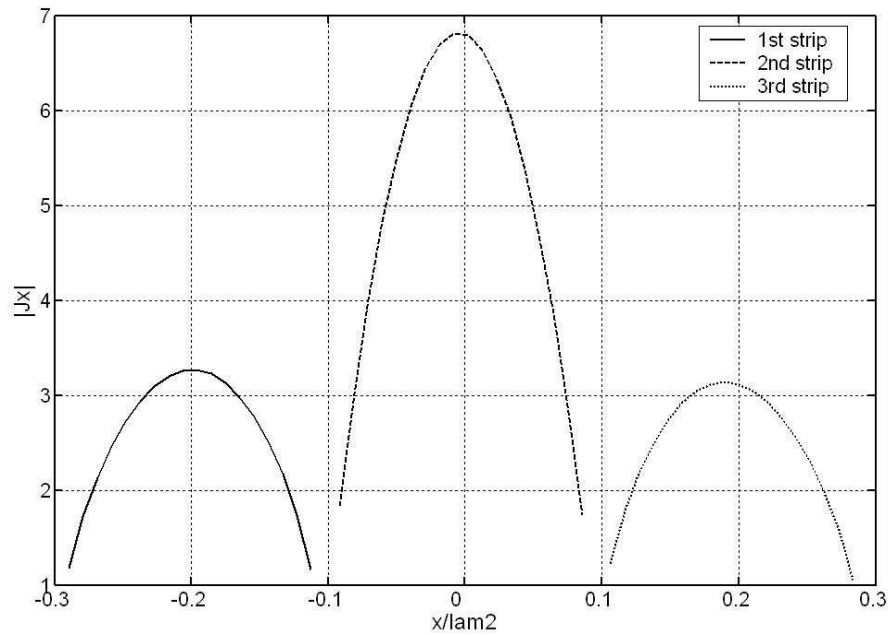


Figure 3.

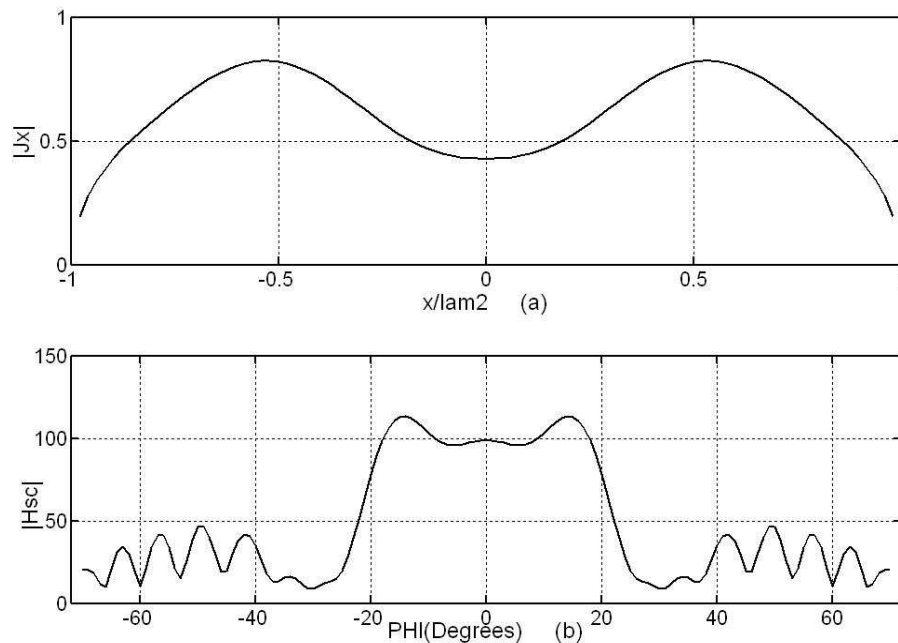


Figure 4.

#### 4. CONCLUSION

In this study, we presented a sinc based MoM formulation and it works in this singular integral equation of the  $H$ -polarization case. The results obtained are verified with the given literature. Also even in the desktop software, it works in a few minutes. The properties of the sinc functions provide us the approximately analytical functions for the main matrix elements. Therefore this reduces the computation time with a given relative error and this error is compatible with the ordinary MoM solutions.

#### REFERENCES

1. Aksun, M. I., F. Çalışkan, and L. Gürel, "An efficient method for electromagnetic characterization of 2-D geometries in stratified media," *IEEE Transactions on MMT*, Vol. 50, No. 5, May 2002.

2. Çalışkan, F., “Efficient methods for electromagnetic characterization of 2-D geometries in stratified media,” MSc thesis submitted to Electrical and Electronics Eng. Department of Bilkent University, August 1997.
3. Oguzer, T. and F. Kuyucuoglu, “Method of moments solution by using sinc type basis functions for the scattering from a finite number of conducting trip grating,” submitted to *Turkish Journal of Electrical Engineering and Computer Sciences*.
4. Oğuzer, T., F. Kuyucuoğlu, and İ. Avgin, “Electromagnetic scattering from strip geometry in the layered medium by the method of moments with the sinc type basis functions,” submitted to *IEEE Transactions on AP*, November 2007.

# Utilizing the Radiative Transfer Equation in Optical Tomography

T. Tarvainen<sup>1,2</sup>, M. Vauhkonen<sup>1</sup>, V. Kolehmainen<sup>1</sup>  
J. P. Kaipio<sup>1</sup>, and S. R. Arridge<sup>2</sup>

<sup>1</sup>Department of Physics, University of Kuopio, P. O. Box 1627, Kuopio 70211, Finland

<sup>2</sup>Department of Computer Science, University College London, Gower Street  
London WC1E 6BT, United Kingdom

**Abstract**— We propose a method which utilizes the radiative transfer equation in optical tomography. In this approach, the radiative transfer equation is used as light propagation model in those regions in which the assumptions of the diffusion theory are not valid and the diffusion approximation is used elsewhere. Both the radiative transfer equation and the diffusion approximation are numerically solved with a finite element method. In the finite element solution of the radiative transfer equation, both the spatial and angular discretizations are implemented in piecewise linear bases.

## 1. INTRODUCTION

In diffuse optical tomography (DOT), images of optical properties of tissues are derived based on measurements of near-infrared light on the surface of the object. The image reconstruction in DOT is a non-linear ill-posed inverse problem. Thus, even small errors in the measurements or modelling can cause large errors in the reconstructions. Therefore, computationally feasible forward models that describe light propagation within the medium accurately are needed.

The radiative transfer equation (RTE) is widely accepted as an accurate model for light propagation in tissues [2]. However, it is computationally expensive, and therefore the most typical approach in DOT has been to use the diffusion approximation (DA) to the RTE as the forward model. The DA is basically a special case of the first order spherical harmonics approximation to the RTE, and thus it has some limitations. Firstly, the medium must be scattering dominated, and secondly, light propagation can not be modelled accurately close to the collimated light sources and boundaries [2].

To overcome the limitations of the diffusion theory, different hybrid methods that combine diffusion approximation with other models have been developed. The radiosity–diffusion model [3] can be used for turbid medium with non-scattering regions. However, it does not model light propagation accurately in low-scattering regions or close to the collimated light sources. Methods which combine Monte Carlo simulation with diffusion theory have also been reported [8, 18]. Monte Carlo is known to describe light propagation accurately. However, it has the disadvantage of requiring a long computation time. Moreover, the hybrid Monte Carlo–diffusion methods often require iterative mapping between the models which increases the computation time even more.

Methods in which the RTE is utilized in DOT by combining it with diffusion theory have been developed. These include the coupled transport and diffusion model [6] and the hybrid radiative transfer–diffusion approach [15] where the transport and diffusion models are coupled and iteratively solved. A coupled RTE–DA model was proposed by the authors in [16]. In the coupled RTE–DA model, the RTE is used as the forward model in sub-domains in which the assumptions of the DA are not valid and the DA is used elsewhere in the domain. The RTE and the DA are coupled through boundary conditions between the sub-domains and they are solved simultaneously using a finite element method (FEM). In this paper, the coupled RTE–DA model is utilized in light transport simulations in realistic two-dimensional (2D) head geometry from a new-born infant's head.

## 2. METHODS

### 2.1. Radiative Transfer Equation

Let  $\Omega \subset \mathbb{R}^n$ ,  $n = 2$  or  $3$  denote the physical domain and  $\partial\Omega$  the boundary of the domain, and let  $\hat{s} \in S^{n-1}$  denote a unit vector in the direction of interest. A widely accepted model for light propagation in tissues is the radiative transfer equation. The frequency domain version of the RTE is of the form

$$\left( \frac{i\omega}{c} + \hat{s} \cdot \nabla + \mu_s + \mu_a \right) \phi(r, \hat{s}) = \mu_s \int_{S^{n-1}} \phi(r, \hat{s}') \Theta(\hat{s} \cdot \hat{s}') d\hat{s}' + q(r, \hat{s}) \quad (1)$$

where  $i$  is the imaginary unit,  $\omega$  is the angular modulation frequency of the input signal,  $c$  is the speed of light in the medium,  $\mu_s$  and  $\mu_a$  are the scattering and absorption coefficients of the medium, respectively,  $\phi(r, \hat{s})$  is the radiance, and  $q(r, \hat{s})$  is the source inside  $\Omega$  [2]. The kernel  $\Theta(\hat{s} \cdot \hat{s}')$  is the scattering phase function which describes the probability that a photon with an initial direction  $\hat{s}'$  will have a direction  $\hat{s}$  after a scattering event. In DOT, we use a vacuum boundary condition for the RTE which assumes that no photons travel in an inward direction at the boundary  $\partial\Omega$ . Including a boundary source  $\phi_0$  at the source position  $\varepsilon_j \subset \partial\Omega$ , the boundary condition can be written as

$$\phi(r, \hat{s}) = \begin{cases} \phi_0(r, \hat{s}), & r \in \cup_j \varepsilon_j, \quad \hat{s} \cdot \hat{n} < 0, \\ 0, & r \in \partial\Omega \setminus \cup_j \varepsilon_j, \quad \hat{s} \cdot \hat{n} < 0, \end{cases} \quad (2)$$

where  $\hat{n}$  is the outward unit normal on  $\partial\Omega$ .

A finite element (FE) solution for the steady-state RTE was derived in [7]. Since then, both the forward and inverse problems have been studied, see e.g., [1, 5, 12]. In the frequency domain, numerical solutions of the RTE have been obtained using finite volume-discrete ordinates method [13], finite element method [15, 17], finite element-spherical harmonics method [19], and finite difference-discrete ordinates method [11]. In this work, the RTE is solved with the FEM. Both the spatial and angular discretizations are implemented in piecewise linear bases.

## 2.2. Diffusion Approximation

In DOT, light propagation in tissues is usually modelled with the diffusion approximation to the RTE. The frequency domain version of the DA is of the form

$$-\nabla \cdot \kappa \nabla \Phi(r) + \mu_a \Phi(r) + \frac{i\omega}{c} \Phi(r) = q_0(r) \quad (3)$$

where  $\kappa = (n(\mu_a + \mu'_s))^{-1}$  is the diffusion coefficient where  $\mu'_s = (1 - g_1)\mu_s$  is the reduced scattering coefficient, and  $g_1$  is the mean of the cosine of the scattering angle,  $\Phi(r) = \int_{S^{n-1}} \phi(r, \hat{s}) d\hat{s}$  is the photon density, and  $q_0(r)$  is a source inside  $\Omega$ . The DA can not satisfy the boundary condition (2). Instead it is often replaced by an approximation that the total inward directed photon current is zero. Further, by taking into account the mismatch between the refractive indices of the medium and surrounding medium, a Robin type boundary condition can be derived. It is of the form

$$\Phi(r) + \frac{1}{2\gamma_n} \kappa A \frac{\partial \Phi(r)}{\partial \hat{n}} = 0, \quad r \in \partial\Omega \quad (4)$$

where  $\gamma_n$  is a dimension-dependent constant which takes values  $\gamma_2 = 1/\pi$  and  $\gamma_3 = 1/4$  and  $A$  is a parameter governing the internal reflection at the boundary  $\partial\Omega$ , with  $A = 1$  for the case of matched refractive index [2, 10]. The light sources at  $\partial\Omega$  are usually modelled in the DA either by the collimated source model or the diffuse boundary source model. In case of the collimated source model, the light source is modelled as an isotropic point source located at a depth  $1/\mu'_s$  below the source site. In case of the diffuse boundary source model, the source is modelled as a diffuse boundary current  $I_s$  at the source position.

The finite element approximation of the DA has been derived in several papers, see e.g., [4]. In this study, the FE-approximation of the DA is constructed similarly as in [15].

## 2.3. Coupled RTE–DA Model

In the coupled RTE–DA model, the domain  $\Omega$  is divided into RTE and DA sub-domains. The RTE is used as a forward model in sub-domain  $\Omega_{\text{rte}}$  in which the assumptions of the DA are not valid. The DA is used as a forward model in sub-domain  $\Omega_{\text{da}}$  which includes the remaining domain. Let  $\partial\Omega_{\text{rte}}$  be the boundary of the domain  $\Omega_{\text{rte}}$ , and  $\partial\Omega_{\text{da}}$  be the boundary of the domain  $\Omega_{\text{da}}$ . Furthermore, let  $\Gamma = \partial\Omega_{\text{rte}} \cap \partial\Omega_{\text{da}}$  denote the interface that separates the sub-domains  $\Omega_{\text{rte}}$  and  $\Omega_{\text{da}}$ . The RTE and DA are coupled through boundary conditions on the interface  $\Gamma$ . For the external boundaries we use the following notations  $\partial\Omega_{\text{rte, out}} = \partial\Omega_{\text{rte}} \setminus \Gamma$  and  $\partial\Omega_{\text{da, out}} = \partial\Omega_{\text{da}} \setminus \Gamma$ . In the frequency domain, the coupled RTE–DA model is of the form

$$\frac{i\omega}{c} \phi(r, \hat{s}) + \hat{s} \cdot \nabla \phi(r, \hat{s}) + (\mu_s + \mu_a) \phi(r, \hat{s}) = \mu_s \int_{S^{n-1}} \Theta(\hat{s} \cdot \hat{s}') \phi(r, \hat{s}') d\hat{s}' + q(r, \hat{s}), \quad r \in \Omega_{\text{rte}} \quad (5)$$

$$\phi(r, \hat{s}) = \begin{cases} \phi_0(r, \hat{s}), & r \in \cup_j \varepsilon_j, \quad \hat{s} \cdot \hat{n} < 0 \\ 0, & r \in \partial\Omega_{\text{rte, out}} \setminus \cup_j \varepsilon_j, \quad \hat{s} \cdot \hat{n} < 0 \end{cases} \quad (6)$$

$$\phi(r, \hat{s}) = \frac{1}{|S^{n-1}|} \Phi(r) - \frac{n}{|S^{n-1}|} \hat{s} \cdot (\kappa \nabla \Phi(r)), \quad r \in \Gamma \quad (7)$$

$$-\nabla \cdot \kappa \nabla \Phi(r) + \mu_a \Phi(r) + \frac{i\omega}{c} \Phi(r) = q_0(r), \quad r \in \Omega_{\text{da}} \quad (8)$$

$$\Phi(r) + \frac{1}{2\gamma_n} \kappa A \frac{\partial \Phi(r)}{\partial \hat{n}} = \begin{cases} \frac{I_s}{\gamma_n}, & r \in \cup_j \varepsilon_j \\ 0, & r \in \partial\Omega_{\text{da, out}} \setminus \cup_j \varepsilon_j \end{cases} \quad (9)$$

$$\Phi(r) = \int_{S^{n-1}} \phi(r, \hat{s}) d\hat{s}, \quad r \in \Gamma. \quad (10)$$

The FE-model for the coupled RTE–DA model was derived in [16] and it was further extended for light propagation in turbid medium with low-scattering and non-scattering regions in [14]. In this study, the FE-calculations are implemented accordingly.

### 3. RESULTS

The coupled RTE–DA model was tested with tissue-like optical properties in a realistic head geometry. The simulations were performed in a 2D segmented image that was done from a magnetic resonance image of a new-born infant head. The 2D head slice is shown in left image of Figure 1. The segmentation consisted of six domains which were: scalp, skull, grey matter, white matter, CSF around the brain, and CSF in ventricles. The optical parameters used in the simulations are given in Table 1. The modulation frequency of the input signal was 100 MHz.

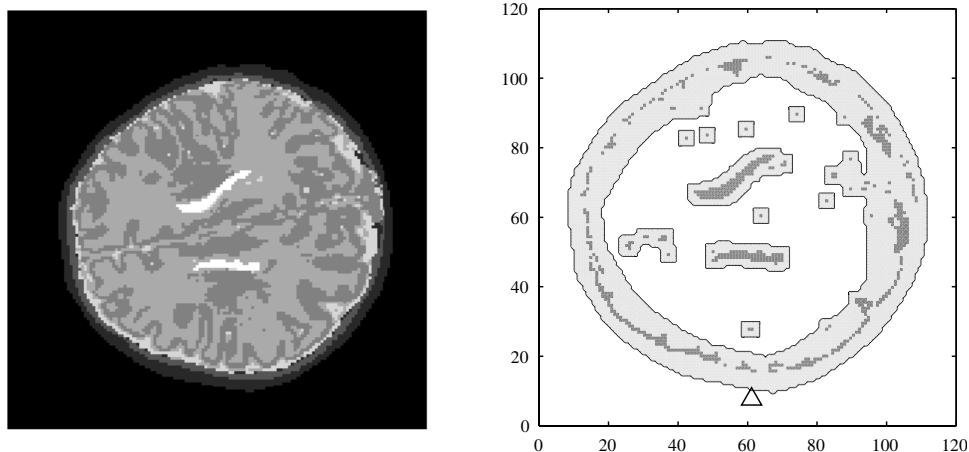


Figure 1: The left image: A segmented image from a new-born infant's head. The right image: The coupled RTE–DA model computation domain; the CSF regions (dark grey colour), the RTE sub-domain (light grey colour), and the DA sub-domain (white colour). The location of the light source is marked with a triangle.

The forward problem was solved with the coupled RTE–DA model in the head slice domain. The computation domain is illustrated in the right image of Figure 1 where the CSF regions are marked with dark grey colour. The domain was divided into the RTE and DA sub-domains,  $\Omega_{\text{rte}}$  and  $\Omega_{\text{da}}$ , which are illustrated in Figure 1 with light grey and white colours, respectively. In simulations, the source was located at the bottom of the computation domain. The location of the source is marked in Figure 1 with a small triangle. The coupled RTE–DA model was solved with the FEM with the streamline diffusion modification applied. For comparison, the FE-solutions of the RTE and the DA were computed in the whole domain. The FE-solutions were computed in the same spatial mesh as the FE-solution of the coupled RTE–DA model. In addition, the results were compared with Monte Carlo simulation. The Monte Carlo simulations were performed as in [9].

The photon densities inside the head slice are shown in Figure 2 which shows the FE-solutions of the RTE, the coupled RTE–DA model, and the DA (images from left to right in respective order). The logarithms of amplitudes are shown on the top row and the phase shifts are shown on the bottom row. The exitances on the boundary of the head slice are shown in Figure 3 which shows the exitances solved with the RTE, the coupled RTE–DA model, the DA, and Monte Carlo. The

Table 1: The absorption coefficient  $\mu_a$  and the scattering coefficient  $\mu_s$  within the head slice.

	Scalp	Skull	Grey matter	White matter	CSF around the brain	CSF in the ventricles
$\mu_a(\text{mm}^{-1})$	0.018	0.016	0.048	0.036	0.0048	0.0048
$\mu_s(\text{mm}^{-1})$	4.75	4	1.25	2.5	0.16	0.006

logarithms of amplitudes are shown on the left and the phase shifts are shown on the right. As it can be seen from Figure 2, the photon densities solved with the RTE and the coupled RTE–DA model look similar. The DA solution differs from both of them. Examining the exitances on the boundary of the domain and comparing the FE-solutions with the Monte Carlo simulations show that the coupled RTE–DA model and the RTE give almost the same results as Monte Carlo. This can be seen from Figure 3. The DA solution differs from the other approaches clearly.

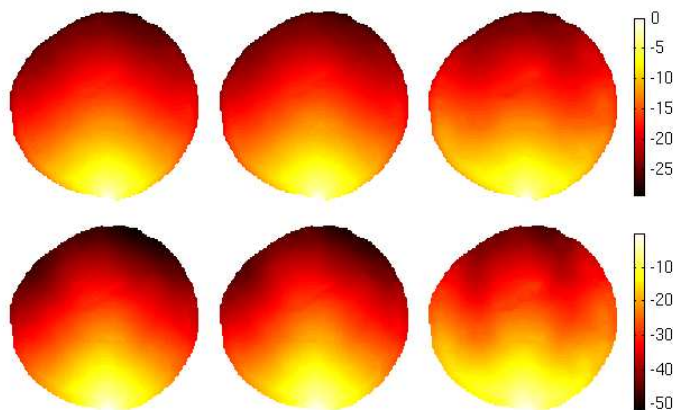


Figure 2: Logarithm of amplitude (top row) and phase shift (bottom row) of photon density within the head slice. From left to right: the RTE solution, the coupled RTE–DA model solution, and the DA solution.

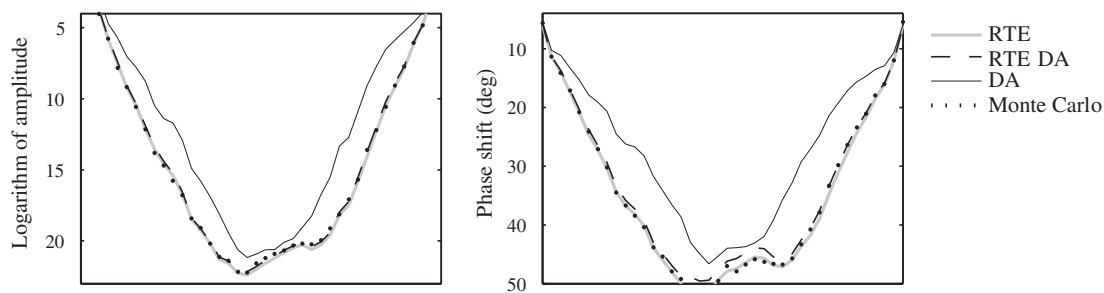


Figure 3: Logarithm of amplitude (on the left) and phase shift (on the right) of exitance on the boundary of the head slice.

Information about FE-matrix sizes and number of non-zero elements in them as well as the computation times are given in Table 2. All the FE-solutions were computed using the biconjugate gradient method with MATLAB<sup>®</sup> version 7.5 (R2007b), (The MathWorks, Inc.). The iterations were proceeded until they converged. As it can be seen from Table 2, the computation times for the RTE and the coupled RTE–DA model are both longer than for the whole domain DA. However, the coupled RTE–DA solution is obtained faster than the solution using the RTE in the whole domain. Moreover, the FE-matrix size and the number of non-zero elements are smaller in coupled RTE–DA model than in the whole domain RTE. This indicates that the coupled model requires less memory when solving the forward problem.

Table 2: FE-matrix sizes, number of non-zero elements, and the forward solution computation times for the RTE, the coupled RTE–DA model, and the DA.

	Matrix size	Non-zeros	Time(s)
RTE:	351040 × 351040	77948928	14383
RTE–DA:	202002 × 202002	42099140	11509
DA:	10970 × 10970	76122	19.594

#### 4. CONCLUSION

Utilizing the RTE in diffuse optical tomography was investigated. Light propagation was modelled with the coupled RTE–DA model, the RTE, the DA, and Monte Carlo in realistic two-dimensional head geometry from a new-born infant’s head. The results show that the coupled RTE–DA model gives almost the same results as the RTE and Monte Carlo. The DA solution, however, differs from the other approaches clearly. The results show that the RTE can be utilized in DOT in situations where the DA is not valid.

#### ACKNOWLEDGMENT

The authors wish to thank Juha Heiskala for doing the Monte Carlo simulations. This work was supported by EPSRC grant EP/E034950/1 and by the Academy of Finland (projects 122499, 119270 and 213476).

#### REFERENCES

1. Abdoulaev, G. S. and A. H. Hielscher, “Three-dimensional optical tomography with the equation of radiative transfer,” *JET*, Vol. 12, No. 4, 594–601, 2003.
2. Arridge, S. R., “Optical tomography in medical imaging,” *Inv. Probl.*, Vol. 15, R41–R93, 1999.
3. Arridge, S. R., H. Dehghani, M. Schweiger, and E. Okada, “The finite element model for the propagation of light in scattering media: A direct method for domains with nonscattering regions,” *Med. Phys.*, Vol. 27, No. 1, 252–264, 2000.
4. Arridge, S. R., M. Schweiger, M. Hiraoka, and D. T. Delpy, “A finite element approach for modeling photon transport in tissue,” *Med. Phys.*, Vol. 20, No. 2, 299–309, 1993.
5. Aydin, E. D., C. R. E. de Oliveira, and A. J. H. Goddard, “A comparison between transport and diffusion calculations using a finite element-spherical harmonics radiation transport method,” *Med. Phys.*, Vol. 29, No. 9, 2013–2023, 2002.
6. Bal, G. and Y. Maday, “Coupling of transport and diffusion models in linear transport theory,” *Math. Model. Numer. Anal.*, Vol. 36, No. 1, 69–86, 2002.
7. Dorn, O., “A transport-backtransport method for optical tomography,” *Inv. Probl.*, Vol. 14, No. 5, 1107–1130, 1998.
8. Hayashi, T., Y. Kashio, and E. Okada, “Hybrid Monte Carlo-diffusion method for light propagation in tissue with a low-scattering region,” *Appl. Opt.*, Vol. 42, No. 16, 2888–2896, 2003.
9. Heiskala, J., I. Nissilä, T. Neuvonen, S. Järvenpää, and E. Somersalo, “Modeling anisotropic light propagation in a realistic model of the human head,” *Appl. Opt.*, Vol. 44, No. 11, 2049–2057, 2005.
10. Kaipio, J. and E. Somersalo, *Statistical and Computational Inverse Problems*, Springer, New York, 2005.
11. Kim, H. K. and A. Charette, “A sensitivity function-based conjugate gradient method for optical tomography with the frequency-domain equation of radiative transfer,” *J Quant. Spectrosc. Radiat. Transf.*, Vol. 104, 24–39, 2007.
12. Klose, A. D. and A. H. Hielscher, “Iterative reconstruction scheme for optical tomography based on the equation of radiative transfer,” *Med. Phys.*, Vol. 26, No. 8, 1698–1707, 1999.
13. Ren, K., G. Bal, and A. H. Hielscher, “Frequency domain optical tomography based on the equation of radiative transfer,” *SIAM J Sci. Comput.*, Vol. 28, No. 4, 1463–1489, 2006.
14. Tarvainen, T., M. Vauhkonen, V. Kolehmainen, S. R. Arridge, and J. P. Kaipio, “Coupled radiative transfer equation and diffusion approximation model for photon migration in turbid medium with low-scattering and non-scattering regions,” *Phys. Med. Biol.*, Vol. 50, 4913–4930, 2005.
15. Tarvainen, T., M. Vauhkonen, V. Kolehmainen, and J. P. Kaipio, “Hybrid radiative-transfer-diffusion model for optical tomography,” *Appl. Opt.*, Vol. 44, No. 6, 876–886, 2005.

16. Tarvainen, T., M. Vauhkonen, V. Kolehmainen, and J. P. Kaipio, “Finite element model for the coupled radiative transfer equation and diffusion approximation,” *Int. J. Numer. Meth. Engng.*, Vol. 65, No. 3, 383–405, 2006.
17. Tervo, J., P. Kolmonen, M. Vauhkonen, L. M. Heikkinen, and J. P. Kaipio, “A finite-element model of electron transport in radiation therapy and a related inverse problem,” *Inv. Probl.*, Vol. 15, 1345–1361, 1999.
18. Wang, L. and S. L. Jacques, “Hybrid model of Monte Carlo simulation and diffusion theory for light reflectance by turbid media,” *J Opt. Soc. Am. A*, Vol. 10, No. 8, 1746–1752, 1993.
19. Wright, S., M. Schweiger, and S. R. Arridge, “Reconstruction in optical tomography using the  $P_N$  approximations,” *Meas. Sci. Technol.*, Vol. 18, 79–86, 2007.

# New Metamaterial Using Dynamic Analysis at Millimeter Waves

Humberto C. C. Fernandes and Davi B. Brito

Federal University of Rio Grande do Norte, Department of Electrical Engineering, Brazil

**Abstract**— Electromagnetic metamaterials are broadly artificial homogeneous electromagnetic structures with unusual properties not readily found in ubiquitous materials with desired dielectric and magnetic characteristics. In this paper the bilateral fin line with EBG — Electromagnetic Band Gap — metamaterial substrate was analyzed using the TTL — Transverse Transmission Line — method. In order to analyze this structure the effective dielectric constant and the attenuation constant are determined. The results obtained for this application and the conclusions are presented.

## 1. INTRODUCTION

Fin lines are widely used as a millimeter wave component due to its various advantages such as reducing size, weight, and cost and in addition because it interfaces easily with other millimeter wave circuits. In this paper the EBG metamaterial is applied to bilateral circuit. The analysis is made using the full wave TTL method. This paper objective is to present the effect of dielectric anisotropy on edge coupled bilateral finlines shown in Fig. 1. The paper discusses the effect of anisotropy on effective dielectric constants and attenuation constant by applying the anisotropy one by one in all three directions.

The EBG medium can not be characterized by assigning a single permittivity and permeability value for throughout the finite structure. In other words, the parameters depend on the spatial coordinates and this causes spatial dispersion. As a result of this, the medium will not be homogenous. For a non-homogeneous structure, the incident wave undergoes a process of multiple scattering. The substrate shown in region 2 of Fig. 1 is modeled by utilizing bianisotropic tensor properties:

$$\mu = \mu_0 \begin{bmatrix} \mu_{xx} & 0 & 0 \\ 0 & \mu_{yy} & 0 \\ 0 & 0 & \mu_{zz} \end{bmatrix} \quad (1)$$

$$\varepsilon = \varepsilon_0 \begin{bmatrix} \varepsilon_{xx} & 0 & 0 \\ 0 & \varepsilon_{yy} & 0 \\ 0 & 0 & \varepsilon_{zz} \end{bmatrix} \quad (2)$$

To calculate the numerical results a computational program in Fortran Power Station and Scilab languages were developed, according to the previous theoretical analyses. Compared to other full wave methods the TTL is an efficient tool to determine the fin line characteristics, making possible a significant algebraic simplification of the equations involved in the process and reducing the computational time.

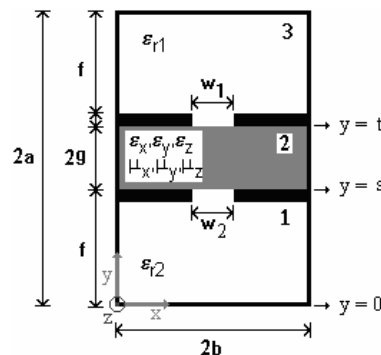


Figure 1: Transversal cut of a bilateral fin line structure with EBG substrate.

## 2. TTL METHOD

The general equations of the fields in the TTL method are obtained after using the Maxwell's equations, as:

$$\begin{bmatrix} \vec{E}_{\Gamma i} \\ \vec{H}_{\Gamma i} \end{bmatrix} = \frac{1}{k_i^2 + \gamma_i^2} \left[ j\omega \nabla_{\Gamma} \times \begin{bmatrix} -\mu \vec{H}_{yi} \\ \varepsilon_1 \vec{E}_{yi} \end{bmatrix} + \frac{\partial}{\partial y} \nabla_{\Gamma} \begin{bmatrix} \vec{E}_{yi} \\ \vec{H}_{yi} \end{bmatrix} \right] \quad (3)$$

where the index 'T' represents the transversal components directions ( $x, z$ ):

$$\vec{E}_{\Gamma i} = \vec{E}_{xi} \hat{x} + \vec{E}_{zi} \hat{z} \quad (4)$$

$$\vec{H}_{\Gamma i} = \vec{H}_{xi} \hat{x} + \vec{H}_{zi} \hat{z} \quad (5)$$

$$\nabla_{\Gamma} = \nabla_x \hat{x} + \nabla_z \hat{z} = \frac{\partial}{\partial x} \hat{x} + \frac{\partial}{\partial z} \hat{z} \quad (6)$$

The equations are used for the analysis in the spectral domain, in the "x" and "z" directions. Therefore it should be applied to the field, equations of double Fourier transform defined as:

$$\tilde{f}(\alpha_n, y, \beta_k) = \int_{-\infty}^{\infty} \int_{-\infty}^{\infty} f(x, y, z) \cdot e^{j\alpha_n x} \cdot e^{j\beta_k z} dx dz \quad (7)$$

After using the Maxwell's equations in the spectral domain, the general equations of the electric and magnetic fields in the TTL method are obtained as:

$$\tilde{E}_{xi} = \frac{1}{\gamma_i^2 + k_i^2} \left[ -j\alpha_n \frac{\partial}{\partial y} \tilde{E}_{yi} - j\omega \mu \Gamma \tilde{H}_{yi} \right] \quad (8)$$

$$\tilde{E}_{zi} = \frac{1}{\gamma_i^2 + k_i^2} \left[ -\Gamma \frac{\partial}{\partial y} \tilde{E}_{yi} - \omega \mu \alpha_n \tilde{H}_{yi} \right] \quad (9)$$

$$\tilde{H}_{xi} = \frac{1}{\gamma_i^2 + k_i^2} \left[ -j\alpha_n \frac{\partial}{\partial y} \tilde{H}_{yi} + j\omega \varepsilon \Gamma \tilde{E}_{yi} \right] \quad (10)$$

$$\tilde{H}_{zi} = \frac{1}{\gamma_i^2 + k_i^2} \left[ -\Gamma \frac{\partial}{\partial y} \tilde{H}_{yi} + \omega \varepsilon \alpha_n \tilde{E}_{yi} \right] \quad (11)$$

where:

$\gamma_i^2 = \alpha_n^2 - \Gamma_i^2 - k_i^2$ , is the propagation constant in "y" direction;  $\alpha_n$  is the spectral variable in "x" direction.

$k_i^2 = \omega^2 \mu \varepsilon = k_0^2 \varepsilon_{ri}^*$  is the wave number of  $i$ th term of dielectric region;

$\varepsilon_{ri}^* = \varepsilon_{ri} - j \frac{\sigma_i}{\omega \varepsilon_0}$  is the relative dielectric constant of the material with losses;

$\varepsilon_i = \varepsilon_{ri}^* \cdot \varepsilon_0$ , is the dielectric constant of the  $i$ th region;

$\Gamma = \alpha_n + j\beta$ , is the complex propagation constant;

$\omega = \omega_r + j\omega_i$  is the complex angular frequency.

### B. The Admittance Matrix

A group of equations are applied, being calculated the  $E_y$  and  $H_y$  fields through the solution of the Helmholtz equations in the spectral domain. A system equations is then obtained, that in a matrix form is given as:

$$\begin{bmatrix} Y_{x^1 x^1} & Y_{z^1 x^1} \\ Y_{z^1 x^1} & Y_{z^1 z^1} \end{bmatrix} \begin{bmatrix} \tilde{E}_{xg} \\ \tilde{E}_{zg} \end{bmatrix} = \begin{bmatrix} \tilde{J}_x \\ \tilde{J}_z \end{bmatrix} \quad (12)$$

Where for example:

$$Y_{x^1 x^1} = \frac{-j}{\omega \mu} \left[ (\alpha_n^2 - \gamma_2^2) \frac{\tanh \gamma_2 g}{\gamma_2} + (\alpha_n^2 - \gamma_3^2) \frac{\coth \gamma_3 f}{\gamma_3} \right] \quad (13)$$

The "Y" matrix is the dyadic Green admittance function of the finline. To eliminate the components of the current density, the method of the moments was applied with the expansion of  $\tilde{E}_{xg}$  and  $\tilde{E}_{zg}$  in terms of known base functions, as:

$$\tilde{E}_{xg} = A_{x1} \tilde{f}_{x1}(\alpha_n) \quad (14)$$

$$\tilde{E}_{zg} = A_{z1} \tilde{f}_{z1}(\alpha_n) \quad (15)$$

As a result, the equation is transformed in an homogeneous matrix equation, whose non-trivial solution corresponds to the characteristic equation, and its roots supply the phase and attenuation constants.

$$\begin{bmatrix} Kx^1x^1 & Kx^1z^1 \\ Kz^1x^1 & Kz^1z^1 \end{bmatrix} \begin{bmatrix} Ax_1 \\ Az_1 \end{bmatrix} = 0 \quad (16)$$

Where for example:

$$Kx^1x^1 = \sum_{-\infty}^{\infty} \tilde{f}x_1(\alpha_n) Yx^1x^1 \tilde{f}x_1(\alpha_n) \quad (17)$$

The characteristic equation for determining the complex propagation constant  $\Gamma$ , is obtained by setting the determinant of the system matrix equal to zero. The effective dielectric constant is determined after numerical solutions of the matrix determinant by the relation between the phase constant and the free space wave number:

$$\varepsilon_{ep} = (\beta/ko)^2 \quad (18)$$

### 3. METAMATERIAL STRUCTURE

Electromagnetic metamaterials (MTMs) are broadly defined as artificial effectively homogeneous electromagnetic structures with unusual properties not readily available in nature [4]. EBGs have been broadened the range of available electromagnetic material properties. These materials have allowed the new solutions to Maxwell's equations not available in naturally occurring materials, fueling the discovery of new physical phenomena and the development of devices.

EBGs are periodic arrangements of dielectric or metallic elements in one, two or three dimensional manners. EBGs inhibit the passage of electromagnetic wave at certain angles of incidence at some frequencies. These frequencies are called partial bandgaps. At a specific frequency band, an EBG does not allow the propagation of wave in all directions and this frequency region is called the complete bandgap or global bandgap.

The characteristic property of stop bands at certain frequencies enables many applications using EBGs. At this stop band, all electromagnetic wave will be reflected back and the structure will act like a mirror. The advantage over a metal reflector is that for an EBG, reflection takes place only at stop band frequency. At other frequencies it will act as transparent medium. This concept is illustrated in Fig. 2.

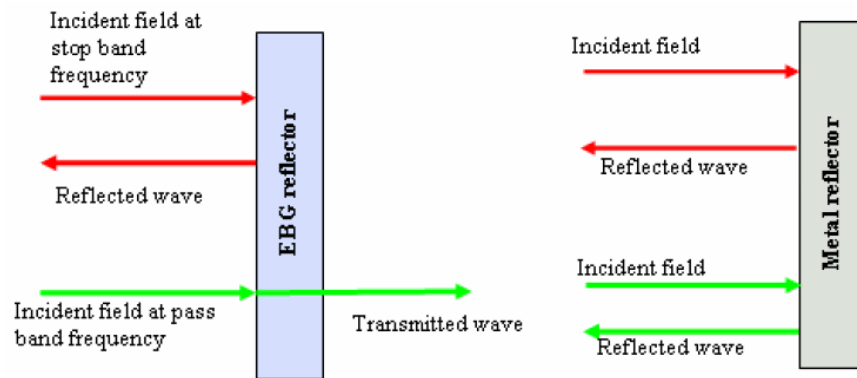


Figure 2: Diagram illustrating the application of EBG.

One characteristic of this material is the negative permittivity,  $\varepsilon$ , and permeability,  $\mu$ . Fig. 3 shows this structure.

If the excitation electric field  $\vec{E}$  is parallel to the “y” axis in the MTM thin-wire shown in Fig. 2(a) so as to induce a current along them and generate equivalent electric dipole moments, this MTM can be characterized by plasmonic-type permittivity frequency function of the form [4],

$$\varepsilon_r(\omega) = 1 - \frac{\omega_{pe}^2}{\omega^2 + \zeta^2} + j \frac{\zeta \omega_{pe}^2}{\omega(\omega^2 + \zeta^2)} \quad (19)$$

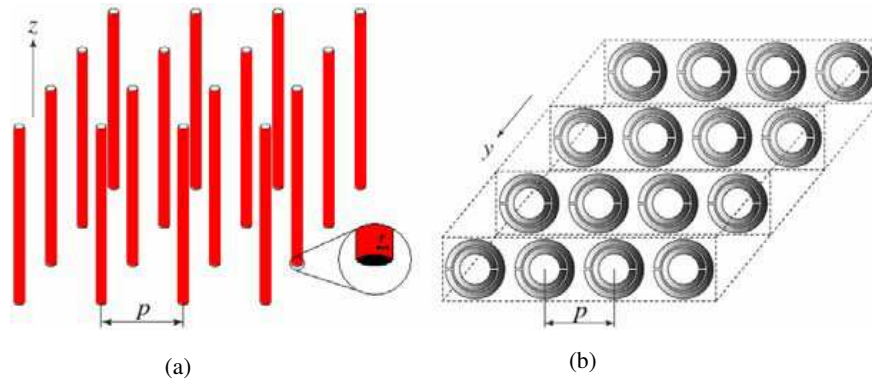


Figure 3: (a) Thin-wires TW, with negative- $\epsilon$ /positive- $\mu$  if  $\vec{E} \parallel y$ , (b) Split-ring resonator SRR positive- $\epsilon$ /negative- $\mu$ , if  $\vec{E} \perp z$  [4].

where:  $\omega_{pe} = \sqrt{\frac{2\pi c^2}{p^2 \ln(\frac{p}{a})}}$  ( $c$ : speed of light,  $a$ : radius of the wires,  $p$ : period) is the electric plasma frequency.  $\zeta = \epsilon_0(p\omega_{pe}/a)^2/\pi\sigma$  is the dumping factor due to metal loss. By analyze the Equation (19), we have:

$$\text{Re}(\epsilon_r) < 0, \text{ for } \omega^2 < \omega_{pe}^2 - \zeta^2 \quad (20)$$

$$\text{If consider } \zeta = 0, \text{ result : } \epsilon_r < 0 \iff \omega^2 < \omega_{pe}^2 \quad (21)$$

If the excitation magnetic field  $\vec{H}$  is perpendicular to the “z” axis in the MTM Split-ring resonator shown in Fig. 2(b). So as to induce a current in the loop of the ring and generate equivalent magnetic dipole moments, this MTM can be characterized by plasmonic-type permeability frequency function of the form [4],

$$\mu_r(\omega) = 1 - \frac{F\omega^2(\omega^2 - \omega_{0m}^2)}{(\omega^2 - \omega_{0m}^2)^2 + (\omega\zeta)^2} + j \frac{F\omega^2\zeta}{(\omega^2 - \omega_{0m}^2)^2 + (\omega\zeta)^2} \quad (22)$$

where:  $F = \pi(a/p)^2$ ,  $\omega_{0m} = c\sqrt{\frac{3p}{\pi \ln(2wa^3/\delta)}}$  ( $w$ : width of the rings,  $\delta$ : radial spacing between the rings) is a magnetic resonance frequency. The Equation (22) analyze, reveals the range of frequency where re permeability is negative:  $\mu_r < 0$ , for  $\omega_{0m} < \omega < \frac{\omega_{0m}}{\sqrt{1-F}} = \omega_{pm}$ , where  $\omega_{pm}$  is the magnetic plasma frequency.

The structure described in the Fig. (b) is a LH is bidimensional, so  $\vec{E}$  has to be directed along the axis of the wires, and two directions are possible for  $\vec{H}$ , then we have the following conditions:  $\epsilon_{xx}(\omega < \omega_{pe}) < 0$ ,  $\epsilon_{yy} = \epsilon_{zz} > 0$ ;  $\mu_{xx} < 0$  for  $\omega_{0m} < \omega < \omega_{pm}$  and  $\mu_{yy}, \mu_{zz} > 0$ .

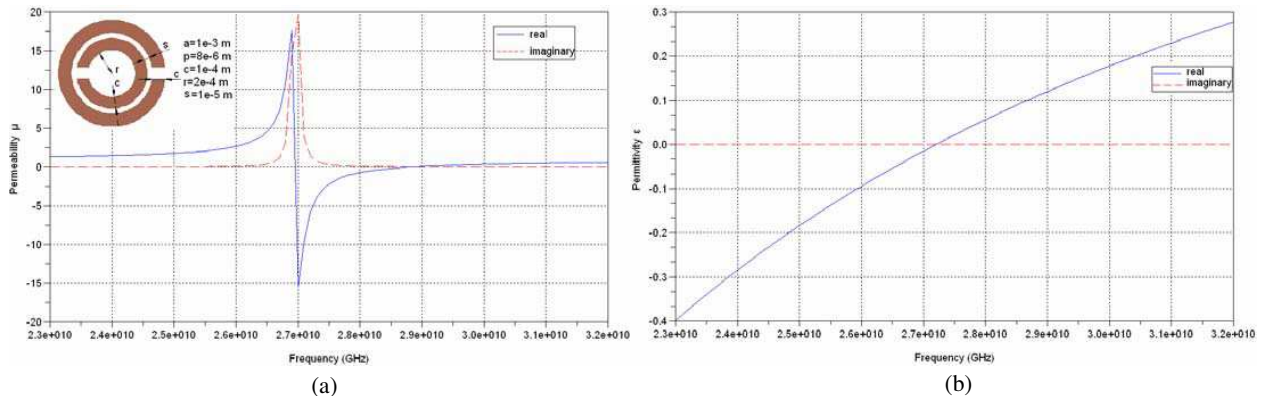


Figure 4: (a) Permeability for the SRR structure, (b) Permittivity for the TW configuration.

#### 4. RESULTS

To calculate the numerical results computational programs in Fortran Power Station language and Scilab were developed, according to the previous theoretical analyses. As illustrated in the previous section the metamaterial present negative permeability  $\epsilon$  permittivity constants. Fig. 4 shows the metamaterial waveforms. The fin line uses a WR-28 millimeter wave guide and at 27.0 GHz (resonance frequency) occurs the Threshold conditions to both curves.

The new results for the bilateral fin line with metamaterial substrate, in a WR-28 millimeter wave guide, according to Fig. 1, with  $2g = 0.125$  mm,  $f = 3.4935$  mm,  $w_1 = w_2 = 0.15$  mm and  $\epsilon_{r1} = \epsilon_{r3} = 1$ ,  $\epsilon_{r2}$  and  $\mu_{r2}$  are given by Figs. 4(a) and (b), are show in Fig. 5.

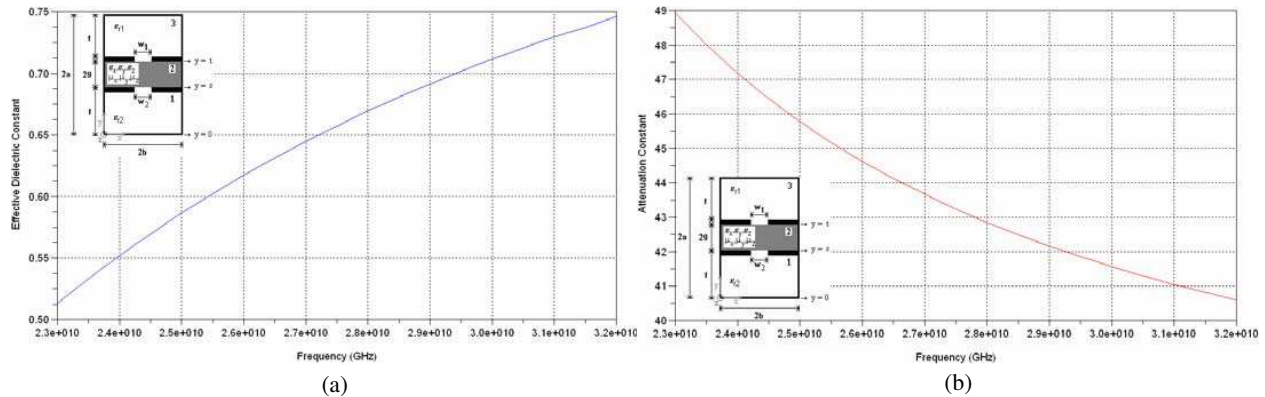


Figure 5: (a) Effective dielectric constant vs. frequency, (b) attenuation constant vs. frequency; for a bilateral fin line in a WR-28 millimeter wave guide with metamaterial substrate.

#### 5. CONCLUSIONS

Theoretical and numerical results have been presented for the bilateral fin line with EBG substrate, and results for the substrate itself. The TTL method, in the Fourier transform domain was used in the determination of the electrical and magnetic fields, in all regions. The results were obtained for the propagation constant, including the attenuation and phase constants, and effective dielectric constant for the fin line structure. It was observed a considerable reduction in the algebraic development using the TTL method and a performance improvement using the metamaterial substrate.

#### ACKNOWLEDGMENT

The authors wish to acknowledge the assistance and support of CNPQ, Brazilian Agency.

#### REFERENCES

1. Fernandes, H. C. C., J. L. G. Medeiros, I. M. Jr., Araújo, and D. B. Brito, "Photonic crystal at millimeter waves applications," *PIERS Online*, Vol. 3, No. 5, 689–694, 2007.
2. Bhat, B. and S. K. Koul, *Analysis, Design and Applications of Fin Lines*, 383–471, Artech House, Inc., Norwood, MA, USA, 1987.
3. Wiersma, D. S., P. Bartolini, A. Lagendijk, and R. Righini, "Localization of light in a disordered medium," *Letters to Nature*, Vol. 390, 18–25, Dec. 1997.
4. Caloz, C. and T. Itoh, *Electromagnetic Metamaterials: Transmission Line Theory and Microwave Applications*, Wiley-IEEE Press, 2005.

# A New Application Metamaterial Antenna

Humberto C. C. Fernandes and M. Bonfim L. Aquino

Department of Electrical Engineering, Federal University of Rio Grande do Norte, Brazil

**Abstract**— Electromagnetic metamaterials (MTM) are artificial homogeneous electromagnetic structures with peculiar properties characteristics, with tensor permeability and permittivity, which can be used in some devices, as: antennas, fin lines devices and filters. In this paper the metamaterial substrate is applied to microstrip antenna. The structure was analyzed using the concise full wave TTL — Transverse Transmission Line — method. In order to analyze this structure the resonant frequency and pattern fields are obtained. The new results are presented and compared with previous another one of the specialized literature.

## 1. INTRODUCTION

The microstrip resonator is widely used as an antenna due to its various advantages such as: reducing size, weight, cost and in addition, because it interfaces easily with other circuits. This device is composed of a rectangular patch, metamaterial substrate and a ground plane. The MTM impedes the propagation of electromagnetic waves in some frequency, which can be used to made devices most efficient, and eliminate unwanted frequencies. The analysis is made using the TTL method, with efficient bases function in both  $x$  and  $z$  directions, as is shown in the Fig. 1 [1]. In order to analyze this structure the resonant frequency and pattern fields are obtained. New results are presented.

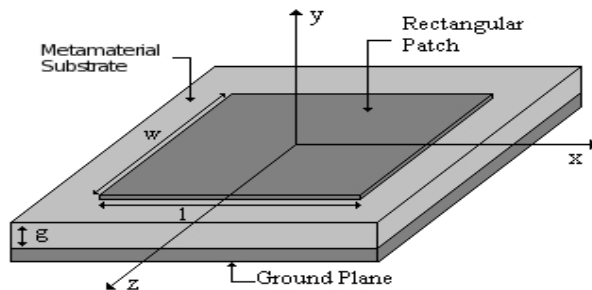


Figure 1: Microstrip resonator with metamaterial.

## 2. METAMATERIAL THEORY

Electromagnetic metamaterials (MTMs) are artificial homogeneous electromagnetic structures with unusual properties not readily available in nature [2,3]. These metamaterials have allowed the new solutions to Maxwell's equations, fueling the discovery of new physical phenomena and the development of devices.

If the excitation electric field  $\vec{E}$  is parallel to the “ $y$ ” axis, in the MTM thin-wire shown in Fig. 2(a), induces a current that generates equivalent electric dipole moments. This MTM can be characterized by plasmonic-type permittivity frequency function of the form [3],

$$\varepsilon_r(\omega) = 1 - \frac{\omega_{pe}^2}{\omega^2 + \zeta^2} + j \frac{\zeta \omega_{pe}^2}{\omega(\omega^2 + \zeta^2)} \quad (1)$$

where:  $\omega_{pe} = \sqrt{\frac{2\pi c^2}{p^2 \ln(\frac{p}{a})}}$  ( $c$ : speed of light,  $a$ : radius of the wires,  $p$ : period) is the electric plasma frequency.  $\zeta = \varepsilon_0(p\omega_{pe}/a)^2/\pi\sigma$  is the dumping factor due to metal loss. By analyze the Equation (1), we have:

$$\text{Re}(\varepsilon_r) < 0, \text{ for } \omega^2 < \omega_{pe}^2 - \zeta^2 \quad (2)$$

$$\text{if consider } \zeta = 0, \text{ result : } \varepsilon_r < 0 \iff \omega^2 < \omega_{pe}^2 \quad (3)$$

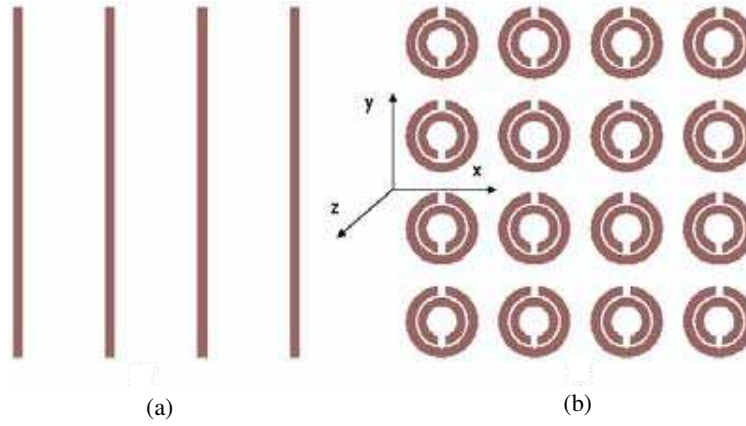


Figure 2: (a) Thin-wires TW, with negative- $\epsilon$ /positive- $\mu$  if  $\vec{E} \parallel y$ , (b) Split-ring resonator SRR positive- $\epsilon$ /negative- $\mu$ , if  $\vec{E} \parallel y$ .

If the excitation magnetic field  $\vec{H}$  is perpendicular to the “z” axis in the MTM Split-ring resonator shown in Fig. 2(b), induces a current in the loop of the ring and generates equivalent magnetic dipole moments. This MTM can be characterized by plasmonic-type permeability frequency function of the form [3],

$$\mu_r(\omega) = 1 - \frac{F\omega^2(\omega^2 - \omega_{0m}^2)}{(\omega^2 - \omega_{0m}^2)^2 + (\omega\zeta)^2} + j \frac{F\omega^2\zeta}{(\omega^2 - \omega_{0m}^2)^2 + (\omega\zeta)^2} \quad (4)$$

where:  $F = \pi(a/p)^2$ ,  $\omega_{0m} = c\sqrt{\frac{3p}{\pi \ln(2wa^3/\delta)}}$  ( $w$ : width of the rings,  $\delta$ : radial spacing between the rings) is a magnetic resonance frequency. The Equation (4) analyze, reveals the range of frequency where re permeability is negative:  $\mu_r < 0$ , for  $\omega_{0m} < \omega < \frac{\omega_{0m}}{\sqrt{1-F}} = \omega_{pm}$ . Where  $\omega_{pm}$  is the magnetic plasma frequency.

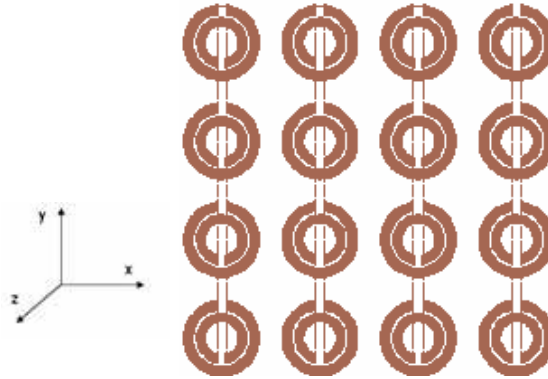


Figure 3: TW-SRR structure composed with SRR and TW metamaterial.

The MTM above is anisotropic, that is characterized using permittivity and permeability tensor, as below:

$$\mu = \mu_0 \begin{bmatrix} \mu_{xx} & 0 & 0 \\ 0 & \mu_{yy} & 0 \\ 0 & 0 & \mu_{zz} \end{bmatrix} \quad (5)$$

$$\epsilon = \epsilon_0 \begin{bmatrix} \epsilon_{xx} & 0 & 0 \\ 0 & \epsilon_{yy} & 0 \\ 0 & 0 & \epsilon_{zz} \end{bmatrix} \quad (6)$$

The structure described in the Fig. 3 is a LH bidimensional.  $\vec{E}$  is directed along the axis of the wires, and two directions are possible for  $\vec{H}$ , then has the following conditions:  $\epsilon_{xx}(\omega < \omega_{pe}) < 0$ ,  $\epsilon_{yy} = \epsilon_{zz} > 0$ ;  $\mu_{xx} < 0$  for  $\omega_{0m} < \omega < \omega_{pm}$  and  $\mu_{yy}, \mu_{zz} > 0$ .

### 3. FIELDS IN STRUCTURE

The metamaterial substrate shown in region 1 of Fig. 1 is modeled by using bianisotropic tensor properties Equations (5) and (6), together with wave equations which are expressed as [4, 5]:

$$\frac{\partial^2 \tilde{E}_y}{\partial y^2} - \gamma^2 \tilde{E}_y = 0 \quad (7)$$

$$\frac{\partial^2 \tilde{H}_y}{\partial y^2} - \gamma^2 \tilde{H}_y = 0 \quad (8)$$

After using the Maxwell's equations in the spectral domain, the general equations of the electric and magnetic fields to the metamaterial resonator are obtained as:

$$\tilde{E}_{xi} = \frac{1}{\gamma_i^2 + k_0^2 \varepsilon_{ri}} \left[ -j\alpha_n \frac{\partial}{\partial y} \tilde{E}_{yi} + \omega \mu_0 \mu_{xi} \beta_k H_{yi} + \omega \mu_0 \mu_{zi} \beta_k \tilde{H}_{yi} \right] \quad (9)$$

$$\tilde{E}_{zi} = \frac{1}{\gamma_{yi}^2 + k_0^2 \varepsilon_{ri}} \left[ -j\beta_k \frac{\partial}{\partial y} E_{yi} - \omega \mu_0 \mu_{xi} \alpha_n H_{yi} - \omega \mu_0 \mu_{zi} \alpha_n H_{yi} \right] \quad (10)$$

$$H_{xi} = \frac{1}{\gamma_{yi}^2 + k_0^2 \varepsilon_{ri}} \left[ -j\alpha_n \frac{\partial}{\partial y} H_{yi} - \omega \varepsilon_0 \varepsilon_{xi} \beta_k E_{yi} - \omega \varepsilon_0 \varepsilon_{zi} \beta_k E_{yi} \right] \quad (11)$$

$$\tilde{H}_{zi} = \frac{1}{\gamma_{yi}^2 + k_0^2 \varepsilon_{ri}} \left[ -j\beta_k \frac{\partial}{\partial y} H_{yi} + \omega \varepsilon_0 \varepsilon_{xi} \alpha_n E_{yi} + \omega \varepsilon_0 \varepsilon_{zi} \alpha_n E_{yi} \right] \quad (12)$$

where:  $i = 1, 2$  represent the dielectric regions of the structure;  $\gamma_i^2 = \alpha_n^2 + \beta_k^2 - k_i^2$  is the propagation constant in  $y$  direction;  $\alpha_n$  is the spectral variable in “ $x$ ” direction and  $\beta_k$  is the spectral variable in “ $z$ ” direction;  $k_i^2 = \omega^2 \mu \varepsilon = k_0^2 \varepsilon_{ri}^*$  is the wave number of the  $i$ th dielectric region;  $\varepsilon_{ri}^* = \varepsilon_{ri} - j \frac{\sigma_i}{\omega \varepsilon_0}$  is the relative dielectric constant of the metamaterial with losses;  $\omega = \omega_r + j\omega_i$  is the complex angular frequency;  $\varepsilon_i = \varepsilon_{ri}^* \cdot \varepsilon_0$  is the dielectric constant of the metamaterial.

The equations above are applied to Helmholtz's wave equations in the spectral domain (7) and (8) [4, 5] to determine the field's equations to the structure in study. The solutions of these equations to the regions are:

For the regions 1 and 2:

$$\tilde{E}_{y1} = A_{1e} \cdot \cosh(\gamma_1 y) \quad (13)$$

$$\tilde{H}_{y1} = A_{1h} \cdot \sinh(\gamma_1 y) \quad (14)$$

$$\tilde{E}_{y2} = A_{2e} \cdot e^{-\gamma_2 y} \quad (15)$$

$$\tilde{H}_{y2} = A_{2h} \cdot e^{-\gamma_2 y} \quad (16)$$

Substituting these solutions in the field's Equations (9) into (12), as functions of the unknown constants  $A_{1e}$ ,  $A_{1h}$ ,  $A_{2e}$  and  $A_{2h}$  are obtained, for example, for the region 1:

$$\tilde{E}_{x1} = \frac{-j \sinh(\gamma_1 y)}{k_1^2 + \gamma_1^2} [\alpha_n \gamma_1 A_{1e} + j\beta_k \omega \mu_0 \mu_{x1} A_{1h} + j\beta_k \omega \mu_0 \mu_{z1} A_{1h}] \quad (17)$$

$$\tilde{H}_{x1} = \frac{-j \cosh(\gamma_1 y)}{k_1^2 + \gamma_1^2} [\alpha_n \gamma_1 A_{1h} + j\beta_k \omega \varepsilon_1 \varepsilon_{x1} A_{1e} + j\beta_k \omega \varepsilon_1 \varepsilon_{z1} A_{1e}] \quad (18)$$

### 4. ADMITANCE MATRIX

The Equations (19) and (20) relate the current densities in the sheets ( $\tilde{J}_{xt}$  and  $\tilde{J}_{zt}$ ) and the magnetic fields in the interface  $y = g$ :

$$\tilde{H}_{x1} - \tilde{H}_{x2} = \tilde{J}_{xt} \quad (19)$$

$$\tilde{H}_{z1} - \tilde{H}_{z2} = \tilde{J}_{zt} \quad (20)$$

Substituting the magnetic field's Equations (11) and (12), into the current Equations (19) and (20), we can get the admittance matrix, like:

$$\begin{bmatrix} Y_{xx} & Y_{xz} \\ Y_{zx} & Y_{zz} \end{bmatrix} \begin{bmatrix} \tilde{E}_{xg} \\ \tilde{E}_{zg} \end{bmatrix} = \begin{bmatrix} \tilde{J}_{xg} \\ \tilde{J}_{zg} \end{bmatrix} \quad (21)$$

$$Y_{xx} = \frac{i}{\omega\mu_0\gamma_1\gamma_2} \left\{ \frac{\gamma_2 \cot gh(\gamma_1 g) [-\beta_k^2 \gamma_1^2 + \omega^2 \alpha n^2 \varepsilon_0 \mu_0 (\varepsilon_{x1} + \varepsilon_{z1}) (\mu_{x1} + \mu_{z1})]}{(\gamma_1^2 + k_1^2) (\mu_{x1} + \mu_{z1})} + \frac{\gamma_1 (-\beta_k^2 \gamma_2^2 + \omega^2 \alpha n^2 \mu_2 \varepsilon_2)}{(\gamma_2^2 + k_2^2) \mu_{r2}} \right\} \quad (22)$$

$$Y_{xz} = \frac{j\alpha n \beta_k}{\omega\mu_0\gamma_1\gamma_2} \left\{ \frac{\gamma_2 \cot gh(\gamma_1 g) [\gamma_1^2 + \omega^2 \varepsilon_0 \mu_0 (\varepsilon_{x1} + \varepsilon_{z1}) (\mu_{x1} + \mu_{z1})]}{(\gamma_1^2 + k_1^2) (\mu_{x1} + \mu_{z1})} + \frac{\gamma_1 (\gamma_2^2 + \omega^2 \mu_2 \varepsilon_2)}{(\gamma_2^2 + k_2^2) \mu_{r2}} \right\} \quad (23)$$

$$Y_{zx} = Y_{xz} \quad (24)$$

$$Y_{zz} = \frac{-j}{\omega\mu_0\gamma_1\gamma_2} \left\{ \frac{\gamma_2 \cot gh(\gamma_1 g) [-\alpha n^2 \gamma_1^2 + \alpha n \beta_k \omega^2 \varepsilon_0 \mu_0 (\varepsilon_{x1} + \varepsilon_{z1}) (\mu_{x1} + \mu_{z1})]}{(\gamma_1^2 + k_1^2) (\mu_{x1} + \mu_{z1})} + \frac{\gamma_1 (-\alpha n^2 \gamma_2^2 + \beta_k^2 \omega^2 \mu_2 \varepsilon_2)}{(\gamma_2^2 + k_2^2) \mu_{r2}} \right\} \quad (25)$$

$$(26)$$

The matrix inversion is used and current densities in the interface are expanded using base functions [4, 5]:

$$\begin{bmatrix} Z_{xx} & Z_{xz} \\ Z_{zx} & Z_{zz} \end{bmatrix} \begin{bmatrix} \tilde{J}_{zg} \\ \tilde{J}_{xg} \end{bmatrix} = \begin{bmatrix} \tilde{E}_{xg} \\ \tilde{E}_{zg} \end{bmatrix} \quad (27)$$

$$\tilde{J}_{xg} = \sum_{i=1}^n a_{xi} \cdot \tilde{f}_{xi}(\alpha_n, \beta_k) \quad (27a)$$

$$\tilde{J}_{zg} = \sum_{j=1}^m a_{zj} \cdot \tilde{f}_{zj}(\alpha_n, \beta_k) \quad (27b)$$

The Fourier transformed to the base functions is [4]:

$$\tilde{f}_x(\alpha_n, \beta_k) = \frac{2\pi^2 l \cdot \cos\left(\frac{\beta_k l}{2}\right)}{\pi^2 - (\beta_k l)^2} \cdot J_0\left(\alpha_n \frac{w}{2}\right) \quad (28)$$

The Galerkin method is applied to (26), to eliminate the current densities, and then is obtained,

$$\begin{bmatrix} K_{xx} & K_{xz} \\ K_{zx} & K_{zz} \end{bmatrix} \cdot \begin{bmatrix} a_x \\ a_z \end{bmatrix} = \begin{bmatrix} 0 \\ 0 \end{bmatrix} \quad (29)$$

Where, for examples,

$$K_{xx} = \sum_{-\infty}^{\infty} \tilde{f}_x \cdot Z_{xx} \cdot \tilde{f}_x^*, \quad K_{xz} = \sum_{-\infty}^{\infty} \tilde{f}_z \cdot Z_{xz} \cdot \tilde{f}_x^* \quad (30)$$

The determinant of (29) solution, supplies the complex resonant frequency.

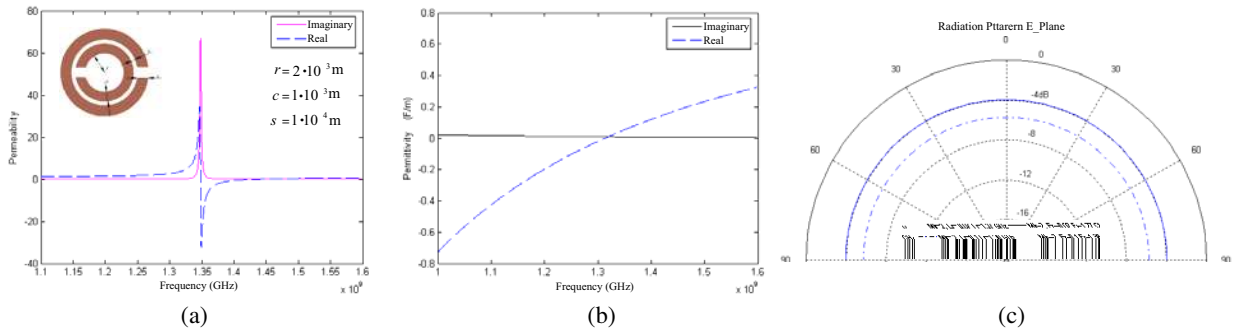


Figure 4: (a) Permeability for the SRR structure, (b) Permittivity for the TW configuration, (c) Radiation Pattern  $E$ -Plane.

## 5. RESULTS

As illustrated in the section one, the metamaterial TW-SRR, can presents negative permeability  $\mu$  permittivity constants. The Fig. 4 shows the waveforms to the structure TW-SRR. At 1.34 GHz (resonance frequency) occurs the threshold conditions to both curves. These characteristics are very important because a range of values available to devices project is increased around the resonance frequency point. It's also shown the far fields compartment to operate in two different ranges (negative  $\mu$ - $\varepsilon$  and positive  $\mu$ - $\varepsilon$ ). Here can be seen that the radiation patterns characteristic can change just varying the operation frequency.

## 6. CONCLUSIONS

The field's equations to rectangular resonator with metamaterial theory were demonstrated using the TTL method. It was shown that can achieved a wide range of permeability and permittivity values, by varying the structure parameters. These characteristics are very important to improve the design of the antenna devices. New results were shown for permeability and permittivity parameters in the GHz range, as well as the far fields and resonance frequency of metamaterial antenna.

## REFERENCES

1. Fernandes, H. C. C. and G. D. F. Alves, "Meta-material multilayer substrate planar resonators with superconductive patch," *Progress In Electromagnetics Research Symposium Abstracts*, 382, Praha, Czech Republic, 2007.
2. Smith, D. R., P. Rye, D. C. Vier, A. F. Starr, J. J. Mock, and T. Perram, "Design and measurement of anisotropic metamaterial that exhibit negative refraction," *IEICE Trans. Electron.*, Vol. E87-C, No. 3, Mar. 3, 2004.
3. Caloz, C. and T. Itoh, *Electromagnetic Metamaterials: Transmission Line Theory and Microwave Applications*, Jonh Wiley & Sons, 2006.
4. Fernandes, H. C. C., M. B. L. Aquino, and D. B. Brito, "Rectangular slot resonator with four dielectrics layers," *PIERS Proceedings*, 2121–2126, Beijing, China, March 26–30, 2007.
5. Fernandes, H. C. C. and D. B. Brito, "Unilateral fin line directional coupler," *International Journal of Infrared and Millimeter Waves*, Vol. 28, No. 8, 651–661, USA, 2007.

# Spectral Enhancement of the SPOT Imagery Data to Assess Marine Pollution near Port Said, Egypt

M. Kaiser<sup>2</sup>, H. Aboulela<sup>1</sup>, H. A. El-Serehy<sup>1</sup>, and H. Ezz Edin<sup>1</sup>

<sup>1</sup>Marine Science Department, Faculty of Science, Suez Canal University, Egypt

<sup>2</sup>Humanities Department, College of Arts and Sciences, Qatar University, Qatar

**Abstract**— Remote sensing is a powerful tool, providing a truly synoptic view of surface water quality. Spectral enhancement of satellite images has improved significantly in recent years. In this research, satellite image data were used to detect, monitor and map different pollutants at five study sites along the El-Gamil beach including; El-Debba, El-Manasra, El-Fardous and El-Gamil inlets and the El-Gamil airport. The images were rectified and analyzed by ERDAS IMAGINE 8.7. Image processing techniques were applied using ENVI 4.2 to analyze the SPOT image data (10 m resolution) for 2006. Image enhancement, principal component analysis (PCA), band ratios and supervised/unsupervised classifications were applied. Water quality degradation, due to high discharge volumes of domestic sewage and the absence of any substantive controls on the release of toxic materials, was monitored. Surface water samples were collected during the winter of 2005 and the summer of 2006. Water contamination was found to be higher in the summer than in the winter. SPOT image data from the summer, therefore, was selected to verify the results of heavy metal analysis. Six metals, at varying concentrations, were detected along the coast: iron (Fe), manganese (Mn), cadmium (Cd), lead (Pb), zinc (Zn) and copper (Cu). The highest concentrations were: Fe (896 µg/l) at El Debba; Mn (198 µg/l) at the El-Gamil airport; Cd (2.7 µg/l) at El Fardous; Pb (56 µg/l) at El Debba; Zn (300 µg/l) at the El Gamil airport; Cu (19.3 µg/l) in El Manasra. Chemical analyses verified the surface water contamination distinguished from the satellite data. El-Gamil airport, El Gamil and El Fardous inlets were the most polluted sites due to intensive discharge of domestic, agricultural and industrial wastes. Different pollutants detected along the El Manasra and El Debba sites are associated with industrial development, and discharge from natural gas companies and electric power generating stations. Satellite imagery data were verified through a field investigation. Significant water pollution was recorded on the eastern side of the coast due to contaminants carried from the Damietta promontory by longshore currents and from other eastern cities by the reverse seasonal currents. Significant water pollution is not unique to this region of the Mediterranean Sea, but is increasingly common at coastal locations throughout the globe. To protect both the marine environment and commercial interests that depend on clean water and beaches (e.g., beach resorts), effective wastewater management practices must be designed, implemented and maintained, along with reasonable development policies. Remote sensing may be an important tool for monitoring the effectiveness of any pollution mitigation strategies.

## 1. INTRODUCTION

Despite major strides in wastewater treatment and control of point and nonpoint source pollution, contamination of surface water remains a major global environmental concern. Developing effective methodology to monitor the quality of surface water has been, and continues to be, a major focus of research [5, 7]. An increasingly important tool for environmental monitoring is remote sensing and related areas of satellite-derived imaging. Remote sensing technologies that can provide important data for multiple coastal water parameters, such as chlorophyll-a, turbidity, dissolved organic matter (DOM), total nitrogen, temperature and salinity, have been under development for nearly two decades [20]. The remote sensing techniques are based on either a radiative transfer algorithm or a statistical correlation model. The most useful water quality data are collected by airborne remote sensing from small, shallow water bodies under cloudless conditions that allow for a high level of spatial resolution. Reliable information has been obtained through multiple satellite remote sensing systems, such as the Multi-spectral Scanner (MSS), Thematic Mapper (TM), Enhanced Thematic Mapper Plus (ETM+), SPOT HRV, IKONOS and Quickbird [8]. These data were recorded as a quantitative measure of electromagnetic radiation that has either been reflected or emitted from terrestrial objects [11]. Yang [20] used ETM+ data to estimate chlorophyll-a concentrations in Pensacola Bay on the Gulf of Mexico. The *in situ* chlorophyll concentrations are estimated using band ratios as independent variables. Band1/Band3 was found to be the most effective in estimating chlorophyll-a. Using this ratio, Yang [20] identified high concentrations of chlorophyll-a along the

Gulf of Mexico coastline. The elevated levels were linked to an abundance of benthic algae, and also may have been due to phytoplankton since the chlorophyll-a measurements were higher near the outlets of several rivers [20]. Change detection is the process of addressing the variation in the state of an object or phenomenon by observing it at different intervals in time. Monitoring these temporal fluctuations is one of the most important applications of remote sensing because of the availability of continuous, or frequent discrete, observations using a uniform data collection method [2, 9, 16–18].

For the current study, SPOT images were used to monitor and analyse coastal water pollution at the El-Gamil area. The image employed in this study was acquired in 2006, with a resolution of 10 m. SPOT data were geometrically corrected based on the corrected images of Kaiser [10] and further rectified to ground control points measured during the field study. Image data, combined with field inspection and chemical analyses, have been successfully applied along the western coast of the Port Said governorate to detect and monitor surface water pollution. The goal of this study was to apply image processing techniques, including image classification, band ratio and principal component analyses, to identify highly contaminated areas along the coastal zone of the study site.

## 2. SURFACE WATER ANALYSES

Thirty surface water samples were collected at a depth of 0.5 m from five selected sites along the El-Gamil coast during the winter of 2005 and summer of 2006. Water samples were collected in one liter, white polyethylene bottles, which were placed in an ice-box following collection, and transferred to the laboratory for storage at 4°C until analysis. Total concentrations of Fe, Mn, Zn, Cu, Pb and Cd metals were analyzed using an atomic absorption spectrophotometer (AAS) (Perkin Elmer, model 1200 A), at the El-Fostat center, Cairo, Egypt, according to Standard Method 3110 [1].

The concentrations of heavy metals were higher in the summer than in the winter (Table 1). Even though there was variability among sites, the overall concentration range for a particular metal was relatively narrow, with no values that appeared to be unusual. Not surprisingly, Fe concentrations were the highest, ranging from 822.6 µg/l at El Fardous to 896 µg/l at El Debba. Cd concentrations were the lowest and ranged from 0.8 µg/l at El Gamil inlet to 2.7 µg/l at El

Table 1: Concentrations of heavy metals in water samples collected from the El-Gamil Coast during winter 2005 and summer 2006.

Metal	Seasons	Sites										Overall	
		El-Gamil Airport		El-Gamil Inlet		El-Fardous		El-Manasra		El-Debba			
		Mean	SD	Mean	SD	Mean	SD	Mean	SD	Mean	SD	Mean	SD
Fe (µg/l)	Winter	786	14.4	793.3	17.0	744	19.0	834.6	50.0	841.3	14.0	799.8	43.0
	Summer	872.6	27.0	832	24.9	822.6	14.7	846.6	30.2	896	15.0	853.9	34.1
Mn (µg/l)	Winter	170	11.1	174.6	7.5	168.6	20.8	162.0	15.0	171.3	7.5	169.3	12.1
	Summer	198	5.2	190.6	9.0	180	7.2	169.3	13.0	187.3	6.4	185	12.4
Cd (µg/l)	Winter	2.4	0.3	2.4	0.11	2.7	1.5	3.1	1.7	2.8	4.2	2.7	0.9
	Summer	2.6	0.2	0.8	1.3	2.7	0.11	2.6	0.2	2.4	0.2	2.6	0.9
Zn (µg/l)	Winter	281.3	21.5	287.3	16.7	242.6	6.4	277.3	16.2	269.3	18.5	271.5	21.4
	Summer	300	17.4	271.3	17.2	283.3	16.2	294.6	32.5	282.6	20.0	286.3	20.9
Cu (µg/l)	Winter	15.3	2.3	14.0	2.0	16.0	2.0	21.3	1.1	17.3	4.1	16.7	3.3
	Summer	13.3	3.0	12.6	2.3	14	2.0	19.3	1.1	18.6	1.1	15.5	3.3
Pb (µg/l)	Winter	34.6	7.0	31.3	5.0	35.3	6.1	44	2.0	50.0	2.0	39.0	8.2
	Summer	42.6	8.0	40	6	41.3	6.4	50.6	4.1	56.0	7.2	46.1	8.4

Fardous inlet.

### 3. IMAGE PROCESSING

Physical parameters related to the earth's surface and atmosphere behave differently when observed at different space-time scales. Monitoring techniques, either remote or ground-based, rely on the principle that alterations in land cover will result in concurrent changes in the spectral signature of the affected land surface. The accuracy of the result is strongly dependent on the processing procedure, consisting mainly of geometric correction, image classification and spectral enhancement.

#### 3.1. Geometrical Correction

Raw digital images usually contain geometric distortions due to variations in altitude, attitude, earth curvature and atmospheric refraction. Random distortions and residual, unknown systematic distortions are corrected by analyzing well-distributed ground control points (GCPs) present within an image and for which accurate ground coordinates are available. In this study, image rectification and registration were completed using ERDAS IMAGINE 8.7 (Leica Geosystems, Atlanta, USA) for the SPOT image in August 2006 (Path 178, Row 38) to monitor surface water pollution. The image was used to distinguish between water pollutants based on collected water samples during the summer of 2006.

A second-order polynomial was used, as it provides an adequate transformation for registering a scene to geographical coordinates (lat/long), in the absence of significant relief [3, 6, 19]. In order to improve the image registration and decrease the RMS errors, 25 well-distributed geographic GCPs were selected from 1:50000 scale topographic maps and measured in the field using a Garmin 38 GPS (Global Positioning System) to be used for the geometric transformation model. These points represent features that are clearly seen in both the satellite image (source points) and topographic map (reference points). Since both the source and the corresponding reference points are representing the same features, but with different  $X$ ,  $Y$  coordinates, corrections were needed. The RMS errors were decreased from 0.4890 in  $X$  and 0.4567 in  $Y$  [10] to 0.2314 in  $X$  and 0.2560 in  $Y$  in the present study. Although the cubic convolution is more complicated than both the nearest neighbour and the bilinear methods, it produces an image without the blackness that can occur with the nearest neighbour method due to the repetition of some pixel values. In addition, the output images do not have the over-smoothing problem associated with the bilinear method, which occurs as a result of the averaging process [15]. The images were geometrically corrected to the Universal Transverse Mercator (UTM) projection with a 10 m grid. In this approach, the transferred "synthetic" pixel values were determined by evaluating a block of 16 pixels from the original image matrix surrounding each output pixel. The most appropriate band combination used to create a false color composite image showing drainage, agricultural and industrial waste products along the El-Gamil coastal zone was 321; RGB (Fig. 1).



Figure 1: False colour composite of three SPOT bands (321 RGB) for 2006. Surface water pollution appears in green along the El Gamil coastal zone.

### 3.2. Image Classification

The basic premise in multi-spectral computer classification is that terrestrial objects possess sufficiently different reflectance properties (digital values commonly known as spectral signatures) in different regions of the electromagnetic spectrum. Based on these spectral signatures, natural and cultural surface features can be discriminated and a new output image created having a specific number of classes or categories [18]. Image classification is used to automatically categorize all pixels in an image into land cover classes or themes. An essential aspect of any classification is the development of training samples for the spectral signatures of all objects existing within the scene. The statistics of these training samples characterize the different classes and enable the software to assign each point in the data to one of these classes. Accordingly, the classification techniques can be divided into two general types: unsupervised and supervised. Unsupervised classification was conducted using a histogram peak cluster technique to identify dense areas or frequently occurring pixels [12]. In the unsupervised approach, spectrally separable classes are determined and defined relative to their informational utility to form a supervised classification scheme. In the supervised approach the useful information categories are defined and examined for their spectral separability. Based on a histogram of the clustering results, five well-defined spectral classes were segregated (Fig. 2), including sea water (dark blue), shallow water (light blue), turbidity and sediment accumulation (green), beach sand (dark red) and polluted water (yellow). Each class was verified in the field using a Garmin 38 GPS unit; more than 25 ground data sites were visited and checked.

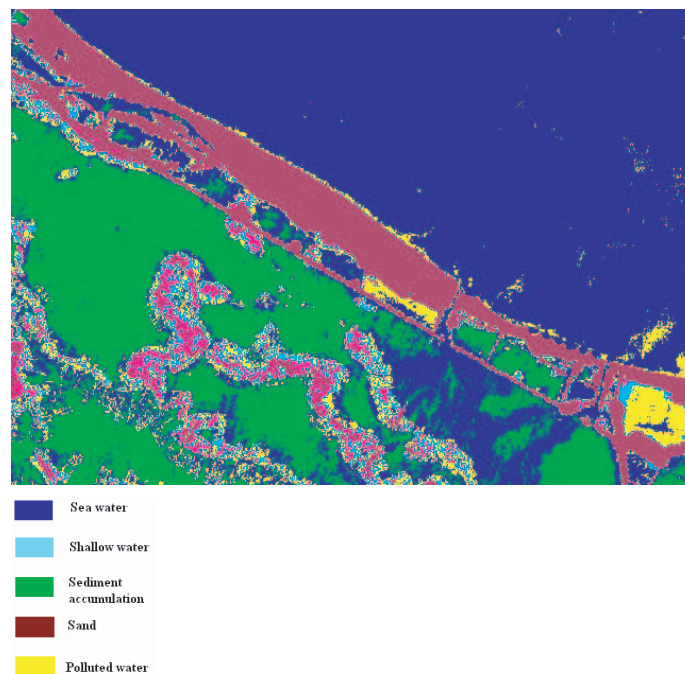


Figure 2: Supervised classification of the SPOT image for 2006, showing spectral classes at the El Gamil coastal zone.

### 3.3. Spectral Enhancement

The principal objective of enhancement techniques is to process a given image so that the result provides more extractable information, is more suitable than the original for a specific application and is more effective for visual display and interpretation. To obtain the maximum benefit from spectral enhancement, modification of a subjective image feature emphasizes certain information and improves the detectability of the target of interest by amplifying what may be very slight differences [13]. Multispectral band ratioing and principal components were used to enhance the identification of surface water pollution at the study area.

#### Spectral Ratioing:

Ratio images are calculated through the division of DN values in one spectral band by corresponding values in another band (Lillesand and Kiefer, 1979). The ratios for each cover type are nearly identical, irrespective of illumination conditions. The spectral ratio depends upon the particular reflectance characteristics of the surface features and capitalizes on small variations that might

otherwise be unquantifiable. These small variations can occur due to a number of factors, one of which is the type of pollution. In this study, the most appropriate band ratio that reflected field observations and the results of chemical analyses was  $b1/b2$  (Fig. 3). Domestic sewage and agricultural discharges through the El Fardous and El Gamil inlets appeared as a dark grey colour while industrial waste products at El Manasra appeared as a light grey colour.

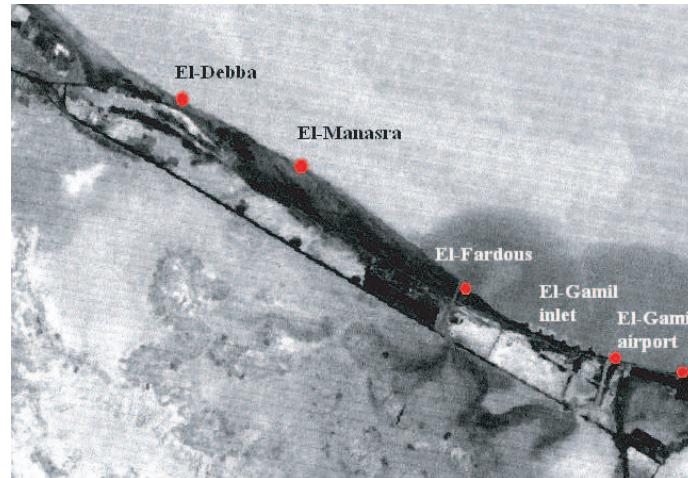


Figure 3: Results of using the  $b1/b2$  band ratio of the SPOT image for 2006, showing different types of surface water pollution in the El Gamil coastal zone.

#### Principal Component Analysis:

Principal component analysis (PCA) is used in a variety of applications, including remote sensing of alteration mapping, geologic mapping and water pollution [4, 14]. PCA was used to reduce redundancy in multispectral data. The original  $n$ -channel data set was compressed into new, and fewer, components. A new set of variables were produced as a result of the calculation of a new coordinate system and condensing of the scene variance in the original data. This procedure enhances the spectral discrimination among different water pollutants.

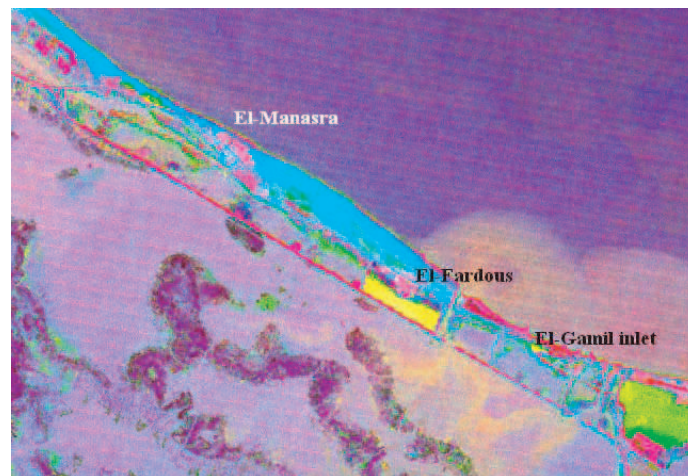


Figure 4: Band combination PC4 (red), PC3 (green) and PC2 (blue) of the SPOT image for 2006. Drainage discharge is shown as a pink colour in front of the El Fardous and El Gamil inlets.

PCA results were verified by comparison to the water pollution distinctions identified through band rationing. Statistical analyses showed that the first three components account for more than 97% of the total variance. A three-band PC coloured composite was comprised of PC1 = red, PC2 = green and PC3 = blue. The three component images may be combined to form a colour composite image which can be treated as original data and used in the classification process and treated as an original data. PC enhancement techniques are particularly appropriate when there is already a certain amount of information about the image [12]. Band combination PC4

(red), PC3 (green) and PC2 (blue) was used to detect surface water pollution originating from drainage discharge through the El-Gamil and El-Fardous inlets (Fig. 4); the pollution appeared as a light pink colour. Red and dark pink colours were found along the coast at El Manasra and the El Fardous and El Gamil inlets. This signature was found to be associated with heavy metals coming from domestic sewage and industrial and agricultural wastes. The natural gas companies Petroget, at El-Fardous, and Petrobel Blaem, at El Manasra, may contribute to this contamination. The band combination, PC1, PC2 and PC3 (Fig. 5), combined with a synthetic colour image through the selection of band 3 as the input band (Fig. 6), were used to monitor surface water pollution. A dark black strip was identified along El-Debba, El-Manasra, El Fardous and El Gamil inlets indicating water heavy metal and organic matter contamination. These pollutants likely originated from industrial and agricultural waste products, as well as the discharge of domestic wastewater along the coast.

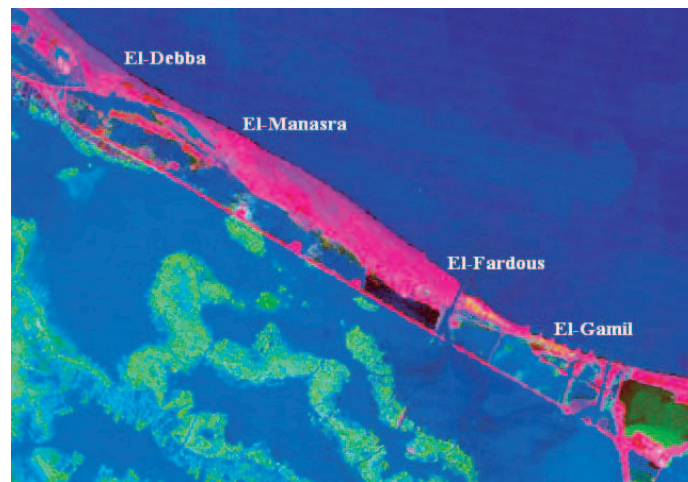


Figure 5: Band combination PC1 (red), PC2 (green) and PC3 (blue) of the SPOT image for 2006. Higher heavy metals and organic matter concentrations are shown as a black strip along the coastal zone.

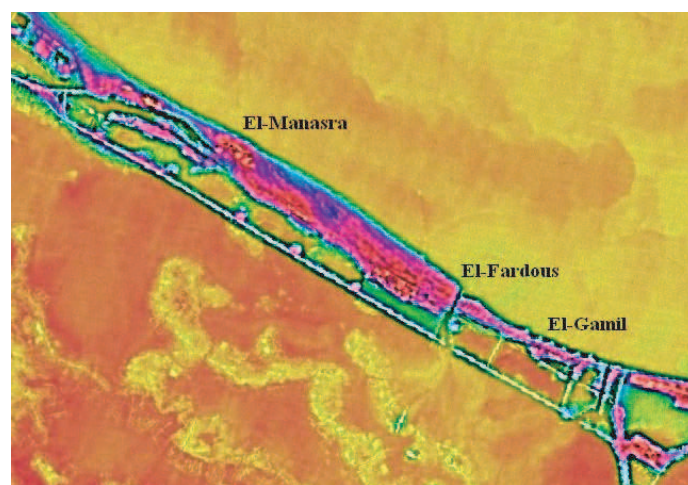


Figure 6: Synthetic colour image of the SPOT image for 2006, showing organic matter (dark strip) at El Manasra, El Fardous and El Gamil sites.

#### 4. CONCLUSION AND DISCUSSION

Spectral enhancement of the data extracted from the 2006 SPOT image (10 m resolution) was used to detect and assess surface water pollution along the western coast of the Port Said governorate. Different types of pollutants, including agricultural, industrial, organic compounds and domestic discharge were identified by analyzing surface water samples collected from the study area for heavy metals. Contaminants originating from agricultural and domestic sources were detected along the

El Fardous and El Gamil inlets. Industrial pollutants were detected at the El Manasra and El Fardous sites. These contaminants were associated with natural gas companies, pipeline industries and an electric power generating station. Image processing using ERDAS imagine 8.7 and ENVI 4.2 were utilized to verify the results obtained through chemical analysis and field observations. Supervised classification was used to identify five classes, including sea water (dark blue), shallow water (light blue), turbidity and sediment accumulation (green), beach sand (dark red) and polluted water (yellow). Band rationing  $b1/b2$  was found to be the most appropriate spectral enhancement method used to detect sewage and agricultural discharges (dark grey colour) at the El Fardous and El Gamil inlets, and industrial waste products (light grey colour) at the El Manasra site. Surface water contamination was also identified by using the band combination of PC4 (red), PC3 (blue) and PC2 (blue), produced from PCA. A light pink colour was characteristic of drainage and sewage discharge at the El Fardous and El Gamil inlets. Elevated levels of heavy metals, from domestic sewage, industrial discharge from the natural gas companies and agricultural wastes at the El Manasra and El Gamil inlets, were distinguished by red and dark pink colours. A dark black strip was detected at the El Manasra, El Fardous and El Gamil inlets by using the band combination PC1, PC2 and PC3. This strip indicated a high concentration of organic matter from agricultural and domestic wastes, in combination with elevated heavy metals produced from industrial activities. In conclusion, spectral enhancement of SPOT image data, coupled with field observations and chemical analyses, allowed for assessment and discrimination of different contaminants along the El Gamil coastal zone.

#### REFERENCES

1. APHA, American Public Health Association, *Standard Methods for the Examination of Water and Wastewater*, 16th edition, Washington, DC, 1992.
2. Anderson, J. R., "Land use and land cover changes — A framework for monitoring," *Journal of Research by Geological Survey*, Vol. 5, 143–153, 1977.
3. Bryant, N. A., A. L. Zobrist, R. E. Walker, and B. Gokman, "An analysis of Landsat Thematic Mapper P-product internal geometry and conformity to earth surface geometry," *Photogrammetric Engineering and Remote Sensing*, Vol. 51, 1435–1447, 1985.
4. Dwivedi, R. S. and T. R. Sankar, "Principal components analysis of Landsat MSS data for delineation of terrain features," *International Journal of Remote Sensing*, Vol. 13, 2309–2318, 1992.
5. Gallie, E. A. and P. A. Murtha, "A modification of chromaticity analysis to separate the effects of water quality variables," *Remote Sensing of Environment*, Vol. 44, 47–65, 1993.
6. Hardy, J. R., "Geometric quality of a Thematic Mapper image of the United Kingdom," Mansel, P. (Editor), *Proceeding of ACSM/ASPRS Convention: Racing into Tomorrow, LIDQUA Final Symposium*, 937–948, 1985.
7. Harrington, J. A., F. R. Schiebe, and J. F. Nix, "Remote sensing of lake Ckicot, Arkansas: Monitoring suspended sediments, turbidity, and secchi depth with landsat MSS data," *Remote Sensing of Environment*, Vol. 39, 25–27, 1992.
8. Hellweger, F. L., P. Schlosser, U. Lall, and J. K. Weisell, "Use of satellite imagery for water quality studies in New York Harbor," *Estuarine Coastal and Shelf Science*, Vol. 61, 437–448, 2004.
9. Ingram, K., E. Knapp, and J. W. Robinson, "Procedure for change detection using Landsat digital data," *International Journal of Remote Sensing*, Vol. 2, 277–292, 1981.
10. Kaiser, M. F. M., "Monitoring and modelling the impact of engineering structures on coastline change, Nile Delta, Egypt," PhD thesis, 270, University of Reading, UK, 2004.
11. Lindgren, D. T., *Landuse Planning and Remote Sensing*, 1–10, Martinus Nijhoff publishers, Dordrecht, 1985.
12. Lillesand, T. M. and R. W. Kiefer, *Remote Sensing and Image Interpretation*, (4th ed.), John Wiley and Sons, New York, 2000.
13. Lillesand, T. M., R. W. Kiefer, and J. Chipman, *Remote Sensing and Image Interpretation*, (5th ed.), John Wiley and Sons, New York, 2004.
14. Loughlin, W. P., "Principal component analysis for alteration mapping," *Photogrammetric Engineering and Remote Sensing*, Vol. 57, 1163–1169, 1991.
15. Mather, P. M., "Computer processing of remotely-sensing images," 1–75, (2nd ed.), John Wiley and Sons, Chichester, New York, 1999.

16. Nelson, R. F., “Detecting forest canopy change due to insect activity using Landsat MSS,” *Photogrammetric Engineering and Remote Sensing*, Vol. 49, 1303–1314, 1983.
17. Singh, A., “Tropical forest monitoring using digital Landsat data in northeastern India,” PhD thesis, 226, University of Reading, UK, 1984.
18. Singh, A., “Digital change detection techniques using remotely-sensed data,” *International Journal of Remote Sensing*, Vol. 10, 989–1003, 1989.
19. Welch, R., T. R. Jordan, and M. Ehlers, “Comparative evaluations of the geodetic accuracy and cartographic potential of Landsat-4 and Landsat-5 Thematic Mapper image data,” *Photogrammetric Engineering and Remote Sensing*, Vol. 51, 1249–1262, 1985.
20. Yang, X., “Remote sensing and GIS applications for estuarine ecosystem analysis: An overview,” *International Journal of Remote Sensing*, Vol. 26, No. 23, 5347–5356, 2005.

# Modal Propagation Analysis Method for the Design of MMI Coupler Based Microring Resonators

Laurence W. Cahill and Thanh Trung Le

La Trobe University, Melbourne, Victoria 3086, Australia

**Abstract**— The multimode interference (MMI) coupler based microring resonator is a versatile component for photonic signal processing applications. Based on this basic building block, many functional devices can be fabricated such as optical switches, filters, modulators, add-drop multiplexers, and true time delay devices. In the analysis and design of such structures it is usually assumed that the MMI coupler is described by a  $2 \times 2$  transfer matrix similar to that of a directional coupler. However, such a simple approximation is inadequate for a detailed design. The purpose of this paper is to present a more appropriate method for the analysis and design of MMI coupler based microring resonators.

In this paper, the modal propagation method is used to determine the fields of the combination of an MMI coupler and a ring resonator. This method has the advantages of good accuracy, and quick computation compared with numerical methods such as FDTD and BPM. It is shown how the structure parameters such as the width and positions of access waveguides, width and length of the MMI coupler, and the waveguide geometry, can be optimized to allow the designer to achieve a prescribed performance. This method can be applied to more complicated structures such as the double ring resonator structure, a  $3 \times 3$  MMI coupler based microring resonator, and microring resonators in series or parallel. The accuracy of the method is checked by comparison with numerical techniques.

## 1. INTRODUCTION

Ring resonators are basic building blocks for various photonic applications such as wavelength division multiplexing, add-drop filtering, optical delay lines and sensing. To obtain high speed photonic signal processing, it is desired to have a ring resonator with an appropriate quality factor (Q). For silicon on insulator (SOI) based waveguides, one approach is to use a directional coupler with a very small gap between the two waveguides to achieve high coupling coefficients. Recently, it has been shown that this method leads to additional loss due to the presence of the mode conversion loss. Therefore, multimode interference (MMI) couplers have been used in ring resonators instead of directional couplers to overcome this problem. MMI couplers have been shown to have many advantages compared with directional couplers such as relaxed fabrication requirements, less sensitivity to the wavelength, and low loss [1].

In this paper, ring resonators based on SOI technology are analyzed and designed. To analyze and design such ring resonator structures, numerical simulation methods such as FDTD or BPM often are used. However, optimization using such techniques may be tedious and time-consuming. In this paper, the problem first will be converted from 3D to 2D by using the effective index method (EIM) for structures using SOI ridge waveguides and by using a 3D eigenmode expansion method (3D EME) [2] for silicon nano-waveguides. Then, the modal propagation method (MPA) is used to obtain the field evolution within the MMI region and waveguides. This enables the transmission characteristics of the device to be determined. The results are compared with well-known numerical methods, namely the FDTD and the transfer matrix method (TMM) [3].

## 2. THEORETICAL ANALYSIS

An MMI coupler based ring resonator is shown in Fig. 1(a). The ridge waveguide structure of the MMI is shown in Fig. 1(b) whilst the nano-waveguide structure is shown in Fig. 1(c). The refractive index of the Si core is  $n_1$  and the refractive index of the cladding is  $n_2$ .

To analyze the device properties, the MMI coupler structures need to be analyzed first. It is well known that by using the modal propagation method, field distributions of the waveguide modes can be determined and this method allows one to easily optimize the device structures. The effective index method is used to reduce the dimensionality of the problem in the cross section from 3D to 2D for the ridge waveguide structure and a 3D-EME algorithm is used to reduce the dimensionality of the silicon nano-waveguide based structures.

Consider a multimode waveguide with a width  $W_{MMI}$  supporting  $m$  guided modes, and having modal field profiles  $\varphi_v(x)$ , where  $v = 0, 1, \dots, m - 1$  is the mode number. A TE input field

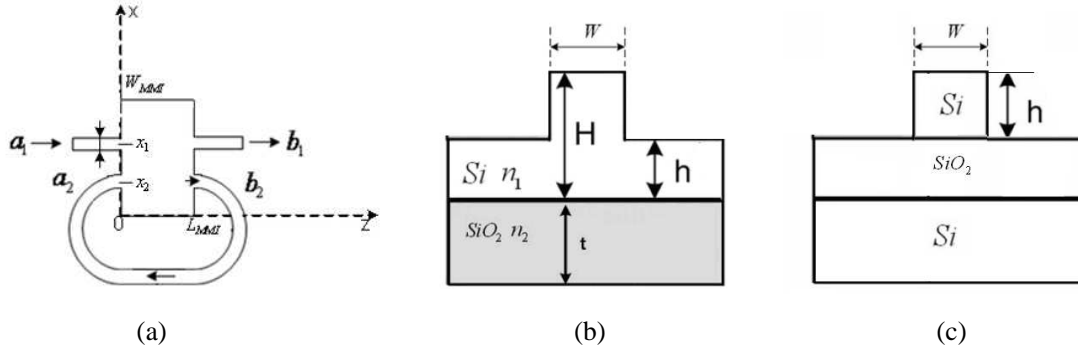


Figure 1: (a) microring resonator based on  $2 \times 2$  MMI coupler (b) SOI ridge cross-section waveguide, and (c) silicon nanowaveguide.

$\psi_1(x, 0)$  is excited at the entrance of the multimode waveguide at position  $x = x_1$  of the access waveguide 1. This field will be decomposed into the modal field distribution of all modes [4]:

$\psi_1(x, 0) = \sum_{v=0}^{m-1} c_{1v} \varphi_v(x)$ , where the field excitation coefficient  $c_{1v}$  is calculated by using overlap integrals,  $c_{1v} = \int E_1(x) \varphi_v(x) dx / \left[ \int \varphi_v^2(x) dx \right]$ . And  $\varphi_v(x)$  is the field profile of the modes in the waveguide with a width of  $W_{MMI}$  and can be given by [4]

$$\varphi_v(x) = \begin{cases} Ae^{\alpha_v x} + Be^{-\alpha_v x}, & x \leq 0 \\ D \cos[\gamma_v(x - W_{MMI}/2)] + E \sin[\gamma_v(x - W_{MMI}/2)], & 0 \leq x \leq W_{MMI} \\ Ge^{\alpha_v(x - W_{MMI})} + He^{-\alpha_v(x - W_{MMI})}, & x \geq W_{MMI} \end{cases} \quad (1)$$

where  $B = E = G = 0$  for even modes ( $v$  even) and  $A = D = H = 0$  for odd modes ( $v$  odd). The remaining constants in (1) can be determined through boundary conditions. The propagation parameters are  $\gamma_v = \sqrt{k_0^2(n_1^2 - N_v^2)}$ ,  $\alpha_v = \sqrt{k_0^2(N_v^2 - n_2^2)}$ . The effective refractive index for mode  $v$  is  $N_v$ , the wavenumber  $k_0 = 2\pi/\lambda_0$ , and  $\lambda_0$  is the optical wavelength.

The field profile  $\psi_1(x, z = L)$  within the MMI at position  $z = L$  then can be calculated as a superposition of all guided modes:  $\psi_1(x, z = L) = \sum_{v=0}^{m-1} c_{1v} \varphi_v(x) e^{-j\beta_v L}$ . The propagation constants

$\beta_v = k_0 N_v$  for the mode  $v$  can be calculated from [4]  $V\sqrt{1-b} = v\pi + 2 \tan(\sqrt{\frac{b}{1-b}})$ , where  $V = kW_{mmi} \sqrt{n_1^2 - n_2^2}$ , and  $b = \frac{N_v^2 - n_2^2}{n_1^2 - n_2^2}$ .

At the end of the MMI section, optical power is transferred to the output waveguide. Each mode of the MMI region will contribute to the mode fields in the output waveguides  $b_1$ , and  $b_2$ . These can be written as  $b_1 = c_{10} \varphi_{10}(x)$ , and  $b_2 = c_{20} \varphi_{20}(x)$ , where  $\varphi_{10}(x)$ ,  $\varphi_{20}(x)$  are the field profiles of the fundamental mode within the output waveguides. The coefficients  $c_{10}$  and  $c_{20}$  can be calculated from the overlap integrals

$$c_{10} = \frac{\int \psi_1(x) \varphi_{10}(x) dx}{\int \varphi_{10}^2(x) dx}, \quad \text{and} \quad c_{20} = \frac{\int \psi_1(x) \varphi_{20}(x) dx}{\int \varphi_{20}^2(x) dx} \quad (2)$$

The signal at output port 2 will travel through the ring waveguides and is then fed back to input port 2. This gives  $a_2 = \alpha \exp(-j\theta) b_2$ , where  $\alpha = \exp(-\alpha_0(2\pi R + L_{MMI}))$  is the transmission loss inside the resonators, and  $\alpha_0$  (dB/cm) is the loss coefficient in the core of the optical waveguides.  $\theta = \beta_0 L$  is the phase accumulated over the ring waveguides with propagation constants  $\beta_0$ , where  $\beta_0 = 2\pi n_{eff}/\lambda_0$ , and  $n_{eff}$  is the effective refractive index of the ring waveguide core.

Similarly, the field evolution within the MMI and the waveguide from the input port 2 can be calculated as before. Therefore, the total field within the MMI region at the position  $z$  is given by

$$\psi(x, z = L) = \psi_1(x, z = L) + \psi_2(x, z = L) = \sum_{v=0}^{m-1} c_{1v} \varphi_v(x) e^{-j\beta_v L} + \sum_{v=0}^{m-1} c'_{1v} \varphi_v(x) e^{-j\beta_v L} \quad (3)$$

where  $c'_{1v}$  is the field excitation coefficient from the input waveguide 2 to the MMI region.

The field at the output ports now can be calculated and the powers in output ports 1 and 2 are given by

$$P_1 = \frac{\left| \int_{-\infty}^{+\infty} \psi(x, z=L) \varphi_{10}(x) dx \right|^2}{\int_{-\infty}^{+\infty} \psi(x, z=L) \psi^*(x, z=L) dx \int_{-\infty}^{+\infty} \varphi_{10}(x) \varphi_{20}^*(x) dx},$$

$$\text{and } P_2 = \frac{\left| \int_{-\infty}^{+\infty} \psi(x, z=L) \varphi_{20}(x) dx \right|^2}{\int_{-\infty}^{+\infty} \psi(x, z=L) \psi^*(x, z=L) dx \int_{-\infty}^{+\infty} \varphi_{20}(x) \varphi_{20}^*(x) dx}$$
(4)

By using wavelength as the variable parameter in (4) the spectral transmission of the device can be determined.

### 3. SIMULATION RESULTS AND DISCUSSION

In this paper, resonators using 3 dB  $2 \times 2$  couplers are considered. Two types of MMI couplers can be used, namely those based on the restricted interference (RI) and those based on general interference (GI). Both ridge and silicon nano-waveguides are considered in this section. For the ridge structure, the thickness of the top silicon layer of the SOI wafer is  $5 \mu\text{m}$ , and the etch depth of the ridge waveguide is  $2 \mu\text{m}$ . The refractive index of the silicon is 3.45 and the refractive index of the  $\text{SiO}_2$  is 1.45 at the wavelength of  $\lambda_0 = 1550 \text{ nm}$ . Using the EIM method, the equivalent refractive indices in 2D is  $n_1 = 3.4767$  for the core region and  $n_2 = 3.4713$  for the cladding region. In our simulations, the width of the MMI was chosen to be  $24 \mu\text{m}$ , and the width of the access waveguides are  $4 \mu\text{m}$ .

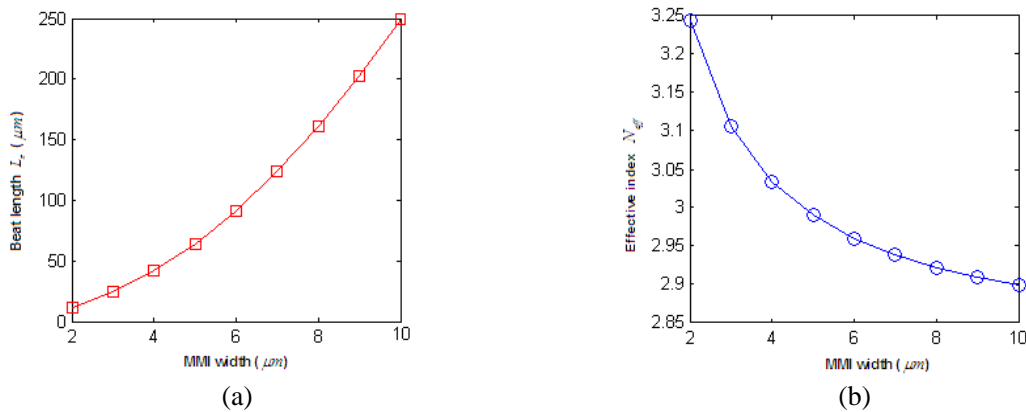


Figure 2: (a) Beat length of the  $2 \times 2$  MMI coupler (b) Equivalent effective index refractive in the 2D dimension.

For the silicon nano-waveguide structures, the height of the silicon guiding layer is  $h = 220 \text{ nm}$ . By using a 3D-EME mode solver, the 3D problem can be converted into a 2D problem, thereby enabling the equivalent effective refractive index  $N_{eff}$  of the core to be determined. Fig. 2(a) shows the beat length and Fig. 2(b) the effective index for the 2D model of a 3 dB MMI coupler based on the RI theory.

After having converted the structure into a 2D problem, the methods for analyzing and designing the device in 2D for both ridge waveguide based structures and silicon nano-waveguide based structures are similar. Therefore this paper now will concentrate on the design of the devices using the ridge structure.

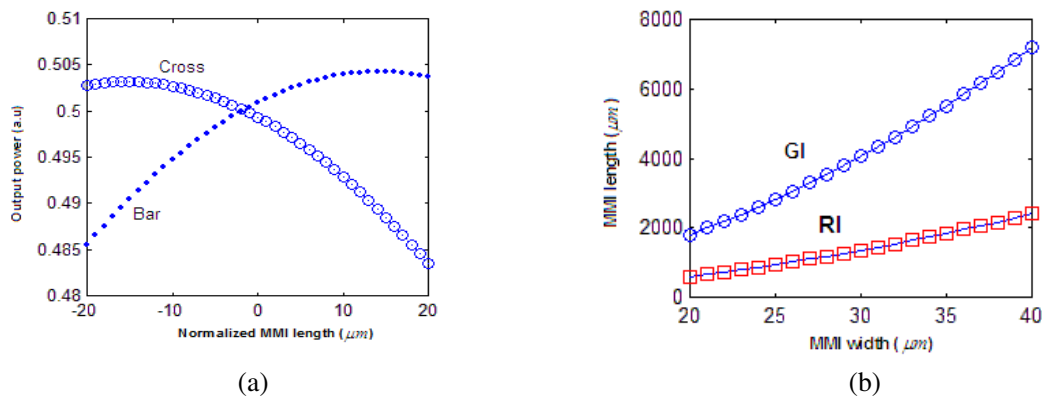


Figure 3: (a) Output powers of the  $2 \times 2$  MMI coupler (b) Optimal lengths for GI and RI MMI couplers.

Figure 3(a) shows the calculated output power at the bar and cross ports of a 3dB RI theory based MMI coupler for different MMI lengths. The access waveguides are assumed to be of width of  $4 \mu\text{m}$ . The results show that the optimum length for best power balance is approximately  $L_{\pi} - 2 (\mu\text{m})$ . Fig. 3(b) illustrates the difference between the optimized length of a 3dB MMI coupler based on the GI approach and those based on the RI theory. It is obvious that the length of the MMI coupler based on RI is much shorter than the one based on RI theory. Therefore, to reduce the size of the device and for ease of integration into more complex structures, the RI theory based MMI couplers are preferred.

The width of the access waveguides have a significant effect on the excess loss of the MMI coupler as shown in Fig. 4(a). As we see, the optimal width of the access waveguide is approximately  $6.5 \mu\text{m}$  to achieve the best performance. However, to prevent the excitation of the higher order modes in the access waveguide, and to obtain low loss in the waveguide, the access waveguides must be appropriately tapered, preferably adiabatically.

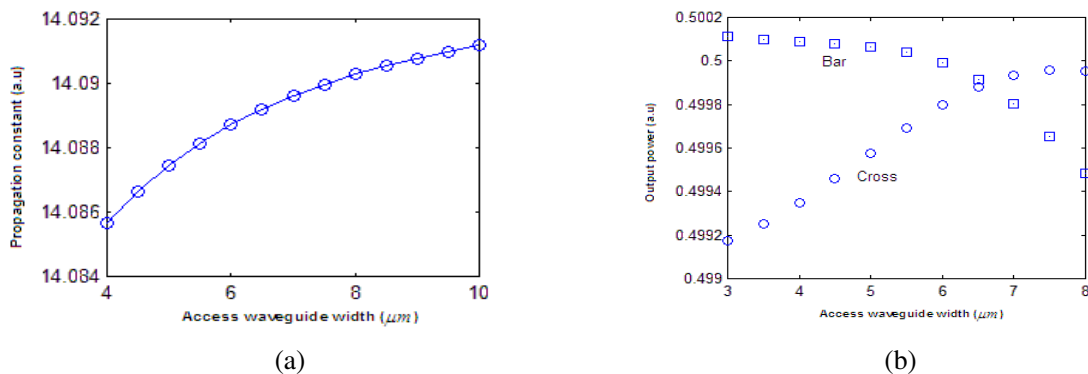


Figure 4: (a) Output powers at different waveguide widths (b) Propagation constants vs. waveguide width.

Using the adiabaticity criteria described in [5], the local taper length scale must be much larger than the coupling length between the fundamental mode and the dominant coupling mode, i.e., the local taper angle must satisfy  $\Omega(z) \leq W(z)(\beta(z) - kn_2)/(4\pi)$ , where  $\beta(z)$  is the local propagation constant at the position  $z$  with a waveguide width  $W(z)$ . The local propagation constant at different widths of the waveguide is plotted in Fig. 4(b). The resultant low-loss, adiabatically tapered access waveguide profiles are shown in Fig. 5.

The spectral transmission characteristics of the device calculated using the MPA approach are plotted in Fig. 6, along with comparable results obtained by using the transfer matrix method (TMM) and the FDTD [6]. The ring radius used in this design is  $250 \mu\text{m}$ . The results show that there is good agreement between our MPA method with the TMM and FDTD methods. However, by using the semi-analytical MPA approach, the device design parameters can be optimized more easily and quickly while still maintaining adequate accuracy for the initial design of resonators [7].

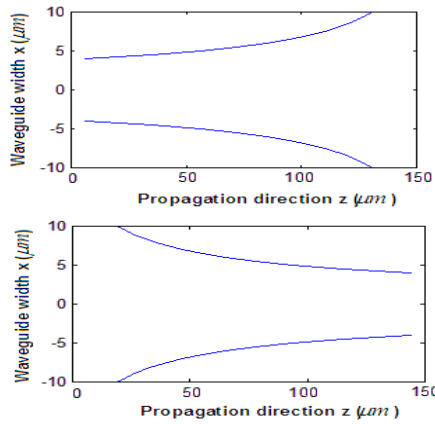


Figure 5: Adiabatic taper access waveguides.

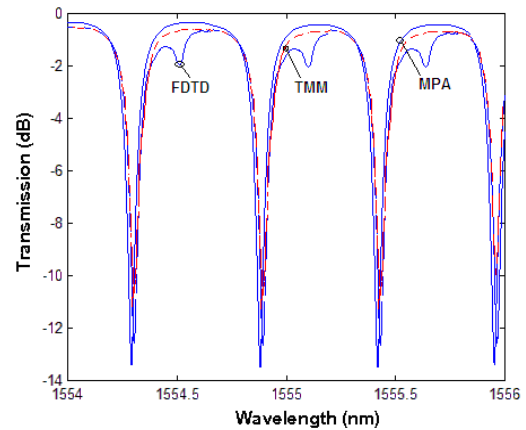


Figure 6: Transmission characteristics using three methods: FDTD, TMM and MPA.

#### 4. CONCLUSIONS

In this paper, the MMI couplers based microring resonators using SOI waveguides has been analyzed and a design procedure outlined. Simulation results have been compared with well-known numerical techniques. The modal propagation method described in this paper has the advantage of rapid calculation thereby allowing device parameters to be optimized easily.

#### REFERENCES

1. Latunde-Dada, K. A. and F. P. Payne, "Theory and design of adiabatically tapered multimode interference couplers," *J. Lightwave Technol.*, Vol. 25, 834–839, 2007.
2. Photon Design, Fimmwave: <http://www.photond.com/>
3. Yariv, A., "Universal relations for coupling of optical power between microresonators and dielectric waveguides," *Electron. Lett.*, Vol. 36, 32, 2000.
4. Le, T. T. and L. W. Cahill, "Accurate modeling and analysis of multimode interference structures by fourier technique," *Proceedings of 10th Conference on CPT 2007*, Vol. 10 G-21, 105–106, Tokyo, Japan, 2007.
5. Love, J., "Application of a low loss criterion to optical waveguides and devices," *IEE Proceedings J.*, Vol. 136, 225–228, 1989.
6. Qiu, M., "Effective index method in heterostructure slab waveguide based two-dimensional photonic crystals," *Appl. Phys. Lett.*, Vol. 81, No. 7, 1163–1165, 2002.
7. Cahill, L. W. and T. T. Le, "Photonic signal processing using MMI coupler-based microring resonators," *Proceedings of LEOS 2007*, 395–396, USA, Oct. 21–25, 2007.

# Medical Diagnostics Using Reflection Method and Waveguide Probes — Feasibility Study

R. Zajíček, T. Smejkal, L. Oppl, and J. Vrba

Department of Electromagnetic Field, Czech Technical University in Prague, Czech Republic

**Abstract**— Paper deals with the complex permittivity measurement of biological tissues. Application of a waveguide probe for this measurement is shown. A non-destructive and non-invasive method based on reflection coefficient measurement attaching the material under test is used. New types of the probes are under investigation — the section of waveguide with H cross-section, the section of waveguide with the rectangular cross-section and with shorted walls, the section of waveguide with inserted dielectric wedge and finally the section of waveguide filled with the liquid dielectric. Properties of these prototypes are studied in the frequency range from 300 kHz to 3 GHz. The method of finite difference in time domain is utilized for the numerical modeling and simulation of the reflection coefficient. The condition for the input reflection coefficient of the waveguide probe is the range from (0.7–0.3) in the broad frequency band. Although the waveguide is a narrowband microwave component, its modifications could have broadband frequency behavior of the reflection coefficient. Results indicate that the most interesting and suitable is the solution with removable dielectric. This liquid dielectric with the low value of permittivity has significant influence on the cut-off frequency of waveguide with dominant mode propagation.

## 1. INTRODUCTION

The knowledge of dielectric parameters of materials is essential for microwave or radio engineers in analysis and synthesis of devices. Relative permittivity, loss factor and conductivity are input parameters for electromagnetic field modeling and simulations. Although for many materials these parameters could be found in the tables, very often their experimental determination is necessary.

Dielectric properties of biological tissues are determining factors for the dissipation of electromagnetic energy in the human body and therefore they are basic parameters in hyperthermia cancer treatment. Measurement of the dielectric parameters of biological tissues is also a promising method in the medical diagnostics and imaging. Knowledge of the complex permittivity in an area under treatment, i.e., knowledge of the complex permittivity of healthy and tumor tissue, is very important for example in the diagnosing of tumor cell-nests in the human body or in the design of thermo-therapeutic applicators which transform electromagnetic energy into thermal in the pathological tissue [1].

## 2. MATERIALS AND METHODS

### 2.1. Complex Permittivity

Permittivity is known from the physics or theory of electromagnetic field [2] as

$$\varepsilon = \varepsilon_0 \varepsilon_c \quad (1)$$

where  $\varepsilon_0$  is free space permittivity and  $\varepsilon_c$  is complex relative permittivity (dielectrics are very often lossy). Complex relative permittivity can be given in turn as

$$\varepsilon_c = \varepsilon_r - j \varepsilon_r \tan \delta \quad (2)$$

where  $\varepsilon_r$  is real part of complex relative permittivity and  $\tan \delta$  is loss factor. For purely conductive losses is

$$\tan \delta = \frac{\sigma}{\omega \varepsilon_0 \varepsilon_r} \quad (3)$$

where  $\sigma$  is the medium conductivity.

### 2.2. Principle of Reflection Method

Reflection method means the measurement of reflection coefficient on the interface between two materials — between microwave probe (and network analyzer) and material under test (MUT, Fig. 1). Reflection coefficient is a voltage quantity which is defined as a ratio between reflected ( $E_r$ ) and incident wave ( $E_i$ ), and assumes values  $R \in \langle 0, 1 \rangle$ .

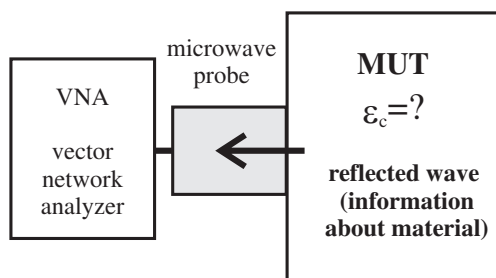


Figure 1: Illustration to the principle of reflection method.

Reflection method is a well-known method for determining the dielectric parameters for example with open-ended coaxial line as a probe [3]. This method is based on the fact that the reflection coefficient of the probe depends on the dielectric parameters of MUT which is attached to it. To calculate the complex permittivity from the measured reflection coefficient it is useful to use an equivalent circuit of the probe.

Figure 1 shows the complex permittivity measurement from the view point of theory of electromagnetic field and propagation of electromagnetic wave on the interface between two materials with different impedances [2]. The probe translates changes in the permittivity of a MUT into changes of the input reflection coefficient of the probe. The interface between the measurement probe and the sample of biological tissue represents an impedance jump (Figs. 1, 2(a)). Biological tissue has extremely high permittivity values. At low frequencies its permittivity is more than 100 and the value of the loss factor more than 0.1. An accurate evaluation is very difficult because the reflection coefficient is close to 1. This means that only a very small part of the incident energy penetrates into the sample.

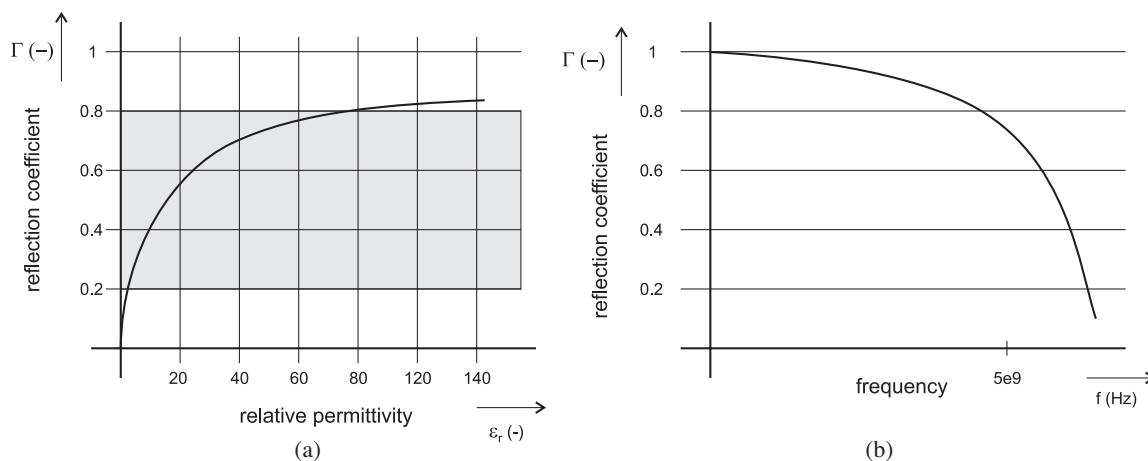


Figure 2: Reflection coefficient versus relative permittivity (a) and frequency (b).

The surface of the sample of MUT must be in the perfect contact with the probe. The thickness of a measured sample must be at least twice an equivalent penetration depth of the electromagnetic wave  $d$ . This assures that the waves reflected from the far MUT interface are attenuated approx.  $-35$  dB, which assures that their effect on the measured reflection coefficient is insignificant [4].

$$d = \frac{1}{\omega} \sqrt{\frac{2}{\mu \epsilon_0 \epsilon_r \tan \delta}} \quad (4)$$

The dependence of equivalent penetration depth  $d$  on dielectric parameters  $\epsilon_r$  and  $\tan \delta$  and also frequency  $f$  denotes Eq. (4).

### 2.3. Measurement System

A typical measurement system using the reflection method consists of the network analyzer, the probe and software (Fig. 3(a)). The probe (in Figs. 1 and 3(a)) is placed in contact with a MUT. Complex permittivity measurement is very fast and proceeds through the three steps. First the

calibration of vector network analyzer is performed. Then the calibration using a reference material (with known dielectric constant  $\epsilon_c$ ) is done. And last the reflection coefficient of MUT is measured. The complex permittivity of MUT is evaluated with the aid of PC (e.g., using MatLab on PC).

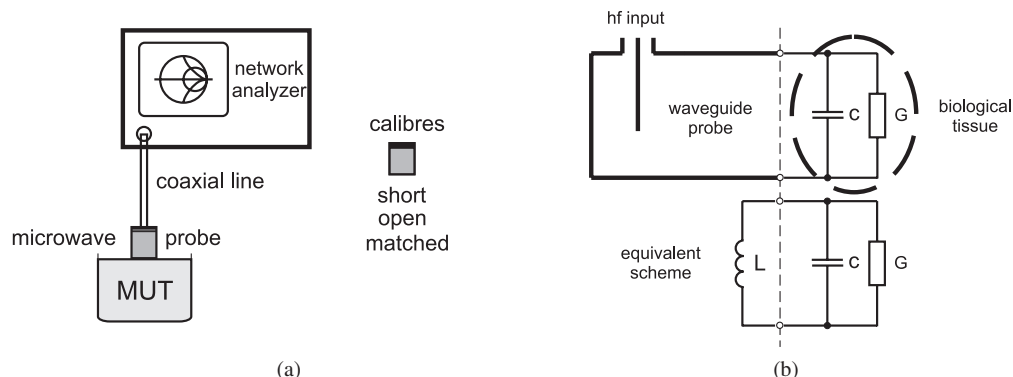


Figure 3: Measurement system (a) and equivalent circuit of probe (b).

## 2.4. Measurement Probes

Microwave technology offers three basic types of components which could be modified for the measurement purposes: *coaxial probes* — for example an adapted standard N and SMA connector [5], *planar probes* — e.g., section of microstrip line and *waveguide probes* — e.g., section of waveguide line. If we want to measure and determine complex permittivity in the broad frequency band, coaxial probe is the most frequently used component. But limitation in frequency is the higher propagation modes excited above waveguide mode cut-off frequency of coaxial probe. First waveguide mode for the N connector with teflon inside dielectric is 5.15 GHz. But if this probe is attaching a sample of biological tissue — lossy dielectric, this cut-off frequency rapidly decreases [3].

## 2.5. Modeling and Simulations

Feasibility study of the waveguide probes is based on numerical calculation and modeling. Numerical simulation utilizes a Finite Integration Technique (FIT implemented in CST Microwave Studio — electromagnetic field simulator) to calculate the reflection coefficient on the interface between the probe and sample of MUT [6]. The system that we modeled consists of two parts, i.e., the sensor and the sample of MUT. The modeling is focused on a model with distilled water — the Debye model of distilled water is implemented [7] and model with agar phantom — equivalent of biological muscle tissue (dielectric description in [5]).

## 2.6. Waveguide Probes

Waveguide probe is a section of metal waveguide with rectangular cross-section excited above the cut-off frequency. This section is shorted from one side and from another side the MUT is attached. A coaxial input is used for feeding the waveguide with electromagnetic energy (Fig. 3(b)). Only the dominant mode propagation is considered.

Design of waveguide probe comes from the design of thermo-therapeutic applicator for microwave hyperthermia working at frequency 434 MHz (2450 MHz respectively). Let's consider different modifications of the applicator in order to achieve non-resonant response of the waveguide probe [8]. Fig. 2(b) illustrates the frequency behavior of reflection coefficient. If the coaxial probe offers measurement up to approximately 2.5 GHz [5], the waveguide probe could cover the higher frequency range.

Figure 3 shows the equivalent circuit of the section of waveguide. Phase constant of this section (for  $f > f_c$ ) is

$$\beta = \sqrt{k^2 - k_c^2} \quad (5)$$

where  $k$  is free space wavenumber and  $k_c$  is cross-section constant of the waveguide.

The cross-section constant for dominant waveguide mode  $TE_{10}$  is

$$k_c = \sqrt{\left(\frac{m\pi}{a}\right)^2 + \left(\frac{n\pi}{b}\right)^2} = k_c(TE_{10}) = \frac{\pi}{a} \quad (6)$$

and for cut-off frequency constant

$$f_c = \frac{k_{cc}}{2\pi\sqrt{\epsilon_r}} = f_c(T E_{10}) = \frac{c}{2a\sqrt{\epsilon_r}} \quad (7)$$

The position of excitation probe is approximately  $\lambda/8$  from the shorted wall of the waveguide [1].

### 2.7. Waveguide with Shorted Walls

Metal waveguide with rectangular cross-section has dimensions: width  $a = 55.5$  mm and height  $b = 30$  mm, probe length  $l = 55$  mm, depth  $d = 21$  mm and distance from the shorted wall  $s = 15$  mm. This configuration is a resonant structure — at frequency 434 MHz is attenuation of reflections about value of  $-35$  dB. Between walls (and excitation probe — internal wire of N connector) is placed shorting stub. Probe is filled with the distilled water.

### 2.8. Waveguide with Inserted Dielectric Wedge

Another modification of the waveguide applicator is the insertion of dielectric wedge inside it. The same section of waveguide described above is used. Dielectric properties of the pentacarbonyl wedge were measured with the aid of coaxial probe [5].

### 2.9. Waveguide with H Cross-section

Commercially available waveguide with H cross-section WRD 475 is used (operating frequency range from 4.75 to 11 GHz). Cut-off frequency is decreased by the distilled water inside the waveguide probe. Specification: length  $l = 30$  mm, probe depth  $p = 5$  mm and distance from the shorted wall  $d = 5$  mm.

### 2.10. Waveguide Filled with Liquid Dielectric

This solution could offer utilization of the only one probe in broad frequency band with removable dielectric inside the probe. The change of permittivity in the range  $\epsilon_r \in (1, 80)$  and its influence of cut-off frequency is under investigation. The commercially available waveguide WR-340 is used.

## 3. RESULTS

Metal stubs placed inside the waveguide probe and also inserted dielectric wedge are not satisfactory solutions for dielectric measurements. Transversal shorted stub positioned in the different places results in a waveguide mode filter. Pentacarbonyl wedge attenuates electromagnetic field and the penetration depth of electromagnetic field into the MUT is then poor.

### 3.1. Waveguide with H Cross-section

Waveguide probe with H cross-section has the response as is shown in Fig. 4.

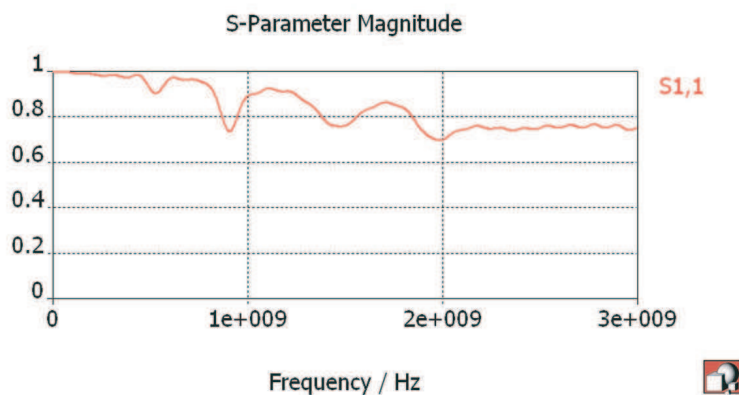


Figure 4: Frequency behavior of probe reflection coefficient.

### 3.2. Waveguide Filled by the Liquid Dielectric

Removable liquid dielectric inside the probe has influence on the cut-off waveguide frequency. Fig. 5 shows the frequency range of dominant mode propagation and also the cut-off frequency of another waveguide mode. Significant influence has small values of permittivity.

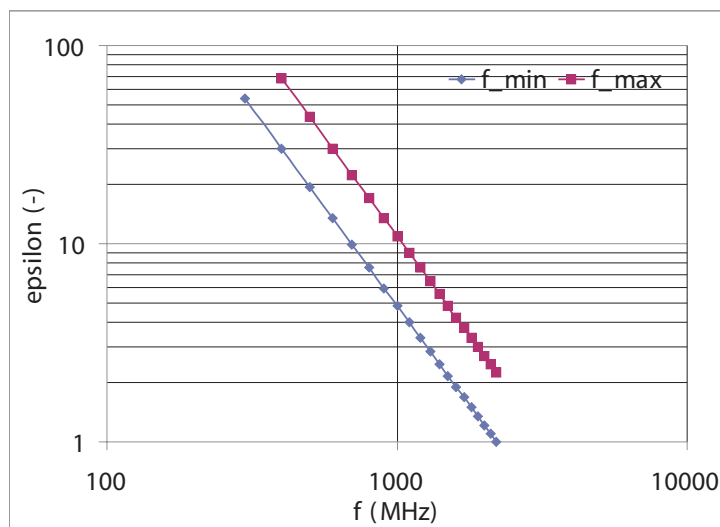


Figure 5: Cut-off frequency dependence on filling dielectric permittivity.

#### 4. CONCLUSION

Some modifications of the waveguides were shown in order to achieve the broadband frequency response of waveguide's reflection coefficient. Another step in our study is the development of a relation between reflection coefficient of the probe and the complex permittivity of MUT.

#### ACKNOWLEDGMENT

This research is supported by Grant Agency of the Czech Republic, project: "Non-standard application of physical fields — analogy, modelling, verification and simulation" (102/08/H081) and by the research program MSM6840770012 "Transdisciplinary Research in the Area of Biomedical Engineering II" of the CTU in Prague, sponsored by the Ministry of Education, Youth and Sports of the Czech Republic.

#### REFERENCES

1. Vrba, J., *Medical Applications of Microwave Technique*, Press CTU in Prague, 2003, (in Czech).
2. Novotný, K., *Theory of Electromagnetic Field*, Press CTU in Prague, 1997, (in Czech).
3. Stuchly, M. A., et al., "Measurement of radio frequency permittivity of biological tissues with open-ended coaxial line: Part I," *IEEE Trans. Microwave Theory Tech.*, Vol. 30, 82–92, 1982.
4. Oppl, L., "Measurement of dielectric properties," Dissertation Thesis, Dept. of EM field, CTU in Prague, 2001, (in Czech).
5. Zajíček, R., et al., "Broadband measurement of complex permittivity using reflection method and coaxial probes," accepted to *Radioengineering*.
6. Hudlicka, M. and P. Hazdra, "Finite integration technique," *Modeling of Fields*, 58–77, IEEE Czechoslovakia Section, 2006.
7. Dekker, J. A., *Solid State Physics*, 145–171, Translation by Martin ernohorsk, Press Academia, Prague, 1966.
8. Smejkal, T., "Waveguide probes for dielectric measurement of biological tissue," Bachelor Thesis, CTU in Prague, 2007, (in Czech).

# Applicators for Treatment of Atherosclerosis

Kateřina Novotná and Jan Vrba

Department of Electromagnetic Field, Czech Technical University in Prague  
Technická 2, 166 27 Prague 6, Czech Republic

**Abstract**— Vascular diseases are the most common cause of death in present time. This project describes the design of two different types of intracavitary applicators for treatment of the atherosclerosis by microwaves. Basic principle of microwave angioplasty is, that heating gained by microwave energy irradiated into artery by microwave applicator, enables safe clear out of atherosclerotic plates in the wall of vessel.

## 1. INTRODUCTION

This paper describes the design of special applicators for microwave angioplasty. As the most acceptable structure to create intracavitary applicators, coaxial quarter wave monopole, was chosen. Described applicators were designed for 2.45 GHz and for numerical modelling electromagnetic field distribution the simulating program was used. In our model the type of applicator for treatment of atherosclerosis was inserted in to the vein with blood and surrounded by phantom of muscular tissue.

## 2. THEORY

The applicator is one of the basic elements of the thermo therapeutic microwave medical device. It decides about efficiency to transfer the high-frequency energy from microwave generator to human body. The applicator decides about the shape and about the size of heated region too. General microwave transmission line which consists two or more conductors can transfer electromagnetic TEM wave. Characteristics and way of propagation Electromagnetic wave depend on the parameters of dielectric space, i.e.,  $\varepsilon$  and  $\mu$ .

The main advantage of the intracavitary applicator like a coaxial line is especially their efficient geometric form, small size and relative cheap technological solution to production. Coaxial applicators are often realized like a half-wave or quarter — wave monopole. These applicators are useful for middle and higher frequencies.

On the Fig. 1 is demonstrated the basic structure of coaxial applicator like a quarter — wave monopole. At point of working plane is finished the outer conductor of the coaxial line and then there is only inner conductor. The length of this section corresponds approximately of quarter of the wave length  $\lambda$  on the conduction. The frequency in which will be radiated maximum power to the biological tissue, is given with this equation

$$f_r = \frac{c_0}{\lambda\sqrt{\varepsilon_r}}. \quad (1)$$

The fundamental conception about the distribution  $SAR$  around the coaxial applicator is that the maximum  $SAR$  is in the plane where finished outer conductor of coaxial line was. The value of  $SAR$  falls symmetrical along the inner conductor and along the outer conductor.

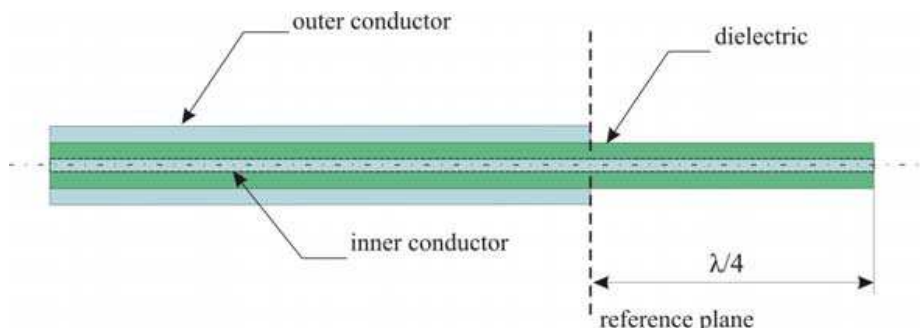


Figure 1: Coaxial quarter wave monopole.

### 3. ORIGINAL SOLUTION

For design of the intracavitary applicator a coaxial cable RG 178 BU was chosen. The main advantage of use is its flexibility because the wall of vessel is very breakable. First instance goal was to obtain good impedance matching between generator and microwave applicator. Then we studied the distribution of absorbed power (*SAR*) along the applicator. The distribution of *SAR* was deciding factor for the future use. The vessel wall is very thin and there is a risk to burn off the wall. We created two different types of applicators:

- simple monopole applicator in blood (Fig. 2),
- simple monopole applicator with ball-shaped tip in blood (Fig. 3).

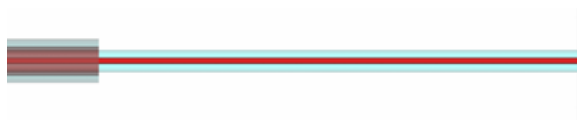


Figure 2: Simple monopole applicator.



Figure 3: Simple monopole applicator with ball-shaped tip.

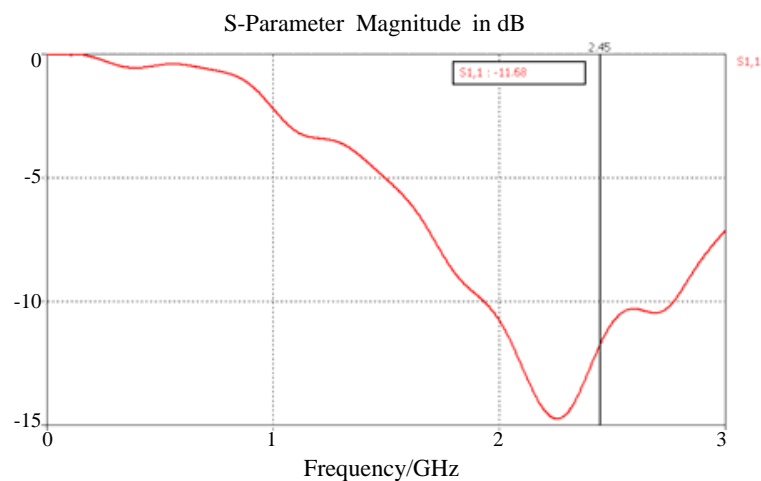


Figure 4: Impedance matching — simple monopole applicator.

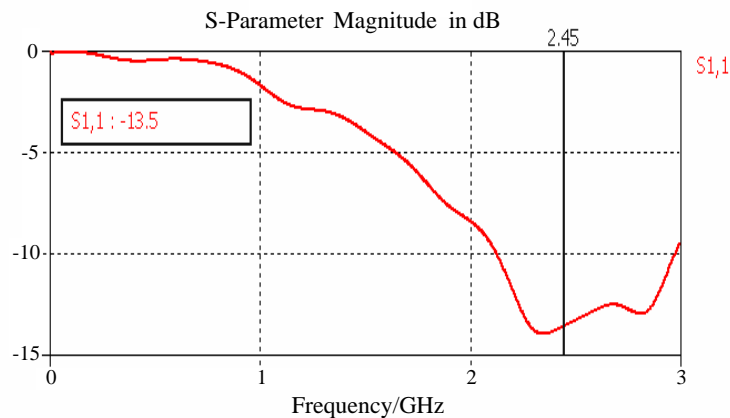


Figure 5: Impedance matching — applicator with ball-shaped tip.

The ball-shaped tip at the end of the applicator (Fig. 5) is better for good impedance matching ( $-13.5$  dB) than simple monopole applicator ( $-11.68$  dB), (Fig. 4). This type of the tip can change the distribution of  $SAR$  along the applicator.

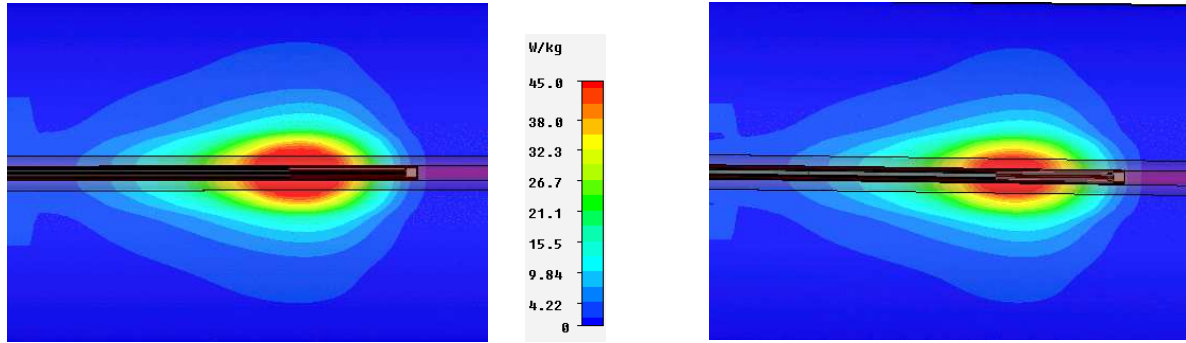


Figure 6: Simple monopole applicator in blood —  $SAR$ .

Figure 7: Simple monopole applicator with ball-shaped tip in blood —  $SAR$ .

#### 4. CONCLUSIONS

This paper describes two technical solutions to design the intracavitary applicators for treatment of atherosclerosis. In the first case (Fig. 6) the maximum of  $SAR$  was at point of termination of outer conductor, but exceeded out of the artery space. This can be dangerous from reason of possible thermal perforation of the wall of the vessel. The second case (Fig. 7) shows from this point of view much better solution. Expected temperature increase is limited to inner part of the vein. This type of applicator is much better for the future use. Final temperature distribution is influenced by blood perfusion too.

The main goal for the future of this project is to determine the optimal temperature distribution and optima distribution of  $SAR$  for different stadium of this illness.

#### ACKNOWLEDGMENT

This research is supported by Grant Agency of the Czech Republic, project: “Non-standard application of physical fields — analogy, modelling, verification and simulation” (102/08/H081) and by the research program MSM6840770012 “Transdisciplinary Research in the Area of Biomedical Engineering II” of the CTU in Prague, sponsored by the Ministry of Education, Youth and Sports of the Czech Republic.

#### REFERENCES

1. Novotná, K., “Intracavitary applicator for microwave angioplasty (in Czech),” Diploma Thesis, Prague 2007.
2. Vrba, J., “Medical applications of microwave thermotherapy (in Czech),” Publishing by CTU, Prague 2003.
3. Rosen, A., et al., “Percutaneous transluminal microwave catheter angioplasty,” United States Patent, number 4643186, Feb. 17, 1987.

# Theory of Evanescent Mode Applicators

Jan Vrba<sup>1</sup>, Paolo Togni<sup>1</sup>, Jan Vrba<sup>2</sup>, and David Vrba<sup>1</sup>

<sup>1</sup>Department of EM Field, Czech Technical University in Prague, Czech Republic

<sup>2</sup>Institute of EM Field Theory, RWTH Aachen University, Germany

**Abstract**— In this contribution we describe our new results dealing with evanescent mode waveguide hyperthermia applicators, typically used for cancer treatment. We have developed theoretical basis of this technology and designed & evaluated different versions of these applicators working below waveguide cut-off frequency.

## 1. INTRODUCTION

The most important factor determining working frequency of high frequency/microwave applicators used in hyperthermia oncology is the penetration depth of the electromagnetic field into biological tissue [1]. The penetration depth is inversely proportional to the imaginary part of complex permittivity and frequency of the electromagnetic field.

$$d = \frac{1}{\sqrt{\pi\sigma\mu f}} \quad (1)$$

With respect to usual operating frequencies of the applicators 27, 434, 915 MHz, which belongs to frequency bands reserved for industrial, scientific and medical applications, and typical (with frequency increasing loss factor) of biological tissue, it is valid that the lower the frequency the bigger the penetration depth. The most common type of applicator would be a rectangular waveguide-based applicator with dominant TE<sub>10</sub> mode. The area of the treated biological tissue limits the dimensions of applicator aperture, so that a situation, where for given dimensions of the aperture the desired operating frequency  $f$  lies under the cut-off frequency  $f_c$  of the waveguide dominant mode, is very often. There are several ways how to solve this problem e.g., modifying the cross-section of the used waveguide, filling the waveguide with high  $k$  dielectric (distilled water), but all these solutions introduces additional weight (limiting handle simplicity), realization complexity and costs. Alternatively a lumped capacitor can be inserted into a piece of waveguide operating under  $f_c$  which together with characteristic impedance of the waveguide (inductive for TE modes) forms a resonant circuit, which transmits high frequency energy into biological tissue.

Microwave circuits with evanescent mode utilize waveguides excited under cut-off frequency [1–5]. This technique allows reducing dimensions of waveguide circuit, producing compact, low weight, easy to tune and handle devices operating on low frequency and thus ensure desired penetration depth.

## 2. THEORY AND DESIGN OF EVANESCENT MODE APPLICATORS

The theory of evanescent mode applicators proceeds from well known waveguide theory. In the design of evanescent mode applicators, the waveguide is excited under the cut-off frequency. Waveguides are usually (radar, industrial applications, ...) operated in frequency band between cut-off frequency of dominant and first higher-order mode. For frequencies in this region propagation constant  $\beta$  and characteristic impedance  $Z_0$  are purely real numbers. However if a particular mode is excited under its cut-off frequency the propagation constant is purely imaginary.

$$\beta = \sqrt{k^2 - k_c^2} = -j\sqrt{k_c^2 - k^2} = -jk\sqrt{\frac{k_c^2}{k} - 1} = -jk\sqrt{\frac{f_c^2}{f} - 1} = -j|\beta|, \quad (2)$$

and characteristic impedance  $Z_{0\text{TE}}$  and  $Z_{0\text{TM}}$  of (rectangular waveguide) TE respective TM mode (e.g., [6] or [7]) is given by

$$Z_{0\text{TE}} = j\frac{k}{\sqrt{k_c^2 - k^2}}\sqrt{\frac{\mu}{\varepsilon}}, \quad Z_{0\text{TM}} = -j\frac{\sqrt{k_c^2 - k^2}}{k}\sqrt{\frac{\mu}{\varepsilon}}. \quad (3)$$

It has been shown Eq. (3) that the rectangular waveguide has an inductive characteristic admittance  $Y_0(1/Z_0)$ . At the same time, the biological tissue has a capacitive admittance  $Y_b = G_b + jC_b$  whose absolute value does not differ to much from that of  $Y_c$  in the frequency range of our interest. The different sign of the imaginary parts of this admittance implies the principal possibility to implement a simple resonator in the shape of prism. The tuning of this type of resonators is usually dependent on the pressure acted on the biological tissue, thus this would need a more complex mechanism in order to obtain it. To find a solution to these problems it is better to insert a separate capacitance into the waveguide and consider the biological tissue just as a load of the resonator.

Connecting the lumped capacitance to the inductive element, a circuit with a desired resonance frequency can be obtained. The inductive element excites a number of TE and TM modes inside the waveguide but since the operating frequency lies under the cut-off frequency, these higher order modes are attenuated according to the attenuation constant described by the Eq. (2).

From Eq. (2) follows that the distance of the inductive element from the biological tissue is a fundamental design parameter since, the proper choice of the distance allows to sufficiently attenuate the undesirable higher order modes. A modal filter can be also employed in order to suppress the unwanted modes and ensure the undisturbed field of the dominant mode at the aperture of the applicator.

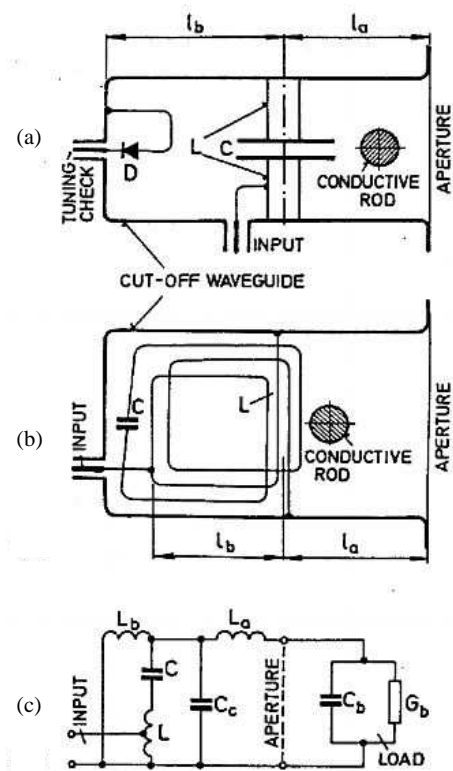


Figure 1: (a), (b) Typical configurations for waveguide evanescent mode applicators; (c) Simplified equivalent circuit for configurations (a) and (b).

Figures 1(a) and 1(b) show two examples of evanescent mode waveguide applicators. Both configurations use a capacitive element  $C$  connected into the waveguide to and inductive element  $L$ . In the first case (a),  $L$  is formed of line section and in the second case (b)  $L$  is a lumped inductance. Often is very advantageous to use a variable capacitance  $C$  in order to have possibility to finely tune the applicator to the frequency of the generator.

In Figure 1(a) it's possible to see also the presence of a diode  $D$  which is used to check the accuracy of tuning and the radiated power. In order to better explain how the applicators described so far works, Figure 1(c) shows a simplified equivalent circuit of these applicators. The main simplification is that this circuit is unbalanced against ground while the real configuration in Figures 1(a) and (b) are balanced. The meaning of  $C$  and  $L$  are the same as in Figures 1(a) and (b);  $L_a$  and  $L_b$  are the equivalent inductances of the two sections of the waveguide with a corresponding lengths  $l_a$  and  $l_b$  respectively;  $C_c$  is an equivalent capacitance explaining the stored energy of electrical field

in the waveguide;  $G_b$  and  $C_b$  express the equivalent conductance and capacitance of the heated biological tissue.

Appropriate arrangement of exciting elements can enlarge effective aperture of the applicator and thereby also influence the heating depth. In this way effective aperture can approach size of the physical aperture (for dominant mode the effective aperture is about half of its physical area). Three different arrangements (see Figure 2) are discussed:

- a) Inductive loops are inside the applicator sufficiently enough from the aperture. Applicator radiates only the dominant mode.
- b) Inductive loops are nearer to the aperture and the radiated field is a superposition of the field of dominant and higher order modes and direct effect of the loops.
- c) Inductive loops are outside of the applicator. Biological tissue is heated by electromagnetic field formed by the loops only.

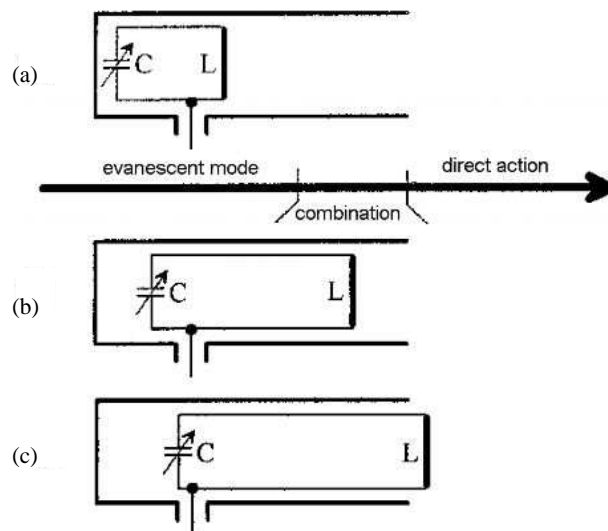


Figure 2: Location of the exciting element inside applicator with evanescent mode: (a) Excitation of the aperture by evanescent mode, (b) Combination of evanescent mode and direct heating, (c) Heating by direct effect of the excitation element only.

### 3. CONCLUSIONS

In this contribution we described our new results dealing with evanescent mode waveguide hyperthermia applicators, typically used for cancer treatment. A theoretical basis of this technology and designed was developed and evaluated with different versions of these applicators working below waveguide cut-off frequency.

This technique allows reducing dimensions of waveguide circuitry, and makes possible to produce compact, low weight, easy to tune and handle devices operating on low frequency and thus ensure desired penetration depth.

### ACKNOWLEDGMENT

This research is supported by the research program MSM6840770012 “Transdisciplinary Research in the Area of Biomedical Engineering II” of the CTU in Prague, sponsored by the Ministry of Education, Youth and Sports of the Czech Republic.

### REFERENCES

1. Vrba, J., *Medical Application of Microwave*, CVUT-FEL, Prague, 2003.
2. Togni, P., “Design and evaluation of a waveguide evanescent mode applicator for microwave thermotherapy,” Master Thesis, Czech Technical University in Prague, 2004.
3. Vrba, Jr., J., J. Boucek, and J. Vrba, “Waveguide applicators for cancer detection and treatment,” *TESLA Electronics*, 2, 1994.

4. Franconi, C., J. Vrba, and F. Montecchia, “27 MHz hybrid evanescent-mode applicators (HEMA) with flexible heating field for deep and safe subcutaneous hyperthermia,” *International Journal of Hyperthermia*, Vol. 9, No. 5, 655–673, 1993.
5. Vrba, J., C. Franconi, M. Lapes, F. Montecchia, A. Kobranov, J. Cervery, and I. Vanucc, “Cutoff waveguide applicators for hyperthermia cancer treatment,” *European Microwave Conference, 21st*, Vol. 2, 1421–1426, 1991.
6. Pozar, D. M., *Microwave Engineering*, 2 edition, John Wiley and Sons, New York, 1998.
7. Harrington, R. F., *Time-Harmonic Electromagnetic Fields*, McGraw-Hill Book Company, New York, 1961.

# Design of an Exposure Chamber for Biological Experiments

L. Visek, J. Vrba, and L. Oppl

Department of Electromagnetic Field, Czech Technical University  
Technická 2, 166 27 Prague, Czech Republic

**Abstract**— The main aim of this work is to design and to simulate an exposure chamber which can simulate mobile phone emission patterns in order to analyze the influence of electromagnetic field on small animals. During our previous research we found the most suitable type of an exposure chamber for this purpose. The basic properties such as electromagnetic field distribution and impedance matching of our designed chamber were optimized and verified by the aid of a 3D electromagnetic field simulator. As a result of our effort a cylinder waveguide chamber with a working frequency 900 MHz has been designed. In the cylindrical structure a circular polarization is excited in order to even the exposure. The chamber is terminated by matched loads on both lateral sides which serve for preventing a possible resonance between sides and the animal.

## 1. INTRODUCTION

In a modern world various sophisticated devices emitting microwave electromagnetic field are ubiquitous. These devices are used in many fields such as industry, medicine and particularly communication. An increasing daily exposure has raised the research activities in order to determine the effects of exposure to the electromagnetic radiation of mobile phones.

Therefore, many experiments on animals have been accomplished. In many cases the animals were fixed to the emitting device in such a way that they could not move. This condition induces stress in the animals and the stress itself can affect the results. Also anesthesia is not a good solution because of its stressful influence. In other cases the elimination of perturbative external electromagnetic field was missing. This condition can also affect results. For these experiments the development of an exposure system where an accurate exposure determination and elimination of stressful conditions are possible is required.

Our motivation is based on the improvements in methods to determine an accurate exposure together with the elimination of external influences which can affect results, such as stress and, of course, external electromagnetic radiation.

## 2. MATERIALS AND METHODS

The main aim of this work is to design and to simulate an exposure chamber in order to analyze the impact of electromagnetic field on small animals and to simulate mobile phone emission patterns.

To design such an exposure system it is important to satisfy the following requirements which arise from the specific purpose mentioned above:

- a working frequency of 900 MHz
- a shielding of electromagnetic field
- enough space for the animal's movement
- an even exposure
- a possibility to measure the exposure accurately
- for a long-term exposure providing illumination and ventilation

The basic structure of the exposure chamber consists of two cylindrical waveguides connected to each other. This structure provides a shielding of electromagnetic field generated inside in order to protect the operators and also generated outside the system in order to eliminate parasitical radiation. Dimensions of the exposure chamber were calculated having in mind two endpoints: desired frequency of operation and the volume needed to expose small animals. The dimensions of the chamber components were computed starting from the waveguide radius because it is a critical value which can affect electromagnetic field excitation and distribution. It is needed to choose radius so that a suitable electromagnetic field distribution can be excited. As the most appropriate mode TE<sub>11</sub> was chosen (see Fig. 1).

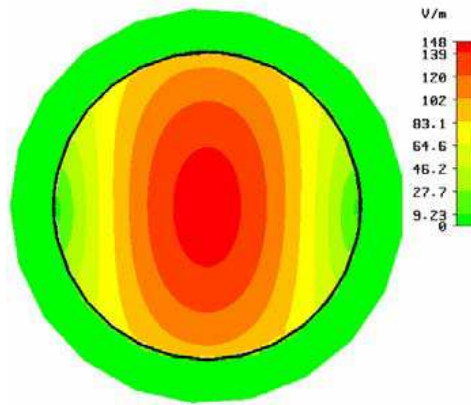


Figure 1: Distribution of electric field strength of mode TE<sub>11</sub>.

By analysis of a waveguide cut-off frequency formula (1) a value of the radius was chosen with respect to the TE<sub>11</sub> mode and the request of large volume for the animal exposure.

$$f_{c11} = \frac{c \cdot p'_{11}}{2\pi r \sqrt{\mu_r \epsilon_r}} \quad (1)$$

where  $c$  is the speed of light,  $r$  is the desired radius of the waveguide,  $\mu_r$  is the relative permeability,  $\epsilon_r$  is the relative permittivity and  $p'_{11}$  is the value 1,84 (see Lit.1).

In order to even the animal's exposure we have chosen a cylindrical structure where a circular polarization can be excited. Electromagnetic field is excited in the chamber by the aid of two capacity screws. There were two possibilities of how to approach the design. First, both capacity screws could be situated perpendicularly in one cutting plane and the signal amplitude being the same on both screws but exciting signal phase shifted to 90 degrees on one of them. Or second, the capacity screws could be at one-fourth of the wavelength distance. Signal amplitude and phase would then be the same on both screws. Screws' lengths itself were chosen to be one-fourth of the wavelength.

To measure an accurate exposure it is desirable to avoid resonance between the terminating sides and the animal. Matched loads on both lateral sides can serve this purpose. In order to avoid reflection and assure an attenuation of power the loads must be made of lossy dielectric material and must have a suitable shape. The electrical resistance of the shape should grow linearly in a direction of the wave's propagation. According to previous conditions the shape was designed as a cylinder with a cone gap (see Fig. 2).

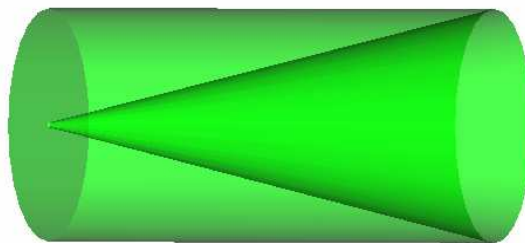


Figure 2: Shape of lossy dielectric material.

We set the length of the cylinder to one wavelength. The dielectric material properties were set to  $\epsilon = 17 + 1.2j$  and  $\mu = 3 + 0.39j$ .

A power balance is determined by the aid of power reading screws which are situated in the same mutual position like the exciting screws. Because the circular polarized wave can be backwards divided into linear polarized waves the power balance can be determined by analysis of  $S$  parameters between measurements of an empty chamber and a chamber with animals and simultaneously

between the corresponding screws. In this way it can be accurately determined how much energy is, in fact, absorbed by the animals.

The exposure chamber was designed to allow long-term exposure of small animals like mice and rats. The waveguide sides are provided with two small holes continuing outside with small waveguides. They serve for a softened illumination and ventilation support. A radius of these two waveguides was chosen to be 20 mm and therefore working like evanescent. Through evanescent waveguides the outside radiation is eliminated.

Basic properties such as electromagnetic field distribution and impedance matching of the designed chamber were optimized and verified by a 3D electromagnetic field simulator.

### 3. RESULTS

We have designed a cylindrical waveguide chamber where a circular polarization can be excited. By analysis of formula (1) with respect to frequency 900 MHz and a propagation in the air, the radius of the cylinder waveguide was obtained. The computed value is 120 mm. The length of the waveguide was set in such a way that enough space for animal movement is assured. Its value was set to 650 mm. There were two possible configurations of the exciting screws — in one cutting plane or shifted. First of them was not a suitable solution because the transmission between screws took a high value — approximately  $-3$  dB. The second configuration reached usable values. Transmissions between screws took a low value — approximately  $-26$  dB (see Fig. 3).

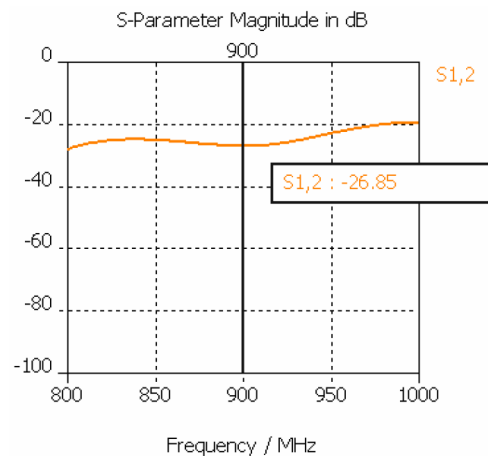


Figure 3: Transmission between exciting screws.

The value of impedance matching for the exposure system is a very important parameter. Values reached are displayed in Figs. 4 and 5.

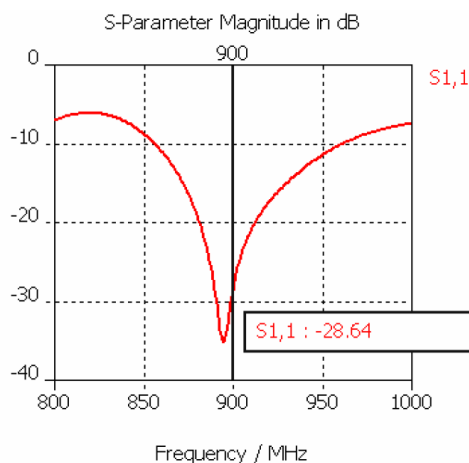


Figure 4: Impedance matching for the first exciting screw.

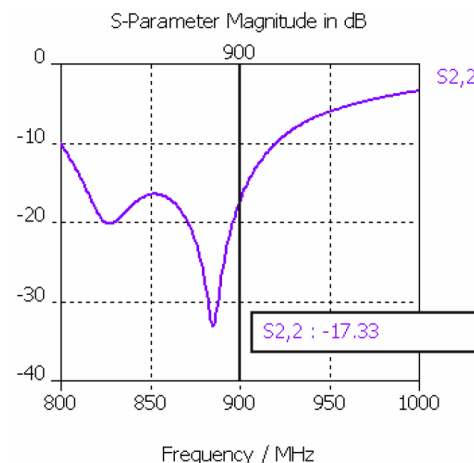


Figure 5: Impedance matching for the second exciting screw.

Figure 6 displays a complete view on the configuration of the designed exposure system.

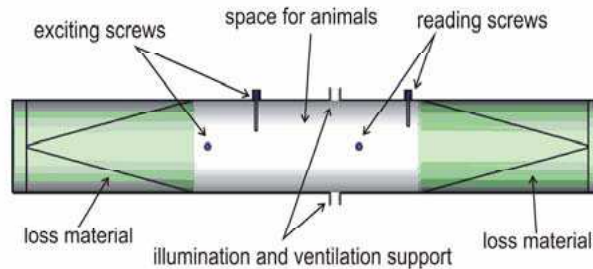


Figure 6: A configuration of designed chamber-longitudinal cutting plane.

#### 4. CONCLUSIONS

As a result of our efforts a cylinder waveguide chamber was designed which satisfies all the requirements for accurately emulating the effects of mobile phone emission on animals. In order to even animals exposure it was chosen cylinder structure where can be excited a circular polarization. The chamber is terminated by matched loads on both lateral sides. These loads serve for preventing a possible resonance between sides and animals and therefore the accurate exposure can be determined. The next important issue is to assure a suitable milieu for animals (support air and light). Evanescent waveguides can serve for this purpose well.

#### ACKNOWLEDGMENT

This research is supported by Grant Agency of the Czech Republic, project: “Non-standard application of physical fields — analogy, modelling, verification and simulation” (102/08/H081) and by the research program MSM6840770012 “Transdisciplinary Research in the Area of Biomedical Engineering II” of the CTU in Prague, sponsored by the Ministry of Education, Youth and Sports of the Czech Republic.

#### REFERENCES

1. Vrba, J., *Úvod do Mikrovlnné Techniky*, CTU Press, 2003.
2. Vrba, J., *Měření na Centimetrových Vlnách*, SNTL, Prague, 1958.
3. Pozar, D. M., *Microwave Engineering*, third edition, John Wiley & Sons, Inc., 2005.
4. Balanis, A. C., *Antenna Theory: Analysis and Design*, second edition, John Wiley & Sons, Inc., 1997.
5. Goiceanu, C., D. D. Sandu, and O. G. Avădănei, “TEM cell as exposure system for biological experiments,” *Romanian J. Biophys.*, Vol. 15, Nos. 1–4, 141–146, Bucharest, 2005.
6. Salford, L. G., A. E. Brun, J. L. Eberhardt, L. Malmgren, and B. R. R. Persson, “Nerve cell damage in mammalian brain after exposure to microwaves from GSM mobile phones,” *Environmental Health Perspectives*, Vol. 111, No. 7, 2003.
7. Ilhana, A., A. Gurelb, F. Armucub, S. Kamislia, M. Irazc, O. Akyold, and S. Ozen, “Ginkgo biloba prevents mobile phone-induced oxidative stress in rat brain,” *Clinica Chimica Acta*, Vol. 340, Nos. 1–2, 153–162, 2004.
8. Visek, L., P. Togni, J. Vrba, and L. Oppl, “Design and comparison of exposure chambers for verification of microwave influence on biological systems,” *PIERS Online*, Vol. 3, No. 8, 1346–1350, 2007.

# Hyperthermia Applicator for Small Superficial Tumor Treatment

P. Togni<sup>1</sup>, J. Vrba<sup>1</sup>, and L. Vannucci<sup>2</sup>

<sup>1</sup>Dept. of Electromagnetic Field, Czech Technical University in Prague, Czech Republic

<sup>2</sup>Dept. Immunology, Institute of Microbiology  
Academy of Sciences of the Czech Republic, Czech Republic

**Abstract**— The use of electromagnetic fields in biomedicine for cancer treatment and diagnostics, nowadays begin to be quite widespread. This paper describes the design and the evaluation of a microwave applicator for treatment of small subcutaneous tumours implanted on animal model. The support of computer simulations was used to evaluate and optimise the fundamental parameters of the applicator and the temperature distribution in the biological tissue. The Results give the prospective to use this applicator for the study of the effects of hyperthermia treatment in relation with the characteristics of the treated tumour.

## 1. INTRODUCTION

Microwave induced hyperthermia (MWIHT) represents an important tool in anti cancer treatments, both as an adjuvant of chemo and radiation therapies and as an ablative procedure, according to the type of applicator used. When the temperature of a part of the body is enhanced over 3°C above its normal value, the cells start to be under thermal stress. Going above 41.5°C this stress begins gradually to induce irreversible damages (cell apoptosis/necrosis), inversely proportional to the ratio heat intensity over time.

Microwaves can induce effective and quite homogeneous hyperthermia, associated to direct effects on cellular molecules and H<sub>2</sub>O. Effective delivery of microwaves depends from precise characteristics of microwave applicators which must be able to focus the electromagnetic energy as better as possible just in cancer tissue in order not to damage the surrounding healthy tissue. In any case, the blood perfusion rate, which is normally higher in the healthy tissues, helps to obtain a better localized temperature enhancement in the cancer. In fact, when the temperature of body part is enhanced, the blood flow increases as well, acting as a cooler. Since the vascular system of tumours is irregular and incompletely developed, this cooling effect is thereby lower than in normal tissues. In these conditions, on equal electromagnetic energy exposure the temperature inside the tumour will be maintained higher with cumulative effects [1]. Also the use of a pulsed power feeding, instead of a constant one, can help in this purpose. For the same reason explained above, during the pause between one pulse and another, the healthy tissue has more possibilities to dispel the heat, with consequent lower thermal stress than in the tumour.

Hyperthermia is newly back in the interest of both, clinical and research oncologists, because its properties to directly produce permanent damage of the treated tumour and to elicit important immunological responses against the cancer cells by changing their immunogenicity [2]. However, this renewed interest for the use of hyperthermia, as an anti-tumour therapy, requests studies that can permit to develop appropriate delivery systems and to establish parameters for evaluating the efficacy of the treatment. In this view we need, on one side applicators able to deliver the right dose in the right volume of tissue, on the other side, we need a method to quickly reveal *in-vivo* the modifications induced in the tissue by the heating. An important aim is to determine the effect of the treatment in relation with the characteristics of the treated tumour.

To do this we study the morphological changes, induced by hyperthermia, in the superficial layers of experimental tumours in animal models by *in-vivo* confocal microscopy. The confocal microscopy has the possibility to make visible, without staining the architecture of tissues, also in fresh samples and *in-vivo* [3], especially with the use of some new methods such as the reflectance mode (RM) and second harmonic generation (SHG- imaging: 2-photon excitation) [4, 5].

## 2. APPLICATOR DESIGN

In the design of this microwave applicator some precise requirements have been taken in to account. Our target is to use this applicator for experiments which will be principally performed on *in-vivo* models made by subcutaneous tumours implanted in mice. The dimensions of such tumours are quite limited, a diameter smaller than 20 mm and a deepness normally smaller than 15 mm. Because of the limited dimensions of the tumours and of the bodies of animals under treatment, for this kind

of experiments, it is necessary to use applicators which guarantee a limited intratissutal penetration of the electromagnetic field. For these reasons the use of a planar structure is more desirable to other kind of applicators like waveguide types, since they can guarantee a smaller penetration depth of the radiated electric field. Also the choice of a quite high working frequency, the ISM band centred at 2450 MHz, reduce the penetration of the treatment in the tissue compared to most common used 434 MHz. The reduction of the penetration depth of the field is also very important in order not to enhance body temperature of the animal, which for its contained dimensions can be easily overheated. Since these tumours are subcutaneous, the use of a water bolus is necessary to protect the skin and prevent burns. The water bolus can also guarantee a good contact between the applicator and the irregular surface of the animal, which is a condition to guarantee a proper impedance matching.

This applicator has a squared planar structure composed by a printed circuit board (PCB) metalized on both sides. The two metalizations are short-circuited all around the applicator obtaining, in such a way, a squared cavity. On one metalization is etched an annular slot [6] which acts as aperture to radiate the microwave energy to the biological tissue. The dimension of the cavity side are such to obtain the first resonance mode  $TE_{101}$  in correspondence of the working frequency. This dimension has been obtained using the relation of the resonance frequency for rectangular waveguide cavities [7]:

$$f_{mnl} = \frac{c}{2\pi\sqrt{\epsilon_r\mu_r}} \sqrt{\left(\frac{m\pi}{a}\right)^2 + \left(\frac{n\pi}{b}\right)^2 + \left(\frac{l\pi}{d}\right)^2} \quad (1)$$

The cavity is filled with dielectric material which permittivity depends on the material used as substrate. In our case this value is  $\epsilon_r = 4.3$  so, for this working frequency, the dimension of the substrate side is  $a = d = 41.75$  mm. Changing the characteristics of the substrate it is then possible to obtain more compact or bigger dimensions for the applicator, according to the dimensions of the area which has to be treated. The thickness of the substrate used is 1.5 mm, in any case, the resonance of the excited mode does not depend on this parameter. To feed the applicator, a  $50\ \Omega$  N-type connector is placed on the metalization on the opposite side of the slot aperture. The internal conductor, passing through the substrate, is welded at the centre of the second metalization. A view of the manufactured applicator is given in Fig. 1.



Figure 1: Pictures of the applicator.

Because of the presence of the connector, which inner conductor is inside the cavity, and the annular ring aperture, some changes of the value of the resonance frequency are expected from the value calculated above. In order to predict this variation and to optimise the dimensions of the applicator, computer simulations were used. The 3D electromagnetic field simulator used was Speag Semcad X based on FDTD method. With the help of the simulator was possible to analyse the dependence of  $S_{11}$  parameter on applicator dimensions shifting the resonance peak in correspondence of working frequency.

The modelled phantom is composed by a homogeneous block of material with characteristics similar to muscles tissue to simulate the biological tissue. Its dimensions are such to have an almost complete attenuation of electromagnetic field in correspondence of the boundaries. The water bolus is modelled with a 20 mm thick block of distilled water. The electromagnetic characteristics of the materials used for the phantom and the bolus are summarized in Table 1.

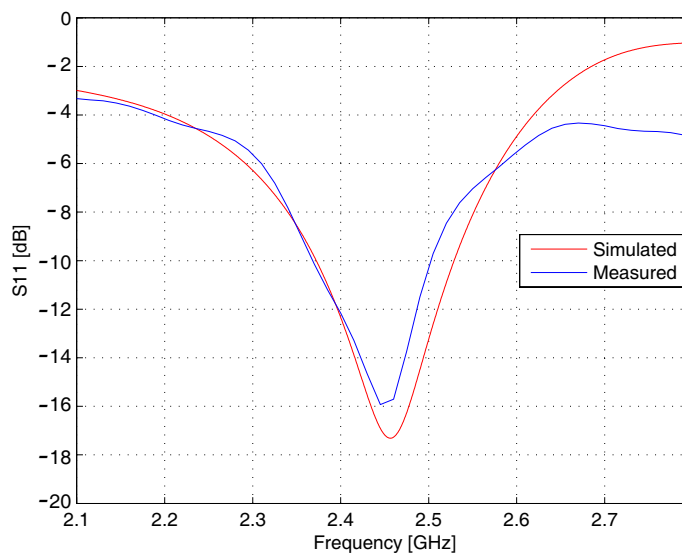
Table 1: Properties of the materials used for simulations.

Material	Relative Permittivity	Electric Conductivity	Density	Thermal Conductivity	Specic Heat	Blood Perfusion Rate	Temp.
	$\epsilon_r$	$\sigma[\text{S m}^{-1}]$	$\rho[\text{Kg m}^{-3}]$	$k [\text{W m}^{-1} \text{ }^\circ\text{C}^{-1}]$	$c [\text{J kg}^{-1} \text{ }^\circ\text{C}^{-1}]$	$F[\text{m}^3\text{kg}^{-1}\text{s}^{-1}]$	$T[^\circ\text{C}]$
Muscles	52.729	1.7388	1020	0.6	3500	$8.6 \cdot 10^{-6}$	37
Dist. Water	76.7	1.2	1000	-	-	-	20
Substrate	4.3	-	-	-	-	-	20

In order to evaluate the deepness and the superficial spreading of the treatment, the simulator was also used to calculate the SAR distribution and the temperature distribution inside the biological tissue. In particular the temperature distribution is important to evaluate the function of the water bolus as superficial cooler [8]. The simulation of the temperature distribution is based on the Bio-Heat Transfer Equation developed by Pennes [9]. The temperature distribution simulations were limited to the phantom, considering the temperature of the bolus at a constant value. On the interface between the biological tissue and water bolus, a Dirichlet boundary condition was used. Another parameter which is considered by the bio-heat equation is the effect of the blood perfusion. In this model this parameter was considered constant for the entire phantom volume. The thermal parameters used for the simulations are also summarized in Table 1.

### 3. RESULTS

From the simulations of the  $S_{11}$  parameter as a function of frequency, was found that the best setting is obtained using a dimension for the applicator side equal to 43 mm and the width of the slot-line equal to 3 mm. To support the results of the simulations, the  $S_{11}$  parameter was then measured with the help of the vector analyzed Agilent E6052. These measurements were made on a flat Agar phantom with electromagnetic characteristics similar to muscles tissue. Since the water bolus was not available, this measurement were made covering the phantom with distilled water and putting the applicator directly in contact with the water at the desired distance to the phantom. The measurement has shown that the best results are obtained reducing the slot-line width to 1 mm. Changing the thickness of water layer on the phantom, it was seen also in this case that the  $S_{11}$  does not depend too much on bolus thickness. In Fig. 2 are shown the result of simulations and measurements for  $S_{11}$  as function of frequency considering a bolus 20 mm thick.

Figure 2:  $S_{11}$  parameter with a water bolus thickness of 20 mm.

The results of the SAR distribution simulations inside the biological tissue are shown in Fig. 3. In Fig. 3(a) is shown the normalized SAR distribution on the surface of the phantom and in Fig. 3(b) the distribution inside the phantom considering a cutting plane passing through the centre of the applicator. From these two figures, it is possible to evaluate the penetration depth and the area covered by the treatment. These distributions show how the requirement of a limited penetration

of the treatment is satisfied. It can be clearly seen from the SAR distribution calculated inside the phantom (Fig. 3(b)), that this penetration can be evaluated within 10 mm. The simulations have also shown, as expected, how the penetration depth of the electric field does not depend on the bolus thickness. On the contrary this thickness plays a key role on determination of the extension of the treatment area. Considering that, the tumours we would like to treat have a diameter between 10 to 20 mm, a bolus thickness of 20 mm is advised in order to cover at best tumours with this dimensions during the experiments. It was also seen from these simulations that the use of this applicator without or with a too thick water bolus crates an hot-spot in correspondence of its centre with the risk of skin burns. Fig. 4(a) shows the results of the temperature distribution simulations inside the phantom using an input power for the applicator of 30 W, after an exposition time of 6 minutes. As expected the penetration of the temperature is deeper than for the SAR because of the temperature diffusion. In any case, the temperature values which can induce thermal damages are with 12–14 mm from the surface. This result can be considered satisfying since in in-vivo, the blood perfusion of the tumours is lower than in the surrounding healthy tissue. Therefore an higher value of temperature is expected in the tumour core. Fig. 4(b) shows the temperature inside the phantom at different times. Both figures show also a good cooling of the surface till 2–3 mm, so no thermal damages of the skin are expected during the treatments.

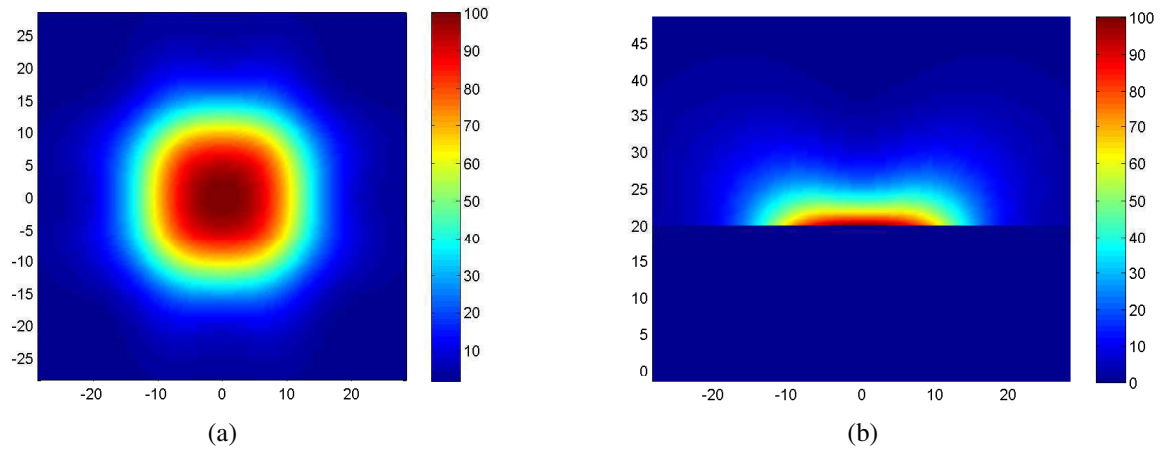


Figure 3: Simulated normalized SAR distribution in %, using a 20 mm water bolus, (a) on the surface, (b) inside the phantom.

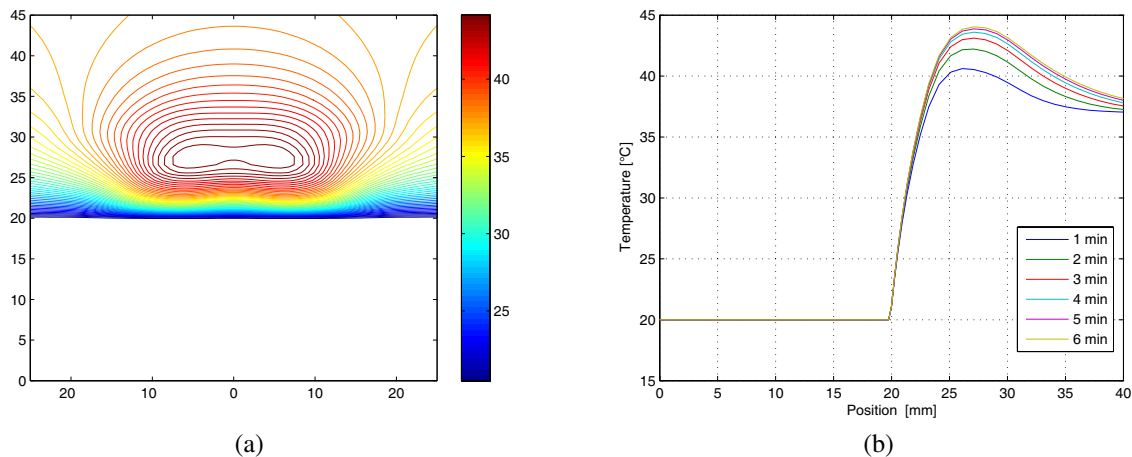


Figure 4: Simulated temperature distribution using a 20 mm water bolus, (a) on the surface, (b) simulated temperature along the agar axis in correspondence of the applicator centre.

#### 4. CONCLUSION

The results of the SAR and temperatures distributions obtained by computer simulations have shown the possibility to use such an applicator for the treatment of superficial tumours with small dimensions. This gives the possibility to carry out experiments on in-vivo tumour model on small animals such as mice. The limited penetration of the electric field in the phantom, could also guarantee a contained risk to radiate also the healthy tissue located below the cancer or to increase to much the body temperature of the animals. The simulations and measurement of the  $S_{11}$  parameters, in correspondence of the applicator input, have shown a real independence of this parameter on the water bolus thickness. This shows the capability for this applicator to be used also on irregular surfaces as could be the body of a mouse. Thanks to this applicator characteristic, a good impedance matching can be guaranteed in the most of the conditions of treatment. The perspective is, after the evaluations of the result on animal model, to use such an applicator in clinical practice for the treatment of small and superficial diseases considering the development of arrays of applicators for the treatment of bigger areas.

#### ACKNOWLEDGMENT

This study is funded by the Grant Agency of the Academy of Sciences of the Czech Republic IAA500200510, Institutional Research Concepts No. AV0Z50200510 and by the Grant Agency of the Czech Republic, Grant No. 102/08/H081.

#### REFERENCES

1. Vrba, J., *Medical Applications of Microwaves*, CTU Press, Prague, Czech, 2003.
2. Baronzio, G., A. Gramaglia, and G. Fiorentini, "Hyperthermia and immunity. A brief overview," *In Vivo*, Vol. 20, No. 6A, 689–95, 2006.
3. Chen, C., M. Elias, K. Busam, M. Rajadhyaksha, and A. Marghoob, "Multimodal in-vivo optical imaging, including confocal microscopy, facilitates presurgical margin mapping for clinically complex lentigo maligna melanoma," *Br. J. Dermatol.*, Vol. 153, No. 5, 1031–6, 2005.
4. Carlson, K., I. Pavlova, T. Collier, M. Descour, M. Follen, and R. Richards-Kortum, "Confocal microscopy: Imaging cervical precancerous lesions," *Gynecol. Oncol.*, Vol. 99, 3 Suppl 1, 84–8, Dec. 2005.
5. Lin, S. J., S. H. Jee, C. J. Kuo, R. J. Wu, W. C. Lin, J. S. Chen, Y. H. Liao, C. J. Hsu, T. F. Tsai, Y. F. Chen, and C. Y. Dong, "Discrimination of basal cell carcinoma from normal dermal stroma by quantitative multiphoton imaging," *Opt. Lett.*, Vol. 31, No. 18, 2756–8, 2006.
6. James, J. R. and P. S. Hall, *Handbook of Microstrip Antennas*, 346–7, by J. R. James and P. S. Hall (Eds.).
7. Pozar, D. M., *Microwave Engineering*, 313–8, 3rd ed., John Wiley & Sons, Inc.
8. Van der Gaag, M. L., M. de Bruijne, T. Samaras, J. van der Zee, and G. C. van Rhoon, "Development of a guideline for the water bolus temperature in superficial hyperthermia," *Int. J. Hyperthermia*, Vol. 22, No. 8, 637–56, Dec. 2006.
9. Pennes, H. H., "Analysis of tissue and arterial blood temperatures in the resting human forearm," *J. Appl. Physiol.*, Vol. 85, 534, 1998.

# Measurement of Yeast Cell Electrical Oscillations around 1 kHz

M. Cifra<sup>1,2</sup>, J. Pokorný<sup>2</sup>, F. Jelínek<sup>2</sup>, and J. Hašek<sup>3</sup>

<sup>1</sup>Department of Electromagnetic Field, Czech Technical University, Czech Republic

<sup>2</sup>Institute of Photonics and Electronics, Academy of Sciences of the Czech Republic, Czech Republic

<sup>3</sup>Institute of Microbiology, Academy of Sciences of the Czech Republic, Czech Republic

**Abstract**— Electric activity of the yeast cells was measured in frequency region 400–1600 Hz. Spectrum analyzer and electrically and electromagnetically screened box with point sensor and amplifiers fed by batteries was used for altogether 50 measurement of nonsynchronized and synchronized cold sensitive tubulin mutant yeast cells. We show that the electric activity of nonsynchronized cells is lower than that of synchronized cells. That corresponds to the findings of Pohl et al. Nanomechanical oscillatory motion in this frequency region was detected by Pelling et al. on yeast cell membrane by atomic force microscopy and evaluated by the Fourier analysis of the height profile signal of horizontally fixed sample-cantilever position.

## 1. INTRODUCTION

Electrically polar vibrations in biological systems have been postulated by Fröhlich [1–4]. Vibrations of electrically polar structures in cells are fundamental source of electromagnetic field in cells. Existence of endogenous electromagnetic field in and around biological systems was therefore assumed. Nanomechanical vibrations of yeast cell in region up to 2.5 kHz and amplitudes of the order of magnitude of 1 nm was detected by Pelling et al. [5, 6] with Atomic Force Microscopy and analyzed by the Fourier transformation of the height profile signal in the fixed cantilever-sample position. Extremely low frequency (up to 30 Hz) of tens to few hundreds of nm large amplitude mechanical oscillations of various cell type membranes was detected by [7–9] with point dark field microscopy. Spatial and time coherence properties of the erythrocyte membrane motions were described from the results of ms time and nm spatial resolution measurements with diffraction phase microscopy [10]. The source of vibrations is estimated to be cooperative action of many motor proteins in [5, 6] and in MgATP dependent actin fluctuations in [7, 8]. Most proteins are polar structures with complex charge distribution. Electrically polar structures with excited mechanical vibrations are generating electromagnetic field. Various factors may influence conditions for the vibration generation processes. High static electric field of the order of magnitude of  $10^6$  to  $10^7$  V/m around cellular organelles may be the cause of nonlinear processes in vibration generation. Cytosol contains negative and positive ions [11]. Static electric field in such a ionic solution is screened within few Debyes lengths. However, it was recently found with voltage dependent fluorescent nanosensors that the electric field from mitochondrial membrane can penetrate much further — up to few  $\mu\text{m}$  to cytosol [12]. The electric field very likely depends on high hydrogen ions concentration in mitochondrial intermembrane space. Authors propose that, electrically, the cytoplasm cannot be described as a simple homogeneous solution, as often approximated, but should rather be thought of as a complex, heterogeneous hydrogel, with distinct microdomains. Microtubules, which are highly electrically polar structures and which consist of tubulin heterodimers, are main organizers of cytoskeleton. Tubulin heterodimers have permanent dipole moment of ca. 1000 Debye ( $10^{-26}$  cm). Energy is supplied to microtubules from GTP hydrolysis [13] and probably also from motor proteins associated with microtubules [5, 6, 14] and possibly also from the wasted energy from citric acid cycle of mitochondria. Closer description on microtubule structure and function from the point of view of molecular biology is given in [11]. Excitation of vibration and generation of electromagnetic field is described in [15–17]. Electromagnetic field emanating from biological systems was detected in optical and infrared [18–21] and MHz [22, 23] region. We have shown preliminary results of kHz yeast cell oscillations in [24]. We present a direct proof of cell electric activity in region 0.4–1.6 kHz in this paper.

## 2. MATERIALS & METHODS

### 2.1. Yeast Cells

Cold sensitive  $\beta$ -tubulin mutant *tub2-401* of yeast cells *Saccharomyces cerevisiae* (strain CUY67 *Mata tub2-401 ura3-52 ade2-101*) was used. Evolution of the cells in the cell cycle can be synchronized by cultivation at the restrictive temperature (lower than 14°C) when the microtubules cannot

be formed. The mutant cells at the restrictive temperature continue in their pathway along the cell cycle up to the point before entering the M phase, which processes depend on the microtubules. Thus after certain time period all the mutant cells are stopped at the same point of the cell cycle. When the temperature is increased to the permissive temperature (above 25°C) microtubules are reassembled and the mitotic spindle is formed. Therefore, start of the M phase in the cells cultivated under the restrictive temperature is triggered by the temperature increase above 25°C. Thus the cells are synchronized. Evolution of the M phase after the warm-up above the permissive temperature is described in detail in [23]. We measured synchronized and nonsynchronized cells in suspension. The cells were suspended in the aqueous sucrose solution. After warming to the permissive temperature, the cells synchronously enter the M phase.

## 2.2. Measurement System

A schematic diagram of the measurement system is shown in the Fig. 1(a). The crucial parts are the sensor, Fig. 1(b), and the preamplifiers, which are located in the temperature stabilized and triple screened box (electrically and magnetically by mumetal box). The effectiveness of the screening was verified in [23]. The batteries for the power supply of the preamplifiers are located inside the screened box, too. At the bottom of a small cuvette there is an evaporated Pt layer forming one electrode. Detecting wire electrode cut at an angle to obtain a point end (about 50 nm) is at a distance of 8  $\mu\text{m}$  above the bottom of the cuvette. Dimension of 8  $\mu\text{m}$  corresponds approximately to the diameter of a yeast cell. After sedimentation cells form a layer at the bottom of the cuvette. Signal from the sensor is amplified inside the screened box. The preamplifier is connected to the spectrum analyzer through semirigid coaxial cable. Control of the spectrum analyzer is provided by a PC program via GPIB interface. Spectrum analyzer Agilent E4448A has been used.

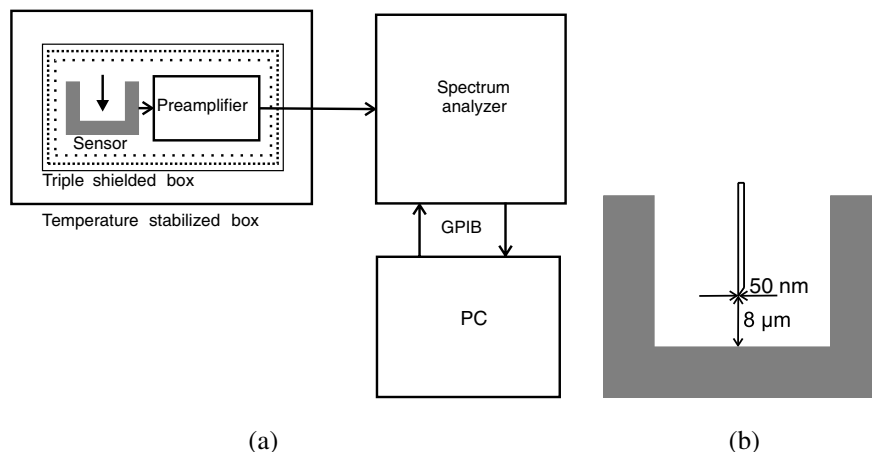


Figure 1: (a) Schematic depiction of the measurement system used (b) Dimensions of the sensor used.

## 2.3. Measurement Protocol

Suspension with synchronized cells was cultivated at the temperature of 14°C. Suspension with nonsynchronized cells was cultivated at the temperature of about 30°C. Before measurement the test tubes with the suspension were warmed in a water bath of 28°C for 3 minutes. Optical density (OD 600) of the suspension was 4.5 [23], which corresponds to concentration of about  $2 \times 10^8$  cells per milliliter. Afterwards, the cuvette was filled with the 60  $\mu\text{l}$  of the suspension. Measurement started immediately after filling the cuvette. Cells sedimented at the bottom of cuvette. Similar measurements of nonsynchronized cells were performed, too.

## 2.4. Data Processing

Measured data have been processed with specified scripts of Python programming language. Modules used: matplotlib, pylab, Numeric, SciPy.

## 3. RESULTS

Measurements of the electrical activity of 25 synchronized cell suspensions and 25 nonsynchronized cell suspensions have been carried out. Each measurement contained at least 400 double sweeps in the region 0.4–1.6 kHz (measured in two subbands 0.6 kHz each) with resolution bandwidth 1 Hz.

Each double sweep and transfer of data to PC took 6 s. Measured power is of the order of magnitude of  $10^{-18} - 10^{-19}$  W. Example of original measurement is in Fig. 2(a). In order to decrease the noise fluctuations, moving average with the windows size of 50 sweeps was used to smooth the curves of time evolution of measured power. The smoothed curves of all measurements are shown in Fig. 2(b).

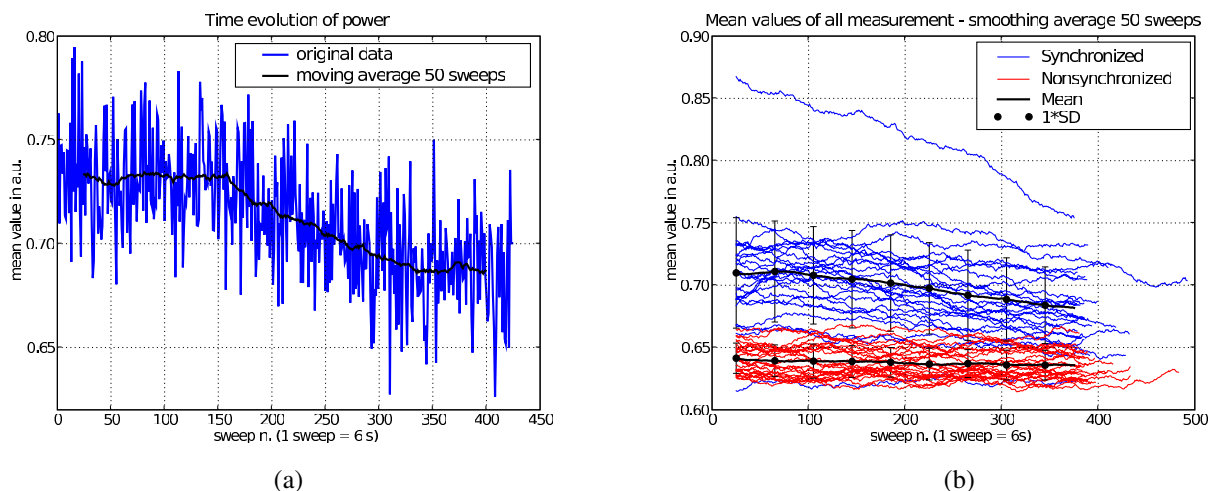


Figure 2: (a) Time evolution of yeast cells electrical activity in spectral region 0.4–1.6 kHz in measurement AHB29 (b) 25 measurements of synchronized and nonsynchronized cells each.

The mean power from measurements of both synchronized and nonsynchronized cells with standard deviation SD as error bars is shown separately in Fig. 3(a) for clarity. It is clearly visible that the electrical activity of yeast cells is higher in the case of synchronized cells than in the case of nonsynchronized cells.

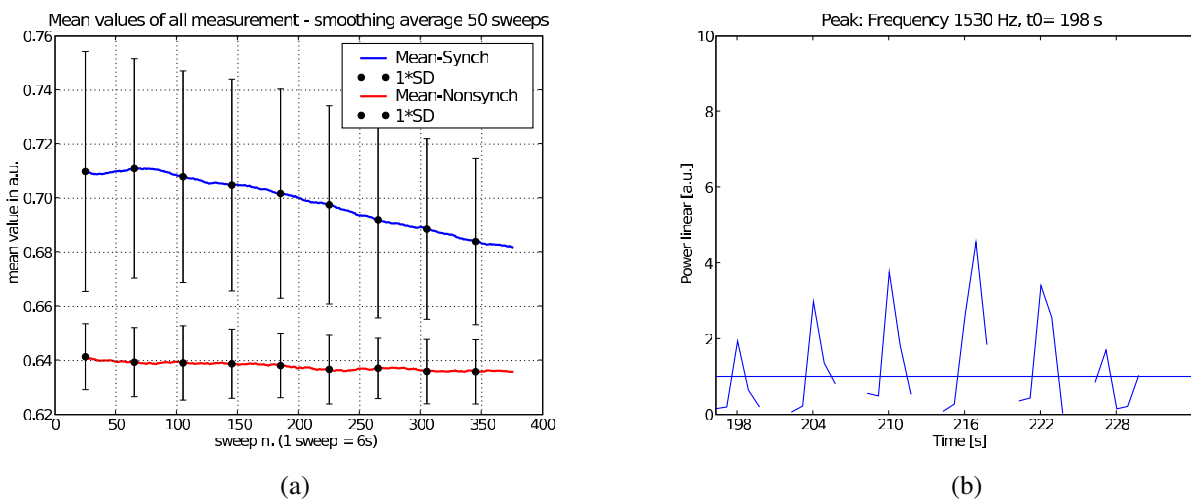


Figure 3: (a) The average power of cellular electrical activity in a frequency band 0.4–1.6 kHz, error bars — symmetric SD (b) Example of long lasting peak, here at 1530 Hz from measurement AHB17. Peak is drawn with two neighbor frequency points on both sides around central frequency. Distance of frequency points is 1 Hz. Horizontal blue line is an average power. See Discussion in text for more on peak detection.

#### 4. CONCLUSION & DISCUSSION

Measurements described in this contribution show that the electrical activity of synchronized cells in the M-phase is greater than that of the nonsynchronized cells. It corresponds to the experimental findings of Pohl et al. [22, 25] based on dielectrophoretic attraction of dielectric particles to yeast cells indicating that their electromagnetic activity is greatest in the M phase. However, in our measurements, lower electrical activity of nonsynchronized yeast cells may be also related to the

energy depletion, since synchronized cells saved their energy reserves when they are kept under restrictive temperature before measurement while nonsynchronized cells were normally active at the room temperature.

We processed the measured signals to detect frequencies which could be attributed to eigen vibration modes of the cellular structures, e.g., microtubules. However, experimental conditions are highly unfavorable since our measurement are of statistical character. Cells sediment in two layers, what can be calculated from number of cells in suspension and the surface of the bottom of cuvette. The sedimented layers were observed by optical microscope. We do not know what is the cell position and if there is any in contact with the point electrode in arbitrary time. From signal processing point of view, the  $1/f^\alpha$  ( $0 < \alpha < 1$ ,  $f$ -frequency) spectral distribution poses a problem for comparison of power on various frequencies in our low frequency region. There was an attempt to solve this problem, it will be published elsewhere. Peaks which lasted over period of at least 18 seconds (triple sweep time) were considered a significant at the first approximation. One example of a long lasting peak is in the Fig. 3(b). The covariance based method was used for detection of long lasting peaks. Spectrum of frequencies was detected by this method. There were bands and frequencies where peaks seemed to appear more frequently. Point detection of fixed cell, sensitive measurement system and other prerequisites are necessary for measurement of single frequencies.

Electrical processes seem to be important for cell activity. Cell cytoskeleton is a probable source of electrical polar vibrations. Endogenous biological electromagnetic field may play important role on temporal and spatial organization of structures and processes in living systems at least on cellular level. Effects on transfer of reaction components, of charge and mass particles were theoretically analyzed [26–28]. Disturbed electromagnetic field can be related to pathological processes. One of the deepest disturbances in organization and regulation in multicellular systems is cancer. In cancer cell, regardless of their viral or other mutagenic origin, dysfunction of mitochondria and disintegration of the cytoskeleton are observed [29, 30]. Vibration states and generated electromagnetic field may be disturbed. The static electric field around mitochondria (and around microtubules too) is diminished, and the wasted energy efflux is cut off (the wasted energy may be used in microtubules in nonlinear processes). Restoration of mitochondrial function in cancer cells by treatment with dichloacetate results in restoration of normal cell function or in apoptosis of aberrant cells [30].

#### ACKNOWLEDGMENT

M.C. is thankful to Grant Agency of the Czech Republic, grant No. 102/08/H081 and FRVS grant agency, grant No. 2300/2008 for the support.

#### REFERENCES

1. Fröhlich, H., “Bose condensation of strongly excited longitudinal electric modes,” *Physical Letters A*, Vol. 26, 402–203, 1968.
2. Fröhlich, H., “Long-range coherence and energy storage in biological systems,” *International Journal of Quantum Chemistry*, Vol. 2, 641–649, 1968.
3. Fröhlich, H., “Quantum mechanical concepts in biology,” *Proceedings of 1st International Conference on Theoretical Physics And Biology 1967*, Vol. 2, 13–22, Versailles, 1969.
4. Fröhlich, H., “The biological effects of microwaves and related questions,” *Advances in Electronics and Electron Physics*, Vol. 53, 85–152, 1980.
5. Pelling, A. E., S. Sehati, E. B. Gralla, J. S. Valentine, and J. K. Gimzewski, “Local nanomechanical motion of the cell wall of *saccharomyces cerevisiae*,” *Science*, Vol. 305, 1147–1150, 2004.
6. Pelling, A. E., S. Sehati, E. B. Gralla, and J. K. Gimzewski, “Time dependence of the frequency and amplitude of the local nanomechanical motion of yeast,” *Nanomedicine: Nanotechnol. Biol. Med.*, Vol. 1, 178–183, 2005.
7. Korenstein, R. and A. Levin, “Membrane fluctuations in erythrocytes are linked to MgATP-dependent dynamic assembly of the membrane skeleton,” *Biophysical Journal*, Vol. 60, 733–737, 1990.
8. Tuvia, S., A. Bitler, and R. Korenstein, “Mechanical fluctuations of the membrane-skeleton are dependent on F-actin ATPase in human erythrocytes,” *The Journal of Cell Biology*, Vol. 141, 1551–1561, 1998.
9. Krol, A. Y., M. G. Grinfeldt, S. V. Levin, and A. D. Smilgavichus, “Local mechanical oscillations of the cell surface within the range 0.2–30 Hz,” *European Biophysics Journal*, Vol. 19, No. 2, 93–99, 1990.

10. Popescu, G., Y.-K. Park, R. R. Dasari, K. Badizadegan, and M. S. Feld, "Coherence properties of red blood cell membrane motions," *Physical Review E*, Vol. 76, 031902, 2007.
11. Alberts, B., D. Bray, J. Lewis, M. Raff, K. Roberts, and J. D. Watson, *Molecular Biology of the Cell*, 3rd ed., Garland, 1994.
12. Tyner, K. M., R. Kopelman, and M. A. Philbert, "Nano-sized voltmeter enables cellular-wide electric field mapping," *Biophysical Journal*, Vol. 93, 1163–1174, 2007.
13. Caplow, M., R. L. Ruhlen, and J. Shanks, "The free energy for hydrolysis of a microtubule-bound nucleotide triphosphate is near zero: All of the free energy for hydrolysis is stored in the microtubule lattice," *The Journal of Cell Biology*, Vol. 127, 779–788, 1994.
14. Kawaguchi, K. and S. Ishiwata, "Thermal activation of single kinesin molecules with temperature pulse microscopy," *Cell Motility and the Cytoskeleton*, 41–47, 2001.
15. Pokorný, J. and T.-M. Wu, *Biophysical Aspects of Coherence and Biological Order*, Academia, Praha, Czech Republic; Springer, Berlin - Heidelberg - New York, 1998.
16. Pokorný, J., "Excitation of vibration in microtubules in living cells," *Bioelectrochemistry*, Vol. 63, 321–326, 2004.
17. Pokorný, J., "Viscous effects on polar vibrations in microtubules," *Electromagnetic Biology and Medicine*, Vol. 22, 15–29, 2003.
18. Belousov, L. V., F.-A. Popp, V. L. Voeikov, and R. Van Wijk, eds., *Biophotonics and Coherent Systems*, Moscow University Press, 2000.
19. Van Wijk, R. and X. Shen, eds., *Biophotonics: Optical Science and Engineering for the 21st Century*, Springer, 2005.
20. Belousov, L. V., V. L. Voeikov, and V. S. Martynyuk, eds., *Biophotonics and Coherent Systems in Biology*, Springer, 2006.
21. Albrecht-Buehler, G., "Rudimentary form of cellular 'vision'," *Proceedings of the National Academy of Sciences of the USA*, Vol. 89, 8288–8293, 1992.
22. Pohl, H. A., "Oscillation fields about growing cells," *International Journal of Quantum Chemistry: Quantum Biology Symposium*, Vol. 7, 411–431, 1980.
23. Pokorný, J., J. Hašek, F. Jelínek, J. Šaroch, and B. Palán, "Electromagnetic activity of yeast cells in the M phase," *Electro- and Magnetobiology*, Vol. 20, 371–396, 2001.
24. Cifra, M., J. Vaniš, O. Kučera, J. Hašek, I. Frýdlová, F. Jelínek, J. Šaroch, and J. Pokorný, "Electrical vibrations of yeast cell membrane," *PIERS Online*, Vol. 3, No. 8, 1190–1194, 2007.
25. Pohl, H. A., *Natural Oscillation Fields of Cells*, 199–210, Springer, Berlin - Heidelberg - New York, 1983.
26. Pokorný, J., J. Hašek, and F. Jelínek, "Endogenous electric field and organization of living matter," *Electromagnetic Biology and Medicine*, Vol. 24, 185–197, 2005.
27. Pokorný, J., J. Hašek, and F. Jelínek, "Electromagnetic field in microtubules: Effects on transfer of mass particles and electrons," *Journal of Biological Physics*, Vol. 31, 501–514, 2005.
28. Pokorný, J., "Endogenous electromagnetic forces in living cells: Implications for transfer of reaction components," *Electro- and Magnetobiology*, Vol. 20, 59–73, 2001.
29. Suresh, S., "Biomechanics and biophysics of cancer cells," *Acta Materialia*, Vol. 55, 3989–4014, 2007.
30. Bonnet, S., S. Archer, J. Allalunis-Turner, A. Haromy, B. Ch., R. Thompson, C. Lee, G. Lopaschuk, L. Puttagunta, G. Harry, K. Hashimoto, C. Porter, M. Andrade, B. Thebaud, and E. Michelakis, "A mitochondria-K<sup>+</sup> channel axis is suppressed in cancer and its normalization promotes apoptosis and inhibits cancer growth," *Cancer Cell*, Vol. 11, 37–51, 2007.

# Comparison of Possibilities Utilization Open-resonator Type and Meandering Type of Microwave Applicators for Textile Industry

M. Pourová and J. Vrba

Faculty of Electrical Engineering, Department of Electromagnetic Field  
Czech Technical University, Technická 2, 166 27 Prague 6, Czech Republic

**Abstract**— In this contribution we would like to describe the possibilities utilization of two different types of microwave applicators. These applicators are designed specially for large thickness sheet of textile materials. We have designed two types of applicators, which we use for testing. There are intended for the drying at factory production of fabrics. The first applicator is derived from the Fabry-Perrot resonator, which is open type resonator. The second one is waveguide type applicator, which is waveguide with a longitudinal slot in wider side of waveguide and it is created by two branches. The textile material goes through the applicator in the maximum of electric field strength, where it can absorb the maximum of energy. The applicators are designed so that only dominant mode  $TE_{10}$  could propagate inside the system. Both applicators work at frequency 2.45 GHz and use different number of magnetrons. The open-resonator type is made by 17 cells that have every one own magnetron. These 17 cells create the whole drying system. The second one — meandering type is now created with two separated cells also excited with magnetrons. This system is designed for testing of new method for surface treatment of textile materials with microwave energy. We have created the model of drying system, which solve the distribution of EM waves inside this structure and we reached the resulting expression, which is used for calculation of electric field strength in the plane of drying textile. This quantity depends on electrical characteristics of wet textile such as permittivity and loss factor. We would like to present the results of measurement parameters of wet textile too. Dielectric parameters are changed with decrease moisture content in textile. The comparison of the simulations of both systems with experimental results has been reported in details. The results of our testing measurements are very good corresponding with simulations and analytical model.

## 1. INTRODUCTION

Microwave heating technology can be used as efficient technology, which can replace conventional heating. Principle of microwave heating is a transformation of electromagnetic field energy to the thermal energy through the field incidence on polar molecules in material. The main target of project is to obtain the most uniform distribution of electric field strength in transit plane of textile. By this way we attain uniform drying in whole textiles plane. In this contribution will be present comparison between two types of single-mode microwave industrial applicators used for microwave drying of textile. The first applicator works on the open-resonator principle and the second one is a waveguide-type applicator. Both applicators are designed to work at frequency 2.45 GHz.

## 2. APPLICATORS FOR MICROWAVE DRYING

### 2.1. Open Resonator Type Applicator

This type of applicator consists of many drying cells (17 in our prototype machine) — each of them is based on the idea of open resonator (i.e., Fabry-Perrot resonator), see Fig. 1. Each of these cells has its own magnetron placed in waveguide holder. Dried textile material is in the middle plane between parallel conductive plates, distance between these plates is equal to  $(3/2)\lambda$ . In this plane is an expected maximum of electric field strength.

### 2.2. Meandering Type Applicator

Meandering applicator is waveguide with a longitudinal slot in wider side of waveguide. This slot is situated in the middle of this side, because maximum of electric field strength is here. Waveguide applicator is pictured on the Fig. 2. This applicator has double drying part with dimension  $80 \times 80$  mm, which is tied with transform to the waveguide with magnetron inside of microwave oven. This applicator was designed for testing the influence of microwave energy on the wet textile. This system is safely because the source of energy is closed in the oven. The bandwidth of dominant mode is 1.85 GHz to 3.75 GHz for this applicator and working frequency 2.45 GHz is in the middle of this band.

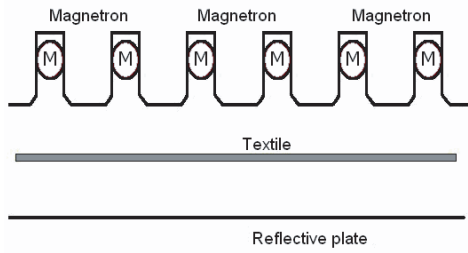


Figure 1: Scheme of open resonator type applicator.

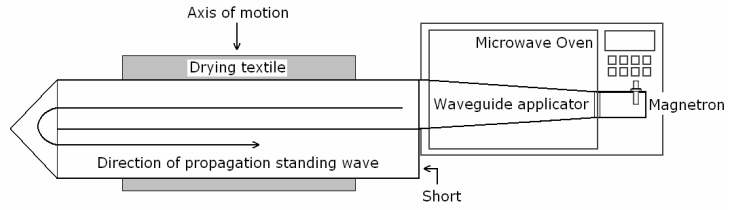


Figure 2: Scheme of meandering type applicator.

### 3. SIMULATIONS IN THE EM FIELD SIMULATOR

For the evaluation of the microwave heating efficiency we can use the quantity SAR (Specific Absorption Rate) or power loss density. SAR can be defined as

$$SAR = \frac{\sigma}{\rho} \cdot \frac{|\vec{E}(x, y, z)|^2}{2}, \quad (1)$$

where  $\sigma$  is the electric conductivity,  $\rho$  is the density of the material and  $\vec{E}(x, y, z)$  is the electric field strength. The distribution of power loss density in the textile material obtained from the simulator is shown in the Fig. 3 and Fig. 4. We tested the applicator with the wet textile. The results of the real drying are shown in the Cap. 3.

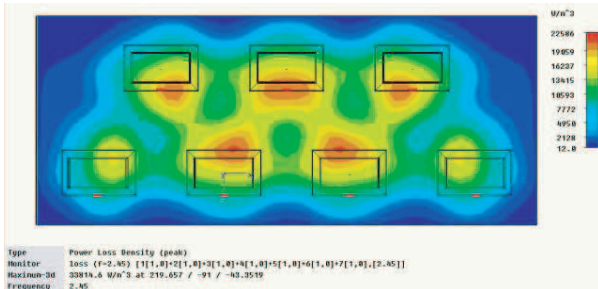


Figure 3: Distribution of power in the resonant applicator.

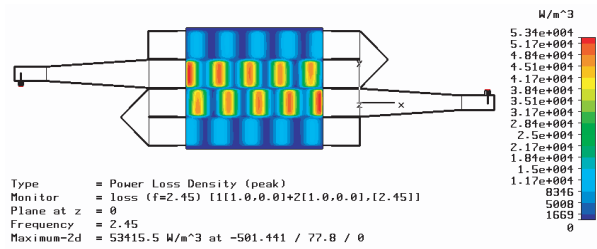


Figure 4: Distribution of power in the meandering applicator.

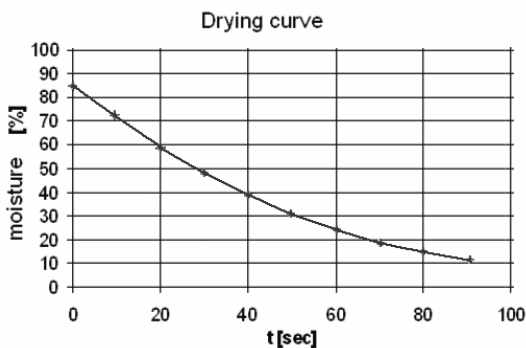


Figure 5: The drying characteristic of resonant applicator.

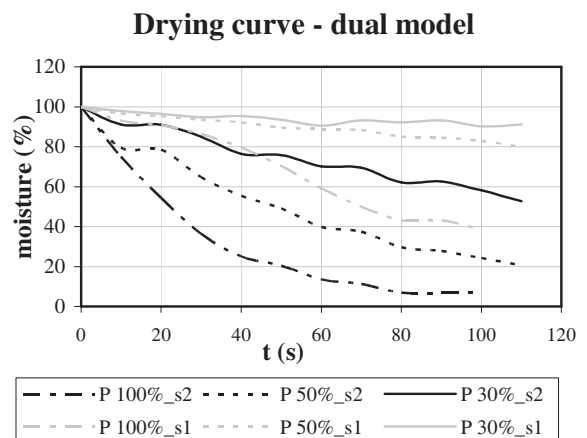


Figure 6: The drying characteristic of meandering applicator.

#### 4. EXPERIMENTAL RESULTS

For our first experiments we have built a one workable cell, which was used for first drying experiments and measurements of drying curve. In the Fig. 5 and Fig. 6 are pictured results of measurement of the moisture content in drying textile with respect to time. The measurement with one cell of resonant applicator was realized with the 100% power and 10s time step. The measurement with meandering applicator was realized with 3 different level of power (30%, 50% and 100%) and 10s time step.

In the Fig. 7 and Fig. 8 are shown the set-up of measurement prototype of both applicators. Resonant system is created by the seventeen cells and meandering system only two cells.



Figure 7: Prototype of resonant system.



Figure 8: Prototype of meandering system.

In the second part of the measurement was used the infra red camera. It was measured the distribution of the temperature in the drying textile (Fig. 9).

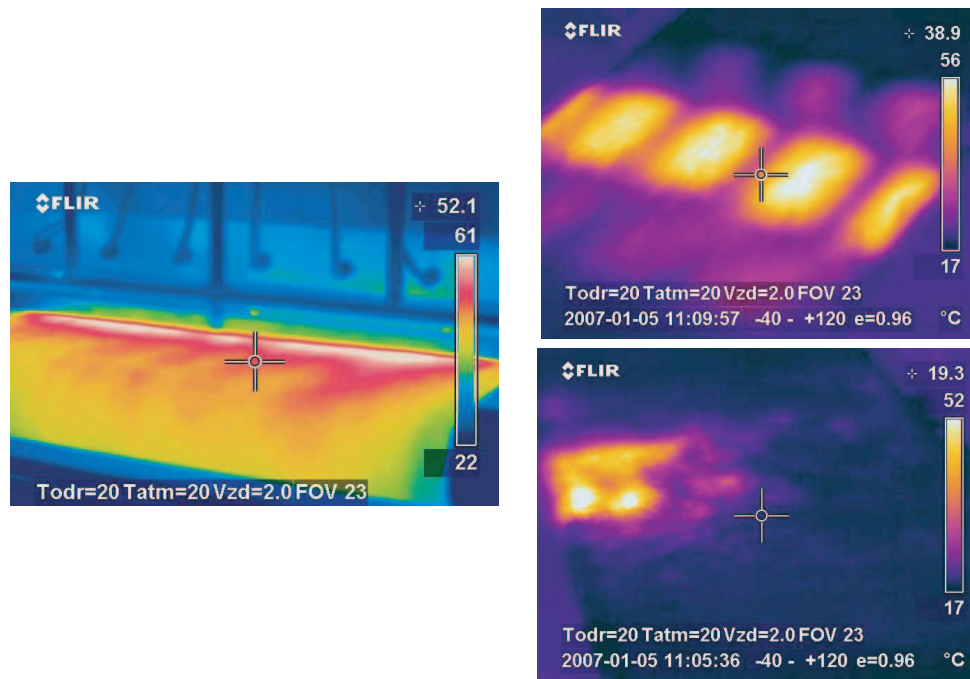


Figure 9: Results of the measurements with infra red camera (resonant prototype — left, meandering prototype — right).

In the left side is resonant prototype, where is the maximum temperature of the drying material around 60°C. The drying textile was in the system 60s. With the same time was measured two

type of fabric (100% cotton, non-woven textile) in the meandering system (right side Fig. 9). In this system was maximal temperature around 55°C.

## 5. CONCLUSIONS

In this contribution was presented two different type of drying system — Open resonant type and Meandering type. These applicators are designed specially for large thickness sheet of textile materials. The comparison of the simulations of both systems with experimental results was reported in details. The results of our testing measurements are very good corresponding with simulations.

## ACKNOWLEDGMENT

This research is supported by Grant Agency of the Czech Republic, project: “Non-standard application of physical fields — analogy, modelling, verification and simulation” (102/08/H081) and by the research program MSM6840770012 “Transdisciplinary Research in the Area of Biomedical Engineering II” of the CTU in Prague, sponsored by the Ministry of Education, Youth and Sports of the Czech Republic.

## REFERENCES

1. Pourová, M. and J. Vrba, “Analytical solutions to the applicators for microwave textile drying by means of zigzag method,” *PIERS Online*, Vol. 3, No. 8, 1204–1207, 2007.
2. Pourová, M. and J. Vrba, “Microwave drying of textile materials and optimization of a resonant applicator,” *Acta Polytechnica*, Vol. 46, No. 5, 3–7, ISSN 1210-2709, 2006.
3. Pourová, M., “Development and optimization of new generation of applicators for microwave heating and drying with increased energy saving,” *Proceedings of Workshop 2007*, Vol. B, 416–417, CTU, Prague, ISBN 978-80-01-03667-9, 2007.
4. Zák, O., “Waveguide applicator for drying of textile materials,” Diploma Thesis, CTU 2005, (In Czech).

# Line Source Wave Scattering by Line Inhomogeneities inside Left-handed Material Slab: Green Function Approach

Yu. N. Barabanenkov<sup>1</sup>, M. Yu. Barabanenkov<sup>2</sup>, and S. A. Nikitov<sup>1</sup>

<sup>1</sup>Institute of Radioengineering and Electronics

Russian Academy of Sciences, Mohovaya 11, Moscow 103907, GSP–3, Russia

<sup>2</sup>Institute of Microelectronics Technology and High Purity Materials

Russian Academy of Sciences, Chernogolovka 142432, Moscow Region, Russia

**Abstract**— We present an analytical approach to study a problem of getting visible image for Veselago's focus inside left-handed material (LHM) slab,  $0 < z < L$ , with the dielectric permittivity  $\epsilon(x, z) = -1 + \delta\epsilon_0 + \delta\epsilon(x, z)$ , where  $\delta\epsilon_0$  and  $\delta\epsilon(x, z)$  are homogeneous and inhomogeneous parts, respectively, and the homogeneous magnetic permeability  $\mu$ , which can be close to  $-1$ . An integral equation for the Green function of  $s$ -polarized electric wave field is derived in a form usual for the potential scattering theory, with including not only a volume potential but also a surface potential proportional to the magnetic permeability jump. Solution to the derived integral equation with the surface potential only gives at magnetic permeability  $\mu = -1$  a perfect Veselago's lens Green function that is obtained also from the empty space Green function by a spatial coordinate transformation for the definite positions of receive and source planes, for which the perfect Veselago's Green function does exist. We rewrite next the derived integral equation in terms of a homogeneous LHM slab Green function and the volume scattering potential accounting for inhomogeneities and solve to the rewritten equation asymptotically in the limit of weak and thin inhomogeneity as a linelike scatterer. The found asymptotic solution reveals a multiplicative quasistatic spatial singularity of the Green function for inhomogeneous LHM slab if the linelike scatterer is placed near the Veselago's focus inside LHM slab, with respect to positions of the receive and the source points.

## 1. INTRODUCTION

In 1968, Veselago [1] introduced into consideration a left-handed materials (LHM's), which possess both negative dielectric permittivity  $\epsilon < 0$  and negative magnetic permeability  $\mu < 0$ . The LHM's lead to numerous interesting optical phenomena, including earlier predicted negative refraction [2] and negative group velocity [3], reversed Cherenkov radiation and reversed Doppler shifts [1], specific resonant scattering properties of a cylinder fabricated from a LHM [4]. The most pronounced property of LHM, predicted by Veselago, is that a perfect planar LHM slab, with  $\epsilon = -1$  and  $\mu = -1$ , could focus the rays from a nearby in free space electromagnetic source into the point images, one inside and the other behind the slab. In a more recent analysis Pendry [5] showed that in addition to the far-field components associated with a source being brought to a focus by the slab, the nonpropagating near-field (evanescent) components could also be recovered in the image. It was, therefore, proposed that the image created by the perfect planar LHM slab could, in principle, contain all of the information associated with the source object, thereby achieving resolution well beyond that of the diffraction limit. For this reason, the perfect planar LHM slab was described as a perfect Veselago's lens.

The resolution enhancement by the perfect Veselago's lens was a surprising result, which gave rise to several approaches for full-wave analysis of Veselago's lens focusing properties, with taking into account different lens imperfections. Rao and Ong [6] discussed a Finite-Difference-Time-Domain (FDTD) method employing to justify the superlensing effect of LHM slabs. They concluded this method is easy to implement but the physical meanings of the simulation results are not easy to be extracted. In other studies [5], [7–10] the authors used frequency domain and wave angular amplitude spectrum decomposition method. A remark of principle on this way was made by Carsia and Nieto-Vesperinas [8] that one should consider the sum over all angular spectrum components to get a result for the total wave field rather than only one component, as in [5], because the total field can in particular diverge inside a perfect Veselago's lens. Luan et al. [11] continued strategy of Ref. [8], having constructed a 2D Green function for Veselago's lens with absorption. Actually, these authors showed that the perfect Veselago's lens transforms a line source wave field into wave field of line source image, in accordance with Veselago prediction [1]. Just recently Shevchenko [12] has obtained similar to [11] result in the form of 3D Green function for Veselago's

lens with absorption. Simultaneously Aniouline [13] published numerical solution to 2D problem of cylindrical wave scattering by ideal Veselago's lens of finite dimensions, with studying the wave field behavior near focus of such lens and applying a method of discrete sources [14, 15].

As one can think, the Luan et al. [11] result relates closely with concept about spatial transformation media [16, 17], which map electromagnetic fields in physical space to the electromagnetism of empty flat space. Note, in this connection, work [18] dates back to 1959 where the covariant Maxwell equations [19] in non-inertial reference system were transformed to usual three dimensional vector form for particular problem of electromagnetic field study in rotating system of reference. In this case the displacement vector  $\vec{D}$  and the magnetic field vector  $\vec{B}$  were expressed through the electric field vector  $\vec{E}$  and the magnetic flux vector  $\vec{H}$  via an constitute equations

$$\vec{D} = \vec{E} - \frac{1}{c} \vec{v} \times \vec{H}, \quad \vec{B} = \vec{H} + \frac{1}{c} \vec{v} \times \vec{E}$$

where  $\vec{v}$  was a local speed of rotating. The formulas were obtained also related the electric field and the magnetic flux in the non-inertial and the inertial systems of reference. In 1960 Plebanski [20] formulated the electromagnetic effect of curved space-time or curved coordinates in concise constitutive equations for general case. The Plebanski's constitutive equations are obtained from above mentioned ones by replacing the first terms in the right hand side (RHS) of these equations to  $\epsilon \vec{E}$  and  $\mu \vec{H}$ , respectively, and by replacing the vector  $\vec{v}$  to  $-\vec{w}$ , where the symmetric matrices  $\epsilon = \mu$  and vector  $\vec{w}$  are written in terms of the space-time metric tensor. Now media with such  $\epsilon$  and  $\mu$  and  $\vec{w}$  are called after Pendry et al. [21] the transformation media. The transformation media lead to modern metamaterials that include LHM's and not only can focus the electromagnetic field as required but are able to avoid objects and flow around them, as it was demonstrated numerically [21] and analytically in terms of bistatic scattering [22].

In the currently presented report we extend the traditional potential wave multiple scattering theory [23] to analytical study an inhomogeneous and absorbing Veselago's lens focusing properties by the Green function method. Specifically we consider a 2D Green function for LHM slab with the dielectric permittivity,  $\epsilon(x, z) = -1 + \delta\epsilon_0 + \delta\epsilon(x, z)$ , where homogeneous part  $\delta\epsilon_0$  saves the Green function convergence whereas  $\delta\epsilon(x, z)$  accounting for inhomogeneities, and the homogeneous magnetic permeability  $\mu$ , which can be close to  $-1$ . Our final aim consists in revealing a specific multiplicative quasistatic singularity of the considered Green function, provided a thin inhomogeneity is placed near focus inside perfect Veselago's lens. We will show that this sort of singularity is directly linked with mentioned concept about spatial transformation media.

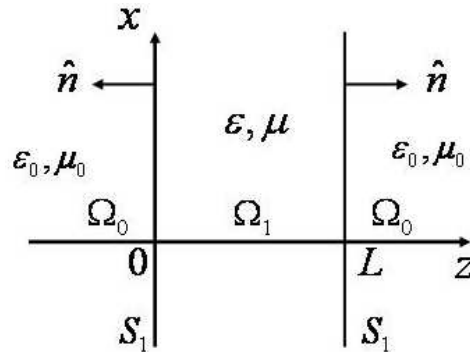


Figure 1: Schematic drawing of  $L$  thick LHM slab (region  $\Omega_1$ ) with  $\epsilon = -1 + \delta\epsilon_0 + \delta\epsilon(x, z)$  and homogeneous  $\mu \rightarrow -1$  surrounded by right and left semispaces (regions  $\Omega_0$ ).

## 2. VOLUME AND SURFACE SCATTERING POTENTIALS OF INHOMOGENEOUS LHM SLAB

### 2.1. Extended Boundary Condition Technique

Let the inhomogeneous LHM slab (see Fig. 1) occupies a region  $\Omega_1$  between the planes  $z = 0$  and  $z = L$  of the Cartesian coordinate system  $x, y, z$ . The surrounding background medium has the permittivity  $\epsilon_0 = 1$  and the permeability  $\mu_0 = 1$  and occupies the region  $\Omega_0$ . The electric field  $E_y(x, z)$  of  $s$ -polarized monochromatic electromagnetic wave with the frequency  $\omega$  has the  $y$ -component only and can be expressed in terms of the Green function  $G(x, z; x', z')$  and the current

density  $j_y(x, z)$  of electromagnetic field source as  $E_y = (4\pi\omega\mu_0/ic^2)Gj_y$ . Here one used an operator denotations and the Gaussian systems of units. Besides, one supposed the source to be placed in the outer region  $\Omega_0$  of the slab. If the source is placed inside region  $\Omega_1$  of the slab,  $\mu_0$  should be replaced to  $\mu$  in the above expression.

The Green function  $G(x, z; x', z')$  consists of four pieces  $G_{ab}(\rho, \rho')$ , with points  $\rho = (x, z)$  and  $\rho' = (x', z')$  being placed inside the regions  $\Omega_a$  and  $\Omega_b$ , respectively, where indices  $a, b = 0, 1$ . Physically  $G_{00}$  describes transmitted through and reflected from the slab wave radiation,  $G_{10}$  and  $G_{01}$  describe incoming into the slab and outgoing from the slab radiation, respectively, and  $G_{11}$  describes radiation propagation inside the slab. These four Green functions are linked between them by the standard boundary conditions of the electric and magnetic field tangential component continuity on the slab boundaries  $S_1$ , that is the quantities  $E_y$  and  $(1/\mu)(\hat{n} \cdot \nabla)E_y$ , with  $\hat{n}$  being the unit vector along the normal to a boundary  $S_1$ .

The above four Green functions are subdivided into two groups consisting (i) incoming  $G_{10}$  and transmitted through and reflected from the slab  $G_{00}$  wave radiation Green functions and (ii) outgoing  $G_{01}$  and propagated inside the slab  $G_{11}$  wave radiation Green functions. The extended boundary condition technique [24] allows to derive, considering the group (i), a specific radiation conditions on the slab boundaries for the Green function  $G_{10}$  of incoming radiation and the integral equation for this Green function with an effective scattering potential as well as a continuous extension of  $G_{10}$  from the slab boundaries to outside region of the slab that gives the Green function  $G_{00}$ . Similarly, one can derive, considering the group (ii), a specific radiation conditions on the slab boundaries for the Green function  $G_{11}$  of propagated radiation and the integral equation for this Green function with effective scattering potential as well as a continuous extension of  $G_{11}$  from the slab boundaries to outside region of the slab that gives the Green function  $G_{01}$ .

## 2.2. Green Functions of Incoming and Transmitted/Reflected Radiation

Consider the Green function  $G_{10}(\rho, \rho')$  of incoming radiation, the receive  $\rho$  and source  $\rho'$  points of which are positioned inside and outside regions relatively to the inhomogeneous LHM slab, respectively. One can derive an integral equation for this Green function by direct applying the scalar Green theorem [25], written for two any functions  $\psi(\rho)$  and  $\varphi(\rho)$ . Let us apply this theorem to region  $\Omega_1$  (see Fig. 1), making choose  $\psi(\rho) = G_0(\rho, \rho'')$ , where point  $\rho''$  has arbitrary position, and  $\varphi(\rho) = G_{10}(\rho, \rho')$ . Such application gives

$$\begin{aligned} & \int_{\Omega_1} d\rho V(\rho)G_0(\rho, \rho'')G_{10}(\rho, \rho') - G_{10}(\rho'', \rho')H(\rho'' \ni \Omega_1) \\ &= \int_{S_1} dS \left[ G_0(\rho, \rho'')(\hat{n} \cdot \nabla)G_{10}(\rho, \rho') - G_{10}(\rho, \rho')(\hat{n} \cdot \nabla)G_0(\rho, \rho'') \right] \end{aligned} \quad (1)$$

Here  $G_0(\rho, \rho') \equiv G_0(\rho - \rho')$  is the Green function in unbounded background medium (empty space), satisfied 2D Helmholtz equation,  $(\Delta + k_0^2)G_0(\rho) = \delta(\rho)$ , and the radiation condition on infinity. We denote  $V(\rho) = k_0^2 - k_1^2(\rho)$  an effective volume scattering potential, with  $k_0 = \omega/c$  and  $k_1 = k_0(\epsilon(x, z)\mu)^{1/2}$  being the wave number in the background and the LHM slab, respectively. The symbol  $H(\rho \ni \Omega_a)$  is a characteristic function of region  $\Omega_a$ , equal to one as  $\rho \ni \Omega_a$  and equal to zero in opposite case. In the surface integral of Eq. (1) RHS an unit vector  $\hat{n}$  at point  $\rho$  of the slab boundary  $S_1$  is directed outwards the slab region  $\Omega_1$ .

Equation (1) includes a normal derivative of the seeking Green function in the term with the surface integral that prevents to utilize the potential scattering theory methods. Therefore we use next a special consequence from the Green theorem in the form of extended boundary condition, which gives, in particular, a possibility to exclude the mentioned normal derivative.

To this end we apply the Green theorem to region  $\Omega_0$  with the same function  $\psi(\rho)$ , but  $\varphi(\rho) = G_{00}(\rho, \rho')$  getting a relation

$$G_{00}(\rho'', \rho')H(\rho'' \ni \Omega_0) = G_0(\rho', \rho'') + \int_{S_1} dS \left[ G_0(\rho, \rho'')(\hat{n} \cdot \nabla)G_{00}(\rho, \rho') - G_{00}(\rho, \rho')(\hat{n} \cdot \nabla)G_0(\rho, \rho'') \right] \quad (2)$$

that is a scalar extended boundary condition similar to the vector version of Ref. [24].

The relation (2) can be transformed identically to some sort of radiation conditions on the slab boundaries for the Green function  $G_{10}$  and continuous extensions of the Green function  $G_{00}$  from the slab boundaries into outside region of the slab. Applying the 1D Fourier transform to Eq. (2)

yields

$$\begin{aligned}
 G_{00}(q, q'; z, z')H(z \ni \Omega_0) &= G_0(q, z - z')\delta_{qq'} - G_0(q, z) \left[ \frac{\partial G_{00}(q, q'; z, z')}{\partial z} \right]_{z=-\eta} \\
 &+ G_{00}(q, q'; z = -\eta, z') i \gamma_q G_0(q, z) \operatorname{sgn}(-z) \\
 &+ G_0(q, z - L) \left[ \frac{\partial G_{00}(q, q'; z, z')}{\partial z} \right]_{z=L+\eta} \\
 &- G_{00}(q, q'; z = L + \eta, z') i \gamma_q G_0(q, L - z) \operatorname{sgn}(L - z) \quad (3)
 \end{aligned}$$

where a sign function  $\operatorname{sgn}(z) = \pm 1$  for  $z > 0$  and  $z < 0$ , respectively. It is seen that the extended boundary condition (2) took form an identity with respect to variable  $z$ , with  $z' < 0$  or  $z' > L$ . In particular case of  $0 < z < L$  and  $z' > L$  the identity is simple resolved in the form of radiation conditions

$$\frac{1}{\mu} \frac{\partial G_{10}(q, q'; z, z')}{\partial z} \Big|_{z=\eta} + i \gamma_q G_{10}(q, q'; z = \eta, z') = 0 \quad (4)$$

and

$$\frac{1}{\mu} \frac{\partial G_{10}(q, q'; z, z')}{\partial z} \Big|_{z=L-\eta} - i \gamma_q G_{10}(q, q'; z = L - \eta, z') = -\exp[i\gamma_q(z' - L)] \delta_{qq'} \quad (5)$$

Substituting these radiation conditions into Eq. (3) leads to continuous extensions

$$G_{00}(q, q'; z, z') = \exp(-i\gamma_q z) G_{10}(q, q'; z = \eta, z') \quad (6)$$

as  $z < 0$  and

$$\begin{aligned}
 G_{00}(q, q'; z, z') &= \frac{1}{2i\gamma_q} \left[ \exp(i\gamma_q |z - z'|) - \exp(i\gamma_q(z + z' - 2L)) \right] \delta_{qq'} \\
 &+ \exp[i\gamma_q(z - L)] G_{10}(q, q'; z = L - \eta, z') \quad (7)
 \end{aligned}$$

as  $z > L$ . Here  $\gamma_q = \sqrt{k_0^2 - q^2}$ ,  $\delta_{qq'} = 2\pi\delta(q - q')$ ,  $z' > L$ , and  $\eta \rightarrow 0$  and  $\eta > 0$ . Klytskin [26] used some kind of radiation conditions similar to (4) in acoustics.

The 1D Fourier transform of the Green function of incoming radiation  $G_{10}$  Eq. (1) with respect to  $x$ -component of the spatial position vector results in an integral equation for  $G_{10}(q, q'; z, z')$ , with including derivatives of this quantity with respect to variable  $z$  on the slab boundaries  $z = 0$  and  $z = L$ . Note, such derivatives can be excluded with the aid of radiation conditions (4) and (5). As a result, Eq. (1) is brought to following form similar for the potential scattering theory

$$G_{10}(q, q'; z, z') = \mu G_0(q, z) \delta_{qq'} + \int_0^L dz'' \int_{q''} G_0(q, z - z'') \hat{V}(q, q''; z'') G_{10}(q'', q'; z'', z') \quad (8)$$

as  $z' > L$ . In this equation  $G_0(q, z) = \exp(i\gamma_q |z|)/(2i\gamma_q)$  is 1D Fourier transform with respect to  $x$  variable of the Green function  $G_0(x, z)$  in unbounded background medium, and  $\int_q = (1/2\pi) \int dq$ . An effective singular potential  $\hat{V}(q, q'; z)$  in the RHS of Eq. (8) consists of two parts

$$\hat{V}(q, q'; z) = V(q - q', z) + V_S(q, q'; z) \quad \text{and} \quad V_S(q, q'; z) = (1 - \mu) i \gamma_q \left[ \delta(z - \eta) + \delta(z - L + \eta) \right] \delta_{qq'} \quad (9)$$

The regular volume part  $V(q - q', z)$  is the 1D Fourier transform of the volume scattering potential  $V(x, z)$  with respect to variable  $x$ . The singular surface part  $V_S(q, q'; z)$  describes the effect of magnetic permeability jump on the slab boundaries.

Resolving the integral Eq. (8) for 1D Fourier transform  $G_{10}(q, q'; z, z')$  of the slab incoming radiation Green function and substituting result into RHS of two continuous extensions (6) and (7) gives 1D Fourier transform  $G_{00}(q, q'; z, z')$  of the slab transmitted and reflected radiation Green function.

### 2.3. Green Functions of Outgoing and Propagated Radiation

Consider the Green function  $G_{11}(\rho, \rho')$  of propagated radiation, the receive  $\rho$  and source  $\rho'$  points of which are positioned inside the inhomogeneous LHM slab. Applying the Green theorem with the same function  $\psi(\rho)$  as in preceding subsection, but  $\varphi(\rho) = G_{11}(\rho, \rho')$  to region  $\Omega_1$  gives

$$\begin{aligned} & \int_{\Omega_1} d\rho V(\rho) G_0(\rho, \rho'') G_{11}(\rho, \rho') + G_0(\rho', \rho'') - G_{10}(\rho'', \rho') H(\rho'' \ni \Omega_1) \\ &= \int_{S_1} dS \left[ G_0(\rho, \rho'') (\hat{n} \cdot \nabla) G_{11}(\rho, \rho') - G_{11}(\rho, \rho') (\hat{n} \cdot \nabla) G_0(\rho, \rho'') \right] \end{aligned} \quad (10)$$

This integral equation is similar to Eq. (1), but includes an additional term  $G_0(\rho', \rho'')$  in the left hand side (LHS). Applying the Green theorem with the same function  $\psi(\rho)$ , but  $\varphi(\rho) = G_{01}(\rho, \rho')$  to region  $\Omega_0$  leads to a relation

$$G_{01}(\rho'', \rho') H(\rho'' \ni \Omega_0) = \int_{S_1} dS \left[ G_0(\rho, \rho'') (\hat{n} \cdot \nabla) G_{01}(\rho, \rho') - G_{01}(\rho, \rho') (\hat{n} \cdot \nabla) G_0(\rho, \rho'') \right] \quad (11)$$

that is similar to extended boundary condition (2), but not includes a term  $G_0(\rho', \rho'')$  in the RHS.

Similar with (2), the relation (11) is transformed identically to radiation conditions on the slab boundaries for the Green function  $G_{11}$  and continuous extensions of the Green function  $G_{01}$  from the slab boundaries into outside region of the slab. The radiation conditions on the slab boundaries have a form

$$\frac{1}{\mu} \frac{\partial G_{11}(q, q'; z, z')}{\partial z} \Big|_{z=\eta} + i\gamma_q G_{11}(q, q'; z = \eta, z') = 0 \quad (12)$$

and

$$\frac{1}{\mu} \frac{\partial G_{11}(q, q'; z, z')}{\partial z} \Big|_{z=L-\eta} - i\gamma_q G_{11}(q, q'; z = L - \eta, z') = 0 \quad (13)$$

as well as two continuous extensions

$$G_{01}(q, q'; z, z') = \exp(-i\gamma_q z) G_{11}(q, q'; z = \eta, z') \quad (14)$$

as  $z < 0$  and

$$G_{01}(q, q'; z, z') = \exp[i\gamma_q(z - L)] G_{11}(q, q'; z = L - \eta, z') \quad (15)$$

as  $z > L$ . As a result, Eq. (10) is brought to a form

$$G_{11}(q, q'; z, z') = G_0(q, z) \delta_{qq'} + \int_0^L dz'' \int_{q''} G_0(q, z - z'') \hat{V}(q, q''; z'') G_{11}(q'', q'; z'', z') \quad (16)$$

This equation is similar to Eq. (8), but has not a factor  $\mu$  at  $G_0(q, z)$  in the RHS.

Resolving the integral Eq. (16) for 1D Fourier transform  $G_{11}(q, q'; z, z')$  of the slab propagated radiation Green function and substituting result into RHS of two continuous extensions (14) and (15) gives 1D Fourier transform  $G_{01}(q, q'; z, z')$  of the slab outgoing radiation Green function.

### 2.4. Green Function Reciprocity

We have shown above how the Green theorem [25], written for any functions  $\psi(\rho)$  and  $\varphi(\rho)$ , is used in the extended boundary condition technique. Note, the function  $\psi(\rho)$  has been chosen to be equal to the Green function in unbounded background medium always and the function  $\varphi(\rho)$  was varied. The same Green theorem is used to derive the reciprocity relations for the Green function in a form

$$\frac{1}{\mu_a} G_{ab}(\rho, \rho') = \frac{1}{\mu_b} G_{ba}(\rho', \rho) \quad (17)$$

by another choosing the function  $\psi(\rho)$ . For example, putting  $\psi(\rho) = G_{00}(\rho, \rho')$  and  $\varphi(\rho) = G_{01}(\rho, \rho')$  and applying the Green theorem to region  $\Omega_0$  jointly with the standard boundary conditions one gets the reciprocity relation in Eqs. (17) at  $a = 1$  and  $b = 0$ . This relation means in details,  $G_{01}(\rho, \rho') = -G_{10}(\rho', \rho)$ , and one can obtain automatically the slab outgoing radiation Green function, provided he knows the slab incoming radiation Green function. The sign minus in the last relation is a consequence of the magnetic permeability jump on the LHM slab boundaries, from  $\mu = 1$  outside to  $\mu = -1$  inside the slab.

### 3. PERFECT PLANAR LHM SLAB AS TRANSFERER OF GREEN FUNCTION SINGULARITY

According to electromagnetism theory in general relativity, a spatial distribution for the dielectric permittivity and the magnetic permeability in the case of perfect Veselago's lens can be obtained from ones for the empty space by 1D coordinate transform of Refs. [16, 17]. For our coordinate system (Fig. 1) this coordinate transformation has a form,  $\tilde{z} = z$  as  $z < 0$ ,  $\tilde{z} = -z$  as  $0 < z < L$ , and  $\tilde{z} = z - 2L$  as  $z > L$ , with  $\tilde{z}$  being a coordinate of electromagnetic (empty) space, and will be referred further LP-transformation. The current section is aimed to consider a relation between the LP-transformation and the perfect Veselago's lens Green function, which will be denoted  $G_{ab}^{(0)}(\rho, \rho')$ .

#### 3.1. Singularity Transfer from Outside to Inside and from One Side to Another of the Slab

In the case of perfect Veselago's lens the effective potential (9) consists of surface part only that simplifies Eq. (8) for 1D Fourier transform of the incoming radiation Green function to algebraic and easy resolved form. Making next the inverse 1D Fourier transform gives the incoming radiation Green function of perfect Veselago's lens as an integral over angular spectrum components

$$G_{10}^{(0)}(x, z; x', z') = \int_q \frac{1}{2i\gamma_q} \exp[iq(x - x')] \exp[i\gamma_q(z - 2L + z')] \quad (18)$$

As one can see, this incoming radiation Green function coincides with the empty space Green function,  $G_0(x - x', z - 2L + z') = G_0(x - x', -\tilde{z} + \tilde{z}')$ , written according to LP-transformation and having singularity at inside focal plane  $z \rightarrow 2L - z'$  under conditions  $z > 2L - z'$  and  $L < z' < 2L$  (left panel of Fig. 2). Under opposite conditions,  $z < 2L - z'$  and  $L < z' < 2L$ , the integral in the RHS of Eq. (18) diverges and the incoming radiation Green function exists as a Schwartz distribution [27] that is as a linear functional kernel, only.

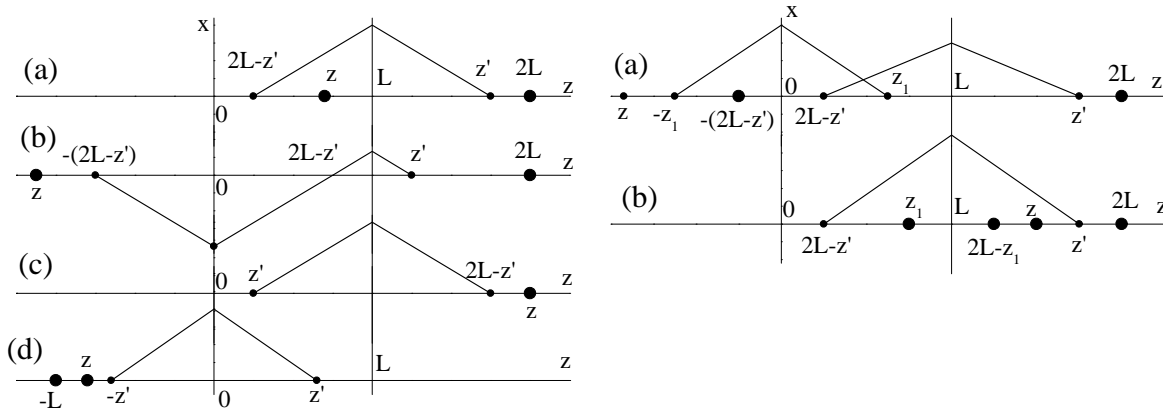


Figure 2: Left panel: Singularity transfer by perfect lens from right outside plane  $z = z'$ ,  $L < z' < 2L$ , to inside (a) and left outside (b) focal planes  $z \rightarrow 2L - z'$ ,  $z > 2L - z'$  and  $z \rightarrow -(2L - z')$ ,  $z < -(2L - z')$ , respectively; singularity transfer from inside plane  $z = z'$ ,  $0 < z' < L$  to right (c) and left (d) outside focal planes  $z = 2L - z'$ ,  $z > 2L - z'$  and  $z \rightarrow -z'$ ,  $z < -z'$ , respectively. Right panel: Multiplicative effect in singularity transfer by LHM slab from right outside plane  $z = z'$  to left (a) and right (b) outside focal planes  $z \rightarrow -(2L - z')$ ,  $z < -z_1 < -(2L - z')$ , and  $z \rightarrow 2L - z_1$ ,  $z' > z > 2L - z_1$ , respectively, via linelike scatterer  $z = z_1$  near inside focal plane  $z_1 \rightarrow 2L - z'$ ,  $z_1 > 2L - z'$ .

Substituting the angular spectrum amplitude of the incoming radiation Green function from Eq. (18) into continuous extensions (6) and (7) leads to transmitted and reflected radiation Green function of perfect Veselago's lens as integral

$$G_{00}^{(0)}(x, z; x', z') = \int_q \frac{1}{2i\gamma_q} \exp[iq(x - x')] \exp[i\gamma_q(-z - 2L + z')] \quad (19)$$

as  $z < 0$  and  $z' > L$ , and as a simple relation

$$G_{00}^{(0)}(x, z; x', z') = G_0(x - x', z - z') \quad (20)$$

as  $z > L$  and  $z' > L$ , respectively. The transmitted radiation Green function (19) coincides with the empty space Green function  $G_0(x - x', -z - 2L + z') = G_0(-\tilde{z} + \tilde{z}')$  written according to LP-transformation and having singularity at left outside focal plane  $z \rightarrow -(2L - z')$  under conditions  $z < -(2L - z')$  and  $L < z' < 2L$  (Fig. 2). Under opposite conditions,  $z > -(2L - z')$  and  $L < z' < 2L$ , the integral in the RHS of Eq. (19) diverges. Eq. (20) shows that the reflected radiation Green function for perfect Veselago's lens coincides with the empty space Green function at all.

Having derived Eqs. (18) and (19), we made assumption that the source plane of the Green function was positioned in the right outside region  $z' > L$  of the perfect planar LHM slab. The values for the Green function in the case of the source plane being positioned in the left outside region  $z' < 0$  of the slab can be obtained automatically from these two equations by formal replacing,  $z \rightarrow -z + L$  and  $z' \rightarrow -z' + L$ , as shows a geometrical consideration. In particular, for the Green function of incoming radiation we obtain

$$G_{10}^{(0)}(x, z; x', z') = \int_q \frac{1}{2i\gamma_q} \exp[iq(x - x')] \exp[i\gamma_q(-z - z')] \quad (21)$$

as  $z' < 0$ . This incoming radiation Green function coincides with the empty space Green function,  $G_0(x - x', -z - z') = G_0(x - x', \tilde{z} - \tilde{z}')$ , written according to LP-transformation and having singularity at inside focal plane  $z \rightarrow -z'$  under condition  $z < -z'$  (left panel of Fig. 2). Under opposite condition,  $z > -z'$ , the integral in the RHS of Eq. (21) diverges, in accordance with Ref. [8].

### 3.2. Singularity Transfer from Inside to Outside of the Slab

In the case of perfect Veselago's lens Eq. (16) for 1D Fourier transform of the propagated inside the LHM slab radiation Green function is simplified to algebraic and easy resolved form, similar with Eq. (8). Substituting this solution into continuous extensions (14) and (15) results in outgoing from the slab radiation Green function of perfect Veselago's lens. Practically one can get this outgoing radiation Green function also applying a reciprocity relation (17) to expressions (18) and (21) for the incoming radiation Green function. The both ways lead to integral representations

$$G_{01}^{(0)}(x, z; x', z') = - \int_q \frac{1}{2i\gamma_q} \exp[iq(x - x')] \exp[i\gamma_q(z' - 2L + z)] \quad (22)$$

as  $z > L$  and

$$G_{01}^{(0)}(x, z; x', z') = - \int_q \frac{1}{2i\gamma_q} \exp[iq(x - x')] \exp[i\gamma_q(-z' - z)] \quad (23)$$

as  $z < 0$ , respectively. As Eq. (22) shows, the Green function of radiation outgoing from inside to the right outside slab region,  $z > L$ , coincides with the opposite in sign empty space Green function,  $-G_0(x - x', z' - 2L + z) = -G_0(x - x', \tilde{z} - \tilde{z}')$ , written according to LP-transformation and having singularity at right outside focal plane  $z \rightarrow 2L - z'$  under condition  $z > 2L - z'$  (left panel of Fig. 2). Under opposite condition,  $z < 2L - z'$ , the integral in the RHS of Eq. (22) diverges. From Eq. (23) we see that the Green function of radiation outgoing to the left outside slab region,  $z < 0$ , coincides with the opposite in sign empty space Green function,  $-G_0(x - x', -z' - z) = -G_0(x - x', \tilde{z}' - \tilde{z})$ , written according to LP-transformation and having singularity at left outside focal plane  $z \rightarrow -z'$  under condition  $z < -z'$  (left panel of Fig. 2). Under opposite condition,  $z > -z'$ , the integral in the RHS of Eq. (23) diverges.

The itself Green function of propagated inside the perfect planar LHM slab radiation is presented by

$$G_{11}^{(0)}(x, z; x', z') = - \int_q \frac{1}{2i\gamma_q} \exp[iq(x - x')] \exp(-i\gamma_q |z - z'|) \quad (24)$$

The integral in the RHS of this equation diverges and the propagated radiation inside perfect LHM slab Green function exists as a Schwartz distribution only.

#### 4. MULTIPLICATIVE SINGULARITY OF GREEN FUNCTION FOR LHM SLAB WITH LINELIKE SCATTERER

##### 4.1. Equation for Inhomogeneous LHM Slab Green Function in Terms of Homogeneous LHM Slab Green Function

As was shown in the preceding section, the perfect Veselago's lens Green function is simple related to the empty space Green function, but for definite positions of receive and source planes only. For another positions of these planes the integral giving the perfect Veselago's lens Green function in angular spectrum representation does diverge because of Pendry's evanescent wave enhancement effect [5]. To save the integral convergence for all receive and source plane positions one can take into account a homogeneous deviation  $\delta\epsilon_0$  of the dielectric permittivity and the magnetic permeability from  $-1$ . In this case the effective volume scattering potential,  $V(x, z) = V_0 + V_1(x, z)$ , consists of homogeneous and inhomogeneous components. The homogeneous component is given by  $V_0 = k_0^2 - k_{01}^2$ , with  $k_{01} = k_0 [(-1 + \delta\epsilon_0)\mu]^{1/2}$  being the wave number in homogeneous LHM slab. The inhomogeneous component  $V_1(x, z) = -k_0^2 [\delta\epsilon(x, z)]\mu$  is accounting for inhomogeneities.

Now the effective singular potential  $\hat{V}(q, q'; z)$ , defined by Eqs. (9), can be rewritten as a sum,  $\hat{V}(q, q'; z) = \hat{V}_0(q, q'; z) + V_1(q - q', z)$ , where  $\hat{V}_0(q, q'; z) = V_0\delta_{qq'} + V_S(q, q'; z)$  is singular potential of homogeneous LHM slab and  $V_1(q - q', z)$  is regular volume potential accounting for inhomogeneities.

We denote the homogeneous LHM slab Green function by  $G_{ab}^{(0)}(\rho, \rho')$ , as was denoted the perfect Veselago's lens Green function in the preceding section. The integral Eqs. (8) and (16) for 1D Fourier transform  $G_{10}^{(0)}(q; z, z')\delta_{qq'}$  and  $G_{11}^{(0)}(q; z, z')\delta_{qq'}$  related to incoming radiation into the homogeneous LHM slab and propagated inside that, respectively, are simple resolved and one can see these solutions in Ref. [11]. It is important for us here that these solutions give possibility to bring Eq. (8) to a new and productive form where evidently one only does see the regular volume potential accounting for inhomogeneities. The new form of Eq. (8) is obtained using a resolvent operator [28] for this equation in the homogeneous LHM slab case and written as follows

$$G_{10}(q, q'; z, z') = G_{10}^{(0)}(q; z, z')\delta_{qq'} + \int_0^L dz'' \int_{q''} G_{11}^{(0)}(q; z, z'')V_1(q - q''; z'')G_{10}(q'', q'; z'', z') \quad (25)$$

as  $z' > L$ . Applying to obtained Eq. (25) the continuous extensions (6) and (7) jointly with (14) and (15) leads after the inverse 1D Fourier transform with respect to the  $q$  and  $q'$  variables to a basic formula for the Green function of transmitted radiation through and reflected radiation from the inhomogeneous LHM slab

$$G_{00}(q, q'; z, z') = G_{00}^{(0)}(x - x'; z, z') + \int dx'' \int_0^L dz'' G_{01}^{(0)}(x - x''; z, z'') \cdot V_1(x'', z'')G_{10}(x'', z''; x', z') \quad (26)$$

as  $z' > L$ . Physically this formula means evidently that transmitted through or reflected from the inhomogeneous LHM slab radiation, created by a point source on the right outside region of the slab, is incoming into the slab next can be scattered by a slab volume inhomogeneities and then is outgoing the slab.

##### 4.2. Approximation of Weak Linelike Inhomogeneity

Consider the basic formula (26) in the limit of inhomogeneity similar to a linelike scatterer, with its axis being parallel to the  $y$  axis and cross section occupied the region,  $x_1 - \Delta x < x < x_1 + \Delta x$  and  $z_1 - \Delta z < z < z_1 + \Delta z$ , where  $0 < z_1 < L$ , in the  $x, z$  plane. We think the scatterer constant potential  $V_1 = k_0^2\delta\epsilon$  to be weak and replace in the formula (26) RHS the unknown Green function  $G_{10}$  for incoming into inhomogeneous LHM slab radiation by known one  $G_{10}^{(0)}$  in the case of perfect Veselago's lens. We replace also in the (26) RHS the transmitted through and reflected from homogeneous LHM slab Green function  $G_{00}^{(0)}$ , as well as the outgoing homogeneous LHM slab Green function  $G_{01}^{(0)}$  to their values in the case of perfect Veselago's lens. This approach gives us

$$G_{00}(x, z; x', z') \cong G_{00}^{(0)}(x - x'; z, z') + V_1 \int_{x_1 - \Delta x}^{x_1 + \Delta x} dx'' \int_{z_1 - \Delta z}^{z_1 + \Delta z} dz'' G_{01}^{(0)}(x - x''; z, z'') G_{10}^{(0)}(x'' - x'; z'', z') \quad (27)$$

as  $z' > L$ . We will simplify the written approximative basic formula for the cases of slab transmitted and reflected radiation separately.

In the case of slab transmitted radiation, with the receive and source planes being placed in the left  $z < 0$  and the right  $z' > L$  outside regions of the slab, respectively, the Green functions of incoming as well as outgoing perfect Veselago' lens radiation in the RHS of formula (27) are given according to (18) by

$$G_{10}^{(0)}(x'' - x'; z'', z') = G_0(x'' - x', z'' - 2L + z') \quad (28)$$

under condition  $z'' > 2L - z'$ , which is satisfied if  $z_1 - \Delta z > 2L - z'$ , as well as according to (23) by

$$G_{01}^{(0)}(x - x''; z, z'') = -G_0(x - x'', -z'' - z) \quad (29)$$

under condition  $z < -z''$ , which is satisfied if  $z < -z_1 - \Delta z$ .

Let us introduce the physically important defocusing parameters  $\delta z$  and  $\delta z'$  for positions of receive and source planes, respectively, relatively the position  $z_1$  of linelike scatterer plane defined by  $\delta z = -z - z_1$  and  $\delta z' = z_1 - 2L + z'$ . Supposing these defocusing parameters are much more the linelike scatterer cross section dimensions,  $\delta z \gg \Delta x, \Delta z$  and  $\delta z' \gg \Delta x, \Delta z$ , and supposing an exact focusing with respect to the  $x$  axis,  $x = x' = x_1$ , one can simplify the formula (27) as follows (right panel of Fig. 2)

$$G_{00}(x, z; x', z') \cong G_0(x = 0, -z - 2L + z') - f_1 G_0(x = 0, \delta z) G_0(x = 0, \delta z') \quad (30)$$

where  $f_1 = V_1 \Delta x \Delta z$  denotes a scattering amplitude of linelike scatterer. Simplification for the approximative basic formula (27) in the case of slab reflected radiation, with the receive and source planes being placed both in the right  $z > L$  and  $z' > L$  outside regions of the slab, is performed similar to the case of transmitted radiation. In the case of slab reflected radiation the defocusing parameters for positions of receive and source planes are defined by  $\delta z = z - 2L + z_1$  and  $\delta z' = z' - 2L + z_1$  and formula (27) is simplified as (right panel of Fig. 2)

$$G_{00}(x, z; x', z') \cong G_0(x = 0, z - z') - f_1 G_0(x = 0, \delta z) G_0(x = 0, \delta z') \quad (31)$$

We will apply the obtained particular basic formulas (30) and (31) to a problem of getting visible image for Veselago's focus inside LHM slab via linelike scatterer.

#### 4.3. Multiplicative Effect in Singularity Transfer

The defined in preceding subsection defocusing parameters  $\delta z$  and  $\delta z'$  were supposed to be much more the linelike scatterer cross dimensions. Nevertheless, these defocusing parameters can be much less the wave number in the background,  $k_0 \delta z \ll 1$  and  $k_0 \delta z' \ll 1$ , until the linelike scatterer cross dimensions are much less the wave number also,  $k_0 \Delta z \ll 1$  and  $k_0 \Delta z' \ll 1$ . Next we remind that the empty space Green function is proportional to the first type Hankel function of the zero order,  $G_0(\rho) = (1/4i)H_0^{(1)}(k_0 \rho)$ , and asymptotically tends to logarithm expression,  $-(1/2\pi) \ln(2/k_0 \rho)$ , in quasistatic limit,  $k_0 \rho \ll 1$ .

Return now to particular basic formulas (30) and (31). We see that the second terms in the RHS of the formulas, described contributions of linelike scatterer into Green function of transmitted through and reflected from the inhomogeneous LHM slab, are proportional to scattering amplitude of the scatterer and product of two Green functions' quasistatic singularities, provided the source and receive points being focused on the scatterer with small defocusing parameters. We call this case as multiplicative quasistatic singularity of the Green function for inhomogeneous LHM slab.

## 5. CONCLUSIONS

In this report we have adopted the usual Green function approach and potential scattering theory to a new area of electromagnetic multiple scattering by inhomogeneous dielectric structure placed inside LHM slab. A specific of the adaptation consisted in appearance not only a volume, but also a surface scattering potential in the derived integral equation for the inhomogeneous LHM slab Green function. First, we verified that the Green function of perfect planar LHM slab can be obtained from the empty space Green function by the spatial coordinate transformation according to concept about spatial transformation media. Nevertheless, this concept demands in our case the definite positions of receive and source planes, for which the perfect LHM slab Green function is presented by convergent integral. Second, we rewrote the derived integral equation for the

inhomogeneous LHM slab Green function in terms of homogeneous LHM slab Green function and volume scattering potential only. The iterative series solution with respect to volume potential to this rewritten integral equation is directly interpreted as wave radiation multiple scattering by inhomogeneities inside LHM slab. We applied the first iteration to study a spatial singularity of the Green function of LHM slab with a linelike scatterer inside slab and showed that singularity can be multiplicative, provided the source and receive planes are focused on the linelike scatterer position, with small defocusing.

This work is supported by the grant from Russian Foundations for basic Research number 06-02-17451; by the Russian Academy of Sciences projects “Passive multichannel radio-and acousto-thermotomography of a human body in the near zone”, “Creation and properties’ investigation of new types of photonic crystals based on semiconductor and magnetic materials for the development of optoelectronic elements of infocommunication nets”.

## REFERENCES

1. Veselago, V. G., “The electrodynamics of substances with simultaneously negative values of  $\epsilon$  and  $\mu$ ,” *Phys. Usp.*, Vol. 10, 509, 1968.
2. Mandel’stam, L. I., “Group velocity in a crystal lattice,” *Zh. Eksp. Teor. Fiz.*, Vol. 15, 475, 1945.
3. Agranovich, V. M. and V. L. Ginzburg, *Crystal Optics with Spatial Dispersion*, Springer-Verlag, Berlin, 1984.
4. Kuzmiak, V. and A. A. Maradudin, “Scattering properties of a cylinder fabricated from a left-handed material,” *Phys. Rev. B*, Vol. 66, 045116, 2002.
5. Pendry, J. B., “Negative refraction makes a perfect lens,” *Phys. Rev. Lett.*, Vol. 85, 3966, 2000.
6. Rao, X. S. and C. K. Ong, “Subwavelength imaging by a left-handed material superlens,” *Phys. Rev. E*, Vol. 68, 067601, 2003.
7. Pendry, J. B. and S. A. Ramakrishna, “Near-field lenses in two dimensions,” *J. Phys.: Condens. Matter.*, Vol. 14, 8463, 2002.
8. Carsia, N. and M. Nieto-Vesperinas, “Left-handed materials do not make a perfect lens,” *Phys. Rev. Lett.*, Vol. 88, 207403, 2003.
9. Ye, Z., “Optical transmission and reflection of perfect lenses by left handed materials,” *Phys. Rev. B*, Vol. 67, 193106, 2003.
10. Dorofeenko, A. V., A. A. Lisyansky, A. M. Merzlikin, and A. P. Vinogradov, “Full-wave analysis of imaging by the Pendry-Ramakrishna stackable lens,” *Phys. Rev. B*, Vol. 73, 235126, 2006.
11. Luan, P. G., H.-D. Chien, C.-C. Chen, and C.-S. Tung, “Imaging properties of a left-handed material slab,” *arXiv: Physics/0311122*, Vol. 25, 11122, 2003.
12. Shevchenko, V. V., “About superfocusing of plane lins from negative material,” *Journal of Radioelectronics*, No. 6, Russian Academy of Sciences, Russia, 2007.
13. Anioutine, A. P., “About field calculation in focus domain of ideal Veselago’s lens of finite dimensions,” *Journal of Radioelectronics*, No. 6, Russian Academy of Sciences, Russia, 2007.
14. Anioutine, A. P., A. G. Kyurkchan, and S. A. Minaev, “About universal modification to the method of discrete sources and its application,” *JQSRT*, Vol. 79–80, 509, 2003.
15. Anioutine, A. P., A. G. Kyurkchan, S. A. Manenkov, and S. A. Minaev, “About 3D solution of diffraction problems by MMDS,” *JQSRT*, Vol. 100, 26, 2006.
16. Leonardt, U. and T. G. Philbin, “General relativity in electrical engineering,” *New J. Phys.*, Vol. 8, 247, 2006.
17. Leonardt, U. and T. G. Philbin, “Quantum optics of spatial transformation media,” *J. Opt. A: Pure Appl. Opt.*, Vol. 9, 289, 2007.
18. Barabanenkov, Yu. N., “Maxwell equations in rotating system of reference,” *Scientific Reports of Higher School, Phys-Math Sciences*, No. 1, 141, 1959.
19. Einstein, A., “Die grundlage der allgemeinen relativitatstheorie,” *Ann. Phys.*, Vol. 49, 769, 1916.
20. Plebanski, J., “Electromagnetic waves in gravitational fields,” *Phys. Rev.*, Vol. 118, 1396, 1960.
21. Pendry, J. B., D. Schurig, and D. R. Smith, “Controlling electromagnetic fields,” *Science*, Vol. 312, 1780, 2006.
22. Chen, H., B.-I. Wu, B. Zhang, and J. A. Kong, “Electromagnetic wave interaction with a metamaterial cloak,” *Phys. Rev. Lett.*, Vol. 99, 063903, 2007.
23. Newton, R. G., *Scattering Theory of Waves and Particles*, McGraw–Hill, New York, 1966.

24. Tsang, L., J. A. Kong, and R. Shin, *Theory of Microwave Remote Sensing*, John Wiley, New York, 1985.
25. Stratton, J. A., *Electromagnetic Theory*, McGraw–Hill, New York, 153, 1941.
26. Klytskin, V. I., *The Imbedding Method in the Theory of Wave Propagation*, Nauka, Moscow, Russia, 1980.
27. Schwartz, L., *Methodes Mathematiques Pour Les Sciences Physiques*, 84, Hermann, Paris, 1961.
28. Riez, F. and B. Sz.-Nagy, *Lecons D'Analyse Fonctionnelle*, 169, Akademiai Kiado, Budapest, 1972.

# Magnetoplasmons and Quasiparticles for Quantum-dots in Graphene

Oleg L. Berman<sup>1</sup> and Godfrey Gumbs<sup>2</sup>

<sup>1</sup>Physics Department, New York City College of Technology, City University of New York, USA

<sup>2</sup>Department of Physics and Astronomy, Hunter College, City University of New York, USA

**Abstract**— We calculate the magnetoplasmon dispersion equation for a square array of quantum dots on a two-dimensional (2D) graphene layer described by the Dirac equation for low-lying excitations. The confining potential is modeled by a linear function of distance from the center of the quantum dot. We map the eigenstates of the Dirac equation for electrons in a magnetic field in the presence of the model confining potential onto a 2D plane of electron-hole pairs in an effective magnetic field without any confinement. The applied magnetic field and the confining potential for quantum dots determine this effective magnetic field. The tight-binding model for the array of quantum dots leads to a wavefunction which results in inter-dot mixing of the quantum numbers associated with an isolated quantum dot. The excitation spectrum of the collective modes preserves the periodicity of the lattice, even with the mixing of the quantum numbers. For chosen slope of the confinement, magnetic field, wavevector and frequency, we plot the dispersion equation as a function of the period  $d$  of the lattice. We obtain those values of  $d$  which yield collective plasma excitations. For the allowed transitions between the valence and conduction bands in our calculations, we obtain plasmons when  $d \lesssim 100\text{\AA}$ .

## 1. INTRODUCTION

A two-dimensional (2D) honeycomb lattice of carbon atoms that form the basic planar structure in graphite (graphene) has recently been produced [1, 2]. Unusual many-body effects in graphene have been attributed to low-lying excitations in the vicinity of the Fermi level [3]. The influence of an external magnetic field on the many-electron properties of graphene results in an unusual quantum Hall effect. The integer quantum Hall effect (IQHE) was discovered in graphene in recent experiments [4–6]. The quantum Hall ferromagnetism in graphene has been studied theoretically [7]. The spectrum of plasmon excitations in a single graphene layer immersed in a material with effective dielectric constant  $\varepsilon_b$  in the absence of magnetic field ( $B = 0$ ) was calculated in Ref. [8]. The collective plasma excitations in layered graphene structures in high magnetic field were obtained in Ref. [9, 10] where the instability of these modes was investigated. Recently, several works were reported for quantum dots in graphene [11–13]. This is just one of the areas of research in the fast-growing field of the electronic and optical properties of graphene [14]. The single-particle states and collective modes in semiconductor quantum dots have long been a subject of interest to both theoreticians and experimentalists [15–17]. The spectrum of collective excitations in a 2D array of quantum dots in semiconductors has been calculated [18].

In this paper, we calculate the dispersion equation for magnetoplasmons in a square array of quantum dots formed by a confining potential which is a linear function of distance from the center of the quantum dot. A strong perpendicular magnetic field  $\mathbf{B}$  is applied. The conditions of the existence of the collective excitations will be investigated.

## 2. SINGLE-ELECTRON EIGENSTATES IN A LINEAR CONFINING POTENTIAL IN GRAPHENE

We now consider an electron in a graphene layer in the presence of a perpendicular magnetic field  $\mathbf{B}$  and a confining potential defined as  $U(r') = \lambda_0|r'|$ , where  $\lambda_0 > 0$  is the slope of the potential. The effective-mass Hamiltonian of an electron in the absence of scatterers in one valley in graphene located in the  $xy$ -plane is given by [19, 20]

$$\hat{H}_{(0)} = v_F \begin{pmatrix} 0 & \hat{\pi}_x - i\hat{\pi}_y \\ \hat{\pi}_x + i\hat{\pi}_y & 0 \end{pmatrix} + \lambda_0|r'|. \quad (1)$$

Here, we neglect the Zeeman splitting and assume energy degeneracy with respect to the two valleys (two pseudospins in graphene). Also, in our notation,  $\hat{\pi} = -i\hbar\nabla + e\mathbf{A}$ ,  $\mathbf{A}$  is the vector potential of an electron,  $v_F = \sqrt{3}at/(2\hbar)$  is the Fermi velocity of electrons with  $a = 2.566\text{\AA}$  denoting the lattice constant and  $t \approx 2.71\text{ eV}$  is the overlap integral between nearest-neighbor carbon atoms in

graphene [21]. The eigenvalue problem of an electron in a linear confining potential can be mapped onto one for a noninteracting electron-hole pair in an effective magnetic field  $\tilde{B}_{\text{eff}}$  under conditions we introduce below.

The eigenfunction  $\psi_\tau$  for the Hamiltonian in Eq. (1) for an electron-hole pair in an effective magnetic field  $\tilde{B}_{\text{eff}}$ , is also the eigenfunction of the magnetic momentum  $\tilde{\mathbf{P}}$  has the form [22–25] and is given by

$$\psi_{\mathbf{P}}(\mathbf{R}, \mathbf{r}) = \exp \left[ \frac{i}{\hbar} \mathbf{R} \cdot \left( \mathbf{P} + e[\tilde{\mathbf{B}} \times \mathbf{r}] \right) \right] \tilde{\Phi}(\mathbf{r} - \rho_0), \quad (2)$$

where  $\mathbf{R} = (\mathbf{r}_e + \mathbf{r}_h)/2$ ,  $\mathbf{r} = \mathbf{r}_e - \mathbf{r}_h$  and  $\rho_0 = [\tilde{\mathbf{B}} \times \mathbf{P}]/(e\tilde{B}_{\text{eff}}^2)$ . The cylindrical gauge for vector potential is used with  $\mathbf{A}_{e(h)} = 1/2[\tilde{\mathbf{B}} \times \mathbf{r}_{e(h)}]$ . The wavefunction of the relative coordinate  $\tilde{\Phi}(\mathbf{r})$  can be expressed in terms of the 2D harmonic oscillator eigenfunctions  $\Phi_{n_1, n_2}(\mathbf{r})$ . For an electron in Landau level  $n_+$  and a hole in level  $n_-$ , the four-component wavefunctions for the relative motion are [26]

$$\tilde{\Phi}_{n_+, n_-}(\mathbf{r}) = \left( \sqrt{2} \right)^{\delta_{n_+, 0} + \delta_{n_-, 0} - 2} \begin{pmatrix} s_+ s_- \Phi_{|n_+|-1, |n_-|-1}(\mathbf{r}) \\ s_+ \Phi_{|n_+|-1, |n_-|}(\mathbf{r}) \\ s_- \Phi_{|n_+|, |n_-|-1}(\mathbf{r}) \\ \Phi_{|n_+|, |n_-|}(\mathbf{r}) \end{pmatrix}, \quad (3)$$

where  $s_\pm = \text{sgn}(n_\pm)$ . The corresponding energy of the electron-hole pair  $E_{n_+, n_-}$  of the Hamiltonian in Eq. (1) is given by [26]

$$E_{n_+, n_-} = \sqrt{2} \left( \frac{\hbar v_F}{\tilde{r}_B} \right) \left[ \text{sgn}(n_+) \sqrt{|n_+|} - \text{sgn}(n_-) \sqrt{|n_-|} \right], \quad (4)$$

where  $r_B^* = \sqrt{\hbar/(e\tilde{B}_{\text{eff}})}$  is an effective magnetic length. The 2D harmonic oscillator wavefunctions  $\Phi_{n_1, n_2}(\mathbf{r})$  are given by [26]

$$\Phi_{n_1, n_2}(\mathbf{r}) = (2\pi)^{-1/2} 2^{-|m|/2} \frac{\tilde{n}!}{\sqrt{n_1! n_2!}} \frac{1}{r_B^*} \text{sgn}(m)^m \frac{r^{|m|}}{r_B^{|m|}} \exp \left[ -im\phi - \frac{r^2}{4r_B^{*2}} \right] L_{\tilde{n}}^{|m|} \left( \frac{r^2}{2r_B^{*2}} \right), \quad (5)$$

where  $L_{\tilde{n}}^{|m|}(x)$  is a Laguerre polynomial,  $m = n_1 - n_2$ ,  $\tilde{n} = \min(n_1, n_2)$  and  $\text{sgn}(m)^m \rightarrow 1$  for  $m = 0$ . The electron-hole eigenfunction given by Eqs. (2), (3), (5) along with the energy eigenvalue in Eq. (4) are the same as the eigenfunction and the eigenvalue of the Hamiltonian in Eq. (1) for an electron in a quantum dot in external magnetic field. The magnetic momentum  $\mathbf{P} = -e[\tilde{\mathbf{B}}_{\text{eff}} \times \mathbf{r}]$  must be the same for the electron and the electron-hole pair at fixed relative coordinate  $\mathbf{r}$ . The effective magnetic field  $\tilde{B}_{\text{eff}}$  depends on the slope  $\lambda_0$  of the confining potential as well as the external magnetic field  $B$  and is given by

$$\tilde{B}_{\text{eff}} = \left( B^2 + \frac{4\lambda_0^2}{e^2 v_F^2} \right)^{1/2}. \quad (6)$$

In the case when there is no electron confinement, i.e.,  $\lambda_0 = 0$ , the effective magnetic field is the same as the applied magnetic field and  $\tilde{B}_{\text{eff}} = B$ . If there is no external magnetic field, i.e.,  $B = 0$ , then there is still an effective magnetic field due to the electron confinement and is given by  $\tilde{B}_{\text{eff}} = 2\lambda_0/(ev_F)$ . The coordinate of the electron-hole relative motion  $r = |\mathbf{r}_e - \mathbf{r}_h|$  is related to the distance  $r'$  of an electron from the center of the confining potential by  $r = r'/2$ .

It should be emphasized that the electrostatic potential for a graphene quantum dot was chosen to have a linear dependence on the coordinate variable  $|r'|$ . This was done because the eigenvalue problem of the Hamiltonian in Eq. (1) described by the Dirac-like equation with a linear potential can be reduced to the Klein-Gordon-type equation with a parabolic potential  $U(r') = \lambda_0^2 r'^2$ . This Klein-Gordon-type equation can then be mapped onto the electron-hole problem in an effective magnetic field  $\tilde{B}_{\text{eff}}$  defined in Eq. (6) under the conditions presented above.

### 3. MAGNETOPLASMONS FOR AN ARRAY OF QUANTUM-DOTS ON GRAPHENE

We now turn our attention to an infinite periodic 2D array of quantum-dots in a graphene plane, shown schematically in Fig. 1. The quantum dots are formed by a periodic linear confining potential defined by  $U(r') = \sum_j \lambda_0 |\mathbf{r}' - \mathbf{r}_j|$ , where  $\mathbf{r}_j$  is the position vector of a quantum dot. We consider this array with the period  $d$  in a perpendicular magnetic field  $\mathbf{B}$  as shown schematically in Fig. 1. For this system, we apply the tight-binding approximation [27, 28]

$$|\mathbf{k}, \alpha\rangle = \sum_{\mathbf{r}_j} e^{i\mathbf{k}\cdot\mathbf{r}_j} \psi_\alpha(\mathbf{r}' - \mathbf{r}_j) \exp\left(-\frac{ie}{\hbar} \mathbf{A} \cdot \mathbf{r}_j\right), \quad (7)$$

where  $\mathbf{k}$  is an in-plane wave vector,  $\psi_\alpha$  is the electron eigenfunction in one quantum dot (which can be represented by the wavefunction of an electron-hole pair in an effective magnetic field as  $\psi_\alpha = \tilde{\Phi}_{n_+, n_-}(\mathbf{r}/2)$ , where  $\tilde{\Phi}_{n_+, n_-}(\mathbf{r}/2)$  is given by Eq. (3). The index  $\alpha = \{n_+, n_-\}$  is a composite quantum number with  $n_+$  and  $n_-$  labeling the electron and hole energy levels, respectively. Also,  $\mathbf{A} = [\mathbf{B} \times \mathbf{r}]/2$  is the vector potential for the externally applied magnetic field  $\mathbf{B}$  expressed in the cylindrical gauge.

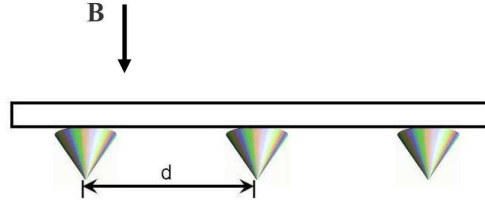


Figure 1: A periodic 2D array of quantum-dots in a graphene plane formed by a linear confinement with a spacing  $d$  in a perpendicular magnetic field  $\mathbf{B}$ .

Following the procedure adopted in Ref. [18], we introduce the quantity  $\Pi_{\alpha\beta}(\omega)$  defined by

$$\Pi_{\alpha\beta}(\omega) = \left(\frac{g_s g_v}{2\pi r_B^*{}^2}\right) \frac{f_0(E_\alpha) - f_0(E_\beta)}{\hbar\omega + E_\alpha - E_\beta + i0^+}, \quad (8)$$

where  $g_s = 2$  and  $g_v = 2$  are the spin and valley degeneracies in graphene,  $\omega$  denotes frequency,  $\alpha = (n_+, n_-)$ ,  $\beta = (n'_+, n'_-)$ ,  $E_{\alpha(\beta)}$  are the electron-hole pair eigenenergies given by Eq. (4) for the Landau levels in an effective magnetic field defined in Eq. (6). Also,  $f_0(E)$  is the occupation function of the two-particle state. At high temperatures or weak magnetic field, when the separation between Landau levels is small so that  $k_B T \gg \hbar v_F / r_B^*$ , the occupation of the Landau levels is given by the Fermi-Dirac distribution function  $f_0(E_\alpha) = (\exp[E_\alpha / (k_B T)] + 1)^{-1}$ .

We now introduce the overlap integral  $F_{\alpha\beta}(\mathbf{q})$  involving the eigenstates with labels  $\alpha = \{n_+, n_-\}$  and  $\beta = \{n'_+, n'_-\}$  through the equation [18]

$$F_{\alpha\beta}(\mathbf{q}) = \int d^2\mathbf{r} e^{i\mathbf{q}\cdot\mathbf{r}} \psi_\alpha^*(\mathbf{r}) \psi_\beta(\mathbf{r}) = s_+ s'_+ s_- s'_- F_{|n_+|-1, |n_-|-1, |n'_+|-1, |n'_-|-1}^{(0)}(\mathbf{q}) \\ + s_+ s'_+ F_{|n_+|-1, |n_-|, |n'_+|-1, |n'_-|}^{(0)}(\mathbf{q}) + s_- s'_- F_{|n_+|, |n_-|-1, |n'_+|, |n'_-|-1}^{(0)}(\mathbf{q}) + F_{|n_+|, |n_-|, |n'_+|, |n'_-|}^{(0)}(\mathbf{q}), \quad (9)$$

where

$$F_{n_1, n_2, n'_1, n'_2}^{(0)}(\mathbf{q}) = \int d^2\mathbf{r} e^{i\mathbf{q}\cdot\mathbf{r}} \Phi_{n'_1, n'_2}^*(\mathbf{r}) \Phi_{n_1, n_2}(\mathbf{r}) \quad (10)$$

and  $\Phi_{n_1, n_2}(\mathbf{r})$  is given by Eq. (5). The angular integral in Eq. (10) can be carried out using the result

$$\int_0^{2\pi} d\theta e^{i\beta \cos(\theta) - im\theta} = 2\pi (-i)^m J_m(-\beta)$$

with  $m$  an integer. If  $m$  is even,  $J_m(-\beta) = J_m(\beta)$ .

We employ the procedure introduced in Ref. [18] for determining the dispersion relation  $\omega = \omega(\mathbf{q})$  for the magnetoplasmon excitation frequencies. This can be calculated from the condition of the vanishing of the determinant of the matrix with elements  $C_{ij}(\mathbf{q}, \omega)$ . In this notation, the subscript  $i$  denotes the pair of quantum numbers  $\alpha$  and  $\beta$  for two different composite electron-hole pairs. Also,  $j$  denotes the quantum numbers  $\alpha'$  and  $\beta'$  for two other composite electron-hole pairs. The matrix elements  $C_{ij}$  are defined as

$$C_{ij}(\mathbf{q}, \omega) = \delta_{ij} - \Pi_i(\omega) \sum_{\mathbf{G}} \frac{2\pi e^2}{\varepsilon_s |\mathbf{q} + \mathbf{G}|} F_i(\mathbf{q} + \mathbf{G}) F_j^*(\mathbf{q} + \mathbf{G}). \quad (11)$$

In this notation,  $\varepsilon_s = 4\pi\epsilon_0\epsilon_b$ , where  $\epsilon_b$  is the average dielectric constant of the medium where the layer of graphene is embedded. We also introduced  $\mathbf{G} = 2\pi/d(n_x, n_y)$  which is a reciprocal lattice vector of the square array of quantum dots with period  $d$  and  $n_x, n_y = 0, \pm 1, \pm 2, \dots$ .

#### 4. NUMERICAL RESULTS AND DISCUSSION

In solving the dispersion equation for plasmon excitations, we chose the slope of the confining potential, magnetic field, wavevector, frequency, temperature and background dielectric constant. We then varied the period  $d$  and calculated the determinant  $\det[C_{ij}(\mathbf{q}, \omega)]$  obtained from Eq. (11). The zeros of the determinant correspond to the collective magnetoplasmon excitations. As is shown in Fig. 2, allowed plasmon resonances appear in the system at specific values of the dot spacing  $d$  corresponding to the condition  $\det[C_{ij}(\mathbf{q}, \omega)] = 0$ . The results of these calculations were obtained by taking into account only transitions between the Landau levels  $n = -1, 0, 1$ . The interdot separations where the plasmons can be excited are given by  $d \lesssim 100\text{\AA}$ . The excitation spectrum of the collective modes preserves the periodicity of the lattice, even with the mixing of the quantum numbers.

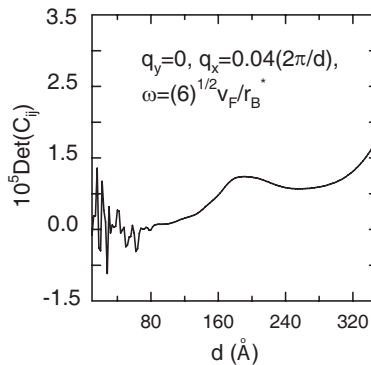


Figure 2:  $\det[C_{ij}(\mathbf{q}, \omega)]$  as a function of an array spacing  $d$  calculated using Eq. (11). We chose the slope of the confinement  $\lambda_0 = 10^{-2}eV/\text{\AA}$ , magnetic field  $B = 1$  T,  $\epsilon_b = 2.5$  and the temperature  $T = 0$  K. The values of spacing  $d$  resulting in  $\det[C_{ij}(\mathbf{q}, \omega)] = 0$  correspond to the existence of magnetoplasmon excitations at chosen frequency and wavevector.

The methodological achievement of the approach presented in this paper is the mapping of the single-electron eigenfunctions (Eq. (3)) and eigenenergies Eq.(4) in magnetic field in linear confinement in graphene onto the eigenfunctions and eigenenergies of a new set of quasiparticles: quasidelectrons and quasiholes without confinement in an effective magnetic field depending on the slope of the confinement (see Eq. (6)).

#### ACKNOWLEDGMENT

This work is supported by contract FA 9453-07-C-0207 of AFRL.

#### REFERENCES

1. Novoselov, K. S., et al., *Science*, Vol. 306, 666, 2004.
2. Zhang, Y., et al., *Phys. Rev. Lett.*, Vol. 94, 176803, 2005.
3. Sarma, S. D., E. H. Hwang, and W.-K. Tse, *Phys. Rev. B*, Vol. 75, 121406(R), 2007.
4. Novoselov, K. S., et al., *Nature*, Vol. 438, 197, London, 2005.

5. Zhang, Y. B., et al., *Nature*, Vol. 438, 201, London, 2005.
6. Zhang, Y., et al., *Phys. Rev. Lett.*, Vol. 96, 136806, 2006.
7. Nomura, K. and A. H. MacDonald, *Phys. Rev. Lett.*, Vol. 96, 256602, 2006.
8. Sarma, S. D. and E. H. Hwang, *Phys. Rev. Lett.*, Vol. 81, 4216, 1998.
9. Berman, O. L., G. Gumbs, and Y. E. Lozovik, *Journal of Electromagnetic Waves and Applications*, accepted, 2008.
10. Berman, O. L., G. Gumbs, and Y. E. Lozovik, *Phys. Rev. Lett.*, submitted, 2008.
11. Pereira, M., P. Vasilopoulos, and F. M. Peeters, *Nano Lett.*, Vol. 7, 946, 2007.
12. Peres, N. M. R., A. H. C. Neto, and F. Guinea, *Phys. Rev. B*, Vol. 73, 241403(R), 2006.
13. Silvestrov, P. G. and K. B. Efetov, *Phys. Rev. Lett.*, Vol. 98, 016802, 2007.
14. Neto, A. H. C., F. Guinea, N. M. R. Peres, K. S. Novoselov, and A. K. Geim, Arxiv; 0709.1163v1, 2007.
15. Brey, L., N. F. Johnson, and B. L. Halperin, *Phys. Rev. B*, Vol. 40, 10647, 1989.
16. Peeters, F. M., *Phys. Rev. B*, Vol. 42, 1486, 1990.
17. Maksym, P. A. and T. Chakraborty, *Phys. Rev. Lett.*, Vol. 65, 108, 1990.
18. Que, W., G. Kirczenow, and E. Castano, *Phys. Rev. B*, Vol. 43, 14079, 1991.
19. Zheng, Y. and T. Ando, *Phys. Rev. B*, Vol. 65, 245420, 2002.
20. Tóke, C., P.-E. Lammert, V. H. Crespi, and J. K. Jain, *Phys. Rev. B*, Vol. 74, 235417, 2006.
21. Lukose, V., R. Shankar, and G. Baskaran, *Phys. Rev. Lett.*, Vol. 98, 116802, 2007.
22. Gorkov, L. P. and I. E. Dzyaloshinskii, *JETP*, Vol. 26, 449, 1967.
23. Lerner, I. V. and Y. E. Lozovik, *JETP*, Vol. 51, 588, 1980.
24. Kallin, C. and B. I. Halperin, *Phys. Rev. B*, Vol. 30, 5655, 1984.
25. Kallin, C. and B. I. Halperin, *Phys. Rev. B*, Vol. 31, 3635, 1985.
26. Iyengar, A., J. Wang, H. A. Fertig, and L. Brey, *Phys. Rev. B*, Vol. 75, 125430, 2007.
27. Huang, D. and G. Gumbs, *Phys. Rev. Lett. B*, Vol. 46, 4147, 1992.
28. Böttger, H. and V. V. Bryksin, *Hopping Conduction in Solids*, Akademie-Verlag, Berlin, 1985.

# Two-photon Absorption Spectra of Cis- and Trans-bifullerene[60]-pentacene Adducts Based on First-principle Simulation

W.-D. Cheng, H. Hu, and J.-Y. Wang

State Key Laboratory of Structural Chemistry

Fujian Institute of Research on the Structure of Matter, Chinese Academy of Sciences

Fuzhou, Fujian 350002, China

**Abstract**— A combined method of time-dependent density functional theory with sum over states formula has been employed to model two-photon absorption spectra of cis- and trans-2[60]-pentacene adducts. The calculated results show that the cis configuration adduct of 2[60]-pentacene exists at lower energy of two-photon absorption peak and has a smaller two-photon absorption cross section. The two-photon absorption peaks of 2[60]-pentacene adducts originate from the charge transfers from condensed aromatics to fullerene cages.

## 1. INTRODUCTION

Utilizing electron acceptor  $C_{60}$  linking to monodisperse  $\pi$ -conjugated oligomer which is taken as photoexcited state electron donors, offers substantially stabilized charge separate states in  $C_{60}$ -based materials and artificial electron transfer systems. These systems have been a subject of great interest due to they are promising candidates for the potential applications, such as artificial photosynthesis, novel molecular electronic and photovoltaic devices, as well as supramolecular chemistry [1–7]. The bisfullerene derivatives form nanostructures, with a wide range of sizes and shapes varying from elongated wires to entangled spheres. The close network of fullerene moieties in the bisfullerene derivatives facilitates the hopping of electron from the parent fullerene to the adjacent molecule, thus increasing the spatial distance between the charge-separated pairs. The cycloadducts of two  $C_{60}$  (2[60]) with pentacene and with diphenylpentacene have been obtained, and their structures, cycloadduct mechanics and electrochemical properties have been discussed by Miller's and Komatsu's group, respectively [8–10]. The trans-arrangement of 2[60]-pentacene and cis-arrangement of 2[60]-diphenylpentacene adducts are compared in stabilization configuration [8, 10], respectively. However, their nonlinear optical properties have not reported up today. In this work, we will model the two-photon absorption (TPA) spectra and understand the origination of two-photon absorption for adducts of 2[60] with condensed aromatics.

## 2. MODLING PROCESS AND METHOD

The molecular two-photon absorption cross section  $\delta(\omega)$  can be characterized by the imaginary part of the molecular third-order nonlinear polarizability, defined at the absorption frequency of  $\omega$ ,  $\text{Im}\gamma(-\omega; \omega, \omega, -\omega)$ , through the relationship of  $\delta(\omega) = 32\pi^4\hbar/(n\lambda)^2 F^4 \text{Im}\gamma(-\omega; \omega, \omega, -\omega)$  and an average TPA cross section of  $\langle\delta(\omega)\rangle = 32\pi^4\hbar/(n\lambda)^2 F^4 \langle\text{Im}\gamma(-\omega; \omega, \omega, -\omega)\rangle$ , in which the third-order polizability  $\gamma$  at degenerate four-wave mixing process can be calculated by sum over states (SOS) method [11, 12]. Here  $\hbar$  is Planck's constant divided by  $2\pi$ ,  $n$  denotes the refractive index of the medium (vacuum assumed in this study),  $F$  corresponds to the local-field factor (equal to 1 for vacuum), and  $c$  is the speed of light and  $\lambda$  is an incident light wavelength. The transition energies, electronic dipole moments and transition moments that are taken as inputs in the SOS calculations are computed by the TDB3LYP method and running in Gaussian 03 code. The input geometries of cis- and trans-configurations of adducts of 2[60] with pentacene were optimized at the B3LYP/6-31G\* level using the DFT method before doing the calculations of TPA properties.

## 3. RESULTS AND DISCUSSIONS

Figure 1 shows the plots of average frequency-dependent TPA cross sections  $\langle\delta(\omega)\rangle$  of the cis and trans 2[60]-pentacene adducts. It is found that the maximum  $\langle\delta(\omega)\rangle$  are 0.28 and 0.53 GM within the studied wavelength ranges, and the location wavelengths of maximum  $\langle\delta(\omega)\rangle$  are 853 and 836 nm for cis and trans 2[60]-pentacene adducts, respectively. The TPA cross section is smaller and the TPA peak is red-shift for the cis 2[60]-pentacene adduct as compared with those for the trans 2[60]-pentacene adduct. The electronic origination of TPA is understood from

state-dependent second hyperpolarizability contributing to the TPA cross section  $\langle\delta(\omega)\rangle$  at a given wavelength. As mentioned above, the  $\delta(\omega)$  value only depends on the imaginary part of the second hyperpolarizability,  $\text{Im}\gamma(-\omega; \omega, \omega, -\omega)$ , while the input frequency is given at the vacuum medium. Accordingly, the two-photon states contributing to  $\text{Im}\gamma(-\omega; \omega, \omega, -\omega)$  also contribute to  $\delta(\omega)$  value. From the simulation of average  $\text{Im}\gamma(-\omega; \omega, \omega, -\omega)$  value *vs* two-photon state at the characteristic wavelength (resonant wavelength), we can find that only one (state  $S_{48}$ ) and two two-photon resonant states (state  $S_{49}$  and state  $S_{50}$ ) makes the greatest contribution to  $\text{Im}\gamma(-\omega; \omega, \omega, -\omega)$ , i.e., to the  $\langle\delta(\omega)\rangle$  values at a given wavelength for the cis and trans 2[60]-pentacene, respectively. An analysis in term of calculated results by the configuration interactions, we find some occupied and empty molecular orbitals involving charge transfer processes. Figures 2 and 3 show the orbitals mostly contributing to  $S_{48}$  of the cis 2[60]-pentacene and to  $S_{49}$  of the trans 2[60]-pentacene adducts, respectively. It is found that the charge transfers from the linker pentacene to the two cage  $C_{60}$  make great contribution to  $\langle\delta(\omega)\rangle$  at the resonant wavelength of 853 and 836 nm for the cis and trans 2[60]-pentacene adducts, respectively.

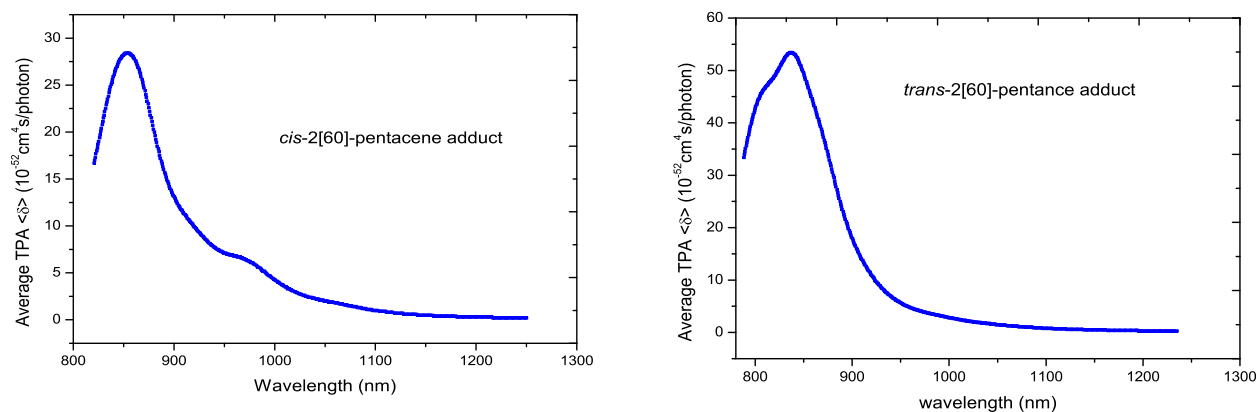


Figure 1: Frequency-dependent two-photon absorption cross section.

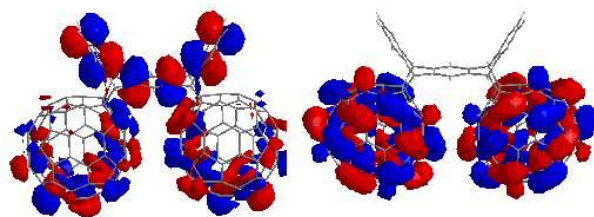


Figure 2: Cis 2[60]-pentacene adduct, molecular orbitals involving charge transfer processes.

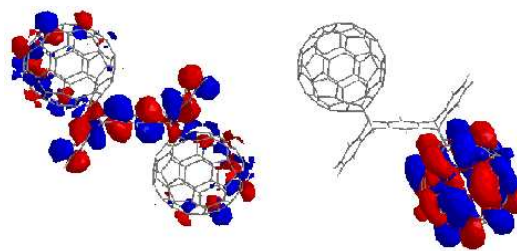


Figure 3: Trans 2[60]-pentacene adduct, molecular orbitals involving charge transfer processes.

#### 4. CONCLUSION

In summary, we have developed a combined method of time-dependent DFT theory with sum over states formula to model nonlinear absorption. The red shift of two-photon absorption peak and reduce of the nonlinear optical absorption for the cis 2[60]-pentacene adduct relative to those of the trans 2[60]-pentacene adduct. The electronic origination of two-photon absorption has been indentified from the excited-state charge transfers from the pentacene to  $C_{60}$  cages for 2[60]-pentacene adducts.

#### ACKNOWLEDGMENT

This investigation was based on work supported by the National Natural Science Foundation of China (No. 20773131), and the National Basic Research Program of China (No. 2007CB815307), and Fujian Key Laboratory of Nanomaterials (No. 2006L2005).

## REFERENCES

1. Wang, G.-W., K. Komatsu, Y. Murata, and M. Shiro, "Synthesis and X-ray structure of dumb-bell-shaped C<sub>120</sub>," *Nature*, Vol. 387, 583–586, 1997.
2. Stepanian, S. G., V. A. Karachevtsev, A. M. Plokhotnichenko, L. Adamowicz, and A. M. Rao, "IR spectra of photopolymerized C<sub>60</sub> films, experimental and density functional theory study," *J. Phys. Chem. B*, Vol. 110, 15769–15775, 2006.
3. Cabrera-Trujillo, J. M. and J. Robles, "Theoretical study of the structural and electronic properties of two-dimensionally polymerized fullerene clusters with 2, 3, 4, and 7 C<sub>60</sub> molecules," *Phys. Rev. B*, Vol. 64, 165408–165414, 2001.
4. Okada, S. and S. Saito, "Electronic structure and energetics of pressure-induced two-dimensional C<sub>60</sub> polymers," *Phys. Rev. B*, Vol. 59, 1930–1936, 1999.
5. Segura, J. L., N. Martín, and D. M. Guldi, "Materials for organic solar cells: The C-60/ $\pi$ -conjugated oligomer approach," *Chem. Soc. Rev.*, Vol. 34, 31–47, 2005.
6. Rispens, M. T. and J. C. Hummelen, *Fullerenes: From Synthesis to Optoelectronic Properties*, ed. D. M. Guldi, and N. Martín, Kluwer Academic Publishers, Dordrecht, 2002.
7. Ono, T. and K. Hirose, "First-principles study of electron-conduction properties of C<sub>60</sub> bridges," *Phys. Rev. Lett.*, Vol. 98, 026804–08, 2007.
8. Murata, Y., N. Kato, K. Fujiwara, and K. Komatsu, "Solid-state [4 + 2] cycloaddition of fullerene C<sub>60</sub> with condensed aromatics using a high-speed vibration milling technique," *J. Org. Chem.*, Vol. 64, 3483–3488, 1999.
9. Miller, G. P., J. Mack, and J. Briggs, " $\pi$ -stacking interactions in *cis*-bisfullerene[60] adducts of 6, 13-disubstituted pentacenes," *Org. Lett.*, Vol. 2, 3983–3986, 2000.
10. Miller, G. P., J. Briggs, J. Mack, P. A. Lord, M. M. Olmstead, and A. L. Balch, "Fullerene-acene chemistry: Single-crystal X-ray structures for a [60]fullerene-pentacene monoadduct and a *cis*-bis[60]fullerene adduct of 6, 13-diphenylpentacene," *Org. Lett.*, Vol. 5, 4199–4202, 2003.
11. Cheng, W.-D., D.-S. Wu, X.-D. Li, Y.-Z. Lan, H. Zhang, D.-G. Chen, Y.-J. Gong, Y.-C. Zhang, F.-F. Li, J. Shen, and Z.-G. Kan, "Design of single-walled carbon nanotubes with a large two-photon absorption cross section," *Phys. Rev. B*, Vol. 70, 155401–6, 2004.
12. Shen, J., W.-D. Cheng, D.-S. Wu, Y.-Z. Lan, F.-F. Li, S.-P. Huang, H. Zhang, and Y.-J. Gong, "Theoretical study of two-photon absorption in donor-acceptor chromophores tetraalkylammonium halide/carbon tetrabromide," *J. Phys. Chem. A*, Vol. 110, 10330–10335, 2006.

# A Novel Parametrically Amplifying Traveling Fast-wave Antenna (PATA) with a High Gain and Directivity as a Modern Version of the Historical Slow-wave Beverage Antenna Utilizing an Induced Fast Surface Wave by an External Sky Wave: Analogous to Traveling-wave Tube Amplification and Negative Resistivity of Esaki Diodes

Hiroshi Kikuchi<sup>1</sup>, S. Tsuruoka<sup>2</sup>, and T. Obata<sup>3</sup>

<sup>1</sup>Institute for Environmental Electromagnetics, 3-8-18, Komagome, Toshima-ku, Tokyo 170, Japan

<sup>2</sup>Takuwa Corporation, 1-4-15, Uchi-Kanda, Chiyoda-ku, Tokyo 101, Japan

<sup>3</sup>Gunma National College of Technology, 580, Toriba-machi, Maebashi 371-0845, Japan

**Abstract**— Parametrically amplifying fast-wave traveling antennas (PATA) utilizing an induced fast surface wave by an external sky wave have been established theoretically and experimentally as a novel travelling wave antenna with a high gain and directivity as a modern version of the historical slow-wave Beverage antenna. The principle of this antenna is to make strong resonance or coupling between the induced surface line-wave with the front velocity of the incident sky wave by coinciding the phase velocity of the induced surface wave with the front velocity of the incident sky wave. The function is something similar to traveling-wave amplification and negative resistivity of Esaki diodes. For the Beverage antenna, on the other hand, the coupling between the induced wire wave or wire-array current with ground return is so weak as a coupling distance becomes a half-wavelength or so, since the phase difference between the induced and the sky wave becomes appreciable. In this way, similarities and differences of both antennas are elucidated in detail.

## 1. INTRODUCTION

Parametrically amplifying travelling-wave antennas (PATA) [1, 2] invented by one of the present authors are somewhat analogous to travelling-wave tubes [3] and Esaki diodes [4] in function and characteristics, though there are essential differences. PATA correspond to amplification of travelling-wave tubes and the incident waves along the line play a role of electron beams. There are, however, essential differences between them. The role of electron beams in travelling-wave tubes is an amplification only when an external microwave is passing through a helical circuit. In contrast, there are twofold roles of an incident wave in PATA. One is to induce a current wave along the line. The other is to amplify its induced current wave at the same time. Further, there is a difference that the coupling of electron beams to a helical circuit is capacitive for travelling-wave tubes but the coupling of incident waves to the line is inductive for PATA. While PATA is expressed by an equivalent active distributed parameter line whose shunt conductance  $G$  is negative in the transition region, the resistance in an equivalent lumped circuit of Esaki diodes is also negative. In this respect, there is some correspondence or analogy between them, though those negative effects are different. The negative shunt conductance of PATA leads to new results that the attenuation constant of the induced wave decreases with increasing frequency and the wave-mode becomes a fast wave, while the negative resistance of Esaki diodes causes current decrease with voltage increase as a result of quantum-mechanical tunnel effects. Progress in gain performance of PATA is presented at a range of frequencies 2~5 GHz where its eigen surface wave becomes a fast wave, being amplified by the sky (space) wave due to a strong coupling, and its guide wavelength reaches as long as  $2\sim 4\lambda$  ( $\lambda$ : wavelength in free space), thus increasing the amplification ratio as high as 0.26~0.4 dB/cm.

## 2. CHARACTERISTICS OF THE WAVE OR BEVERAGE ANTENNA

Structure of the wave antenna used by Beverage for long wave communications below 100 KHz in frequency or beyond 3 km in wavelength is a wire or parallel wires above ground as schematically shown in Fig. 1, where 9 is a conducting wire of the order of one wavelength long and several to ten meters high, and is installed within the plane of wave incidence, 10 is the earth return, 3 is the input end on the transmitter side, 4 is the receiver end, and 5 is a receiving set. When the signal



Figure 1: Experimental setup of PATA.

wave reaches the antenna, an electromotive force is induced in the horizontal wire. A small current thus induced in each element of the wire starts to flow toward the receiver end, where the total current cumulated by successive additions is led to the receiver. Thus, the wave antenna utilizes the fact that the amplitude of the induced current becomes maximum at a point on the wire. The first wave reception by the wave antenna was performed by Beverage in 1923 at Long Island in the suburb of New York for a transmitting wave from England<sup>1</sup>. In contrast to most of antennas in use that are metallic, the Beverage antenna is using the earth as return that is a poor conductor and hence has been regarded as a heterogeneous antenna in mechanism of transmittance and reception. Although the Beverage antenna was used specifically as a transmitter for one-way communication to submarines as developed by the US Navy in context of the so-called Project SUNGUINE, this antenna has been used usually as a receiving antenna. Its receiving mechanism is such that the incident sky wave induces the eigen-mode of an earth-return circuit on its arrival. Then the line current induced along each wire element is being piled up and is increasing the amplitude of the total current, thus obtaining the gain at the receiving end. As seen in Beverage paper (Fig. 2 in p.259 in Ref. [1]), however, the interference effects due to the difference between the phase velocity of induced wave less than the velocity of light (slow wave) and the front velocity of the incident wave

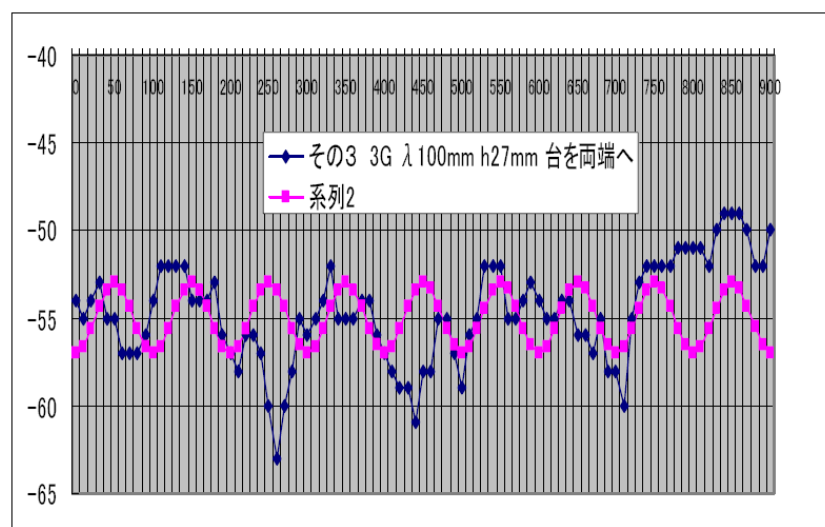


Figure 2: Sample data of the standing wave induced along the line (blue), showing a decrease of the guide wavelength ( $\lambda$ ) in comparison with the space wave in free space (purple). The centre of almi-pipe is 27 mm high above the base plate.  $F = 3$  GHz.

(fast wave  $\geq$  velocity of light) tend to develop at a certain distance of nearly half-one wavelength, though the induced current on the wire builds up at first (refer to Appendix 1).

Soon later, electromagnetic theory of wave propagation along a wire above ground was treated by Carson<sup>2</sup> and Pollaczek<sup>3</sup> independently in 1926 and can apply to the Beverage antenna at low frequencies.

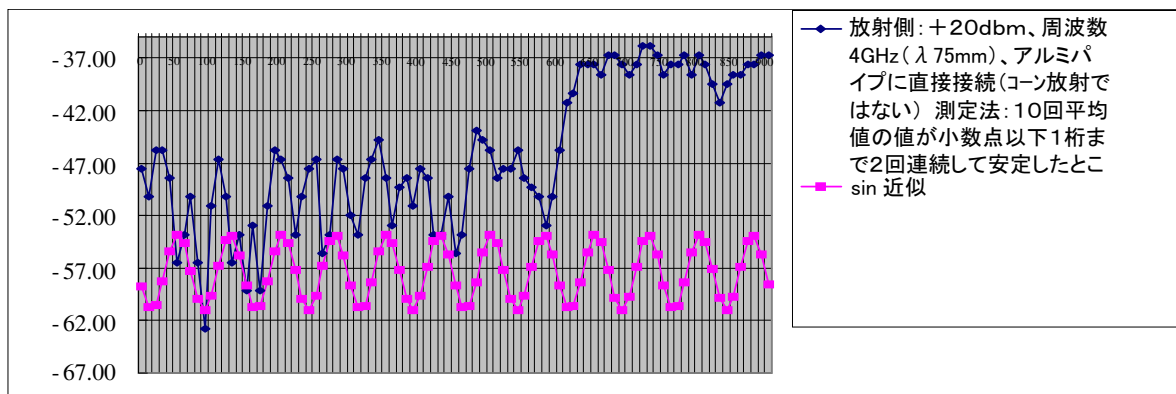


Figure 3: Another sample data of the standing wave induced along the line (blue), showing a decrease of the guide wavelength ( ) in comparison with the space wave in free space (purple). The centre of almi-pipe is 27 mm high above the base plate.  $F = 3$  GHz.

### 3. HISTORY OF STUDIES OF WAVE PROPAGATION ALONG WIRE ABOVE GROUND AT HIGH FREQUENCIES

The breakthrough of the problem of wave propagation along a wire above ground at high frequencies opened up in 1956 with an preliminary experiment over a frequency range of 1 to 20 MHz. Attenuation constant turned to decrease around 10 MHz from a monotonous increase with increasing frequency for a wire 7.5 m high with a radius of 2.5 mm. According to Carson-Pollaczek's theory, attenuation should increase endlessly with increasing frequency. It was indicated that this is because Carson-Pollaczek's theory does not take into account the displacement current within the earth and air and the effect of field concentration around the wire with increasing frequency. In fact, the displacement current in the earth becomes comparable to the conduction current in the earth around the 10 MHz. In addition, the effect of field concentration forces the electric lines of force to go back to the wire at high frequencies. An extended theory to take these effects into account has a new mathematical technique<sup>4~7</sup>. The solutions were also represented in terms of an equivalent been developed by solving Maxwell's equations as a combined eigen- and boundary-value problem with the aid of distributed parameter line. The numerical results of frequency character

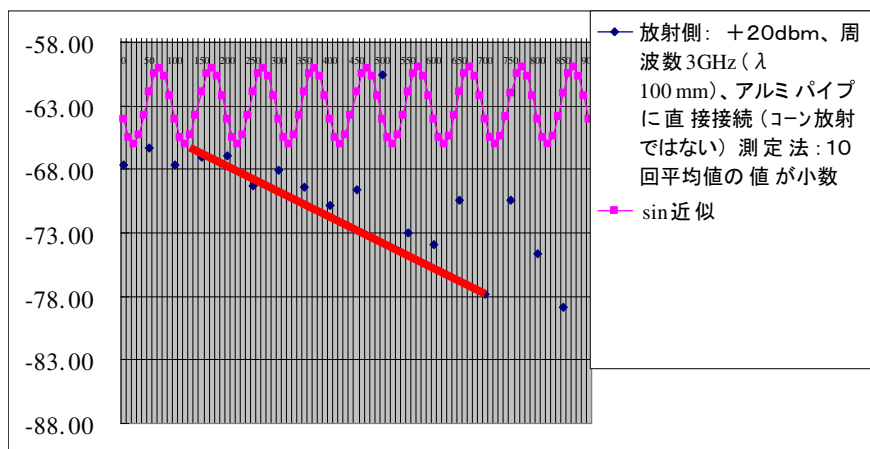


Figure 4:  $H = 27$  mm,  $f = 3$  GHz, amplification rises up to 0.4 db/cm as approaches the end. In general, wave fields are composed of space waves and surface waves induced. As is shown in Fig. 6, most of wave fields are the incident space waves near the input end. But become the induced surface waves as approaching the output end, being amplified by the space waves, increasing its amplification ratio as high as 0.4 dB/cm.

#### 4. EXPERIMENTAL SETUP

Whole setup of PATA is composed of a bare copper (or aluminum) wire (tube) or its array (1 m long with (outer) diameter 2.75 cm) connected with a guide-horn above a lossy dielectric (foam polyethylene) base-plate and wire or tube centre is 2.7~8 cm high) above the base-plate whose bottom side is grounded as seen in Fig. 1.

#### 5. EXPERIMENTAL RESULTS

**5.1. Phase Characteristics Showing a Fast Wave Induced ( $g = \text{guide wavelength} > 2\sim 4$ )**

**5.2. Amplification Characteristics (0.4~5 GHz)**

#### 6. CONCLUSION

Parametrically amplifying fast-wave traveling antennas (PATA) utilizing an induced fast surface wave by an external sky wave have been established theoretically and experimentally as a novel travelling wave antenna with a high gain and directivity as a modern version of the historical sloe-wave Beverage antenna.

#### REFERENCES

1. Kikuchi, H., Parametrically Amplifying Traveling-wave Antenna, UK Patent 2276985, 1996; US Patent 5,469,179, 1995; French Patent 9404020, 1997; Japanese Patent 2636164, 1997; German Patent 4411720, 2004.
2. Pierce, J. R., *Traveling-wave Tubes*, D. Van Nostrand, Princeton, 1950.
3. Esaki, L., *Phys. Rev.*, Vol. 109, 603, 1958.

# Analysis and Design of Minigenerator

P. Fiala and T. Jirku

Department of Theoretical and Experimental Electrical Engineering  
Faculty of Electrotechnical Engineering and Communication, Brno University of Technology  
Kolejni 2906/4, Brno 612 00, Czech Republic

**Abstract**— The paper presents results of the analysis of the vibrational generator. The paper deals with the design of a vibrational generator that is used as a power supply for independent electric circuits. The vibrational generator can be used in the various areas, e.g., traffic, electronics, special-purpose machines, and robotics. The proposed design employs magnetic damping of the core movement. It was numerically evaluated and it was shown that it was possible to obtain significantly larger output voltage and output power than in experimental settings used previously [1].

## 1. INTRODUCTION

The development of any new device always lays strong requirements on its reliability. The areas where reliability demands are of particular importance are transport, robotic and automotive applications.

One of the ways to increase the sensor reliability is their supplying from autonomous power sources. Sensors used in industry and automotive systems can be placed at critical points, without supply and data transmission systems. These sensors monitor important quantities during the system operation. In the course of the revision, the operator just scans the device under test, and by using wireless transmission the needed data are retrieved from all sensors. These data can be then compared with those from a previous system operation and all other data available.

This paper presents the results of a vibrational mini-generator (MG) analysis. The MG is intended to provide power for the above sensors. The principle of its operation is based on the utilization of changes of the external mechanical forces, which can be described by Faraday's law [1, 2]. The required output parameters are: output voltage between 3–5 V in the ideal case, output power 200–1000  $\mu\text{W}$ . The value of output power depends on the type of the sensor used.

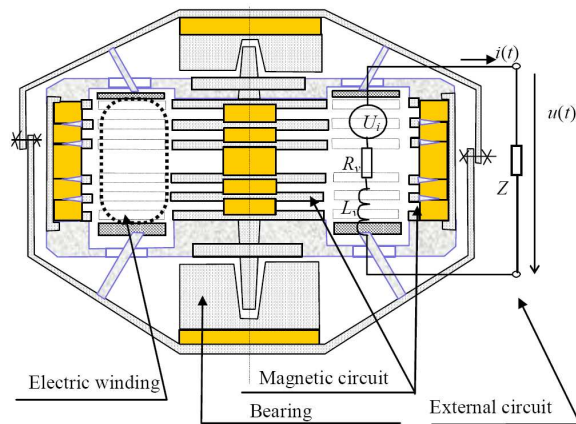


Figure 1: The basic arrangement of the investigated device.

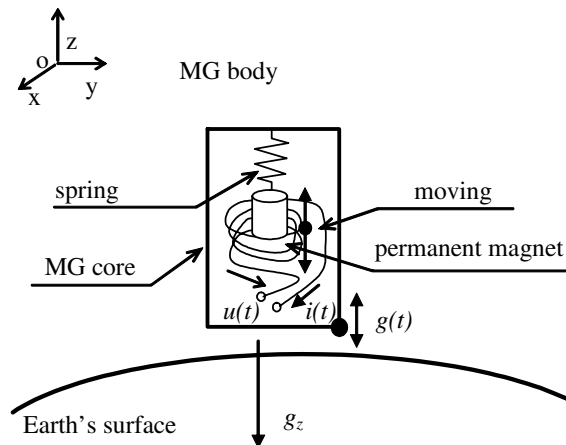


Figure 2: The principle of a vibrational minigenerator.

The basic arrangement of the vibrational generator is in Fig. 1. The MG body is tightly connected with the source of vibration — the fuselage, and thanks to the oscillation of the whole system the MG core starts moving with respect to the fuselage. The mechanical part of the MG is designed such that the MG core driven by external vibrations performs non-damped oscillations. The design of the MG allows oscillations of the MG core within quite a wide spectrum of external oscillation frequencies. The operation of the MG is based on Faraday's law as follows from Fig. 2. The core containing ferromagnetic parts and permanent magnets (with high density of the stored energy, e.g., FeNdB, SmCo) that moves with respect to the winding connected to the shell induces

in it a voltage and the external current connected to it starts carrying a current. Both the induced voltage and current in the external circuit are generally complex functions of time. Typical oscillation frequencies of the vibration source that were measured at two places of one investigated device (aircraft) are, for an illustration, shown in Fig. 3. The graphs express the square of amplitude of the movable parts on external oscillation frequencies (the amplitudes are, moreover, related to quantity  $g = 9.81 \text{ m/s}^2$ ).

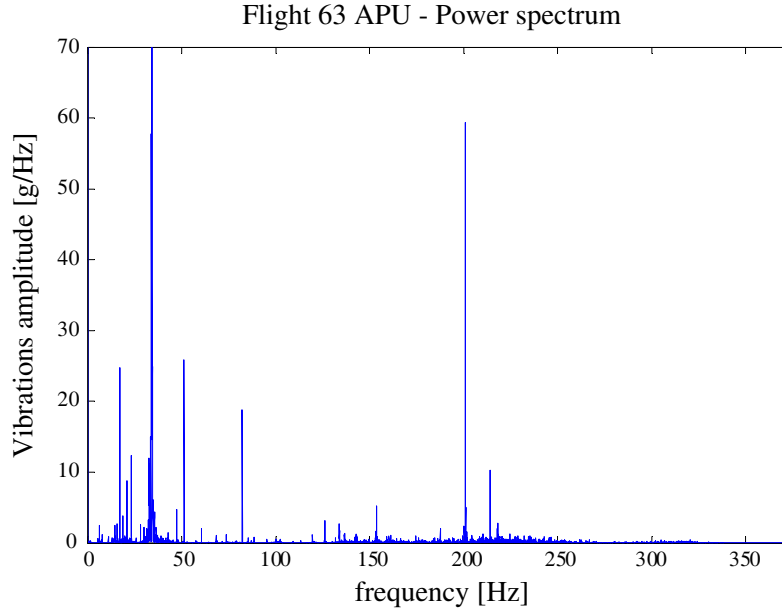


Figure 3: Squared relative amplitudes of vibrations versus external frequency of oscillations (measured at two different places of an aircraft).

## 2. MATHEMATICAL MODEL

The mathematical model of the problem consists of a partial differential equation describing the distribution of electromagnetic field in the device and two ordinary nonlinear differential equations describing the behavior of external electric circuit and mechanical movement the movable parts of the generator. The electromagnetic and mechanical phenomena strongly influence one another. The generator (Fig. 4(a)) whose volume is denoted by letter  $\Omega$  contains several important subdomains (Fig. 4(b)) of different physical parameters. These subdomains are denoted as  $\Omega_{Fe}$  — ferromagnetic parts of the magnetic circuit,  $\Omega_p$  — permanent magnets,  $\Omega_w$  — windings. Other subdomains are, for example, spring, shell and air. The electromagnetic part of this coupled model may be described by the reduced Maxwell equations:

$$\text{curl} \mathbf{H} = \mathbf{J} \text{ in } \Omega, \quad \text{div} \mathbf{B} = 0 \text{ in } \Omega, \quad \text{curl} \mathbf{E} = -\frac{d\mathbf{B}}{dt} \text{ in } \Omega_w \quad (1)$$

where  $\mathbf{H}$  is the magnetic field strength vector,  $\mathbf{B}$  the magnetic flux density vector and  $\mathbf{J}$  the current density vector, material relations are represented by relations

$$\text{div} \mathbf{J} = 0 \text{ in } \Omega_w, \quad \mathbf{B} = \mu_0 \mu_r \mathbf{H} \text{ in } \Omega_{Fe}, \quad \mathbf{B} = \mu_0 \mu_r \mathbf{H} + \mu_0 \mathbf{M} \text{ in } \Omega_p, \quad \mathbf{J} = \gamma \mathbf{E} \text{ in } \Omega_\gamma \quad (2)$$

where  $\mathbf{E}$  is the electric field strength vector, where  $\mu_0$  is the permeability of vacuum,  $\mu_r$  the relative permeability,  $\mathbf{M}$  the remnant intrinsic magnetisation vector of permanent magnet,  $\gamma$  the specific electric conductivity and  $\Omega_\gamma$  any from the above subregions with nonzero electrical conductivity. After introducing magnetic vector potential by equations

$$\text{curl} \mathbf{A} = \mathbf{B}, \quad \text{div} \mathbf{A} = 0, \quad \mathbf{E} = -\text{grad} \varphi - \frac{d\mathbf{A}}{dt}, \quad (3)$$

Eddy currents in the electrically conductive parts (that are not connected to external sources) of density  $\mathbf{J}_t$  generally consist of two components: current density due to temporal ( $\mathbf{J}_{eddy}$ ) and spatial

( $J_m$ ) changes of magnetic field. Similarly, the voltage induced at the terminals of the winding consists also of two components due to temporal and spatial variation of magnetic field. The total current passing through the external circuit is then given from solution of the corresponding circuit equation whose form depends on the character of the load (consisting mostly of a resistance and inductance). The electromagnetic model together with the circuit equation has to be supplemented with another nonlinear ordinary differential equation for the mechanical circuit. Considering that the movement is realized in the direction of axis  $z$ , this equation may be written in form

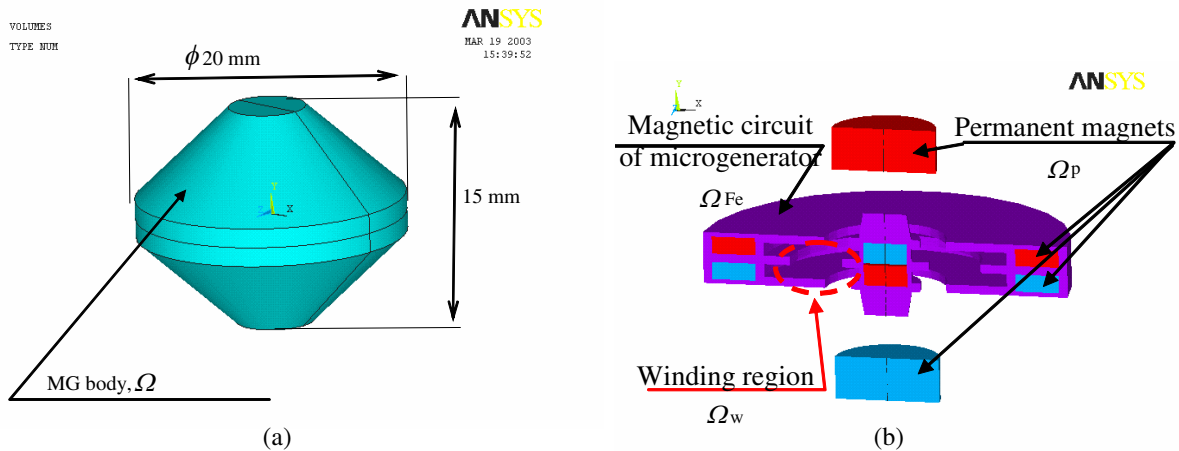


Figure 4: (a) Overall view of the device, (b) Particular subregions in the device.

$$m\ddot{z} + l_c\dot{z} + kz = \sum F \quad (4)$$

where  $m$  denotes the total mass of the moving elements,  $l_c$  the coefficient of damping,  $k$  the constant of the spring and  $\sum F$  the total external force acting on the movable parts that consists of their weight and forces of magnetic origin. After applying of the Galerkin method the continuous model is transformed to a finite-element model. The equation has been solved using ANSYS supplemented with a number of own scripts and macros.

### 3. MODEL OF MINI-GENERATOR IN ANSYS PROGRAM

The geometrical model was created with standard tools in the ANSYS program [5] and with the aid of automated mesh generator. The element applied is SOLID97. The ferromagnetic material is non-linear with the  $B$ - $H$  curve of steel given by the ČSN 15670 standard. The properties of the SmCo permanent magnet were taken over from the data sheet of the magnet manufacturer.

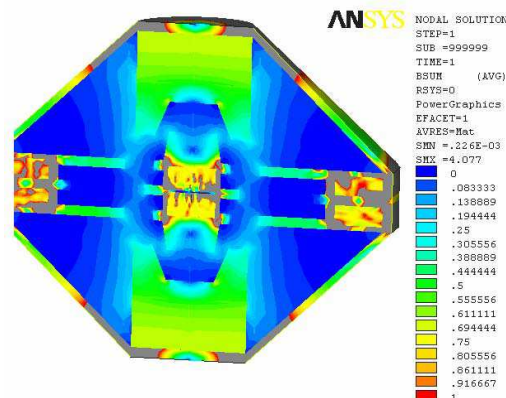


Figure 5: Evaluation of modules of magnetic field density  $B$ .

#### 4. RESULTS OF NUMERICAL ANALYSIS

The modules of vector functions of magnetic flux density  $B$  and field strength  $H$  are shown in Fig. 5.

The model is fully 3D. No symmetries were used in the model. This is due to the convergence evaluation and error estimation [6, 7].

#### 5. EXPERIMENTAL REALIZATION OF VIBRATIONAL GENERATOR

Several prototypes of mini-generators of different constructions were realized. Fig. 6 shows the prototype of a minigenerator of output  $P_{out} = 10 \div 100$  mW. The prototypes were tested on a vibrational bench during their development. The non-harmonic periodical voltage transients were obtained by measurement for vibration displacement within the range  $\Delta x \in < 0.1, 0.4 >$  mm. The vibration bench measurements were performed for various bench displacements (see Tab. 1). The theoretical values of generator output parameters are listed in Tab. 1. This is necessary to verify by experiment.

Table 1: Measured values of generator output voltage.

$\Delta x$ (mm)	$U_{pp}$ (V)	$f$ (Hz)	$U_{\max-p}$ (V)	$a$ ( $\text{ms}^{-2}$ )/ $g$	$f_{cent}$ (Hz)
0.4	26	27-38	46	0.586149	36-37
0.2	14	27-38	36	0.293074	38
0.1	8	27-38	18	0.146537	38
0.05	4	28-38	7	0.073269	31

$f_{cent}$  — peak of the resonant curve,  $g$  is Earth gravitational acceleration.

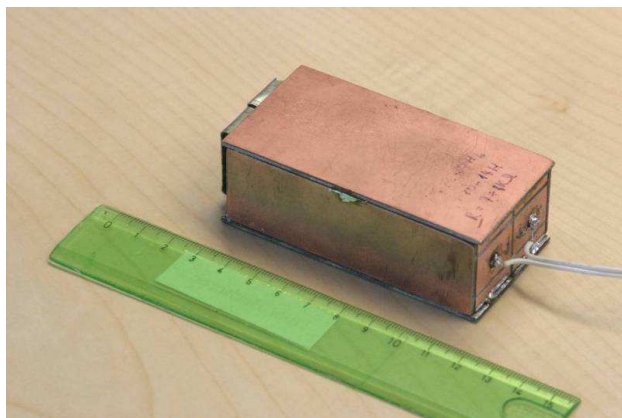


Figure 6: Functional sample of a generator version (10–100) mW.

#### 6. CONCLUSION

The paper represents a part of an introductory study of the vibrational MG design. It is intended as a preparation for a proposal of the 6th General European Project.

The paper presents results of the distribution of magnetic and electric field strengths and flux densities. In order to get voltage of required time dependence it is possible to suitably modify the shape of the winding (the details are discussed in [4]). The time domain simulations were performed using the lumped equivalent circuit in the MATLAB program. This approach is not very accurate in comparison with FEM capabilities. However, this approach is substantially faster. The results of the analysis serve as a foundation for the design of the minigenerator.

#### ACKNOWLEDGMENT

The paper was prepared within the framework of the research plan MSM 0021630516 of the Ministry of Education, Youth and Sports of the Czech Republic, WISE — Wireless Sensing STREP 6FP Project No. FP6-2003-AERO-1.

**REFERENCES**

1. Li, W. J., Z. Wen, and P. K. Wong, “A micromachined vibration induced power generator for low power sensors of robotic systems,” *World Automation Congress*, Maui, Hawaii, July 11–16, 2000.
2. Stratton, J. A., *Theory of Electromagnetic Field*, SNTL, Prague, Czech Republic, 1961.
3. Fiala, P., T. Vojtek, and I. Běhunek, “Analysis and test of vibrational minigenerators,” *Proc. IC SPETO 2006*, Vol. 1, 155–158, Gliwice-Ustron, Poland.
4. Fiala, P., “Conception of vibrational microgenerator,” 102, Research report UTEE FEKT VUT in Brno, UTEE FEKT in Brno, Czech Republic, Jan. 30, 2003.
5. ANSYS, *User’s Manual for Revision 5.1–8.0*, Vol. 1–4, Swanson Analysis System, Inc., Houston, USA, 1994–2003.
6. Fiala, P., “Modeling of transformers during short-circuit,” 111, Doctoral Thesis, UTEE FEI VUT in Brno, UTEE FEKT in Brno, Czech Republic, Dec. 30, 1998.
7. Fiala, P., “Solution of electric field at a bushing support from distribution frame,” Research Report No. 1/96, Laboratory of Modeling and Optimization of Fields in Electromechanical Systems, FEI VUT Brno and ABB EJV, a.s. Brno, 24.7.1996.
8. Patent No. PV-2006-571, Czech Republic.
9. Patent No. PUV-2006-18391, Czech Republic.

# An Electric Field Test Using the MRI

P. Fiala<sup>1</sup> and K. Bartusek<sup>2</sup>

<sup>1</sup>Department of Theoretical and Experimental Electrical Engineering  
University of Technology Brno, Kolejní 4, Brno 612 00, Czech Republic

<sup>2</sup>Institute of Scientific Instruments, Academy of Sciences of the Czech Republic  
Královopolská 147, Brno 612 64, Czech Republic

**Abstract**— The paper describes a test of an electric field on water molecules based on the present knowledge of the problem as discussed by references [6–11]. The basic configuration of the test was experimentally verified at the Institute of Scientific Instruments, Academy of Sciences of the Czech Republic. We also prepared other tests using a different type of substance to find the relation between the MRI and the macroscopic electric field intensity. As a matter of fact, it respects the classical Electrodynamics and Material Wave Theory (MWT). The experiments are intended for future applications in the field of health service.

## 1. INTRODUCTION

In recent years the research in this field has been focused on the search of different ways of treating various types of diseases like tumors, viruses, and other micro- and nanoscopic problems [1, 2]. The papers referred to in this study analyze the impact of an external electric field application on the development and persistence of tumor diseases. For example, paper [3] analyzes — depending on the effect of external influences, namely electromagnetic fields — the mechanisms of emergence of a cell and its uncontrolled development phase. The research carried out by the laboratory specialists of Norfolk University, USA [4, 5] features the analysis of the impact of impulse electromagnetic fields on tissue structure changes, genetic code changes, and the types of controlled variation in selected parts of an organism.

The basic experiments and studies of the impact of electric and electromagnetic fields on the development of tumor diseases have been presented by prof. Kikuchi [6]. The previous published studies [2], however, had not entirely respected the complex electro- magneto- hydro- dynamic (EMHD) principles of approach. According to the data available, the phases of a tumor disease development are classified into four stages as related to the status of a cell. The first two of these stages are reversible; within the remaining ones, however, distinctive changes in the cell metabolism are recorded and, given the standardly weak EMHD effects in the latter two stages, the principles of cell change become irreversible. The research conducted by Norfolk University is markedly oriented toward analyzing the latter two stages in the development of a cell within a tumor formation. In comparison with this research orientation, we have focused our research distinctly on the former two development stages.

The elementary approach to the problem consists in finding a suitable numerical model to analyze the impact of an electromagnetic field on the basic chemical structure elements. Within the process of numerical analysis, we perform the testing of the impact of an electric field on a small volume of purified homogeneous H<sub>2</sub>O water. In this respect, the interdependence is sought between the impacts of size, direction, and instantaneous course of the electric field intensity on the molecular properties of the material (water). Further, experiments are performed using the Nuclear Magnetic Resonance (NMR) and the Magnetic Resonance Imaging (MRI), and the shift and variation of the spectral line of the examined sample are monitored. In the process of the verification of laws resulting from the MWT and the available plus verifiable theories [7–13], the procedure of an electric field impact analysis will be directed toward more complex organic structures. The elementary findings of the sample status in the NMR testing are further completed with numerical analysis [13].

## 2. MRI EXPERIMENTS

In order to set the NMR method, both the impacts thereof on the resulting image and the material inhomogeneity impact on the processing of the NMR image were examined and numerically modelled [15]. Further, to support the analysis of the impact of an electric field depending on the instantaneous value and size of electric field  $\mathbf{E}$  intensity on the samples that can be located close to the operator, we developed special controlled voltage sources with output voltage regulation of

$U_{out} = 1\text{--}100\text{ kV}$  and current limitation (to the value of current manageable by a human organism) within the range of  $I_{out}$  0–1 mA. Figs. 1 and 2 show the conception of the controlled, high-voltage source. This problem is analyzed in greater detail by the [14] reference study.

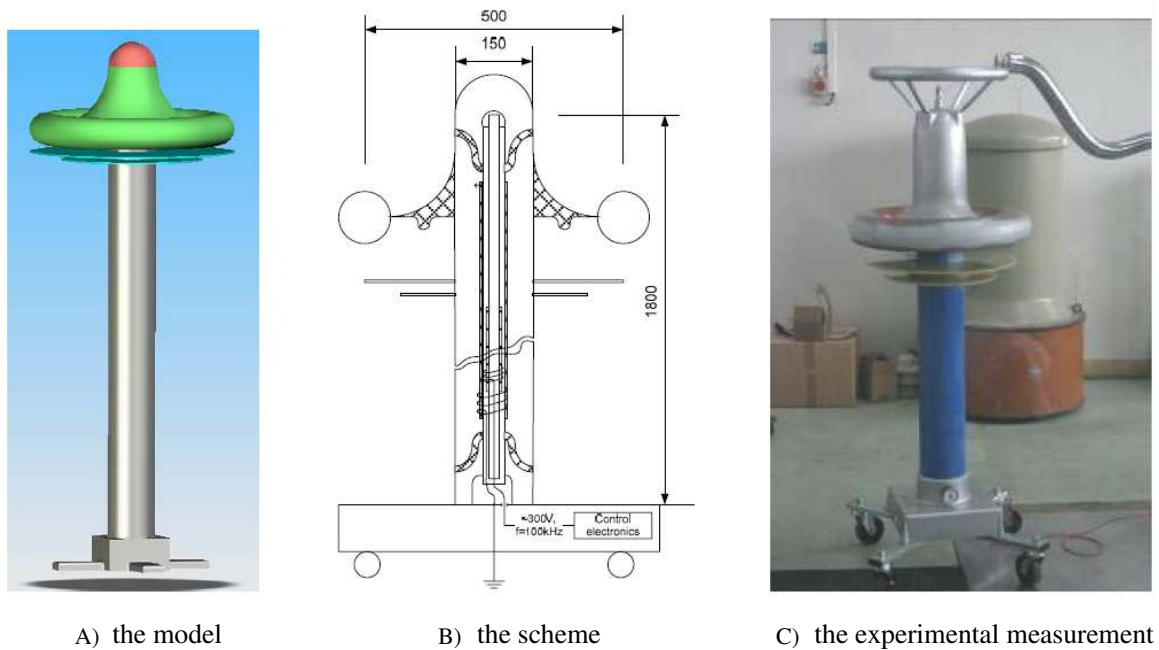


Figure 1: A high voltage source compact conception.

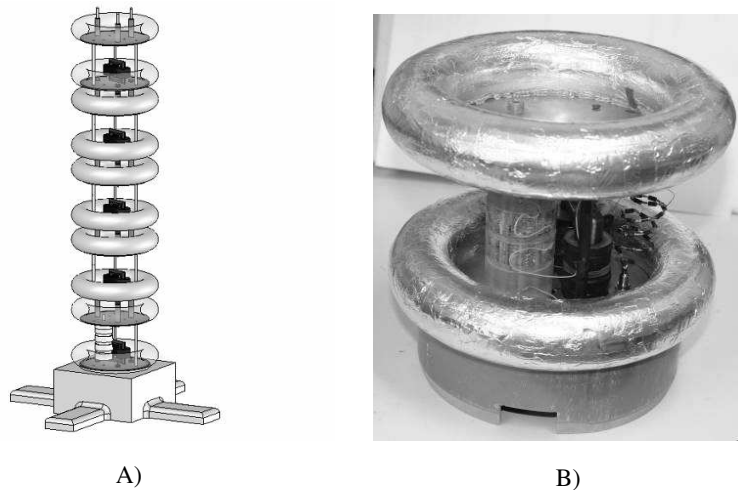


Figure 2: High voltage source component conception A), one module of the source.

This work deals with the design of an electronically controlled high-voltage power source used for special purposes. The source will be used to set up the intensity of an electric field on predefined shapes of material samples, from simple inorganic to complex organic materials. The design must fulfill the condition of a constant setting of the source's output current. The regulation ranges should be: output voltage  $U_o = 1\text{--}100\text{ kV}$ , electric current  $I_{max} = 10\ \mu\text{A}\text{--}10\text{ mA}$ , frequency  $f = 0\text{--}1\text{ KHz}$ . The device must satisfy safety requirements specified by Czech standards (ČN). Several designs have been prepared on the basis of available materials, and one was selected and realized: a circuit with an offline flyback regulator, regulated with pulse-width modulation frequency  $f_m = 30\text{ KHz}$ . The power source was realized and its specifications were experimentally verified. The electronic control wiring diagram of the high-voltage source with current limitation is shown in Fig. 3. The numerical analysis results were experimentally verified using the 200 MHz/75 mm MR tomograph at

the ISI, AS CR (Fig. 5). The tomograph elementary magnetic field  $B_0 = 4,7000 \text{ T}$  is generated by a superconducting horizontal magnet produced by the Magnex Scientific company. The resonance frequency for the cores  $^1\text{H}$  is 200 MHz. From the measurements performed using the MRI we obtained the results of the electric field intensity  $E$  impact on the cores of the  $\text{H}_2\text{O}$  sample; an overview of these results is provided in Tab. 1. Further, experiments were carried out on the  $\text{H}_2\text{O}$  sample using a device with a system of electrodes. There was a distance of 20 mm between the electrodes, which were fixed to a laboratory beaker containing the water sample. The fixation was realized in such a manner as to eliminate the displacement current effects on all the surfaces and dielectric volumes. Leakage current was secured, with the resulting assurance of operator safety. Then, the first measurement without the electric field intensity  $E$  impact on the examined sample showed the centre on the frequency of  $f_0 = 184 \text{ Hz}$ . After connecting voltage to the electrodes and producing the electric field intensity of 50 kV/m–4050 kV/m, we managed repeatedly to measure the resonance line shift of  $\Delta f = 4 \text{ Hz}$ . Thus, the influence was experimentally proved of the electric field static intensity on the motion and behaviour of water molecule cores. According to the well-known relation between the change of frequency and the change of magnetic induction [15], the change of magnetic induction is

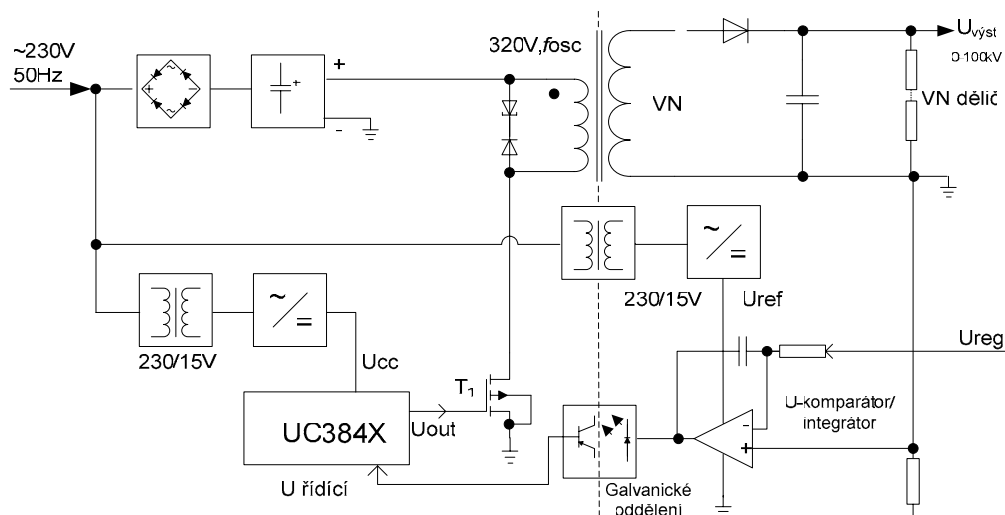


Figure 3: High voltage source diagram of electronic control.

$$\Delta B = \frac{2\pi\Delta f}{\gamma} = \frac{2\pi\Delta f}{2,67 \cdot 10^8} \quad (1)$$

where  $f[\text{Hz}]$  is the frequency,  $\gamma[\text{T}^{-1} \cdot \text{s}^{-1}]$  is the gyromagnetic ratio of water, and  $\Delta B[\text{T}]$  is the change of magnetic flux density module distribution in the sample. Then, the change of magnetic induction corresponds with  $\Delta B = 94.1 \text{ nT}$ .

Figures 4 and 5 show the experimental MRI laboratory.

Table 1: The measured resonance frequency shifts.

Electric Field Intensity $E_z$ [kV/m]	Resonance frequency offset [Hz]
+4050	+4
+2025	+4
0	0
-2025	+3
-4050	+3

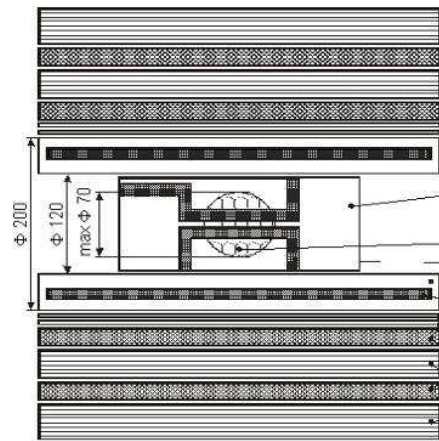


Figure 4: Elementary configuration of the MR magnet for the 200 MHz tomograph, ISI ASCR.

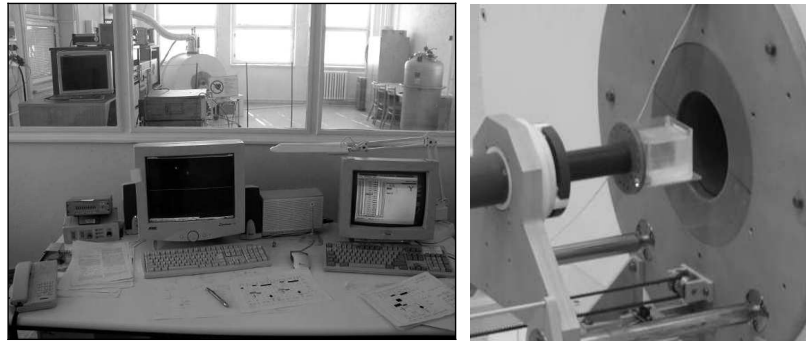


Figure 5: MR experimental workplace and equipment.

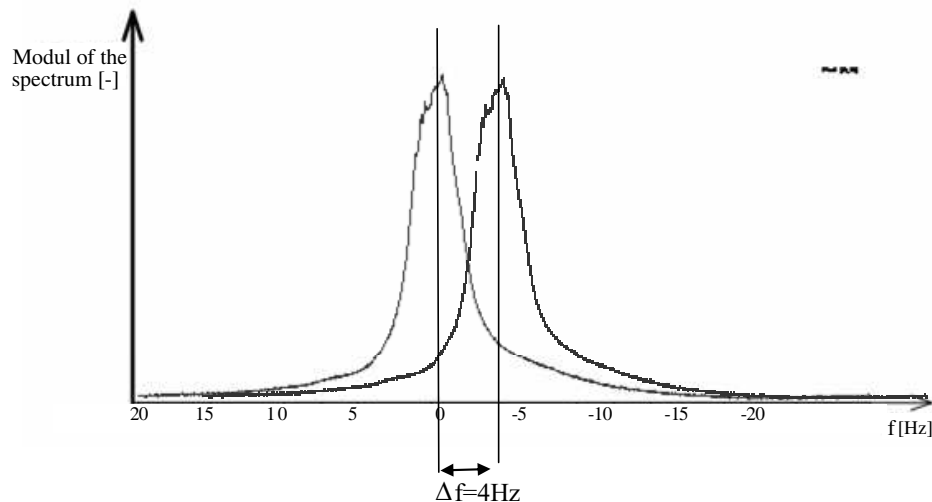


Figure 6: The measured spectral characteristics of the water sample,  $\Delta f = 4 \text{ Hz}$  (resonance frequency without the electric field is  $f_0 = 184 \text{ Hz}$ ).

### 3. CONCLUSION

The presented paper contains the results of experiments analyzing the impact of an electric (static) field on the behaviour of elementary compounds cores. The study represents a step forward in the analysis of the more complex chemical substances behaviour as related to the impact of an electric field. The results of EMHD theories were taken into account in studying the task, and an MWT-based model was used for the numerical support thereof.

**ACKNOWLEDGMENT**

The research described in the paper were financially supported by FRVŠ by research plan No. MSM 0021630516, ELCOM-No. MSM 0021630513, grant GAAV No. B208130603 and Prof. H. Kikuchi for the consultations and advises.

**REFERENCES**

1. Schoelkopf, R. J. and S. M. Girvin, “Wiring up quantum systems,” *Nature, the International Weekly Journal of Science*, 7th of February, 2008.
2. *The European Journal of Surgery*, Supplement 574, Proceedings of the IABC International Association for Biologically Closed Electric Circuits (BCEC) in Medicine and Biology, Scandinavian University press, Oslo-Copenhagen-Stockholm, 1994.
3. Daivid, E., “Effectiveness and risk during application of NLW from the medical point of view,” *Non-lethal Options Enhancing Security and Stability, 3rd European Symposium on Non-lethal Weapons*, Ettlingen, SRN, May 10–12, 2005.
4. Heeren, T., J. T. Camp, J. F. Kolb, K. H. Schoenbach, S. Katsuki, and H. Akiyama, “250 kV sub-nanosecond pulse generator with adjustable pulse-width,” *IEEE Trans. Diel. Electr. Insul.*, Vol. 14, 884–888, 2007.
5. Sun, Y., S. Xiao, J. A. White, J. F. Kolb, M. Stacey, and K. H. Schoenbach, “Compact, nanosecond, high repetition-rate, pulse generator for bioelectric studies,” *IEEE Trans. Diel. Electr. Insul.*, Vol. 14, 863–870, 2007.
6. Kikuchi, H., “Electro-plasma macrostructure and functioning of a mono-cancer-tumor or scatered fine-grained tumors analogous to a dust grain or grains in dusty plasmas,” *Progress In Electromagnetics Research Symposium, USA*, March 1999.
7. Van Vlaenderen, K. J. and A. Waser, “Electrodynamics with the scalar field,” *Physics*, Vol. 2, 1–13, 2001.
8. Kikuchir, H., *Electrohydrodynamics in Dusty and Dirty Plasmas: Gravito-electrodynamics and EHD*, Kluwer academic publishers, Dordrecht, Boston, London, 2001.
9. Van Vlaenderen, K. J., “A charge space as the orogin of sources, fields and potentials,” *Physics*, Vol. 1, No. 16, 1–13, arXiv:physics/9910022, October 1999.
10. Hofer, W. A., “A charge space as the origin of sources, fields and potentials,” *Physics*, Vol. 3, No. 17, arXiv: quant-ph/9611009, April 1997.
11. Prosser V a kolektiv, “Experimentální metody biofyziky,” *Academia*, Praha, 1989.
12. Delong, A., “Verbal information,” *Czech Academy of Science, ISI Brno*, 7.2.2006 Brno, 2006.
13. Bartusek, K. and P. Fiala, “A simple numerical simulation of internal structure of particles test,” *PIERS Online*, Vol. 2, No. 6, 653–656, 2006.
14. Fiala, J., “Special electronics controlled HV sources,” Diploma Thesis, 73, Brno: FEEC BUT v Brno, Czech Republic, 2007.
15. Bartusek, K. and P. Fiala, “Experiments with the effect of non-homogenous parts into materials,” *PIERS Proceedings*, 1081–1084, Hangzhou, China, March 24–28, 2008.

# Numerical Modelling of the Special Light Source with Novel R-FEM Method

P. Fiala, E. Kroutilova, and T. Kriz

Department of Theoretical and Experimental Electrical Engineering  
Brno University of Technology, Kolejní 4, Brno 612 00, Czech Republic

**Abstract**— This paper presents information about new directions in the modelling of lighting systems, and an overview of methods for the modelling of lighting systems. The novel R-FEM method is described, which is a combination of the Radiosity method and the Finite Elements Method (FEM). The paper contains modelling results and their verification by experimental measurements and by the Matlab simulation for this R-FEM method.

## 1. INTRODUCTION

The paper contains information about verification of the design of the special light sources by the numerical simulation of the R-FEM method and verification by experimental measurements.

## 2. THE R-FEM METHOD

The R-FEM method is a new direction in the modelling of lighting systems. It utilizes the similarity between physical models. This paragraph demonstrates the usage of analogy between different physical models for the modelling of light problems. The R-FEM method is able to solve tasks that fulfill the condition  $\lambda_S \ll \max(D) \wedge \lambda_S < 10 \cdot \max(D)$ , where  $\lambda_S$  is the source of light wavelength and  $D$  is one of the geometrical dimensions of the modelling task. It can be used for to model more complicated physical problems than the methods mentioned up to now. An example of a more complicated physical problem, which we can solve by the R-FEM method, is the modelling of light intensity distribution in interior or exterior spaces with non-homogeneous environment, where the light has passed through some impure air (e.g., filled with smoke, fog, mist, vapour, dust, etc.).

## 3. THE DESIGN BY R-FEM METHOD

In technical praxis we often encounter conjugate problems. A necessary part of the design process during the development and measurement of light sources is the modelling and experimental verification of results. The most accurate mathematical models of the sources of light include models based on the radiation principle. One possibility is to use standard oneCpurpose programs while another possibility offers the usage of sophisticated numerical methods, among them the finite element method, for example the ANSYS program.

The ANSYS program uses standard program tools such as modelling, discretization into a net of elements, solvers, evaluation, and interpretation of the results. The crux of the whole problem lies in the transformation of thermal field quantities into optical quantities. This can be done using the general rules described in [19]. In the following text the basics of modelling the primitive light problem are described. The verification of the model of light source is done via experiment and then it continues to the hollow light guide problems and it was also verified by experiment (for more information, see references [17–19]). The geometrical situations that were modeled and verified is shown in the Fig. 1.

## 4. BUILDING THE NUMERICAL MODEL

The formulation of the basic thermal model is based on the first law of thermodynamics

$$q + \rho c v \cdot \text{div}T - \text{div}(k \text{grad}T) = \rho c \left( \frac{\partial T}{\partial t} \right) \quad (1)$$

where  $q$  is the specific heat,  $\rho$  is the specific weight,  $c$  is the specific solidification heat,  $T$  is the temperature,  $t$  is the time,  $k$  is the coefficient of calorific conduction,  $\nu$  is the the velocity of flow. This model can, with respect to the application of Snell's principles and according to the Stefan-Boltzmann principles, heat transfer by way of radiation between surfaces with relative indexes  $i, j$  is formulated as be simplified into the form

$$q_{ri} = \sigma \varepsilon_i A_{i,j} S_i (T_i^4 - T_j^4) \quad (2)$$

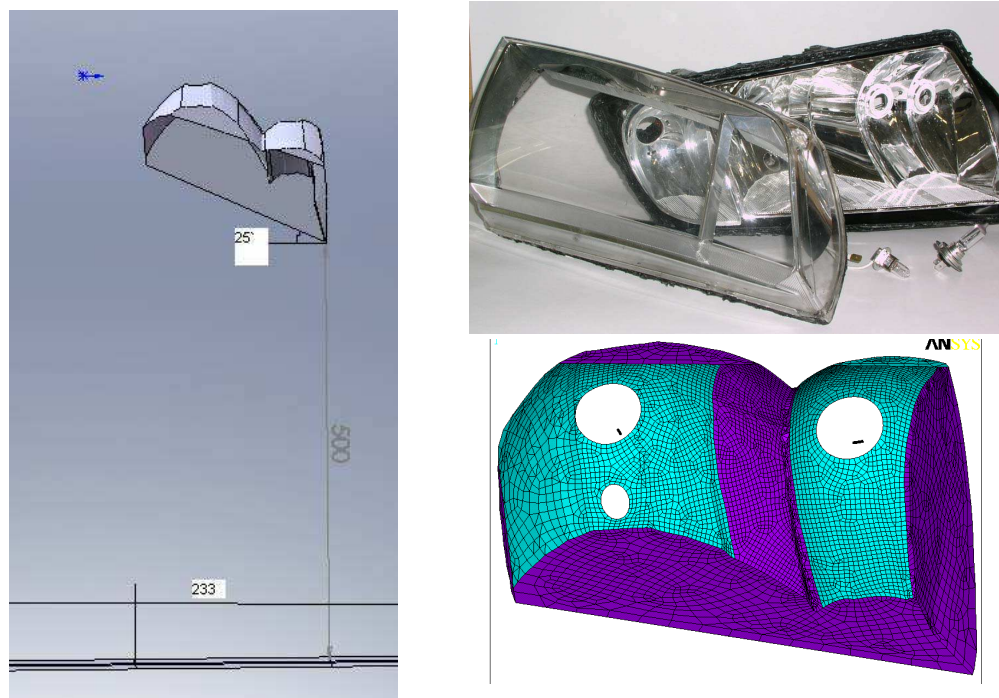


Figure 1: Geometrical configuration of the special light source.

where  $q_{ri}$  is the specific heat transferring from surface with index  $i$ ,  $\sigma$  is the Stefan-Boltzmann constant,  $\varepsilon_i$  is the emissivity of surface,  $A_{i,j}$  is the projection factor of surface with index  $i$  to surface with index  $j$ ,  $S_i$  is the area of surface with index  $i$ ,  $T_i$ ,  $T_j$  are the temperature of surfaces  $i$ ,  $j$ . When the projection factor is determined, it is possible to use the Galerkin principles for converting this problem into model (1). Marginal and initial conditions must be respected.

$$[K]\{T\} = \{Q\} \quad (3)$$

where  $K$  is the coefficients matrix,  $T$  is the columnar matrix of sought temperatures,  $Q$  is the columnar matrix of heat sources. Thermal flow  $T_f$  is determined from temperature  $T$  as

$$T_f = -(k \text{ grad} T) \quad (4)$$

By the radiation principle, the elements of column matrix of heat sources  $Q$  and adjusting for mathematical model yields

$$Q_{i,j} = \overbrace{S_i A_{i,j} \varepsilon_i \sigma}^K (T_i^2 - T_j^2) (T_i + T_j) (T_i - T_j) \quad (5)$$

The heating model will be used for the modelling of light problem using the Snell principles in optics. Light source with lighting intensity  $E(lx)$  corresponds to equivalent heat quantity density of heat flow  $q''$ , light flow  $\Phi(lm)$  corresponds to equivalent quantity of heat flow  $q'$ . The resulting light flow is defined by equation (6).

$$\Phi_e = \frac{T_{f,e}}{S_{n,e}} \quad (6)$$

where  $\Phi_e$  is the flow of light on the element,  $T_{f,e}$  is the equivalent of the thermal flow through the element,  $S_{n,e}$  is the normal surface to the element (more can be found in [19]). The result of modeling by the R-FEM method is shown in the Fig. 2.

## 5. VERIFICATION OF THE R-FEM

The results of the verification of the R-FEM via experiments is given in Fig. 3. There are differences between the values obtained by modelling and experimental measurement, ranging from 5–15%, depending on the distribution of the net of elements. When the elements of the net are of a lower density, the differences are also lower. This problem requires the net of elements to be optimized.

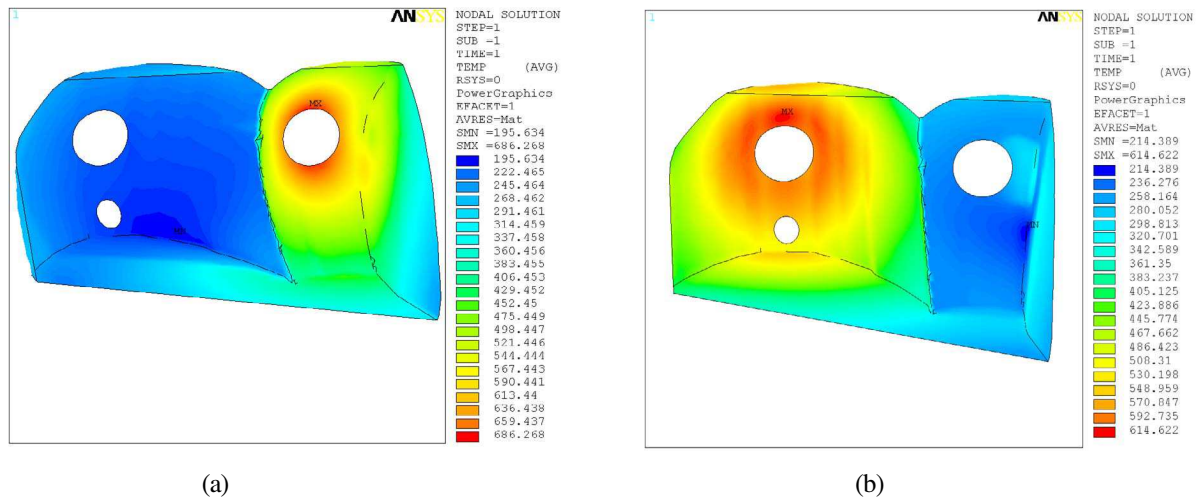


Figure 2: (a) The result of the R-FEM method — thermal flux, module of vector, distribution on central line, (b) The result of the R-FEM method — lighting intensity  $E(lx)$ .

## 6. ADVANTAGES OF THE R-FEM

One of the biggest advantages of this method is the wide spectrum of its usage. We can design the interior and also exterior scenes with its specifications in the materials quality, climatic dissimilarities and geometrical dimension varieties. We can use all types of sources of light with their diversity of the colour distribution in the light spectrum. The designers are not limited by the geometrical dimension varieties, colour distribution in the light spectrum, material qualities or climatic dissimilarities. The other advantage is that the method is very accurate. The degree of accuracy can be chosen by choosing the method of generating nets of elements and the solution algorithm because all this is provided by the ANSYS standard program tools.

## 7. THE FULL FEM WAVE SOLUTION

FEM is the short form for the Finite Elements Method modelling. The light problems that fulfill the condition  $\lambda_S \ll \max(D) \wedge \lambda_S < 10 \cdot \max(D)$ , where  $\lambda_S$  is the source of light wavelength and  $D$  is one of the geometrical dimensions of the modelling assignment, will be solved by the FEM using

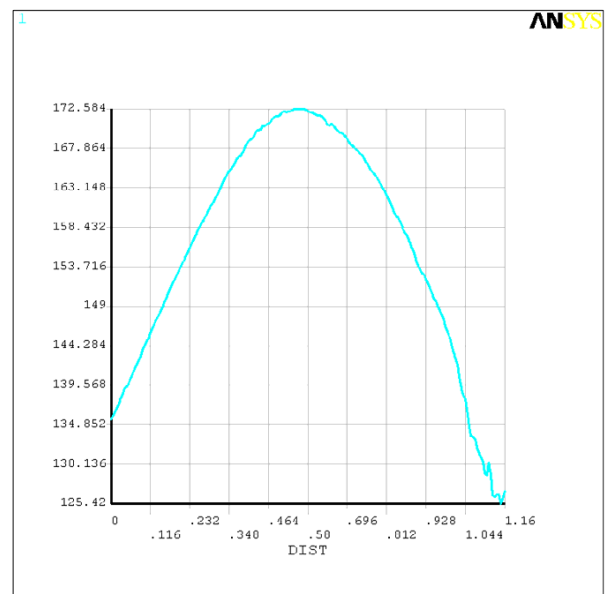


Figure 3: The results of the modeling by the Matlab — Lighting intensity  $E[lx]$ .

the full wave equation, which was used to define light emissions. This method of the solution yields highly accurate results, but is demanding as regards geometrical declaration, and time-consuming (for example, for incoherent sources of light the calculation is too long). The Full FEM wave solution is suitable for a specific purpose.

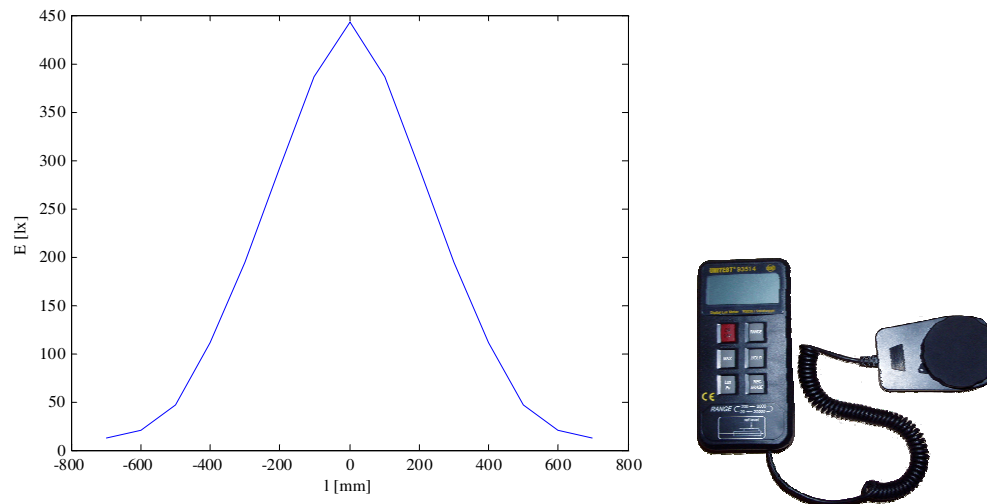


Figure 4: Results of the light intensity by the experiment with the luxmeter.

## 8. VERIFICATION THE R-FEM SIMULATION

The results of the verification of the R-FEM via two experiments are given in Figs. 3, 4 and 5. Experimental measurements were used as first verification. The comparison modeling and experimental values is given in Fig. 6.

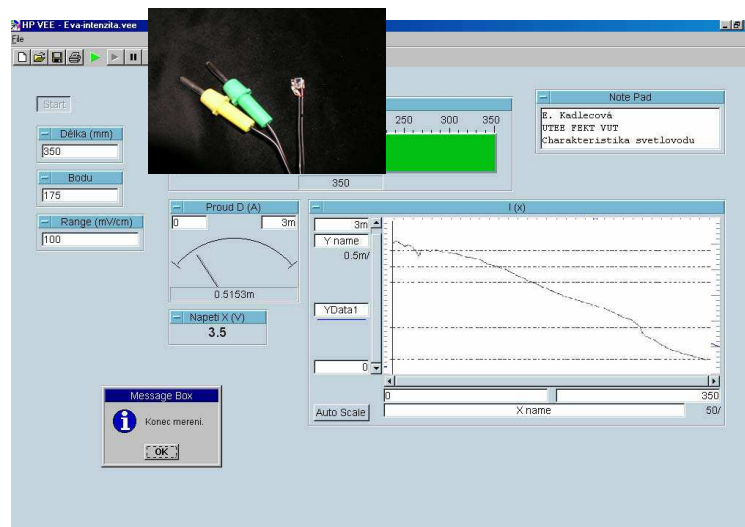


Figure 5: The shape of distribution of the light intensity by experiment with the LED.

## 9. CONCLUSION

This article describes novel numerical methods (R-FEM) of modelling lighting problems, which are used in Computer Graphics and in Lighting Engineering. Main novel described method exploits FEM ANSYS system for partial solution. Article also describes the R-FEM method, which has been verified and found to be a great asset for the modern trends in modelling lighting problems. It can solve specific light problems have been solved by using with the full geometry.

**ACKNOWLEDGMENT**

The research described in the paper were financially supported by FRVŠ by research plan No MSM 0021630516 and grant GAAV No. B208130603.

**REFERENCES**

1. [http://www.lighting-technologies.com/Products/Photopia/Photopia2\\_pod.htm](http://www.lighting-technologies.com/Products/Photopia/Photopia2_pod.htm)
2. Kadlecová, E., M. Bernard, and P. Fiala, "Illumination of interiors by the hollow light guides," *14th International Conference Light 2003*, ISBN 80-233-0488-7, Bratislava, 2003.
3. Kadlecová, E. and P. Fiala, "Light guide modeling," *Energy Forum 2004*, 338–341, ISBN 80-986-1619-1, Technical University, Sofia, Bulgaria, 2004.
4. Kadlecová, E., Automated System of Calculation of Reflecting Surface of Light Sources, Ph.D. Thesis, VUT v Brně, FEKT, Brno, srpen 2004.
5. Kroutilova, E., Patent No. PV 2008-65, Zpusob návrhu odrazných ploch reflexních zařízení pomocí analogie teplotního pole- radiace a vlnové rovnice a zařízení v podobě světelné soustavy určené pro numerickou optimalizaci požadovaných světelných parametru odrazných ploch, Czech Republic, leden 2008.

# The Measurement of Temperature Characteristics of Cu Bulk Resistivity

Karel Bartušek<sup>1</sup>, Pavel Fiala<sup>2</sup>, and Premysl Dohnal<sup>3</sup>

<sup>1</sup>Institute of Scientific Instruments, Academy of Sciences of the Czech Republic  
Královopolská 147, Brno 612 00, Czech Republic

<sup>2</sup>Department of Theoretical and Experimental Electrical Engineering  
Faculty of Electrical Engineering and Communication, Brno University of Technology  
Kolejní 4, Brno 612 00, Czech Republic

<sup>3</sup>Department of Languages, Brno University of Technology  
Údolní 53, 602 00 Brno, Czech Republic

**Abstract**— This contribution contain a presentation of a results of the numerical modeling during design of measurement method for determine of thermal characteristic of specific resistance of Cu bulk. Combine of numerical modeling and experimental verification brings very effective procedure during suggestion and application in cryogenic region. Results of this work are used in research activities of Czech Academy of Science, ISI-Brno.

## 1. INTRODUCTION

In the process of development and designing of cryotechnical devices, the problem of thermal transmission from a metal wall to gas is studied. The transmission of heat from the material surface is proportional to its thermal conductivity. It is a well-known fact that thermal conductivity value can be estimated on the basis of electric conductivity. Thermal conductivity measurement in metals within the thermal range of LN2 (77 K) to 300 K is a very demanding process. For that reason, it is rather more suitable to measure the electric conductivity of material that is designed for thermal conduction and to empirically determine the thermal conductivity parameters. The aim of the described process of measurement is to determine the resistivity of the material of a Cu disc featuring a low ratio between the diameter/thickness and the resistivity thermal coefficient. The described disc could not, however, be used to produce a suitable sample for measurement using the four-point material resistance measurement. The elementary precondition for the application of this measurement method is a material sample in the shape of a long thin cylinder or baulk. In measuring the resistivity of thin layers, the currently used method is the one devised by der Pauw. The necessary precondition of precise measurement is a homogeneous sample of the measured material in the form of a thin sheet of any shape. All the four contacts are located in the corners of the sample. From the values of resistance between all clamps and taking into account the final size of the contacts, the material resistivity is calculated. It would be suitable to facilitate the measurement using the classical 4-point resistance or conductivity measurement method. In respect of the fact that we had at our disposal a cylinder of 325 mm in diameter and 30 mm in thickness, namely a cylinder that can not be further divided and used in making a test sample, the 4-point modified resistance measurement method was applied.

## 2. METHOD DESCRIPTION

The described method of measuring a large Cu disc resistance is based on the idea that the potential measured on two defined points on the surface of the disc in current passage through the disc is proportional to the disc material resistivity. Voltage clamps are located symmetrically around the disc centre in the distance of  $\pm l/2$ . The resistivity  $\rho$  is given by the relation

$$\rho(T) = k_s \frac{U_m(T)}{I_0} \quad (1)$$

where  $U_m$  is the voltage measured on the points  $\pm l/2$ , [V],  $I_0$  is the excitation current, [A],  $k_s$  is the constant dependent on the geometrical configuration of the measured disc, [m]. The proportionality constant  $k_s$  is dependent on the current field distribution in the measured sample and on the distribution of the scalar electric potential  $\varphi$  equipotentials. This distribution for the selected configuration can be calculated using the finite element method.

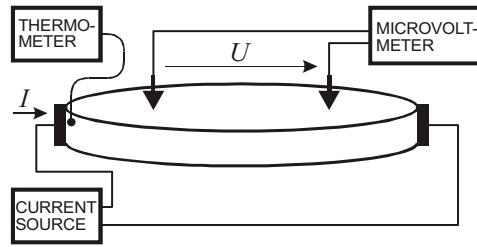


Figure 1: Principle of measurement method of Cuprum bulk conductance.

### 3. MATHEMATICAL MODEL

The description of the electrostatic model is based on the reduced Maxwell's equations and on the expression for the material relation between the functions

$$\operatorname{div} \mathbf{J} = 0, \quad (2)$$

$$\operatorname{rot} \mathbf{E} = 0, \quad (3)$$

$$\mathbf{J} = \gamma \mathbf{E}, \quad (4)$$

$$\mathbf{E} = -\operatorname{grad} \varphi, \quad (5)$$

where  $\mathbf{J}$  is the current density vector,  $\mathbf{E}$  is the electric field intensity vector,  $\varphi$  is the scalar electric potential,  $\gamma$  is the measurable conductivity of the environment. The area  $\Omega$ , where Equation (2) will be applied, is divided into areas: with measurable conductivity  $\gamma_{Cu}$   $\Omega_{Cu}$ , with measurable conductivity  $\gamma_{uz}$  (air area)  $\Omega_0$ . For these, there holds  $\Omega \equiv \Omega_{Cu} \cup \Omega_0$ . The boundary conditions are described by the relations

$$\begin{aligned} \mathbf{n} \times (-\gamma_i \operatorname{grad} \varphi_i + \gamma_j \operatorname{grad} \varphi_j) &= 0 & \text{na hranici } \Gamma_0, \\ \mathbf{n} \times (\operatorname{grad} \varphi_i + \operatorname{grad} \varphi_j) &= 0 & \text{na hranici } \Gamma_0 \end{aligned} \quad (6)$$

where  $\mathbf{n}$  is the normal vector to the area surface  $\Omega$ ,  $\Gamma_0$  is the surface of the area  $\Omega_0$ . By applying the relations (2) to (5) we obtain the expression

$$-\operatorname{div} \gamma \operatorname{grad} \varphi = 0. \quad (7)$$

The discretization of the expression (7) can be realized using the approximation of the scalar magnetic potential

$$\varphi = \sum_{k=1}^{N_\phi} \phi_k(t) W_k(x, y, z), \quad \forall (x, y, z) \in \Omega, \quad t \geq 0 \quad (8)$$

where  $\phi$  is the node value of the scalar magnetic potential,  $W$  is the base function,  $N_\phi$  is the number of the discretization mesh nodes. By applying the approximation (8) in relation (7), by applying the Galerkin method, and by respecting the boundary and initial conditions (5) and (6), we obtain the semidiscrete solution

$$\sum_{j=1}^{N_\phi} \phi_j \int_{\Omega} \gamma_j \operatorname{grad} W_j \cdot \operatorname{grad} W_i d\Omega = 0, \quad i = 1, \dots, N_\phi, \quad (9)$$

The system of equations (9) can be written briefly using the expression

$$[K_{ij}] \{\phi_j\} = 0, \quad i, j = 1, \dots, N_\phi. \quad (10)$$

The coefficient for the modified system of equations (10) to the system of equations (11) are written as

$$k^e = \int_{\Omega^e} \gamma_j^e \operatorname{grad} W_j \cdot \operatorname{grad} W_i d\Omega, \quad i, j = 1, \dots, N_e, \quad (11)$$

where  $\Omega^e$  is the area of the selected type of the discretization mesh element,  $\gamma^e$  is the specific conductivity of the selected element environment,  $N_e$  is the number of nodes of the discretization mesh element. The system of equations (10) changes into

$$[K^e] \{\phi\} = 0, \quad e = 1, \dots, N_e. \quad (12)$$

The system of equations (12) can be solved using standard algorithms.

#### 4. NUMERICAL MODEL

The geometrical model based on the Finite Element Method (FEM) in the ANSYS program was made using standard algorithms generating the mesh of elements and nodes. The mathematical model was applied with the help of the SOLID232, 233 elements. The basic characteristics of the nodes are described by the number of nodes = 32527, the number of elements=19506, and the degree of freedom = 32527. The geometrical model of the task is described in Fig. 2.

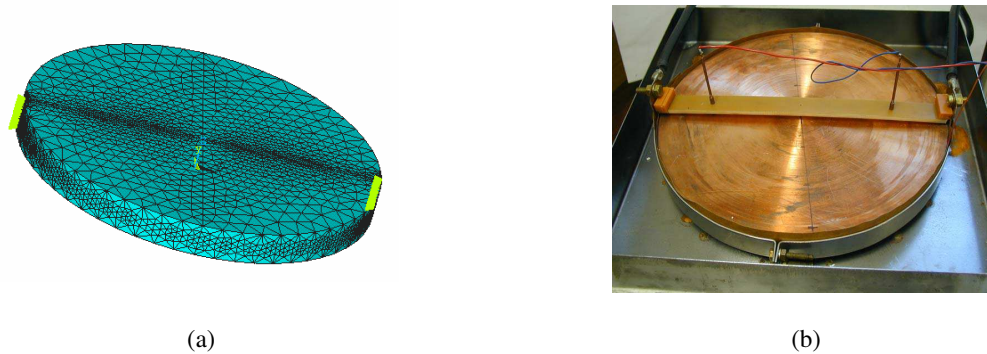


Figure 2: (a) The geometrical model for the Cu block conductivity measurement; (b) The experiment.

#### 5. NUMERICAL ANALYSIS RESULTS

The description of the evaluation of electric potential  $\varphi$  and current density  $\mathbf{J}$  in the copper disc area is shown in Figs. 3 and 4. Another objective of the task consisted in defining the distribution of the electric scalar potential along the external transversal trajectory of the disc. On the basis of this distribution (Fig. 5), the limit position of the contact points is determined; on these points, electric potential will be scanned and voltage drop evaluated in order to facilitate the determination of resistivity according the relation (1). The points were set to the distance of 100 mm from the center.

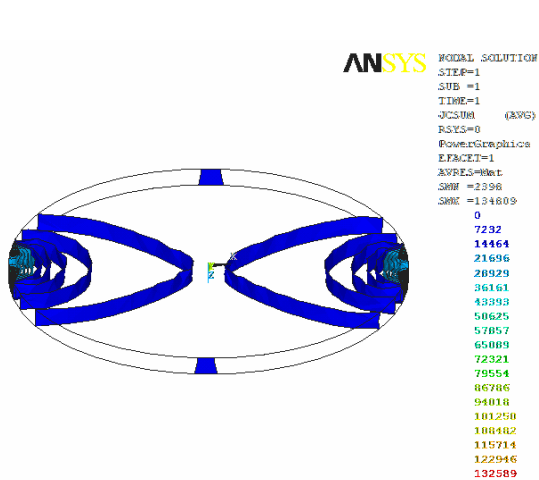


Figure 3: The distribution of current density  $\mathbf{J}$  module in the model of the Cu block conductivity measurement.

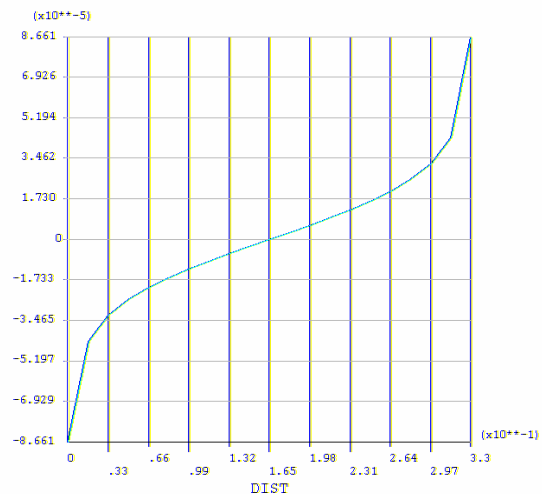


Figure 4: The distribution of electric scalar potential  $\varphi$  along potential  $\varphi$ .

#### 6. EXPERIMENTAL RESULTS

The concrete form of the measured sample was a disc of 325 mm in diameter 30 mm in height. The disc had been designed for the purposes of the production of thermal structures parts using a cryostat. The measurement configuration is described in Fig. 6. The current of  $I_0 = 100$  A from a CRYOGENICS stabilized current source passes via parallel groove clamps through the entire volume

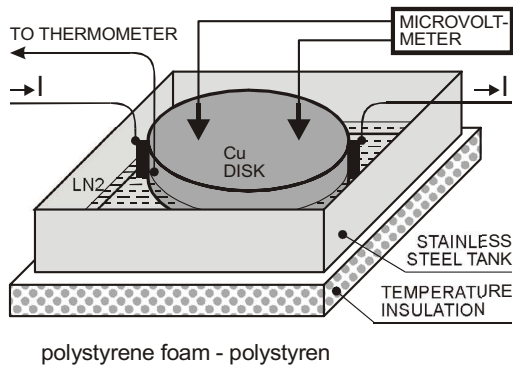


Figure 5: The electric conductivity  $\gamma$  measurement scheme.

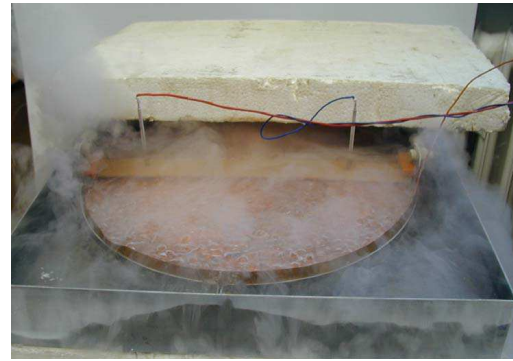


Figure 6: The dependence of electric conductivity  $\gamma$  on temperature: The measurement configuration.

of the measured sample. The clamps were constructed using a Cu wire (3 mm in diameter), and they were located on the disc perimeter; the current from the clamps was conducted away through an item of Cu sheet metal to the clamps of the supply cables. By this configuration, the contact surface of current contact is defined as  $84 \text{ mm}^2$  ( $2.8 \times 30 \text{ mm}$ ). Then, the disc is spanned — over an insulation sheet — with a non-corrodible tightening belt, which, after being tightened, will produce force  $F$  sufficient to press the supply parallel groove clamps. The results of the measurement of thermal characteristics of the Cu disc resistivity applying the above-described method are shown in Fig. 7. The dependence corresponds with the theory; the linear and thermal coefficient of the measured material resistivity is  $\alpha = 8.24 \times 10^{-5} \Omega \text{mm}^2 \cdot (\text{m}^\circ \text{K})^{-1}$ . The resistivity of the measured material is  $0.01711 \Omega \text{mm}^2 / \text{m}$  for  $273^\circ \text{K}$ .

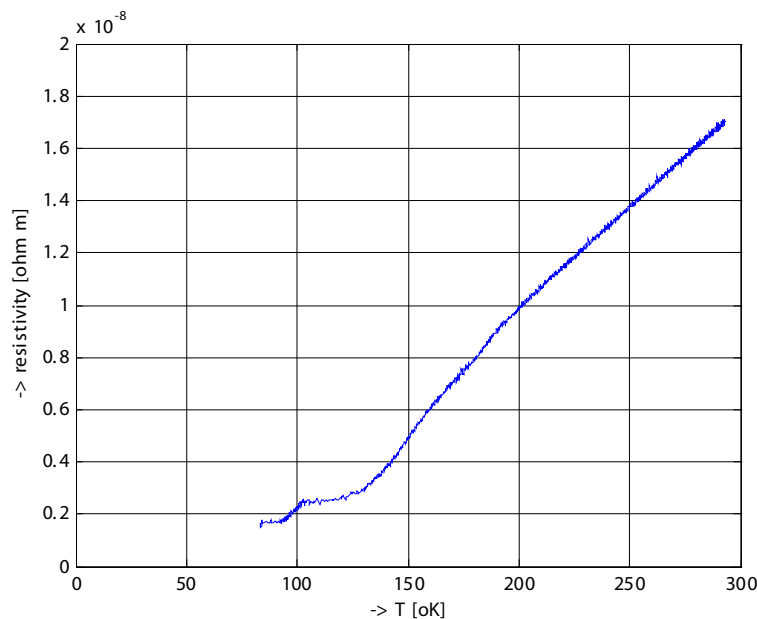


Figure 7: The Cu resistivity dependence on temperature.

## 7. CONCLUSION

Using the modified four-point measurement method and the simulation of potential distribution during the process of excitation by current, the resistivity and its thermal coefficient for the Cu disc material was determined, namely within the range of 77 to  $293^\circ \text{K}$ . Subsequently, the results were applied in drafting the design of a cryostat with minimized evaporation of liquid gases.

**ACKNOWLEDGMENT**

The research described in the paper were financially supported by FRVŠ by research plan No. MSM 0021630503 and grant GAAV No. B208130603.

**REFERENCES**

1. Kanagawa, T., R. Hobara, I. Matsuda, T. Tanikawa, A. Natori, and S. Hasegawa, "Anisotropy in conductance of a quasi-one-dimensional metallic surface state measured by a square micro-four-point probe method," *Ph. Rev. L.*, Vol. 91, No. 3, 2003.
2. Han, K., A. Ishmaku, and J. D. Embury, "Role of nanotwins and dislocations in high strength and high conductivity bulk Cu," National High Magnetic Field Laboratory Reports, Vol. 11, No. 1, MacMaster Univ., Materials Science and Engineering, Hamilton, Canada, 2004.
3. Webster, J. G., *Electrical Measurement, Signal Processing, and Displays*, CRC Press LLC, ISBN 0-8493-1733-9, London, 2004.
4. Van der Pauw, L. J., "A method of measuring specific resistivity and Hall effect of discs of arbitrary shape," *Philips Res. Rep.*, Vol. 13, 1–9, 1958.

# Processing of MR Images in Temporomandibular Joint Examination

K. Bartusek<sup>1</sup>, Z. Smékal<sup>2</sup>, O. Liberda<sup>3</sup>, and A. Sprlakova<sup>4</sup>

<sup>1</sup>Institute of Scientific Instruments, Academy of Sciences of the Czech Republic v.v.i  
Kralovopolska 147, Brno 612 00, Czech Republic

<sup>2</sup>Faculty of Electrical Engineering and Communication, Brno University of Technology  
Purkynova 118, Brno 612 00, Czech Republic

<sup>3</sup>Faculty of Medicine, Clinic of Oral and Maxillofacial Surgery, Masaryk University  
Komenskeho nam. 2, Brno 662 43, Czech Republic

<sup>4</sup>Faculty of Medicine, Department of Radiodiagnostics, Masaryk University  
Komenskeho nam. 2, Brno 662 43, Czech Republic

**Abstract**— The paper deals with the post-processing treatment of MR images in the examination of temporomandibular joints. Increasing the contrast that corresponds to the nucleus relaxation time  $T_2$  in the MR image and enhancing the arthritic areas of the afflicted temporomandibular joint were achieved by digital filtering using the wavelet transform and by processing two MR images measured at different echo times. The enhanced area indicates arthritic changes in the temporomandibular joint, which will be compared with conclusions from arthroscopy examination.

## 1. INTRODUCTION

Magnetic resonance is one of the most important and advanced medical diagnostic techniques [1]. In images detected by the technique of magnetic resonance (MR images) it is possible to distinguish the properties of individual human tissues and the distribution of proton nuclei, and to image the difference in the relaxation properties of nuclei in the tissues being measured. These parameters can be used to obtain a more accurate diagnosis of the disease. MR diagnostic results in medicine are indisputable.

The number of temporomandibular joint examinations using the MR methods has recently been increasing and the results obtained are compared with those provided by sonographic examination and CT imaging.

The magnitude contrast in an MR image is given by many physical parameters of live tissues. The most important parameters are the spin density of proton nuclei, relaxation times  $T_1$  and  $T_2$ , and the kinetics of molecules of water (such as flows, diffusion and perfusion) [2]. Contrast in an MR image always depends on several parameters simultaneously. By choosing the type of the measuring pulse sequence and by setting its parameters such as the spin echo time  $T_E$ , the experiment repetition time  $T_R$ , the magnitude of flip angle, the nucleus inversion time  $T_I$ , etc., the contrast given by one of the above parameters can be increased and, simultaneously, the effect of the other parameters reduced. In this way it is possible to increase the contrast and make visible the pathological areas of the tissue being examined [3, 4]. The intensity of the signal acquired by the MRI technique depends on echo time  $T_E$  and on repetition time  $T_R$  of successive scans. An appropriate choice of  $T_R$  and  $T_E$  for suitable  $T_1$  and  $T_2$  weights is an important factor in determining image contrast in medical imaging. Measuring by these pulse sequences results in images with enhanced contrast of one relaxation time (either  $T_1$  or  $T_2$ ) and with undesirable contrast given by the other relaxation time and by the spin density [5–7]. Pulse sequences of greater complexity are proposed, which include a multi-step preparatory phase, employing gradients [8] or a special detection technique [9] with the aim of suppressing this undesirable contrast.

The value  $T_2$  can be calculated from several (6–10) MR images scanned at different echo times TE via linear or non-linear least-squares curve fitting in all image pixels [10]. This method requires obtaining a great number of images scanned by means of classical or fast MR methods.

The amount of proton nuclei—the spin density—determines the basic contrast of MR images, and changing this amount can be used to affect the contrast. The present paper describes a measuring method suitable to distinguish between the effect of weighting the MR image by spin density and by relaxation time  $T_2$  of sample nuclei. This method of image processing is based on measuring the MR images by the spin echo technique for two time values ( $T_E$ ) and on the calculation of their quotient. The result is an MR image weighted by relaxation time  $T_2$  with the effect of this spin density suppressed. With increasing time  $T_E$  the intensity of the signal being measured and the

signal-to-noise ratio in the MR image will be decreasing. For this reason the MR images being measured need to be digitally filtered, with optimally chosen parameters.

## 2. PROPOSED METHOD OF MEASURING AND PROCESSING

One of the current techniques of detecting MR images is the spin echo (SE) method [11]. The obtained image of a chosen layer is weighted by spin density  $M_0(x, y)$  and, simultaneously, by the magnitude of relaxation constant  $T_2$ . The effects of spin-lattice relaxation  $T_1$  and diffusion can be considered negligible. The magnitude of an MR image can be expressed by the expression:

$$M(x, y) = M_0(x, y) \exp(-T_E/T_2) \quad (1)$$

In the commonly conducted experiments for the determination of relaxation times  $T_2$  it is necessary to measure a series of images with different echo times  $T_E$  and to estimate the  $T_2$  value at each point of the images via curve fitting according to relation (1). In this way the effect of spin density in the chosen place can be limited. A simplified method consists in measuring one MR image for a suitably chosen value  $T_E$  with respect to the expected relaxation times  $T_1$  and  $T_2$  in the tissues being measured [1 and 8]. In this case the image magnitude will not be weighted by relaxation times several times shorter than the chosen time  $T_E$ , and the contrast in the image will correspond to relaxation times  $T_2 > T_E$ . For a more accurate determination of the spin relaxation time in a chosen local place of the image it is of advantage to eliminate the effect of spin density. We measure the MR images for two times  $T_E$ . On the basis of definition (1) their magnitudes can be expressed as follows:

$$M_1(x, y) = M_0(x, y) \exp\left(-\frac{T_{E1}}{T_2}\right) \quad M_2(x, y) = M_0(x, y) \exp\left(-\frac{T_{E2}}{T_2}\right) \quad (2)$$

Time  $T_{E1}$  should be as short as possible and it is limited by the measuring sequence and by the magnitudes of the gradients used. Time  $T_{E2}$  is chosen according to the assumed relaxation times in the sample measured (20 ms and 90 ms). The quotient of images  $M_1(x, y)$  and  $M_2(x, y)$  can be used to eliminate the effect of spin density on the contrast of MR image:

$$\frac{M_1(x, y)}{M_2(x, y)} = \exp\left[-\frac{(T_{E1} - T_{E2})}{T_2}\right] \quad (3)$$

At each point of the image the relaxation times are then given by the relation:

$$T_2 = -\frac{(T_{E1} - T_{E2})}{\{\ln [M_1(x, y)] - \ln [M_2(x, y)]\}} \quad (4)$$

The processing of MR images in the above way is limited by the noise in the image because noise is enhanced by this modification.

Various types of digital filtering can be used to reduce noise in an MR image. Based on earlier experience, the wavelet transform was used. The result of filtering was assessed visually on a

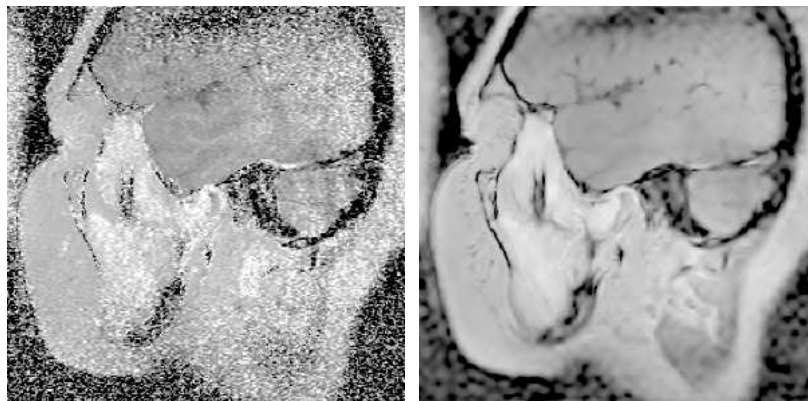


Figure 1: MR image of temporomandibular joint; (a) non-filtered, (b) digitally filtered with wavelet function *coif 4*.

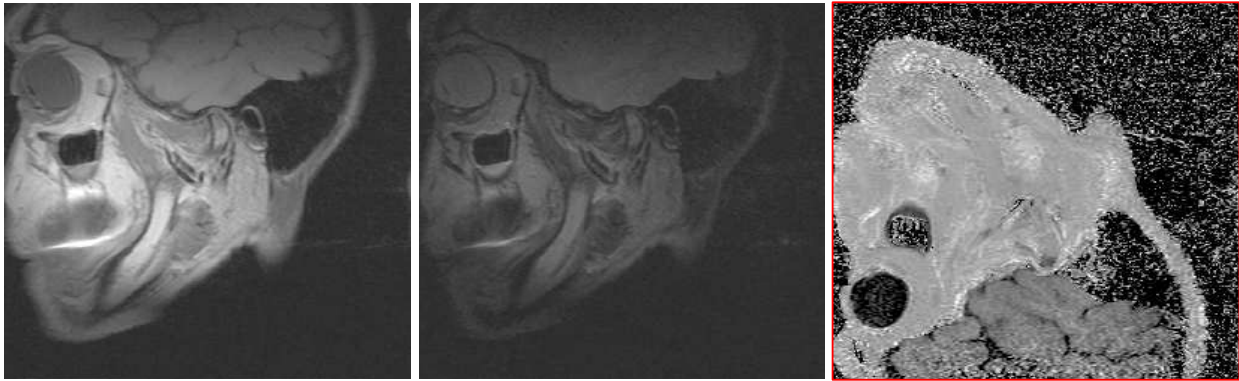


Figure 2: MR images of the head near the temporomandibular joint; (a) for  $T_E = 20$  ms, (b) for  $T_E = 90$  ms, (c) resultant MR image weighted by relaxation time  $T_2$ .

detail of MR image of the human brain near the temporomandibular joint. The following wavelet functions were used: haar, db 6, bior 2.4, rbio 2.6 version 2, coif 4, sym 3, sym 4, and dmey. Judging from the details of the filtered image we regard the coif 4 function as optimum. The resultant image contains the greatest number of details with high contrast. This function was used to filter all MR images. Fig. 1 gives a non-filtered and a filtered MR image ( $256 \times 256$  pixels) taken at an echo time of 90 ms. The wavelet transform with the coif 4 wavelet function is efficient in suppressing noise in the image, with minimum blur of the image.

### 3. EXPERIMENTAL WORK

Examination of temporomandibular joint was performed on a 1T Magnetom Impact Siemens MR tomograph at the Faculty of Medicine of Masaryk University in Brno. Image processing by the proposed method was performed in Matlab and Marevisi programs. In the group of patients under examination the MR images of temporomandibular joint were measured at echo times of 20 ms and 90 ms. The efficiency of the described method of data processing is shown on a selected MR image of the temporomandibular joint of a female patient 34 years old.

Figs. 2(a) and (2b) give the MR images of the head in the area of temporomandibular joint ( $256 \times 256$  pixels) taken at echo times of 20 and 90 ms. Wavelet filtering of the two images markedly reduces

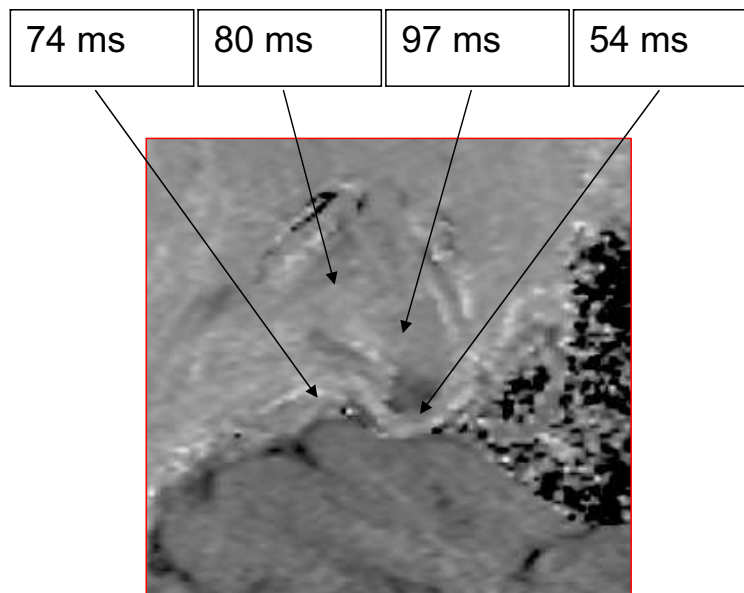


Figure 3: Evaluation of the magnitude of relaxation times  $T_2$  in a detail near the temporomandibular joint.

image noise. In the two images, the contrast is due to spin density and also to relaxation time  $T_2$ . Fig. 2(c)) gives the resultant image after processing the two images according to relation (4), weighted by relaxation time  $T_2$ .

It is evident from Fig. 2 that the resultant image has a low contrast because the relaxation time values are close to each other. The difference between muscles, bones and brain tissues are greater. The evaluation of relaxation times for the detail of temporomandibular joint is given in Fig. 3. The temporomandibular joint has the relaxation constant  $T_2 = 54$  ms and at their end the relaxations are markedly longer,  $T_2 = 97$  ms. A longer relaxation time indicates more freely bonded molecules of water in this place and this means that there have been arthritic changes in the temporomandibular joint.

#### 4. CONCLUSION

Using the above method to modify an MRI image weighted by relaxation time  $T_2$  yielded an enhanced contrast resolution of the image. Suppressing the effect of spin density at each point of the image resulted in increased image contrast weighted by relaxation time  $T_2$ .

Experimental verification of the described method of data processing proves the suitability of using the wavelet transform. Images weighted by relaxation time  $T_2$  make the freely bonded molecules of water more pronounced and enable making visible the area with arthritic changes in temporomandibular joints. The method can also be applied in other MR examinations.

The method described above can be applied to most MR imaging techniques as the effect of spin density in images weighted by relaxation time  $T_2$  is always manifest. For tissues with a short relaxation time  $T_2 < T_1$  it is possible to obtain new information. An advantage of this method can be seen in measuring two MR images. The knowledge of the exact values of relaxation times in MR images can lead to some new information in medical diagnostics and examination.

#### ACKNOWLEDGMENT

This work was supported within the framework of project No. 102/07/1086 of the Grant Agency of the Czech Republic.

#### REFERENCES

1. Kimmich, R., *NMR Tomography, Diffusometry, Relaxometry*, Springer-Verlag Berlin Heidelberg, New York, 1997.
2. Gass, A., "White matter diseases," *Proc. ESMRMB2004*, S8, Copenhagen, 2004.
3. Dijkhuizen, R., "Ischemic stroke," *Proc. ESMRMB2004*, S8, Copenhagen, 2004.
4. Tintera, J., "Contrast mechanisms," *Proc. ESMRMB2004*, S2, Copenhagen, 2004.
5. Haacke, E. M., P. A. Wielopolski, J. A. Tkach, and M. T. Modic, "Steady-state free precession imaging in the presence of motion: Application for improved visualization of the cerebrospinal fluid," *Radiology*, Vol. 175, 545–552, 1990.
6. Duerk, J. L., J. S. Lewin, M. Wendt, and C. Petersilge, "Remember true FISP? A high SNR, near 1-second imaging method for  $T_2$ -like contrast in interventional MRI at 2T," *J. Magn. Reson. Imaging*, Vol. 8, 203–208, 1998.
7. Schmitz, B., T. Hagen, and W. Reith, "Three-dimensional true FISP for high-resolution imaging of the whole brain," *European Radiology*, Vol. 13, No. 7, 1577–1582, 2003.
8. Mugler, J. P., T. A. Spraggins, and J. R. Brookeman, " $T_2$ -weighted 3-dimensional MP-range MR imaging," *JMRI-Journal of Magnetic Resonance Imaging*, Vol. 1, No. 6, 731–737, 1991.
9. Butts, R. K., F. Farzaneh, S. J. Riederer, et al., " $T_2$ -weighted spin-echo pulse sequence with variable repetition and echo times for reduction of MR image acquisition time," *Radiology*, Vol. 180, No. 2, 551–556, 1991.
10. Watrin-Pinzano, A., J. P. Ruaud, Y. Cheli, et al., "Evaluation of cartilage repair tissue after biomaterial implantation in rat patella by using  $T_2$  mapping," *Magnetic Resonance Materials in Physics Biology and Medicine*, Vol. 17, No. 3–6, 219–228, 2004.
11. Bartusek, K., "Processing of MR images weighted by relaxation time  $T_2$  to increase their contrast resolution," *Measurement Science and Technology*, Vol. 17, No. 4, 727–730, 2006.

# Software Implementation of a New Multi-scale Method for Fractal-shaped Structures' Diffraction Analysis

T. BenSalah and T. Aguli

L. Syscom, ENIT, BP 37 Le Belvedere 1002, Tunis, Tunisia

**Abstract**— This paper proposes a new software implementation for a new EM Analysis method named MS-MGEC which stands for *Multi Scale Method of Generalized Equivalent Circuit*. With this method, analyzing multi scale antennas with fractal [1–4] shapes — for example — is made easy with interesting results. The Software is developed in the Java™ platform aiming to become a complete EM analysis platform.

## 1. INTRODUCTION

We are interested, in this paper, in a couple of fractal structures placed in an infinite waveguide and excited with the fundamental mode. We will focus on the analysis of the diffraction of this mode on the structures. We are interested, particularly, in Cantor Iris (1D) (Fig. 1) and Sierpinski Gasket structures (2D) (Fig. 2).

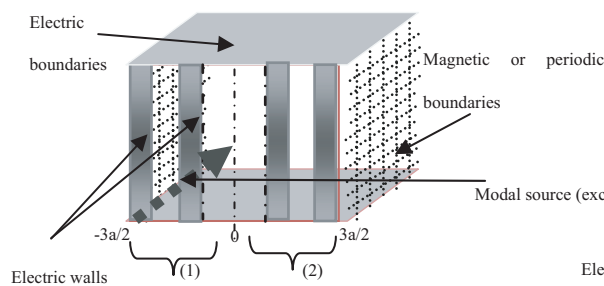


Figure 1 : Cantor Iris ( $k=2$ ).

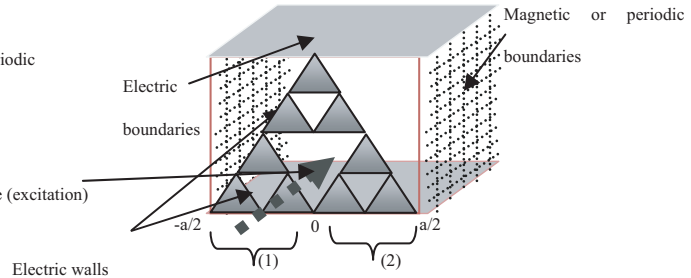


Figure 2 : Sierpinski Gasket ( $k=2$ ).

Fractal structures such as Fig. 1 may seem to be quite simple to study. Due to their self-similarity characteristics, known methods, like MoM lack efficiency. Indeed, multi-scale structures require adapting calculation precision to different elements of the simulated structure: Big elements require less precision while small elements require more precision. Adaptive meshing too can not bring a convincing solution, because it still needs lots of resources (both memory and execution time). However — in this case — the structure is very regular (set of rectangular shapes).

Fractal structures are well adapted to recursive algorithms, and many works have been deployed to enhance performance and resource usage in such algorithms [7].

The following paragraph will discuss a new method that is well adapted to the fractal geometry. Then, we present a new software implementation for that method, and finally we will use the software to analyze the structures of Fig. 1 and Fig. 2.

## 2. MULTI SCALE METHOD OF GENERALIZED EQUIVALENT CIRCUIT

The proposed method is an extension of the MGEC [5,6] method (a MoM based method) in which we introduce a new formulation using a Surface Impedance Operator (multi-port model) for bypassing conventional 'scalar' surface impedance limitations.

Indeed, by applying the multi-port model in conjunction with the cut and plug approach to study the structure at the  $k$ th stage, we do — first of all — cut and study the same structure at the  $k - 1$ th stage (small guides) by calculating its input impedance (seen by  $n$  fundamental/excitation modes). Then we re-plug an equivalent structure as a substitute for it (Fig. 3). Actually, that equivalent structure is a multi port (Fig. 4) that corresponds to the former input impedance. We shall mention that if we excite with a single mode ( $m = 1$ ) we come back to the traditional Surface Impedance Model [5] with a scalar value. It is important to mention also that the equivalent structure for the initial fractal at  $k$ th stage is the structure at the first stage (generator element) where metal will be replaced by surface impedance [8,9].

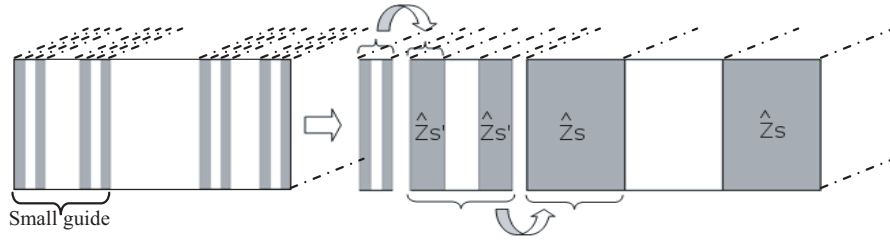
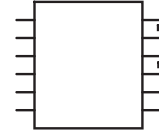

 Figure 3: Application of the  $Z_{S_k}$  operator.


Figure 4: Equivalent multipoint.

So, using this method we will always study structures no more complex than the generator element. The final iteration will be simply the study of the generator element itself (without multipoint).

Using the MGEN, we translate relations between Electric and Magnetic fields into equivalent Circuit as shown in Fig. 5.

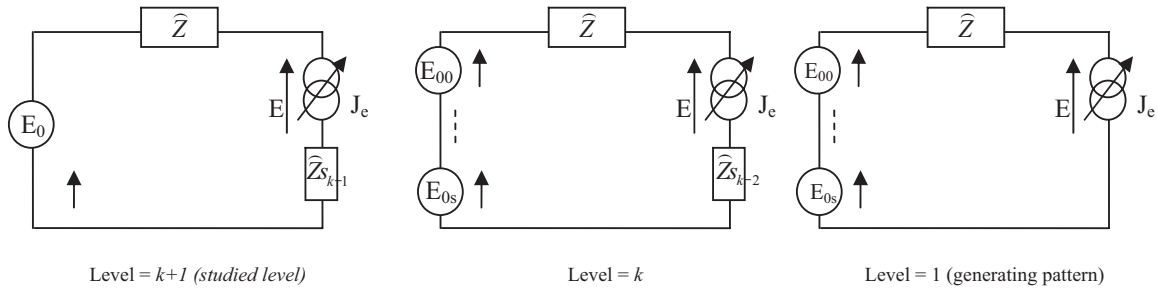


Figure 5: Equivalent circuit for different stages.

Then, we deduce  $[Z_{in}]$  matrix expression for each iteration (on  $k$ th stage) using Galerkin method.

$$[Z_{in}] = ([B]^t[A]^{-1}[B])^{-1} \quad (1)$$

where

$$[B] = [\langle g_p, F_n \rangle]_{0 \leq p \leq NE \wedge 0 \leq n < m} \quad (2)$$

$$[A] = [\hat{Z}] + [\hat{Z}_S] \quad (3)$$

$$\hat{Z} = \sum |F_n\rangle z_n \langle F_n| \Rightarrow [\hat{Z}] = \sum \langle g_p F_n \rangle z_n \langle F_n g_q \rangle_{p,q} \quad (4)$$

$$\hat{Z}_S = \sum |f_n\rangle z_n \langle f_n| \Rightarrow [\hat{Z}_S] = \sum \langle g_p f_m \rangle z_{s(m,n)} \langle f_n g_q \rangle_{p,q} \quad (5)$$

$\{g_p\}$  are the (current) test functions,  $\{F_n\}$  the big guide ( $k+1$ th stage) base functions (modes) and  $\{f_n\}$  the small guide ( $k$ th stage) base functions.

We note that, this method makes possible to study one scale at a time so that difficult multi-scale problems imposed by the fractal aspect of the structures are bypassed in a suitable manner.

### 3. NEW SOFTWARE IMPLEMENTATION

We have developed a multi-purpose EM simulation software (Fig. 6) that initially supports only the MCEG method for simulating mainly planar structures. The software was designed for researchers who know well MoM method by providing them all needed parameters to explore different types of meshing and different types of test functions (according to the selected meshing of course). Then, we have extended this software to include the MS-MGEN method and fractal structures.

In fact, the software is designed in such a way that new applications can be dealt with by simply adding pertinent models and functions that may be used for analyzing a wide range of planar structures. It is designed in a modular manner that enables its usage either as an extensible stand alone Desktop GUI application or as an embedded library. Indeed, new structure types, new test

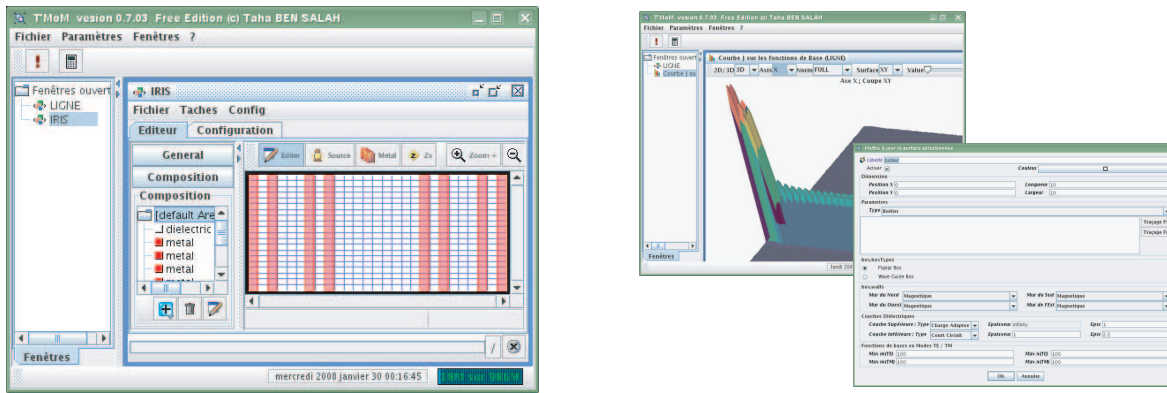


Figure 6: Software screen samples (WYSIWYG editor, 2D/3D fields plotting, wizards...).

functions, and new meshing algorithms are highly customizable. And, because it is implemented in the Java™ language, it is easy to include a new implementation of any of the software components. Further, it benefits the platform independence of such a language and runs indifferently on many operating systems.

Actually, planar antennas radiation and wave-guided structure diffraction can be simulated by the software to obtain  $Z_{in}$ ,  $S$  parameters, Surface Currents, Electric fields ... In fact, the new software (more than 800 classes) aims to become a complete simulation platform for EM analysis.

#### 4. APPLICATION TO FRACTAL STRUCTURES

Using this software we define structures (Fig. 1) and (Fig. 2) as follows (Table 1):

Table 1: Fractal structures definition using scripting language in the software. (a) Cantor Iris Fractal definition, (b) Sierpinski Gasket Fractal definition.

<pre>#Cantor Iris Pattern : polygon((0,0), (1,0), (1,1), (0,1)) as \$1 Transform : resize(\$1,1/3) as \$1 ; move(resize(\$1,1/3),2/3,0) as \$1</pre>	(a)
<pre>#Sierpinski Gasket Pattern : polygon((0,0), (0.5,1), (1,1)) as \$1 Transform : resize(\$1,0.5) as \$1 ; move(resize(\$1,0.5),0.5,0) as \$1;            move(resize(\$1,0.5),0.25,0.5) as \$1</pre>	(b)

Then we calculate the input impedance of Fig. 1 (stage 2) and Fig. 2 (stage 2) by two means: on the one hand using a reference method that is actually the well known MoM method (supported by the software); and on the other hand using the MS-MGEC method while varying the number  $m$  of excitation modes. As we have mentioned earlier, when  $m = 1$  we fall back into the surface impedance model. The Fig. 7 shows the relative error ( $E_m$ ) between  $Z_{in-ref}$  ( $Z_{in}$  calculated using the reference method) and each of the  $Z_{in-mod-m}$  ( $Z_{in}$  calculated using MS-MGEC using  $m$  excitation modes for each small guide) for  $m = 1, 2$  and  $3$ . Relative error is given while  $Z_{in}$  value is converging in terms of test and base functions count. At convergence, for Iris Cantor structure,  $E_1 = 16.5\%$ ,  $E_2 = 7.3\%$  and  $E_3 = 1.9\%$ . Concerning Sierpinski Gasket structure,  $E_1 = 19.2\%$ ,  $E_2 = 4.0\%$  and  $E_3 = 4.1\%$ , we can not do further improvements by increasing  $m$  value due to B matrix conditioning (the bigger  $m$  we use, the worst conditioning A matrix we experience).

This shows how important is the use of surface impedance operator (multiport model) instead of the traditional surface impedance model. Besides, to highlight the numerical interest of the suggested method, we note that if we use  $m$  base (mode) functions and  $n$  test functions per element (so that total test functions count is  $N = 3^{k-1}n$  for Sierpinski Gasket), the total time spent on  $Z_{in}$

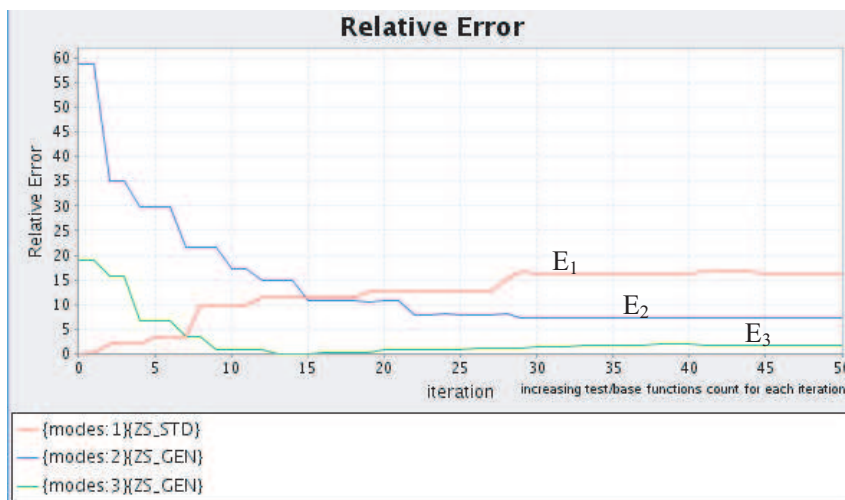


Figure 7:  $Z_{in-mod-m}$  (modes:  $m$ ) relatively to  $Z_{in-ref}$  for Cantor Iris structure.

calculation for the stage  $k$  is: For direct calculation using Method Of Moments:

$$T_{dir}^k = T_s \left( 3^{(k-1)}n \right) m + T_c \left( 3^{(k-1)}n \right)^2 m + T_i$$

For the proposed method:

$$T_{prop}^k = k(T_s n m + T_c n^2 m + T_i)$$

where  $T_s$  is the scalar products calculation time,  $T_c$  is the A matrix ( $(3^k n) \times (3^k n)$  dimension) cell calculation time and  $T_i$  is the matrix inversion time. We note that  $T_i \gg T_s \gg T_c$ .

This ensures that calculation time becomes linear (for fixed  $n$  and  $m$  values) instead of exponential (Fig. 8). Hence — as mentioned in the second paragraph — the studied structure will be always remodelled to the generator element ( $k = 1$ ) which ensures that test functions count is not getting to explode when  $k$  (fractal stage) is increasing, so that A Matrices (1) remains with modest dimensions. Moreover, thanks to the self similarity of fractal structures, all small guides of a particular structure at stage  $k$  (big guide) will be replaced with the same  $\hat{Z}_{s_{k-1}}$ . In this way, when calculating  $Z_{in(k=2)}$  (stage 2) for Sierpinski Gasket structure, we need to calculate once  $Z_{in(k=2)}$  and use it three times for replacing the three small guides. That is to say, we will spend

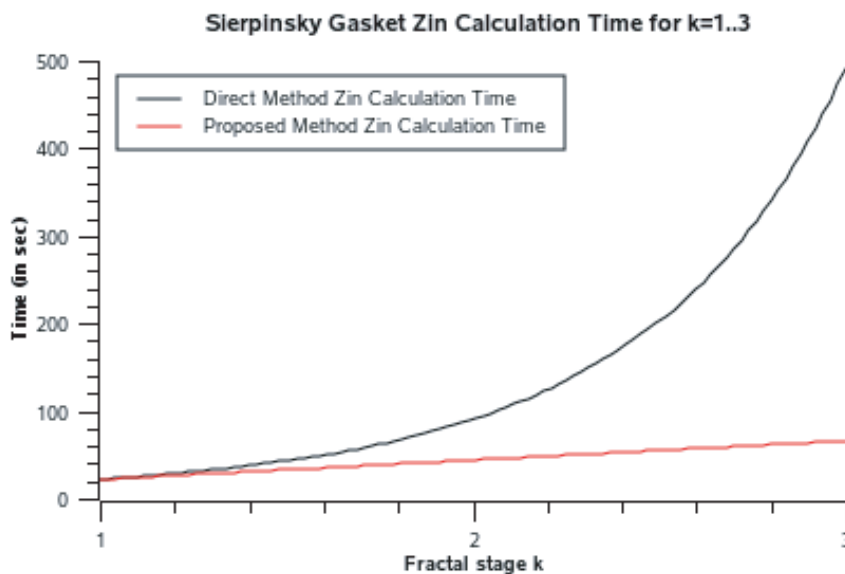


Figure 8: Sierpinski Gasket calculation time for  $k = 1, 2, 3$ .

time calculating 2 matrices of dimension  $n$  (one for  $k = 1$  and one for  $k = 2$  by applying multiport model) instead of calculating one of dimension  $3n$ , where  $n$  is the test functions count needed for the generator element ( $k = 1$ ).

## 5. CONCLUSION

In this paper we have proposed a new software implementation of the MS-MGEC Method (a MoM based method) — a well adapted to multi scale and fractal structures method — and have validated it by comparing its result to a reference implementation of the MoM method. While providing less than 2–4% of error, the software gives valuable speed enhancements for a couple of fractal structures. The originality of this work is that although it applies a recursive method to a fractal shaped planar antenna — as does [7] for fractal antenna arrays — it ensures a linear calculation time and a fixed Matrix size (independent of stage  $k$ ). Besides, thanks to the multi port-model, it provides interesting enhancements in precision compared to the surface impedance model presented in [5].

## REFERENCES

1. Madelbrot, B., *Fractal Objects*, Flammarion, 1975.
2. Romeu, J. and et al., “Generalized Sierpinski fractal multiband antenna,” *IEEE Trans. on Antenna and Propagation*, Vol. 49, 1237–1239, August 2001.
3. Elkamchouchi, H. M. and M. N. Abd El-Salam, “Square loop antenna miniaturization using fractal geometry,” *Proceedings of the Twentieth National Radio Science Conference, NRSC 2003*, B4-1–8, March 18–20, 2003.
4. Werner, D. H. and S. Ganguly, “An overview of fractal antenna engineering research,” *Antennas and Propagation Magazine, IEEE*, Vol. 45, 38–57, February 1, 2003.
5. Aguilu, T., “Modélisation des composants SHF planaires par la méthode des Circuits Equivalents généralisés (MGEC),” *Thesis Manuscript*, Enit Tunis, 2000.
6. Alatan, L. and et al., “Analytical evaluation of MoM matrix elements,” *IEEE Transactions on Microwave Theory and Techniques*, Vol. 44, No. 4, 519–525, April 1996.
7. Werner, D. H., D. Baldacci, and P. L. Werner, “An efficient recursive procedure for evaluating the impedance matrix of linear and planar fractal arrays,” *IEEE Transactions on Antennas and Propagation*, Vol. 52, 380–387, February 2, 2004.
8. Surre, F., A. S. Saleh, and H. Aubert, “Selective microwave filters based on self similar and lacunar structures,” *2002 IEEE Antennas Propagation Symposium, Conference Proceedings*, Vol. 2, 840–843, San Antonio, Texas, June 16–21, 2002.
9. Surre, F., A. S. Saleh, and H. Aubert, “Frequency response of self similar planar waveguides,” *Microwave and Optical Technology Letters (MWOLT)*, Vol. 27, No. 3, May 5, 2003.

# Multilayer Antenna with Metamaterial and Arbitrary Substrate

H. C. C. Fernandes, R. R. C. França, and A. F. Gomes

Department of Electrical Engineering, Federal University of Rio Grande of Norte, Brazil

**Abstract**— This paper presents a study and development of equations consisting metamaterials of negative refraction index. The equations developed for this structure are based in full wave Transverse Transmission Line (TTL) method. This method possibility a significant algebraic simplification of the equations involved in the process. In order to analyze this structure the complex resonant frequency were determined. The results obtained for this application are presented.

## 1. INTRODUCTION

Microstrip antennas are widely used due to its various advantages such as reducing size, weight, and cost and in addition because it interfaces easily with other microwave circuits, compatibility with integrated hybrid circuits and the possibility of acting with dual frequency [1]. They can be used in several systems, such as: radars, wireless, mobile telephony and communication by satellites. This paper presents an application of multilayer antenna with metamaterial. The analysis is made using the concise full wave TTL method.

However, most of the designs are still in the stage of theory and there is a big challenge to integrate antennas with dielectric multilayer has advantages, such as, the flexibility in the operation frequency band and a smaller physical size.

The TTL — Transverse Transmission Line method is used in the determination of the electromagnetic field components in the Fourier transform domain (FTD), for the three regions of the structures shown in the Fig. 1. The moment method is applied and adequate basis functions are used to expand the current densities in the metallic strip.

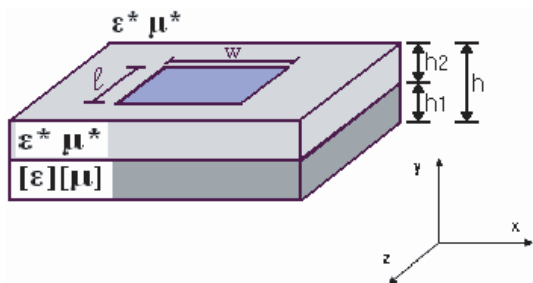


Figure 1: Multilayer microstrip antennas.

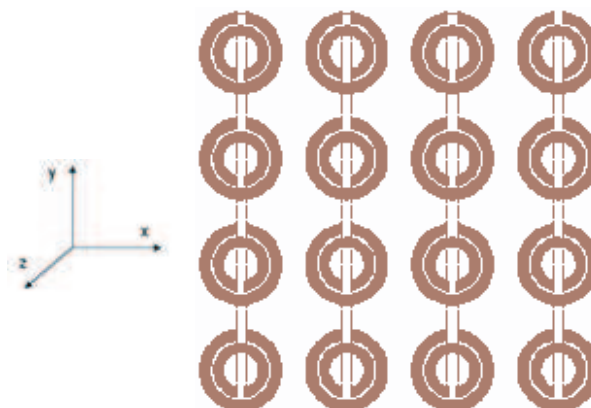


Figure 2: TW-SRR Structure compost with SRR and TW metamaterial.

The metamaterial substrate depends on the spatial coordinates and this causes spatial dispersion. As a result the medium will be no homogenous. For a no homogeneous structure, the incident wave undergoes a process of multiple scattering. The substrate shown in region 1 of Fig. 1 is modeled by utilizing the anisotropic tensor properties, which are expressed as [2]:

$$\mu = \mu_0 \begin{bmatrix} \mu_{xx} & 0 & 0 \\ 0 & \mu_{yy} & 0 \\ 0 & 0 & \mu_{zz} \end{bmatrix} \tag{1}$$

$$\varepsilon = \varepsilon_0 \begin{bmatrix} \varepsilon_{xx} & 0 & 0 \\ 0 & \varepsilon_{yy} & 0 \\ 0 & 0 & \varepsilon_{zz} \end{bmatrix} \tag{2}$$

## 2. METAMATERIAL THEORY

The term electromagnetic metamaterial has been applied to artificial structures, that possess properties beyond those available in naturally materials. The identification of a permittivity and permeability with an inhomogeneous structure allows the properties of the metamaterial to be expressed conveniently, often in analytic form. The ability to describe an otherwise complicated inhomogeneous structure as a continuous material characterized by homogenized material parameters is the heart of the metamaterial concept. Although the terms photonic crystal, artificial material or metamaterial are often used interchangeably, it is the key term that best fits the type of structures presented here in Fig. 2 [1].

## 3. FIELDS THEORY

The TTL — Transverse Transmission Line method in the Fourier transform domain, uses a component of propagation in the  $y$  direction, treating the general equations of electric and magnetic field as functions of  $\tilde{E}_y$  and  $\tilde{H}_y$  [3–5].

Starting from the Maxwell equations, and after several algebraic manipulations, the equations that represent the electromagnetic fields in the  $x$  and  $z$  directions are obtained as a function of the electromagnetic fields the in the  $y$  direction.

The metamaterial substrate shown in region 1 of Fig. 1 is modeled by utilizing bianisotropic tensor properties Equations (2.6) and (2.7), together with wave equations which are expressed as [2, 3]:

$$\frac{\partial^2 \tilde{E}_y}{\partial y^2} - \gamma^2 \tilde{E}_y = 0 \quad (3)$$

$$\frac{\partial^2 \tilde{H}_y}{\partial y^2} - \gamma^2 \tilde{H}_y = 0 \quad (4)$$

After using the Maxwell's equations in the spectral domain and the previous definitions above, the general equations of the electric and magnetic fields to the resonator, are obtained as:

$$\tilde{E}_x = \frac{1}{\gamma_y^2 + k_0^2 \varepsilon_r} \left[ -j\alpha_n \frac{\partial}{\partial y} \tilde{E}_y + \omega\mu_0\mu_{xx}\beta_k \tilde{H}_y + \omega\mu_0\mu_{zz}\beta_k \tilde{H}_y \right] \quad (5)$$

$$\tilde{E}_z = \frac{1}{\gamma_y^2 + k_0^2 \varepsilon_r} \left[ -j\beta_k \frac{\partial}{\partial y} \tilde{E}_y - \omega\mu_0\mu_{xx}\alpha_n \tilde{H}_y - \omega\mu_0\mu_{zz}\alpha_n \tilde{H}_y \right] \quad (6)$$

$$\tilde{H}_x = \frac{1}{\gamma_y^2 + k_0^2 \varepsilon_r} \left[ -j\alpha_n \frac{\partial}{\partial y} \tilde{H}_y - \omega\varepsilon_0\varepsilon_{xx}\beta_k \tilde{E}_y - \omega\varepsilon_0\varepsilon_{zz}\beta_k \tilde{E}_y \right] \quad (7)$$

$$\tilde{H}_z = \frac{1}{\gamma_y^2 + k_0^2 \varepsilon_r} \left[ -j\beta_k \frac{\partial}{\partial y} \tilde{H}_y + \omega\varepsilon_0\varepsilon_{xx}\alpha_n \tilde{E}_y + \omega\varepsilon_0\varepsilon_{zz}\alpha_n \tilde{E}_y \right] \quad (8)$$

where  $i = 1, 2, 3$ , represent the dielectrics regions of the structure;  $\gamma_i^2 = \alpha_n^2 + \beta_k^2 - k_i^2$  is the constant of the propagation in  $y$  direction;  $\alpha_n$  is the spectral variable in “ $x$ ” direction and  $\beta_k$  the spectral variable in “ $z$ ” direction;  $k_i^2 = \omega^2 \mu \varepsilon = k_0^2 \varepsilon_{ri}^*$  is the wave number of dielectric region;  $\varepsilon_{ri}^* = \varepsilon_{ri} - j \frac{\sigma_i}{\omega \varepsilon_0}$  is the dielectric constant relative of the material with losses;  $\omega = \omega_r + j\omega_i$  is the complex angular frequency;  $\varepsilon_i = \varepsilon_{ri}^* \cdot \varepsilon_0$  is the dielectric constant of the material;

The solutions of Helmholtz's equations for the three regions of the antenna are given by:

For region 1:

$$\tilde{E}_{y1} = A_{1e} \cdot \cosh(\gamma_1 y) \quad (9)$$

$$\tilde{H}_{y1} = A_{1h} \cdot \cosh(\gamma_1 y) \quad (10)$$

For region 2:

$$\tilde{E}_{y2} = A_{2e} \cdot \sinh(\gamma_2 y) + B_{2e} \cdot \cosh(\gamma_2 y) \quad (11)$$

$$\tilde{H}_{y2} = A_{2h} \cdot \sinh(\gamma_2 y) + B_{2h} \cdot \cosh(\gamma_2 y) \quad (12)$$

For region 3:

$$\tilde{E}_{y3} = A_{3e} \cdot \cosh[\gamma_3(da - y)] \quad (13)$$

$$\tilde{H}_{y3} = A_{3h} \cdot \cosh[\gamma_3(da - y)] \quad (14)$$

Substituting these solutions in the equations of the fields, in function of the unknown constants  $A_{1e}$ ,  $A_{1h}$ ,  $A_{2e}$  and  $A_{2h}$  is obtained, for example, for the region 1 [3]:

$$\tilde{E}_{x1} = \frac{-j}{k_1^2 + \gamma_1^2} [\alpha_n \gamma_1 A_{1e} \sinh(\gamma_1 y) + (\mu_{x1} + \mu_{z1}) j \beta_k \omega \mu_0 A_{1h} \sinh(\gamma_1 y)] \quad (15)$$

$$\tilde{E}_{z1} = \frac{-j}{k_1^2 + \gamma_1^2} [\beta_k \gamma_1 A_{1e} \sinh(\gamma_1 y) - (\mu_{x1} + \mu_{z1}) j \omega \mu_0 \alpha_n A_{1h} \sinh(\gamma_1 y)] \quad (16)$$

$$\tilde{H}_{x1} = \frac{-j}{k_1^2 + \gamma_1^2} [\alpha_n \gamma_1 A_{1h} \cosh(\gamma_1 y) - (\varepsilon_{x1} + \varepsilon_{z1}) j \beta_k \omega \varepsilon_1 A_{1e} \cosh(\gamma_1 y)] \quad (17)$$

$$\tilde{H}_{z1} = \frac{-j}{k_1^2 + \gamma_1^2} [\beta_k \gamma_1 A_{1h} \cosh(\gamma_1 y) + (\varepsilon_{x1} + \varepsilon_{z1}) j \omega \varepsilon_1 \alpha_n A_{1e} \cosh(\gamma_1 y)] \quad (18)$$

To the determination of the unknown constants described above the boundary conditions are applied in the structure shown in Fig. 1, in  $y = h_1$  and  $y = h = h_1 + h_2$ . The electromagnetic fields general equations as function of  $\tilde{E}_{xh}$  and  $\tilde{E}_{zh}$ , which are the tangential components of the electric fields are obtained to calculate the propagation constant.

$$\tilde{E}_{x1} = \tilde{E}_{x2}, \quad \tilde{H}_{x1} = \tilde{H}_{x2} \quad (19)$$

$$\tilde{E}_{z1} = \tilde{E}_{z2}, \quad \tilde{H}_{z1} = \tilde{H}_{z2} \quad (20)$$

After several calculations are obtained the following constant values:

$$A_{1h} = \frac{\beta_k \tilde{E}_{xy} - \alpha_n \tilde{E}_{zy}}{\sinh(\gamma_1 y) \omega \mu_0 (\mu_{xx} + \mu_{zz})} \quad (21)$$

$$A_{1e} = \frac{j(\alpha_n \tilde{E}_{xy} + \beta_k \tilde{E}_{zy})}{\gamma_1 \sinh(\gamma_1 y)} \quad (22)$$

$$A_{2e} = \frac{j(\alpha_n \tilde{E}_{xh} + \beta_k \tilde{E}_{zh})}{A} \left[ \frac{\gamma_1}{\gamma_2} \cosh(\gamma_2 h_2) \sinh(\gamma_1 h_1) - \frac{\varepsilon_1}{\varepsilon_2} \sinh(\gamma_2 h_2) \cosh(\gamma_1 h_1) \right] \quad (23)$$

$$A_{2h} = \frac{(\beta_k \tilde{E}_{xh} - \alpha_n \tilde{E}_{zh})}{\omega \mu B} \left[ \frac{\gamma_1}{\gamma_2} \cosh(\gamma_1 h_1) \cosh(\gamma_2 h_2) - \sinh(\gamma_1 h_1) \sinh(\gamma_2 h_2) \right] \quad (24)$$

$$B_{2e} = \frac{j(\alpha_n \tilde{E}_{xh} + \beta_k \tilde{E}_{zh})}{A} \left[ \frac{\varepsilon_1}{\varepsilon_2} \cosh(\gamma_1 h_1) \cosh(\gamma_2 h_2) - \frac{\gamma_1}{\gamma_2} \sinh(\gamma_1 h_1) \sinh(\gamma_2 h_2) \right] \quad (25)$$

$$B_{2h} = \frac{(\beta_k \tilde{E}_{xh} - \alpha_n \tilde{E}_{zh})}{\omega \mu B} \left[ \sinh(\gamma_1 h_1) \cosh(\gamma_2 h_2) - \frac{\gamma_1}{\gamma_2} \cosh(\gamma_1 h_1) \sinh(\gamma_2 h_2) \right] \quad (26)$$

$$A_{3h} = \frac{\beta_k \tilde{E}_{xy} - \alpha_n \tilde{E}_{zy}}{\omega \mu} \quad (27)$$

$$A_{3e} = \frac{-j(\alpha_n \tilde{E}_{xy} + \beta_k \tilde{E}_{zy})}{\gamma_3} \quad (28)$$

where

$$A = \gamma_1 \sinh(\gamma_1 h_1) \cosh(\gamma_2 h_2) + \gamma_2 \frac{\varepsilon_1}{\varepsilon_2} \cosh(\gamma_1 h_1) \sinh(\gamma_2 h_2) \quad (29)$$

$$B = \sinh(\gamma_1 h_1) \cosh(\gamma_2 h_2) + \frac{\gamma_1}{\gamma_2} \cosh(\gamma_1 h_1) \sinh(\gamma_2 h_2) \quad (30)$$

#### 4. ADMITANCE MATRIX

The following equations relate the current densities in the sheets ( $\tilde{J}_{xy}$  and  $\tilde{J}_{zy}$ ) and the magnetic fields in the interface  $y = h_1 + h_2$ :

$$\tilde{H}_{x2} - \tilde{H}_{x3} = \tilde{J}_z \quad (31)$$

$$\tilde{H}_{z2} - \tilde{H}_{z3} = -\tilde{J}_x \quad (32)$$

After the obtaining of the electromagnetic fields components, the magnetic boundary conditions are applied, being  $[Y]$  the dyadic Green matrix.

$$\begin{bmatrix} Y_{xx} & Y_{xz} \\ Y_{zx} & Y_{zz} \end{bmatrix} \begin{bmatrix} \tilde{E}_x \\ \tilde{E}_z \end{bmatrix} = \begin{bmatrix} \tilde{J}_x \\ \tilde{J}_z \end{bmatrix} \quad (33)$$

The matrix inversion is used and the current densities in the interface are expanded using base functions [4]:

$$\begin{bmatrix} Z_{xx} & Z_{xz} \\ Z_{zx} & Z_{zz} \end{bmatrix} \begin{bmatrix} \tilde{J}_{zh} \\ \tilde{J}_{xh} \end{bmatrix} = \begin{bmatrix} \tilde{E}_{xh} \\ \tilde{E}_{zh} \end{bmatrix} \quad (34a)$$

$$\tilde{J}_{xh} = \sum_{i=1}^n a_{xi} \cdot \tilde{f}_{xi}(\alpha_n, \beta_k) \quad (34b)$$

$$\tilde{J}_{zh} = \sum_{j=1}^m a_{zj} \cdot \tilde{f}_{zj}(\alpha_n, \beta_k) \quad (34c)$$

Applying the Galerkin technique, the electric fields out of the metallic strip are eliminated. The current densities are expanded in terms of appropriate basis functions, and become a homogeneous complex matrix as shown in (35).

$$\begin{bmatrix} K_{xx} & K_{xz} \\ K_{zx} & K_{zz} \end{bmatrix} \cdot \begin{bmatrix} a_x \\ a_z \end{bmatrix} = \begin{bmatrix} 0 \\ 0 \end{bmatrix} \quad (35)$$

Each element of the  $[K]$  characteristic matrix is shown in (36)–(39):

$$K_{xx} = \sum_{-\infty}^{\infty} \tilde{f}_x(x, z) Z_{xx} \tilde{f}_x^*(x, z) \quad (36)$$

$$K_{xz} = \sum_{-\infty}^{\infty} \tilde{f}_z(x, z) Z_{xz} \tilde{f}_x^*(x, z) \quad (37)$$

$$K_{zx} = \sum_{-\infty}^{\infty} \tilde{f}_x(x, z) Z_{zx} \tilde{f}_z^*(x, z) \quad (38)$$

$$K_{zz} = \sum_{-\infty}^{\infty} \tilde{f}_z(x, z) Z_{zz} \tilde{f}_z^*(x, z) \quad (39)$$

#### 5. RESULTS

Figure 3 shows the results of the resonance frequency depending on the length  $L$  of the patch resonator, simulated for two cases.

- Case 1: 1 layer dielectric substrate comprised of PBG 2D considering focusing on the wave polarization  $s$ , 2 dielectric layer composed of RT Duroid 5880 and dielectric layer 3 is the air;
- Case 2: 1 layer dielectric substrate comprised of PBG 2D considering focusing on the wave polarization  $p$ , 2 dielectric layers composed of RT Duroid 5880 and dielectric layer 3 is the air.

The analysis of Fig. 3, we can conclude that when the material PBG is the first layer beneath the patch irradiator, the frequency of resonance does not suffer significant changes with the change in the wave incidence in the substrate (polarization  $s$  or  $p$ ). This effect is due to difference in heights of layers, as the  $\epsilon_r = 2.2$  predominates on the PBG material.

Comparing the first two layers of the structure mentioned in Fig. 1, with another one antenna structure of one layer, we see that the results are similar, as shown in Fig. 4.

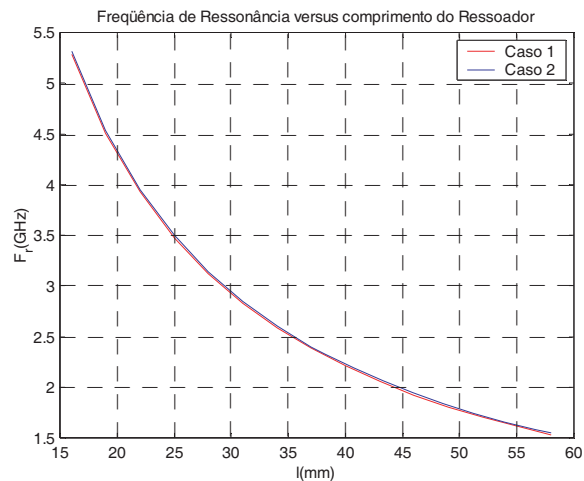


Figure 3: Frequency of resonance as a function on the length of patch material for PBG 2D for the polarization  $s$  or  $p$ .

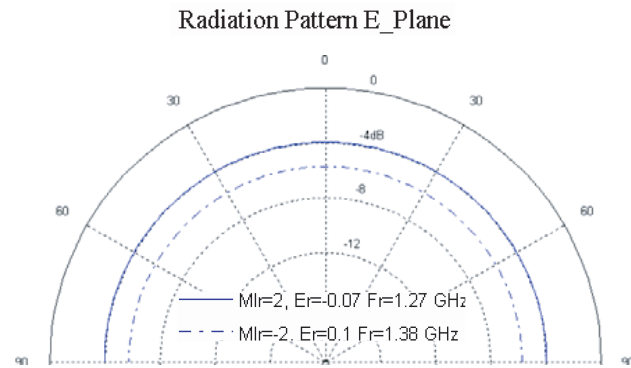


Figure 4: Radiation pattern  $E$ -plane.

## 6. CONCLUSIONS

The results obtained can be used to the design of novel meta-materials with potential applications in wireless systems.

The full wave Transverse Transmission Line — TTL method, was used to obtain the numeric results of the planar antennas with three metamaterial layers.

In this work, the insertion of the metamaterial influence was realized through of the use in tensor permeability and permittivity, and good results were obtained.

## REFERENCES

1. Caloz, C. and T. Itoh, *Electromagnetic Metamaterials: Transmission Line Theory and Microwave Applications*, Jonh Wiley & Sons, 2006.
2. Smith, D. R., P. Rye, D. C. Vier, A. F. Starr, J. J. Mock, and T. Perram, "Design and measurement of anisotropic metamaterial that exhibit negative refraction," *IEICE Trans. Electron.*, Vol. E87-C, No. 3, Mar. 3, 2004.
3. Fernandes, H. C. C. and G. D. F. Alves, "Meta-material multilayer substrate planar resonators with superconductive patch," *Progress In Electromagnetics Research Symposium Abstract*, Praha, Czech Republic, 2007.
4. Fernandes, H. C. C., H. D. de Andrade, D. B. Brito, and M. B. L. de Aquino, "Rectangular slot resonator with four dielectrics layers," *PIERS Proceedings*, 2121–2126, Beijing, China, March 26–30, 2007.
5. Fernandes, H. C. C. and D. B. Brito, "Unilateral fin line directional coupler," *International Journal of Infrared and Millimeter Waves*, Vol. 28, No. 8, 651–661, USA, 2007, ISSN 0195-9271.

# Design and Analysis of Resonant Leaky-mode Broadband Reflectors

M. Shokooh-Saremi and R. Magnusson

Department of Electrical and Computer Engineering, University of Connecticut  
371 Fairfield Road, U-2157, Storrs, CT 06269-2157, USA

**Abstract**— Devices based on the guided-mode resonance (GMR) effect are very promising elements in the areas of optics and electromagnetics. They can provide variety of spectral responses only founded on periodically patterning of a single optical layer on a substrate or as a free-standing membrane. Although the main manifestation of the GMR effect is sharp resonances in the reflection spectra, by proper selection of device parameters, attainment of variety of optical spectral responses such as narrow bandpass/bandstop filters, broadband reflectors, polarizers and so on is possible. Since in this kind of elements, light is coupled into waveguide leaky modes through a subwavelength grating structure, the device works in the second (leaky) stopband. Response of such devices is highly dependent on the modal characteristics of the guiding layer. Broadband high reflectors, based on periodically patterned single layers (with substrate or as a membrane), are promising and attractive elements in the area of optical devices and have recently found practical application as top mirror in tunable vertical cavity surface emitting lasers (VCSELs). In this paper, a single layer, strongly-modulated GMR-based broadband high reflector is designed for 1.45–2.0  $\mu\text{m}$  band for TE and TM polarizations using particle swarm optimization (PSO) technique; a robust, easy to implement evolutionary technique inspired from the behavior of particles in a swarm searching for their requirements resources. A silicon-on-insulator (SOI) structure has been chosen in which the binary patterned silicon layer act as both grating and waveguide. The spectral and modal characteristics of these elements are analyzed utilizing rigorous electromagnetic techniques like rigorous coupled-wave analysis (RCWA) and modal techniques. The designed reflector for TM and TE polarizations provide  $\sim 520$  nm and  $\sim 125$  nm bandwidth at  $> 99\%$  reflectance, respectively. Also, showing the reflection and transmission maps as well as the mode profiles, we investigate the effect of refractive index modulation and the thickness of the grating on device's spectral response.

## 1. INTRODUCTION

Devices based on the guided-mode resonance (GMR) effect are promising in areas of optics and optical engineering [1, 2]. They can provide variety of spectral responses based on periodically patterning of a single optical layer on a substrate or as a free-standing membrane [3, 4]. Although the main manifestation of the GMR effect is a sharp, Lorentzian-shape resonance in the reflection spectra, by proper selection of device parameters, attainment of variety of optical spectral responses is possible [3–5]. Recently, there have been reports on the potential application of single-layer, one-dimensional guided-mode resonance (GMR) gratings as optical elements like narrow bandpass/bandstop filters, broadband reflectors, and polarizers [3]. These devices are based on the resonant coupling of an incident light beam into a light-guiding layer through a surface relief diffraction grating. The period of the grating, its thickness, and the refractive indices of comprising materials and their distribution along the period, as well as the refractive indices of surrounding media, are basic parameters of a GMR element. These parameters can greatly influence the behavior of the device, since GMR devices are proven to be highly sensitive to their structural parameters. In a single layer device, the subwavelength grating acts as the incident light coupler as well as the light guiding medium. The subwavelength grating couples the incident light into leaky waveguide mode(s), provided that the phase matching condition is satisfied. Since the light is coupled into leaky modes, the device works in the second (leaky) stopband [6]. The spectral response of such devices is highly dependent on the modal characteristics of the guiding layer.

Broadband high reflectors, based on periodically-patterned single layers (on a substrate or as membranes), are useful in many optics applications and have recently found practical application as mirrors in vertical cavity surface emitting lasers (VCSELs) [7]. The objective of this paper is to provide insights into the electromagnetic properties of these kinds of optical elements. Accordingly, in this paper, broadband high reflectors are designed for the 1.45–2.0  $\mu\text{m}$  band using particle swarm optimization (PSO) technique and their spectral and modal behavior for both TE and TM polarizations is studied and discussed.

## 2. DEVICE STRUCTURE AND DESIGN

Figure 1 illustrates the structure of the device. It is basically a silicon-on-insulator (SOI) element. The grating layer, which also acts as the waveguide, is defined by its period ( $\Lambda$ ), thickness ( $d$ ), and filling factor ( $F$ ). For designing the broadband reflector, normal incidence and both TE and TM polarizations are considered. The grating period has two sections consisting two materials with different refractive indices; one of them has higher refractive index ( $n_H > n_L$ ).

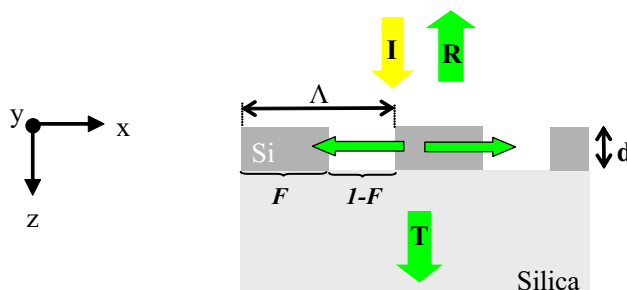


Figure 1: Schematic of a typical single-layer, silicon-on-insulator GMR device.  $\Lambda$ ,  $d$  and  $F$  are period, thickness, and filling factor, respectively. The incidence medium is air ( $n = 1.0$ ) and the substrate is silica ( $n = 1.48$ ). The case of normal incidence is treated here.

The particle swarm optimization (PSO) technique is utilized to design the broadband reflector. The design target is set to be 100% reflectance over the  $1.45 \mu\text{m}$  to  $2.0 \mu\text{m}$  band. The parameters to be optimized by the PSO to achieve the target reflectance are taken to be  $\Lambda$ ,  $d$ , and  $F$ . The basics of the PSO technique for designing diffraction gratings have been reported elsewhere [8].

## 3. FEATURES OF THE BROADBAND HIGH REFLECTORS

### 3.1. TM Polarization

Figures 2(a) and (b) show the reflectance and transmittance spectra (linear and logarithmic scales) of the designed two-part, SOI, broadband high reflector for TM polarization, in which  $\Lambda = 0.766 \mu\text{m}$ ,  $d = 0.490 \mu\text{m}$ , and  $F = 0.726$ . The width of the high reflectance band ( $R_0 > 0.99$ ) is  $\sim 520 \text{ nm}$  over  $1.45$  to  $2.0 \mu\text{m}$  range. As seen in Fig. 2(b), there are three transmittance dips inside the reflection band, each of which corresponds to a guided-mode resonance. It should be noted that under guided-mode resonance conditions, in which the incident light is coupled into a leaky waveguide mode, the transmittance theoretically approaches zero. Therefore, Fig. 2 shows co-existence, or a blend, of three modes. Figure 3(a)–(c) illustrates the amplitude of the magnetic (modal) field ( $H_y(z)$ ) inside the grating structure and also in the surrounding media for the three resonances at  $1.495$ ,  $1.620$ , and  $1.839 \mu\text{m}$  and for the zeroth, first and second diffraction orders. As displayed, the modal

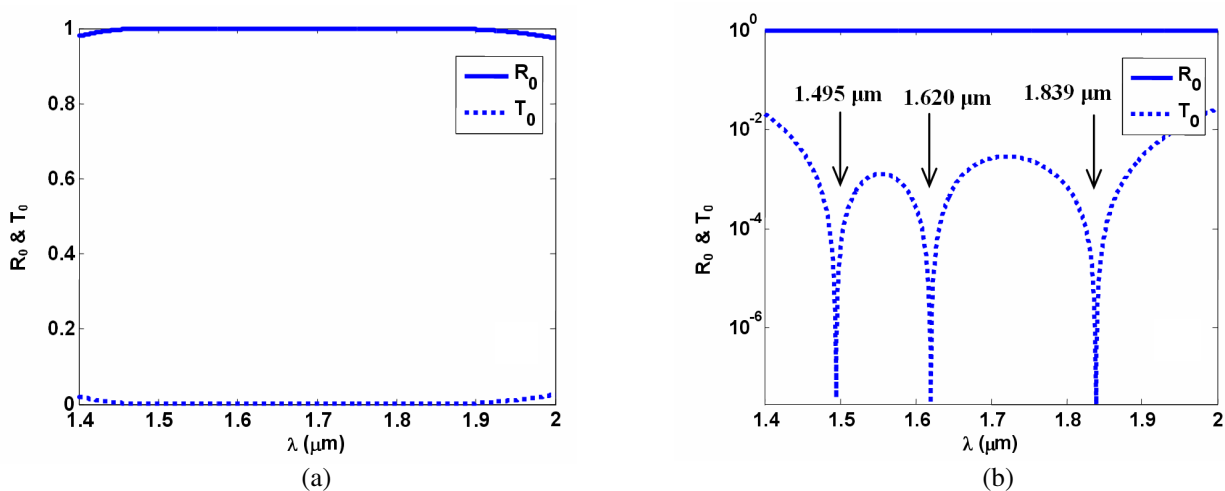


Figure 2: Reflectance and transmittance spectra (a) linear and (b) logarithmic scale of the broadband TM reflector.

profiles for the first diffraction order ( $S_1$ ) at three resonant wavelengths show mixed mode states.

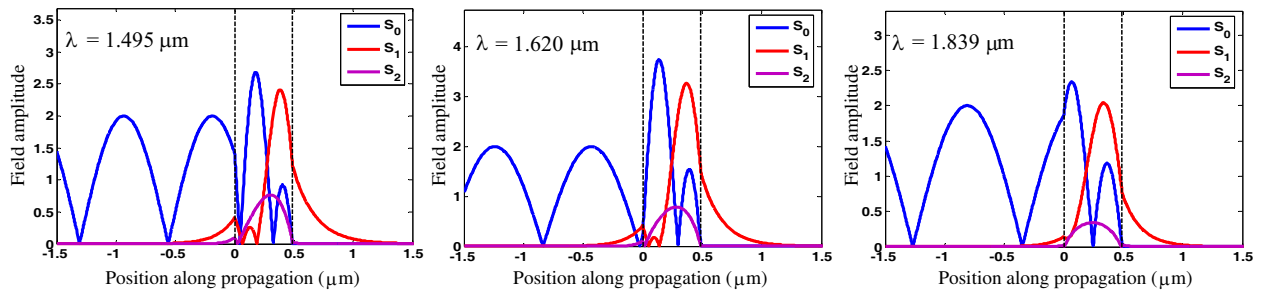


Figure 3: Amplitude of the magnetic (modal) field inside the grating structure and the surrounding media for the three resonances.

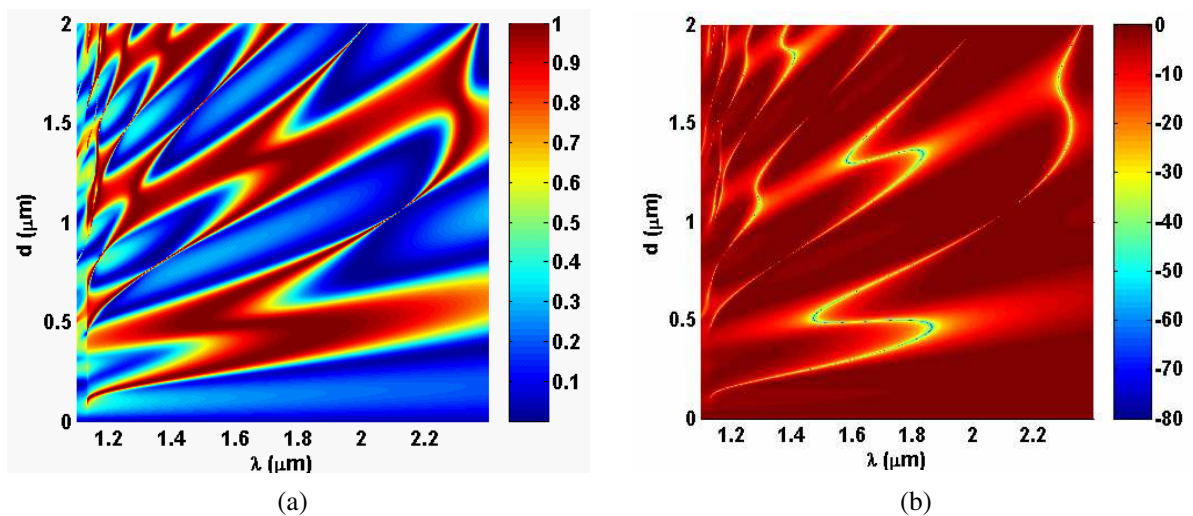


Figure 4: (a) Color-coded reflectance map  $R_0(\lambda, d)$  drawn versus wavelength and grating thickness. (b) Transmittance map  $T_0(\lambda, d)$  in dB.

Figure 4(a) displays a color-coded reflectance map  $R_0(\lambda, d)$  drawn versus wavelength and grating thickness. This map shows the qualitative modal behavior of the grating structure, which is highly dependent on the thickness. As evident from Fig 4(a), “S” shaped high-reflection areas

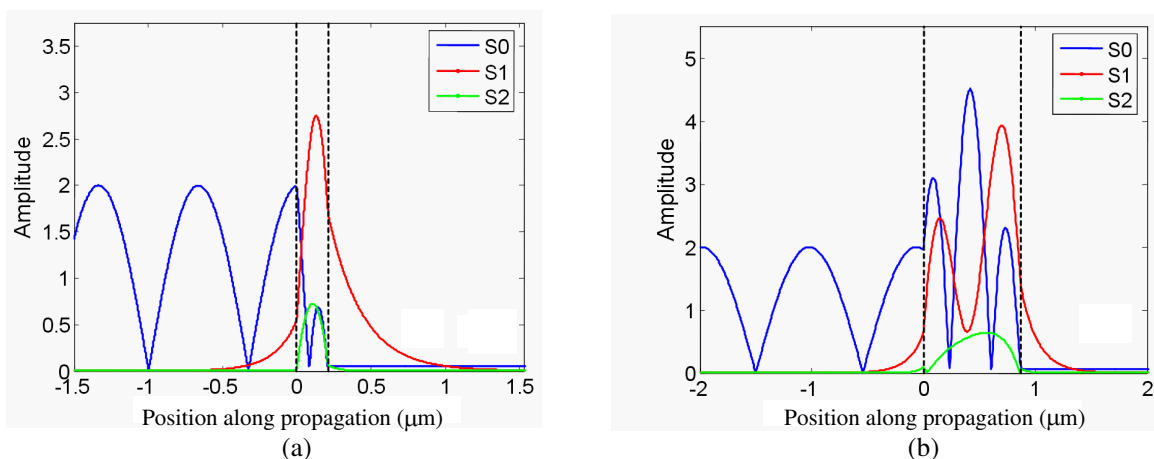


Figure 5: Modal field profiles for two resonance points far from the broadband reflection region, (a)  $d = 0.212 \mu\text{m}$  and  $\lambda = 1.345 \mu\text{m}$ , (b)  $d = 0.870 \mu\text{m}$  and  $\lambda = 1.919 \mu\text{m}$ .

show the evolution of the reflection band from a nearly single narrow resonance to a broad one. Figure 4(b) illustrates the associated transmittance versus wavelength and thickness in dB. As seen, the transmittance dip also has an “S” shape. The calculations for the reflection spectra are done using rigorous coupled-wave analysis (RCWA) [9] and modal analysis techniques [10]. Both methods yield results that are in complete agreement. Figure 5 shows the modal field profiles for two points on the reflection band in Fig. 4(a) but far from the broadband reflection region. As seen, for thicknesses well below the design thickness,  $TM_0$  is the main excited leaky mode, while above the design thickness  $\sim TM_1$  is excited.

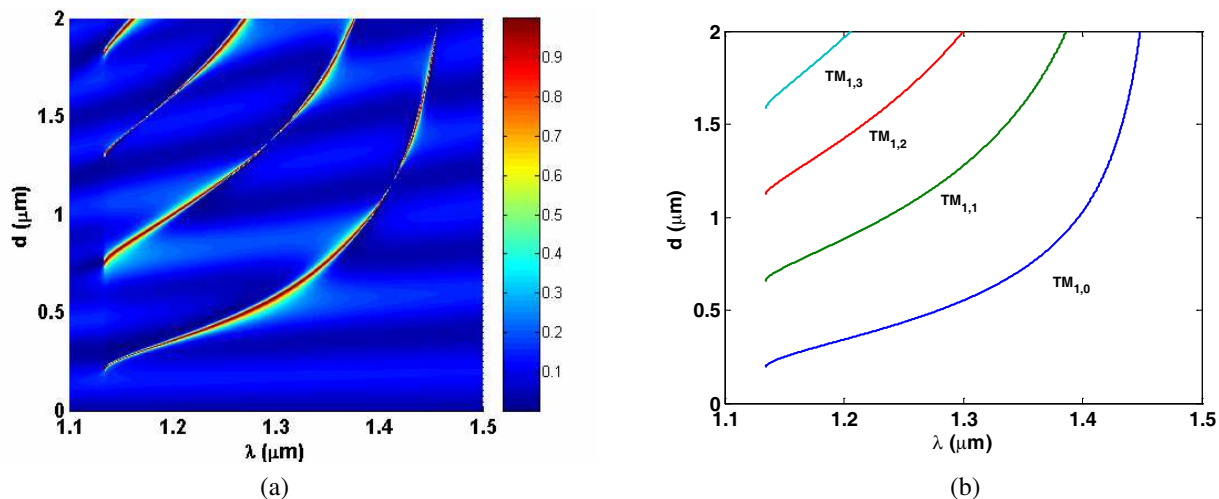


Figure 6: (a)  $R_0(\lambda, d)$  map for low refractive index modulation;  $n_H = 2.0$ ,  $n_L = 1.3417$ . (b) Calculated modal curves for the first four modes excited by the first diffraction order considering a thin film waveguide with  $n_f = 1.92$ .

The  $R_0(\lambda, d)$  map in Fig. 4(a) can be considered as a qualitative counterpart for modal curves of an equivalent homogeneous slab waveguide. Modal curves can be obtained by solving the eigenvalue equation of the equivalent homogenous slab waveguide system [4]. To investigate the modal behavior of this system and provide a clearer view of the physics, we reduce the index modulation of the structure while keeping the average refractive index of the waveguide layer fixed at 1.7314 (zero-order effective index) [1]. This reduces the linewidth of the resonances and enhances the visibility of the modal curves. By considering  $n_H = 2.0$  and  $n_{ave} = 1.7314$ ,  $n_L$  is calculated to be 1.3417. Figure 6 shows the  $R(\lambda, d)$  map for this low-index modulation structure as well as the calculated

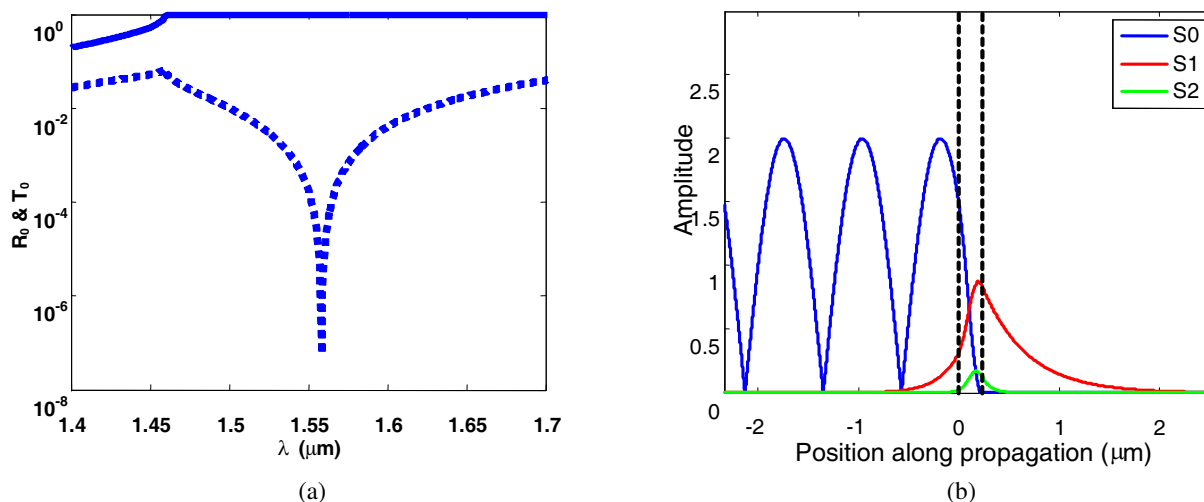


Figure 7: (a) Reflectance (solid line) and transmittance (dashed line) spectra of the designed reflector for TE polarization (in logarithmic scale). (b) Amplitude of electric field in the grating layer and incident and substrate media ( $\lambda = 1.559 \mu\text{m}$ ).

modal curves for the first four modes excited by the first diffraction order considering  $n_f = 1.92$ . It is seen that there is a good qualitative agreement between the two graphs. Also, this shows that in single layer broadband high reflector, a modal mixture takes place when a high refractive index contrast is present and will make different modes contribute to the broadband reflection. The value of  $n_f$  is also qualitatively in reasonable agreement to the second-order effective index of the equivalent homogenous layer which is 1.82 [1].

### 3.2. TE Polarization

Broadband high reflector can be also designed to work with TE polarized incident light. Using PSO as the design tool, a two-part period reflector is designed for the 1.45–1.7  $\mu\text{m}$  band based on a SOI structure. The designed parameters are:  $\Lambda = 0.986 \mu\text{m}$ ,  $d = 0.228 \mu\text{m}$ , and  $F = 0.329$ . Figure 7(a) illustrates the reflectance and transmittance spectra of the device in logarithmic scale. The transmission dip, which shows the resonance wavelength, falls at 1.559  $\mu\text{m}$ . The reflection band of the filter for  $R_0 > 0.99$  is  $\sim 125 \text{ nm}$ . Figure 7(b) shows the amplitude of electric field in the grating layer as well as in incident and substrate media. As evident from this figure, the leaky mode has  $\sim \text{TE}_0$  characteristics.

Figure 8(a) displays a color-coded map  $R_0(\lambda, d)$ , which qualitatively represents the modal behavior of the device. As seen in this figure, at the design thickness ( $d = 0.228 \mu\text{m}$ ), the reflection spectrum exhibits maximum width. Figure 8(b) shows the  $T_0(\lambda, d)$  map in dB, in which the blue traces represent the position of the resonance. In this structure, in part due to higher modal cut-off wavelength than for TM, a kind of folding back regions appear. The zero-order effective medium refractive index (average refractive index) of the structure is 2.159 and the second-order effective

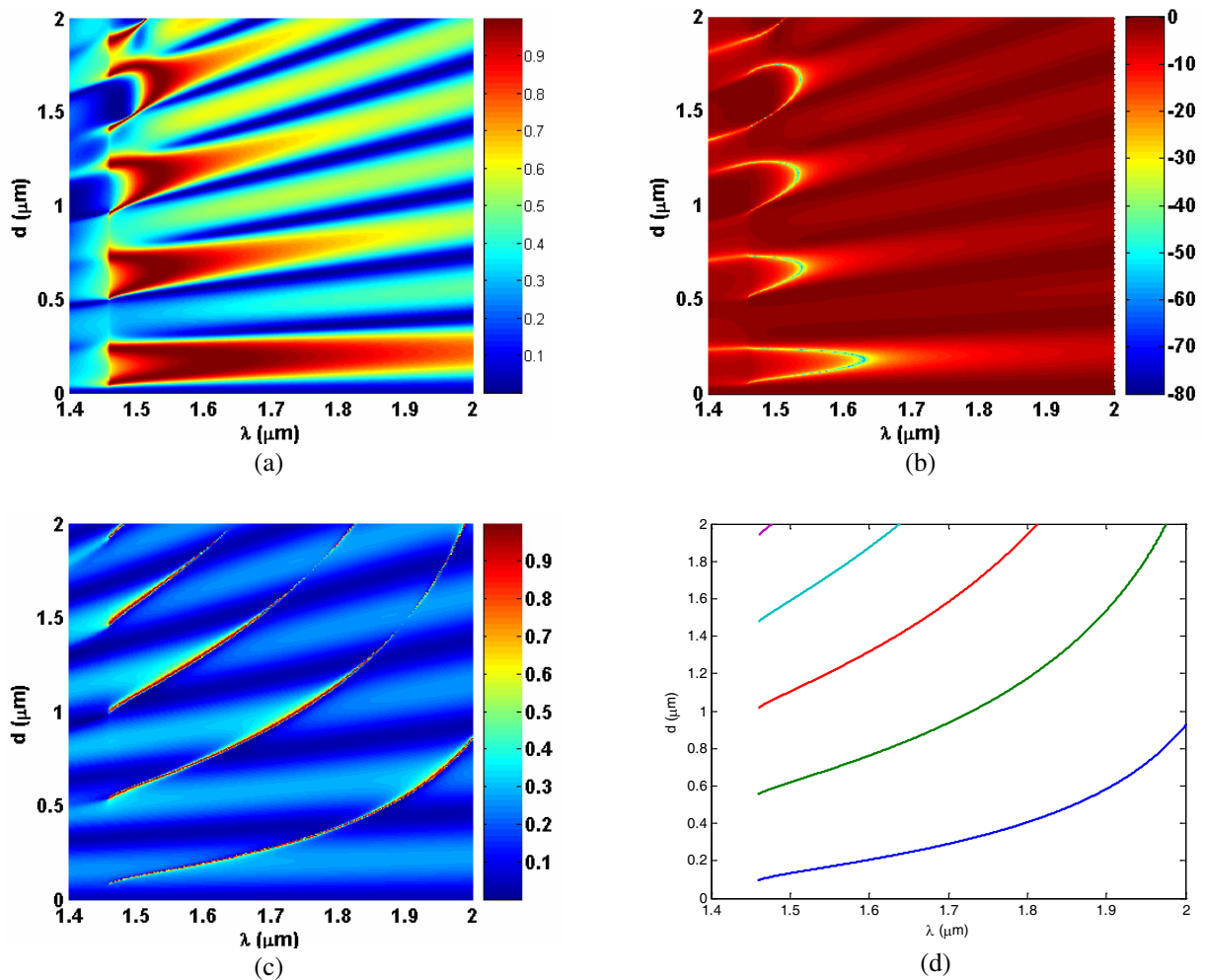


Figure 8: (a)  $R_0(\lambda, d)$  map for the reflector designed for TE polarization. (b)  $T_0(\lambda, d)$  map in dB. (c) Reflection map for the reduced refractive index modulation structure ( $n_H = 2.3$  and  $n_L = 2.086$ ) and (d) Modal characteristic curves for the equivalent homogeneous layer with refractive index of  $n_f = 2.1696$ .

medium refractive index is 3.365. Keeping the average refractive index fixed, by reducing the refractive index contrast, the reflection map can qualitatively represent the leaky-mode curves of the equivalent homogenous layer. Figure 8(c) shows the reflection map for the reduced modulation structure ( $n_H = 2.3$  and  $n_L = 2.086$ ) and Fig. 8(d) illustrates the modal characteristic curves for the equivalent homogeneous layer with refractive index assumed to be  $n_f = 2.1696$ , which is the second order effective medium refractive index of the structure at  $1.7\ \mu\text{m}$ . There is a clear resemblance between the two figures, showing the modal origin of the broad reflection spectra, as in the TM case.

#### 4. CONCLUSIONS

In this paper, we have presented the basics of the broadband high reflector rooted in guided-mode resonance effect. The modeling and simulation results of this device show that the high refractive index contrast of the grating can be responsible for exciting a blend of leaky modes and providing the maximum reflection linewidth for the optimal design parameters. It is important to use effective inverse methods to determine the parameters providing the proper spectra. Broadband high reflectors with two-part periods have been designed for both TE and TM polarizations. The design and analysis results show that a maximum reflection linewidth can be obtained by incorporating a mixture of TE or TM modes.

#### ACKNOWLEDGMENT

This material is based, in part, upon work supported by NSF under Grant No. ECS-0524383.

#### REFERENCES

1. Magnusson, R. and D. Shin, "Diffractive optical components," *Encyclopedia of Physical Science and Technology*, 3rd ed., Vol. 4, 421–440, 2002.
2. Kikuta, H., H. Toyota, and W. Yu, "Optical elements with subwavelength structured surfaces," *Optical Review*, Vol. 10, 63–73, 2003.
3. Ding, Y. and R. Magnusson, "Resonant leaky-mode spectral-band engineering and device applications," *Opt. Express*, Vol. 12, 5661–5674, 2004.
4. Wang, S. S. and R. Magnusson, "Theory and applications of guided-mode resonance filters," *Appl. Opt.*, Vol. 32, 2606–2613, 1993.
5. Tibuleac, S. and R. Magnusson, "Reflection and transmission guided-mode resonance filters," *J. Opt. Soc. Am A*, Vol. 14, 1617–1626, 1997.
6. Ding, Y. and R. Magnusson, "Band gaps and leaky-mode effects in resonant photonic-crystal waveguides," *Opt. Express*, Vol. 15, 680–694, 2007.
7. Huang, M. C. Y., Y. Zhou and C. J. Chang-Hasnain, "A surface-emitting laser incorporating a high-index-contrast subwavelength grating," *Nature Photonics*, Vol. 1, 119–122, 2007.
8. Shokooch-Saremi, M. and R. Magnusson, "Particle swarm optimization and its application to the design of diffraction grating filters," *Opt. Lett.*, Vol. 32, 894–896, 2007.
9. Gaylord, T. K. and M. G. Moharam, "Analysis and applications of optical diffraction by gratings," *Proc. IEEE*, Vol. 73, 894–937, 1985.
10. Peng, S. T., T. Tamir, and H. L. Bertoni, "Theory of periodic dielectric waveguides," *IEEE Trans. Microwave Theory Tech.*, Vol. 23, 123–133, 1975.

# Design of Two-band 150–220 GHz Superconducting Bolometric Detection Structure

D. Raully<sup>1</sup>, A. Monfardini<sup>2</sup>, A. Colin<sup>3</sup>, and P. Febvre<sup>1</sup>

<sup>1</sup>IMEP-LAHC, UMR 5130 CNRS/INPG/UJF/USAVOIE  
MINATEC, Grenoble and Le Bourget du Lac, France

<sup>2</sup>Institut Néel, CNRS/UJF dept MCBT, Grenoble, France

<sup>3</sup>Instituto de Fisica de Cantabria (CSIC-UC), Santander, Spain

**Abstract**— We propose a pixel design, aimed to be included in an array, receiving and detecting simultaneously two bands of the Cosmic Microwave Background (CMB). It is composed of a bowtie antenna, feeding a diplexer structure to separate the signal towards two bolometric detectors at 150 and 220 GHz. The diplexer makes use of differential transmission lines of Coplanar Striplines (CPS) and Broadside Coupled Lines (BCL) types, for filtering and separation purposes. The antenna and diplexer are planned to be fabricated in a superconductive niobium thin film deposited on a Silicon substrate, while NbSi bolometers will lie on a SiN membrane. The device has been simulated by means of ADS (Agilent), CST Microwave Studio and HFSS (Ansoft) softwares. Final dimensions that take into account the kinetic inductance of the superconducting lines are proposed. Promising computation results are found, with signal separation up to 20 dB.

## 1. INTRODUCTION

Nowadays, a large number of astrophysical studies based on CMB observation require multi-band measurements. As an example, the detection of clusters of remote galaxies can be performed by comparing CMB photon fluxes at 150 and 220 GHz, using the model of spectral deformation of the Planck law, due to the Sunayev-Zeldovich (SZ) effect [1].

This requirement can be met by means of optical filtering, defining appropriate photometric bands, but it generally consumes a higher surface of the available focal plane. Multi-frequency detector arrays, using antenna-coupled bolometers associated with filtering functions may overcome this problem. These functions are classically achieved by millimeter circuits composed of planar transmission lines. Several designs, based on microstrip lines, have been proposed in the past [2, 3].

Microstrip transmission lines are often used coupled with slot antennas [4]. However, when an antenna of differential type is used, like a bow-tie antenna, a balun must be inserted between the feeding microstrip line and the antenna, in order to keep the symmetry of the currents repartition in the structure and not to affect the radiation pattern.

The design presented in this paper (see Fig. 5) proposes a bow-tie antenna coupled to a diplexer circuit exclusively composed of balanced differential transmission lines, thus avoiding the need for a balun. The strategy for elaborating the whole diplexer structure, consists of utilizing high-impedance CPS lines connected on one end to the source antenna, and to the other end to the low-impedance BCLs. The BCLs are connected to the resistive bolometers on their other end (see Fig. 5). CPS lines facilitate the decoupling between both 150 and 220 GHz sub-circuits, while BCLs lower the influence of the membrane supporting the loads and the bolometers.

## 2. ANTENNA DESIGN

The antenna is a bow-tie fabricated with superconductive Nb on 30  $\mu\text{m}$ -thick Si substrate, with a reflector back plane located 300  $\mu\text{m}$  below the antenna plane. The two triangles of the antenna (height 580  $\mu\text{m}$  and base 580  $\mu\text{m}$ ) are separated by a 2  $\mu\text{m}$  gap. Fig. 1 shows other geometric parameters for the computation. The metallization has been assumed to be 1  $\mu\text{m}$ -thick perfect conductor material. Open radiation type boundaries have been defined for the surrounding box.

Figure 2 compares results computed by HFSS (Ansoft) and CST Microwave Studio softwares, in terms of real and imaginary part of the antenna impedance, seen from the 2- $\mu\text{m}$  gap.

It exhibits an out-of band resonance at 100 GHz, found somewhat sharper with CST than with HFSS. Both results show good fit for the impedance values  $Z_{ant} = 54.2 - j84.0 [\Omega]$  at 150 GHz and  $Z_{ant} = 108.7 + j8.5 [\Omega]$  at 220 GHz. Consequently, the diplexer structure studied in the next paragraph must be designed in order to deliver the complex conjugate of the antenna impedance, for optimal microwave power matching.

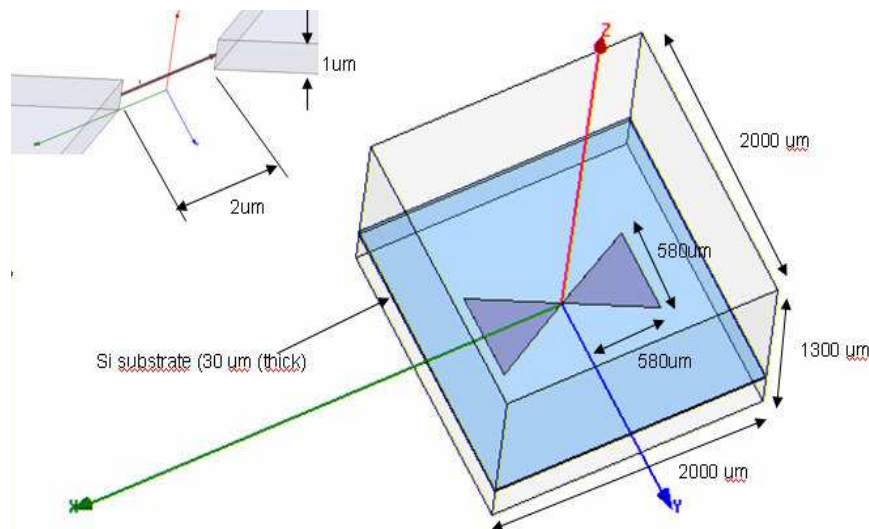


Figure 1: Geometry of the bow-tie antenna with HFSS-CST computation parameters.

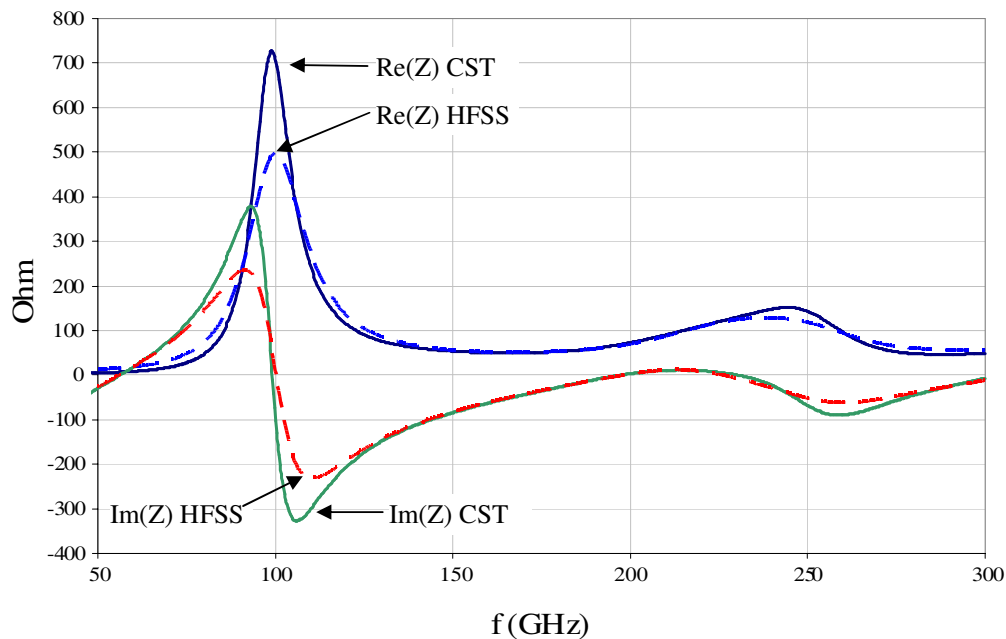


Figure 2: HFSS and CST computed antenna complex impedance.

### 3. DIPLEXER DESIGN

The diplexer is designed according to the simple scheme shown in Fig. 3. At this step of the project development, no severe slope has been specified for the transmission coefficient versus frequency variation. Focus is put on low insertion losses at the desired frequency, and high rejection at the undesired frequency. In this approach, each filtering sub-circuit is thus composed by only two transmission line elements, in order to meet the low-size requirement for the whole device.

In Fig. 3, Port 1 represents the antenna, modeled by its complex impedance imported from HFSS and CST computations (see Fig. 2), while Ports 2 and 3 represent the resistive loads associated to the bolometric detection. ADS Optimization has been performed with 0-dB-goals for  $S_{21}$  and  $S_{31}$  at 150 and 220 GHz respectively.

Optimized values of the characteristics impedance and electrical lengths (degrees) of the lines are given in Fig. 3. The corresponding results are plotted in Fig. 4, in terms of reflection and transmission coefficients. It exhibits return losses and signal separation better than 20 dB, with 0 dB insertion losses at the central frequencies. Undesirable transmissions occur at 110 and 290 GHz

towards the 220-GHz and 150-GHz detectors respectively, but they can be filtered, by means of a 120–240 GHz optical filter using combined metal cross-mesh and low-pass.

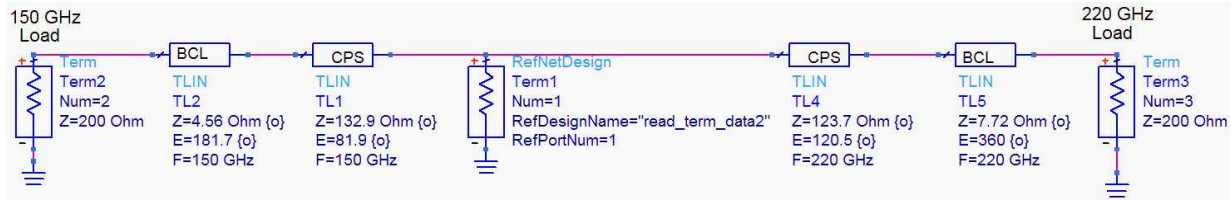


Figure 3: Schematics of the diplexer.

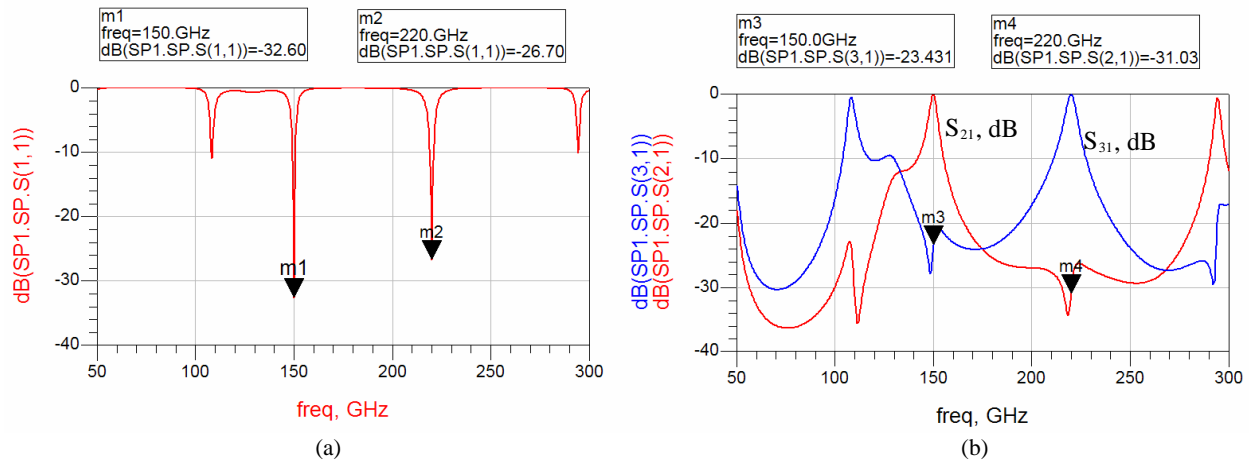


Figure 4: (a) Reflection coefficient of the structure, seen from the antenna port. (b) Transmission coefficients from antenna to 150-GHz load ( $S_{21}$  dB) & 220-GHz load ( $S_{31}$  dB).

#### 4. LAYOUT AND PHYSICAL DIMENSIONS

The whole device is represented in Fig. 5. Notice that the strips in CPS lines TL1 and TL4 are vertically offsetted by a  $0.3 \mu\text{m}$   $\text{SiO}_2$  layer in order to permit the transition to the BCLs.

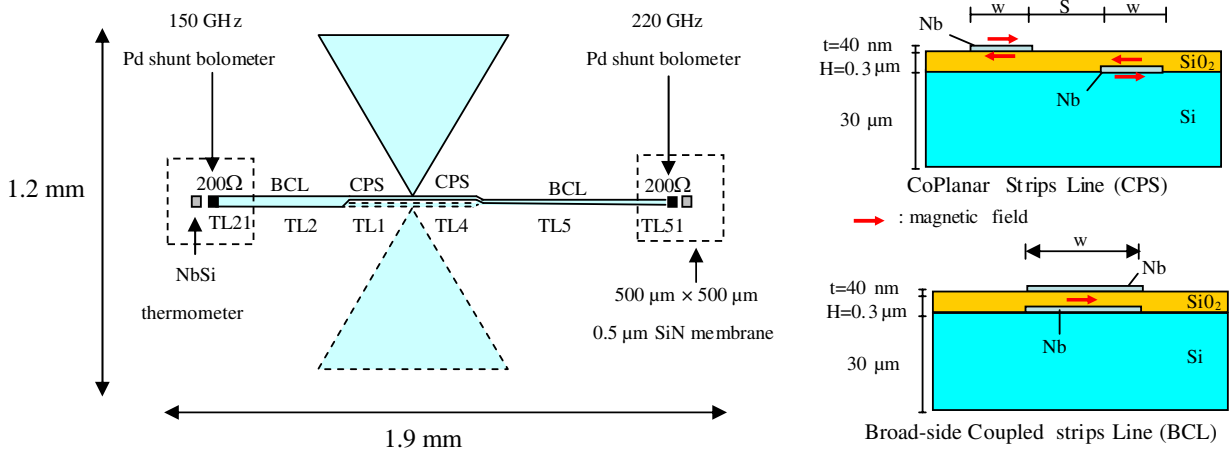


Figure 5: Left: Layout of one pixel of the detector structure. Right: Cross-section of CPS lines and BCLs.

Physical dimensions of the transmission lines have been determined using an iterative procedure. In a first step, geometrical (or external) line inductance  $L_{geo}$  and capacitance  $C$  have been deduced from CST simulations assuming perfect conductor materials, as shown in Table 1. Next, the kinetic inductance, inherent to the superconducting state of niobium material at 0.1 K is evaluated as follows [5].

Table 1: Final dimensions of the structure and calculations of lines parameters with  $\lambda_L = 39$  nm.

TL	Phys. dim. $\mu\text{m}$	$Z_c, \Omega$ , CST (perf. cond)	$\epsilon_{\text{eff}}$ , CST (perf. cond.)	$L_{\text{geo}}$ , nH/m	C, pF/m	$2 \cdot L_{\text{kin}}$ nH/m	$Z_{\text{superc}}, \Omega$ (eq.3)	$Z_{\text{superc}}, \Omega$ HFSS	$Z_c, \Omega$ required
<b>TL1:</b> CPS	W=3.6 $\mu\text{m}$ S=10 $\mu\text{m}$ L = 186 $\mu\text{m}$	129.9	5.8	1042	61.7	28.8	<b>131.7</b>	<b>133.1</b>	132.9
<b>TL2:</b> BCL	W=14 $\mu\text{m}$ H=0.3 $\mu\text{m}$ L = 441 $\mu\text{m}$	3.9	3.8	25	1693	9.1	<b>4.5</b>	<b>4.8</b>	4.6
<b>TL4:</b> CPS	W= 4.5 $\mu\text{m}$ S=10 $\mu\text{m}$ L = 186 $\mu\text{m}$	122.5	5.80	988	65.9	23.1	<b>123.9</b>	<b>127</b>	123.7
<b>TL5:</b> BCL	W=8 $\mu\text{m}$ H=0.3 $\mu\text{m}$ L = 597 $\mu\text{m}$	6.6	3.8	43	978	16	<b>7.8</b>	<b>8.3 (Si)</b> <b>7.8 (memb)</b>	7.7

For the BCLs, we assumed that the magnetic field is confined between strips, without variation in the transverse direction (horizontal in Fig. 5) due to the high aspect ratio of the BCLs. Thickness  $t$  is taken into account since it is of the same order of magnitude as the London penetration depth ( $\lambda_L = 39$  nm for bulk Nb), and the commonly adopted assumption  $t \gg \lambda_L$  is no more applicable here. As the temperature 0.1 K is far from the critical temperature of Nb 9.2 K, the electrical conductivity  $\sigma$  is assumed purely imaginary [6]. The kinetic inductance can be written as follows, where  $W$  is the strip width [5]:

$$L_{\text{kin-BCL}} = \mu_0 \frac{\lambda_L}{W} \coth\left(\frac{t}{\lambda_L}\right) [\text{H/m}] \quad (1)$$

For the CPS lines, attention must be paid to the magnetic field repartition, which can be considered equal, but of opposite signs, on upper and lower surfaces of the strip (see Fig. 1). The kinetic inductance then becomes [5]:

$$L_{\text{kin-CPS}} = \mu_0 \frac{\lambda_L}{2W} \coth\left(\frac{t}{2\lambda_L}\right) [\text{H/m}] \quad (2)$$

Then, assuming that all superconducting films have the same London penetration depth and thickness  $t$ , the final expression of the characteristic impedance  $Z_{\text{superc}}$  and electrical length  $E$  are:

$$Z_{\text{superc}} = \sqrt{\frac{L_{\text{geo}} + 2L_{\text{kin}}}{C}} \quad (3)$$

$$E = 360 \sqrt{(L_{\text{geo}} + 2L_{\text{kin}})C} \cdot F \cdot P [\text{degrees}] \quad (4)$$

where  $F$  is the frequency and  $P$  the physical length. Table 1 gives the calculations and final dimensions of the lines composing the diplexer. An imposed part (250  $\mu\text{m}$ ) of BCLs lines length is lying on the SiN membrane, but negligible correction (2%) of the strip width has been found in order to keep constant the characteristic impedance and the effective permittivity.

These results are then compared with HFSS computations where the superconductive strips are replaced by a boundary surface with purely reactive surface impedance as in reference [5]. Low dispersive effects have been found ( $Z_c$  varies less than 0.5%) but greater influence of the membrane on BCLs is revealed (see Table 1).

## 5. CONCLUSIONS

The design of a two band 150–220 GHz detection structure, with pixel-size and 20 dB signal separation requirements, has been revealed feasible. It implies rigorous modeling of the superconducting transmission lines, and the method proposed in this paper could be applied to other structures for similar applications.

**REFERENCES**

1. Nati, F., et al., “The OLIMPO experiment,” *New Astronomy Reviews*, Vol. 51, 385–389, 2007.
2. Kuo, J. and E. Shih, “Microstrip stepped-impedance resonator bandpass filter with an extended optimal rejection bandwidth,” *IEEE Trans. MTT*, Vol. 51, No. 5, 1554–1559, May 2003.
3. Meyers, M. J., et al., “An antenna-coupled bolometer with an integrated microstrip bandpass filter,” *APL* 86, 114103, 2005.
4. Knorr, J. B., “Slot line transition,” *IEEE Trans. MTT*, Vol. 22, No. 5, 548–554, May 1974.
5. Febvre, P., C. Boutez, S. George, and G. Beaudin, “Models of superconducting microstrip and coplanar elements for submillimeter applications,” *Proc. of the Int. Conf. on Millimeter and Submillimeter Waves and Applications II*, Vol. SPIE 2558, 136–147, San Diego Convention Center, July 9–14, 1995.
6. Mattis, D. C. and J. Bardeen, “Theory of anomalous skin effect,” *Phys. Rev.*, Vol. 111, No. 2, 412–417, 1958.

# Stability and Interactions of Moving Bragg Grating Solitons in a Semi-dual Core System

Yazhuo Li and Javid Atai

School of Electrical and Information Engineering, The University of Sydney, NSW, 2006, Australia

**Abstract**— In this paper, we investigate the existence of moving solitons in the model proposed in Ref. [5]. Using the relaxation technique we have been able to obtain moving soliton solutions. The stability of these solitons are investigated numerically. A key finding is that for fixed parameters the stability borders depend on the velocity of solitons and detuning frequency. We have also considered the collision of counterpropagating in-phase and  $\pi$ -out-of-phase moving solitons in this model.

## 1. INTRODUCTION

Periodic modulation of the linear dielectric constant in an optical medium results in a photonic band structure. This band structure gives rise to a cross-coupling between counterpropagating waves. As a result, such a medium becomes highly dispersive. An example of an optical medium with these characteristics is a fiber Bragg grating (BG). In this case, the effective dispersion due to the grating is approximately 6 orders of magnitude greater than the underlying chromatic dispersion of the fiber. At sufficiently high intensities the BG-induced dispersion may be counterbalanced by Kerr nonlinearity resulting in a Bragg grating soliton.

BG solitons have been the subject of intense theoretical and experimental research over the past three decades (see for example Refs. [1–4]). It has been shown that BG solitons in a uniform Bragg grating form a two-parameter family of solutions. One of these parameters is related to soliton's velocity, which can range between zero and the speed of light in the medium, and the other is dependent on the detuning frequency, peak power and soliton width. Due to their potential application in optical buffers and storage devices, significant efforts have been directed toward the generation of zero-velocity (quiescent) solitons. To date, moving BG solitons with a velocity in excess of 50% of speed of light have been observed. The existence and stability of solitons have also been investigated in more sophisticated systems. For instance, in Ref. [5] it has been shown that a family of BG solitons exists in a dual core system with nonidentical cores where one core is linear, which may or may not have a Bragg grating, and the other is nonlinear and equipped with a Bragg grating.

## 2. MODEL AND EQUATIONS

The system we are modeling is a semilinear dual-core system. The BG is written either on the nonlinear core only or on both cores. Following the derivation of the GMTM (Generalized Massive Thirring Model) [5] and of the standard equations of a dual-core fiber, a general model for the semilinear dual-core BG system can be described by the following set of normalized equations.

$$i\frac{\partial u}{\partial t} + i\frac{\partial u}{\partial x} + \left[|v|^2 + \frac{1}{2}|u|^2\right] u + v + \kappa\phi = 0 \quad (1)$$

$$i\frac{\partial v}{\partial t} - i\frac{\partial v}{\partial x} + \left[|u|^2 + \frac{1}{2}|v|^2\right] v + u + \kappa\psi = 0 \quad (2)$$

$$i\frac{\partial \phi}{\partial t} + ic\frac{\partial \phi}{\partial x} + \kappa u = 0 \quad (3)$$

$$i\frac{\partial \psi}{\partial t} - ic\frac{\partial \psi}{\partial x} + \kappa v = 0 \quad (4)$$

Here,  $u$ ,  $v$  present the forward- and backward- propagating waves in the nonlinear core,  $\phi$  and  $\psi$  are their counterparts in the linear core,  $\kappa$  is the coefficient of linear coupling between the cores,  $c$  is the relative group velocity in the linear core.

In the case we are studying, we assume there is no BG written in the linear core. We also set  $c = 0$  (no relative group velocity in the linear core).

### 3. STABILITY

Through numerical simulation, we have been able to find the stability range for moving solitons with different velocities in the nonlinear core. Fig. 1 shows the stability of moving solitons whose velocities are in the range of 0.0–0.5 (0 to 50% speed of light).

In Fig. 1, Area I shows the region when stable solitons are found. In Area II the solitons are unstable.

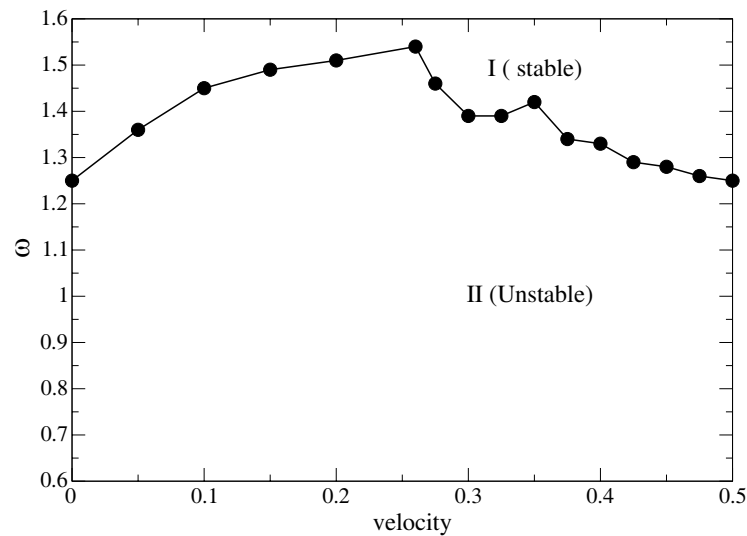


Figure 1: Stability diagram for moving solitons.

### 4. INTERACTIONS AND COLLISIONS

We have also investigated the collisions and interactions of in-phase and out-of-phase counterpropagating solitons.

In Ref. [6, 7] the interactions of counterpropagating gap solitons in a Bragg grating (i.e., Eqs. (1) and (2) with  $\kappa = 0$ ) were investigated. Of particular interest is the merging of the counterpropagating pulses into a quiescent solitary pulse after the collision (See area M in Fig. 2 of [7], and area I in Fig. 2 and Fig. 3 of [6] for the parameter regions this occurs in). However this behaviour is absent in the general model for the semilinear dual-core BG system described above in Eqs. (1)–(4). Typical behaviour of the collisions of two counterpropagating in-phase solitons is shown in Fig. 2

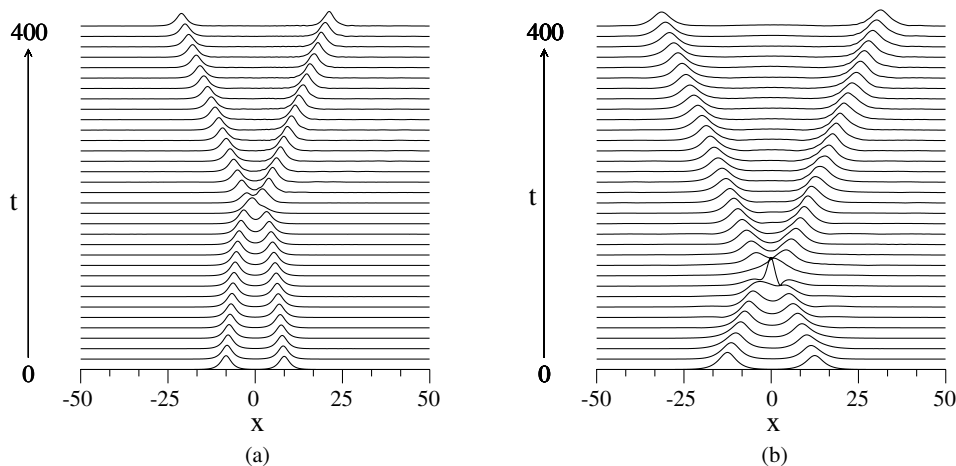


Figure 2: Examples of the interaction of counter-propagating in-phase solitons. (a) velocity = 0.05,  $\omega = 1.4$ , (b) velocity = 0.2,  $\omega = 1.53$ .

and Fig. 3. In Fig. 2 the pulses initially attract one another. Further propagation shows that they continue to be attracted and pass through each other. In Fig. 3 the in-phase solitons initially repel

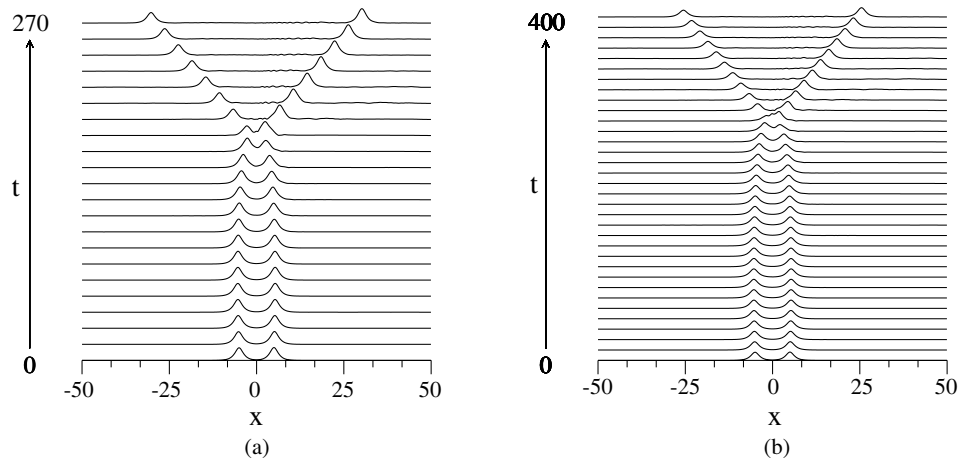


Figure 3: Examples of the interaction of counter-propagating in-phase solitons for (a) velocity = 0.05,  $\omega = 1.43$ , (b) velocity = 0.1,  $\omega = 1.47$ , as it is shown, initially repel each other but subsequently they attract one another and collide.

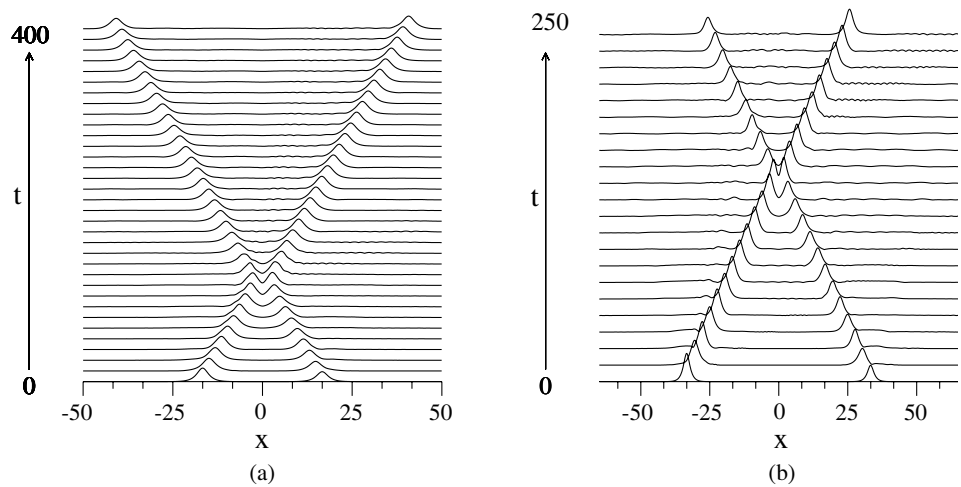


Figure 4: Examples of the interaction of counter-propagating solitons with a  $\pi$  phase difference. (a) velocity = 0.3,  $\omega = 1.43$ , (b) velocity = 0.5,  $\omega = 1.3$ .

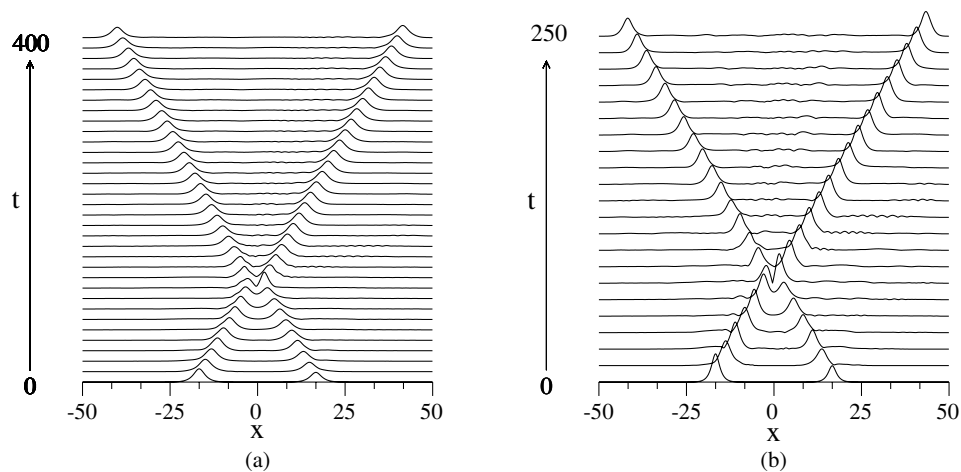


Figure 5: Examples of the interaction of counter-propagating solitons with a  $\pi/2$  phase difference. (a) velocity = 0.3,  $\omega = 1.43$ , (b) velocity = 0.5,  $\omega = 1.3$ .

one another. However, upon further propagation, the pulses then attract one another, resulting in the formation of a lump which subsequently separates into two solitons. (See Fig. 3.)

The collision of counterpropagating out-of-phase gap solitons was investigated for both  $\pi$  and  $\pi/2$  phase differences. Examples of the collision are shown in Fig. 4 (with phase difference equals  $\pi$ ) and Fig. 5 (with phase difference equals  $\pi/2$ ). In both these cases the solitons always bounced off each other. This contrasts with the case of the standard model [7] where, depending on the initial conditions, the solitons were also observed to pass through one another [6].

## 5. CONCLUSION

In this paper, we have investigated the stability and interactions of soliton waves in a dual-core system. We found the stability of solitons in this system relies on the detuning frequency and velocities of moving solitons. Moreover, we also investigated the interactions of two counterpropagating solitons. It is found that the collision dynamics are dependant on detuning frequency and soliton velocities as well as phase informations.

## ACKNOWLEDGMENT

Yazhuo Li likes to thank Daniel R. Neill for helpful discussions.

## REFERENCES

1. De Sterke, C. M. and J. E. Sipe, *Prog. Opt.*, Vol. 33, 203, 1994.
2. Aceves, A. B. and S. Wabnitz, *Phys. Lett. A*, Vol. 141, 37, 1989.
3. Eggleton, B. J., C. M. De Sterke, and R. E. Slusher, *J. Opt. Soc. Am. B*, Vol. 14, 2980, 1997.
4. Taverner, D., N. G. R. Broderick, D. T. Richardson, R. I. Laming, and M. Ibsen, *Opt. Lett.*, Vol. 23, 328, 1998.
5. Atai, J. and B. A. Malomed, *Phys. Rev. E*, Vol. 62, 8713, 2000.
6. Neil, D. R. and J. Atai, *Phys. Lett. A*, Vol. 353, 416, 2006.
7. Mak, W. C. K., B. A. Malomed, and P. L. Chu, *Phys. Rev. E*, Vol. 68, 026609, 2003.

## Plastic Optical Fiber Microbend Sensors

W. S. Fegadolli<sup>1</sup>, J. E. B. Oliveira<sup>1</sup>, and V. R. Almeida<sup>2</sup>

<sup>1</sup>Instituto Tecnológico de Aeronáutica — ITA, Brazil

<sup>2</sup>Instituto de Estudos Avançados — IEAv, Brazil

**Abstract**— Nowadays, it is well known that optical fiber sensors play a major role on the performance of various state of the art measurement devices and systems, namely: gyroscopes, accelerometer, strain and temperature sensors, among many other. In order to increase the range of applications of such kind of sensors a great deal of researcher activities has been guided towards the design and implementation of low-cost sensors. This work addresses design, implementation and characterization of a plastic optical fiber microbend sensor, and points out its potential as a low-cost anti-squeeze sensor. Quite reasonable results were obtained using plastic optical fiber sensor and standard optoelectronic detection scheme.

### 1. INTRODUCTION

The principle of operation of microbend fiber optic sensors addressed in this publication relies on the change of fiber propagation characteristic induced by strain, via the photoelastic effect. Such change may lead to the coupling between optical guided mode and optical leaky modes, therefore the sensor's performance depends on the fiber optical radius of curvature created by the microbend [1, 2]. Such kind of sensors may be implemented using plastic fiber optic, hence they have potential to enable low-cost anti-squeeze optical sensors. In order to develop model for this type of sensors one may relies on the so-called coupled wave equations which yields the optical power dependence on the fiber optic radius of curvature. Based on this understanding, a sensor configuration was designed and tested in order to validate some of the predictions obtained based on a rather simple proposed modeling. As a whole, the sensor comprises three major building blocks, namely: the electromechanical conversion (the actual fiber optic sensor), the optical detection unity and the electronic signal processing device. The former block takes care of correlating the mechanical force which causes the fiber optic squeezing to the change of optical intensity transmitted through the fiber optic. On the other hand, the optical detection and electronic processing are assembled in such fashion which may enable the application of rather insightful optoelectronic techniques, which were validated by means of experimental results obtained while testing the plastic fiber sensors addressed in this publication. In order to gain better qualitative understanding of the sensor principle of operation, one may relies on the schematics shown in Figure 1. It shows, on its left hand side, that a CW laser source after propagating throughout a certain length of fiber optic squeezed by means of an external force, feeds the optical detection unity. In such way, the optical power at the exit of the fiber turns displays characteristics of the induced mechanical bending. Furthermore, the electronic signal available at the optical detection unity is properly delivered to the electronic signal processing unity.

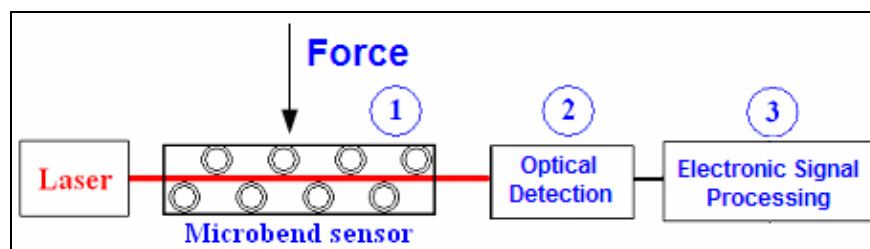


Figure 1: Schematic representation of a fiber optic microbend sensor.

It should be stated that in this publication the electronic signal processing was designed based on the assumption that the sensor would operate as a warning device. In other words, it emphasizes the situation in which one needs to determine whether the external force lies within a certain range of values, rather than accurately measure its intensity.

## 2. SENSOR MODELING

First of all, it is assumed that the microbend pattern generated by the external force exhibits a sinusoidal pattern along the fiber optics axis. In such situation, one may rely on a standard approach based on the Coupled Mode Theory (CMT), in order to investigate the dependence of the coupling between guided and leaky optical modes with respect to microbend pattern characteristics, such as period and radius of curvature [2]. One insightful result which stems from this analysis has to do with the optical power leakage as a function of the microbend radius of curvature. For instance, when such radius is smaller than the value specified by Equation (1), in order to properly model the optical fiber power transmission characteristics, one has to take into account the mode coupling,

$$R_c \cong \frac{3n_1^2\lambda_0}{4\pi(n_1^2 - n_2^2)^{3/2}} \quad (1)$$

where  $n_1$  and  $n_2$  are the fiber core and cladding refractive index, respectively, and  $\lambda_0$  is the free space optical wavelength.

Furthermore, for radius of curvature smaller than  $R_c$  the analysis based on the Coupled Mode Theory leads to the following expression for the optical power at the fiber optic output,

$$P_{out} = P_{in}e^{-2\alpha z} \quad (2)$$

$$2\alpha = \frac{\pi^{1/2}\kappa^2 e^{\left(\frac{-2\gamma^3 R_{eff}}{3\beta^2} - 2\gamma a\right)}}{2R_{eff}^{1/2}\gamma^{3/2}V^2 K_{m-1}(\gamma a)K_{m+1}(\gamma a)} \quad (3)$$

with,

$$R_{eff} = \frac{R}{1 - \frac{n^2}{2}[P_{12} - v(P_{11} + P_{12})]} \quad (4)$$

where  $P_{in}$  is the incoming optical power,  $2\alpha$  is the optical power loss coefficient due to the fiber curvature,  $\kappa$ ,  $\gamma$ ,  $\beta$  are the core transversal, the cladding transversal and the fiber longitudinal propagations constants, respectively,  $a$  is the fiber optic core radius,  $K_{m+1}$  and  $K_{m-1}$  are modified Bessel's function of second kind,  $R$  is the fiber curvature radius,  $P_{12}$  and  $P_{11}$  are photoelastic constants and  $v$  is the fiber Poisson ratio [1].

In order to experimentally observe some of the predictions based on the modeling described by Equations (1) to (3), a rather simple sensor set-up was assembled, as shown in Figure 2. It should be noticed that the microbend pattern imprinted in the fiber is generated by the squeezing of a plastic fiber optic with the aid of two periodic array of cylinder rods. It should be pointed out that sensor works even with plastic fiber optic having a very thick jacket.

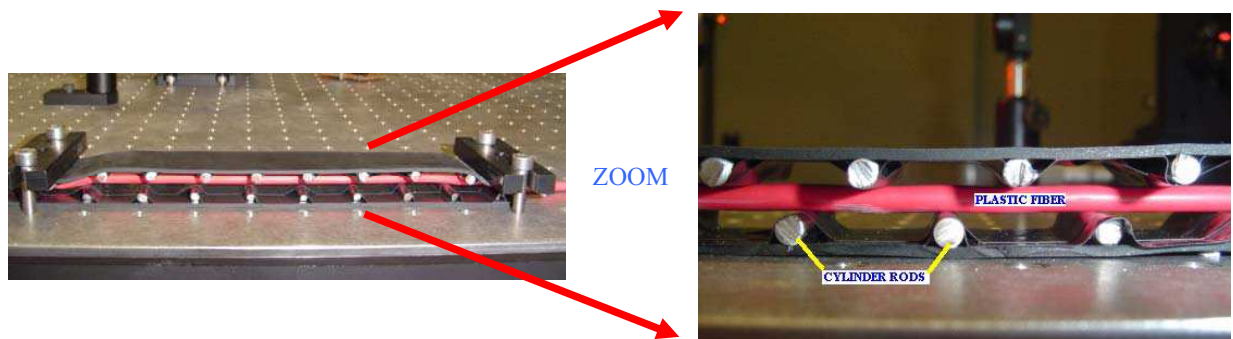


Figure 2: Plastic fiber optic sensor: Microbend pattern generation.

The plastic fiber microbend sensor, as a whole, which was assembled according to the schematics presented in Figure 1, is shown in Figure 3.

The technique chosen for imprinting the microbend pattern into the fiber optic turned out to be very practical and also yielded a robust sensor set-up.

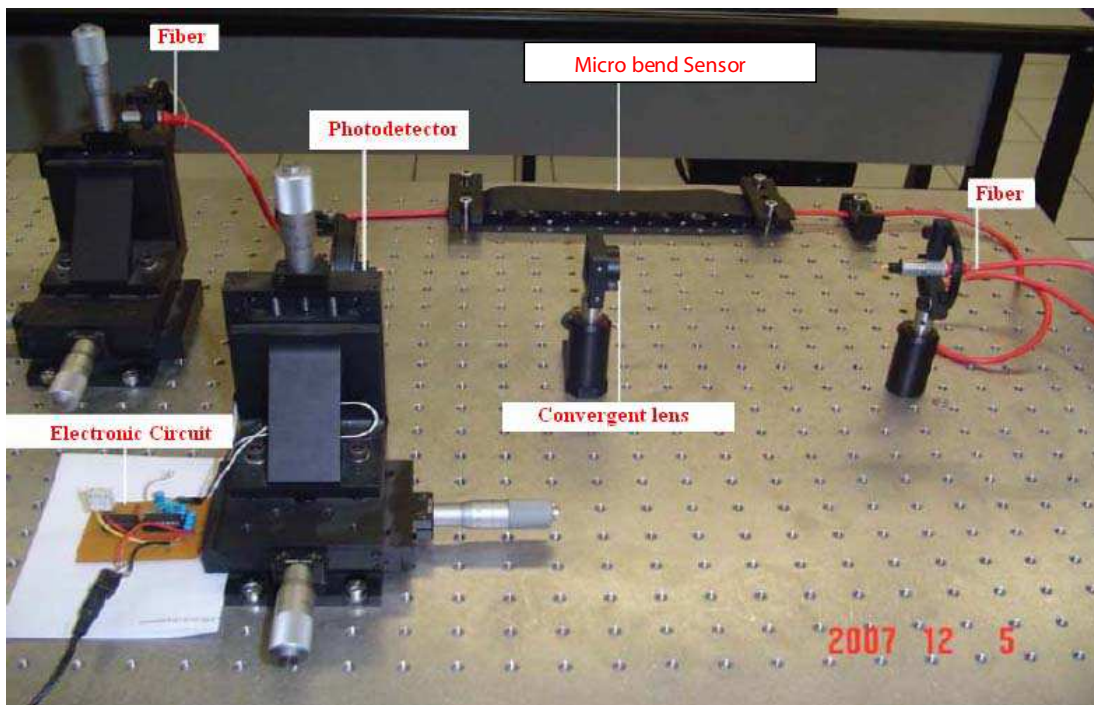


Figure 3: Plastic fiber optic microbend sensor set-up.

### 3. EXPERIMENTAL RESULTS

Based on the accurate understanding obtained based on the rather simple modeling and using low-cost optical and electronics components a very interesting sensor prototype was assembled and tested. This section gives some experimental results obtained using an electronic processing unity based on the integrated circuits HIN 232 and 74HC14N. Figure 4, part A, shows that the output voltage has a linear dependence with respect to the applied force, with a scale factor around 0.1 V/Kgf. On the other hand, part B of the same figure is related to the performance of the sensor as a microbend warning device; Its electronic processing unity was assembled to provide an output voltage swinging as high as 4 volts. When the applied force exceeds 3.2 Kgf the sensor identifies that squeezing is taking place. However, owing to its simplicity the assembled electronics does not yields good results when the force ranges from 2.1 Kgf to 3.2 Kgf. Moreover, Figure 5 displays results obtained when an output of  $-10$  volts means squeezed state and 10 volts means squeeze free state. These results show that one has certain degree of freedom to set the threshold force beyond which a squeezing state is warned [3].

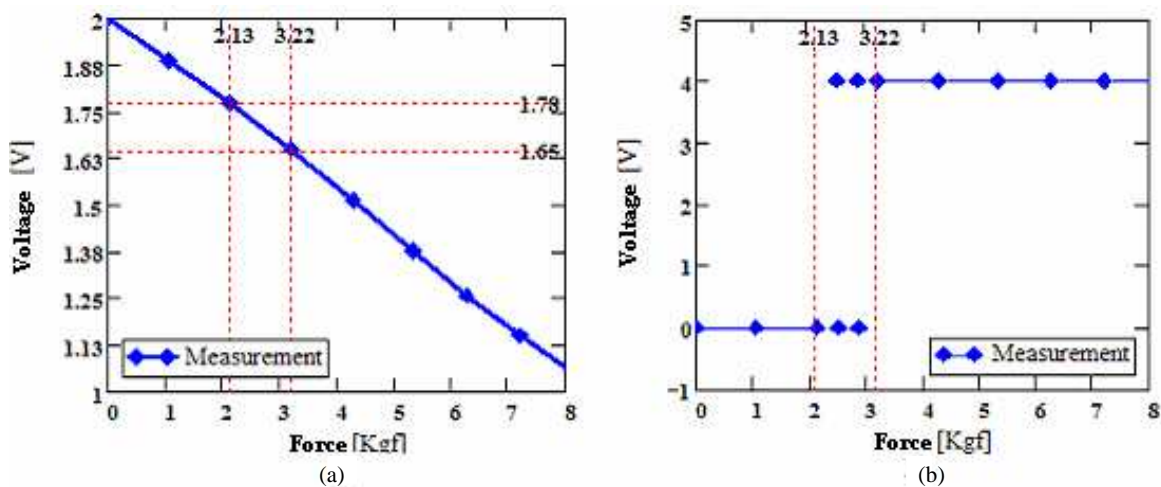


Figure 4: Electronic signal processor output, with 4 V voltage swinging (a) analog and (b) digital.

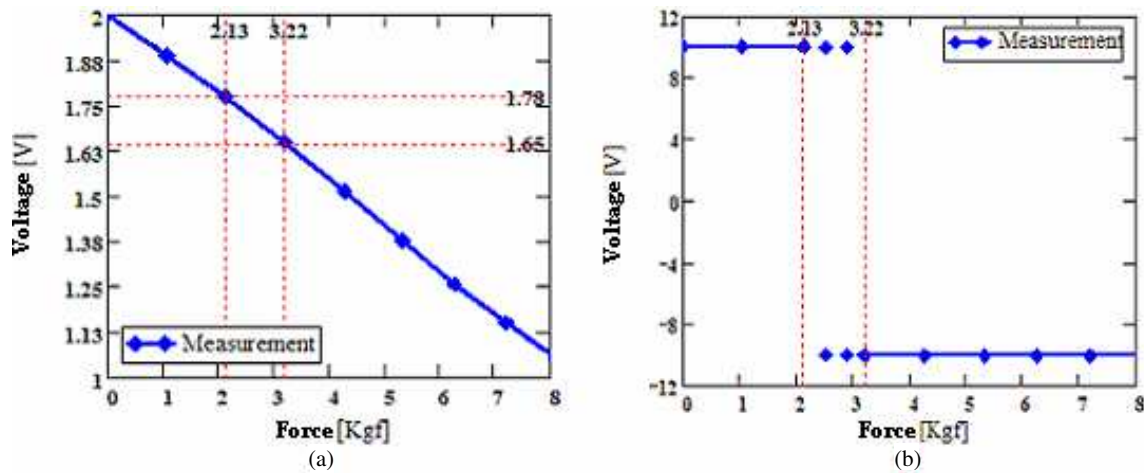


Figure 5: Electronic signal processor output, with 20 V voltage swinging (a) analog and (b) digital.

#### 4. CONCLUSION

This publication reports experimental results obtained using plastic fiber microbend sensor implemented with low-cost optical and electronic components. Its modeling illustrates a rather simple application of the coupled mode theory. The results point out that such kind of sensor may be very useful in applications related to safety, automatic control, among many others. Above all it may be widely used as laboratory tool for training graduate and undergraduate on the subject of optoelectronic devices and sensors applications.

#### REFERENCES

1. Schermer, R. T. and J. H. Cole, "Improved bend loss formula verified for optical fiber by simulation and experiment," *IEEE Journal of Quantum Electronics*, Vol. 43, No. 10, October 2007.
2. Linec, M. and D. Donlagic, "A plastic optical fiber microbend sensor used as a low-cost anti-squeeze detector," *IEEE Sensors Journal*, Vol. 7, No. 9, September 2007.
3. Fegadolli, W. S., "Implementação de um sistema de comunicação de Dados Através da Tecnologia FSO," Trabalho de graduação — Unisaesiano, 87, 2006.

# Design of a Broadband Filter

Manidipa Bhattacharya

SAMEER, Plot L2, Block GP, Sector-V, Salt Lake Electronic Complex  
Kolkata 700091, West Bengal, India

**Abstract**— Design of a compact filter having a broad pass band (73.3%) and low insertion loss (2.0 dB) is presented. Here broadside coupled resonator elements are used for synthesis of the filter in suspended stripline configuration. A general synthesis method for broadband filter design is demonstrated and the realization of the filter in suspended stripline configuration is also discussed. A specific example of fifteen section filter having broadside-coupled resonator elements in edge coupled configuration is described here. The design has been verified by the simulation and results are presented.

## 1. INTRODUCTION

Suspended stripline (SSL) is a suitable transmission medium with moderate loss and a wide range of possible circuit configurations, especially for filters [1]. SSL consist of a dielectric substrate suspended symmetrically between two ground planes. The attractive features of SSL compared to conventional stripline or microstrip are reduced ohmic/dielectric losses over wide bandwidth, better temperature stability over a wide temperature range, low dispersion and good fabrication tolerances. The SSL structure under consideration for synthesis of broadband filter is a broadside coupled resonator printed on a substrate suspended in a shielded channel as shown in Fig. 1. Broadside coupled resonators are basically an arrangement of strip elements on both sides of the substrate for improved coupling between filter elements. Thus the use of two layer configuration for the filter makes the design flexible and compact. The bandpass filter under consideration (Fig. 2) uses quarter wavelength resonators and the capacitive coupling is realized through the supporting dielectric, thereby eliminating the need for precision etching.

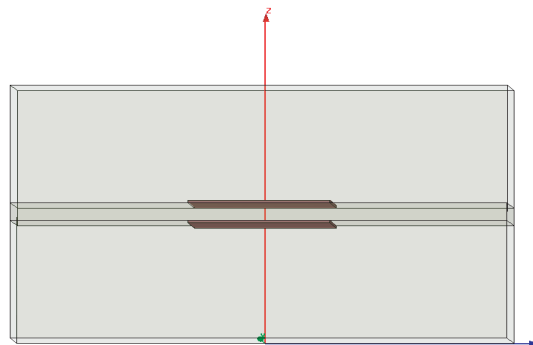


Figure 1: Cross sectional view of the broadside-coupled resonator in suspended stripline configuration.

## 2. DESIGN METHODOLOGY

The design procedure can be summarized as below.

- (i) Suspended stripline operating range and corresponding cutoff frequency can be decided from knowledge of mode propagation within an enclosed structure.
- (ii) From the passband and stopband requirements the order of the filter and normalized element values are obtained [2].
- (iii) Evaluation of the coupling coefficients from the normalized element values and selected terminating impedances. Here admittance inverter model for each broadside coupled resonator is considered and coupling coefficients are derived from the even and odd mode impedances values for all section of the filter [3–5].

- (iv) Physical dimension of the strips for each filter elements in suspended stripline has been evaluated from a simple analysis [5]. Here coupling coefficients against width of the strips are evaluated.
- (v) Simulation of the filter structure for verification of the design and further optimization.

### 3. DESIGN DETAILS

In order to achieve broad bandwidth (octave or more) with edge-coupled transmission lines the line separation required to achieve the necessary impedance values becomes too small to fabricate. In SSL with broadside-coupled resonator configuration large range of impedance values can be realized and this makes practical design dimension calculated from the filter synthesis.

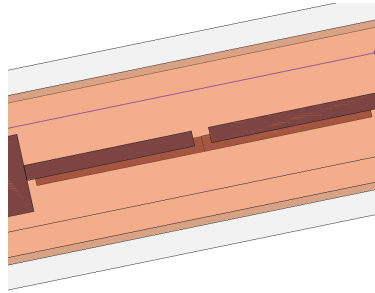


Figure 2: Layout of the band pass filter (top view).

The starting point of the design is L-C low pass prototype of order  $N$  which was used to transform the theoretical band pass response from  $N + 1$  broadside coupled sections [2]. From the desired center frequency and bandwidth the normalized element values [3] and corresponding odd and even mode impedances of the coupled line sections are obtained [4]. The coupling coefficients are then calculated for each filter section. Each broadside coupled section are then designed for the corresponding coupling level [5]. The length and width of the quarter wavelength resonators are determined for the suspended channel dimensions based on theoretical computation [5] and verified by simulation (HFSS) of the filter sections (Fig. 3). The internal impedance levels are set to have the desired Q of the resonator sections. Although the length of the resonator is ideally quarter wavelength at the center frequency, the average value of the effective dielectric constant for even and odd modes are used to determine the length of the coupled lines.

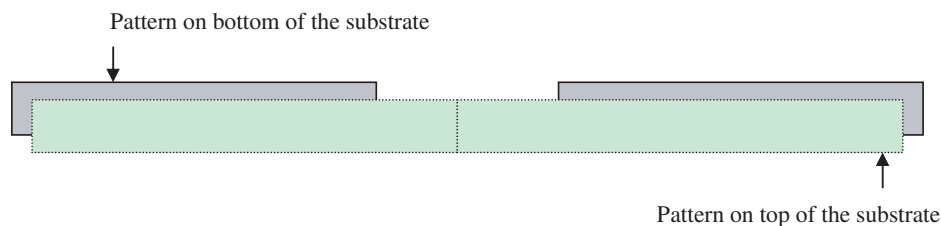


Figure 3: Edge-coupled configuration for two adjacent broadside-coupled sections of the filter.

### 4. DESIGN DATA

Here fifteen broadside-coupled sections are used to design the broadband filter at K-Ka band (75.8% fractional bandwidth) with Chebyshev response having 0.5 dB ripples. The suspended stripline channel was designed for dominant TEM mode propagation up to 60.28 GHz with the following channel dimensions.

Channel Width = 2.4 mm.

Channel Height = 1.0 mm.

Dielectric Constant of the Suspended Substrate = 2.2.

Substrate Thickness = 5 mil.

A theoretical analysis [5] has been done for tabulating the coupling coefficients as a function of normalized strip width for the broadside coupled strips with different dielectric constants as shown in Fig. 4. It is clear that for the same coupling coefficient the substrate having lower dielectric

constant can be used to get the wider strip width with easier mechanical fabrication. With this logic the dielectric constant for the suspended substrate has been chosen as 2.2. The same analysis is used to tabulate even and odd mode impedance of the broadside coupled strips as a function of their normalized width. A plot for the same using the suspended channel dimensions has been generated and verified by HFSS simulation as shown in Fig. 5. This plot has been used to find out the physical dimension of the coupled strips as per the required coupling coefficients. The required coupling level of first eight resonators and the corresponding width and length of the same are tabulated in Table 1. The last 8 sections have the same value in reverse order.

Table 1: Computed design data for first 8 sections suspended stripline broadside-coupled filter.

Filter Sections	g values	Coupling Coefficients	Width of Strip	Length of Strip
1	1.7635	0.6361	0.205	1.9039
2	1.2791	0.6238	0.185	1.9052
3	2.6920	0.5426	0.094	1.9125
4	1.3826	0.5278	0.083	1.9135
5	2.7654	0.5227	0.079	1.9138
6	1.3991	0.5204	0.078	1.9139
7	2.7811	0.5193	0.077	1.9140
8	1.4024	0.5189	0.076	1.9141

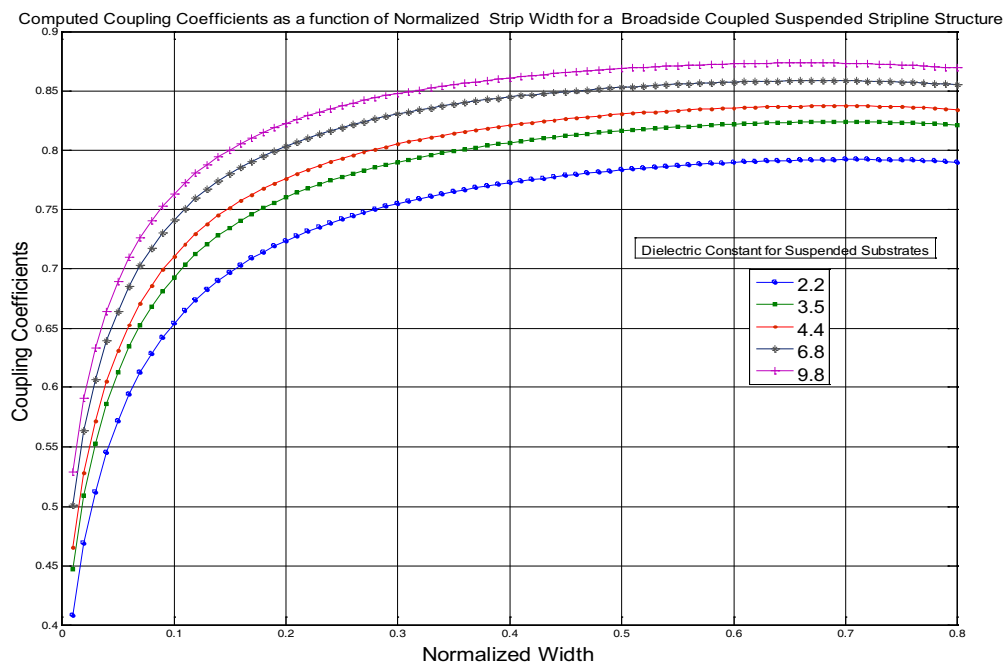


Figure 4: Computed plot of coupling coefficients as a function of normalized strip width.

## 5. SIMULATION RESULTS

The filter sections are capacitively coupled through a gap of 0.2 mm along the length (40 mm). The effect of inserting 0.2 mm gap was to alter the cutoff frequencies and to lower the the operating frequency band slightly. To compensate the effect of the gap capacitance the resonator length can be scaled down appropriately or the target design frequency may be kept at higher value to maintain the filter response for the desired operating band. The most accurate results will be obtained using this type of structures with a homogeneous dielectric where even and odd mode phase velocities are same. The structure has been simulated in HFSS and Fig. 7 shows the simulated response of the

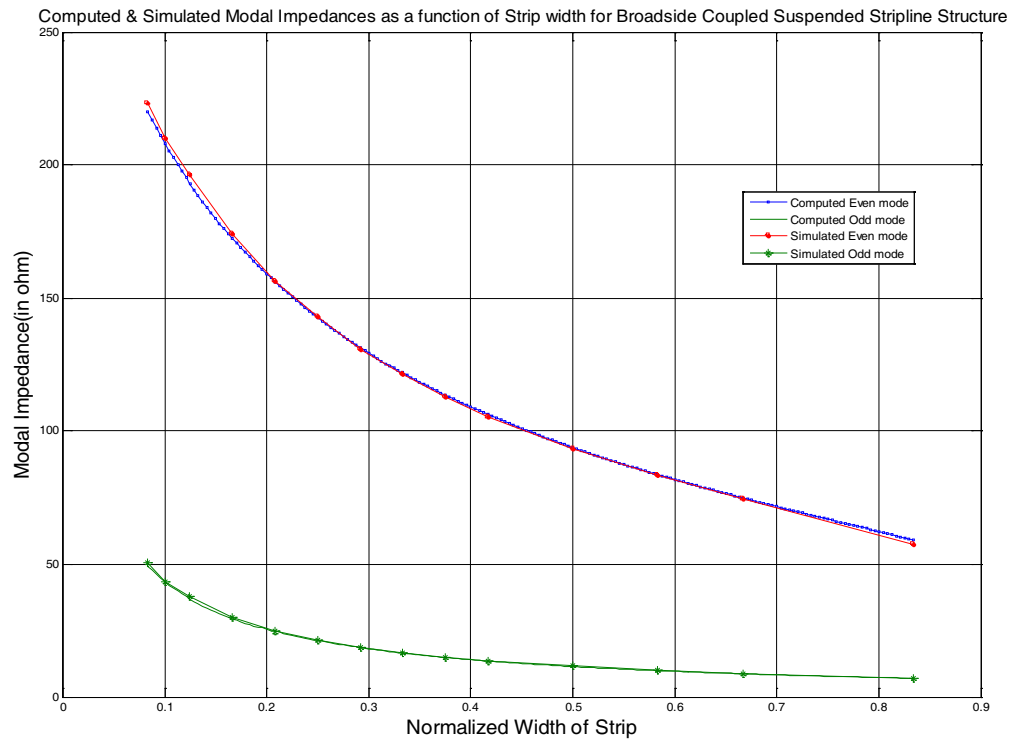


Figure 5: Computed/Simulated plot of even and odd mode impedance as a function of normalized strip width.

filter. The simulated filter pass band shows a 73.3% bandwidth (19.0–41.0 GHz) with a loss of 2.0 dB over the operating band. So this design can be implemented with proper fabrication facilities to develop a broadband filter.

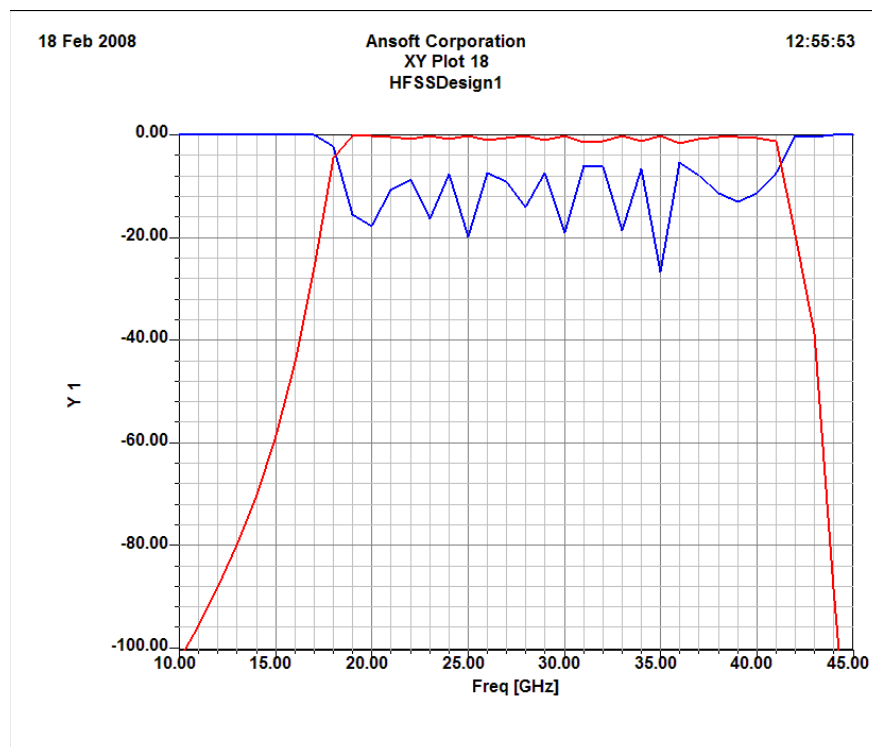


Figure 6: Simulated response of the suspended substrate broadside coupled filter.

## 6. CONCLUSIONS

The design of a wide band filter has been demonstrated with commonly used edge-coupled configuration with broadside-coupled elements in suspended stripline configuration. However there is future scope to modify this design using asymmetrically coupled elements where fabrication difficulties can be further minimized.

## ACKNOWLEDGMENT

I am grateful to SAMEER-Kolkata for publishing this work.

## REFERENCES

1. Dougherty, R. M., "mm-wave filter design with suspended stripline," *Microwave Journal*, 75–84, Jul. 1986.
2. Matthei, G. L, E. M. T. Jones, and L. Young, *Microwave Filters, Impedance-matching Networks and Coupling Structures*, Chapter 10, Artech House, 1980.
3. Matthei, G. L., "Design of wide-band band pass filters on the insertion loss basis," *IRE Trans. MTT*, 580–592, Nov. 1960.
4. Cho, C. and K. C. Gupta, "Design methodology for multilayer coupled line filters," *IEEE MTT-S Digest*, 1997.
5. Sturdivant, R., "A capacitively coupled BPF design using a suspended substrate stripline," *Microwave Journal*, 71–76, Nov. 1993.

# Dynamical Control of Terahertz Metamaterial Resonance Response Using Bimaterial Cantilevers

H. Tao<sup>1</sup>, A. Strikwerda<sup>2</sup>, C. Bingham<sup>3</sup>  
W. J. Padilla<sup>3</sup>, X. Zhang<sup>1</sup>, and R. D. Averitt<sup>2</sup>

<sup>1</sup>Department of Manufacturing Engineering, Boston University, Brookline, MA 02446, USA

<sup>2</sup>Department of Physics, Boston University, Boston, MA 02215, USA

<sup>3</sup>Department of Physics, Boston College, Chestnut Hill, MA 02467, USA

**Abstract**— In this work, we report a novel method for the dynamical control of the resonant electrical response of terahertz (THz) metamaterials. Our approach is based on planar arrays of split-ring resonators (SRRs) coupled with microfabrication methods to create a bimaterial-cantilever-based THz metamaterial switch. Our device exhibits a tunable resonant response centered at 0.75 THz and operates by modifying or shorting the SRR capacitive gap with the bimaterial cantilevers. These results demonstrate the potential of bimaterial-cantilever-based MMs for creating THz devices including, as examples, switches, dynamic filters, and phase shifters.

## 1. INTRODUCTION

Artificially structured electromagnetic (EM) materials are an extremely active research area because of the possibility of creating materials which exhibit novel EM responses not available in natural materials, such as negative refractive index [1]. Such EM composites, often called metamaterials (MMs), are especially important for the technologically relevant terahertz (1 THz =  $10^{12}$  Hz) frequency regime where there is a strong need to create components to realize applications ranging from spectroscopic identification of hazardous materials to noninvasive imaging [2–4]. For many of these potential applications, it is desirable to create MMs that exhibit a controlled active and/or tunable response [5, 6].

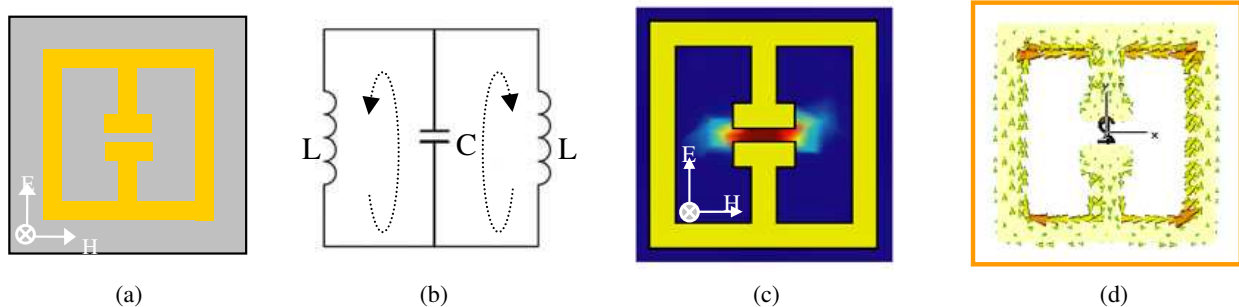


Figure 1: (a) The electrically resonant metamaterial is based on the balanced split resonator ring (balanced-SRR) structure, which consists of two single SRRs put together on the split gap side; (b) Equivalent circuit of the electrically resonant metamaterial; (c) Simulation results show that the effective LC resonance results in a frequency dependent transmission where, on resonance, a strongly enhanced electric field is concentrated in the gap of the SRR; (d) The simulated surface current density distribution, which provides a simple way to visualize the absence of a magnetic response in balanced-SRR; namely, the magnetic fields created by circulating surface currents cancel due to clockwise and counterclockwise components in adjacent regions of the particle. (All simulations were conducted by using a finite difference time domain Maxwell's equations solver, CST STUDIO SUITE<sup>TM</sup> 2007).

## 2. DESIGN AND SIMULATION

Currently, most implementations of MMs are based on SRR structures to obtain a magnetic response and wire structures to obtain an electric response. One disadvantage of obtaining electric MMs by the use of wire media is the difficulty in fabrication of continuous wires with good electric connections for large 2D/3D arrays. The canonical SRR structure, which was originally designed for its unique magnetic response, also displays an electric response under normal incidence radiation

with the magnetic field lying completely in the SRR plane and electric field perpendicular to the SRR gap. This allows the electric field to drive the inductive-capacitive (LC) resonance. The SRR structure normally shows a bianisotropic response, coupling to both electric and magnetic fields. To address the difficulty in identifying the electric resonance from the bianisotropic responses, a novel metamaterial element was used in this work, referred as a balanced-SRR, which couples strongly to a uniform electric field, and negligibly to a uniform magnetic field [7], as shown in Fig. 1.

In our device, an individual THz electric metamaterial resonance switch element consists of a balanced-SRR with a cantilever sitting above the gap, as shown in Fig. 2. The effective LC resonance results in a frequency dependent transmission where, on resonance, a strongly enhanced electric field is concentrated in the gap of the SRR; the resonance disappears when the cantilever bends down to touch the SRR and shorts the gap.

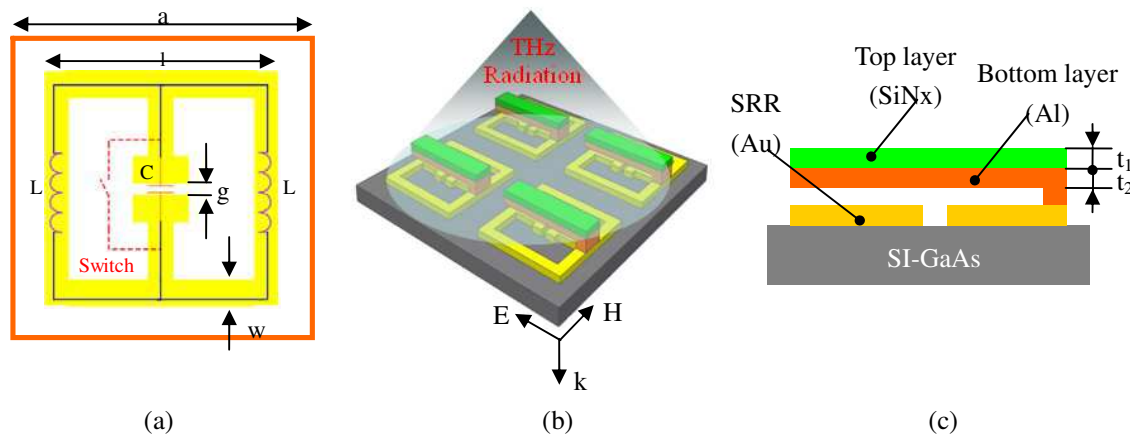


Figure 2: The device consists of two single SRRs put together on the split gap side with a cantilever sitting above. Design dimensions: Unit cell length ( $a = 50 \mu\text{m}$ ), length of the ring ( $l = 36 \mu\text{m}$ ), width of the ring ( $w = 4 \mu\text{m}$ ), gap distance ( $g = 2 \mu\text{m}$ ), thickness of bimaterial cantilever ( $t_1 = t_2 = 200 \text{ nm}$ ), width is  $6 \mu\text{m}$ , and length is  $32 \mu\text{m}$ . (a) Equivalent circuit of THz MM resonance switch, the resonance disappears when the cantilever bends down to touch the SRR and shorts the gap; (b) Planar periodic array exposed to normal incident THz radiation with electric field perpendicular to the SRR gap; (c) Cross-section view of one individual element.

### 3. FABRICATION

Figure 3(a)~3(h) detail the fabrication process using a surface micromachining process: (a) A semi-insulating GaAs wafer was chosen because it is highly transmitting at THz frequencies; (b) AZ5214e image reversal photoresist was patterned using direct laser writing with a Heidelberg<sup>TM</sup> DWL 66 laser writer; (c) 200 nm-thick Au/Ti was E-beam evaporated followed by lift-off with rinsing in Acetone for several minutes; (d) 1.3  $\mu\text{m}$ -thick photoresist of Shipley S1813 was spin-coated as the sacrificial layer; (e) anchors were patterned by standard photolithography; (f) a 200 nm-thick Aluminum (Al) layer was E-beam evaporated, followed by sputtering of a 200 nm-thick Silicon Nitride (SiNx) layer; (g) 6  $\mu\text{m}$  (width)  $\times$  32  $\mu\text{m}$  (length) cantilevers were patterned by standard photolithography, and etched by reactive ion etch of SF<sub>6</sub>/He and Al etchant respectively; (h) isotropic release etching of photoresist was conducted by high density oxygen plasma asher; (i) photographs of the fabricated samples.

### 4. MEASUREMENT

The bimaterial cantilevers were designed to have an initial downward curvature to touch the SRRs due to residual stress induced by the microfabrication process. This is the “on” (highly transmitting) state. The switch can be turned “off” by controlling the ambient temperature to make the bimaterial cantilevers bend up due to the different thermal expansion of Al and SiNx. Surface profiles of the switch “on/off” were obtained using a 3D Optical Profiler, as shown in Figs. 4(a) & 4(b). Spectroscopic measurements were performed using a Fourier transform interferometer (FTIR) in the far infrared over the range from 16~66  $\text{cm}^{-1}$  with 0.5  $\text{cm}^{-1}$  spectral resolution. The samples were mounted in the FTIR at normal incidence with the electric field perpendicular to the SRR

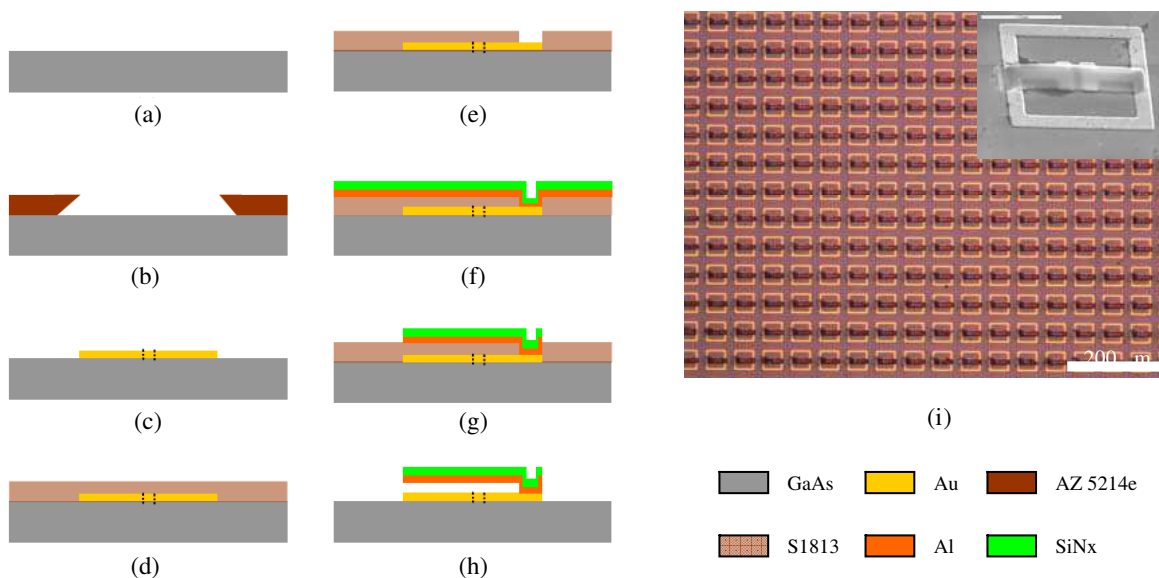


Figure 3: Fabrication process and sample picture of THz MM resonance response switch.

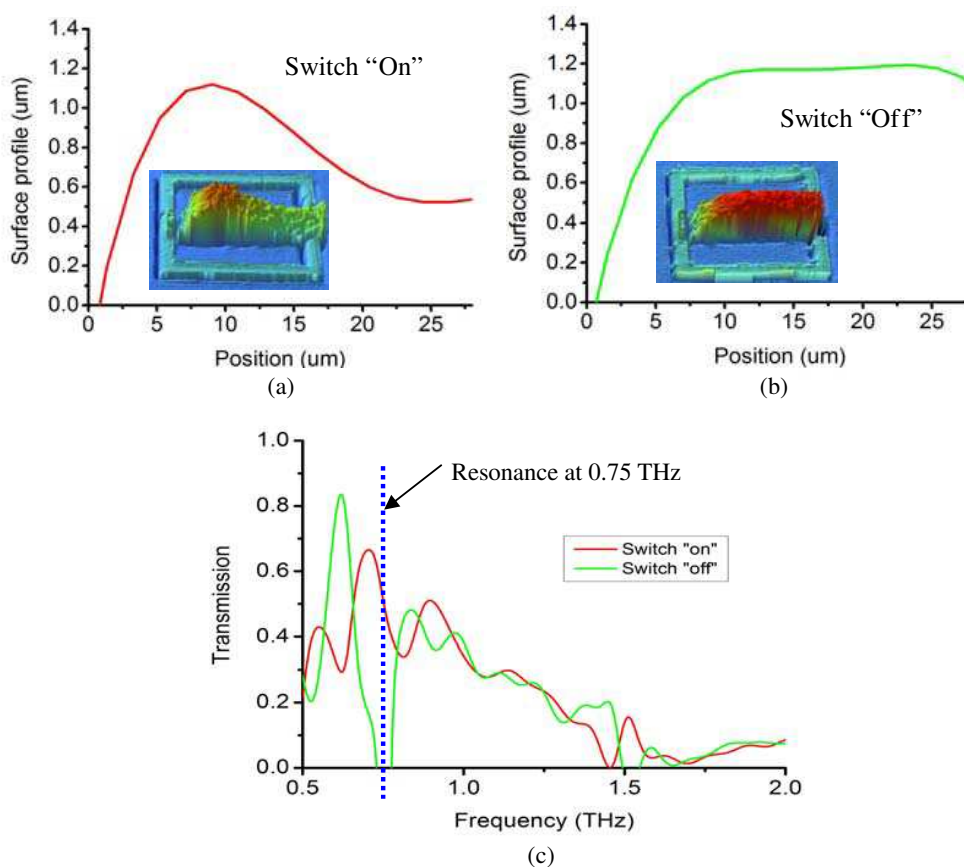


Figure 4: (a) & (b) Surface profiles of cantilever switches at “on” & “off” using ZYGO<sup>TM</sup> New View 6000 Series 3D optical profiler; (c) Preliminary testing results of THz MM switch using Bruker<sup>TM</sup> VERTEX 80v FTIR spectrometer.

gap. Preliminary results show that the THz transmission resonance ( $\sim 0.75$  THz) of the MM with bimaterial cantilevers can be modulated by nearly 50%, which makes it an ideal candidate as THz switch/modulator, as shown in Fig. 4(c). The modulation can be further improved by choosing

high-Q SRRs and optimizing the geometry of cantilevers.

## 5. CONCLUSION

In summary, we have demonstrated dynamical control of terahertz metamaterial resonance response using bimaterial cantilevers. The response of MMs could be further improved by geometric optimization of the resonators and substrate, such as increased filling fraction, thicker samples, and extension to multiple layer structures. Furthermore, MMs have been demonstrated over many decades of frequency, thus our results are not limited only to terahertz frequencies but may be used over much of the electromagnetic spectrum.

## ACKNOWLEDGMENT

This project has been supported in part by the DOD/Army Research Laboratory through grant W911NF-06-2-0040. The authors would like to thank the Photonics Center at Boston University for all of the technical support throughout the course of this research.

## REFERENCES

1. Smith, D. R., W. J. Padilla, D. C. Vier, S. C. Nemat-Nasser, and S. Schultz, "Composite medium with simultaneously negative permeability and permittivity," *Phys. Rev. Lett.*, Vol. 84, 4184–4187, May 1, 2000.
2. Padilla, W. J., M. T. Aronsson, C. Highstrete, M. Lee, A. J. Taylor, and R. D. Averitt, "Electrically resonant terahertz metamaterials: Theoretical and experimental investigations," *Physical Review B*, Vol. 75, Jan. 2007.
3. Yen, T. J., W. J. Padilla, N. Fang, D. C. Vier, D. R. Smith, J. B. Pendry, D. N. Basov, and X. Zhang, "Terahertz magnetic response from artificial materials," *Science*, Vol. 303, 1494–1496, Mar. 5, 2004.
4. Federici, J. F., B. Schulkin, F. Huang, D. Gary, R. Barat, F. Oliveira, and D. Zimdars, "THz imaging and sensing for security applications — Explosives, weapons and drugs," *Semiconductor Science and Technology*, Vol. 20, S266–S280, Jul. 2005.
5. Chen, H. T., W. J. Padilla, J. M. O. Zide, A. C. Gossard, A. J. Taylor, and R. D. Averitt, "Active terahertz metamaterial devices," *Nature*, Vol. 444, 597–600, Nov. 30, 2006.
6. Padilla, W. J., A. J. Taylor, C. Highstrete, M. Lee, and R. D. Averitt, "Dynamical electric and magnetic metamaterial response at terahertz frequencies," *Physical Review Letters*, Vol. 96, Mar. 17, 2006.
7. Schurig, D., J. J. Mock, and D. R. Smith, "Electric-field-coupled resonators for negative permittivity metamaterials," *Applied Physics Letters*, Vol. 88, Jan. 23, 2006.

# Controlling the Emission of Electromagnetic Source

Yu Luo<sup>1</sup>, Jingjing Zhang<sup>1</sup>, Lixin Ran<sup>1</sup>  
Hongsheng Chen<sup>1,2</sup>, and Jin Au Kong<sup>1,2</sup>

<sup>1</sup>The Electromagnetics Academy at Zhejiang University  
Zhejiang University, Hangzhou 310058, China

<sup>2</sup>Research Laboratory of Electronics, Massachusetts Institute of Technology  
Cambridge, Massachusetts 02139, USA

**Abstract**— The coordinate transformation on the space that contains electromagnetic sources is studied. We find that, not only the permittivity and permeability tensors of the media, but also the source inside the media will take another form in order to behave equivalently as the original case. It is demonstrated that, a source in the free space can be replaced by another source of arbitrary shape with an appropriate metamaterial coating around it without being detected by outer observers, because the emission of the source can be controlled at will in this way. As examples, we show how to design conformal antennas and electrically small antennas by covering the sources with transformation media. The method proposed in this letter provides a completely new approach to develop novel active EM devices.

## 1. INTRODUCTION

In 2006, J. Pendry et al. proposed the pioneering coordinate transformation concept to arbitrarily control EM fields [1, 2]. In his approach, a space consisting of the normal free space can be transformed into a new space with different volume and space-distributed constitutive parameters [1, 3], which could be realized by artificial metamaterial, whose permittivity and/or permeability can be designed to continuously change from negative to positive values [4–6]. Following this approach, some novel EM devices [7–19] can be realized to obtain unusual EM behaviors. In this letter, we further illustrate that such coordinate transformation can even be applied to a space containing EM sources. The closed-form solution obtained from an analytical full wave method shows that in this case, not only the permittivity and permeability tensors, but also the EM sources can be transformed at will. In particular, a source in the free space can be replaced by another source of arbitrary shape, given access to a properly designed metamaterial coating, without being detected by outer observers. This generates a powerful path to electromagnetic design and can encompass all forms of electromagnetic phenomena. As examples, we show how to apply the theory on the design of conformal antenna, which still remains a problem in engineering, as well as reducing the size of traditional antennas. The method proposed in this letter not only provides a completely new approach in the development of novel active EM devices, but also enlightens a wider exploration in the field of coordinate transformation.

## 2. FORMULAS

We start from considering a general coordinate transformation between the initial and the transformed spherical coordinate systems  $(r', \theta', \varphi')$  and  $(r, \theta, \varphi)$  by

$$\bar{r}' = \bar{F}(\bar{r}) \quad \text{or} \quad r' = f(r, \theta, \varphi) \quad \theta' = g(r, \theta, \varphi) \quad \varphi' = h(r, \theta, \varphi) \quad (1)$$

Here  $\bar{F}$  represents a deformation mapping from coordinate system  $(r', \theta', \varphi')$  to  $(r, \theta, \varphi)$  on a closed domain  $V$ , of which the boundary is matched to free space ( $\bar{r} = \bar{F}(\bar{r})|_{\partial V}$ ). The relation between the two operators  $\tilde{\nabla} = \hat{r} \frac{\partial}{\partial r'} + \hat{\theta} \frac{\partial}{\partial \theta'} + \hat{\varphi} \frac{\partial}{\partial \varphi'}$  and  $\nabla = \hat{r} \frac{\partial}{\partial r} + \hat{\theta} \frac{\partial}{\partial \theta} + \hat{\varphi} \frac{\partial}{\partial \varphi}$  is given by

$$\begin{cases} \nabla \times \bar{A} = \det(\bar{J}) \bar{J}^{-1} \cdot \tilde{\nabla} \times \left[ (\bar{J}^T)^{-1} \cdot \bar{A} \right] \\ \nabla \cdot \bar{A} = \det(\bar{J}) \tilde{\nabla} \cdot \left[ \frac{\bar{J} \cdot \bar{A}}{\det(\bar{J})} \right] \end{cases} \quad (2)$$

By substituting Equations (2) into Maxwell's equations, we obtain the desired physical material constants in terms of the constants in the original coordinate

$$\begin{cases} \bar{\epsilon} = \det(\bar{J}) \bar{J}^{-1} \cdot \bar{\epsilon}' \cdot (\bar{J}^T)^{-1}, \quad \bar{\mu} = \det(\bar{J}) \bar{J}^{-1} \cdot \bar{\mu}' \cdot (\bar{J}^T)^{-1} \\ \rho(\bar{r}) = \det(\bar{J}) \rho'(\bar{F}(\bar{r})), \quad \bar{j}(\bar{r}) = \det(\bar{J}) \bar{J}^{-1} \cdot \bar{j}'(\bar{F}(\bar{r})) \end{cases} \quad (3)$$

where  $\bar{\bar{J}} = \frac{\partial(f, g, h)}{\partial(r, \theta, \varphi)}$  is the Jacobian transformation matrix. The surface current  $\bar{J}_s$ , current  $\bar{I}$ , and charge  $q$  in the transformed coordinate can also be described with the mapping matrix  $\bar{F}$  as

$$\bar{J}_s(\bar{r}) = \bar{\bar{J}}^T \cdot \bar{J}'_s(\bar{F}(\bar{r})), \quad \bar{I}(\bar{r}) = \bar{I}'(\bar{F}(\bar{r})), \quad q(\bar{r}) = q'(\bar{F}(\bar{r})) \quad (4)$$

Note that under this transformation, Maxwell equations still remain their form invariance in the new coordinates  $(r, \theta, \varphi)$ , but the permittivity, permeability, charge density and current density will be expressed in a different form.

The electromagnetic field in the transformed coordinates on domain  $V$  which contains sources  $\bar{j}(\bar{r}_0)$  and  $\rho(\bar{r}_0)$  can therefore be calculated by introducing the vector potential  $\bar{A}$  ( $\bar{B} = \nabla \times \bar{A}$ ) and scatter potential  $\phi$  ( $\bar{E} = i\omega\bar{A} - \nabla\phi$ ). Applying gauge condition  $\nabla \cdot (\bar{T}^{-1} \cdot \bar{A}) - i\omega\mu_0\varepsilon_0\phi = 0$ , where  $T = \bar{\bar{J}}^T \bar{J} / \det(\bar{\bar{J}})$  is the metric tensor, the partial differential equation of the vector potential  $\bar{A}$  is given by

$$\tilde{\nabla}^2 \left[ \left( \bar{\bar{J}}^{-1} \right)^T \cdot \bar{A} \right] + k_0^2 \left( \bar{\bar{J}}^{-1} \right)^T \cdot \bar{A} = \frac{\mu_0 \bar{\bar{J}} \cdot \bar{j}(\bar{r}_0)}{\det(\bar{\bar{J}})} \quad (5)$$

Then the exact expression of the electric field can be written with Green's function

$$\bar{E} = i\omega\mu_0 J^T \cdot \left( \bar{I} + \frac{\tilde{\nabla}\tilde{\nabla}}{k^2} \right) \cdot \iiint d^3\bar{r}'_0 \frac{e^{ik|\bar{r}'-\bar{r}'_0|}}{4\pi|\bar{r}'-\bar{r}'_0|\det(\bar{\bar{J}})} \bar{\bar{J}} \cdot \bar{j}(\bar{r}_0) \quad (6)$$

with  $\bar{r}' = \bar{F}(\bar{r})$ ,  $\bar{r}'_0 = \bar{F}(\bar{r}_0)$ .

The above analysis implies that, by applying the coordinate transformation  $\bar{F}$ , a point source located at  $\bar{r}' = \bar{F}(\bar{r}_0)$  in the initial coordinates will be transformed to  $\bar{r} = \bar{r}_0$  in the transformed coordinates. Thus looking from the outside of the transformed region, a source located at  $\bar{r} = \bar{r}_0$  will appear to radiate at  $\bar{r} = \bar{F}(\bar{r}_0)$ . By selecting appropriate transformation  $\bar{F}$ , a source can be transformed into almost any required shape. This principle can be applied in the design of conformal antenna and electrically small antenna, which will be related in detail in the latter parts of this letter.

### 3. CONFORMAL ANTENNAS

Pendry et al. [1] suggested that with certain transformation, the electromagnetic field in a spherical region  $r < R_2$  can be compressed into the annulus region  $R_1 < r < R_2$ . Here we consider such a transformation as:  $\frac{x'^2+y'^2}{a^2(r)} + \frac{z'^2}{b^2(r)} = 1$ , with  $a(r) = \frac{R_2}{R_2-R_1}(r-R_1)$  as the major axis of the ellipse and  $b(r) = \frac{R_2-\frac{d}{2}}{R_2-R_1}(r-R_1) + \frac{d}{2}$  (Here  $d$  is a constant.) as the minor axis of the ellipse. In contrast to Pendry's transformation, it is different in that a line of the length  $d$  with respect to the original  $(x', y', z')$  axes instead of the origin is transformed to a spherical surface  $r = R_1$ , which stands for the inner boundary of the annulus. Suppose there is a line source of length  $d$  which is located at the origin, as shown in Fig. 1(a). Under the proposed transformation, the current of source is mapped to the surface current at the inner boundary ( $r = R_1$ ), and in the spherical region  $r < R_2$ , the electric field radiated by the dipole will be squeezed into the annulus. This assumption can be verified analytically with the method related above.

To begin with, we calculate the expression of the surface current at the inner surface  $r = R_1$ , in order that it will behave exactly the same as a dipole  $\bar{J}'_s = \lim_{r \rightarrow R_1} \frac{I_0}{2\pi a(r)} \hat{z} \rightarrow \infty$  to an outer observer.

With Equation (4), the surface current  $\bar{J}_s$  in the physical domain can be given as

$$\bar{J}_s = \bar{\bar{J}}^T \cdot \bar{J}'_s = -\frac{I_0 \sin \theta}{2\pi R_1} \hat{\theta} + \lim_{r \rightarrow R_1} o(a(r)) = -\frac{I_0 \sin \theta}{2\pi R_1} \hat{\theta} \quad (7)$$

Figure 1(b) displays the surface current on a spherical surface which works equivalently to the dipole under the aforementioned transformation. The electromagnetic field in the transformed coordinate can be obtained from Equations (6). By comparing the electric field distribution of this spherical surface current with that of the corresponding single dipole, we can notice that the fields outside the spherical region ( $r < R_2$ ) are exactly the same. Fig. 2(a) depicts the electric field produced by a line source, and Fig. 2(b) shows the field distribution of the equivalent surface

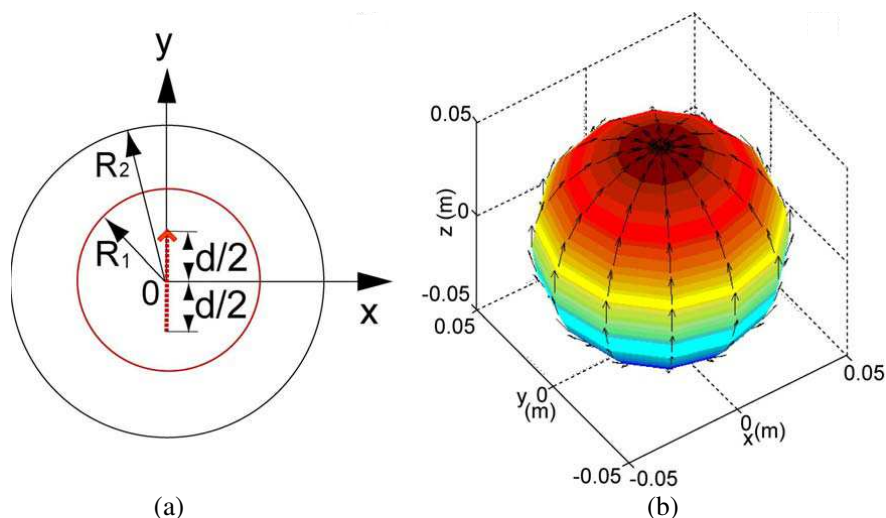


Figure 1: (a) Schematic of a spherical conformal antenna. Red dashed line is a dipole in the initial virtual domain. Red solid line is the radome surface where current is distributed. The outer surface is a sphere conformal to the inner radome. (b) Current distribution on a spherical surface in the transformed physical domain.

current at the inner boundary of a transformation medium shell. As a comparison, we also plot the difference between the fields in the two cases, which is shown in Fig. 2(c). This phenomenon can be comprehended like this, if we design a spherical shell with the above transformation, the surface current on the inner boundary will behave as a line source at the origin when detected from the outer space of the coating. This has something in common with the idea of cloaking, which can smoothly guide the wave around a volume so that the detector outside the cloaking shell will feel that the region inside the shell is empty.

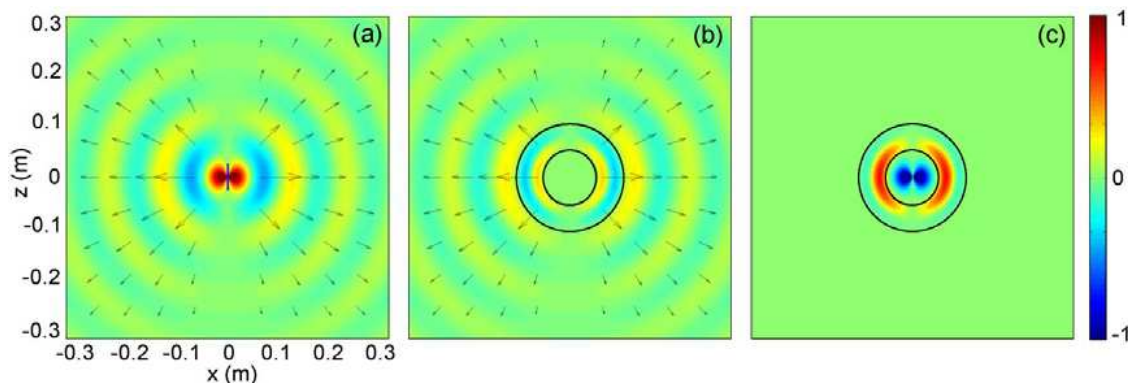


Figure 2: (a) Field distribution of a dipole in the initial virtual domain (free space). (b) Field distribution of the spherical conformal antenna in the transformed physical domain. (c) The difference between the fields in (a) and (b).

The above theory provides the basic principle for the design of conformal antenna using coordinate transformation. Given the metamaterial whose permittivity and permeability are appropriately designed, the emission of the source can be controlled in the expected way and the conformal antenna can be physically realized. As long as we find a mapping  $\bar{F}(f, g, h)$ , which can transform the inner domain of the radome, then we can fabricate such a radome with metamaterials to control the current, and consequently, the radiation. The outer surface of the radome is matched to free space while the current on a surface of arbitrary shape inside the radome can be mapped to the inner surface. As a result, the conformal antenna will have exactly the same radiation pattern as the original virtual antenna emitting in the free space.

#### 4. ELECTRICALLY SMALL ANTENNAS

Except for conformal antenna, how to reduce the size of an antenna is another topic that people are concerning about recently. Sometimes we make an antenna smaller at the cost of the performance in order to satisfy some size restriction in engineering. However, we find that by covering an antenna by a substrate composed of transformation media, an image that is much larger than the source will be produced, which will perform as a bigger antenna. In another word, we can realize a small antenna which behaves equivalently to a bigger one by covering it with a substrate designed with coordinate transformation. For simplicity, here we choose the substrate coating to be contained within the annulus  $R_1 < r < R_2$  and consider a simple transformation,

$$r' = f(r) \quad \theta' = \theta \quad \varphi' = \varphi \quad \text{with} \quad f(R_2) = R_2 \quad (8)$$

If  $f(r)$  is a multi-valued mapping expressed by a non-monotonic function, as shown in Fig. 3(a), the constitutive parameters of the corresponding medium will be obtained with Equation (3):

$$\bar{\epsilon} = \epsilon_r(r) \hat{r}\hat{r} + \epsilon_t(r) \hat{\theta}\hat{\theta} + \epsilon_t(r) \hat{\varphi}\hat{\varphi}, \quad \bar{\mu} = \mu_r(r) \hat{r}\hat{r} + \mu_t(r) \hat{\theta}\hat{\theta} + \mu_t(r) \hat{\varphi}\hat{\varphi} \quad (9)$$

where  $\epsilon_t = \epsilon_0 f'(r)$   $\epsilon_r = \epsilon_0 \frac{f^2(r)}{r^2 f'(r)}$ ,  $\mu_t = \mu_0 f'(r)$   $\mu_r = \mu_0 \frac{f^2(r)}{r^2 f'(r)}$

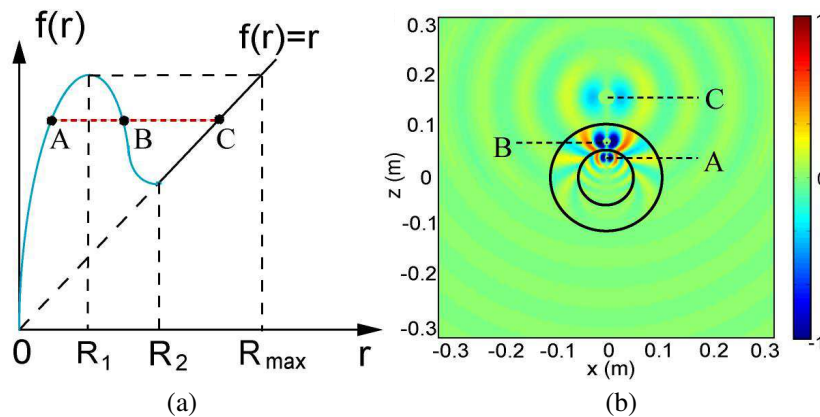


Figure 3: (a) Schematic figure of the transformation functions  $f(r)$  which is non-monotonic.  $r'$  of certain value in the initial virtual coordinate corresponds to  $r$  of three different values in the transformed coordinate, which are denoted by A, B, and C. (b) Electric field distribution of a coated source. The source is covered by a substrate created with transformation function  $f(r)$ , and is located at A, which is also denoted in subfigure (a). Two images are produced as a result, located at B and C, corresponding to point B and C in subfigure (a) respectively. It is easy to find the source is magnified in the imaging.

When  $r < R_1$ ,  $f(r)$  is monotone increasing while in the region  $R_1 < r < R_2$   $f(r)$  is monotone decreasing. From Equation (9) we can easily see that the medium from right-handed (RH) to left-handed (LH) [20] after crossing the boundary  $r = R_1$ . From Fig. 3(a), we noticed that a definite value of  $f(r)$  corresponds to three different  $r$  (depicted by A, B, and C in Fig. 3(a)). Thus if we put a source at point A, two images will be produced, which are located at points B and C respectively. The most remarkable is, different with the images formed with a left-handed material slab [21], the two images, one inside the left-handed region and one in the free space, are both magnified compared with the source. The reason is that, under this transformation, the field in the spherical domain ( $0 < r < R_{\max}$ ) is radially compressed into a smaller region ( $0 < r < R_1$ ), and as long as we embed a source within the sphere ( $0 < r < R_1$ ), an image which is even larger than the substrate coating ( $0 < r < R_1$ ) will be formed in the annulus ( $R_2 < r < R_{\max}$ ). This is verified by numerical simulations based on finite element method. When a point source is embedded in the RH region ( $r < R_1$ ), as shown in Fig. 3(b), two magnified images are produced. One is in the LH region ( $R_1 < r < R_2$ ) while the other is in the free space ( $r > R_2$ ), and the one outside the coating is even larger than the one in the LH region. Since the boundaries at  $R_1$  and  $R_2$  are matched, both B and C are perfect images of the source A.

Suppose an electric linear antenna with the current density  $\bar{j}(\bar{r}'') = \hat{z}I_0(1 - \frac{|z''|}{l})\delta(x'')\delta(y'')$  ( $l = 2R_1$ ) is placed at the origin. After covering the antenna with a spherical substrate whose

permittivity and permeability components are described by Equation (9), the electromagnetic fields inside and outside the substrate can be calculate with Equation (6). Fig. 4(a) shows the electric field distribution of an antenna with length  $2R_{\max}$  in free space; Fig. 4(b) shows the electric field distribution of a small antenna covered by the aforementioned complex RH-LH coating of radius  $R_2$ . From Fig. 4(c) which shows the difference between the fields of the two cases, we can easily conclude that the coated small antenna has the equivalent performance to the original large one.

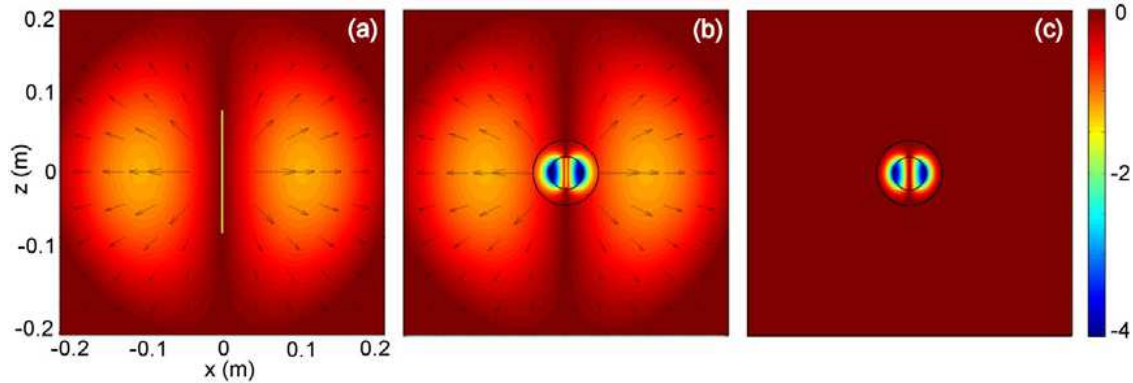


Figure 4: (a) Field distribution of an electric linear antenna with length  $2R_{\max}$  in the initial virtual domain (free space). (b) Field distribution of a electric linear antenna with length  $2R_1$  embedded in the substrate (with diameter  $2R_2 < 2R_{\max}$ ) in the transformed physical domain. (c) Difference of the fields in (a) and (b).

## 5. CONCLUSION

Coordinate transformation is not restricted to source-free cases. The transformation on those domains containing sources can be studied by manipulating the Maxwell's equations. Under transformations, not only the space but also the sources can be transformed, and given access to proper metamaterials, the initial source can be replaced by another source of almost any required shape with the same radiation properties. This makes the realization of some active EM devices, such as conformal antenna and electric small antenna, a practical possibility.

## ACKNOWLEDGMENT

This work is sponsored by the Chinese National Science Foundation under Grant Nos. 60531020 and 60671003, the NCET-07-0750, the China Postdoctoral Science Foundation under Grant No. 20060390331, the ONR under Contract No. N00014-01-1-0713, and the Department of the Air Force under Air Force Contract No. F19628-00-C-0002.

## REFERENCES

1. Pendry, J. B., D. Schurig, and D. R. Smith, *Science*, Vol. 312, 1780, 2006.
2. Leonhardt, U., *Science*, Vol. 312, 1777, 2006.
3. Schurig, D., J. B. Pendry, and D. R. Smith, *Opt. Express*, Vol. 14, 9794, 2006.
4. Pendry, J. B., et al., *Phys. Rev. Letts.*, Vol. 76, 4773, 1996.
5. Pendry, J. B., et al., *IEEE Trans. Microwave Theory Tech.*, Vol. 47, 2075, 1999.
6. Smith, D. R., et al., *Phys. Rev. Letts.*, Vol. 84, 4184, 2000.
7. Schurig, D., et al., *Science*, Vol. 314, 5801, 2006.
8. Cummer, S. A., et al., *Phys. Rev. E*, Vol. 74, 036621, 2006.
9. Cai, W., et al., *Nat. Photonics*, Vol. 1, 224, 2007.
10. Chen, H., et al., *Phys. Rev. Letts.*, Vol. 99, 063903, 2007.
11. Cai, W., et al., *Appl. Phys. Letts.*, Vol. 91, 111105, 2007.
12. Weder, R., eprint ArXiv: 0704. 0248, 2007.
13. Sihvola, A. H., *Progress In Electromagnetics Research*, PIER 66, 191, 2006.
14. Zhang, J., et al., *Phys. Rev. B*, to be published.
15. Rahm, M., et al., eprint ArXiv: 0706. 2452, 2007.
16. Yaghjian, A. D. and S. Maci, eprint ArXiv: 0710. 2933, 2007.
17. Chen, H. and C. T. Chan, *Appl. Phys. Letts.*, Vol. 90, 241105, 2007.

18. Tsang, M. and D. Psaltis, eprint ArXiv: 0708. 0262, 2007.
19. Kildishev, A. V. and E. E. Narimanov, eprint ArXiv: 0708. 3798, 2007.
20. Veselago, V. G., *Sov. Phys. Usp.*, Vol. 10, 509, 1968.
21. Pendry, J. B., *Phys. Rev. Letts.*, Vol. 85, 3966, 2000.

# Effect of Losses in a Layered Structure Containing DPS and DNG Media

J. R. Canto, S. A. Matos, C. R. Paiva, and A. M. Barbosa

Instituto de Telecomunicações and Department of Electrical and Computer Engineering  
Instituto Superior Técnico, Av. Rovisco Pais 1, 1049-001 Lisboa, Portugal

**Abstract**— The problem of reflection and transmission of plane electromagnetic waves in a periodic multilayered structure containing double-negative (DNG) media is analyzed using a matrix formalism. A Lorentz model with a single resonance is used to describe the dispersion of the DNG medium. It is shown that the introduction of losses, in accordance with the Kramers-Kronig relations, is essential in order to obtain correct results on the performance of the structure.

## 1. INTRODUCTION

Although the concept of a DNG medium (i.e., a double-negative medium with  $\varepsilon < 0$  and  $\mu < 0$ ) was first proposed by Veselago [1], it took many years until experimental evidence for the existence of such a medium was presented [2]. In order to uphold the causality principle, a dispersive model should include losses according to the Kramers-Kronig relations [3]. In fact, for plane wave propagation of the form  $\exp[i(nk_0z - \omega t)]$ , the refractive index of the unbounded passive medium is given by  $n = \pm\sqrt{(\varepsilon\mu)}$  and, in order to select the correct sign, losses must be taken into account. Hence, the condition  $\text{Im}\{n\} > 0$  imposes that, for the DPS (double-positive) case, we should have  $n = \sqrt{(\varepsilon\mu)}$  whereas, for the DNG case, we should have  $n = -\sqrt{(\varepsilon\mu)}$  instead. Accordingly, in this communication, the following Lorentz model is used to describe DNG media

$$\varepsilon(\omega) = 1 - \frac{\omega_{ep}^2}{\omega^2 - \omega_{eo}^2 + i\gamma_e\omega}, \quad \mu(\omega) = 1 - \frac{\omega_{mp}^2}{\omega^2 - \omega_{mo}^2 + i\gamma_m\omega} \quad (1)$$

where  $\omega_{ep,mp}$  are the plasma frequencies,  $\omega_{eo,mo}$  the resonance frequencies and  $\gamma_{e,m}$  the loss coefficients. In this work we will focus on the reflection and transmission of electromagnetic waves in a periodic multilayered structure containing DPS and DNG layers as the one depicted in Fig. 1. The problem of multilayered structures [4] has already been studied in the literature when DNG layers are included [5, 7], although a causal model for dispersion, thereby taking losses into account, has never been taken into account — as far as the authors are aware. In fact, we show herein that losses deeply change the global behavior of the whole structure: the reflectance and transmittance present completely different characteristics for these two distinct situations. The transmittance, in particular, is strongly attenuated even for very small losses, thereby limiting the number of periods that can be used. Furthermore, the forbidden bands also increase significantly when losses are included. Accordingly, our main conclusion is that a causal model, that takes both dispersion and losses into account, is an essential tool for the study of multilayered structures containing DNG media.

## 2. ANALYTICAL APPROACH

For a simple interface between two isotropic media one has  $(n\omega/c)^2 = k_z^2 + k_x^2$ . As already mentioned before, the sign for the root in  $n = \pm\sqrt{(\varepsilon\mu)}$  depends on whether a DPS or a DNG medium is considered.

One also has  $k_z = n(\omega/c) \cos(\theta)$ , where  $\theta$  is the incidence angle of the wave vector with respect to the interface. For TE modes, the field components are given by

$$E_y = A \exp(ik_z z) + B \exp(-ik_z z), \quad H_x = -\frac{k_z}{\omega\mu} [A \exp(ik_z z) - B \exp(-ik_z z)] \quad (2)$$

where  $A$  and  $B$  are the amplitudes of the forward and backward traveling waves. After imposing the boundary conditions to the field components as given by (2), we get

$$D_1 \begin{bmatrix} A_1 \\ B_1 \end{bmatrix} \Big|_{z=0^-} = D_2 \begin{bmatrix} A_2 \\ B_2 \end{bmatrix} \Big|_{z=0^+} \quad (3)$$

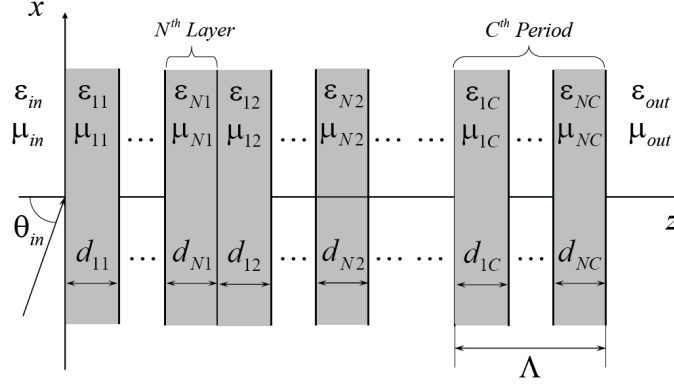


Figure 1: Structure containing  $N$  layers of isotropic media of thickness  $d_i$  and parameters  $\varepsilon_i$ ,  $\mu_i$ , repeated over  $C$  periods of length  $\Lambda$ .

where  $D_i$  is the transmission matrix for the  $i$ -th layer. For TE and TM modes, we have respectively

$$D_i^{\text{TE}} = \begin{bmatrix} 1 & 1 \\ \frac{n_i}{\mu_i} \cos \theta_i & -\frac{n_i}{\mu_i} \cos \theta_i \end{bmatrix}, \quad D_i^{\text{TM}} = \begin{bmatrix} \cos \theta_i & \cos \theta_i \\ \frac{n_i}{\mu_i} & -\frac{n_i}{\mu_i} \end{bmatrix}. \quad (4)$$

The field amplitudes at an interface can be then related through

$$\begin{bmatrix} A_1 \\ B_1 \end{bmatrix} \Big|_{x=0^+} = D_1^{-1} D_2 \begin{bmatrix} A_2 \\ B_2 \end{bmatrix} \Big|_{x=0^-}. \quad (5)$$

In order to apply these results to the structure defined in Fig. 1 it is also necessary to define the propagation matrix  $P_i$ , to account for propagation inside the layer of thickness  $d_i$

$$\begin{bmatrix} A_i \\ B_i \end{bmatrix} \Big|_{z=z_i-d_i} = P_i \begin{bmatrix} A_i \\ B_i \end{bmatrix} \Big|_{z=z_i}, \quad P_i = \begin{bmatrix} \exp(-ik_{zi}d_i) & 0 \\ 0 & \exp(ik_{zi}d_i) \end{bmatrix} \quad (6)$$

where  $k_{zi} = n_i(\omega/c) \cos(\theta_i)$  and  $\theta_i$  is the angle for the  $i$ -th layer so that  $k_{xi} = n_i(\omega/c) \sin(\theta_i)$ . For a structure with a single period, the relation between the amplitude of the incident waves  $A_{in}$  and  $B_{in}$ , at  $z = 0$ , and the transmitted waves  $A_{out}$  and  $B_{out}$ , at  $z = \Lambda$ , can be written as

$$\begin{bmatrix} A_{in} \\ B_{in} \end{bmatrix} = D_{in}^{-1} D_1 P_1 D_1^{-1} D_{out} \begin{bmatrix} A_{out} \\ B_{out} \end{bmatrix}. \quad (7)$$

Hence, the transmission matrix for the whole structure presented in Fig. 1 is

$$\begin{bmatrix} A_{in} \\ B_{in} \end{bmatrix} = \mathbf{M} \begin{bmatrix} A_{out} \\ B_{out} \end{bmatrix}, \quad \mathbf{M} = D_{in}^{-1} \left[ \prod_{i=1}^N D_i P_i D_i^{-1} \right]^C D_{out}. \quad (8)$$

The transmittance and reflectance of the structure can then be obtained through (8). For left incidence,  $B_{out} = 0$  and the total reflectance  $R$  and transmittance  $T$  are given by

$$R = \left| \frac{B_{in}}{A_{in}} \right|_{B_{out}=0}^2 = \left| \frac{M_{21}}{M_{11}} \right|^2, \quad T = \left| \frac{A_{out}}{A_{in}} \right|_{B_{out}=0}^2 = \left| \frac{1}{M_{11}} \right|^2. \quad (9)$$

The structure under analysis is periodic. Hence, according to Floquet's theorem, the solutions of the wave equations are of the form

$$E_K(x, z) = E_k(z) \exp(iKz + ik_x x) \quad (10)$$

with  $E_K(z + \Lambda) = E_K(z)$  and where  $K$  is the Bloch wavenumber. The periodicity can be expressed as

$$\begin{bmatrix} A_1 \\ B_1 \end{bmatrix} \Big|_{z=d_1} = \exp(-iK\Lambda) \begin{bmatrix} A_1 \\ B_1 \end{bmatrix} \Big|_{z=d_1+\Lambda} \quad (11)$$

which, combined with the previous matrix formalism (8), leads to

$$\begin{bmatrix} L_{11} & L_{12} \\ L_{21} & L_{22} \end{bmatrix} \begin{bmatrix} A_1 \\ B_1 \end{bmatrix}_{z=d_1+\Lambda} = \exp(-iK\Lambda) \begin{bmatrix} A_1 \\ B_1 \end{bmatrix}_{z=d_1+\Lambda}, \quad \mathbf{L} = D_1^{-1} \left[ \prod_{i=2}^N D_i P_i D_i^{-1} \right] D_1 P_1, \quad (12)$$

where a new matrix  $\mathbf{L}$  was introduced. The problem then reduces to a simple equation:  $\det[\mathbf{L} - \exp(-iKz)\mathbf{I}] = 0$ . Since  $|\mathbf{B}\mathbf{A}\mathbf{B}^{-1}| = |\mathbf{A}|$ , we get  $\det(\mathbf{L}) = 1$  (i.e.,  $\mathbf{L}$  is unimodular, as expected, since it relates two equivalent layers with the same index of refraction). The Bloch wave function is finally obtained through the equation

$$\cos(K\Lambda) = \frac{1}{2} \text{tr}(\mathbf{L}). \quad (13)$$

Henceforth only the case with  $N = 2$  for a structure immersed in air, with a unit cell composed of a DNG and a DPS layers, will be considered. Then, for TE modes, (13) reduces to

$$\cos(K\Lambda) = \cos(k_{z1}d_1) \cos(k_{z2}d_2) - \frac{1}{2} \left( \frac{\mu_1 k_2}{\mu_2 k_1} + \frac{\mu_2 k_1}{\mu_1 k_2} \right) \sin(k_{z1}d_1) \sin(k_{z2}d_2). \quad (14)$$

The Bloch wave number  $K$  defines propagating waves when  $\text{Im}\{K\} = 0$  and evanescent waves when  $\text{Im}\{K\} \neq 0$ . Whenever losses are taken into account,  $\varepsilon$  and  $\mu$  become complex as well as  $K$ . Strictly speaking, all wave solutions then become complex. Therefore, we introduce the ratio  $\text{Im}\{K\}/\text{Re}\{K\}$  so that we can have a criterion to enable the distinction between propagating and evanescent-like waves.

### 3. NUMERICAL RESULTS

In this section only TE modes on a structure, immersed in air, with  $C = 10$  periods and  $N = 2$  (Fig. 1) are numerically analyzed. The unit cell includes a DNG ( $\varepsilon_1, \mu_1$ ) slab, with a medium described by (1), and a DPS ( $\varepsilon_2 = 1.5, \mu_2 = 1$ ) slab. The adopted numerical values for the parameters were the following:  $\omega_{ep} = 2\pi \times 10^{10} \text{ rads}^{-1}$ ,  $\omega_{mp} = 2\pi \times 3.52 \times 10^9 \text{ rads}^{-1}$ ,  $\omega_{eo} = 2\pi \times 10^8 \text{ rads}^{-1}$ ,  $\omega_{mo} = 2\pi \times 4 \times 10^9 \text{ rads}^{-1}$  and  $4.2 < f[\text{GHz}] < 5.2$ . To analyze the effect of losses, two cases were studied: (i)  $\gamma_e = \gamma_m = 0 \text{ rads}^{-1}$ ; (ii)  $\gamma_e = \gamma_m = 2\pi \times 10^7 \text{ rads}^{-1}$ . The reflectance and transmittance for the first case are shown in Figs. 2 and 3, respectively. The passbands and stopbands that can be observed, which are typical of a multilayered structure containing DNG media, decrease when the incidence angle increases. The results obtained for the reflectance and transmittance reveal severe changes, even when both coefficients  $\text{Im}\{\varepsilon\}/\text{Re}\{\varepsilon\}$  and  $\text{Im}\{\mu\}/\text{Re}\{\mu\}$  remain below 0.5%, as shown in Figs. 4 and 5. One should also stress that the transmittance curve is the most affected due to the cumulative effect of losses introduced by each DNG layer of the structure, therefore limiting the maximum length of the structure.

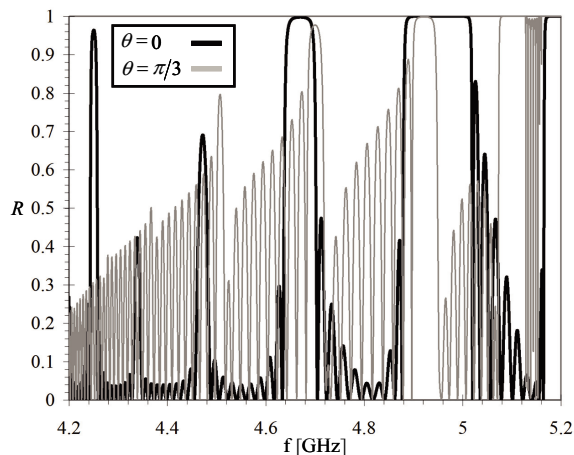


Figure 2: Reflectance for  $\gamma_e = \gamma_m = 0 \text{ rads}^{-1}$ .

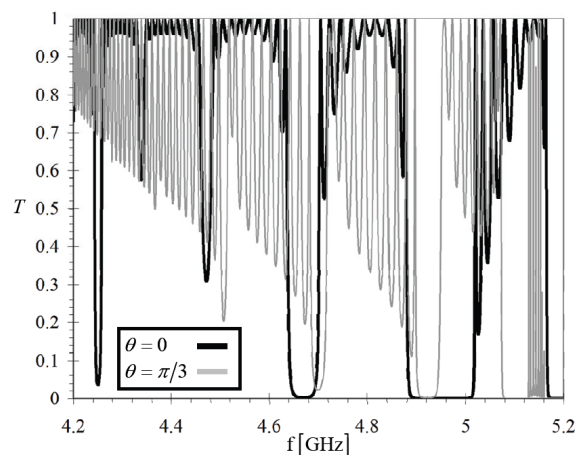
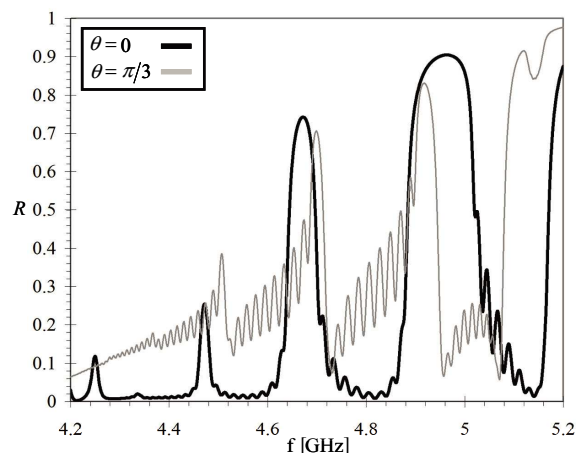
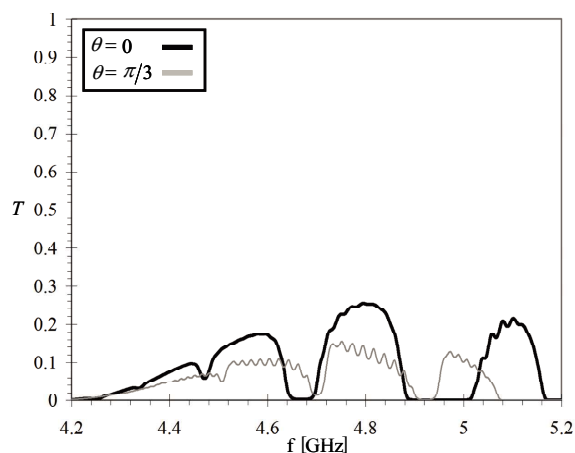
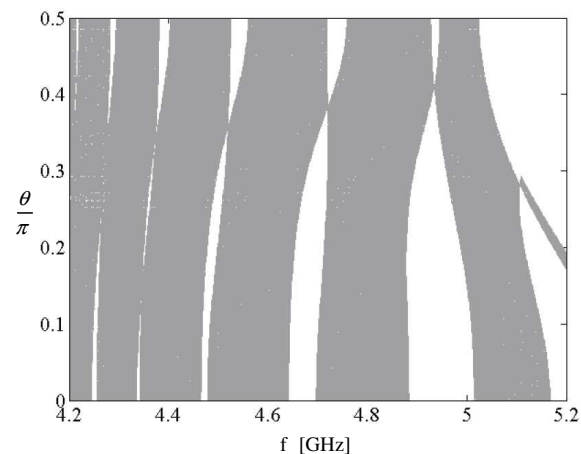
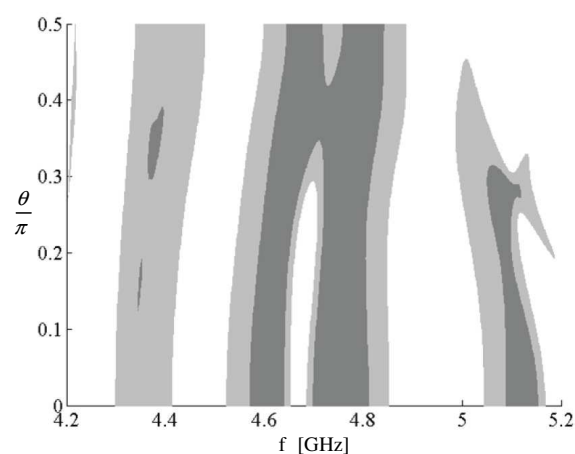


Figure 3: Transmittance for  $\gamma_e = \gamma_m = 0 \text{ rads}^{-1}$ .


 Figure 4: Reflectance for  $\gamma_e = \gamma_m = 2\pi \times 10^7 \text{ rads}^{-1}$ .

 Figure 5: Transmittance for  $\gamma_e = \gamma_m = 2\pi \times 10^7 \text{ rads}^{-1}$ .

According to (14), the passbands corresponding to propagating Bloch waves are presented in Fig. 6, case (i), and Fig. 7, case (ii), for several values of the incident angle. For the lossless case, presented in Fig. 6, the passbands are defined as  $\text{Im}\{K\} = 0$  and depicted in grey. When losses are taken into account, the Bloch wave number becomes complex. Hence, in Fig. 7, that represents case (ii), different tone grey areas are used to represent different criteria for the definition of passbands, namely: (a) dark grey –  $\text{Im}\{K\}/\text{Re}\{K\} < 5\%$ ; (b) light grey –  $\text{Im}\{K\}/\text{Re}\{K\} < 10\%$ . A comparison between Figs. 6 and 7 reveals the significant effect of losses: the passbands change with an increase width of the forbidden bands. Thus, a causal dispersion model has to be used in order to derive the proper behavior of the structure, even when losses remain below 0.5%.


 Figure 6: Passbands for  $\gamma_e = \gamma_m = 0 \text{ rads}^{-1}$ .

 Figure 7: Passbands for  $\gamma_e = \gamma_m = 2\pi \times 10^7 \text{ rads}^{-1}$ .

#### 4. CONCLUSIONS

It was found that a causal Lorentz model, to account for both dispersion and losses in a DNG medium, is an essential tool for a correct electromagnetic characterization of a multilayered structure when using these type of media. It has been shown that, even when very small losses are introduced, significant changes do emerge. These losses affect the transmittance values and justify an increase in the number of forbidden bands, and these effects must be taken into account when these type of structures are used for filter design.

#### REFERENCES

1. Veselago, V. G., "The electrodynamics of substances with simultaneously negative values of  $\epsilon$  and  $\mu$ ," *Sov. Phys.-Usp.*, Vol. 10, No. 4, 509–514, 1968.

2. Smith, D. R., W. J. Padilla, D. C. Vier, S. C. Nemat-Nasser, and S. Schultz, “Composite medium with simultaneously negative permeability and permittivity,” *Phys. Rev. Lett.*, Vol. 84, No. 18, 4184–4187, 2000.
3. Peiponen, K. E., V. Lucarini, E. M. Vartiainen, and J. J. Saarinen, “Kramers-Kronig relations and sum rules of negative refractive index media,” *Eur. Phys. J. B*, Vol. 41, 61–65, September 2004.
4. Yeh, P., *Optical Waves in Layered Media*, 1988, 118–134, Wiley, New York, 2005.
5. Tretyakov, S., *Analytical Modeling in Applied Electromagnetics*, 251–353, Artech House, Boston, 2003.
6. Alù, A. and N. Engheta, “Pairing an epsilon-negative slab with a mu-negative slab: Resonance, tunneling and transparency,” *IEEE Trans. Antennas Propagat.*, Vol. 51, No. 10, 2258–2571, October 2003.
7. Jiang, H. and H. Chen, “Omnidirectional gap and defect mode of one-dimensional photonic crystals containing negative-index materials,” *Appl. Phys. Lett.*, Vol. 83, No. 26, 5386, December 2003.

# Complex Aberration Effect in Moving Dispersive DNG Media: A Spacetime Algebra Approach

S. A. Matos, J. R. Canto, C. R. Paiva, and A. M. Barbosa

Instituto de Telecomunicações and Department of Electrical and Computer Engineering  
Instituto Superior Técnico, Av. Rovisco Pais 1, 1049-001 Lisboa, Portugal

**Abstract**— Using spacetime algebra, the Doppler shift, aberration and the refractive index covariance, relating the co-moving and laboratory frames, are readily obtained. Lorentz transformations and the cumbersome constitutive relations in the laboratory frame are circumvented altogether. The theory of a moving double-negative medium (DNG) is developed by using a lossless model to account for material dispersion. The normal surfaces and the Doppler effect are analyzed. We show that a complex index of refraction may arise in the laboratory frame as a result of a complex aberration effect. A physical interpretation for this new type of aberration is also presented.

## 1. INTRODUCTION

In recent years, DNG (double-negative) media, theoretically proposed by Veselago [1], have become a research topic of growing interest. In the electromagnetic theory of moving isotropic — either DPS (double-positive) or DNG — media, negative refraction [2] and negative phase velocity [3] are now well-known effects, although the influence of material dispersion has been neglected so far. Čerenkov radiation in a lossy DNG medium was already addressed in [4]. Here we analyze plane wave propagation in a moving DNG medium by considering a lossless dispersive model to account for material dispersion. The laboratory frame moves with constant velocity relative to the proper (or co-moving) frame where the medium is at rest and, hence, seen as a DNG medium. Our main goal is to characterize this DNG medium from the perspective of the lab frame where it is seen as a bianisotropic medium. However, to circumvent the cumbersome calculations that such complex constitutive relations with magnetoelectric coupling impose, we will use the mathematical approach of Clifford's geometric algebra [5–7]. With this new formalism the vectors of Minkowski spacetime (absolute vectors) are related to the vectors of regular space (relative vectors) in a straightforward way. Using this new mathematical tool [5] we present a new method to obtain the Doppler shift, aberration and the refractive index covariance relating the co-moving and laboratory frames. All these effects are derived from a single geometric equation which depends exclusively on the (absolute) wave and velocity vectors. Both the normal surfaces and the Doppler effect in moving DNG media are analyzed for the first time, as far as the authors are aware. The analyses presented in the literature so far only handle normal surfaces not taking into account the Doppler effect. Herein, however, both effects interplay (as they should) and hence they have to be taken into account at the same time. The normal surfaces of a moving isotropic medium have already been analyzed by Chen [8]. However, in DNG media, the influence of dispersion on those surfaces was never reported (to our knowledge). We also show how dispersion has a decisive role, namely when the modulus of the refractive index is below one. In fact, in this case, a complex index of refraction is obtained in the lab frame as a new complex aberration effect arises. For this particular case the Doppler effect is, indeed, inconsistent: a real Doppler effect is found for the lab frame; from the proper frame perspective, however, there is a complex Doppler effect. We claim that the only consistent way to analyze this region is by taking losses into account. One should not forget that causality is an important issue in DNG media: dispersion is correlated to losses, as shown through the Kramers-Kronig relations [9]. Furthermore, we also stress that the distinction between a medium with a negative-index of refraction and a DNG medium is mandatory whenever losses are included [10].

## 2. SPACETIME ALGEBRA

Geometric algebra can be applied to an arbitrary space. For the Minkowski spacetime the algebra is named  $\mathcal{Cl}_{1,3}$  or  $\mathcal{Cl}_{3,1}$ , depending on the metric. We adopt the  $\mathcal{Cl}_{1,3}$  metric, i.e., for the unit orthogonal vectors ( $\mathbf{e}_0, \mathbf{e}_1, \mathbf{e}_2, \mathbf{e}_3$ ) we have:  $\mathbf{e}_0^2 = 1, \mathbf{e}_1^2 = \mathbf{e}_2^2 = \mathbf{e}_3^2 = -1$ . A general element of  $\mathcal{Cl}_{1,3}$ , which we call a multivector, is given by a (graded) sum of a scalar, a vector, a bivector, a trivector

and a quadrivector. The geometric product is defined between any elements of  $C\ell_{1,3}$ . This product is associative and verifies the contraction property. The geometric product between two vectors is defined as the sum of a scalar (the usual dot or inner product) with a bivector (resulting from the outer or exterior product,  $\wedge$ ):  $\mathbf{ab} = \mathbf{a} \cdot \mathbf{b} + \mathbf{a} \wedge \mathbf{b}$ . A vector  $\mathbf{a}$ , when  $\mathbf{aa} > 0$ , is called a time-like vector and, when  $\mathbf{aa} < 0$ , is called a space-like vector. Therefore, a vector can be decomposed as:  $\mathbf{a} = a_0\mathbf{e}_0 + \vec{a}$ , where  $a_0$  is the time component and  $\vec{a} = a_1\mathbf{e}_1 + a_2\mathbf{e}_2 + a_3\mathbf{e}_3$  is the spatial component. With spacetime algebra there is a new way of relating spacetime (or absolute) vectors with vectors of  $\mathbb{R}^3$  (relative vectors). The geometric product of a vector with a unit time vector gives a graded sum of a scalar with a bivector:  $\mathbf{ae}_0 = a_0 + \vec{a}\mathbf{e}_0$ . The relative “vector” is actually the bivector  $\mathbf{A} = \vec{a}\mathbf{e}_0$ . In fact,  $\mathbb{R}^3$  is isomorphic to the subspace of bivectors ( $\mathbf{e}_1\mathbf{e}_0, \mathbf{e}_2\mathbf{e}_0, \mathbf{e}_3\mathbf{e}_0$ ) [5]. The scalar  $a_0$  and the bivector  $\mathbf{A}$  are relative quantities, i.e., they are frame dependent. Within the context of special relativity, the proper frame ( $\mathbf{f}_0, \mathbf{f}_1, \mathbf{f}_2, \mathbf{f}_3$ ) moves with constant velocity relative to the lab frame ( $\mathbf{e}_0, \mathbf{e}_1, \mathbf{e}_2, \mathbf{e}_3$ ). Accordingly, an absolute vector has a different representation in different frames. For our analysis we will only introduce two absolute vectors: the wave vector  $\mathbf{k} = (\omega_1/c)(\mathbf{e}_0 + \vec{n}_1) = (\omega_2/c)(\mathbf{f}_0 + \vec{n}_2)$ . and the velocity vector of a material point in the lab frame  $\mathbf{u} = c\mathbf{e}_0 = \gamma(c\mathbf{f}_0 - \beta\vec{u})$ , where  $\gamma = 1/\sqrt{1 - \beta^2}$  and  $\beta = v/c$  is the normalized velocity between frames. According to reversion, an operation that verifies the properties  $(\mathbf{ab})^\sim = \mathbf{ba}$ ,  $\tilde{\mathbf{A}} = -\mathbf{A}$  and  $\tilde{a}_0 = a_0$ , relative quantities are related by

$$(\mathbf{ke}_0)(\mathbf{ue}_0)^\sim = (\mathbf{kf}_0)(\mathbf{uf}_0)^\sim. \quad (1)$$

Furthermore,  $\mathbf{ue}_0 = c$ ,  $\mathbf{uf}_0 = \gamma c(1 - \beta\hat{\mathbf{U}})$ ,  $\mathbf{ke}_0 = (\omega_1/c)(1 + n_1\hat{\mathbf{N}}_1)$ ,  $\mathbf{kf}_0 = (\omega_2/c)(1 + n_2\hat{\mathbf{N}}_2)$ , where  $\hat{\mathbf{U}}$  is the relative velocity “vector” and  $\hat{\mathbf{N}}_i = n_i\hat{\mathbf{N}}_i$  is the relative refractive index “vectors”. Then, according to (1),  $\omega_1(1 + n_1\hat{\mathbf{N}}_1) = \gamma\omega_2(1 + n_2\hat{\mathbf{N}}_2)(1 + \beta\hat{\mathbf{U}})$  and hence

$$\begin{cases} \omega_1 = \gamma\omega_2 \left(1 + \beta n_2 \hat{\mathbf{N}}_2 \cdot \hat{\mathbf{U}}\right) \\ n_1 \hat{\mathbf{N}}_1 = \gamma \frac{\omega_2}{\omega_1} \left(n_2 \hat{\mathbf{N}}_2 + \beta \hat{\mathbf{U}} + \beta n_2 \hat{\mathbf{N}}_2 \wedge \hat{\mathbf{U}}\right). \end{cases} \quad (2)$$

The Doppler effect is explicitly obtained in (2). Solving (2), we get

$$n_1 \hat{\mathbf{N}}_1 = \frac{n_2 \hat{\mathbf{N}}_2 + \beta \hat{\mathbf{U}} + \beta n_2 \hat{\mathbf{N}}_2 \wedge \hat{\mathbf{U}}}{1 + \beta n_2 \hat{\mathbf{N}}_2 \cdot \hat{\mathbf{U}}}. \quad (3)$$

All terms in (3) are bivectors. The term  $\hat{\mathbf{N}}_2 \wedge \hat{\mathbf{U}}$  is the exterior product of two bivectors and, in this case, it is also a bivector. Nevertheless, bivectors  $\hat{\mathbf{N}}_2$  and  $\hat{\mathbf{U}}$  are time-like whereas  $\hat{\mathbf{N}}_2 \wedge \hat{\mathbf{U}}$  is space-like. From (3), after calculating  $\hat{\mathbf{N}}_1 \hat{\mathbf{N}}_1$  and  $\hat{\mathbf{N}}_1 \cdot \hat{\mathbf{U}}$ , we get

$$n_1^2 = \frac{n_2^2 (1 - \beta^2 \sin^2 \theta_2) + 2\beta n_2 \cos \theta_2 + \beta^2}{(1 + \beta n_2 \cos \theta_2)^2}, \quad \cos \theta_1 = \frac{1}{n_1} \frac{n_2 \cos \theta_2 + \beta}{1 + n_2 \cos \theta_2}, \quad (4)$$

where  $\theta_i$  is the angle between  $\hat{\mathbf{N}}_i$  and  $\hat{\mathbf{U}}$ . Since both Equations (4) are still valid with the transformation  $n_1 \leftrightarrow n_2$ ,  $\theta_1 \leftrightarrow \theta_2$  and  $\beta \leftrightarrow -\beta$ , we obtain, after some simple algebra, the more traditional expressions

$$n_1 = \frac{-\xi \beta \cos \theta_1 \pm \sqrt{1 + \xi (1 - \beta^2 \cos^2 \theta_1)}}{1 - \xi \beta^2 \cos^2 \theta_1}, \quad \tan \theta_1 = \frac{1}{\gamma} \frac{\sin \theta_2}{\cos \theta_2 + \beta/n_2}, \quad (5)$$

where  $\xi = \gamma^2(n_2^2 - 1)$ . The plus (minus) sign in (5) corresponds to a DPS (DNG) medium.

### 3. DISPERSION EFFECT

The following dispersive model (in the proper frame) is used throughout [11]:  $\varepsilon(\Omega) = 1 - (\Omega_p/\Omega)^2$ ,  $\mu(\Omega) = 1 - F\Omega^2/(\Omega^2 - 1)$ , where  $\Omega$  is the normalized frequency  $\Omega = \omega_2/\omega_m$ ,  $\omega_m$  is the magnetic resonance frequency, and the parameter  $\Omega_p$ , given by  $\Omega_p = \omega_p/\omega_m$ , is the normalized electrical resonance frequency. The numerical values  $F = 0.56$  and  $\Omega_p = 5/2$  were also adopted. According to this model, the medium behaves as DNG for  $1 < \Omega < (1 - F)^{-1/2}$ . In the proper frame the refractive index is  $n_2 = \pm\sqrt{\varepsilon\mu}$ , the negative (positive) sign is chosen if the medium is DNG

(DPS). The results for the problem under consideration depend on two parameters: the emitted frequency  $\Omega$  and the relative velocity  $\beta$  between frames. The polar plots of the phase velocity, given by  $v_p = c/n_1$ , and the frequency shift, given by the parameter  $1 + z = \omega_1/\omega_2$ , are presented in Fig. 1 for  $\beta = 0.3$ . This polar diagram has a simple graphical interpretation: in the lab frame and for a given direction, the receiver recognizes the frequency received and the corresponding phase velocity. The frequency surfaces reveal a complementary variation to the normal surfaces. For relative velocities above the phase velocity (the Čerenkov point), as is in Fig. 1(a), double solutions occur for some angles (not only for the normal surfaces but also for the frequency plot). However, this type of solution occurs in the first quadrant for the normal surfaces and in the third quadrant for the frequency surfaces. For  $\Omega \approx 1$  the index of refraction presents high values, thereby leading to a low phase velocity. This explains why in Fig. 1(a) the Čerenkov point is crossed for low values of  $\beta$ . By increasing the frequency the index of refraction decreases and hence the Čerenkov point is not crossed anymore, Fig. 1(b). In Fig. 1(c), the case where the index of refraction is very close to one is shown and two isotropic-like surfaces occur as expected.

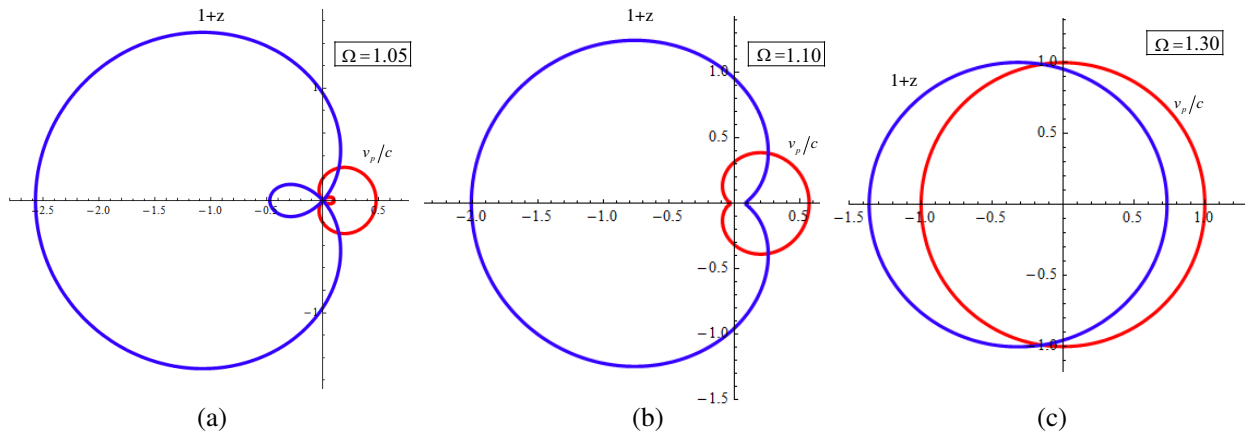


Figure 1: Normal and frequency surfaces for  $\beta = 0.3$ .

For lower values of the index of refraction a new effect may occur: in (5), if the argument of the square root is negative, the index of refraction becomes complex. This occurs for  $|n_2| < \beta < 1$  and implies that complex Doppler and aberration effects are present. However, the Doppler effect described in terms of the proper frame parameters,  $\omega_1 = \gamma\omega_2(1 + n_2\beta \cos\theta_2)$ , seems to predict only real frequencies. Indeed, these two approaches are not consistent as only one of them predicts complex values. In what follows we will present a physical explanation that will shed light on this matter. Let us assume that  $\theta_2$  is complex:  $\theta_2 = \theta'_2 + i\theta''_2$ . According to aberration (5), a complex angle in the lab frame has a real representation in the proper frame whenever

$$\text{Im} \left( \frac{1}{\gamma \cos \theta_2 + \beta/n_2} \right) = 0 \Rightarrow \frac{\cos h(\theta''_2)}{\cos \theta'_2} = -\frac{\beta}{n_2}. \quad (6)$$

One can then conclude from (6) that, for  $|n_2| < \beta$ , a complex angle can have a real representation in the lab frame. This is the same limit as predicted before. Accordingly, the problem at hand is actually consistent as long as we allow for the existence of complex angles in the proper frame. A complex angle in the proper frame implies a complex index of refraction which means that losses must be taken into account. This is not surprising at all: in fact, whenever dispersion is included in the analysis, causality implies that we should have a lossy medium according to the Kramers-Kronig relations. Our main conclusion is that losses must be accounted for so that the entire problem can be formulated in a consistent way.

#### 4. CONCLUSIONS

The influence of dispersion on a moving DNG medium was discussed. Using the formalism of spacetime algebra, a new simple derivation of the Doppler effect, aberration and refractive index covariance was presented. The normal surfaces and the Doppler effect were studied from the lab frame perspective. By representing these two effects in the same polar plot a complementary behavior was found between the two surfaces. It was shown that the influence of frequency dispersion

deeply changes the nature of the problem. For emitted frequencies that correspond to high values of refractive index, the relativistic effects start to occur for lower velocities between frames. On the other hand, for a frequency band where  $|n_2| < \beta$  a new result was reported: the Doppler and aberration effects can be complex. We found that aberration can indeed relate complex angles (measured in the proper frame) with real angles (measured in the lab frame). We claim that a proper interpretation of this problem requires that losses should be taken into account in our dispersion model, so that causality is respected as imposed by the Kramers-Kronig relations.

#### REFERENCES

1. Vesalago, V. G., "The electrodynamics of substances with simultaneously negative values of  $\epsilon$  and  $\mu$ ," *Soviet Physics USPEKHI*, Vol. 10, 509–514, 1968.
2. Grzegorzcyk, T. M. and J. A. Kong, "Electrodynamics of moving positive and negative refraction," *Phy. Rev. B*, Vol. 74, 033102.1–033102.4, July 2006.
3. Mackay, T. G. and A. Lakhtakia, "Negative phase velocity in a uniformly moving, homogeneous, isotropic, dielectric-magnetic medium," *J. of Phy. A*, Vol. 37, 5697–5711, May 2004.
4. Lu, J., T. M. Grzegorzcyk, Y. Zhangm, J. Jr. Pacheco, B.-I. Wu, and J. A. Kong, "Čerenkov radiation in materials with negative permittivity and permeability," *Opt. Express*, Vol. 11, No. 7, 723–734, April 2003.
5. Doran, C. and A. Lasenby, *Geometric Algebra for Physicists*, Cambridge University Press, Cambridge, 2003.
6. Paiva, C. R. and M. A. Ribeiro, "Doppler shift from a composition of boosts with Thomas rotation: A spacetime algebra approach," *Journal of Electromagnetic Waves and Applications*, Vol. 20, No. 7, 941–953, 2006.
7. Matos, S. A., M. A. Ribeiro, and C. R. Paiva, "Anisotropy without tensors: a novel approach using geometric algebra," *Opt. Express*, Vol. 15, No. 23, 15175–15186, 2007.
8. Chen, H. C., *Theory of Electromagnetic Waves: A Coordinate-Free Approach*, 229–314, McGraw-Hill, New York, 1985.
9. Peiponen, K.-E., V. Lucarini, E. M. Vartiainen, and J. J. Saarinen, "Kramers-Kronig relations and sum rules of negative refractive index media," *Eur. Phys. J. B*, Vol. 41, 61–65, September 2004.
10. McCall, M. W., A. Lakhtakia, and W. S. Weiglhofer, "The negative index of refraction demystified," *Eur. J. Phys.*, Vol. 23, 353–359, May 2002.
11. Shadrivov, I. W., A. A. Sukhorukov, and Y. S. Kivshar, "Guided modes in negative-refraction-index waveguides," *Phy. Rev. E*, Vol. 67, 57602, May 2003.

# Wide Band Gap Semiconductor High-power Coherent THz Source

V. I. Litvinov<sup>1</sup>, H. Morkoc<sup>2</sup>, and J. Xie<sup>2</sup>

<sup>1</sup>WaveBand Division, Sierra Nevada Corporation, 15245 Alton Pkwy, Irvine, CA 92618, USA

<sup>2</sup>Department of Electrical and Computer Engineering, Virginia Commonwealth University  
601 West Main Street, Room 338, P. O. Box 843072, Richmond, Virginia 23284, USA

**Abstract**— Formation of the electrical domains in semiconductor superlattices prevents Bloch oscillations to occur. Despite this, it is practical to explore a microwave source where the domains themselves may provide high-frequency operation. Negative differential dc-conductivity (NDC) in semiconductor superlattices has proven to cause traveling electrical domains oscillations at 147 GHz in InGaAs/GaAs device. High-power operation requires the use of materials capable of withstanding large current/voltage swings. Therefore, the wide band gap semiconductor is a material of choice for the active region of the device. We study III-Nitride material system, a wurtzite (0001) AlGaIn/GaN superlattice, where the polarization fields affect the dynamics of miniband electrons. Polarization fields stem from the bulk spontaneous polarization and the lattice-mismatch-induced piezoelectric component. We explore the short-period GaN/AlGaIn Stark superlattice as a potential high-power sub-millimeter wave source. We calculate the electron energy, width of the first miniband, and the mobility-field relation. These results create a base for simulation of the source performance using the Atlas-Silvaco package capable of simulating Gunn-type devices. Superlattice source performance (oscillation frequency and power efficiency) depends on the material parameters of its active region and could be of (500–600) GHz with the intrinsic power efficiency of (9–18)%. The frequency of the output signal is tunable by an applied voltage and a series resistance. The GaN superlattices have been grown and characterized. It is shown that the dc-current-voltage characteristics have NDC region that is the prerequisite for the formation of electrical domains.

## 1. INTRODUCTION

Since the negative differential dc-conductivity (NDC) in semiconductor superlattices (SL) was found [1], the study of traveling electrical domains in SLs [2–4] resulted in fabrication of a 147 GHz InGaAs/GaAs microwave source [5]. The output power of this device depends on the current and voltage swings in the NDC region. High-power operation requires the use of materials capable of withstanding large current/voltage swings. Therefore, the wide bandgap semiconductor, for example GaN, is a material of choice for the active region of the SL sources designed for high power operation. In addition, the performance of GaN-based electronic and optoelectronic devices is less sensitive to a high dislocation density as compared to their GaAs-InAs counterparts.

III-Nitride material system for high-frequency source was proposed in [6, 7]. In this paper we further explore the short-period GaN/AlGaIn Stark SL as a perspective high-power sub-millimeter wave source. We calculate the electron band dispersion, the width of the first miniband, and the mobility-field relation in GaN-based SL. These results create a base for simulation of the source using the Atlas-Silvaco semiconductor simulator. The SLs have been grown, characterized, and their dc current-voltage characteristics are reported.

## 2. MOBILITY-FIELD RELATION AND OSCILLATION SPECTRA

The electron mobility in a dc-biased SL is given in Ref. [8, 9]. It can be approximated by a standard model used for Gunn diode simulations:

$$\mu(F) = \frac{\mu_0 + (v_{sat}/F)(F/F_{crit})^2}{1 + (F/F_{crit})^2}. \quad (1)$$

The structure under study comprises fifty 24 Å-long periods ( $L = 0.12 \mu\text{m}$ ) of AlGaIn/GaN superlattice. The SL with Al-content of  $x = 0.42$  has the following characteristics:  $F_{crit} = 100 \text{ kV/cm}$ ,  $\mu_0 = 50 \text{ cm}^2/\text{Vs}$ ,  $v_{sat} = 10 \text{ cm/s}$ . Complete screening of the polarization fields (flat-band SL) leads to a 10% decrease in the miniband width (low-field mobility). That slow change allows neglecting the carrier concentration dependence of the SL parameters. Both sides of the sample are connected to highly doped ( $10^{19} \text{ cm}^{-3}$ ) 0.01  $\mu\text{m}$ -thick layers to provide good ohmic contacts. Additional  $p$ -doped layer ( $p = 1.5 \cdot 10^{17} \text{ cm}^{-3}$  in Fig. 1) prevents spillover of electrons from the metal contact.

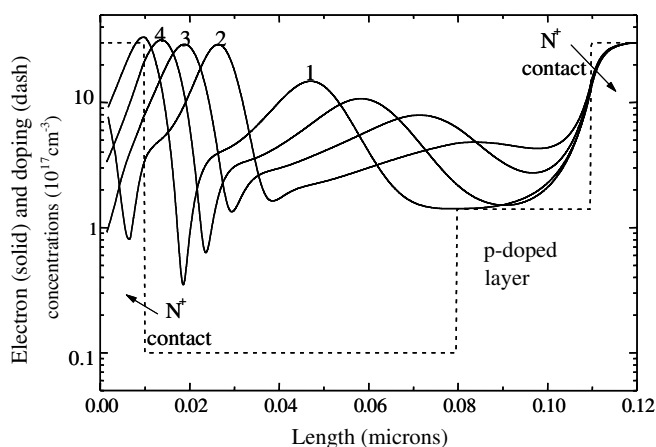


Figure 1: Spatial distribution of the electron (solid) and doping (dashed) concentration at consecutive times: 1-3T/8, 2-T/2, 3-3T/4, 4-7T/8, where T is the period of oscillations.

The lattice temperature is assumed to be 300 K. The spatial electron density and time evolution of the electrical domains in a 4.7 V-biased SL is shown in Fig. 1.

As shown in Fig. 3, at low current density the device reveals coherent oscillations. The spectrum becomes rich when current increases as illustrated in Fig. 4.

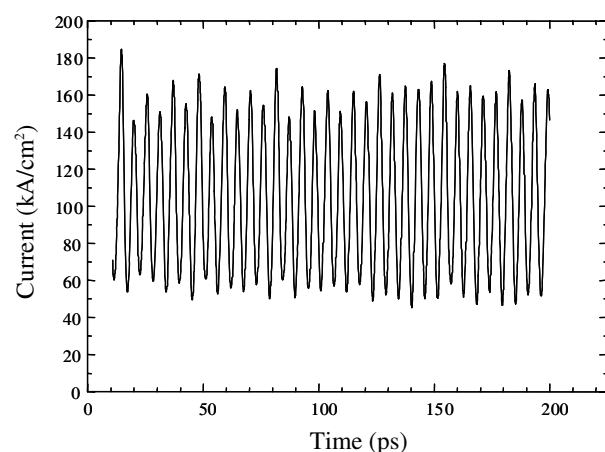


Figure 2: Current oscillations.

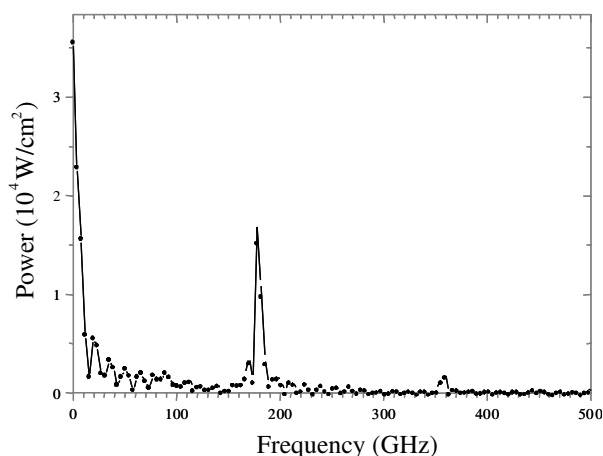


Figure 3: Power spectrum of a superlattice,  $J = 100 \text{ kA/cm}^2$ .

Oscillation frequency illustrated in Fig. 4 correlates with the average current through the device. For instance, the current of  $800 \text{ kA/cm}^2$  results in the main harmonic of 400 GHz. Note, that the GaN material system allows withstanding high voltage and current.

From simulation results it is possible to estimate the power characteristics of the diode, namely, RF output

power  $P_f = \frac{J_{sw} V_{sw}}{8}$ , and intrinsic power efficiency  $\eta = \frac{P_f}{P_{dc}}$ . If we take as an example the SL with harmonic oscillations at 200 GHz (see Fig. 3), then for the typical mesa area of  $100 \mu\text{m}^2$  we have  $P_f = 12.5 \text{ mW}$  and  $\eta = (3 - 6)\%$ . This estimation shows that this type of oscillator may provide high coherent output power. However, what is more important is that if we relax our requirement to pure harmonic oscillations, it is possible to get high-harmonic output at high frequency and efficiency (as shown in Fig. 4: 18.6% at 500 GHz, 16.3% at 485 GHz, and 9.3% at 635 GHz). The estimations do not account for matching to an external circuit (waveguide or free space) and for the dc voltage drop on lump elements external to a superlattice. The device is tunable with the applied dc-voltage and each harmonic can be fetched by an appropriate resonant cavity.

### 3. EXPERIMENTAL RESULTS AND CONCLUSIONS

We have grown and characterized the AlGaIn/GaN SLs. The typical dc I-V curve is shown in Fig. 5.

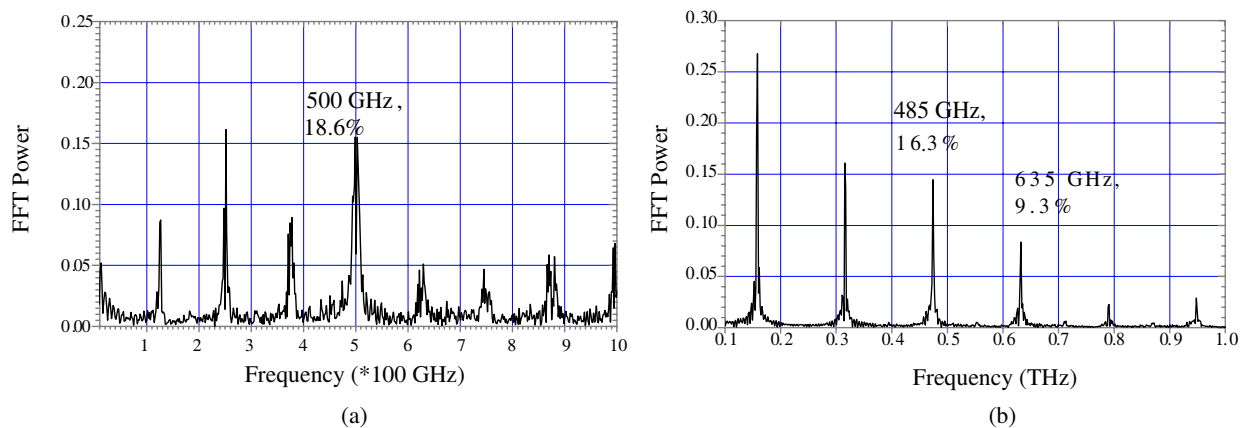


Figure 4: Power spectrum of a superlattice.  $J = 2000 \text{ kA/cm}^2$ ; (a) dc bias=3.2 V, (b) 3.7 V. Harmonic frequency and corresponding intrinsic power efficiency are indicated on the picture.

The dc-IV characteristics reveal an NDC region shown in Fig. 5. That makes possible to achieve self-sustainable current oscillations in GaN-based SLs.

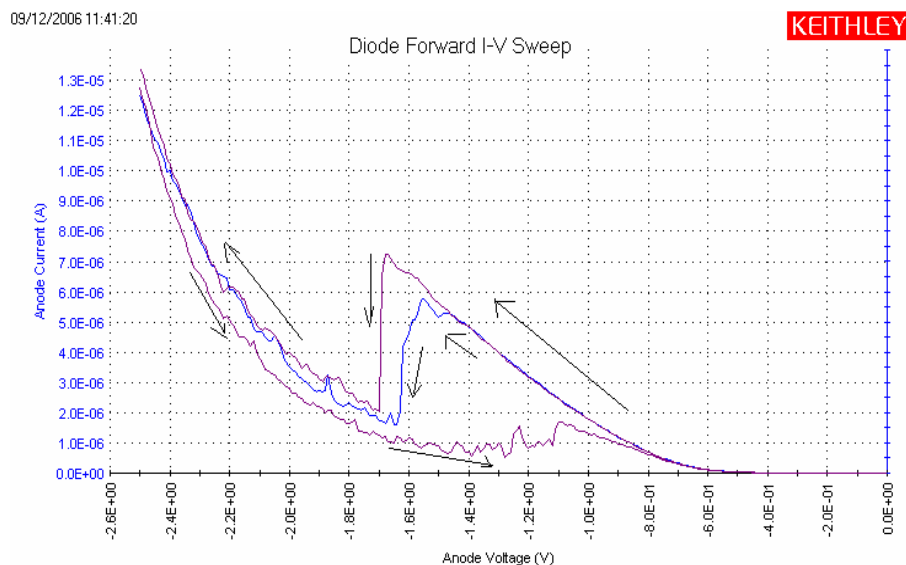


Figure 5: Dc current-voltage characteristics of an AlGaIn/GaN superlattice diode.

In conclusion, we discussed the feasibility of sub-millimeter wave high power signal generation by III-Nitride superlattices. GaN-based submillimeter wave source promises high-power and high efficiency performance. The frequency of the output signal is tunable by an applied voltage. The electrical characteristics of the device in the NDC region require further study toward the source fabrication and microwave characterization.

## REFERENCES

1. Esaki, L. and R. Tsu, *IBM J. Res. Dev.*, Vol. 14, No. 1, 61–65, 1970.
2. Schomburg, E., R. Scheuerer, S. Brandl, K. F. Renk, D. G. Pavel'ev, Yu. Koschurinov, V. Ustinov, A. Zhukov, A. Kovich, and P. S. Kop'ev, *Electron. Lett.*, Vol. 35, 1491–1492, 1999.
3. Blomeier, T., E. Schomburg, K. Hofbeck, J. Grenzer, S. Brandl, I. Lingot, A. A. Ignatov, K. F. Renk, D. G. Pavelev, Yu. Koshurinov, B. Melzer, V. Ustinov, S. Ivanov, and P. S. Kop'ev, *Phys. Stat. Solidi (b)*, Vol. 204, 485–488, 1997.
4. Scheuerer, R., E. Schomburg, K. F. Renk, A. Wacker, and E. Schöll, *Appl. Phys. Lett.*, Vol. 81, 1515–1517, 2002.

5. Schomburg, E., S. Brandl, K. Hofbeck, T. Bloemeier, J. Grenzer, A. A. Ignatov, K. F. Renk, D. G. Pavel'ev, Yu. Koschurinov, V. Ustinov, A. Zhukov, A. Kovich, S. Ivanov, and P. S. Kop'ev, *Appl. Phys. Lett.*, Vol. 72, 1498–1500, 1998.
6. Litvinov, V. I., V. A. Manasson, and L. Sadovnik, *Proc. SPIE*, Vol. 4111, 116–123, 2000.
7. Gordion, I., A. Manasson, and V. I. Litvinov, *IEEE Trans. Electron. Devices*, Vol. 53, 1294–1299, 2006.
8. Litvinov, V. I. and A. Manasson, *Phys. Rev. B*, Vol. 70, 195323, 2004.
9. *Superlatt. and Microstruct.*, Vol. 37, 217–226, 2004.

# Microwave Characterization of Nickel

Stepan Lucyszyn

Imperial College London, UK

**Abstract**— In recent years, nickel has found new applications in RF microfabricated filters and MEMS switches, as it is proving to be a convenient structural material and suitable for realizing power-efficient electrothermal buckle-beam microactuators. While nickel is becoming a material of choice for processing engineers, there is a serious issue of RF characterization at microwave frequencies. This paper investigates some of the issues associated with both measurement and modelling of nickel. It has been found that RF engineers are currently faced with the problem that there is insufficient data available to undertake simulation designs with a high level of confidence at microwave frequencies.

## 1. INTRODUCTION

Nickel has for many decades been used for realizing ferrites, employed in radio frequency (RF) applications, due to its high magnetic permeability at low frequencies. However, in recent years, electroplated nickel has been used as a structural material in RF microfabricated circuits [1] and even radio frequency microelectromechanical systems (RF MEMS [2]) applications [3–5]. With the former, at around 30 GHz, weakly magnetized nickel has twice the surface resistance of silver or copper, but is chemically and mechanically more robust [1]. Moreover, it has a relatively small deleterious effect [1]. Also, when used in electrothermal buckle-beam microactuators, since nickel's thermal expansion coefficient is approximately five times greater than that of polysilicon, the same displacements can be obtained at a much lower temperatures [5]. Therefore, its use in RF transmission lines and microactuators permits co-fabrication, having the same lithographic steps [5]. On the other hand, creep and high-cycle fatigue of nickel structures, particularly at elevated temperatures, may still limit their use in electrothermal microactuators for some applications, due to the impact on their reliability and lifetime [5].

It is very important for the RF designer to understand and know the frequency characteristics of all the materials to be employed in the development of a future device, circuit or system. Surprisingly, very little has been reported on the magnetic permeability of nickel. A survey of textbook values is given in Table 1, along with additional data from a leading commercial 3D electromagnetic simulation software package: Ansoft's High Frequency Structure Simulator (HFSS<sup>TM</sup>).

Table 1: Textbook survey of dc bulk conductivity and magnetic relative permeability.

Reference	$\sigma_o$ [S/m] $\times 10^{-7}$	$\mu_r$
Brown et al. [1]	1.4	1
Olver [6]	1.15	50
Carter [7]	1.28	600
Popovic and Popovic [8]	1.28	600
HFSS <sup>TM</sup> [9]	1.45	600

Clearly, within Table 1, very little consensus exists on the combined values of dc bulk conductivity and magnetic relative permeability. Indeed, with the latter, no information is given as to whether the values represent dc values. Also there is no information on how the nickel was deposited or its level of purity. This makes the design of nickel structures for microwave applications very difficult indeed. This paper tries to address the issue of characterizing the frequency dispersive nature of magnetic permeability for nickel.

## 2. GENERAL FREQUENCY BEHAVIOUR

When an alternating magnetic field is applied, at low frequencies, the magnetic domains respond to it and produce a high permeability material. This works up to hundreds of megahertz with insulating ferrites but only up to a few kilohertz for conducting ferromagnets like nickel. The initial

permeability is measured with almost no externally applied magnetic field, where the domain walls are just beginning to move from their equilibrium state. The present investigation is concerned with the measurement of the initial permeability in small magnetic fields, where all boundary movements are reversible. At low frequencies the permeability is high, because the domains can follow the applied field. As frequency increases, movement of the domains lag behind the applied field and the resulting increase in loss, caused by friction, is represented by the associated increase in the imaginary part of initial permeability. At infrared frequencies and shorter wavelengths, the domains cannot follow the applied field and so there is no loss from trying to follow it and the relative initial permeability approaches unity. Therefore, the dc value of initial permeability must fall off as frequency increases and the greatest frequency dispersion generally occurs between 0.1 and 10 GHz; the decrease in permeability for nickel is in the neighbourhood of 1 GHz [10].

### 3. SURVEY OF MEASURED MICROWAVE DATA

Scientists have been investigating the properties of magnetic materials for a century. In 1951, Bozorth collated all the data that was available during that time for the frequency dispersion characteristics of permeability. The collated graphs are reproduced in Fig. 1 [10].

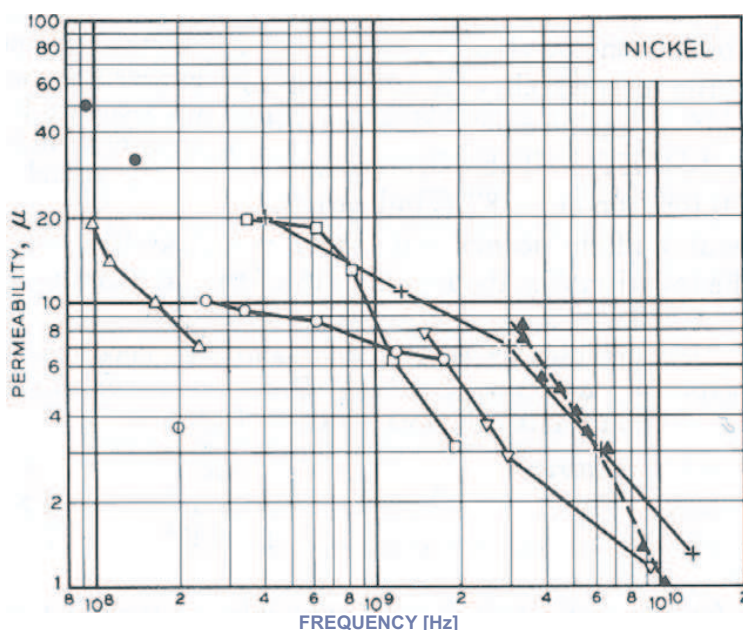


Figure 1: Measured frequency characteristics of initial permeability for nickel [10].  
(+ Arkadiew [11],  $\nabla$  Simon [12],  $\blacktriangle$  Hodsmen et al. [13])

From Fig. 1, it can be seen that the frequency behaviour does indeed show a low frequency value that drops off at around 1 GHz. However, at any one frequency, the results from different researchers give large discrepancies in their measured values. Surface conditions are thought to be an important factor at microwave frequencies. For example, a thin oxide film, formed on the metal during heat treatment, may cause the apparent permeability to decrease by a factor of 10 [10]. Moreover, Arkadiew also noted an increase of high-frequency permeability when magnetic material is annealed [11].

This inconsistency in measurement data makes the characterization of nickel very difficult. The following reviews some of the experimental approaches undertaken and highlights key findings.

#### 3.1. Arkadiew [11]

Back in 1919, reflectivity measurements were performed by Arkadiew with fine wire gratings made from ferromagnetic materials. Here, initial permeability was shown to decrease from 20 at 0.41 GHz down to approximately 1.2 at 12.3 GHz [11]. Unfortunately, the reflection coefficients from ferromagnetic and non-ferromagnetic metals, having medium to high conductivities, for both plane and guided waves, do not differ sufficiently to allow direct measurement [13].

### 3.2. Hodsman et al. [13]

In 1948, measurements are carried out by comparing the attenuation constants of 1.4 m length coaxial transmission lines having an inner conductor made from 99.5% purity nickel and reference nonferromagnetic (e.g., constantan or German silver) wire. Here, the attenuation constants are derived from circles on an impedance Smith chart, which were produced by measuring the standing-wave patterns in the transmission line for different positions of a movable short circuit that were then transformed into values of input impedances. The results are given in Table 2. Calculations showed that the probable error in the recorded values for permeability is of the order of 15% for nickel.

Table 2: Measured initial permeability [13].

Frequency [GHz]	dc	3.356	3.374	3.956	4.545	5.062	5.564	6.522	8.772	9.615	10.084
Initial Permeability	17	8.3	7.5	5.6	5.0	4.1	3.4	3.0	1.5	1.03	1.0

### 3.3. Hsu et al. [14]

Hsu et al. recently attempted to model the 20 to 40 GHz frequency band power loss behaviour of 8, 10 and 16 mm length nickel CPW transmission lines [14]. A high-resistivity silicon (HRS) substrate was employed that also has a 300 nm layer of thermally grown silicon dioxide. The nickel lines are deposited by electroplating a low-stress 2  $\mu\text{m}$  thick nickel layer on top of a thin Ti/Ni (80/50 nm) seed layer. The feed lines were made from gold, using a low-stress RF sputtering process. Parameter extraction techniques were then used to determine values of relative initial permeability within a 20 to 40 GHz frequency range of interest.

While this may at first appear to be a valid approach, on closer inspection there are a number of issues. For example, on the experimental side, bond-wires or air bridges were not introduced at the launch discontinuities or at regular intervals along the line in order to suppress unwanted slot-line modes. Also, it can be assumed that the RF on-wafer measurement samples were tested directly on a metal wafer chuck. As a result, while the lowest-order TM mode can be calculated to be approximately 61 GHz, for an ideal lossless 500  $\mu\text{m}$  thick silicon wafer [15], the onset into this mode will be seen at much lower frequencies, due to the dramatic reduction in the resistivity of the HRS silicon wafers  $\rho_s$  caused by the high temperatures involved in the growth of the silicon oxide layer. In theory, the dielectric constant of the HRS  $\epsilon_{rs}$  will also change. Finally, no mention was made of the level of nickel oxidation immediately prior to measurement.

## 4. MODELLING STRATEGIES

### 4.1. Relaxation-effect Models

The speed at which the boundary movements can follow a high frequency alternating field must ultimately depend on the speed at which the spin rotations can be accomplished. As the period of the applied magnetic field approaches the relaxation time of the spin rotations, the boundary movements lag further behind the applied field and the apparent permeability would decrease to unity.

Frequency dispersion of initial permeability,  $\mu$ , for ferromagnetic materials was first proposed by Becker with the following overly simplified model [16]:

$$\mu(\omega) = \frac{\mu(0)}{1 + j(\omega/\omega_c)} \quad \text{and} \quad \mu(\omega) \equiv \mu(\omega)' - j\mu(\omega)'' \equiv (1 + \chi_m(\omega)) \quad (1)$$

where  $\mu(0)$  = initial permeability at dc and  $\omega_c$  = critical frequency, which is a function of the domain length and dc characteristics of the material [13]. For nickel, a very approximate fit can be obtained with  $f_c = \omega_c/2\pi \sim 0.5 - 1.6$  GHz, indicating a domain length of  $\sim 4$   $\mu\text{m}$  [13].

This rather crude model can be improved upon by using the following well-known Drude model for magnetic susceptibility,  $\chi_m(\omega)$ :

$$\chi_m(\omega) = \frac{\chi_m(0)}{1 - (\omega/\omega_o)^2 + j\omega\tau} \quad \text{where} \quad \tau = \frac{1}{\omega_o^2\tau_o} \quad \text{and} \quad \chi_m(\omega) \equiv \chi_m(\omega)' - j\chi_m(\omega)'' \quad (2)$$

where  $\chi_m(0)$  = static magnetic susceptibility,  $\omega_o$  = resonance frequency and  $\tau_o$  = characteristic damping time.

#### 4.2. Parameter Extraction Techniques

Hsu et al. adopted a brute-force approach to characterizing the relative initial permeability,  $\mu_r$ , of nickel. First, a value for dc bulk conductivity of  $\sigma_o = 7.99 \times 10^6$  S/m was extracted from over-simplified multimeter measurements of line resistance. It should be noted that this value is considerably lower than those quoted in Table 1. If one employs the standard 4-point probe test approach then a more accurate value for dc bulk conductivity can be determined. The authors expected a value of  $14.5 \times 10^6$  S/m, which represents an 81% increase in value. This could potential cause a source of error. The attenuation constant of a CPW line, due to conductor loss, is directly proportional to surface impedance and this, in turn, is directly proportional to  $\sqrt{\mu_r/\sigma_o}$ . Therefore, any error in their extracted value of conductivity could be translated directly to their value of relative initial permeability.

Second, a loss tangent value of  $\tan \delta = 10 \times 10^{-4}$  for the HRS was extracted by modelling a 15 mm length non-ferromagnetic (i.e., gold) CPW line using HFSS<sup>TM</sup>. Using the measured value of  $\sigma_o$  for the nickel and the extracted value  $\tan \delta$  for the HRS, Hsu et al. extracted a frequency-independent value of  $\mu_r = 1.7$  for the relative initial permeability of nickel.

It is well known that HFSS<sup>TM</sup> can produce results that do not conform to measurements, due to problems when assigned boundary conditions, wave port dimensions, solve functions, solution frequencies, convergence targets, etc. [17]. As a result, by entering wrong values of  $\rho_s$ ,  $\epsilon_{rs}$ ,  $\sigma_o$  and  $\mu_r$  it is possible to force simulation results to exactly match measurements within narrow bandwidths, especially when transmission phase angle is not considered.

Hsu et al. also performed analytical calculations of attenuation constant due to conductor loss, based on the work of Holloway et al. [18]. Using this alternative method, Hsu et al. determined another frequency independent value of  $\mu_r = 2.1$  for the relative permeability of nickel.

On closer inspection, both the simulated and calculated frequency responses only manage to cut across the measured frequency responses, within the 20 to 40 GHz frequency range of interest. In other words, exact fits only occur at a single frequency, and this frequency changes with length of transmission line. It can, therefore, be concluded that the extraction technique as described and the resulting values for relative permeability cannot be considered accurate, even though these values are close to the expected value of unity.

## 5. CONCLUSIONS

Frequency dispersion characteristics of magnetic permeability for nickel have been investigated, from the issues of measurement and modelling. It has been found that RF engineers are currently faced with the problem that there is insufficient data available to undertake simulation designs with a high level of confidence at microwave frequencies. While some experimental data exists for the real part of the relative initial permeability, there is still considerable uncertainty as to how this relates to the deposition process, material purity and level of oxidation. Moreover, to the best of the author's knowledge, no measured data exists for the imaginary part of permeability. The well-known Drude model is expected to be able to give an empirical fit to future experimental data. In addition, extraction techniques using 3D electromagnetic modelling software may offer another way forward. Here, both the magnitude and phase angle of the transmission characteristics for impedance-matched transmission lines must be considered, in order to be able to produce frequency-dependent complex values of permeability at microwave frequencies.

## REFERENCES

1. Brown, E. R., A. L. Cohen, C. A. Bang, M. S. Lockard, B. W. Byrne, N. M. Vandelli, D. S. McPherson, and G. Zhang, "Characteristics of microfabricated rectangular coax in the Ka band," *Microwave and Optical Technology Letters*, Vol. 40, No. 5, 365–368, Mar. 2004.
2. Lucyszyn, S., "Review of radio frequency microelectromechanical systems (RF MEMS) technology," *IEE Proceedings — Science, Measurement and Technology*, Vol. 151, No. 2., 93–103, Mar. 2004.
3. Peroulis, D., S. P. Pacheco, K. Sarabandi, and L. P. B. Katehi, "Electromechanical considerations in developing low-voltage RF MEMS switches," *IEEE Transactions on Microwave Theory and Tech.*, Vol. 51, No. 1, 259–270, Jan. 2003.

4. Pranonsatit, S., A. S. Holmes, I. D. Robertson, and S. Lucyszyn, “Single-pole eight-throw RF MEMS rotary switch,” *IEEE/ASME Journal of Microelectromechanical Systems*, Vol. 15, No. 6, 1735–1744, Dec. 2006.
5. Girbau, D., L. Pradell, A. Lázaro, and À. Nebot, “Electrothermally actuated RF MEMS switches suspended on a low-resistivity substrate,” *IEEE/ASME Journal of Microelectromechanical Systems*, Vol. 16, No. 5, 1061–1070, Oct. 2007.
6. Olver, A. D., *Microwave and Optical Transmission*, John Wiley & Sons, 378, 1992.
7. Carter, R. G., *Electromagnetic Waves: Microwave Components and Devices*, Chapman and Hall, 320, 1990.
8. Popovic, Z. and B. D. Popovic, *Introductory Electromagnetics*, Prentice Hall, 2000.
9. Ansoft HFSS™, Version 10, Materials Library.
10. Bozorth, R. M., *Ferromagnetism*, D. Van Nostrand Co. Inc., 1951.
11. Arkadiew, W., “Absorption of electromagnetic waves in two parallel wires,” *Ann. Physik*, Vol. 58, 1919.
12. Simon, I., “Magnetic permeability of Ni in region of cm waves,” *Nature*.
13. Hodsman, G. F., G. Eichholz, and R. Millership, “Magnetic dispersion at microwave frequencies,” *Proceedings of the Physical Society Section B*, 377–390, 1949.
14. Hsu, H.-H., S. W. Lee, and D. Peroulis, “K-Band loss characterization of electroplated nickel for RF MEMS devices,” *IEEE Antennas and Propagation International Symp. Dig.*, 289–292, Jun. 2007.
15. Collier, R. J., “Coupling between coplanar waveguides and substrate modes,” *29th European Microwave Conference Dig.*, 382–385, Munich, Germany, Oct. 1999.
16. Becker, R., *Ann. Physik*, Vol. 27, 123, 1936.
17. Choi, J. Y. and S. Lucyszyn, “HFSS modelling anomalies with electrically thin-walled metal-pipe rectangular waveguide simulations,” *10th IEEE High Frequency Postgraduate Student Colloquium (10th HF-PgC) Digest*, 95–98, Leeds, UK, Sep. 2005.
18. Holloway, C. L. and E. F. Kuester, “A quasi-closed form expression for the conductor loss of CPW lines, with an investigation of edge shape effects,” *IEEE Transactions on Microwave Theory and Tech.*, Vol. 43, No. 12, Dec. 1995.

# A Non-surgical Interrogating Vector Field Brain Activity Recovery Method

D. Cohoon<sup>1</sup>, G. Erdmann<sup>2</sup>, R. Albanese<sup>2</sup>, J. Harvey<sup>3</sup>  
R. Medina<sup>3</sup>, and S. Samn<sup>2</sup>

<sup>1</sup>West Chester University of Pennsylvania, USA

<sup>2</sup>Air Force Research Laboratory, USA

<sup>3</sup>L-3 Communications, USA

**Abstract**— We have created inverse source methods which have the potential for non-surgical recovery of brain activity using magnetoencephalogram or electroencephalogram recordings. Our objective is to enable an amputee to operate an artificial limb with his thoughts. To test the theory we developed computer simulations of two inverse source methods which use measurements taken outside the skull to recover simultaneously the orientation and precise time profile of current dipole sources in the brain tissue. These computer simulations assumed a layered spherical model of the head with the permittivity of the brain and bone tissue regions being derived from Gabriel's Cole-Cole model [2].

We first solved the forward problem, starting with the Hirvonen expansion [3] of the vector potential of an array of arbitrarily oriented dipoles in terms of vector spherical harmonics [7]. By changing the indices of summation we found that we could predict, through the solution of the inside-to-outside boundary value problem [1], the electric and magnetic fields outside the head that are created by brain activity.

For the inverse problem, we use a mathematically infinite family of interrogating vector fields that satisfy the vector Helmholtz equation in each tissue region. These vector fields and their curls have tangential components which are continuous across tissue interfaces. For each interrogating vector field at each frequency, there is a linear equation relating measurements outside the head to the vector of current components on each of the generally oriented dipoles. These dipoles simulate neuronal activity of the model brain. We created more equations than unknowns. As a check on our Gauss divergence theorem-based equations, we made sure that the outside-the-head surface integrals matched the brain tissue volume integrals. We then solved the large matrix equation for the a priori unknown dipole currents, using a modification of the singular value decomposition program written by Argonne National Laboratory.

We show the basic equations relating surface measurements to neuronal currents. Our recovery of neuronal orientation and Hodgkin-Huxley-generated current moments matched to many significant digits.

We have used similar equations to go from head surface voltage distributions derived from electroencephalogram recordings to neuronal current vectors, and these use solutions of the scalar Helmholtz equation in each tissue region as the means of interrogating the scalp surface voltage distribution. The boundary conditions used in this scalar method are that both the scalar and vector potentials are continuous across boundaries.

## 1. BIOPHYSICAL MODEL

Brain, skull, and other tissue regions of the human head are dispersive materials at brain activity frequencies [2]. Our model determines and makes use of the frequency-dependent complex permittivities of different tissue regions when solving the boundary value problem, yielding the electric field  $\mathbf{E}$  and magnetic field  $\mathbf{H}$  outside the head that are stimulated by internal brain waves.

We programmed the original 1952 Hodgkin and Huxley formulation description of nerve axon activity [4], using the stiff differential equation subroutines of Morris [5]. The dependent variables in this model are transmembrane voltage, potassium and sodium channel access probabilities, and channel inhibition probabilities. The neuronal currents that stimulate the magnetoencephalogram are then derived from the voltage differential equation as the product of the transmembrane capacitance and the voltage derivative. To achieve good accuracy and stability using the stiff differential equation package developed by Morris [5], we used analytical, closed-form Jacobians in this solver.

Hodgkin and Huxley provided values of parameters for the above system of differential equations ([4], page 520).

In addition to using the complete Hodgkin and Huxley model, we also used a data-derived non-physiological Rinzel model [6] as modified by Wilson [8]. The parameter values chosen for the Rinzel model were numerically fitted to produce good approximations of the human neocortical neuron action potential. The computer program reproduced the human neocortical neuron action potential with a constant input current  $I$  in the Rinzel voltage equation of 1.57 nano Amperes. This Rinzel system was solved successfully without resorting to the stiff differential equation solver of Morris [5].

## 2. MATHEMATICAL INVERSION METHOD

To recover brain activity through the skull, we need to interrogate, or derive information from, the electromagnetic fields outside the head that were stimulated by brain activity. For this purpose, we used members of an infinite family of interrogating vector fields  $\mathbf{M}$  which all satisfied the vector Helmholtz equation in each tissue region and had the property that they and their curls had tangential components that were continuous across tissue interfaces. Thus, for a set of dipoles representing neurons, the volume and surface integral relationships are

$$\begin{aligned}
& \int_{\partial\Omega} [\mathbf{M} \times \text{curl}(\mathbf{E}) - \mathbf{E} \times \text{curl}(\mathbf{M})] \cdot \mathbf{n} \, d\text{area} \\
&= \int_{\Omega} -\mathbf{M} \cdot \text{curl}[\text{curl}(\mathbf{E})] + \mathbf{E} \cdot \text{curl}[\text{curl}(\mathbf{M})] \, d\text{volume} \\
&= \int_{\Omega} -\mathbf{M} \cdot \text{curl}(i\omega\mu_0\mathbf{H}) + \mathbf{E} \cdot k^2\mathbf{M} \, d\text{volume} \\
&= \int_{\Omega} -\mathbf{M} \cdot i\omega\mu_0(-i\omega\epsilon\mathbf{E} + \mathbf{J}_{\text{brain wave}}) + \mathbf{E} \cdot k^2\mathbf{M} \, d\text{volume} \\
&= \int_{\Omega} -\mathbf{M} \cdot k^2\mathbf{E} - \mathbf{M} \cdot (i\omega\mu_0\mathbf{J}_{\text{brain wave}}) + \mathbf{E} \cdot k^2\mathbf{M} \, d\text{volume} \tag{1} \\
&= \int_{\Omega} -i\omega\mu_0\mathbf{M} \cdot \mathbf{J}_{\text{brain wave}} \, d\text{volume} \\
&= \sum_{q=1}^Q -i\omega\mu_0 p_q(\omega) [M_x \sin(\alpha_q) \cos(\beta_q) + M_y \sin(\alpha_q) \sin(\beta_q) + M_z \cos(\alpha_q)] \\
&= \sum_{q=1}^Q M_x P_x(q, \omega) + M_y P_y(q, \omega) + M_z P_z(q, \omega)
\end{aligned}$$

Table 1 shows a comparison between the area integral above and the sum which is the evaluated volume integral above.

Table 1: Comparison of surface  $S(\omega)$  integrals and evaluated volume  $V(\omega)$  integrals in (1) for two frequencies.

$S(1079.4306)$	$(-7.513096429263251 - 6.310030795022107i) \times 10^{-9}$
$V(1079.4306)$	$(-7.513096432396249 - 6.310030799265132i) \times 10^{-9}$
$S(9714.8755)$	$(-9.090836630124369 + 3.925661599580988i) \times 10^{-8}$
$V(9714.8755)$	$(-9.090836626263916 + 3.925661622573461i) \times 10^{-8}$

The system of equations representing equality of each side of (1) is solved for the a priori unknown complex current amplitudes for each neuronal source

$$(P_x, P_y, P_z)(q, \omega) = -i\omega\mu_0 p_q(\omega) (\sin(\alpha_q) \cos(\beta_q), \sin(\alpha_q) \sin(\beta_q), \cos(\alpha_q)) \tag{2}$$

We solve for the complex vector current components  $P_x$ ,  $P_y$ , and  $P_z$  at each frequency  $\omega$  for each dipole index  $q$  and solve for the orientation angles  $\alpha_q$  and  $\beta_q$ . In numerical tests,  $\alpha_q$  and  $\beta_q$  have been the same for every frequency  $\omega$ , which serves as a confirmation of the mathematics. If real data exhibit this feature, we could exploit it to speed up the algorithm. We give a sample of the complex current recovery in Tables 2 and 3.

Table 2: Comparison of recovered and actual complex current amplitudes  $P_x$ ,  $P_y$ , and  $P_z$  for a test dipole  $q$  at frequency  $\omega = 1079.4306$ .

$P_x$ recovered	$(-4.55075342692135 + 0.609023465847673i) \times 10^{-6}$
$P_x$ actual	$(-4.55075313768083 + 0.609023160131540i) \times 10^{-6}$
$P_y$ recovered	$(-3.42923867493659 + 0.458931766801319i) \times 10^{-6}$
$P_y$ actual	$(-3.42923845791739 + 0.458931868923525i) \times 10^{-6}$
$P_z$ recovered	$(-1.41034411501906 + 0.188745049963244i) \times 10^{-5}$
$P_z$ actual	$(-1.41034415856988 + 0.188745078086793i) \times 10^{-5}$

Table 3: Dipole orientation prediction and the actual orientation angles (in degrees).

$(\alpha, \beta)$ recovered	(22.0, 37.0)
$(\alpha, \beta)$ actual	(22.0, 37.0)

### 3. A COMPUTER SIMULATION OF THE INTERROGATING VECTOR FIELD METHOD FOR NONSURGICAL BRAIN ACTIVITY RECOVERY

To test our brain activity inversion program, we place a computer-generated cortical neuron trans-membrane current on three arbitrarily oriented and arbitrarily located dipoles. We solve the forward problem by exact formulae to find the electric and magnetic fields outside the skull which are stimulated by the brain activity. We then, with our brain activity inversion program, attempt to recover the generating trans-membrane currents using brain-activity independent interrogating vector fields. In Figure 1 we display the overlaid graphs of (i) the original stimulating trans-membrane and (ii) our attempt to recovery this trans-membrane current for one of the dipoles. The graphs are visually indistinguishable.

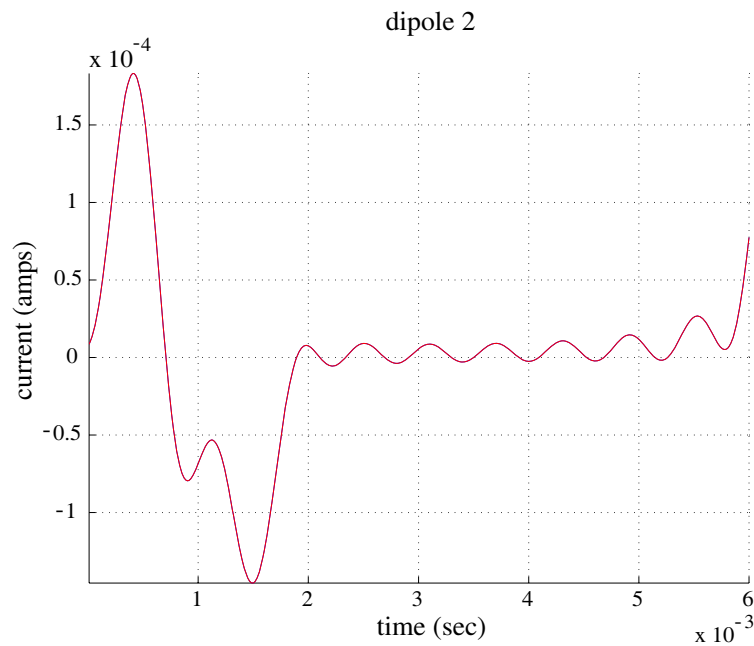


Figure 1: Overlaid graphs of stimulating trans-membrane current and recovered current for a dipole. The graphs are visually indistinguishable.

#### REFERENCES

1. Cohoon, D. K., "An exact solution of mie type for scattering by a multilayer anisotropic sphere," *Journal of Electromagnetic Waves and Applications*, Vol. 3, No. 5, 421–448, 1989.

2. Gabriel, C., *Compilation of the Dielectric Properties of Body Tissues at RF and Microwave Frequencies*, AL/OE-TR-1996-0037, Brooks AFB, Texas 78235-5102: Occupational and Environmental Health Directorate, RadioFrequency Radiation Division, June 1996.
3. Hirvonen, M. T., “Electromagnetic field of an oscillating point dipole in the presence of spherical interfaces,” *Acta Polytechnica Scandinavica Ma39*, 1–37, 1983.
4. Hodgkin, A. L. and A. F. Huxley, “A quantitative description of membrane current and its application to conduction and excitation in nerve,” *Journal of Physiology*, 500–544, 1952.
5. Morris, Jr., A. H., *NSWC Library of Mathematics Subroutines*, NSWCDD/TR 92/425, 608, January 1993.
6. Rinzel, J. and B. Ermentrout, “Analysis of neural excitability and oscillations,” Koch, C. and I. Segev, editors, *Methods in Neuronal Modeling from Ions to Networks*, 251–291, MIT Press, Cambridge, Massachusetts, 1998.
7. Stratton, J., *Electromagnetic Theory*, McGraw Hill, New York, 1941.
8. Wilson, H. R., “Simplified dynamics of human and mammalian neocortical neurons,” *Journal of Theoretical Biology*, Vol. 200, 375–388, 1999.

# Resonance as a Tool to Transfer Information to Living Systems: The Effect of 7 Hz Calcium Ion Energy Resonance on Human Epithelial Cells (HaCaT) Differentiation

Antonella Lisi<sup>1</sup>, Alberto Foletti<sup>2</sup>, Mario Ledda<sup>1</sup>, Flavia De Carlo<sup>1</sup>  
Livio Giuliani<sup>3</sup>, Enrico D'Emilia<sup>3</sup>, and Settimio Grimaldi<sup>1</sup>

<sup>1</sup>Istituto di Neurobiologia e Medicina Molecolare CNR, Rome, Italy

<sup>2</sup>BITITALIA, Milan, Italy

<sup>3</sup>ISPEL, DIPIA, Rome, Italy

**Abstract**— The specific aim of the present work concerns the effectiveness of low frequency electromagnetic fields treatment to modify biochemical properties of human keratinocytes (HaCaT).

Cells exposed to a 7 Hz electromagnetic field and 9.2  $\mu$ T static magnetic field ( $B_0$ ) and 9 for one hour (twice daily), showed by Scanning Microscopy modification in shape and morphology; these modifications were also associated to different actin distribution revealed by phalloidin fluorescence analysis.

Indirect immunofluorescence with fluorescent antibodies against involucrin and  $\beta$  catenin, both differentiation and adhesion markers, revealed an increase in involucrin and  $\beta$  catenin expression, supporting that exposure to electromagnetic field carries keratinocytes to an upper differentiation level.

## 1. INTRODUCTION

In the last twenty years there has been an increasing interest to investigate the possible effect of extremely low frequency (ELF) electromagnetic and magnetic fields (Chiabreara et al. 1985, Zhadin 2001) on human health. The experimental approach to the electromagnetic field (EMF) effects on living systems is complicated by various reported non linearities (intensity, frequency and time windows of the fields) and peculiarities (cell type, age, treatment) so that extrapolation or replications among laboratories can hardly be made. The possible mechanisms of the induced effects are still not known, although a number of theoretical models have been proposed (Glaser 1992, Liburdy 1992, Barnes 1996,). This may be partially due to the difficulties in demonstrating reproducible results.

The aim of the present work is to clarify the action's mechanism at cellular level of an electrotherapy procedure performed by an electro-medical device still in clinical use and so easily reproducible in each bio-physical setting like frequency, intensity and exposure's time.

Moreover a second aim of this work is to validate the effectiveness of the current clinical application protocols.

This work concerns the effect of 7 Hz electromagnetic field exposure on morphological and biochemical properties of normal human keratinocytes.

Keratinocytes (HaCaT) are epithelial cell line, ideal to understand if a physical agent such as electromagnetic field exposure (7 Hz) can interfere with cell morphology, biochemistry and modulate keratinocytes differentiation.

Our results indicate that two ours exposure daily to 7 Hz electromagnetic field could be responsible to a different morphological and cytoskeletal aspect on HaCaT, together with the increase in involucrin expression, suggesting that EMF brings such cells at an upper differentiation level.

This data strongly support the efficacy of 7 Hz therapy for the treatment of skin diseases as well as a co adjuvant in the therapy of undifferentiated diseases.

## 2. MATERIALS AND METHODS

### 2.1. Cell Cultures

Cells were grown in Serum Free Medium (GIBCO Laboratories, Scotland) supplemented with antibiotics (110 IU/ml of penicillin and 100  $\mu$ g/ml of streptomycin) at  $37 \pm 0.3$  °C, 5% CO<sub>2</sub>, and sub-cultivated once a week at a 1:3 ratio.

## 2.2. Exposure System

Cells were exposed twice daily for 1 hours to a 7 Hz electromagnetic field at 100 mV using a commercially available electromedical device (Vega Select 709) in a cells incubator under controlled condition (37 °C and 5% CO<sub>2</sub>).

As a control experiment other sample of the same cells was placed in the cell incubator with no field, in the same conditions of the exposed one.

No differences were detected between control and sham cells.

## 2.3. Fluorescence Microscopy

The fluorescence was monitored using a LEICA TCS 4D Confocal Microscope supplemented with Argon Krypton laser and equipped with 40 × 1.00 – 0.5 and 100 × 0.6 oil immersion lenses. Four experiments were performed analysing a total 150 cells for each data point. Images were recorded employing the pseudo-colour representation.

## 2.4. Immunofluorescence Assay

HaCaT cells were cultured in SFM medium, starting at a concentration of 6 × 10<sup>5</sup>/ml. Exposed cells were cultivated in the same conditions in the exposure system at 7 Hz electromagnetic field for 72 hours. Cells were washed, air dried, fixed in paraformaldehyde 4% in PBS for 15 minutes and tested by indirect immunofluorescence for the presence of involucrin and  $\beta$  catenin. Antibody against involucrin (Sigma) was used at 1:100 dilution, anti  $\beta$  catenin (Calbiochem) at a 1:500 dilution. After 45 minutes incubation in primary antibody, the slides were washed three times with PBS, dried and stained with fluorescein — isothiocyanate- conjugated goat antiserum to human immunoglobulin G (Amersham) at a dilution of 1:200. After further incubation for 45 minutes the slides were washed and examined by fluorescence microscopy. Four different sets of experiments were performed.

## 3. RESULTS AND DISCUSSION

Electromagnetic therapy is a treatment method in which an electromagnetic or magnetic stimulus is used to achieve physiological changes in the cells, into specific organs or into the whole body. The middle of the eighties was marked with the discovery by Blackman (Blackman et al. 1985) and Liboff (1985) of a surprising phenomenon: a low frequency alternating (AC) magnetic field (MF) changed free calcium concentration in nervous tissue only in the presence of a simultaneously acting static (DC) MF. The most prominent effect was observed at the AC field frequency close to the cyclotron frequency of a calcium ion. The cyclotron frequency is defined (Liboff, 1985) as

$$f_C = \frac{q}{2\pi m} B_0,$$

where  $q$  and  $m$  are the charge and mass of the ion, and  $B_0$  is the DC field. These works opened a new line of research in Bioelectromagnetics.

There were three unexpected qualities in this phenomenon: 1) the necessity simultaneous action of DC and AC MFs, 2) the resonance effect on cyclotron frequency, and 3) very small values of acting MFs, measured with tens of  $\mu T$ , and extremely low frequencies of AC MFs, measured with several tens of Hz. Therefore, these results evoked a suspicion in the scientific community. Afterwards, many confirmations for these data were obtained in works performed on different objects and in different experimental situations (Liboff et al. 1987; Lerchi et al. 1991; Blackman et al. 1994; Zhadin et al. 1999; and others) which convinced the scientific community of the real existence of the above effects.

The specific target of our study concerns the effectiveness of low frequency electromagnetic fields treatment to modify biochemical properties of human keratinocytes (HaCaT).

Cells exposed to a 7 Hz electromagnetic field 100 mV for one hour (twice daily), using a commercially available wave generator (Vega Select 719) showed by Scanning Microscopy modification in shape and morphology; these modifications were also associated to different actin distribution revealed by phalloidin fluorescence analysis.

Indirect immunofluorescence with fluorescent antibodies against involucrin and  $\beta$  catenin, both differentiation and adhesion markers, revealed an increase in involucrin (Fig. 1 and Tab. 1) and  $\beta$  catenin (Fig. 2 and Tab. 1) expression, supporting that exposure to electromagnetic field carries keratinocytes to an upper differentiation level.

Such study confirmed our previous observation and support the hypothesis that 7 Hz electromagnetic field, can modify cell biochemistry and interfere in differentiation and cellular adhesion of normal keratinocytes.

Our results strongly suggests the possibility to use physical inputs such as electromagnetic or magnetic field, in support to fight epithelial proliferation diseases, as well as all the diseases in which cells are characterized to a lower differentiation state.

#### 4. FIGURE LEGENDS

Figure shows modulation of involucrin expression in control (left Panel) and exposed cells (right Panel).

Figure is representative of cells at 72 hours growth and exposure. The number of HaCaT cells positive to indirect involucrin immunofluorescence is reported in Tab. 1.

Expression of  $\beta$  — catenin in control (left Panel) and exposed cells (right Panel). Figure is representative of cells at 72 hours growth.

Table 1: HaCaT viability.

	% Viable Cells
Control	$90 \pm 0.5$
7 Hz Exposed	$88 \pm 0.8$
$\pm$ S.D	

Table 2: Involucrin and  $\beta$  catenin immunofluorescence positivity after 7 Hz electromagnetic treatment.

	% Positive Cells
Involucrin	$58 \pm 1$
$\beta$ Catenin	$81 \pm 1$
$\pm$ S.D	

#### ACKNOWLEDGMENT

This work has been supported by grant ISPESL B1/42/DIPIA/04 and B1/45/DIPIA/04. Specially thanks for the realisation of this work is due to Italian Medical Society for Bio-Physical Information Therapy.

#### REFERENCES

1. Adey, W. R., "Tissue interaction with non-ionizing electromagnetic field," *Physiological Review*, Vol. 61, 435–514, 1981.
2. Adey, W. R., "Biological effects of electromagnetic fields," *J Cell Biochem*, Vol. 51, No. 4, 410–6, 1993.
3. Barnes, P. S., "Effect of electromagnetic field on the rate of chemical reactions," *Biophysics*, Vol. 41, 801–808, 1996.
4. Basset, C. A. L., "Beneficial effects of electromagnetic fields," *Journal of Cellular Biochemistry*, Vol. 51, 387–393, 1993.
5. Batta, K., E. L. Rugg, N. J. Wilson, N. West, H. Goodyear, E. B. Lane, M. Gratian, P. Dopping-Hepenstal, C. Moss, and R. A. Eady, "A keratin 14 'knockout' mutation in recessive epidermolysis bullosa simplex resulting in less severe disease," *Br J Dermatol*, Vol. 143, No. 3, 621–7, 2000.
6. Chiabrera, A., C. Nicolini, and H. P. Schwan, *Interactions between Electromagnetic Fields and Cells*, In Chiabrera eds, Plenum, New York, 1985.
7. Dominey, A. M., X. J. Wang, L. King, L. B. Nanney Jr, T. A. Gagne, H. Sellheyer, D. S. Bundman, M. A. Longley, J. A. Rothnangel, D. A. Greenhalg, et al., "Targeted over expression of

- transforming growth factor alpha in the epidermis of transgenic mice elicits hyperplasia, hyperkeratosis, and spontaneous, squamous papillomas," *Cell Growth Differ.*, Vol. 4, 1071–1082, 1993.
8. Fukunaga, M., M. Oka, M. Ichihashi, T. Yamamoto, H. Matsuzaki, and U. Kikkawa, "UV-induced tyrosine phosphorylation of PKC delta and promotion of apoptosis in the HaCaT cell line," *Biochem, Biophys, Res., Commun.* 30, Vol. 289, No. 2, 573–9, 2001.
  9. Glaser, R., "Current concepts of the interaction of of weak electromagnetic fields with cells," *Bioelectrochem. Bioener.*, Vol. 27, 255–268, 1992.
  10. Hinsenkamp, M., A. Jercinovic, Ch. De Graef, F. Wilaert, and M. Heenen, "Effects of low frequency pulsed electromagnetic current on keratinocytes in vitro," *Bioelectromagnetics*, Vol. 18, 250–254, 1997.
  11. Hsu, M., T. Andl, G. Li, J. L. Meinkoth, and M. Herlyn, "Cadherin repertoire determines partner-specific gap junctional communication during melanoma progression," *J Cell Sci.*, Vol. 113, (pt9), 1535–42, 2000.
  12. Kaiser, F., "Theory of non-linear excitation," Frolich H., et al. (eds), *Biological Coherence and Response to External Stimuli*, 25–48, Springer Heidelberg, Germany, 1988.
  13. Karabakhtsian, R., N. Bronde, N. Shalts, S. Kochlatyi, R. Goodman, and A. S. Henderson, "Calcium is necessary in the cell response to EM fields," *FEBS Lett.*, Vol. 301, 53–59, 1994.
  14. John, C. F., K. Morris, B. R. Jordan, B. Thomas, S. A.-H. Mackerness, "Ultraviolet-B exposure leads to up-regulation of senescence-associated genes in Arabidopsis thaliana," *J. Exp. Bot.*, Vol. 52, No. 359, 1367–73, 2001.
  15. Jost, M., C. Kari, and U. Rodeck, "The EGF receptor-an essential regulator of multiple epidermal functions," *Eur. J Dermatol.*, Vol. 10, 505–510, 2000.
  16. Laemmli, U. K., "Cleavage of structural proteins during the assembly of the head bacteriophage T4," *Nature*, Vol. 227, 680–685, 1970.
  17. Liburdy, R. P., "Calcium signalling in lymphocytes and ELF fields: Evidence for an electromagnetic field metric and a site of interaction involving calcium ion channels," *FEBS Lett.*, Vol. 301, No. 1, 53–59, 1992.
  18. Leszczynski, D., C. M. Pitsillides, R. K. Pastila, R. Rox Anderson, and C. P. Lin, "Laser-beam-triggered microcavitation: A novel method for selective cell destruction," *Radiat. Res.*, Vol. 156, No. 4, 399–407, 2001.
  19. Medema, J. P., M. W. Sark, C. Backendorf, and J. L. Bos, "Calcium inhibits epidermal growth factor-induced activation of p21ras in human primary keratinocytes," *Mol. Cell Biol.*, Vol. 14, No. 11, 7078–85, 1994.
  20. Pilla, A. A. and M. S. Markov, "Bioeffects of weak electromagnetic fields," *Rev Environ Health*, Vol. 10, No. 3–4, 155–69, 1992.
  21. Phillips, J. L., W. Haggren, W. J. Thomas, T. I. Jones, and W. Adey, "Magnetic field-induced changes in specific gene transcription," *Biochimica Biophysica Acta.*, Vol. 1132, 140–144, 1992.
  22. Peus, D., L. Hamacher, and M. R. Pittelkow, "EGF-receptor tyrosine kinase inhibition induces keratinocytes growth arrest and terminal differentiation," *J. Invest. Derm.*, Vol. 109, 751–756, 1997.
  23. Pletnev, S. D., "The use of millimeter band electromagnetic waves in clinical oncology," *Crit. Rev. Biomed. Eng.*, Vol. 28, No. 3–4, 573–87, 2000.
  24. Rusovan, A. and M. Kanje, "Magnetic fields stimulate peripheral nerve regeneration hypophyctomia rats," *Neuroreport*, Vol. 3, No. 12, 1039–1041, 1992.
  25. Savitz, D. A., N. Pearce, and C. Poole, "Update on methodological issues in the epidemiology of electromagnetic fields and cancer," *Epidemiological Reviews*, Vol. 15, 558–566, 1987.
  26. Santoro, N., A. Lisi, D. Pozzi, E. Pasquali, A. Serafino, and S. Grimaldi, "Effect of extremely low frequency (ELF) magnetic field exposure on morphological and biophysical properties of human lymphoid cell line (Raji)," *Biochim. Biophys. Acta.*, Vol. 1357, 281–290, 1997.
  27. Szabo, I., M. A. Rojavin, T. J. Rogers, and M. C. Ziskin, "Reactions of keratinocytes to in vitro millimeter wave exposure," *Bioelectromagnetics*, Vol. 22, 358–364, 2001.
  28. Tenforde, T. S., "Interaction of extremely low frequency electromagnetic and magnetic fields with humans," C. Polk, E. Postow, *Handbook of Biological Effects of Electromagnetic Fields*, 2nd Ed., 185–230, CRC Press, Boca Raton, 1995.

29. Vasioukhin, V., C. Bauer, L. Degenstein, B. Wise, and E. Fuchs, “Hyperproliferation and defects in epithelial polarity upon conditional ablation of alpha-catenin in skin,” *Cell* 23, Vol. 104, No. 4, 605–617, 2001.
30. Weaver, J. C. and R. D. Astumian, “The response of living cells on very weak electromagnetic fields: The thermal noise limit,” *Science*, Vol. 247, 459–462, 1990.
31. Walleczeck, J., “Electromagnetic field effect on cells of the immune system: The role of calcium signalling,” *Faseb Journal*, Vol. 6, 3177–3185, 1992.
32. Zhadin, M. N., “Review of russian literature on biological action of DC and low-frequency AC magnetic fields,” *Bioelectromagnetics*, Vol. 22, No. 1, 27–45, 2001.

# Temperature Induced Changes of Spontaneous Photon Emission from Human Hands

M. Cifra<sup>1,2</sup>, E. P. A. van Wijk<sup>3</sup>, and R. van Wijk<sup>3,4</sup>

<sup>1</sup>Dept. of Electromagnetic Field, Czech Technical University, Prague, Czech Republic

<sup>2</sup>Institute of Photonics and Electronics

Academy of Sciences of the Czech Republic, Prague, Czech Republic

<sup>3</sup>International Institute of Biophysics, Neuss, Germany

<sup>4</sup>Faculty of Biology, Utrecht University, Utrecht, The Netherlands

**Abstract**— Ultra weak photon emission (UPE) in visible spectral region from human hands was measured by low-noise photomultiplier system situated in light-tight darkroom. Dominant hands of three subjects were measured for baseline value of photon emission and skin surface temperature before, during and after the cooling of palms by ice cube. Example temperature and UPE and dynamics are shown. Ratios of UPE and temperature values before and after cooling are calculated. It is shown that the relation of the UPE intensity and skin surface temperature is not linear or other processes are involved.

## 1. INTRODUCTION

Ultra weak spontaneous optical photon emission (UPE) arises from living organisms. It is also called biophoton emission. It can be considered a part from the broad spectrum of endogenous electromagnetic field generated by biological systems above thermal level ranging from few Hz to the optical part of the spectrum [1–8]. Many experiments with cell cultures or parts of cells explored the relation between UPE properties and various physical and non-physical parameters. However, experiments looking for these relationships in human are not numerous. One of the most basic questions is the relation between temperature and UPE. Nakamura and Hiramatsu [9] reported a positive correlation between skin surface temperature and UPE intensity on the human hand while changing the ambient temperature of air. However, Inaba [10] reported no correlation between temperature and UPE of various hand locations. In these experiments no changes in ambient temperature were introduced.

We report here results from measurements of the UPE and surface skin temperature of the hand while cooling it with the ice block.

## 2. MATERIALS & METHODS

### 2.1. Materials

A special darkroom (2 m × 2 m × 1 m) and photon counting device were used to record photon emission of the subjects. Walls and ceiling of that darkroom were covered with black matt paint. The temperature of the dark room was registered before and after every set of measurement. The darkroom could be vented. The darkroom had a bed inside and subjects could be easily measured in lying or sitting position. The darkroom was built inside a control room without windows, and separated by a light tight door and black matt curtain to ensure that there is no light leakage to the dark room. The control room contained the electrical equipment (high voltage supply for photomultiplier tube (PMT), PMT shutter and steering system), an active air moisture filter, a cooling unit for PMT as well as a remote computer system for the photomultiplier. The control room was illuminated by red light.

The photomultiplier tube (EMI 9235 QB, selected type) used could be manipulated in three directions. It is a 52-mm diameter, especially selected, low noise, end window photomultiplier that was mounted in a sealed housing under vacuum with a quartz window. An additional ring at the front of the photomultiplier tube allowed measuring a 9-cm-diameter area at a fixed distance from the body (70 mm). The photomultiplier had a spectral sensitivity range of 160–630 nm. During the experiments it was maintained at a low temperature of  $-25^{\circ}\text{C}$  in order to reduce the dark current (electronic noise). Typical dark current (electronic noise) under these conditions was about 5 counts per second (cps). Temperature measurements were carried out on a defined point in the middle of the palmar and dorsal side of the hand with a thermocouple thermometer with red LCD display and sensitivity of  $0.1^{\circ}\text{C}$ .

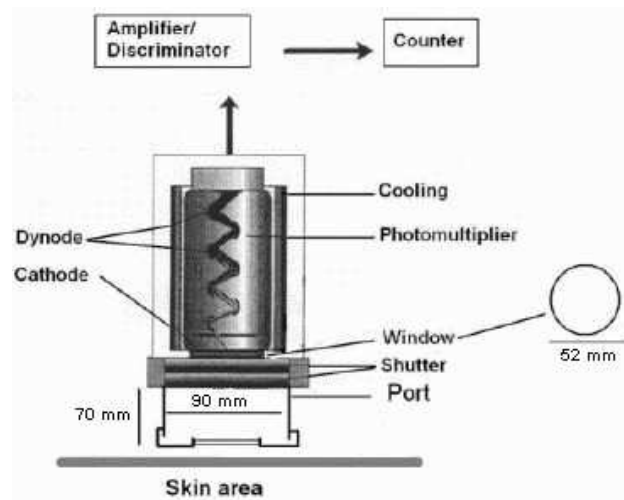


Figure 1: Dimensions of the photomultiplier.

## 2.2. Methods

In 10 experiments, temperature changes of the hand have been induced by external cooling using an ice cube. In all experiments UPE was recorded, however, temperature recordings were made in 7 out of 10 experiments. In the first part of the experiment, dark accommodated palm and dorsal side of the subject's dominant hand have been measured to obtain baseline values of UPE and temperature under the stable temperature conditions. In the second part of the experiment, a palm sized ice cube, covered with thin plastic to avoid the skin moistening during contact, was used to cool down the palm side while the photon emission of dorsal side of the hand was measured. In the third part of the experiment, the ice cube was removed to allow recovery of the temperature. The UPE and the temperature have been measured directly after the removal of the ice as well as during the recovery.

## 3. RESULTS EXPERIMENT

The results of the ice cooling experiments for the palmar and dorsal side of the dominant hand are presented in Table 1 and 2, respectively. In the first three experiments only the UPE from dorsal sides was measured, continuously, with small breaks for applying and removing ice. Recovery value to baseline value ratio and ice value to baseline value ratio for the temperature for and the UPE

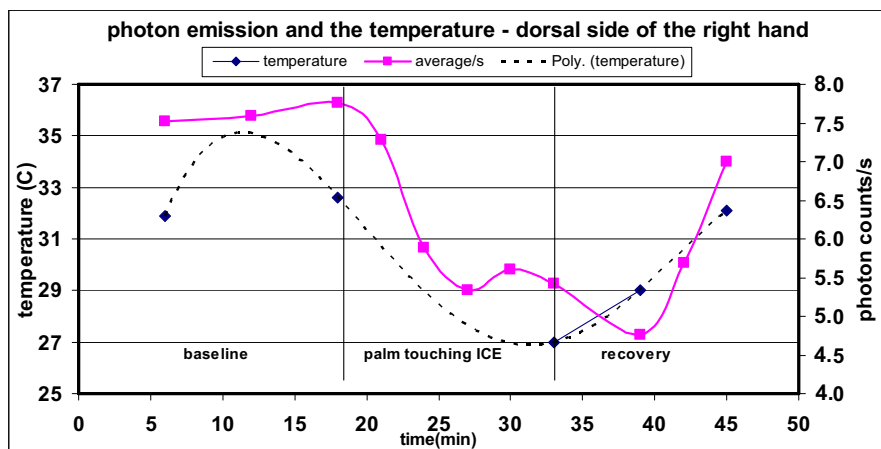


Figure 2: Mc04 — typical dynamics of the UPE and the skin surface temperature of the cooling(ice under the palm) and the recovery of the dorsal side of the hand. Photon signal with background noise already subtracted. The 6th order polynomial fitting was used to connect the separate temperature values for better visualization. It should be noted that the rise and drop of temperature in the baseline period does not correspond to the reality, it is just artifact of the fitting.

is listed on the end of both tables. Baseline values correspond to the period before cooling, ice values are measured just after the cooling, directly after the ice is removed and recovery values are measured after 15 min recovery (no ice).

To compare the effect of cooling by ice and recovery values to baseline values, we introduced ratios of these values for the UPE and temperature as well. Average ratios and the corresponding standard deviations calculated from the values in the Tables 1 and 2 are provided in the Table 3.

Figure 2 presents the typical dynamics of UPE and skin surface temperature during cooling (ice block under the palm) and recovery of the dorsal side of the hand. All the values of the UPE intensity are in counts/s, background noise  $\sim 5$  c/s subtracted.

Table 1: Palm of the dominant hand. Skin surface temperature [ $^{\circ}\text{C}$ ] and the UPE [c/s] — [number of photons/s] — [counts/s] during the baseline measurement, right after the ice cooling (15 min) and after the recovery from coldness (15 min). Background noise subtracted.

PALMAR SIDES	mc04		mc05		mc06		mc07		Ew01		sb01		sb02	
	$^{\circ}\text{C}$	c/s	$^{\circ}\text{C}$	c/s	$^{\circ}\text{C}$	c/s	$^{\circ}\text{C}$	c/s	$^{\circ}\text{C}$	c/s	$^{\circ}\text{C}$	c/s	$^{\circ}\text{C}$	c/s
<b>BASELINE 15 minutes</b>	34	12.04	32.5	7.30	31.45	9.19	32.8	9.83	34.5	10.76	28	3.46	30	4.80
<b>ICE 15 minutes</b>	18.5	7.40	12.6	3.50	12	5.48	15.5	4.75	25	6.32	14	4.36	17	4.16
<b>RECOVERY 15 minutes</b>	34	11.65	32.5	5.11	29.50	9.10	32	7.84	32	8.69	27	1.44	32	5.66
<b>T. – temperature P. - UPE</b>	T.	P.	T.	P.	T.	P.	T.	P.	T.	P.	T.	P.	T.	P.
Ratio recovery/baseline	1.01	0.97	1.00	0.70	0.94	0.99	0.98	0.80	0.93	0.81	0.96	0.42	1.07	1.18
Ratio ice/baseline	0.55	0.61	0.39	0.48	0.38	0.60	0.47	0.48	0.72	0.59	0.50	1.26	0.57	0.87

Table 2: Dorsal side of the dominant hand. Skin surface temperature [ $^{\circ}\text{C}$ ] and the UPE [c/s] — [number of photons/s].

DORSAL SIDES	mc01	mc02	mc03	mc04		mc05		mc06		mc07		ew01		sb01		sb02	
	c/s	c/s	c/s	$^{\circ}\text{C}$	c/s	$^{\circ}\text{C}$	c/s	$^{\circ}\text{C}$	c/s	$^{\circ}\text{C}$	c/s	$^{\circ}\text{C}$	c/s	$^{\circ}\text{C}$	c/s	$^{\circ}\text{C}$	c/s
<b>BASELINE 15 minutes</b>	3.60	2.96	4.34	32.25	7.62	30.95	4.48	29.55	5.08	31.25	4.97	33	9.44	28.5	1.93	30	2.42
<b>ICE 15 minutes</b>	2.00	1.18	2.47	27	5.42	26.5	3.53	25.5	3.29	26.6	3.94	30	6.12	24	1.33	24	1.29
<b>RECOVERY 15 minutes</b>	2.27	3.29	2.62	32.1	7.00	30.2	3.05	25.00	5.02	28.8	3.88	30.5	7.11	24.5	2.23	27	1.38
<b>T. – temperature P. - UPE</b>	P.	P.	P.	T.	P.	T.	P.	T.	P.	T.	P.	T.	P.	T.	P.	T.	P.
Ratio recovery/baseline	0.63	1.11	0.60	1.00	0.92	0.98	0.68	0.85	0.99	0.92	0.78	0.92	0.75	0.86	1.16	0.90	0.57
Ratio ice/baseline	0.55	0.40	0.57	0.84	0.71	0.86	0.79	0.86	0.65	0.85	0.79	0.91	0.65	0.84	0.69	0.80	0.53

Table 3: Average recovery/baseline and ice/baseline ratios of temperature.

RATIOS	DORSALS		PALMS	
	UPE	Temperature	UPE	Temperature
recovery/baseline	$0.82 \pm 0.21$	$0.92 \pm 0.06$	$0.84 \pm 0.24$	$0.98 \pm 0.05$
ice/baseline	$0.63 \pm 0.12$	$0.85 \pm 0.03$	$0.61 \pm 0.28$	$0.51 \pm 0.12$

#### 4. DISCUSSION & CONCLUSIONS

Positive correlation of the UPE intensity and the skin surface temperature from the dorsal and the palmar side of the hand is clear. It confirms the finding of Nakamura et al. [9]. However, they also found that higher oxygen content in the ambient air also increases the UPE intensity. Recovery/baseline ratios of temperature are different from the recovery/baseline ratio for the UPE (Table 3). This indicates that also other parameters than temperature are responsible for the changes of the UPE intensity. The ice/baseline ratio of the UPE are nearly same for the dorsal and palmar sides of the hand. However, the ice/baseline ratio of temperature is significantly different. Another indication that also other processes than temperature are involved in the UPE dynamics in cooling. The UPE intensity is also dependent on anatomic location — typical anatomic pattern of UPE intensity was found [11, 12].

Laager et al. [13] found increased UPE of the wrist during the exercise relating it to the higher ROS production in the tissue, since the surface skin temperature was still rising after the exercise although the UPE intensity decreased and intensity was correlated more with oxygen uptake of the measured subjects. They also found that heart beat does seem to correlate with the UPE intensity in the rising period (during the exercise), but it does not correlate after the exercise ceased — heartbeat drops but the UPE intensity rises.

Most of the measured data found in the literature concerning skin temperature and the UPE intensity come from the hands. However, our preliminary measurements of the UPE and skin temperature from 12 locations on the body shows that although correlation of temperature and the UPE intensity is high on the hands, it is usually much lower or unstable on the other parts of the body. We may conclude that generally, processes which are related to higher ROS production are accompanied with increased UPE intensity. We can say there is a positive correlation of the UPE intensity and the skin surface temperature when changing the temperature externally within the physiological range on the hands. Further research focused on the measurement of UPE from the other parts of the body is needed to elucidate whether the ROS reactions directly are the main contributor to measured UPE intensity. Not only intensity of the UPE, but also statistical parameters of photocount distribution should be of the high interest.

#### ACKNOWLEDGMENT

This work was made possible by funding from the Samueli Institute of Information Biology (SIIB) and the Rockefeller- Samueli Center for Research in Mind-Body Energy. Its contents are solely the responsibility of the authors and do not necessarily represent the official views of SIIB. This work was carried out utilizing the whole body photomultiplier device constructed under supervision of Dr. F. A. Popp (International Institute of biophysics, patent G9417845.3). M. C. is also thankful to Grant Agency of the Czech Republic, grant No. 102/08/H081 and to FRVS grant agency, grant n. 2300/2008 for the support.

#### REFERENCES

1. Cifra, M., J. Vaniš, O. Kučera, J. Hašek, I. Frýdlová, F. Jelínek, J. Šaroch, and J. Pokorný, “Electrical vibrations of yeast cell membrane,” *PIERS Online*, Vol. 3, No. 8, 1190–1194, 2007.
2. Pokorný, J., J. Hašek, F. Jelínek, J. Šaroch, and B. Palán, “Electromagnetic activity of yeast cells in the M phase,” *Electro- and Magnetobiology*, Vol. 20, 371–396, 2001.
3. Pohl, H. A., “Oscillationg fields about growing cells,” *International Journal of Quantum Chemistry: Quantum Biology Symposium*, Vol. 7, 411–431, 1980.
4. Popp, F.-A., K. H. Li, and Q. Gu, eds., *Recent Advances in Biophoton research and its Applications*, World Scientific, Singapore, London, New York, Hong Kong, 1992.

5. Popp, F.-A. and L. V. Belousov, eds., *Biophotonics, Non-equilibrium and Coherent Systems in Biology, Biophysics and Biotechnology*, Bioinform Services, Moscow, 1996.
6. Belousov, L. V., F.-A. Popp, V. L. Voeikov, and R. van Wijk, eds., *Biophotonics and Coherent Systems*, Moscow University Press, 2000.
7. Van Wijk, R. and X. Shen, eds., *Biophotonics: Optical Science and Engineering for the 21st Century*, Springer, 2005.
8. Belousov, L. V., V. L. Voeikov, and V. S. Martynyuk, eds., *Biophotonics and Coherent Systems in Biology*, Springer, 2006.
9. Nakamura, K. and M. Hiramatsu, “Ultra weak photon emission from human hand: Influence on temperature and oxygen concentration,” *Journal of Photochemistry and Photobiology B: Biology*, Vol. 80, 156–160, 2005.
10. Inaba, H., “Measurement of biophoton from human body,” *J. Intl. Soc. Life Info. Sci.*, Vol. 18, No. 2, 448–453, 2000.
11. Van Wijk, R., M. Kobayashi, and E. P. A. van Wijk, “Anatomic characterization of human ultra-weak photon emission with a moveable photomultiplier and ccd imaging,” *Journal of Photochemistry and Photobiology B: Biology*, Vol. 83, 69–76, 2006.
12. Van Wijk, E. P. A. and R. van Wijk, “Multi-site recording and spectral analysis of spontaneous photon emission from human body,” *Forsch Komplementärmed Klass Naturheilkd*, Vol. 12, 96–106, 2005.
13. Laager, F., S.-H. Park, J.-M. Yang, W. Song, and K.-S. Soh, “Effects of exercises on biophoton emission of the wrist,” *European Journal of Applied Physiology*, 2007.